Universitat Autònoma de Barcelona

Synthesis of T-shaped molecules for their deposition over three-terminal devices

Daniel Riba López

Synthesis of T-shaped molecules for their deposition over three-terminal devices

Daniel Riba López

Doctoral Thesis

Ph.D. in Chemistry

Supervisor: ICREA Prof. Núria Aliaga Alcalde

Supervisor: Dr. Arántzazu González Campo

Tutor: Dr. Ramón Alibés Arqués

Departament de Química-Facultat de Ciéncies (UAB)

Institut de Ciència de Materials de Barcelona (ICMAB-CSIC)

2023

Universitat Autònoma de Barcelona

INSTITUT DE CIÈNCIA DE MATERIALS DE BARCELONA

EXCELENCIA SEVERO OCHOA

CSIC
CONSEJO SUPERIOR DE INVESTIGACIONES CIENTÍFICAS

Universitat Autònoma de Barcelona

Departament de Química-Facultat de Ciències

Doctorat en Química

Synthesis of T-shaped molecules for their deposition over three-terminal devices

Thesis submitted for the degree of Doctor in Chemistry by

Daniel Riba López

Supervisor

ICREA Prof. Núria Aliaga Alcalde

Supervisor

Dr. Arántzazu González Campo

Tutor

Dr. Ramón Alibés Arqués

Bellaterra, Gener 2023

Abstract

Curcuminoids (CCMoids) are a group of small organic molecules that present two aromatic rings linked by a seven-carbon conjugated chain together with a keto-enol moiety in the central position of their backbone. This type of molecules can be achieved using straightforward methods that allows the easy modification of their structure by (i) changing the nature of the lateral aromatic substituents, (ii) inserting additional functional groups in the central carbon of the alkene chain CCMoid skeleton, and/or (iii) modifying chemically the keto-enol chelating unit, including this, the coordination with metals and metalloid centres. CCMoids have been extensively used in the biomedical field. However, in this doctoral thesis we focus on the design of new CCMoids toward their applications in the field of Molecular Electronics. In the last years our group has been working on the deposition of CCMoids over graphene-based three-terminal devices. These devices function as field effect transistor (FET), having two electrodes (source and drain) made of graphene supported on the top of the third one (gate) of Si, where SiO_2 is used as insulator among them. The CCMoids published in such studies have displayed anthracene rings on the arms, acting as good anchoring groups with the graphene electrodes through π–π interactions. The efficient attachment, CCMoid-graphene electrodes, is still under study, far from optimal, due to the weak nature of the attachment and also because of the variety of shapes and edge composition of the graphene electrodes. From a chemical point of view, it is necessary to search for a new type of CCMoids that can improve the anchoring strength to the graphene electrodes and can react with the additional parts of the devices (SiO_2 substrate) through functional groups fixing the molecules and making the final device more robust and efficient at low and room temperatures.

Consequently, new CCMoids are introduced in this thesis containing polycyclic aromatic hydrocarbon (PAH) groups in both extremes of the molecules, to strength the interaction with graphene, and secondly T-shaped CCMoids are also presented that contain the same PAH units and, in addition, a short functionalized group (with alkyl or alkene endings) located in the centre of the CCMoid chain that, by hydrosilylation reaction, can have silane endings groups capable to react with the Si-OH groups of the activated SiO_2 support from the three-terminal hybrid devices to fix the CCMoids to the final system.

For that, this thesis shows the detailed characterization of all the presented CCMoids using solution (^{1}H-, ^{13}C-NMR, UV-Vis and electrochemistry) and solid-state (Raman, FTIR, UV-Vis, MS MALDI-TOF and TGA) techniques, which allow comparative studies with optical/electrochemical-structural correlations regarding the insulator-semiconductor nature for each CCMoid under study.

Furthermore, in this thesis initial steps towards the creation of CCMoids containing reactive groups at the CCMoid chain ends have been carried out, being the obtained molecules future precursors in the creation of nanoribbons with CCMoid skeleton.

Resum

Els curcuminoids (CCMoids) són un grup de petites molècules orgàniques que presenten dos anells aromàtics units per una cadena conjugada de set carbonis i una fracció ceto-enol en la posició central de les seves estructures. Aquest tipus de molècules poden ser obtingudes mitjançant mètodes directes que permeten modificar la seva estructura canviant la naturalesa dels seus substituents aromàtics laterals, inserint grups funcionals addicionals en el carboni central de la cadena d'alquens de l'esquelet CCMoide i/o modificant químicament la unitat quelant ceto-enol, incloent en aquesta possibilitat, la coordinació amb metalls o centres metal·loides. Els CCMoids han estat utilitzats extensament en biomedicina. No obstant, en aquesta tesis doctoral ens hem centrat en el disseny de nous CCMoides per a la seva aplicació en el camp de l'Electrònica Molecular. En els últims anys el nostre grup ha estat treballant en la deposició de CCMoids sobre dispositius de tres terminals basats en grafè. Els dispositius funcionen com a transistors d'efecte camp (FET), formats per dos elèctrodes (font i drenatge) fets de grafè i suportats sobre un tercer (porta) de Si, on una capa de SiO_2 és utilitzada com aïllant entre ells. Els CCMoids publicats posseeixen anells antracènics en els braços, actuant com a bons grups d'ancoratge amb els elèctrodes de grafè a través d'una interacció π-π. L'eficiència d'aquest contacte, lluny de ser òptima, es troba encara sota estudi donat la seva dèbil naturalesa d'ancoratge i també la seva varietat de formes i la composició de les vores dels elèctrodes de grafè. Des d'un punt de vista químic, és necessari buscar un nou tipus de CCMoides que puguin millorar la força d'ancoratge als elèctrodes de grafè i que permeti reaccionar amb una part addicional als dispositius (elèctrode de Si, porta) a través de grups funcionals, fixant les molècules i fent el dispositiu final més robust i eficient a temperatures baixes i ambient. Així doncs, en aquesta tesis es presenten nous CCMoides que contenen hidrocarburs aromàtics policíclics (PAH) en ambdós extrems de la molècula, per millorar la interacció amb el grafè, i en segon lloc, CCMoides amb aparença de T que contenen també aquestes unitats PAH i grups funcionals curts (acabats amb alquins o alquens) en el centre de la cadena del CCMoid, que mitjançant reaccions de hidrosililació es poden obtenir grups silans terminals capaços de reaccionar amb el els -Si-OH del suport activat de SiO_2 del dispositiu híbrid de tres terminals, fixant així els CCMoids al sistema final.

En aquest sentit, alguns dels nous CCMoids presentats en aquesta tesis s'han dissenyat amb una estructura que conté molts anells aromàtics en els braços

i, a més a més, d'altres que contenen també una cadena alquílica curta situada en el centre de la cadena central d'alquens conjugada que hauria de proporcionar millors posicions d'ancoratge amb les diferents parts del dispositiu seleccionat, un dispositiu híbrid de tres terminals.

A més a més, la caracterització detallada de tots els CCMoids sintetitzats se s'ha dut a terme amb tècniques en dissolució (^{1}H-, ^{13}C-NMR, UV-Vis i electroquímica) i en estat sòlid (Raman, FTIR, UV-Vis, MS MALDI-TOF i TGA), permetent la comparació de les correlacions estructurals òptiques/electroquímiques respecte la naturalesa de aïllant-semiconductor de cada CCMoid.

Finalment, en aquesta tesis també es presenta els primers passos per a la creació de nous CCMoids amb grups reactius en els braços, essent els precursors per a la creació de nanocintes de grafè amb esquelet CCMoid.

Outline

In this doctoral thesis, a group of new organic molecules belonging to the curcuminoid (CCMoid) family, with a characteristic diarylheptanoid chain that contains a keto-enol group in the centre and polycyclic aromatic hydrocarbon (PAH) groups in both sides of the chain, have been synthesized. In addition, T-shaped CCMoids containing the former PAH arms and including an extra functional group situated in the centre of the CCMoid framework ended in an alkyl/alkene reactive unit, have also been accomplished. Both types of CCMoids have been designed toward their future insertion in graphene-based field effect transistors (FETs).

The general introduction displays a brief overview on the structural features of CCMoids and the available synthetic methods to achieve them, including some of the most important precedents existing regarding the use of such molecules and others as active nanowires in single-electron transport studies within the field of Molecular Electronics.

Chapter I shows the synthetic protocols for obtaining a new CCMoid that contains alkyne groups in the *para*- position of the aromatic units. In the following chapters, this CCMoid will be the precursor to obtain larger molecules; here, special attention is paid to the characterization of the new CCMoid and its derivatives (protecting the triple bond endings and coordinating with BF_2 units through the keto-enol moiety). Finally, the deposition of the alkyne CCMoid on a hybrid device is carried out to study its electronic properties. The results presented in this chapter have been collected in a publication (appendix II): D. Riba-López, R. Zaffino, D. Herrera, R. Matheu, F. Silvestri, J.F. da Silva, E.C. Sañudo, M. Mas-Torrent, E. Barrena, R. Pfattner, E. Ruiz, A. González-Campo and N. Aliaga-Alcalde. Dielectric behaviour of curcuminoid polymorphs on different substrates by direct soft vacuum deposition. *iScience* **2022**, 105686, 1-29.

Chapter II describes the synthetic methodology for the synthesis of a new generation of CCMoids that contain polycyclic aromatic hydrocarbons (PAHs) in both sides of the CCMoid skeleton, including CCMoids with PAH groups that may allow the growth of their arms through latter reactivity. The chapter display the proper characterization of these molecules in solution and in the solid-state providing the general steps to follow for the series of novel PAH-based CCMoids.

Chapter III describes the synthetic procedure to obtain new T-shaped CCMoids; the molecular systems contain the PAHs described in previous chapter but, in addition, short and reactive functional groups (alkyne/alkene ending units) located in the central part of the CCMoid skeleton towards their future use as nanowires that can be fixed chemicallyin graphene-based FETs.

Finally, in the conclusions section, some final considerations on the achievements of this doctoral thesis are made.

Acronyms

Attenuated total reflection	ATR
Acetonitrile	ACN
Acetylacetone	acac
Atomic force microscope	AFM
Bis(cyclooctadiene)nickel	$Ni(cod)_2$
Bisdemethoxycurcumin	BDMC
Curcumin	CCM
Curcuminoid	CCMoid
Cyclic voltammetry	CV
Demethoxycurcumin	DMC
Density functional theory	DFT
Dichloromethane	DCM
Differential pulse voltammetry	DPV
Differential scanning calorimetry	DSC
Differential thermal analysis	DTA
Dimethylsulfoxide	DMSO
Direct current	DC
Electrochemistry	EC
Elemental analysis	EA
Energy gap	E_g
Ethyl acetate	EtOAc
Ferrocene	Fc
Few graphene layers	FGL
Field-effect transistors	FET
Fourier transform infrared spectroscopy	FTIR
Graphene nanoribbon	GNR
Highest occupied molecular orbital	HOMO
Karstedt catalyst	KC
Lowest unoccupied molecular orbital	LUMO
Matrix-assisted laser desorption/ionization- Time of flight	MALDI-TOF
Mechanically controlled break-junction	MCBJ
Metal-organic framework	MOF
Methanol	MeOH
Micro-contact printing	μ-CP
Microwave	MW
Mass spectrometry	MS
Nanographene	NG

Nuclear magnetic resonance spectroscopy	NMR
Nuclear overhauser effect	NOE
Polycyclic aromatic hydrocarbons	PAH
Room temperature	RT
Scanning electron microscopy	SEM
Tetrabutylammonium hexafluorophosphate	$TBAPF_6$
Tetrachloroethane	TCE
Tetrachloro-*p*-benzoquinone or 2,3-dichloro-5,6-dicyano-1,4-benzoquinone	DDQ
Thermogravimetric	TGA
Thin-layer chromatography	TLC
Trimethylsilyl	TMS
Ultraviolet-Visible	UV-Vis
Ultra high vacuum	UHV
X-rays diffraction	XRD
X-ray photelectron spectroscopy	XPS

Acknowledgements

Agrair profundament a les meves directores de la tesi, la Núria per confiar en mi per a la realització d'aquest projecte i a l'Arancha moltes gràcies per compartir el vostre coneixement, la paciència que heu tingut aquests anys i el vostre suport en els moments complicats de la tesis que no deu a ver sigut fàcil.

Em sento molt honrat d'haver compartit aquests anys amb grans companys en el grup Funnanosurf (Raúl, Wenjie, Ezhil, Niki, Pablo, Josep, Ona, Álvaro, Maripaz, Yolimar, Beltzane, …), encara que sigui poc tots meu donat consells o ajudat en alguna cosa per petita que sigui. Gràcies Andrea, ha sigut un plaer poder haver participat en el teu TFG.

Moltes gràcies al Prof. Diego Peña de la Universitat de Santiago de Compostela per ajudar-me en el meu primer any i la seva amabilitat per acollir-me en el seu grup. També a tots els estudiants que vaig conèixer del seu grup: la Fátima, el Iago, el Jesús i la Dulce gràcies de tot grat per la vostra ajuda. Agraïments també a tota la gent que m'ha ajudat amb les tècniques de caracterització i els serveis tècnics del ICMAB, ICN2, UAB i UB.

Només tinc paraules d'agraïment de tot cor pel Dani H. he après moltíssim de tu, m'has ajudat a aclarir molts dubtes i sempre recordaré el meu company del laboratori Danis & Teresa. Rossella, moltíssimes gràcies per estar allí, escoltar-me i donar-me els teus consells savis en moments de frustració, no tinc paraules suficients per agrair tot l'esforç que has fet per ajudar a tirar endavant l'article i a més que les teves classes d'estiraments m'han ajudat també a descarregar tensió acumulada, sens dubte la millor post-doc que he conegut, moles molt no canviïs mai!.

Durant aquest viatge he fet molts companys però sobretot amics que han fet molt més lleuger el viatge i que la seva amistat espero no perdre mai per lluny que siguem: Albert , Álex , Sandra, Sole, Joseline, Chiara, Jorik, Marc, Matteo, Paolo, Nanthilde, Yvan, Thomas, Cris, Wid i sobretot Teresa, Marta, Amanda (map) i Laura (sense tu no estaria on estic). També agrair el suport que m'han donat tots els meus amics de la uni, els lalas i els meus companys de pis que m'han aguantat en els meus pitjors dies d'estrès Jordi i Eric. I a la Johanna, estic molt content d'haver-te conegut en el meu últim any i el teu suport m'ha ajudat molt a acabar molt més feliç, moltes gràcies de tot cor.

I per últim a la meva germana i els meus pares, us estimo i moltes gràcies pel vostre suport, sabeu tot el que he passat en aquest camí i m'heu ajudat moltíssim en tot, sense vosaltres no seria qui sóc.

Table of contents

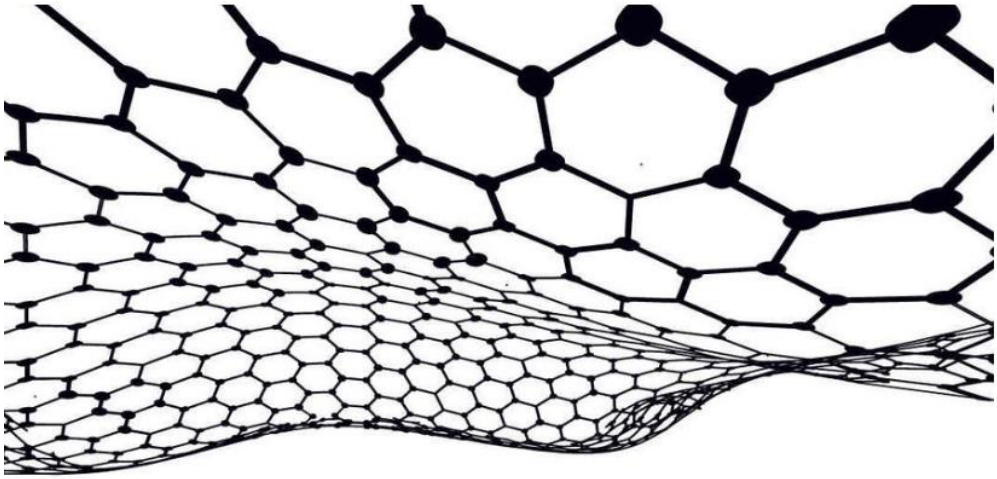

GENERAL

INTRODUCTION

GENERAL INTRODUCTION

In this PhD thesis, novel organic curcuminoid molecules (CCMoids) containing polycyclic aromatic hydrocarbons (PAHs) have been synthesized for their function as connectors between two graphene electrodes on hybrid graphene/SiO_2/Si three-terminal electronic devices. A brief introduction of these molecules and their future use in the field of Molecular Electronics are provided in this chapter.

G.1. CURCUMINOIDS (CCMoids)

CCMoids[1] are a group of organic molecules formed by a conjugated diarylheptanoid chain that functions as the skeleton of the molecule (body in figure G1), that contains in the centre a *keto-enol* moiety (head, figure G1); the central carbon within the chain displays a single H due to the conjugation and the already mentioned *keto-enol* group, but this position can be modified introducing several carbon-based functional groups (leg, figure G1).[2,3] Finally, the backbone ends with aromatic rings that can have different substituents as well (arms, Figure G1)[4]

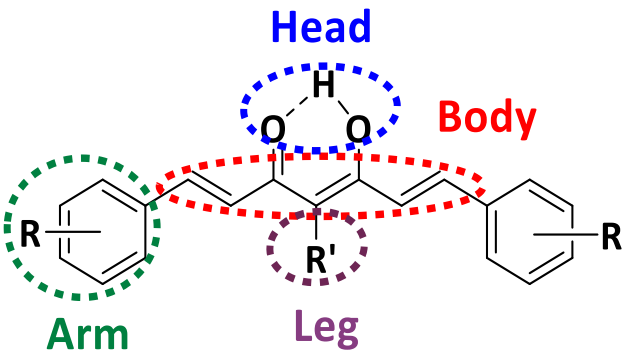

***Figure G1**: Schematic representation of the structure of the CCMoids in the keto-enol form.*

CCMoids can be found in nature but also be synthesized in the laboratory.[5,6] In nature, there are three known CCMoids: curcumin (CCM), desmethoxycurcumin (DMC) and bisdemethoxycurcumin (BDMC), respectively (figure G.2). These three compounds are extracted from turmeric, also called *Curcuma longa* plant. This plant is included in the Zingiberaceae family, and is cultivated mainly in Asia, in tropical and subtropical regions.[7] These CCMoids appear in a percentage between 2-8

wt%, being CCM the most abundant (70-80 wt%), followed by DMC (15-25 wt%) and BDMC (3-10 wt%), in that order.[7] CCM has one hydroxyl and one methoxy group in each ring, in the *para* and *meta* positions (figure G2). For years, it has been used as culinary component, in the Hindu gastronomy, being one of the principal ingredients of the curry. Moreover, it has also been used in the alternative *ayurveda* medicine.[8]

The first study regarding the properties of the CCM go back to 1748, by Loeber and Buechner;[9] however, CCM was not isolated until 1842 by Vogel *et al*.[10], its chemical formula was described in 1910 by Milobedzka *et al*.[11] and the first synthetic protocol was described by the same group in 1913.[12]

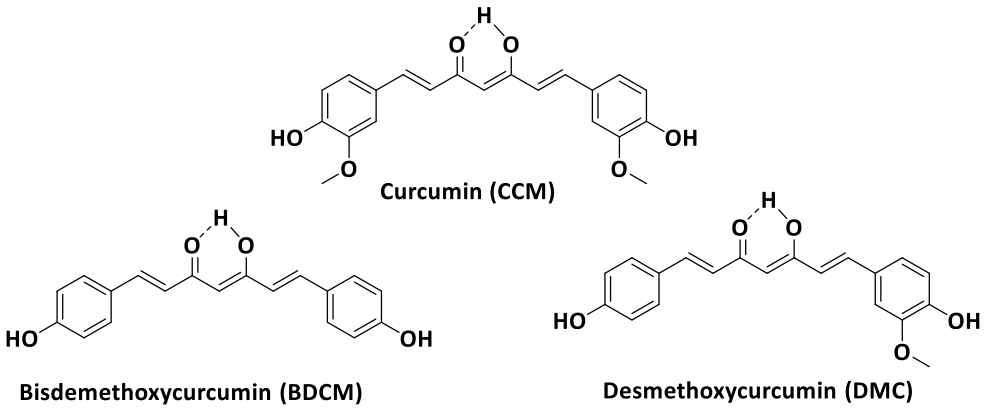

***Figure G2**: Molecular structures of natural CCMoids.*

G.2. SYNTHESIS OF CCMoids

Another possible and general definition of CCMoids is that they are described as a family of molecules that resemble CCM. To replicate this molecule, the most well-known methodology is that created by H.J.J. Pabon in 1964.[5]

This synthetic path is the most widely used protocol for the synthesis of CCM but also to achieve natural and synthetic CCMoids, due to the enormous range of possible starting materials to which this process can be applied. It is based on the Knoevenagel condensation reaction between the methylene side groups of acetylacetonate (acac) and an aldehyde, using butylamine as a catalyst, as it is shown in Scheme G1 and Figure G3.

The first step in this reaction implies the formation of a complex between acac and boron trioxide (B_2O_3). This process is necessary to avoid the Knoevenagel

condensation reaction with the central carbon of the molecule. The reaction continues with the addition of a boronic ester (in our case tributyl borate) that shifts the equilibrium of the reaction towards the formation of the boron complex and helps to eliminate the water molecules formed in the condensation process.[13] Subsequently, the desired aromatic aldehyde is also incorporated to the mixture and, after 2 hours, the catalyst, butylamine, is added to enhance the Knoevenagel condensation towards the methyl groups of the acac. The final product of this reaction is a 2:1 complex of the CCMoid with boron, which is hydrolysed with a diluted acid to give the final free CCMoid.

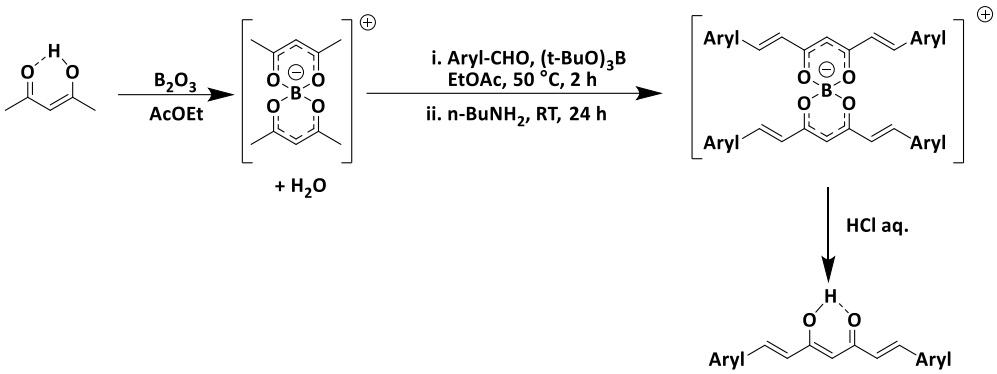

***Scheme G1**: Pabon's methodology for the synthesis of the curcuminoids.*

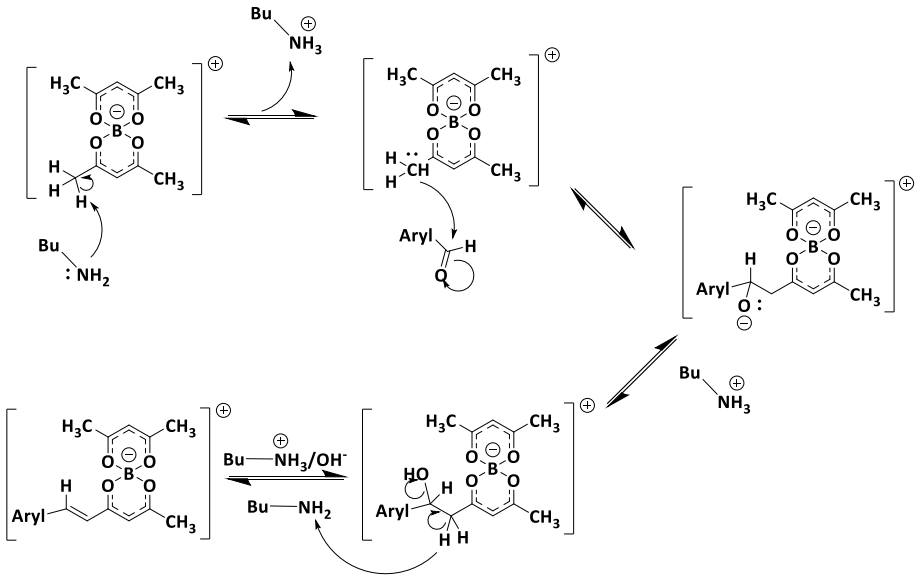

***Figure G3:** Mechanism of the Knoevenagel condensation.*

This methodology has been extended by other groups to the creation of new CCMoids that share the same core structure. This way, Roughley *et al*.[14] in 1973, Matthes *et al*.[15] and A. Mukhopadhyay *et al*.[16] in 1982 mentioned the preparation, among other molecules, of some symmetrical and unsymmetrical CCMoids with modifications specially in the arms (aromatic groups), showing in all the cases that in solution (by NMR) all the CCMoid systems exist in the *keto-enol* form, with no presence of the other tautomer (diketone form). However, in practice, and also in this thesis, the term "β-diketone" is more commonly used to refer to the head of the CCMoid (figure G1), without explicitly referring to its tautomer nature. Continuing along historical lines, in 1985, Pedersen *et al*.[6] focused their investigation on the synthesis of several symmetric and asymmetric CCMoids. In this case, the asymmetry was given by the synthesis of CCMoids with different aromatic groups of the sides (Scheme G2); the work shows CCMoids that not only contain several substituents on the aromatic rings but also modifications in the central part of the hydrocarbonated alkene chain, hence, in the leg position (figures G1 and Scheme G3). In this extensive study, they corroborated the mechanistic study of the condensation reaction for the synthesis of CCMoids,[5] promoting as well the reactivity of the aromatic substituents with a straightforward acetylation of the hydroxyl groups.[15] Interestingly, they also show the study of the alkylation reaction[14] of CCM, which show that O-alkylation took place at the phenolic oxygens exclusively and, even further, C-alkylation took place in central carbon of the conjugated alkene chain; therefore, no alkylation was seen at the oxygen of the enol form, and that, in all of the cases, the diarylheptanoid chain showed an *E* configuration.[6]

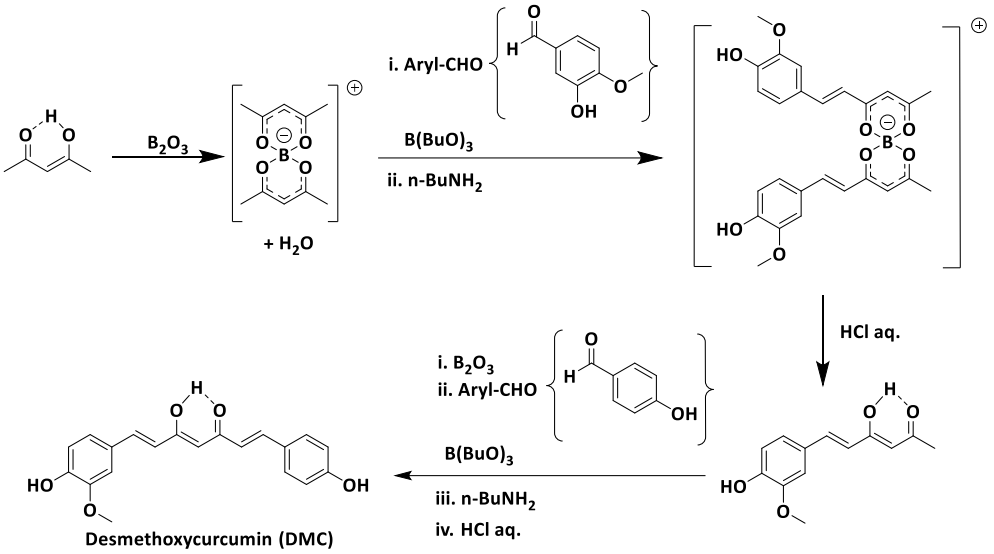

***Scheme G2**: Synthesis of the CCMoid: desmethoxycurcumin (DMC).*

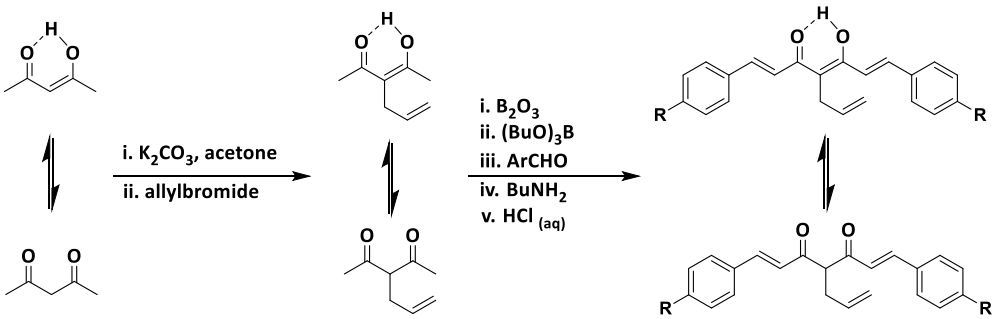

***Scheme G3**: Example of a synthesis of leg-CCMoid.*

Another way to obtain asymmetric CCMoids involves the synthesis of Hemicurcuminoids. In 2011, Wichitnithad *et al*.[17] studied the synthesis of an asymmetric CCMoid which consists basically in the same methodology as explained before but using 1 eq. of aldehyde (vanillin) and, afterwards, the addition of another aldehyde (4-hydroxybenzaldehyde). The intermediate species are called Hemicurcuminoids (HemiCCMoids, figure G4), defined as CCMoids molecules that only possess half of the π-conjugated backbone. Later on, this methodology has been used by other groups for a huge variety of aldehydes.[18-20]

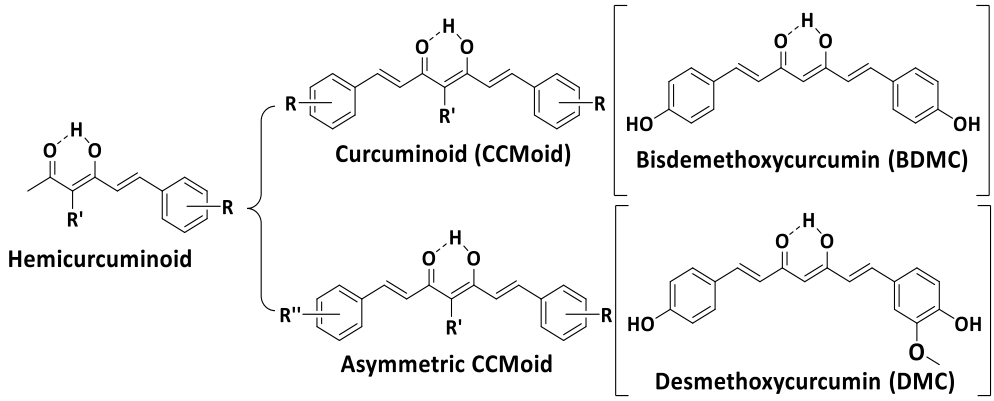

***Figure G4**: Chemical structures of the hemicurcuminoid (HemiCCMoid, DMC), symmetric and asymmetric curcuminoid (CCMoid) where R and R' are possible different substituents.*

During the last decades, new, synthetic CCMoid molecules have been created with a huge variety of lateral substituents to answer the requirements of multiple applications mostly the biomedical field, using CCMoids as anti-inflammatory,[21,22] antitumoral,[23-29] antibacterial[30,31] and antioxidant agents.[32,33]

However, the singular structure of CCMoids and straightforward synthetic path (Figure G5) makes practical their used in many other fields such as sensoring,[34,35] organic solar cells,[36] electronic transport[37-39] and coordination polymers.[40] For example, the central *keto-enol* group allows the coordination of CCMoids with several metal and semi-metal centers together with additional organic molecules that can modify the electrochemical and the optical properties of the CCMoids under study.[41-48] In addition, the aromatic groups situated on the ending of the conjugated alkene chain (arms) promote multifunctional molecular/polymeric systems with a variety of properties (chirality, fluorescence, electronic, magnetic...).[37,38,49,50] And finally, in the middle of the chain, we can introduce different functional groups, that depending on their nature can add an extra anchoring point for the molecule to a substrate, using supramolecular or covalent bonds.[36,51-54]

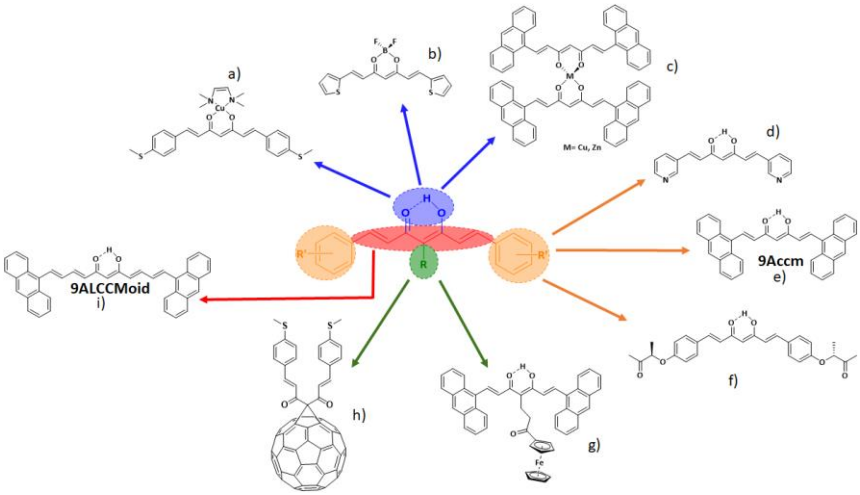

***Figure G5**: CCMoid structure and some derivatives molecules: a) Olavarría-Contreras et al.[45(50)], b) Olavarría-Contreras et al.[45(50)], c) Aliaga-Alcalde et al.[36(43)], d) Rodríguez-Cid et al.[51(55)], e) Prins et al.[37], f) Qian[52(56)], g) Díaz-Torres[46(51)], h) Dulić et al.[47(52)] and i) Burzurí et al.[38]*

In this thesis, we focus on the design of new CCMoids toward their use in the field of Molecular Electronics, where our group has been working during the last years[37,38,41,48,50,57,58] taking advantage of the CCMoid design.

G.3 MOLECULAR ELECTRONICS

G.3.1. Brief summary on the electronic challenges

Moore's law is the principle that has been driven the information technology revolution since the 1960s. Moore's law states that the number of transistors and other electronic elements on a microprocessor chip will double every 2 years (Figure G6).[59,60] It is known that the global semiconductor industry is governed by three main goals to make devices: smaller, faster and cheaper, and in this sense, silicon chips have been the basis for the rapid development of this industry. Making them smaller, than present and previous technologies, involves diminishing the size and improving the packing of the elements that form part of the chips, while maintaining optimal response, hence, electrons will be able to move between them in an efficient way. Regarding this matter, there are two main problems with this procedure: the heat generated when the circuitry is crowded and the appearance of electron's quantum effects, the two combined situations make new nano-transistors unreliable.[59,60]

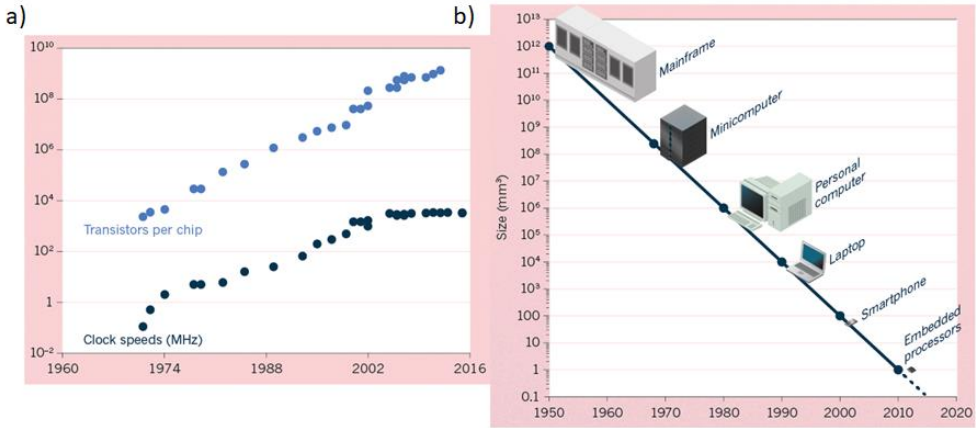

***Figure G6**: Moore's law representation of a) the number of transistors per microprocessor among time and their 'clock speed' or rate to execute instructions and b) decrease in size of the computers through the years while increasing in power.[55(60)] Reprinted with permission from Springer Nature.*

Working in this matter, there are interesting candidates as an alternative to conventional silicon devices, from 2D graphene-like systems to spintronic materials. In addition, a great effort has done into scaling down electrical circuits based on single-molecule electronics, being molecules the smallest stable structures imaginable.[61,62]

Molecular-scale electronic devices are those based on the use of individual or collections of few molecules to create functional electrical circuits. Being molecules capable of functioning as conductive nanowires, rectificators, together with memory, and/or switching elements. In addition, it has several advantages compared to silicon-based electronic devices. First, the extremely small size of the molecules, between 1 and 100 nm, allows for increased capabilities (efficiency and power dissipation) and faster performance.[62,63] Second, the diversity in the molecular structures, that can be introduced, allows for new and novel effects and physical phenomena that are not accessible using traditional materials (e.g., molecule transport, binding effects and optical properties, among others).[60,63-65] And thirdly, the low manufacturing cost due to the universal availability of molecules that can be used in bulk synthetic processes.[60-65] However, one of the major drawbacks for the development of molecular electronics is the instability at high temperatures.[61]

In addition, reproducibility is also a crucial issue. Typically, the step current detected is small (~nA) when the target unit is downscale to the scale of a single molecule, and therefore the current is highly sensitive to noise effects

and environmental changes. Finally, another important point is to develop a technology for mass production of single-molecule devices at low cost. Thus, decreasing the unit size and increasing the level of integration without sacrificing cost remains a challenging task in the future.[61]

G.3.2. Curcuminoids in molecular electronics

During the last decade our group has used CCMoids as molecular platforms to include and measure them in a variety of devices thanks to the collaboration with specialized groups. Toward the characterization of the electronic nature of CCMoids at the single scale different techniques have been used over time. Here a summary of them, including the work of other groups in related subjects:

<u>Mechanically controlled break-junction (MCBJ)[66] with gold electrodes</u>

CCMoids have been used as linkers to create various dimensional architectures, from 0D to 3D.[37,38,41,49,50,58,67,68] In 2016,[58] a new thiophene CCMoid family was designed to study their single-molecule conductance, using them as nanowires, between gold electrodes (Figure G7). In general, to design these type of ligands three principal aspects must be considered. First, the ligands must have a proper anchoring group to enable attachment to the electrodes, in this case, sulphur atoms within the aromatic rings were selected and the disposition of the sulphur atom (in *ortho*-, 2-thiopheneCCMoid, and *meta*-, 3-thiopheneCCMoid) was achieved in a straight way using Pabon´s method in good yields. In addition, to achieve a good molecular conductance, short and conjugated skeletons are required. In this sense, CCMoids can possess the two aspects and, additionally they can provide structural flexibility to accommodate between the two gold electrodes.

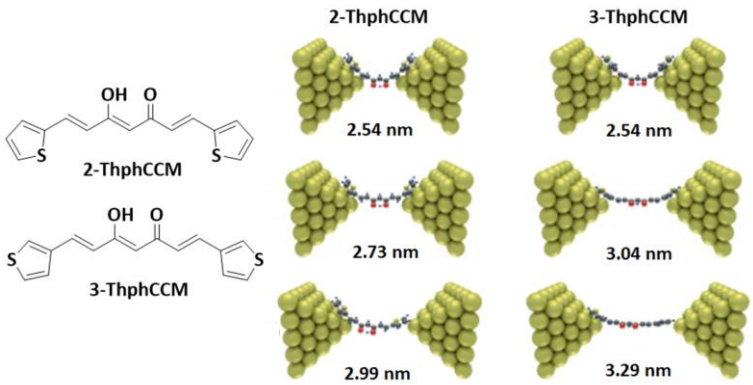

***Figure G7**: Chemical structures of 2-thphCCM, 3-thphCCM and the representation of three possible different molecular junction configurations for both molecules.[54(58)] Reprinted with permission from Wiley Online Library.*

A drop of the molecular solution was deposited on a device formed by gold electrodes and then the conductance measurements were performed with the controllable mechanical break junction technique (MCBJ).[69] MCBJ provides a tuneable gap size between two tip-shaped electrodes with mechanical stability for the characterization of single molecules. With advanced lithography techniques, the electrode can be reduced to molecular dimensions, which is well suited for single-molecule measurements. It is based on a small piece of a ductile metal wire fixed on a flexible substrate, called a bending beam. A vertical movement of the push rod promotes the bending of the beam, the metal wire starts to elongate producing a fracture of the metal wire (Figure G8). After the breakage, two nanoelectrodes are generated and the distance between them is controlled by bending or relaxing the substrate. The molecules are then integrated into the gap between the electrodes bridging them and allowing the measurement of the electronic properties of the molecules. A scheme of MCBJ is shown in Figure G8.[69,70]

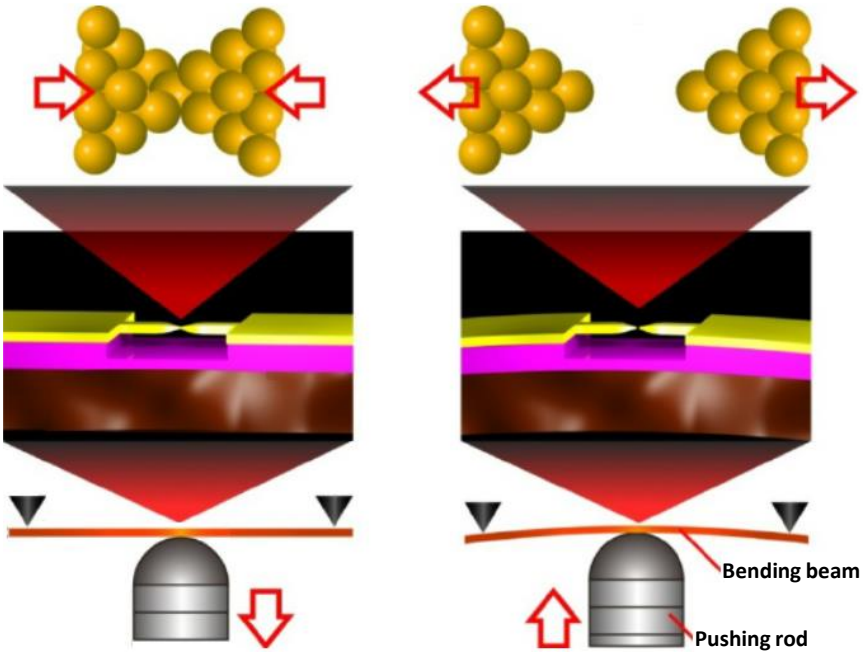

***Figure G8**: Scheme of the Mechanically Controllable Break-Junction procedure.[62(66)] Reprinted with permission from MDPI. 2012, 12, 7259–7298.*

The 2- and 3-thphCCMs presented conductance values of $3x10^{-5}$ and $3x10^{-4}$ G_0, respectively.[58] The results pointed out the relevance of the disposition of the anchoring group, presenting the 3-thphCCM one order of conductance higher than the 2-thphCCM. Nevertheless, it was seen a limitation in the stability of the junction molecule-gold, due to the poor yield (number of experiments where the CCMoids were in between the gold electrodes and therefore it was possible to measure molecular conductance).

Afterwards, in 2018,[50] using the same methodology than before, the molecular conductance behaviour of a new set of CCMoids was also studied. These new molecules presented methylthio groups in their ending groups (arms) and the *keto-enol* moiety was coordinated with the groups BF_2 and Cu^{II} (Figure G9).

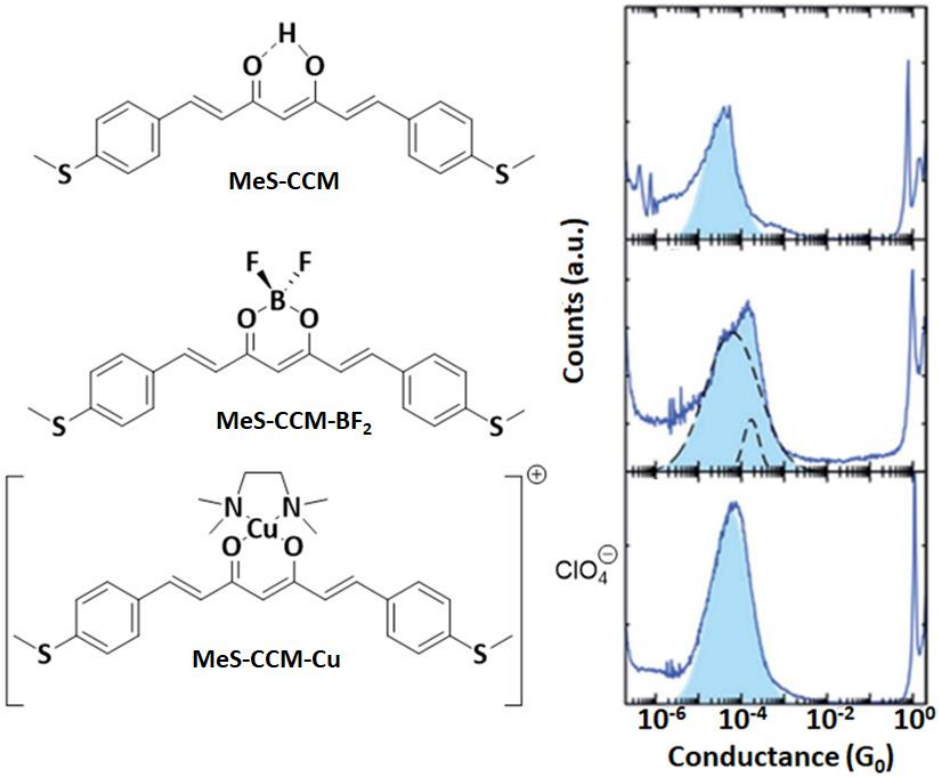

***Figure G9**: Schematic representation of the free and coordinated curcuminoid molecules MeS-CCM, MeS-CCM-BF_2 and MeS-CCM-Cu and the one-dimensional histograms of each one.[45(50)] Reprinted with permission from RSC.*

In this study it was compared the effect of the free ligand (a) with those of the coordination compounds containing one of them a metalloid ion (b) and the other a 3d metal centre (c). It was seen that once the free ligand was coordinated with the Cu^{II} ion, a slight increase in the conductance was promoted, whereas the -BF_2 coordination group showed a bistability effect in the conductance measurements. Theoretical calculations allowed us to explain this bistability behaviour due to the coordination of the -BF_2 group and the promotion of conformational changes between flat and non-flat molecular structures, related to the disposition of the methyl group of the methylthio units, which together, produced a difference in the dipole moment.[50]

In another work, in 2020,[52] our group, together with collaborators, studied a hybrid family of fullerene-CCMoids, where the fullerene group was always attached to the central carbon atom of the CCMoid skeleton (**Figure G10**). It was shown that the arrangement of the fullerene-CCMoids promoted different conductance values, some of CCMoid nature and others related to

the fullerene group. Density Functional Theory calculations corroborated that the conductance values of the fullerene CCMoid are found to be similar to those of a planar curcuminoid molecule without a fullerene attached.

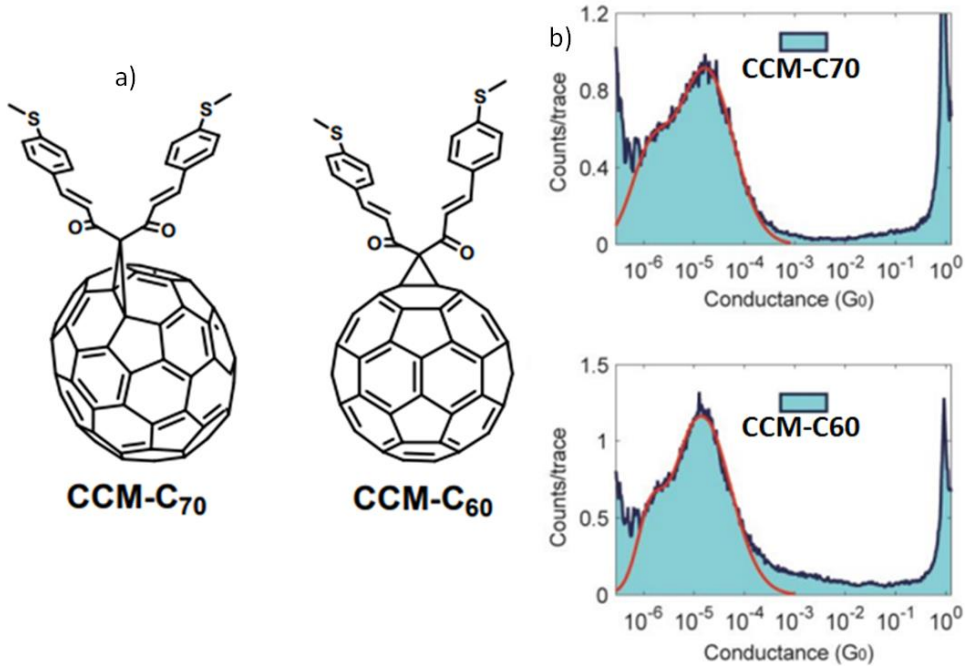

***Figure G10**: Rerpresentation of the fullerene CCMoids CCM-C_{70} and CCM-C_{60} (left) and one-dimensional histograms of CCM-C70, CCM-C60 (right)where the red lines are the most probable conductance values.[52] Reprinted with permission from ACS publications.*

Despite the information gathered in these studies it is known that gold electrodes present major disadvantages: they are thick metal electrodes which may lead to a large screening of a backgate potential, and molecules can adopt many binding geometries which can lead to bad defined metal-molecule-metal conductance which can also strongly limit the junction's mechanical stability.[62,71]

<u>Break-junction in graphene</u>

Taking into account the disadvantages that gold presents (malleability and high atomic mobility, which makes it unstable and therefore not applicable as a robust electrode), more and more new technologies have been focused on different materials including carbon-based systems.[37,72,73] In the latter, graphene presents a suitable solution for the connectivity with single molecules in the terms of stability and reproducibility. Within this layered

material, the covalent sp^2 hybridization of the carbon atoms in the graphene electrodes promotes a high stability even in ambient conditions. In addition, graphene can promote the formation of supramolecular and covalent bonds with molecules, which enables the creation of strong attachments stable for room-temperature applications.[74]

Graphene is an allotrope of carbon consisting of a two-dimensional honeycomb arranged in a base of two carbon atoms network (Figure G11). Within the layer, the distance between the carbon atoms is 1.42 Å, existing strong bonds among all them. Graphene is a zero-overlap semi-metal and has opened up enormous possibilities in the fabrication of electronic devices due to its high charge carrier mobility.[75] Graphene has also been used as a conducting electrode in memory devices,[76] field-effect transistors (FETs),[77] and dye-sensitized solar cells.[78]

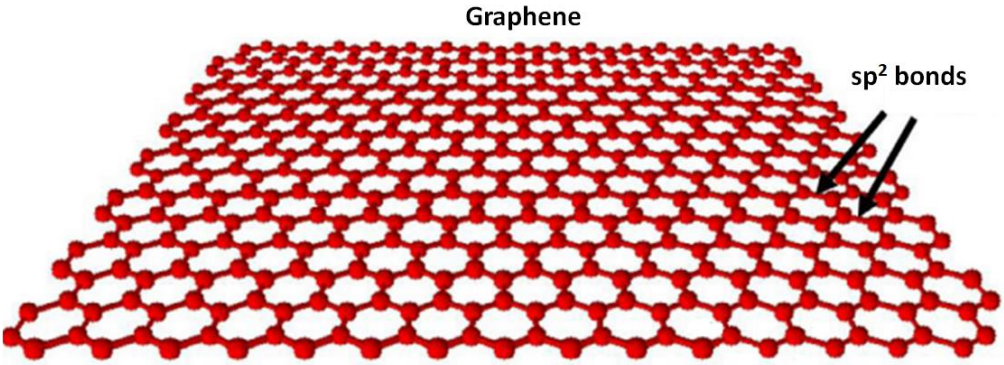

***Figure G11**: Scheme of the graphene honeycome with sp_2 hybridized carbon atoms.[75(79)] Reprinted with permission from Elsevier.*

The best way of using graphene as electrodes, without disturbing the properties of this 2D material, involves the anchoring of molecules by π-π stacking. The higher the number of aromatic groups within the molecules, the so-called polycyclic aromatic hydrocarbons (PAH), the most stable is the contact. PAHs are a type of organic molecules consisting mainly of C and H atoms organized in conjugated aromatic cycles. They can be seen as small graphene fragments and the largest representatives are also referred to as nanographenes or graphene nanoribbons (Figure G12).[80]

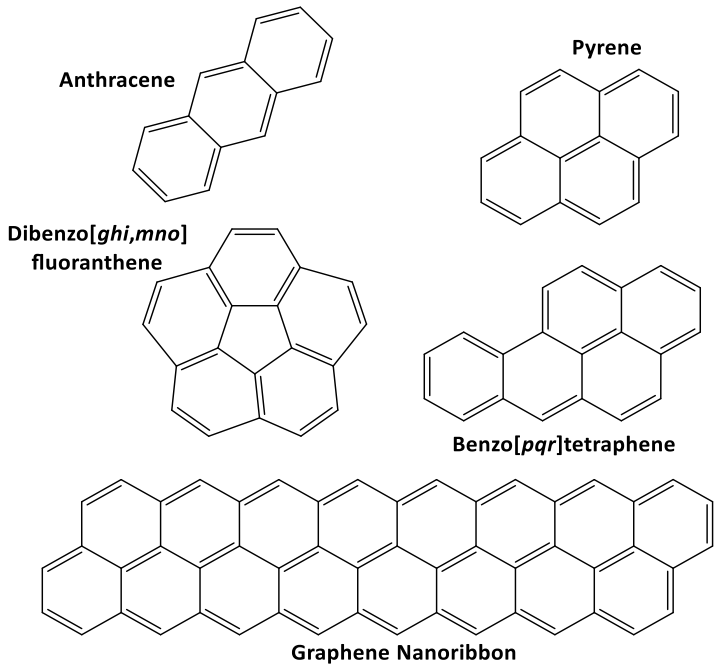

***Figure G12**: Examples of PAHs and a piece of a graphene nanoribbon.*

In nature, PAH*s* are found in different substances, such as oil, coal, and tar, and are produced in combustion processes.[81] Due to the mutagenic and carcinogenic properties of some PAH*s* they are of concern as pollutants.[81,82] However, in some areas of material science, PAH*s* are very promising molecules, as in Molecular Electronics, taking into account that the systems under development require small quantities of PAHs. As in the case of the graphene, the exceptional structural order of the π-conjugated PAH systems confers them an enhanced stability, particular electronic properties, and the ability to conduct charges along the aromatic backbones.[80,82,83] For that reason they have been studied in the molecular electronic field for the assembly of field-effect transistors and photovoltaic cells.[80,82-86]

Nevertheless, the control of the positioning of single molecules in strategic locations on the graphene hybrid devices and the maintenance of the stability of the system along with its performance and the reproducibility has been difficult issues to deal with in the development of the single molecular electronics.[37,38,57] The general idea has been the reinforcement of the molecule-electrode interface. There have been several groups that, in the recent years, are working on the use of carbon-based devices using graphene as electrodes and PAH-based molecules as bridges, connecting through the π-π stacking electrodes of graphene.

Hybrid graphene-based three-terminal devices were fabricated for the first time by Professor Herre Van der Zant´s group at Delf University.[87] They have worked on the fabrication of transistor-like graphene-based devices that consisted of two single layers of graphene separated by a nanogap, that act as source and drain electrodes, respectively, both situated over a Si/SiO_2 layer that behaves as a gate of the final device (Figure G13). The three electrodes: graphene and Si are separated by SiO_2 that acts as insulator (< 300 nm thick). The final system resembles a nanoFET (nano-field effect transistor), where the gate does not inject electrons but is capable of adjusting the energy of the molecular energy levels to the Fermi levels of the source and drain electrodes.[37,38,50,52,57,58,74,88]

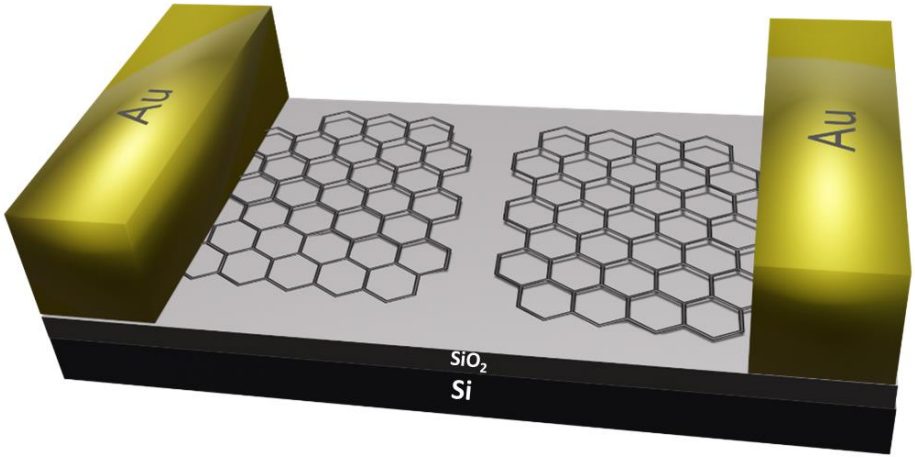

Figure G13*: Schematic representation of the three-terminal devices.*

The separation of the graphene layer forming a small nanogap between them can be produced by few specific techniques. One of them is the already mentioned MCBJ technique (Figure G14). As explained before, this bases on the formation of a bridge in the middle of the graphene layer supported on a flexible metal substrate. Then, the substrate bents promoting a stretching of the graphene bridge until it ruptures. This bending is produced in a reversed way, which causes that the graphene edges can be in touch making the electrical current flow between them allowing multiple measurements to be performed.[37,38,74]

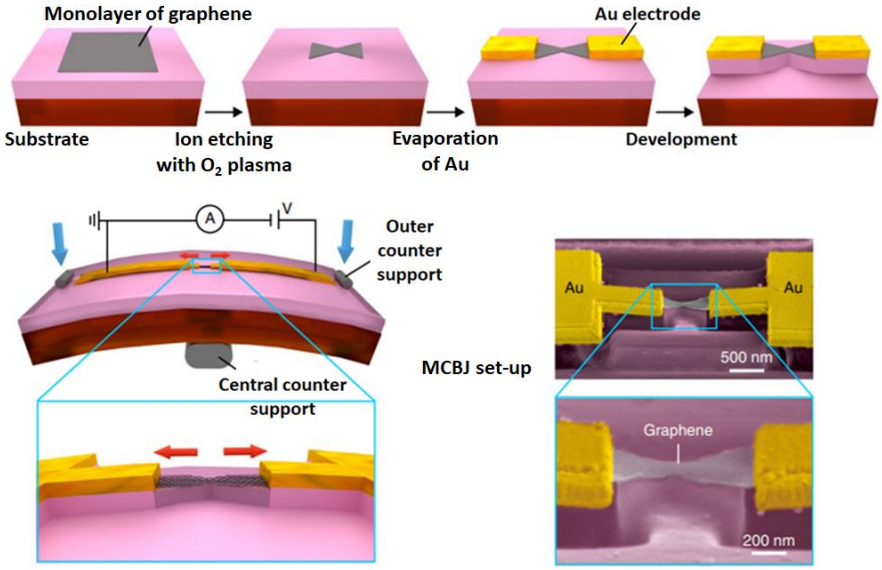

***Figure G14**: Example of the stapes taken for the nanofabrication of graphene device with the MCBJ technique.[89] Reprinted with permission from Springer Nature.*

They observed that with this technique, it could be obtained a large conductance oscillation as a function of nanometre displacement between the two overlapping graphene sheets. Furthermore, they have seen that gap size of the graphene layer can be adjusted with high precision and stability meaning that graphene MCBJs technique could be used as a powerful tool for single molecule conductance measurements over electronic devices to introduce statistics and therefore capable of providing information regarding the most probably conformations of molecules once they contact the electrodes.[37,38,74]

Another technique performed for the obtention of a nanogaps is called the feedback-controlled electroburning. It consists of the chemical reaction between carbon atoms and oxygen at high temperatures, induced by Joule heating at high current densities. The procedure involves first the application of ramps of voltage (V) to a graphene layer (or few graphene layers, FGLs), while the current (I) is controlled. Then, the variation in conductance (G=I/V) is monitored with a feedback condition at a >10% drop in G when a certain limit of potential is achieved. Upon this potential limit, the voltage is swept back to zero and immediately after, a new sweep starts repeating the process. This process promotes eventually a breaking of the layer (Figure G15), where in certain parts of the junction the distance among the electrodes is between 1-2 nm.[37]

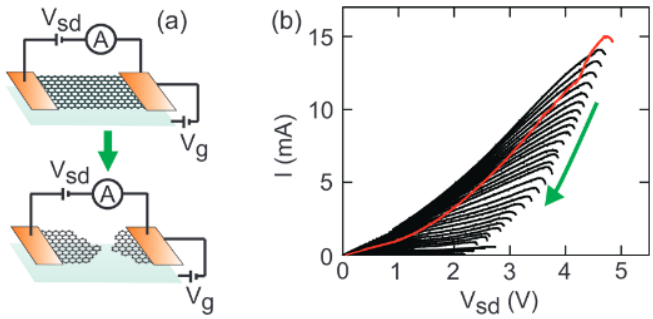

***Figure G15**: a) Scheme of the feedback-controlled electroburning formation of the nanometer sized gap. (b) Graphic of the current-voltage (IV) evolution during the electroburning procedure. The first IV trace is displayed in red.[37] Reprinted with permission from ACS publications.*

After the deposition of the desired molecules over the device, conductance measurements can be measured and represented using I-V graphs (Figure G16a) and also Coulomb diamond blockade (Figure G16b) diagrams, respectively. The latter, called diamonds, are V_{bias} vs. V_{gate} representations of the charge situation between source-drain and gate electrodes, where it could be differentiated the low current regions, where current is blocked, from the regions where there is electron transport (high current regions) produced by the molecule appearing in the diagram with a diamond shape. Inside the diamonds is also possible to observe and measure high current electron transport areas (indicated by the black and white arrows, Figure G16b) related to the single-electron transport excitations of the molecules anchored that, with the help of DFT calculation, they can be related to vibrations of the molecule and, therefore the different oscillations of the molecule coupled with the graphene electrodes.[38]

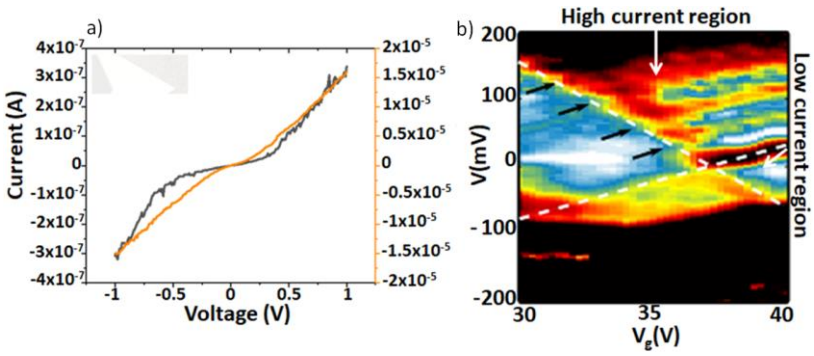

***Figure G16**: Examples of: a) Current–voltage diagram of a graphene electrode device before (brown) and after (black) the gap is created and b) Coulomb diamond diagram where it can be distinguished the high and low current regions separated by dashed white lines. The black arrows show the different single-electron transport excitations.[38] Reprinted with permission from ACS publications.*

During the last decade, few groups as that formed by Professors Mol and Briggs, from the University of Oxford, have deposited porphyrin-based molecules/chains of different dimensions on three-terminal devices based on graphene. Each porphyrin unit are conformed by heterocyclic macrocycles based on pyrrole subunits (Figure G17), functionalised with anchor groups designed to bind the molecule directly with the graphene electrodes via π–π stacking and van der Waals interactions. This type of molecules has been deposited in solution over the graphene-based devices and its conductance measured at low temperatures (approximately 10 K).[72,84,89]

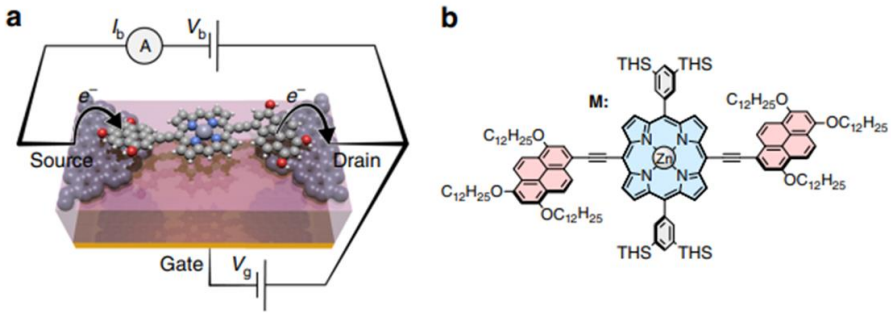

***Figure G17**: Schematic representation of: a) porphyrin-device and b) porphyrin molecule with a porphyrin core (blue), solubilising aryl groups on the porphyrin meso-positions (grey) and π-stacking anchor groups on the other meso-positions (red).[90] Reprinted with permission from Springer Nature under the Creative Commons Attribution 4.0 International License.*

As expected, small molecules display weak attachment with the graphene electrodes, and it has been highlighted the necessity to design supramolecular assemblies, to be able to precisely control the molecular environment and therefore control the orientations of the molecules across the gap and make more stable the contact with the electrodes.

Professor Guo's group, at the Peking University, have been working also in the fabrication of single molecule devices using a layer of graphene. In their case, by using ultrahigh-resolution electron-beam lithography and gradual oxygen plasma, they created ribbon terminal endings of the graphene layer giving some characteristics to the edges such as carboxylic acid groups (Figure G18a). Then, they covalently connect molecules with the ending groups. For that, the designed molecules possessed two terminal amine units capable of reacting with the carboxylic groups, from the ending graphene electrodes, forming amide covalent bonds (Figure G18b). This technique and performance provide robust devices although the gaps are between 8-12 nm and therefore the molecules use must have a long chain-like structure.[90] In

their case, the success on the creation of single-molecule/chain bridges was indicated by the electrical currents measurements and they showed that their devices provide good yields and are stable and function after more than one year.[61,91]

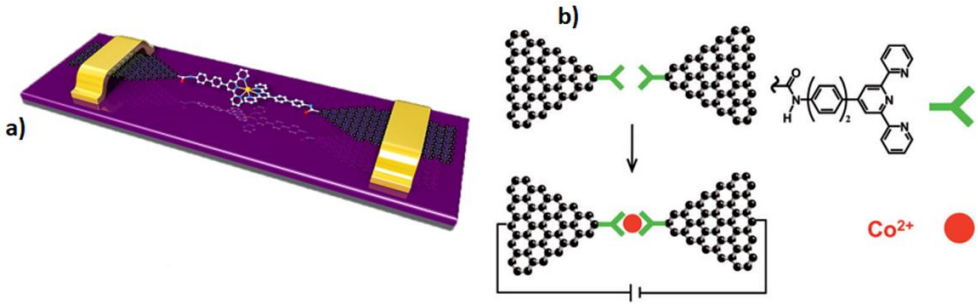

***Figure G18**: Schemes of: a) The graphene device-molecule anchoring and b) the coordination reaction.[91] Reprinted with permission from AIP publishing.*

During the development of this thesis, and with a similar idea to fix molecules on the three terminal devices and therefore, the preparation of reproducible and controllable electronic features at room temperature, the group of Professor Calame, from the University of Basel, has been focused on the functionalization of the SiO_2 substrate attaching covalently molecules to graphene-based three terminal devices (Figure G19).[92-94] Therefore, after the gap between the graphene layers is formed the molecule depicted in Figure G19 was anchored directly to the SiO_2 substrate, using a terminal trimethoxysilane group (blue square Figure G19) through a silanization process which is a common procedure, used to cover surfaces with an alcoxysilyl group.[95-97] Apart from the silyl group, these molecules also contain, in their structure, head groups that consisted in aromatic rings (PAHs, green square Figure G19) which promote the π–π stacking interaction that allows the electronic flow between the neighbour molecules and also enhance the stability of the system. This way, Calame´s group demonstrate that these types of molecular devices allowed a stable current–voltage (I–V) measurement and a high reproducible transport in the temperature range from 20 to 300 K.[92]

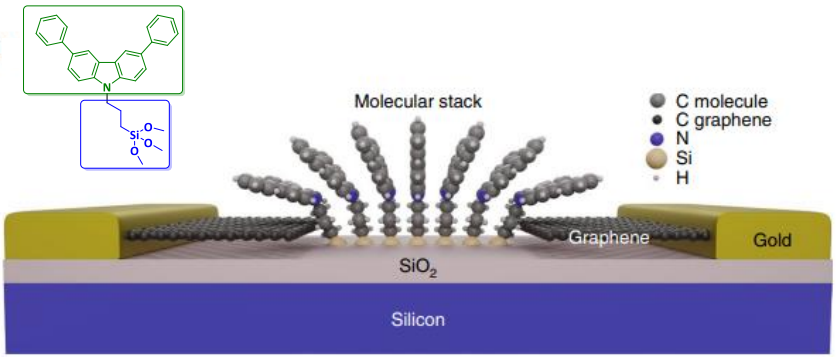

***Figure G19**: Scheme of the molecular anchoring through the silane group (blue) anchor to the substrate and the collection of molecules are brdging the graphene electrodes through π–π-stacing interaction.[92] Reprinted with permission from Springer Nature.*

The disadvantage of their procedure resides in the need of several molecules aligned to fit into the gap, between the electrodes, to promote the electron transport. Their calculations demonstrate that there is a crucial role of π–π-stacked head groups in the transport, and they used molecules without PAHs as a control to compare the difference in current.[93]

In a parallel way, our group, in collaboration with the group of Herre Van der Zant, have reported few works regarding single-electron transport using single CCMoids deposited over graphene devices.[(37,38,50,52,57,58)] The first molecule selected as a nanowire in this type of three-terminal devices was an anthracene-based CCMoid (9Accm, Figure G5e, and Figure G20). The anthracene-groups made proper interactions with the π-system of the graphene layer, thus providing a strong anchor to the electrodes. The molecules were placed over the device putting the system on a chloroform solution (0.1 mM of the CCMoid) and letting them overnight at room temperature. After that, the devices were taken out and dried by a flow of N_2.[37]

Conductance measurements of the devices at room temperature showed that there was an increase in conductance after deposition (IV graph, Figure G20). In addition, at room temperature, the conductance was shown to be dependent on the gate voltage displaying an increase as higher positive gate values voltages were applied. As it happens in room temperature, at low temperatures (10 K), the conductance also showed a clear changing towards more positive values of the gate voltage. Although explained in the last part of the introduction, this was the first work published on single-molecule electron transport at room temperature, in 2011, and the pioneer work that inspired the rest of groups explained above.

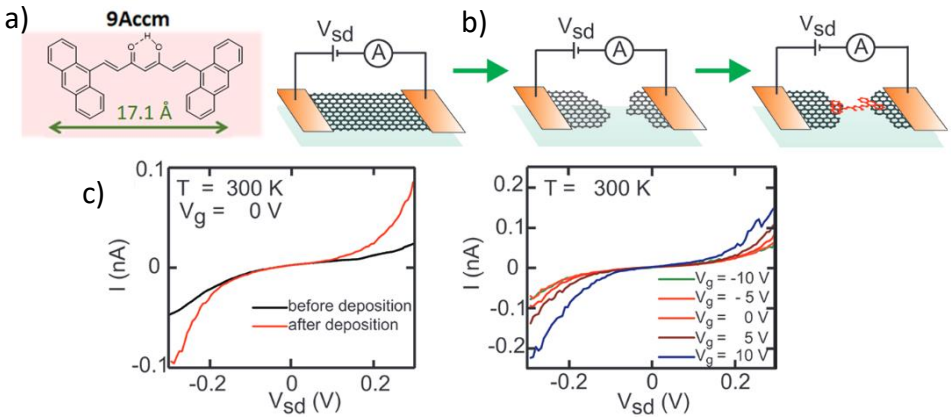

***Figure G20**: a) Chemical structure of 9Accm, b) representation of the procedure for the nanogap formation and bridging of 9Accm molecule to the graphene nanogap, and c) Graph of the IV measurents before and after the deposition of 9Accm molecules at 300 K.[37] Reprinted with permission from ACS publications.*

As it was pointed by the low yield of the results, the π–π-contact point of 9Accm was limited by the variety of shapes and composition of the edges of the electrodes,[99] being similar in size the nanogap and the molecule. For that reason, in a latter work, a longer molecule, similar to the previous CCMoid, but having now a longer chain (11 C atoms instead of 7 C skeleton) was designed, without disturbing the CCMoid conjugation and possessing the same anchoring groups as before (9Accm). This way it was thought to improve the π-π interactions far from the edges of the graphenes, to minimize the influence of the different shapes of their endings.

With this hypothesis on mind, a new anthracene curcuminoid-based molecule (9ALCCmoid, Figure G5i, and Figure **G21**) was synthesized which contains an extension of the conjugated alkene chain backbone.[38]

Here, the CCMoid molecules were deposited at room temperature by drop-casting of a 0.1 mM solution of the synthesized molecules in DCM. They showed an increase of the current after molecule deposition showing the typical I-V representation for this type of fabricated junctions.[37,38,73] This way, the current increases around 2 orders of magnitude with respect the measurements before the deposition which make the results obtained comparable with the 9Accm ones.[38]

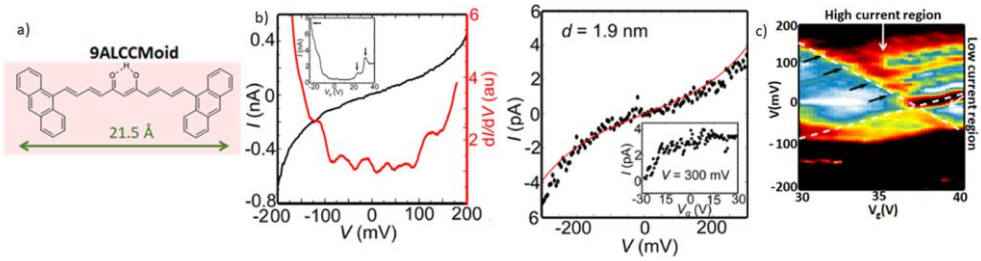

***Figure G21**: a) Scheme of the chemical structure of 9ALCccmoid, b) Graph of the IV measurements before (left) and after (right) molecular deposition measured at T= 4 K and Vg= 0 and c) Coulomb diamond diagram where several single-electron transitions excitations (marked with black arrows) appear bias at positive bias.[38] Reprinted with permission from ACS publications.*

The comparable conductance results obtained from the fabricated devices after the deposition for both anthracene derivates together with DFT calculations indicated that even though 9ALCccmoid was longer than 9Accm, and therefore conductance values were expected to be lower, the enhancement of the CCMoid-electrode interaction compensated for the possible decrease in conductance.

Considering these works related to CCMoids, it can be seen that, although anthracene molecules had demonstrated to behave as good anchoring groups with the graphene electrodes, this π–π-contact show still some limitations, taking into account the variety of shapes and nature of the edges of the graphene electrodes after the electroburning process. For this reason, it is necessary the search for a new type of molecules that can promote not only a better anchoring point through π-π systems with the graphene electrodes (than the ones obtained for the 9Accm and the 9ALCCMoid), but also a more robust system that resist the temperature effect on the device which causes the vibration of the molecules and therefore promotes the deterioration of the intermolecular molecule-graphene interaction, affecting the performance of the device. Consequently, the new CCMoids presented in this thesis have been designed to minimize such aforementioned effects, while improving the reproducibility and performance of the final devices compared with the ones before.

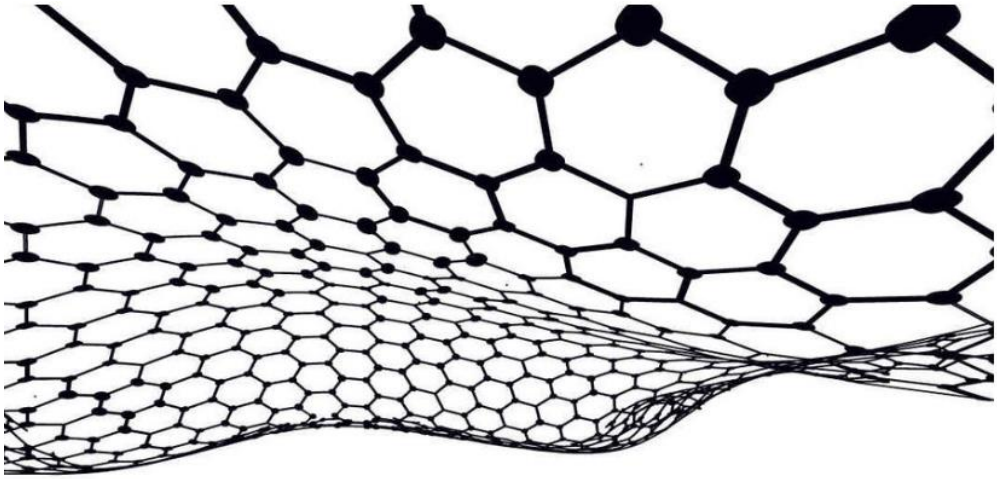

OBJECTIVES

OBJECTIVES

In this thesis we explore the best conditions for the straightway synthesis and the proper characterization of new PAH-CCMoids and T-shaped PAH-CCMoids. Our approach resides in the creation of basic CCMoids that can be used as starting or intermediate materials thanks to the reactivity of their functionalized ending groups

- Toward the main objective, the first synthetic goal was to create CCMoids containing acetylene groups in *para* position of the terminal aromatic rings. Figure O1 shows three new CCMoids that could act as source to synthesize PAH-CCMoids for their future use in Molecular Electronics.

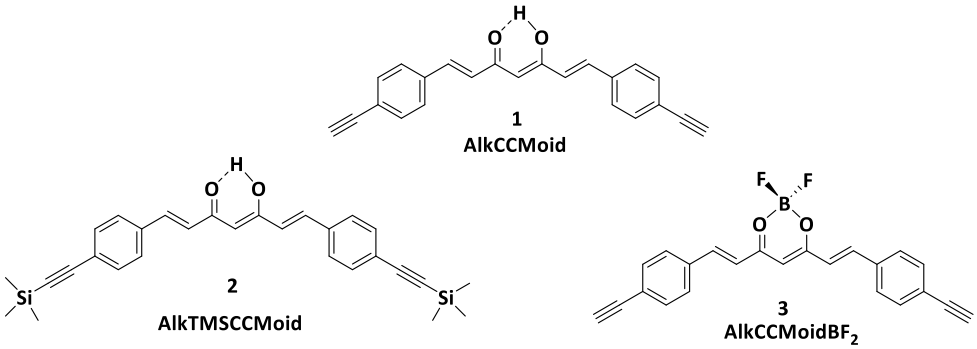

***Figure 22**: Molecular structure of **1, 2** and **3**.*

- The second aim was to find a suitable synthetic strategy to transform the above units into PAH-CCMoids (figure O2), starting with reagents that could be purchased (e.g.: to create 4PhAntCCMoid, **5**) and be synthesized (e.g.: for the creation of 2Br12PhCCMoid, **7**); the two systems contain small nanographene (NGs) units in the sides of the CCMoid skeletons that will improve the π-π stacking with graphene substrates/electrodes. In addition, the designed arms have groups (system, **7**) that can continue growing being the source of nanoribbons-based CCMoids.

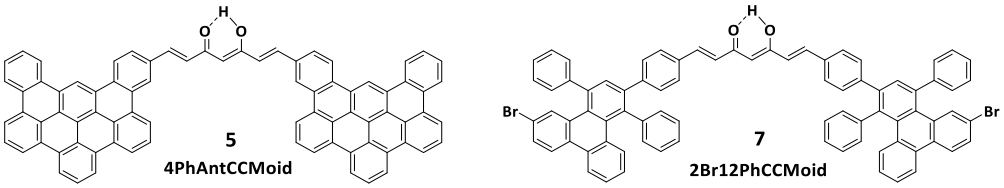

***Figure 23**: Chemical structure of CCMoids **5** and **7**.*

- The third objective in the creation of new CCMoids was to use the knowledge gathered previously to achieve now T-shaped CCMoids containing PAHs groups in both sides of the CCMoid framework and, in addition, insert a short reactive functional group (with alkyl or alkene endings) in the central part of the CCMoid skeleton (figure O3).

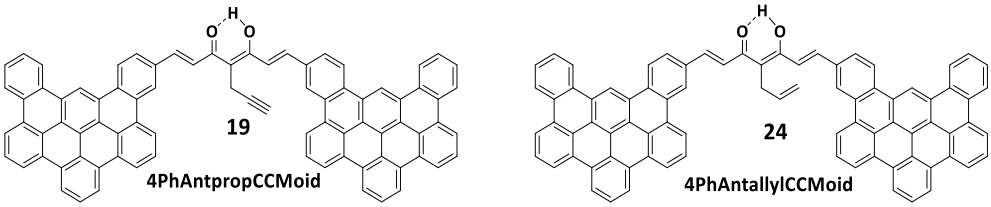

Figure 24: *Chemical structure of CCMoids **19** and **24**.*

Due to the novelty of such molecular systems and the expected characteristics of PAH molecules (e.g.: planarity, insolubility), an important objective of this thesis has been the establishment of a protocol of useful techniques for the identification/characterization of the molecular-based materials and their electrochemical/optical properties in solution and in solid state.

Finally, studies on the deposition of some of the molecules on different substrates/devices are explored, toward a better understanding of the electronic behaviour of these molecules and the possibility of designing new and improved PAH-CCMoid prototypes in the future.

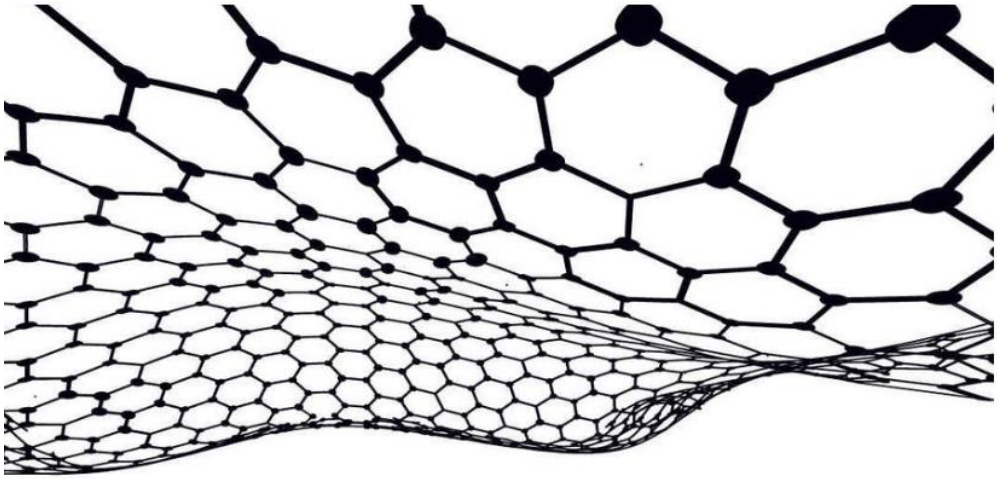

CHAPTER I

1. CHAPTER I: SYNTHESIS AND CHARACTERIZATION OF A NEW CCMOID WITH ACETYLENE ENDING GROUPS, ALKCCMOID 1

1.1 INTRODUCTION

As previously mentioned in the introduction section, using the versatile chemistry of CCMoids based on well-established methods[37,42,46,47,58,99-101] we planned the synthesis and study of new molecular platforms for their use in the field of Molecular Electronics toward their inclusion on hybrid graphene devices. For this purpose, new functionalized CCMoids combined with polycyclic aromatic hydrocarbons (PAHs) have been designed.

Considering both types of units, this thesis shows our first attempts matching their characteristics towards the creation of molecular wires, with molecular systems that contain a CCMoid skeleton and bulky graphene-like ending groups on the sides, to strengthen the molecular anchoring to graphene electrodes. In the development of such systems, two main paths, using both of them the general Pabon´s reaction, were considered.

The first possibility was the synthesis of aldehydes containing the PAHs units to be used later to perform the synthesis of new CCMoids (Scheme 1.1, route 1).[28,50] This methodology is realistic, but previous experience in the group showed us that PAH-based aldehydes (starting materials for the new CCMoids) entails problems derived from their solubility, such as impurities, low yields, including the achievement of mixtures of CCMoids (symmetric and hemi-CCMoids), complicating the achievement of the final molecules. Therefore, a second strategy was analyzed, where CCMoids units would contain reactive groups on their arms that could coordinate with the desired PAHs groups (Scheme , route 2). To carry out this reaction cascade, the synthesis of new functionalized CCMoids had to be performed.

This chapter shows the steps followed toward the synthesis and characterization of CCMoids with reactive groups in their arms.

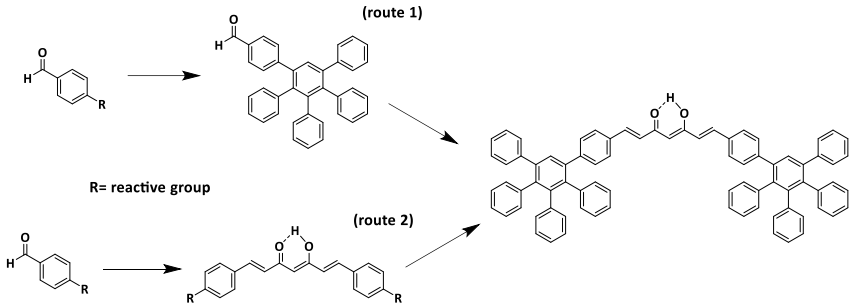

***Scheme 1.1**: Methodologies for the synthesis of CCMoids containing PAH precursors. R is a reactive group that latter would allow the achievement of the bulky CCMoids.*

1.2 OBJECTIVES

In this chapter we explore the best conditions for the straightway synthesis and the proper characterization of a new CCMoid with acetylene groups in *para*- position of the terminal aromatic rings, that allows the introduction of additional PAH groups for their in Molecular Electronics.

The analysis of the optical and electronic behaviour of the final system has been also targeted, to compare it with already synthesized CCMoids reported in previous works, and taking into account that the new system would display common CCMoid features (a conjugated backcbone, a central *keto-enol* moiety and aromatic groups on the arms).

Another relevant point shown in this chapter is how to deposit the functionalized CCMoid on different substrates including three-terminal devices, through sublimation, to directly analyse their electronic behaviour, providing structural-electronic correlations.

1.3 RESULTS AND DISCUSSION

The chemistry in solution of alkyne groups is well-known; they are highly reactive and can undergo catalytic reactions, like Glasser coupling trimerization, addition of nucleophilic or electrophilic reagents, hydration reactions, as well as hydroboration and oxidation reactions, among others.[106] Alkynes can even give place to cycloaddition reactions,[107-109] which allows promoting C-C bonds, and therefore the continuation of conjugation and an increase in the length of the molecule, introducing new aromatic rings, which will be further explained in chapter 2 and 3. Apart from the above-mentioned reactivity in solution, they can promote on-surface reactions as well, anchoring molecules into some functionalized surfaces, like in the famous click chemistry reactions.[110-114]

Considering all the above possibilities, an acetylene functional group was introduced in the terminal aromatic rings in *para*-position of a CCMoid giving rise to a new system called AlkCCMoid **1** (Figure 25).

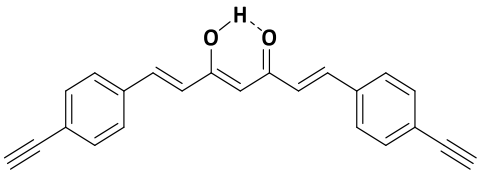

***Figure 25**: Schematic representation of AlkCCMoid **1**.*

1.3.1. Synthesis of AlkCCMoid 1 and alkyne modified CCMoid 2 and 3

The molecules **1-3** (Figure 1.26) display the expected structure of symmetric CCMoids; this includes a 7-carbon atom conjugated chain, with a central *keto-enol* functional group and two terminal, and functionalized, aromatic rings. In all the cases, the aromatic groups are substituted in *para*- position with alkyne groups.

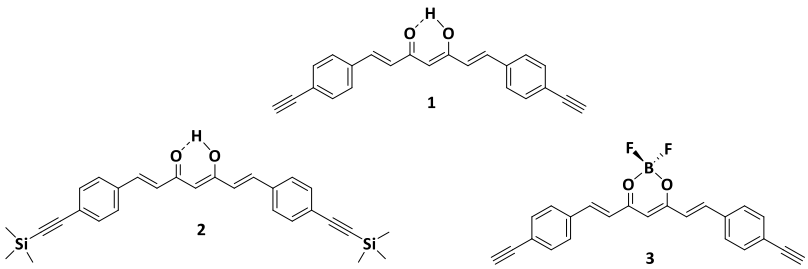

***Figure 1.26**: Molecular structure of **1**, **2** and **3**.*

1 was synthesized by a modification of Pabon´s method,[5] presented in Scheme **1.2**1.2. In general, symmetric CCMoids present straightforward syntheses that can be scaled up and chemically tuned by varying the nature of the aldehyde used.

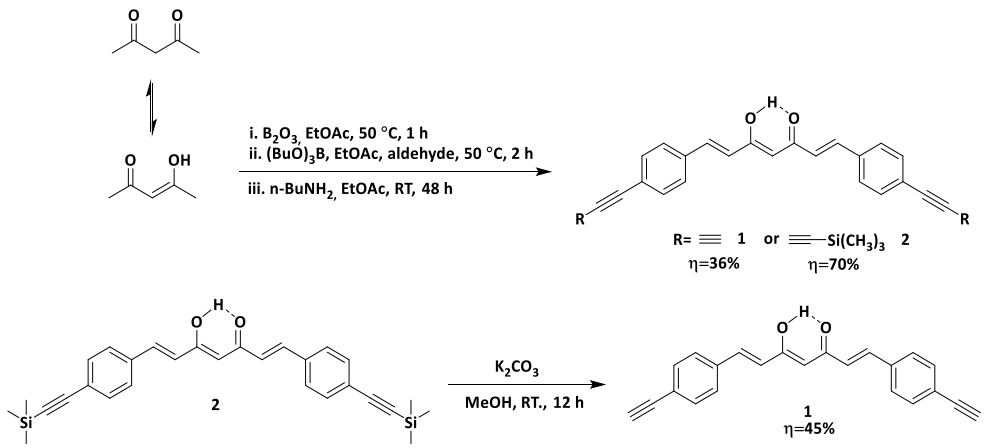

***Scheme 1.2**: Synthetic paths in the achievement of molecules **1** and **2**.*

We came up with a two synthetic methodology for **1** based on one and two-step synthesis. Both synthetic methodologies started with the Pabon's reaction, using an aldehyde with a trimethylsilyl (TMS) protected alkyne group or without this protecting unit. Providing, in the case of the protected one, a CCMoid in higher yield, (45% instead of the 36% for the unprotected one), as well as more soluble in organic solvents, due to the TMS moieties. Then, next step was the removal of the TMS group using potassium carbonate in methanol at RT. System **2** was previously synthesized in the group,[111] however, the complete characterization and reactivity studies have been performed during this thesis process.

Here, it is important to mention that CCMoids have been used for the coordination to different transition metals and metalloids through the *keto-enol* moiety.[40-45,48,50,112] Regarding the metalloids, and more precisely the coordination with -BF_2 groups, it is well-known the effect on the HOMO-LUMO energy levels (bandgap) of the coordinated CCMoid. In all cases, it is reported the reduction of the bandgap, caused by the formation of a donor-acceptor-donor system (Figure 27), including here previous work of our group with different CCMoids in the field of molecular-electronic devices.[41,50]

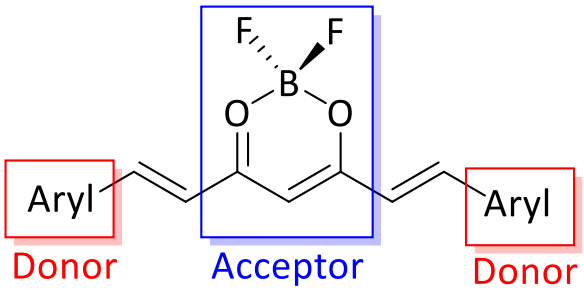

***Figure 27**: Structure of the -BF$_2$ complexes where is highlighted the electron donor-acceptor-donor system.*

To test the effect of such coordination on the electronic properties of **1** the BF$_2$-complex **3** was achieved. For that, **1** was mixed with BF$_3$·OEt$_2$ (Scheme **1.3**1.3). Our approach includes modifications on the methodology reported in the literature,[113-115] using a microwave reactor instead of conventional heating, decreasing reaction times from 16 h approximately to 10 min; moreover, the introduction of the -BF$_2$ moiety provides changes in the solubility of the molecule making it more soluble in polar solvents.[116]

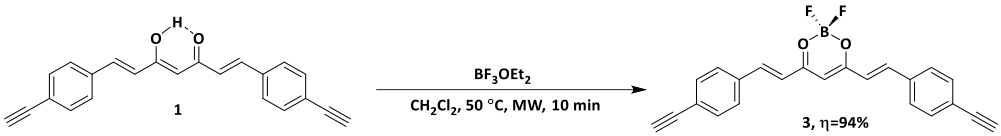

***Scheme 1.3**: Schematic representation of the formation of the BF$_2$-complex 3.*

The three CCMoids (**1**-**3**) were characterized in solution using nuclear magnetic resonance (NMR), UV-Vis absorption spectroscopy and electrochemistry. In the solid state, we gathered crystallographic data for **1** and **2**, which agree with the information achieved for these molecules in solution. Furthermore, we used additional characterization techniques (IR, Raman, MALDI, UV-Vis, EA, and TGA) to verify the structures, the purity and analyse further optical and electronic properties of the systems.

In the following sections, it is presented the comparison between the **1**-**3** compounds. Spectra of the different techniques used for the analysis of each individual molecule can be found in the appendix section.

1.3.2. ^{1}H NMR and ^{13}C NMR spectroscopy for CCMoids 1, 2 and 3

In general, the NMR analysis in solution of CCMoids provides clear information regarding its nature, purity and coordination, being the first to be used in our characterisation process.

Figure 28 and**Figure** display the ^{1}H NMR and ^{13}C NMR spectra of **1**, **2** and **3**, in that order. Regarding the overall appearance of the ^{1}H and ^{13}C chemical shifts, a similar trend is observed in the case of the backbone of all three CCMoids, having in common comparable signals for the linear alkene chain and the aromatic groups. Nevertheless, for **3** all the signals appear shifted towards lower fields (higher ppm) due to the presence of the -BF_2 moiety, an electronegative group that promotes a polarisation of the proper nucleus, making them more prone to suffer the effect of the external magnetic field.[114,116,117] This group produces a decrease in the electronic density by the electron-withdrawing effect of the surrounding atoms and therefore they feel more the external magnetic field applied. This phenomenon is called deshielding effect and it has been extensively reported in the past.[114,118,119]

Analysing the ^{1}H shifts, the signals that appears at the lowest field H_a and H_g correspond to the *keto-enol* protons present in **1** and **2** (15.81 and 15.82 ppm respectively), absent in **3** due to the coordination of the -BF_2 group. In addition, H_b, H_d, H_h, H_j, H_m and H_o appear for all the systems in the range of 8.0 to 6.5 ppm; they correspond to the two types of protons of the conjugated skeleton that display two doublets each, with identical and large coupling constants typical from alkene protons disposed in *trans* position ($^{3}J_{HH}$ = 15.8-15.6 Hz).[120] The *keto-enol* group produces a deshielding effect for the H_b, H_h and H_m protons, towards lower fields with respect to H_d, H_j and H_o which appear always at higher fields. It is remarkable to observe that systems **1** and **2** have almost identical shifts, showing that the terminal units, -H or -TMS, do not have a strong impact in the conjugated chain. Instead, the coordination with the -BF_2 unit shifts them in a greater manner (H_m and H_o), to lower fields, and produces an improvement of the aromatic nature.[114,116,117] In the arms of the molecules, the signals corresponding to the aromatic protons H_c and H_i appear together, as a singlet, for **1** and **2**, integrating in both cases eight protons. Again, for **3**, this signal (H_n) splits as a doublet of doublets with a coupling constant typical of phenyl groups ($^{3}J_{HH}$ = 8.43 Hz). The difference between **3** and **1** and **2**, in this respect, could be attributed to the presence of the -BF_2 moiety that produce a broadening effect in the coupling constant of the aromatic protons.[121] The central proton in the alkene chain H_e, H_k and H_p

suffers the shielding effect of the *keto-enol* moiety and, in the case of **3**, it also suffers the deshielding effect of coordination to the $-BF_2$ group which make them appear as a singlet and practically at the same position for **1** and **2,** but being shifted at lower fields in the case of **3**.

Finally, the terminal protons of the triple bond in the arms, for **1** and **3** appear almost at the same position, approx. at 3.25 ppm, as other terminal alkyne groups in the literature.[122] The similarities between the two systems suggest that at the edges they do not feel the effect of coordination of the $-BF_2$. As expected, system **2** displays an intense signal, which relates to the trimethylsilyl groups at high fields (H_l, 0.05 ppm).

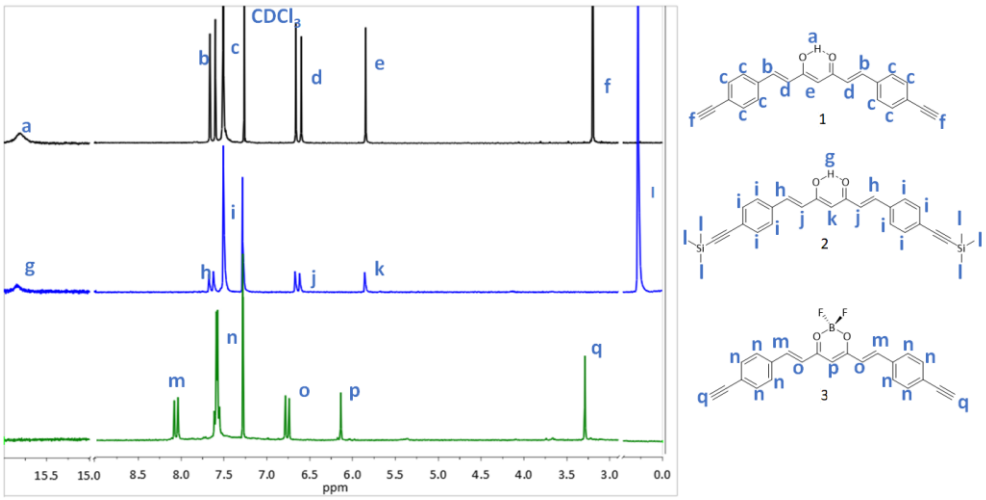

***Figure 284**: ^{1}H NMR comparison between **1** (black), **2** (blue), and **3** (green) in $CDCl_3$ at 360 MHz.*

The ^{13}C NMR spectra of the three molecules present many similarities as well, with few particular carbon shifts. This way, for **1** and **2**, the *keto-enol* carbons (C_a and C_k, 183.2 ppm) appear as a unique signal, which could be explained for the efficient interconversion between both functional groups, situating this signal at lower fields with respect to a typical ketone carbonyl group (≈200 ppm).[120] For **3**, this signal presents a shift towards higher fields (at ≈179 ppm) which is comparable with other reported works, indicating that the inductive effect produced by the O group is less effective due to the presence of the B group that promotes an smaller polarization of the C-O bond.[50,116,117] The region comprising 140-120 ppm contains the aromatic and conjugated alkene chain signals, being the most intense those related to the aromatic carbons C_d, C_e, C_n, C_o, C_x, and C_y, and the less intense to the quaternary one carbons C_c, C_g, C_m, C_p, C_w, and C_α due to the slower relaxation time and lack of

NOE enhancement.[102] The remaining ones in this region come from the alkene chain C_b, C_f, C_l, C_p, C_v and C_z. Another differentiate signal is the corresponding to the central carbon of the alkene chain C_h, C_q and C_β, appearing in a separate area from those before, and in all cases approximately between 104-102 ppm, because of the shielding effect of the *keto-enol* group. It is particularly interesting to observe that coordination of the $-BF_2$ does not affect in great manner this shift in the case of the carbon atoms probably because the deshielding effect in this region is not as strong as in the other carbons of the alkene chain.

Finally, the carbon atoms of the triple bonds C_i, C_j, C_γ, and C_δ for **1** and **3** appear between 83-79 ppm, in agreement with similar moieties described in the literature.[120] Here, the same signals for **2** are shifted to lower fields compared to the others because of the steric interactions caused by the presence of a trimethylsilyl group which influences the nucleus of the alkynyl group promoting a deshielding effect.[122] Again, it can be identified another extra signal related to the trimethylsilyl groups at high fields C_t, 0.05 ppm.

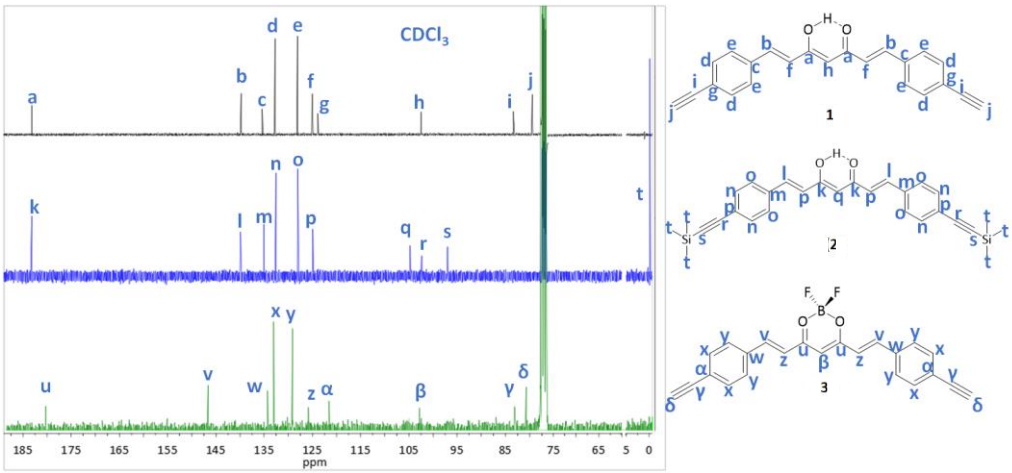

Figure 1.5: *$^{13}C\{1H\}$ NMR spectra with comparison between **1** (*black*), **2** (*blue*) and **3** (*green*) in $CDCl_3$* at 90 MHz.

1.3.3. ATR-FTIR spectra for CCMoids 1, 2 and 3

In parallel to the solution studies, ATR-FTIR was used to identify the main functional groups for each system. The comparative between all the CCMoids also gave us information about the presence of significant bands that could be useful for the proper analysis of advanced (and insoluble) compounds that would be shown in the following chapters.

Figure 296 shows that molecules **1** and **3** display the characteristic sharp band corresponding to the stretching vibrational mode of the triple bond, ν(≡C-H), which appears at around 3200 cm^{-1} together with a band at 614 cm^{-1} which corresponds to the bending mode, δ(≡C-H), confirming the presence of this functional group in both systems. Instead, for **2**, a sharp band at 2142 cm^{-1} is observed characteristic to the stretching ν(C≡C) signal.[120] Interestingly, in all compounds, there is a broad signal between 1650-1625 cm^{-1}, assigned to the ν(C=O) band of the *keto-enol* conformation for the *keto-enol*. Additional bands corresponding to the ν_{ar}(C-C) vibrational mode appear between 1570-1495 cm^{-1}. Moreover, for system **2**, appears a band at 1247 cm^{-1} that can be related to the out-of-plane bending vibration of the TMS group, δ(Si-CH_3). Also, **3** shows at 1393 cm^{-1} a band that could be related to the ν(B-O). However, no assignation of the ν(B-F) was attempted, due to the huge range in which it should appear (around 1500-700 cm^{-1}) and the overlap within additional bands.[120]

Finally, to conclude this analysis, an intense and sharp signal could be observed in the three systems (around 831-821 cm^{-1}) which corresponds to the δ(C-H_{oop}) *para*-substituted aromatic ring.[120]

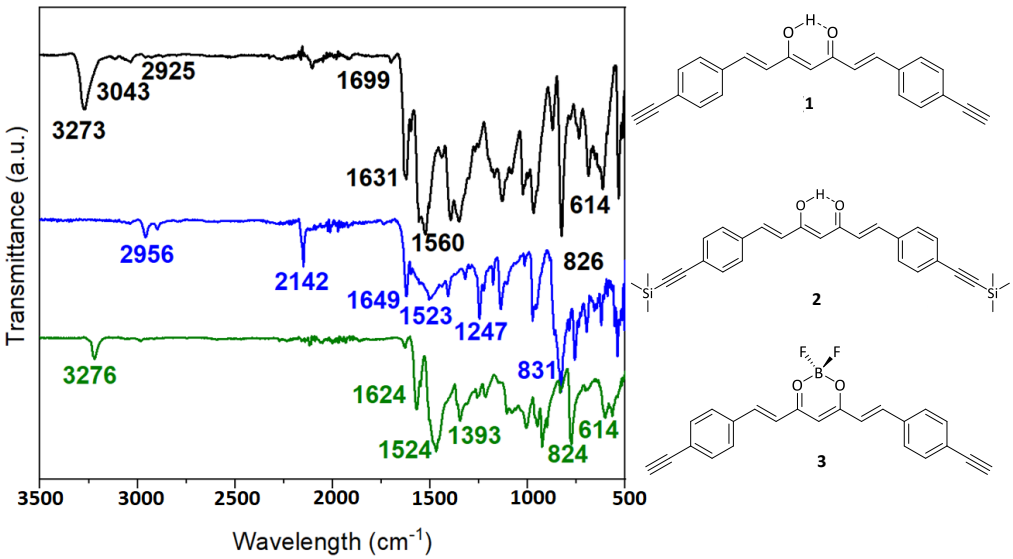

***Figure 296**: Comparative ATR-FTIR spectrum between **1** (black), **2** (blue) and **3** (green).*

1.3.4. Raman spectroscopy for CCMoids 1, 2 and 3

Raman also allows the confirmation and comparison of the vibrational modes of different functional groups. Moreover, thanks to the data reported for the curcumin molecule (CCM), and due to its resemblance to our structures, our results could be contrasted and corroborated.[51,123]

Figure 307 shows that all systems present a vibrational mode around 2100-2200 cm^{-1} assigned to the stretching mode of the triple bond, ν(C≡C)[124], being shifted for **2**, due to the presence of the trimethylsilyl groups.[125] Following the analysis, at around 1630-1640 cm^{-1} it is recognized the vibration assigned to the ν(C=O), and the next sharp band at around 1600 cm^{-1} corresponds to the stretching mode ν_{ar}(C=C). Then, at 1175 cm^{-1}, the signals found are related to the bending vibrational mode δ(C-O-C) of the *keto-enol* groups together with the stretching *v* and bending δ(C-C-H) of the aromatic ring.[51,123]

For system **3**, two more signals could be seen, at 1512 and 984 cm^{-1}, which assigned to the ν(B-O) mode.[126,127] Again, the B-F vibrational mode could not be seen, in this case a possible explanation of this phenomenon could be the polarized nature of the bond, being this band inactive in Raman.[128,129]

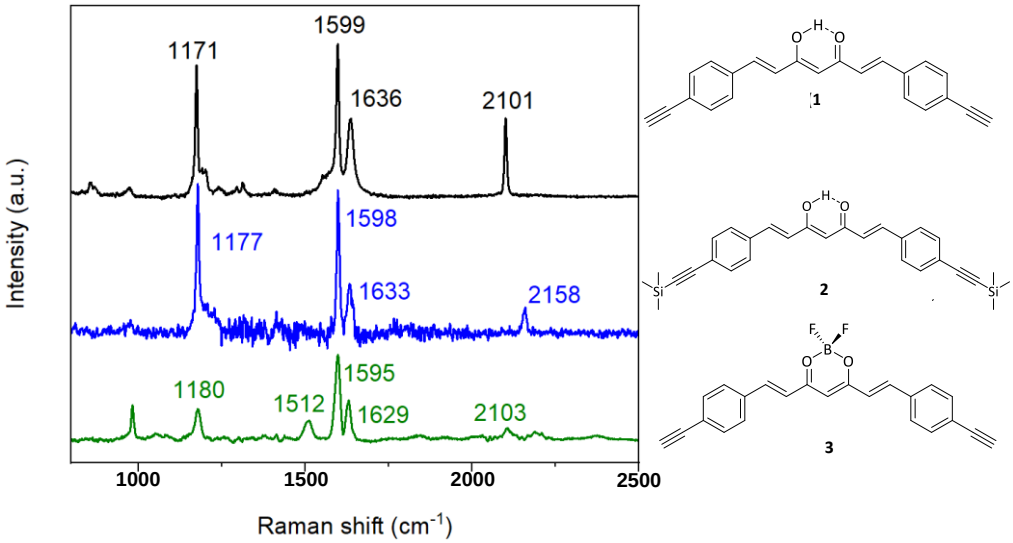

***Figure 307**: Comparative Raman spectrum between **1** (black), **2** (blue) and **3** (green).*

Raman measurements were performed with the assistance of Dr.Tariq Jawhari (from the Centre Científics i Tecnològics de la Universitat de

Barcelona (CCiTUB)) and Dr. Rossella Zafino from our group (Fuctional Nanomaterials and Surfaces, Funnanosurf).

1.3.5. Crystallographic data for CCMoids 1 and 2

To further characterize the systems in the solid state, and with the aim of achieving additional information regarding conformations and polymorphism, recrystallization of the systems was pursued, and crystallographic data (of single crystals and powder) gathered.

Among the different approaches in the literature, in this thesis crystals were achieved using vapour phase-diffusion technique (Figure 318). For that, two vials, one contained inside the other, were used, sealing the outer. In the inner vial, a solution of the compound with a volatile solvent is placed and in the outer vial another volatile solvent, which our CCMoid is insoluble in, is set and the system is left undisturbed for days. With time, the outer solvent gradually diffuses into the inner one, making slow the process of nucleation and precipitation of the system, in form of crystals.

With this methodology, the crystal structures of **1** and **2** were obtained. The latter made by a former student in the group, Jesse Ferreira da Silva.

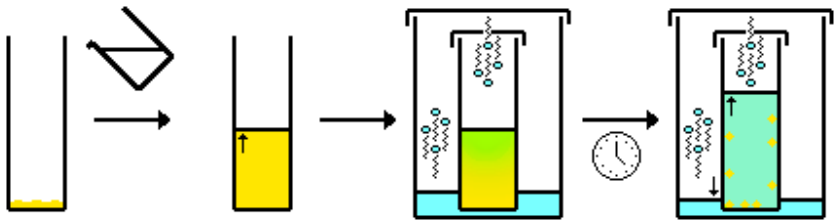

***Figure 318**: Vapour phase-diffusion crystallization process. (Photography extracted from: https://web.mit.edu/x-ray/cystallize.html)*

Crystallographic data of **1** and **2** were collected using synchrotron radiation and resolved by Dr. Eva-Carolina Sañudo (Inorganic department of the University of Barcelona, UB)).[40,41,45,50,55,130] Figure 329 and Figure **33** show the data of the two CCMoids units and packing of molecules, respectively, and Table 1.1 displays the most significant crystallographic parameters. System **1** shows a monoclinic space group *Cc*, while **2** presents the triclinic space group *P$\bar{1}$*, presenting both four molecules in their respective asymmetric unit cells. The *keto-enol* moiety of the two molecules species displays the C=O/C-OH distances ranging from 1.294 Å for **1**, and 1.298 Å for **2**, correspondingly and the C-C and C=C distances of the alkene chain between 1.345-1.464 Å for **1**,

and 1.354-1.471 Å for **2**. The terminal alkyne groups exhibit the shortest distances, presenting C≡C lengths of 1.200 Å in the case of **1** and 1.213-1.225 Å for **2**.

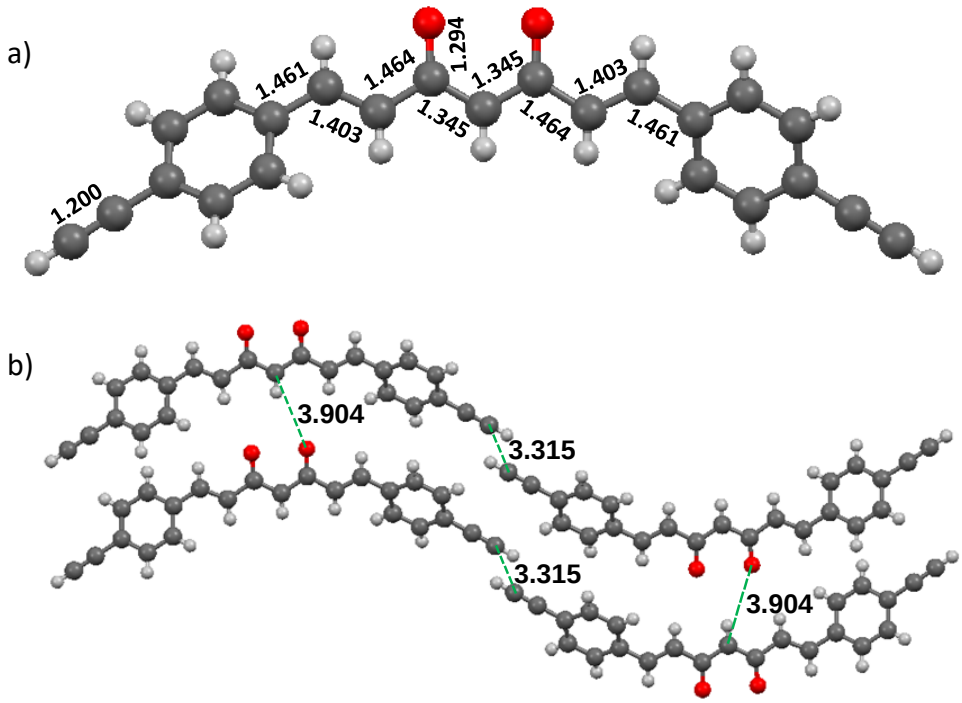

***Figure 329**: Crystal structure of **1**: representations of a) a single molecule and b) the packing of molecules of 1 including the most relevant intermolecular interactions.*

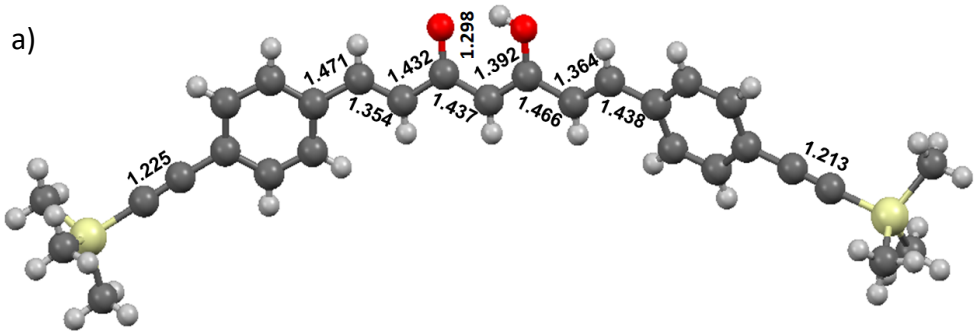

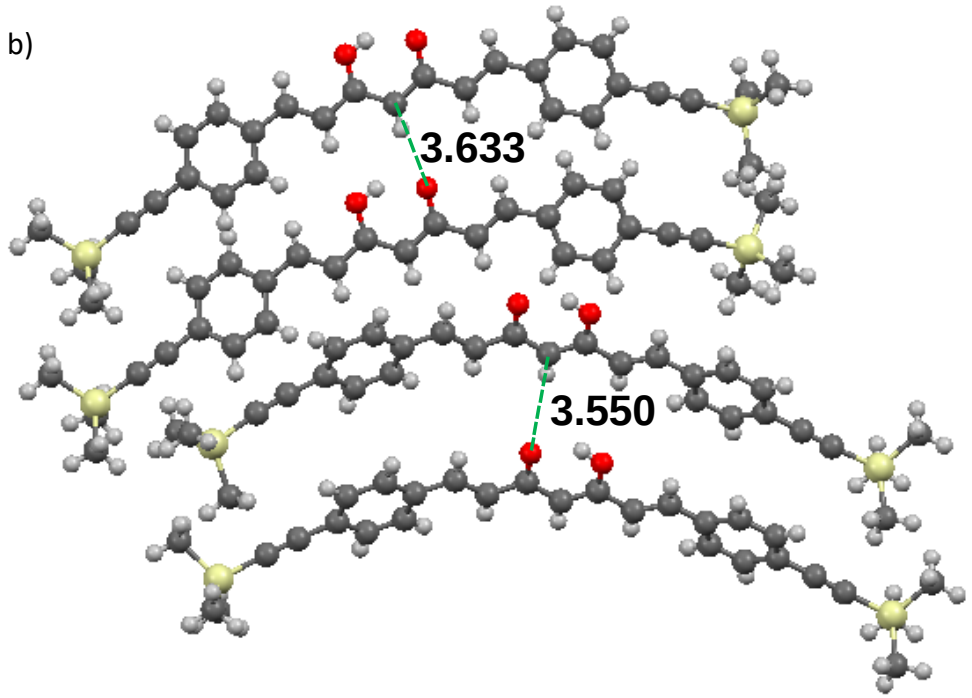

Figure 3310*: Crystal structure of CCMoid* ***2****: representations of a) a single molecule and b) the packing of molecules of* ***2*** *including the most relevant intermolecular interactions.*

Both systems presented the typical CCMoid trends,[40,41,45,50,55,130] with alternating single and double C-C and C-O bonds of the alkene chain and the *keto-enol* moiety, respectively. However, there are some differences in the conformation of the molecules. On the one hand, **1** presents a twisting of the aromatic rings and the triple bonds with respect to the backbone of the molecule producing a curvy shape (Figure 329). On the other hand, **2** shows an arched conformation with the aromatic, triple bond and silane groups, which resemble to a buckle conformation (Figure 3310). In both cases, it is shown that two nets of molecular units are fused in opposite directions. **2** exhibits intermolecular interactions between the O atoms of the *keto-enol* moiety of one molecule and the methine group (H-C) of the neighbour molecule that are in the same direction with distances of 3.550 Å and 3.633 Å and angles close to 150°. For **1**, these interactions are weaker due to longer distances (3.904 Å and 155°) nevertheless it possesses other interactions through the triple bonds with molecules in opposite directions (C···C distances of 3.315 Å, Figure 32) producing supramolecular 1D networks.

*Table 1.1: Crystallographic data of CCMoids **1** and **2**.*

Name	AlkCCMoid (**1**)	AlkTMSCCMoid (**2**)
Formula	$C_{23}H_{15}O_2$	$C_{29}H_{32}O_2Si_2$
Formula weight	323.35	468.75
Crystal system	monoclinic	monoclinic
Space group	Cc	$P\bar{1}$
a (Å)	39.30	34.87
b(Å)	5.68	11.20
c (Å)	7.58	29.90
α (◦)	90	90
β (◦)	90.61	113.33
γ (◦)	90	90
V (Å)	1691.94	10722
Z	4	8
ρ (gcm^{-3})	1.27	1.16
Temperature (K)	100	293
Wavelength (Å)	0.73	0.73
μ(mm^{-1})	0.08	0.16
F(000)	676.4	4000
Reflections collected	14828	88952
Independent reflections	2687	28609
R_{int}	0.13	0.09
Parameters	51	1217
Restraints	0	2
Goodness-of-fit on F^2	3.32	1.05
R1 [I>2σ(I)]	0.19	0.10
wR2 [I>2σ(I)]	0.45	0.25
R1 (all data)	0.19	0.09
wR2 (all data)	0.47	0.23

1.3.6. Ultraviolet-Visible spectroscopy (UV-Vis) in solution and in solid state for CCMoids 1, 2 and 3

UV-Vis absorption studies in solution and in the solid state were performed to further characterize systems **1**-**3**, while extracting electronic information, including this the calculation of the optical band gap (E_g^{op}) in the case of the solid state.

The experiments in solution were taken in DCM, in a concentration of 10^{-5} M (Figure 341), showing a similar number of bands all of them with displacements very similar in the case of **1** and **2**, between 403 and 410 nm, respectively, assigned to π-π* transitions related to the CCMoid skeleton and *keto-enol* moiety. **3** presents the same band but further shifted to higher wavelengths is due to the presence of -BF_2, as described in other reported works.[114,118,119] Following bibliography, we assign the band located between 260-273 nm to the transition σ-π* of the aromatic region of each CCMoid.[59,120]

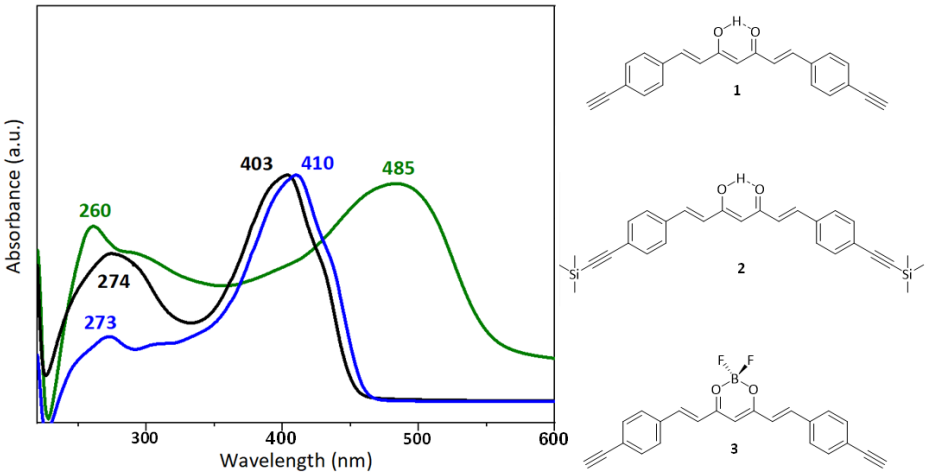

***Figure 341**: Comparative UV-Vis spectrum in solution (DCM 10^{-5} M) between **1** (black), **2** (blue) and **3** (green).*

It is well described that in solution CCMoids present solvatochromic effects, displaying shifts in the wavelengths of the different bands.[36,52,112,114,120] For example, Tønnesen *et al*.[131] studied the UV-Vis absorption and emission spectra of the bisdemethoxycurcumin (BDMC) in several solvents and they observed a shift to the red region in the fingerprint absorption bands, while increasing the polarity of the solvents. Therefore, in order to analyse the optical bandgap, UV-Vis absorption experiments were performed in the solid-state (Figure 35). To do that, pellets of each compound mixed with KBr were used, reaching micromolar concentrations of $1*10^{-6}$ mmol of compound/mg of KBr and the pellet was measured using an integrated sphere accessory.[41,48,113,114]

All of them present a similar distribution of bands between 280-315 nm, corresponding as before, to the σ-π* transition of the aromatic region, but

they differ with the experiment in solution in the bands identified with the π-π^* transition. This way, for **1**, this band seems to overlap with the ones of higher energy. Instead, **3** shows the same behaviour than in solution, with a broad band shifted to the red region of the spectra at higher wavelengths (lower energies) due to an electronic delocalization by the coordination of the -BF_2, effect that is also observed when some CCMoids were coordinated with paramagnetic metals increasing the polarizability of the molecule.[42,51,112]

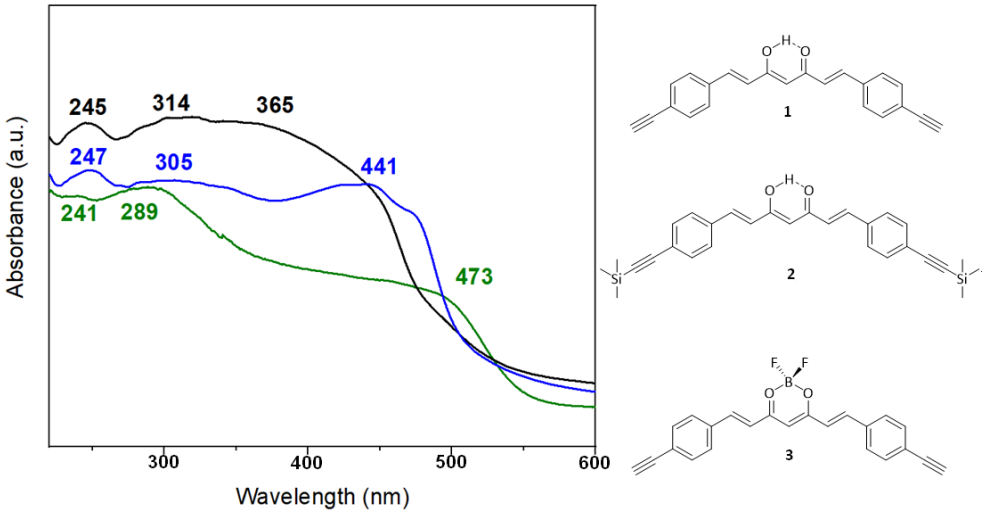

***Figure 35**: Comparative UV-Vis spectrum in solid state (10^{-6} mmol compound/mg KBr) between **1** (black), **2** (blue) and **3** (green).*

As explained above, the calculation of the optical band gap for each molecule was performed in solid state. To do that, Tauc's plot was used as the suitable mathematical tool.[132-134] The absorbance and frequency values obtained from the UV-Vis spectra were used in **Equation 1.1** and the representation of the values using the direct and indirect allowed transitions are showed in

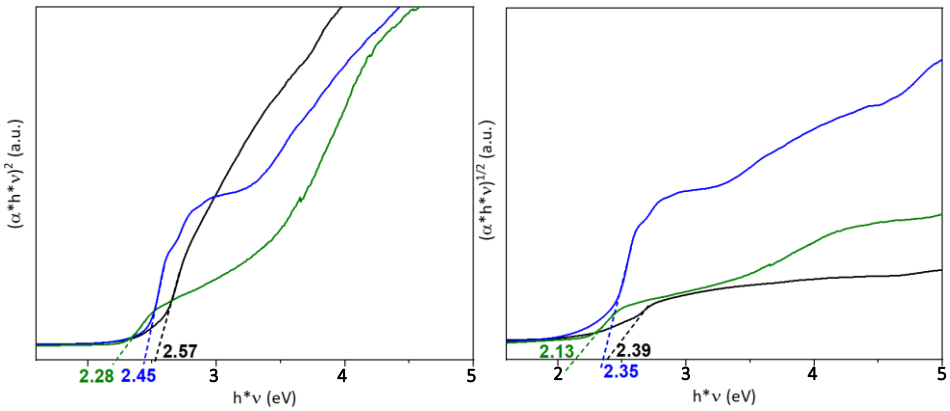

Figure **36**3.

$$(\alpha * h * \nu)^{\frac{1}{n}} = B * (h * \nu - E_g)$$

***Equation 1.1**: Tauc's equation for the direct and indirect transitions of the energy gap calculation.*

Where:

- α = 2.303·Abs/l (absorption coefficient)
- l = sample thickness
- n = ½ for direct transitions and 2 for indirect transitions
- h = Planck's constant

Then, the crossing point between the x-axis and a tangent line made from the curve corresponds to the E_g^{op} value. Table 1.2 shows the average between the direct and indirect allowed transitions values obtained for **1**, **2** and **3**. The optical band gap values agree with other CCMoids in the literature, showing that **1** and **2** display a similar band gap. Instead, **3** possess a lower bandgap, improving a bit the semiconductor character.

***Table 1.2**: Summary of the optical properties of **1**, **2** and **3**. Band gap energies in eV. E_g^{op} stand for the optical energy gap.*

CCMoids	E_g^{op} solid state	Colour of the powder
1	2.48	Brown
2	2.40	Yellow
3	2.20	Red

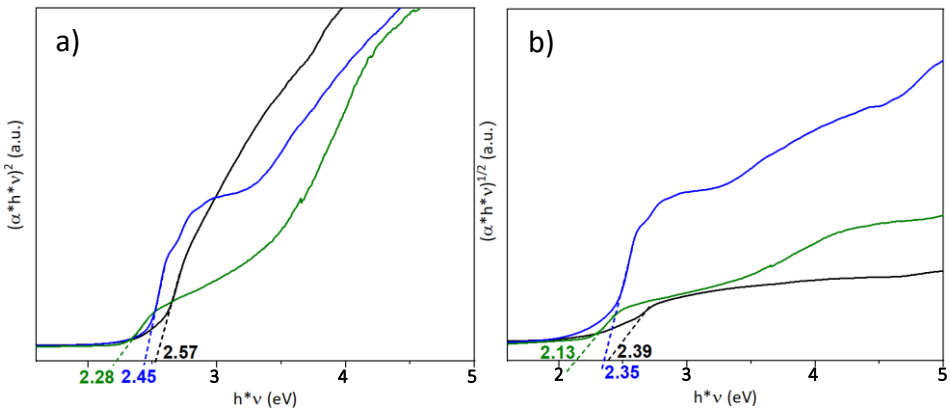

***Figure 36**: Comparative UV-Vis spectrum in solid state using the Tauc's plot of direct transition a) and indirect transition b) representations for the analysis of the optical band gap. **1** (black), **2** (blue) and **3** (green).*

1.3.7. Electrochemistry (Cyclic Voltammetry and Differential Pulse Voltammetry) for CCMoids 1, 2 and 3

The calculation of the optical band gap was compared with the analysis of the electrical band gap (E_g^{ec}), using cyclic voltammetry (CV) and differential pulse voltammetry (DPV). These studies were carried out dissolving the sample with DCM in a concentration of 10^{-3} M, using tetrabutylammonium hexafluorophosphate ($TBAPF_6$) as electrolyte in an inert atmosphere of Ar. The spectra were recorded at 100 mV/s. Figure 374 and Figure **38**5 display the CV and DPV spectra of the three systems, with the corresponding reduction (right) and oxidation (left) pattern.

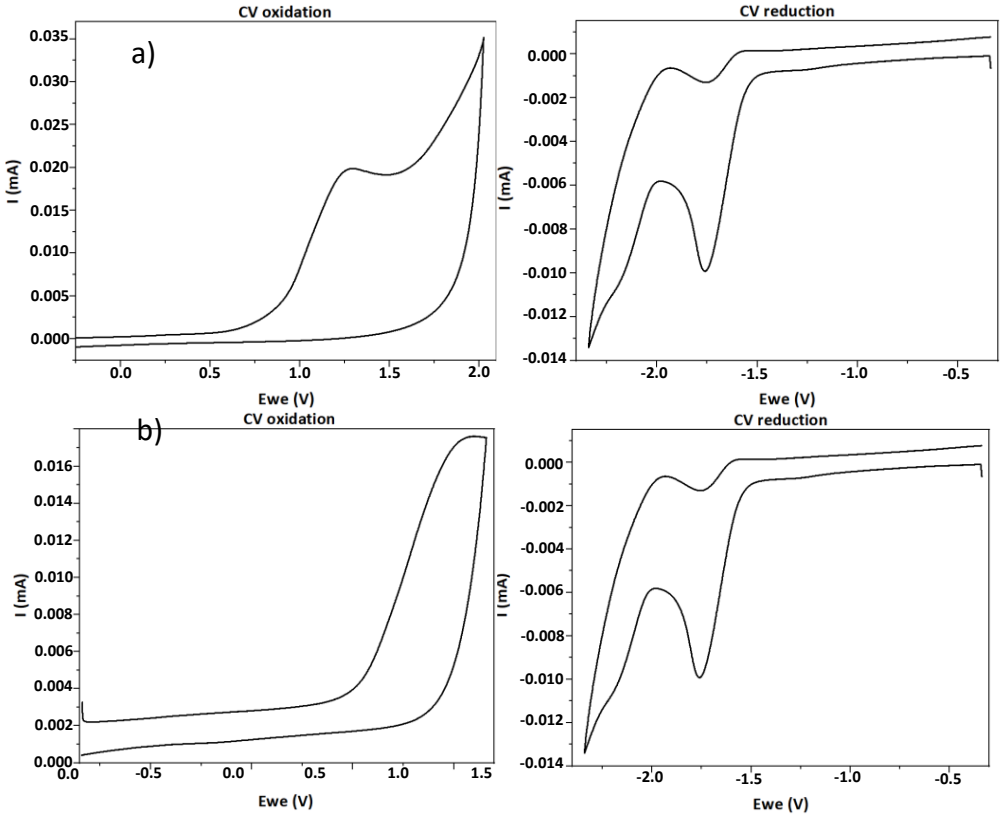

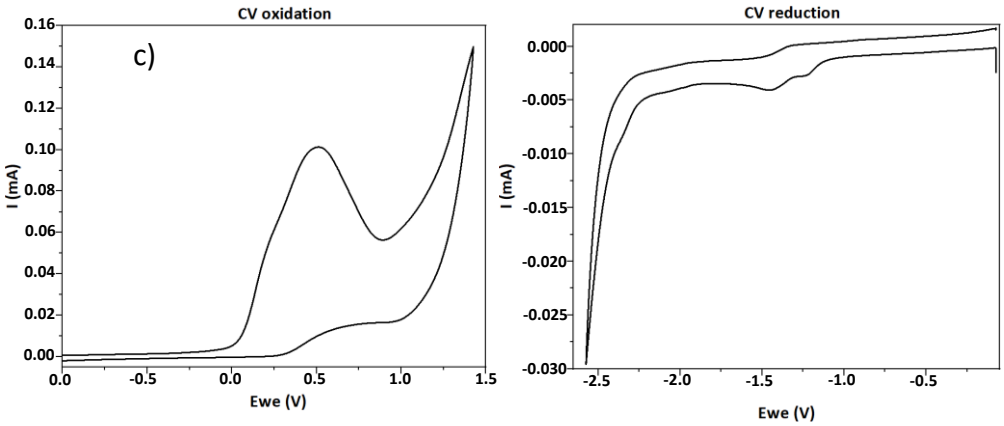

***Figure 374**: Oxidation and reduction cyclic voltammogram spectra of: a) **1**, b) **2** and c) **3**.*

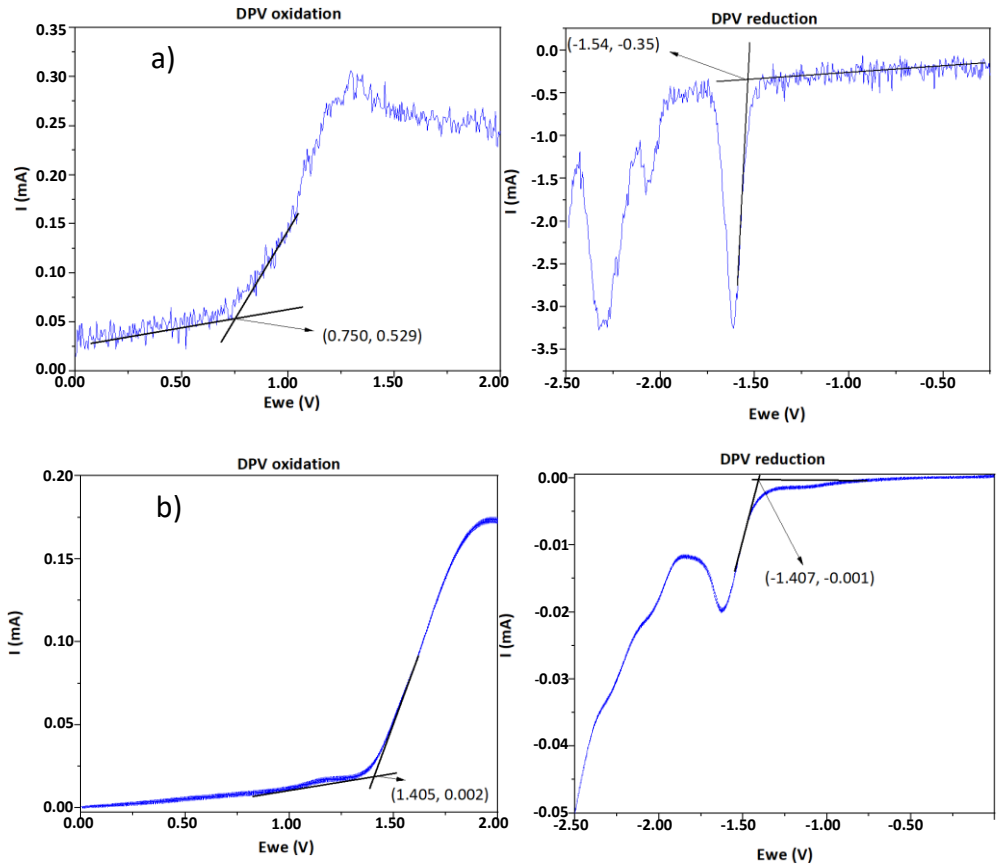

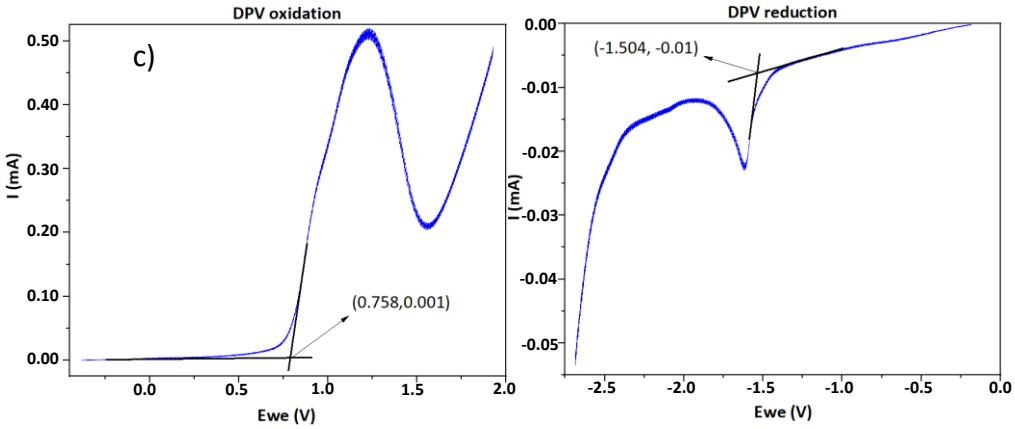

Figure 385**: Oxidation and reduction differential pulse voltammogram spectra of: a) **1**, b) **2** and c) **3

All the systems show oxidation and reduction processes as irreversible bands, in a window between -2.5 and 2.0 V. In this range, a broad oxidation process is always observed, for **1**, **2** and **3**. On the other hand, in the reduction processes the first one is always more intense than the rest. This pattern is typical for most of CCMoids described in the literature.[59] The electrochemical gaps are provided by the difference between the HOMO process (related to the first oxidation observed) and the LUMO process (first reduction process), considering that they rely to the extraction and addition of electrons in the outer molecular orbitals (Equation 1.2 and Equation **1.3**).[51,117,135] For comparative purposes, the values obtained of the HOMO, LUMO, electrochemical and optical band gap energy levels for the three molecules are shown together in Table 1.3 and Figure 396.

***Table 1.3**: Summary of the physical properties of **1**, **2** and **3**. Potential values in V, referenced to Fc/Fc⁺. Band gap energies in eV. Eg^{ec} and Eg^{op} stand for the electrochemical and optical energy gaps, respectively.*

CCMoid	1st Oxid.	1st Red.	E_{HOMO}	E_{LUMO}	E_g^{ec}	E_g^{op}	Colour of the powder
1	0.90	-1.54	-5.70	-3.26	2.44	2.48	Brown
2	0.41	-1.95	-5.21	-2.85	2.36	2.40	Yellow
3	0.76	-1.50	-5.56	-3.30	2.26	2.20	Red

We used **Equation 1.2** to calculate the energy of the HOMO and LUMO vs. the ferrocene molecule under vacuum conditions:

$$E_{HOMO} = -\left((E_{onset})^{(oxid)}\right) + 4.8\ eV$$

$$E_{LUMO} = -\left((E_{onset})^{(red)}\right) + 4.8\ eV$$

***Equation 1.2**: Equations for the calculation of the HOMO and LUMO energy levels.*

The value of 4.8 eV corresponds to the potential of the ferrocene (Fc/Fc^{+}) couple below the vacuum level. Finally, the energy gap is calculated by Equation 1.3:

$$E_g^{ec} = (E_{LUMO}) - (E_{HOMO})\ eV$$

***Equation 1.3**: Calculation of the electrochemical energy band gap.*

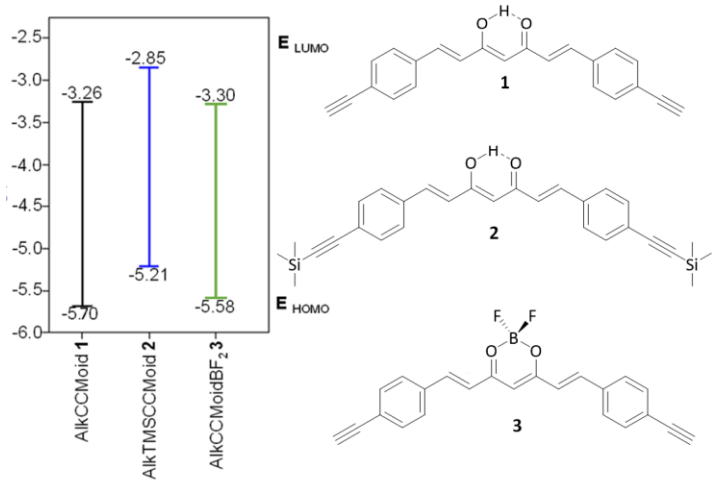

***Figure 39**: HOMO and LUMO energy levels of CCMoids **1**, **2**, and **3**.*

The comparison of the estimated HOMO-LUMO values between the three systems shows that **1** and **3** present a very similar gap and energy displacement but being lower for **3**, conferring the molecule with a more semiconductive behaviour. In contrast, **2** possess a LUMO level higher than the other two, which means that this molecule is less prone to accept electrons than the others.

The energy band gap values assessed from the optical and electrochemical experiments, agreed well and were consistent with other CCMoids in the literature, showing the tree of them a borderline semiconductor-insulator character, and being close to the work function of gold metal (-5.0 eV).[62]

1.3.8. Thermogravimetric analysis (TGA), melting and sublimation analysis for CCMoids 1, 2 and 3

In order to attain information regarding the thermal stability of the samples, thermal analyses were performed. This way, the melting point analysis show at what temperature the molecules undergo a physical change. At 175 ºC system **1** changed its colour from brown to black. A similar behaviour was observed for molecule **2** at the temperature of 220 ºC but not for molecule **3** which did not suffer any change even when the temperature limit of the machine was reached (300 ºC).

Subsequently and to corroborate these results, a thermogravimetric analysis of the three molecules was performed to know at what temperature the molecules undergo a structural change and decompose (Figure A 27-Figure **A 29**). To do the analysis, the molecules were heated up to 800 °C under N_2 with a mass flow rate of 100 mL/min and a heat ramp of 10 °C/min. **1** showed at 207 °C an exothermic peak that could be related to a melting or sublimation point under these conditions. As the melting analysis showed no melting point, this exothermic peak is more likely to be related to a sublimation point. For molecule **2**, an endothermic peak around 225 °C is observed which could be related to several processes like vaporization, crystallization, adsorption or a glass point transition. And for molecule **3**, there is an endothermic peak around 82 °C which again could be related to several processes as mentioned before and an exothermic peak at 225 °C which could be related to a melting, sublimating or adsorption point.

TGA measurements were performed by Sonia Pérez technician of the Institut de Química Avançada de Catalunya (IQAC-CSIC).

Finally, the last thermal analysis performed was the sublimation process using a standard sublimation system, which contains a long Schlenk tube where, at the bottom, the sample is deposited. Then, inside this Schlenk, there is a cold finger container with cold water recirculating inside. The whole system is connected to a vacuum pump through an arm that contains a stopcock adapter and a pressure of 1mbar is applied to the system (Figure 407). Then, for molecule **1**, when the system reached 160 °C the cold finger acquired a yellow tonality and these conditions were maintained for 2 h. After that, the system was cooled down to RT and the solid stacked at the cold finger was analysed by ^{1}H NMR confirming that this solid corresponded to molecule **1**. However, in the case of molecules **2** and **3** no solid was observed in the cold finger, despite reaching 300 °C with the above conditions. Furthermore, the remaining solids in the bottom of the Schlenk tubes were also analysed by ^{1}H

NMR showing that there is a mix of signals indicating decomposition of the samples.

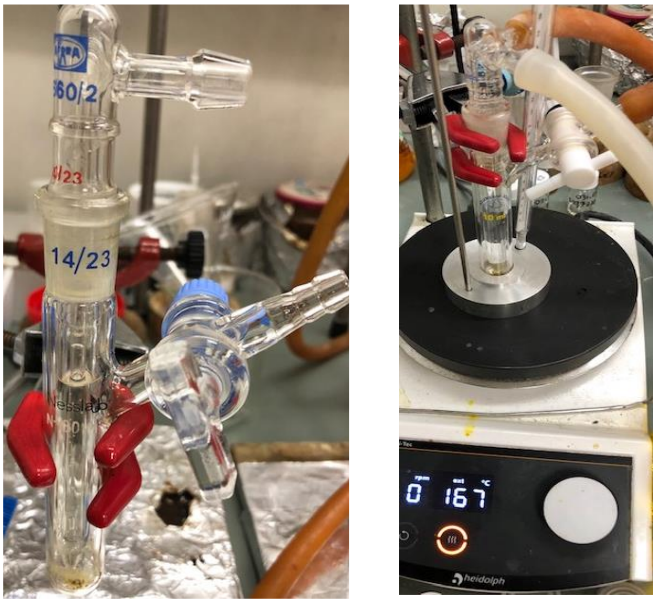

Figure 40*: Image of the standard sublimation system and the sublimation process.*

1.3.9. Deposition of CCMoid 1 on different substrates

Likewise, as already explained before, molecule **1** will be selected as the initial system for the construction of CCMoids with PAHs for their use in Molecular Electronics. For this reason, in the search of a direct method that allow us to estimate the electronic nature of CCMoids on surfaces, taking into account that this molecule is relatively simple, comparing with the ones in the rest of the chapters, and considering that showed a sublimating point relatively low, we decided to perform the deposition of system **1** on Au(111) and Si/SiO_2 surfaces. These surfaces were selected because they will be part of the device, together with the graphene monolayers, of the three-terminal device chosen for the electronic measurements. The handmade system for the sublimation process was designed in our group by Dr. Daniel Herrera (Figure 41, patent pending).[136] The procedure goes by adding microcrystalline powder of **1** (≈ 5 mg) to the bottom of a ground glass vessel, which is coupled to a stopcock adapter connected to a vacuum pump. Inside, a cylinder, acting as a frame, supports the surface to be studied, orienting it towards the solid.

***Figure 41**: Picture of the hand-made sublimator used in the sublimation process and deposition over a surface.*

The experiments were done by, fixing the distance between the solid and the substrate, then, the system was connected to the vacuum (1 mbar) and the vessel heated up on a silicon bath until 160 °C during different periods of time (1 h, 2 h, 6 h and 24 h). Raman spectroscopy and optical microscope (Figure 42 and Figure **43**) were the techniques used to distinguish which were the best conditions for the sublimation process and to determine the morphology and the chemical structural changes. They showed that for periods longer than 6 h, there is a change in the morphology and in the chemical structure of the system; moreover, the solid at the bottom of the sublimator suffer a change of colour from pale to dark brown due to side reactions. This change of colour is accompanied by changes in the solubility of the solid and could be explained with the presence of polymeric species of CCMoid units linked through ethylene bonds, providing amorphous and insoluble materials.[106-108]

However, when the sublimated molecules of **1** after 1 h and 2 h over the two types of substrates (Au(111) and (Si/SiO_2) were compared with the non-sublimated solid, in the Raman spectra, similar results were obtained showing nondestructive deposition of the molecules (Figure 429). In all samples it appears the ν(C≡C-H) at 2100 cm^{-1}, the ν(C=C) and ν(C=O) at 1640 and 1600 cm^{-1}, respectively, from the CCMoid skeleton.[51,123]

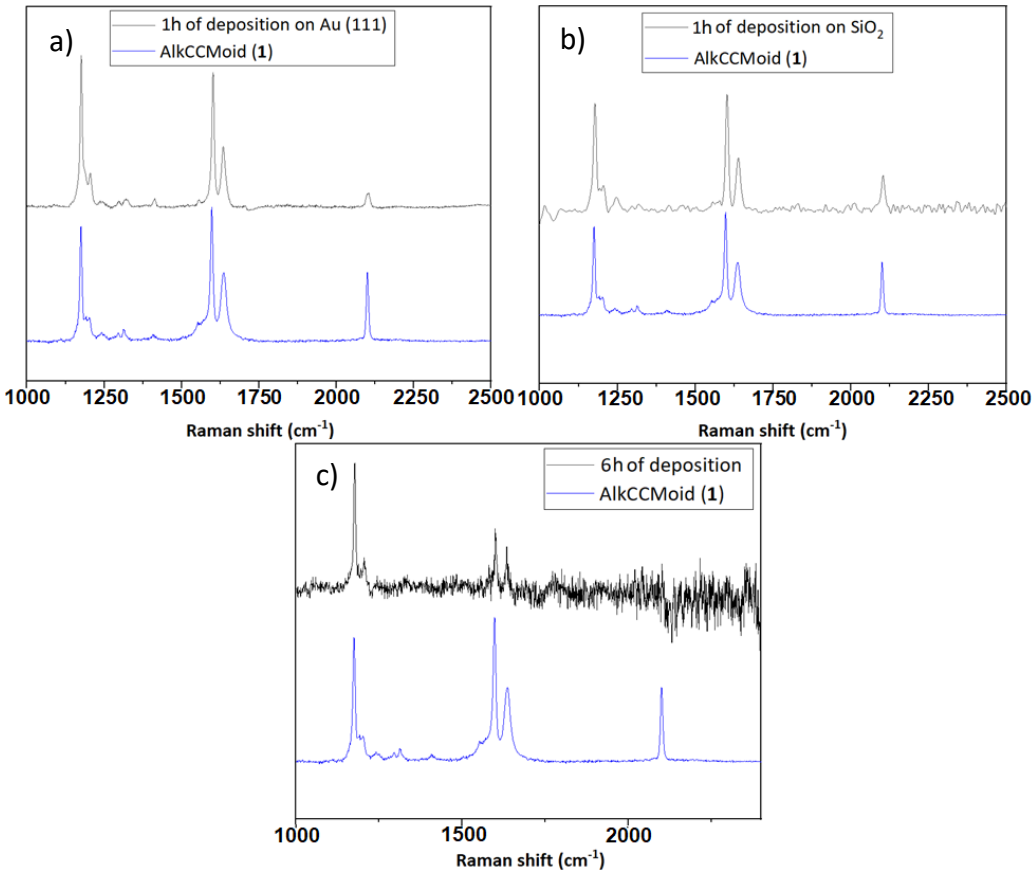

Figure 429: *Comparative Raman spectra between the deposition of **1** (black) and the non-sublimated molecule (blue) over the two types of substrates and the time: a) 1 h of deposition on Au (111) and b) 1 h of deposition on Si/SiO₂ c) 6 h of deposition on Si/SiO₂.*

SEM and optical microscope (Figure 439 and Figure **44**) were also used to assist in the analysis of the morphology and homogeneity of the sublimated material. It can be seen that aggregates of different sizes and shapes are formed on gold substrates, where some of them show a butterfly shape (Figure 43a and Figure **44**a). On the Si/SiO_2 substrate, however, the shapes are present in an elongated prismatic form (Figure 43b and Figure **44**b). Furthermore, in the optical microscope images, on Au (111) (Figure 43a) **1** displays amorphous/round islands with different height and surface area, while, on Si/SiO_2 (Figure 43b), they are disposed in more ordered form, as a pseudo-cuboid microcrystals. In addition, in the last one, fuzzy branched sheet-like structures are observed, which indicates that the molecule tend to nucleate and grow in a different shape in the deposition process depending on the surface.[137]

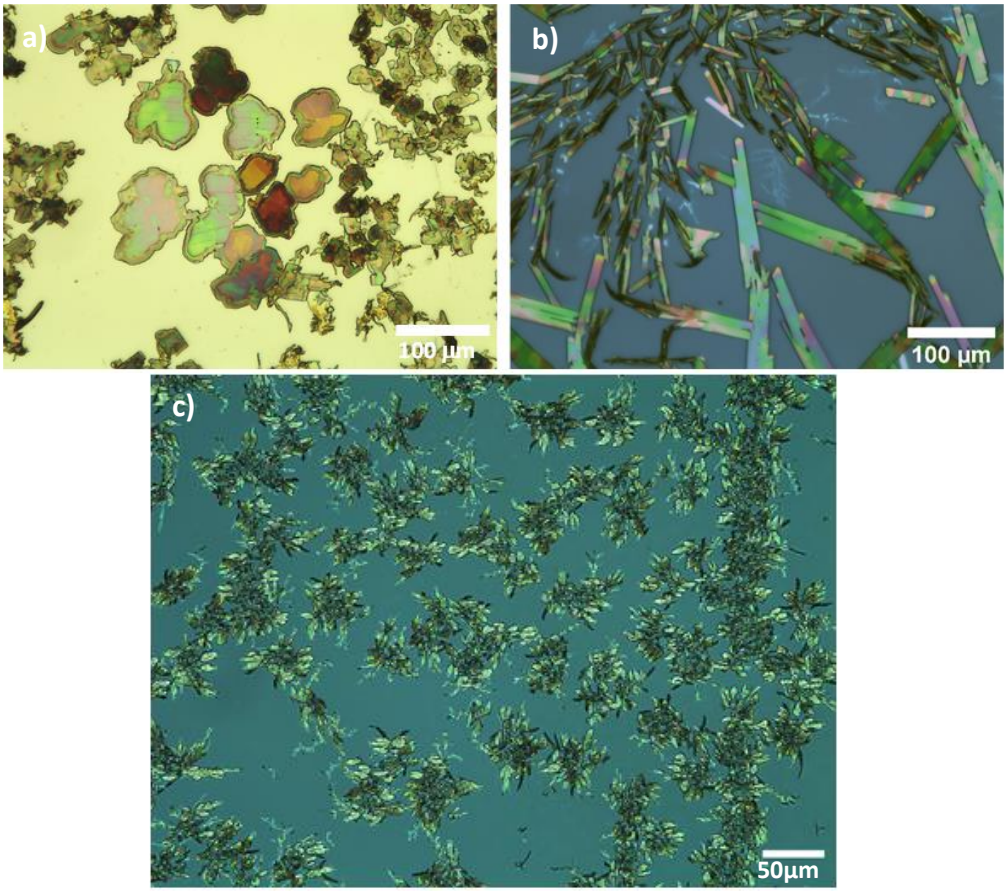

Figure 43: *Optical microscope images of the deposition process of* ***1*** *over a) Au (111) 1h of sublimation, b) Si/SiO_2 1 h of sublimation and c) Si/SiO_2 6 h of sublimation.*

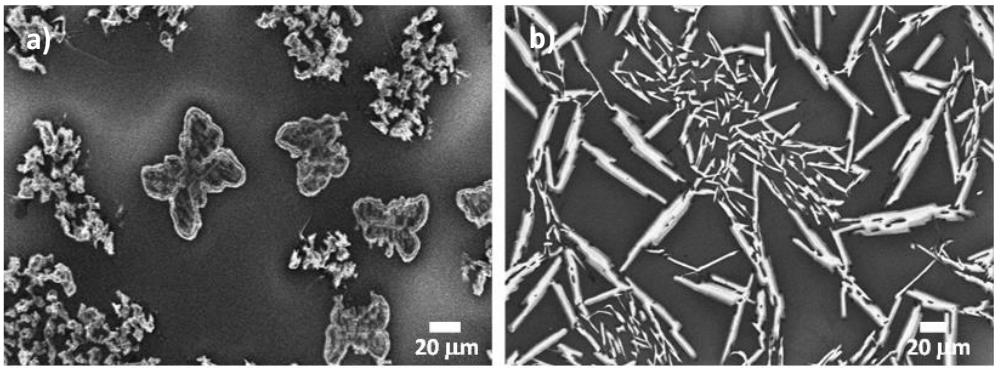

Figure 44*: SEM images of the deposition process of* ***1*** *over a) Au (111) and b) Si/SiO_2.*

AFM was also another technique used to characterize the sublimated system over the surfaces providing a topography that corroborates the formation of crystallites with heights of few hundred of nanometers giving flat facets. AFM

measurements were performed with contact mode using a tapping mode giving images of 20x20 µm with heights between 150-800 nm (Figure 45).

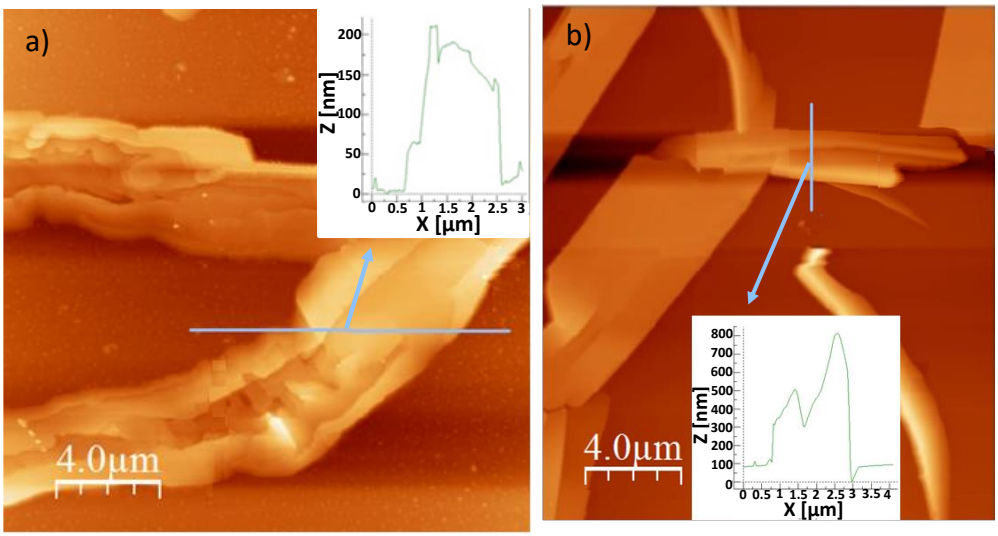

***Figure 45**: AFM images of the deposition of **1** on the two types of substrates: a) Au (111) and b) Si/SiO_2.*

Dr. Rossella Zafino performed Raman, optical miscroscope and SEM measurements. Andrés Gómez, technician at the ICMAB, performed AFM measurements and Dr. Francesco Silvestri performed UHV-AFM from the Physical Chemistry of Surfaces and Interfaces (SURFACES) group from ICMAB.

1.3.10. Deposition on three-terminal hybrid devices and its electrical measurements

To end this study and as mentioned before, **1** was sublimated on a three-terminal hybrid device, fabricated in the group by Dr. Rossella Zaffino, to characterize the electronic behaviour of **1** and to compare with previous UV-Vis absorption and electrochemistry studies. The device was prepared by depositing gold on SiO_2/Si substrates, where gold will act as source and drain electrodes of the system, and Si as a bottom gate electrode (Representation of the device on Figure 462a). Laser lithography was used to produce the pattern of gold thin films over the SiO_2/Si system, after that, metal bilayer of Cr/Au was evaporated over the system and then lift-off process was done. Once the sublimation of **1** was done, it could be observed that the microcrystals do not form a continuous film, but they bridge contacts between micro spacing of the electrodes (Figure 463b).

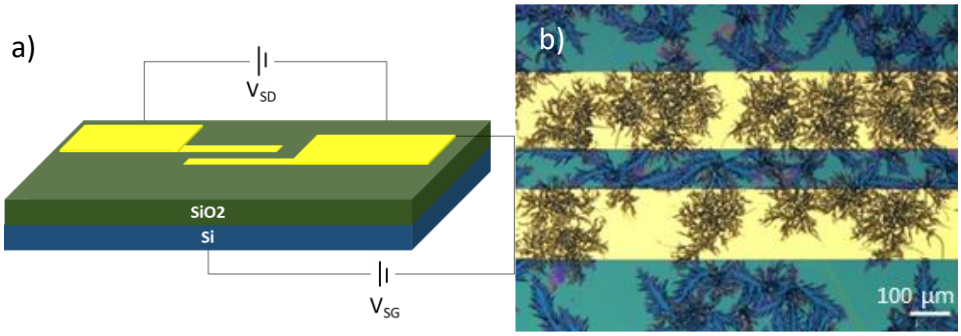

***Figure 463**: a) Picture of the designed electrodes with separation lengths of 40 µm after the sublimation of system **1**, b) Optical microscope image of the gap between the two gold electrodes with the molecule **1** sublimated.*

Then, electrical properties of **1** were measured under direct current (DC) measurements (Figure 474). First, two different conditions of the current-voltage measurements were performed: at ambient conditions and in vacuum (<10^{-5} mbar). From these measurements, it was possible to calculate the resistivity values, using the Equation 1.4:

$$R = \rho \frac{L}{A}$$

***Equation 1.4**: Electrical resistance formula applied for a material.*

Where ρ is the resistivity of the gold, L is the length of the micro-gap and A is the area of the micro-gap covered by the molecules that was estimated by optical pictures using the software ImageJ and where the current goes through. These values, were arranged between 6.5×10^{2} and 2.3×10^{3} Ω·cm.

Furthermore, conductivities values between 1.5×10^{-7} and 2.7×10^{-7} S·cm were given with the Equation 1.5:

$$\sigma = \frac{1}{\rho}$$

***Equation 1.5**: Relationship between conductivity and resistivity.*

These values are associated with an insulator behavior and are in good agreement with the DC conductivity values reported for natural CCMoid films grown on Si substrates.[138]

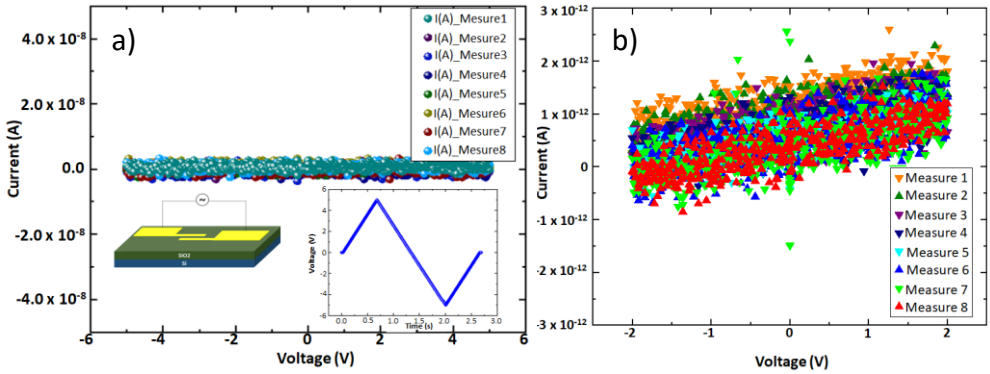

Figure 47: Current-Voltage for each micro-gap of the molecular chip obtained after sublimation measured in: a) air and b) under vacuum.

To be certain of these results, another experiment was done with a single crystal of **1** that was transferred electrostatically to a Si/SiO_2 substrate (Figure 48). This crystal was manually connected to external metallic aluminum electrodes by using graphite ink. Then, Au wires were also connected to the graphite as electrodes and the measurements were performed under vacuum conditions. The setup and experiment were performed in collaboration with Dr. Raphael Pfattner from the Molecular Materials for Electronic Devices (eMolMat) and Dr. Zaffino both at the ICMAB.

The measured current-voltage curves provide a conductivity value of about $(8.50 \pm 0.03)\times10^{-10}$ S/cm, agreeing with the sublimated ones, which means that after sublimation the electrical properties of the material remain unchanged maintaining its insulating nature.

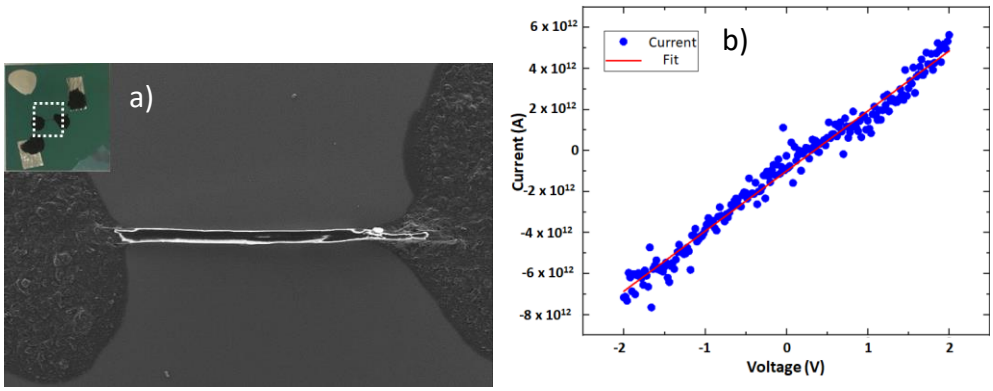

Figure 48: a) SEM image of the crystal embedded between graphite ink electrodes. The inset shows the microscopic picture of one the device incorporating a single crystal. b) The corresponding current-voltage curve measured for this device.

Furthermore, all these results are related to the values obtained from the optical and electrochemical band gap measurements. So, taking into account the electronic characteristic of our compound, the weak communication among molecules and the configuration of our devices, the dielectric properties of the system were measured in detail, to see if they could be used as energy storage of an electrical field energy. For this purpose, to see the time dependence variation, for one week a broadband of dielectric spectroscopy measurements under ambient conditions were performed where a pellet of **1** was loaded into a capacitor cell and sandwiched between the aluminium contacts (Figure 49).

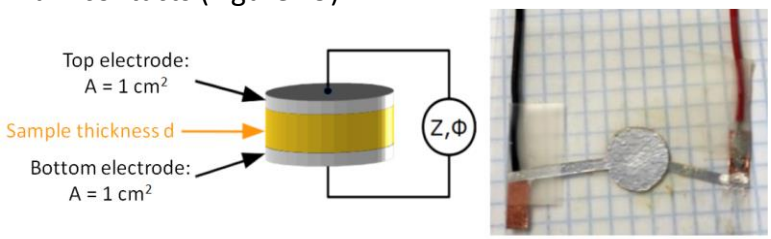

a) b)

***Figure 496**: Broadband dielectric spectroscopy setup. a) Sample geometry and b) optical micrograph with cell dimensions: A = 0.993 ± 0.002 cm² and d sample thickness.*

From these measurements it was demonstrated that **1** is highly stable at ambient conditions and that the values obtained are in good agreement with literature data found for small, conjugated molecules.[139] After that, the temperature dependence was also measured after heating at temperatures ranging from 15 °C to 55 °C showing only small and reversible variations of the conductivity and an irreversible increase of the permittivity which means that the insulating behaviour of **1** is not greatly affected by temperature (Figure 507).[39]

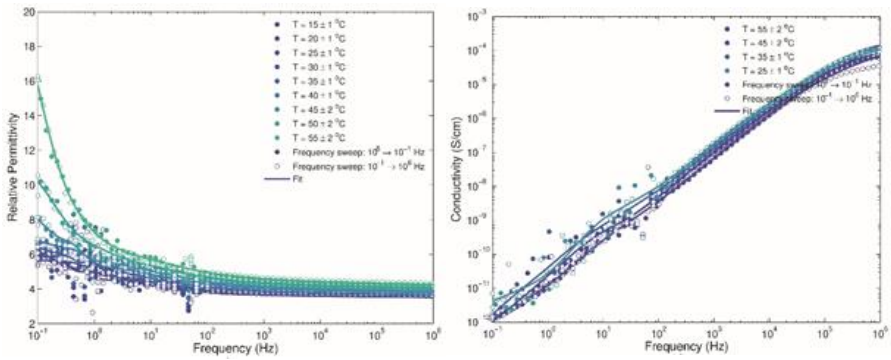

a) b)

***Figure 507**: Broadband dielectric spectroscopy. Permittivity and Conductivity evolution upon: a) heating and b) cooling.*

This irreversible increase in permittivity can be related to a structural change in the supramolecular morphology of **1**. In order to confirm this hypothesis, XRD analysis of the powder sample before and after the heating/cooling treatment was performed and showed that the annealed sample maintains the same pattern (Figure 518). Nevertheless, additional broad peaks with poor signal-to-noise ratio appeared, which reinforces the idea of structural changes affecting the permittivity parameter. Then, DFT theoretical calculations were performed in collaboration with Prof. Eliseo Ruiz of the University of Barcelona obtaining different polymorphs depending on the treatment of **1**: single crystal, microcrystalline powder or sublimated material. Moreover, the calculations explained how the microcrystalline powder could be converted to the polymorph found in the small broad signals of the XRD, which can also confirm the changes observed in the permittivity after heating at 55 °C.

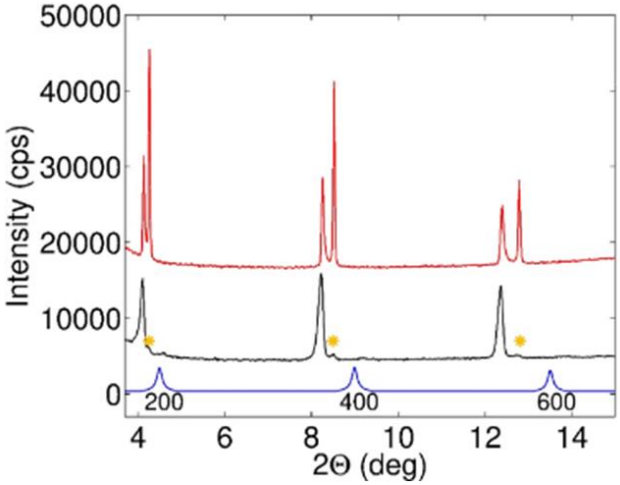

***Figure 518**: XRD spectra of **1** in a) in single crystal (blue), b) microcrystalline powder (black) and sublimated material (red) deposited on Si/SiO₂.*

1.4 CONCLUSIONS

Two methodologies were performed for the obtention of CCMoid **1**: The first one with a straightforward one step reaction with a yield of 36% and the second one with a two-step reaction obtaining a 32% yield.

The modifications in the different parts of **1** (arms with **2** and head with **3**) have showed some slight variations in the optical and electrical properties of the molecule changing the distance of the HOMO and LUMO (E_g) towards lower levels for **2** and a bigger change for **3**.

Thanks to the sublimation process CCMoid **1** can produce, under reproducible conditions, thin and stable aggregates on substrates (Au (111) and Si/SiO_2) in relatively short period of time (<60 minutes). AFM, SEM, optical microscope, and Raman spectroscopy confirmed the stability of **1** after the sublimation process. This sublimation process was also applied over a three-terminal hybrid device and electrical measurements at ambient conditions and in vacuum ($<10^{-5}$ mbar), corroborates that, after sublimation, the electrical properties of the material remain unchanged, and it has an insulator behaviour giving a similar conductivity and resistivity values for both sublimated and single crystal molecules.

As the compound had insulator properties, dielectric measurements of the device system were performed founding that no significant variations of the conductivity with either low or high frequencies. However, at low frequencies, a decrease in the relative permittivity was found, which could be explained by variations of the relative humidity. Furthermore, no temperature dependence was obtained after experiments heating from 15 ˚C to 55 ˚C showed only small and reversible variations of the conductivity values and an irreversible increase of the permittivity. These results assist in the reading of the electronic properties of CCMoid molecules further than the values obtained from the optical and electrochemical band gap measurements.

Finally, the irreversible increase in permittivity was demonstrated to be related to a structural change in the supramolecular morphology of **1** by XRD analysis and DFT theoretical calculations.

1.5 EXPERIMENTAL SECTION

1.5.1. Measurements

Single crystal X-ray diffraction data for **1** were collected at the XALOC beamline 13 of Alba-CELLS Synchrotron (Spain). Data for **1** using a Bruker D8 Venture diffractometer at 293 K (λ = 0.72932 Å). The simulated powder patterns were calculated from the single crystal crystallographic data using Mercury 3.7 software.

Fourier transform infrared (FTIR) spectra were obtained using an FT-IR JASCO 4700LE using the ATR (attenuated total reflectance) accessory in the range between 500 and 4000 cm^{-1}, 2 mg of the powdered samples were deposited covering the crystal of the ATR accessory and pressed with the pressure tip.

Elemental analyses were carried out using a PerkinElmer 2400 series II analyzer.

^{1}H-NMR and ^{13}C-NMR spectra were obtained on a Bruker Advanced at 300 MHz and 298 K.

Thermogravimetric analysis was performed under a N_2 atmosphere from r.t. to 1000 °C at a heating rate of 10 °$Cmin^{-1}$, using a simultaneous thermogravimetric analysis (TG)-differential scanning calorimetry/differential thermal analysis (heat flow DSC /DTA) system NETZSCH-STA 449 F1 Jupiter.

MALDI-TOF mass spectra were recorded with an ULTRAFLEXTREME mass spectrometer (Bruker) at Servei de Proteòmica i Biologia Estructural (SePBioEs) from UAB.

UV/Vis absorption spectra of liquid samples were obtained with a Varian Cary 780 spectrometer by using quartz cells with operating range of 200–600 nm, mainly in reflectance or transmittance mode. For solid samples the Diffuse Reflectance Sphere DRA-2500 accessory of a Varian Cary 780 UV/Vis/NIR spectrophotometer was used with operating range of 200–700 nm, mainly in reflectance or transmittance mode.

Raman scattering spectra were measured on a XploraTM Plus system from Horiba Scientific model with a solid-state laser, emitting at 785 nm wavelength. The laser power at the sample was about 10% of 5 mW.

SEM images of molecules sublimated on different surfaces were obtained with a Zeiss Auriga 40 Field Emission microscope at an acceleration voltage of 2kV and a working distance below 4 mm without metallization of the samples.

The DC electrical characterization of three-terminal devices with sublimated molecules was carried out in a Probe Station by Lakeshore at ambient condition and under vacuum by using two system measurement units (SMU) 2450 from Keithley and a home-made python routine. Resistance measurements were done recording 2 probes current-voltage characteristics applying back and forward voltage sweeps in the range between ±1V. The electrical characterization of the FET was performed under vacuum and applying gate-source voltage V_{GS} between ±40V to the bottom Si acting as a gate electrode. Temperature sweeps were carried out employing a *Peltier* element which was connected to a PID temperature controller for temperature stabilization.

1.5.2. Materials

Acetylacetonate ($C_5H_7O_2$, acac), boron trioxide (B_2O_3), tributyl borate ($(BuO)_3B$, $C_{12}H_{27}BO_3$), *n*-butyl amine (n-$BuNH_2$, $C_4H_{11}N$), ethynyl benzaldehyde ($HC{\equiv}CC_6H_4CHO$), 4-[(Trimethylsilyl)ethynyl] benzaldehyde ($(CH_3)_3SiC{\equiv}CC_6H_4CHO$), potassium carbonate ($K_2CO_3$), boron trifluoride diethyl etherate ($BF_3{\cdot}OEt_2$) were provided by Sigma Aldrich and Fluorochem. Ethyl acetate (EtOAc), methanol (MeOH), and acetonitrile (MeCN) were supplied by Carlo Erba. Dicloromethane (DCM) was provided by ChemLab. Deuterium chloroform ($CDCl_3$) was provided by Eurisotop. Double polished n-type Si (100) wafers covered with a variable thickness of SiO_2 were obtained from the Institute of Microelectronic of Barcelona (IMB-CNM).

1.5.3. Synthesis of 1. AlkCCMoid (1*E*,4*Z*,6*E*)-1,7-bis(4-ethynylphenyl)-5-hydroxyhepta-1,4,6-trien-3-one

Two synthesis routes (A and B) were used to obtain this molecule.

(A) 200 mg (2 mmol) of acac and 100 mg of B_2O_3 (0.7 eq, 1.4 mmol) were solubilized in 2 mL of EtOAc. The mixture was stirred and heated at 50 °C for 1 hour. Then 1.1 mL (4 mmol) of $(BuO)_3B$ was added, followed by the addition of a solution of 809 mg of 1-ethylbenzaldehyde (4 mmol) in 2 mL of EtOAc. The reaction was stirred at 50 °C for two hours and then cooled to RT Next, a

solution of n-$BuNH_2$ (100 µL, 1 mmol) in EtOAc (1.3 mL) was added dropwise and the reaction was stirred at r.t. for two days. TLC was used to monitor the progress the reaction (Hexane/EtOAc: 95/5, Rf: 0.25). Finally, an HCl aqueous solution (0.1 M) was added to the solution and the mixture was stirred at 40 ^{o}C for 1 h. The resulting precipitate was filtered and washed with cold MeOH. Recrystallisation was achieved by dissolving the solid in MeCN and leaving the solution in the refrigerator at 0 °C. **1** was obtained as a brown powder in 36% yield. ^{1}H NMR (δ in ppm, 360 MHz, $CDCl_3$): 15.83 (s, 1H), 7.64 (d, $^{3}J_{HH}$ = 15.8 Hz, 2H), 7.51 (s, 8H), 6.63 (d, $^{3}J_{HH}$ = 15.8 Hz, 2H), 5.85 (s, 1H), 3.20 (s, 2H). ^{13}C{^{1}H} NMR (δ in ppm, 90 MHz, $CDCl_3$): 183.2, 139.8, 135.4, 132.8 128.1, 125.1, 123.9, 102.5, 83.4 and 79.5. ATR-FTIR (cm^{-1}): 3273 (ν:≡C-H), 3033 (ν:=C-H and ν_{ar}:C-H), 2958-2929 (ν:-C-H), 2162 (ν:-C≡C-), 1698 (ν:C=O *keto-enol*), 1629 (ν:C=O *keto-enol*, with intermolecular H-bonds), 1495 (ν_{ar}:C-C, skeleton vibrations), 1136 ($\delta_{ip\ ar}$:C-H), 974 (δ:CH) 822 (ν_{ar}:C-H ρ-disubstituted and δ_{oop}: CH) and 623 (δ:≡C-H). MS MALDI-TOF (m/z): calc. for $C_{23}H_{16}O_2$[M]: 324.11; found[M-1]$^{-}$: 322.94. Elemental analysis calculated for **1**·2MeCN ($C_{27}H_{22}N_2O_2$): C, 79.78; H, 5.46. Found: C, 79.35; H, 5.08.

(B). The second synthetic route is based on the preparation of the TMS-protected analog CCMoid **2** followed by the deprotection in basic media. 200 mg of **2** (2 mmol) and 590 mg of K_2CO_3 (20 mmol) were solubilized in 45 mL of MeOH and the mixture was stirred at RT. overnight. Then, an aqueous HCl solution (0.1 M) was added, and the resulting solution was concentrated at the rotary evaporator. The final system was extracted with DCM and washed three times with 10 mL brine. System **1** was obtained without further purification as a brown powder in 70% yield.

1.5.4. Synthesis of 2. AlkTMSCCMoid (1*E*,4*Z*,6*E*)-5-hydroxy-1,7-bis({4-[2-(trimethylsilyl)ethynyl]phenyl})hepta-1,4,6-trien-3-one

200 mg (2 mmol) of acac and 100 mg of B_2O_3 (0.7 eq, 1.4 mmol) were solubilized in 2 mL of EtOAc. The mixture was stirred and heated at 50 °C for 1 h. Then 1.1 mL (4 mmol) of $(BuO)_3B$ was added, followed by the addition of a solution of 809 mg of 4-[(trimethylsilyl)ethynyl] benzaldehyde (4 mmol) in 2 mL of EtOAc. The reaction was stirred at 50 °C for two hours and then cooled to RT. Next, a solution of n-$BuNH_2$ (100 µL, 1 mmol) in EtOAc (1.3 mL) was added dropwise and the reaction was stirred at r.t. for two days. TLC was used to monitor the progress of the reaction (Hexane/EtOAc: 95/5, Rf: 0.25). Finally, an aqueous HCl solution (0.1 M) was added to the solution and the mixture was left stirring at 40 ^{o}C for 1 h. The resulting precipitate was filtered

and washed with cold MeOH. Recrystallisation was achieved by dissolving the solid in MeCN and leaving the solution in the refrigerator at 0 ºC. **2** was obtained as a yellow powder in 45% yield. ^{1}H-NMR (ppm, 360 MHz, $CDCl_3$) δ 15.84 (s, 1H), 7.65-7.59 (d, $^{3}J_{HH}$ = 15.8 Hz, 2H), 7.48 (s, 8H), 6.65-6.59 (d, $^{3}J_{HH}$ = 15.8 Hz, 2H), 5.83 (s, 1H), 0.27 (s, 9H). $^{13}C\{^{1}H\}$ NMR (ppm, 90 MHz, $CDCl_3$) δ 183.2, δ 139.9, δ 136.1, δ 132.6, δ 128.0, δ 124.9, δ 124.9, δ 104.8, δ 102.4, δ 97.0 and δ 0.1. ATR-FTIR data (cm^{-1})**:** 2956 (ν:-C-H), 2149 (ν:-C≡C-), 1649 (ν:C=O *keto-enol* form, with intermolecular H bonds), 1501 (ν_{ar}:C-C, skeleton vibrations), 1135 ($\delta_{ip\ ar}$:C-H), 972 (δ_{oop}:CH) and 831 (ν_{ar}:C-H ρ-disubstituted and δ_{oop}:CH). MS MALDI-TOF (m/z): calc. For $C_{29}H_{32}O_2Si_2$[M]: 468.19; found $[M-1]^-$: 466.84. Elemental analysis calculated for **2**·MeCN ($C_{31}H_{35}N_1O_2Si_2$): C, 73.04; H, 6.92. Found; C, 73.15; H, 6.66.

1.5.5. Synthesis of 3. AlkCCMoidBF$_2$ 4,6-bis[(1*E*)-2-(4-ethynylphenyl)ethenyl]-2,2-difluoro-2H-1lambda3,3,2lambda4-dioxaborinine.

50 mg (0.15 mmol) of acac and 30 μL of $BF_3{\cdot}OEt_2$ (1.4 eq, 0.2 mmol) were solubilized in 1.5 mL of DCM. The mixture was heated with the microwave in a dynamic program of 50 °C for 10 min at 600 rpm. TLC was used to monitor the progress the reaction (hexane/EtOAc: 8/2, Rf: 0.28). Finally, the reaction was cooled down to RT, the solid obtained was filter and washed with Et_2O and hexane. **3** was obtained as a red powder in 93.6 % yield. ^{1}H NMR (360 MHz, CDCl3) δ=8.04 (d, $^{3}J_{HH}$ = 15.6 Hz, 2H), 7.56 (q, $^{3}J_{HH}$ = 8.43 Hz, 8H), 6.74 (d, $^{3}J_{HH}$ = 15.6 Hz, 2H), 6.12 (s, 1H), 3.27 (s, 2H). $^{13}C\{^{1}H\}$ (ppm, 90 MHz, $CDCl_3$) δ179. 8, 146.6, δ134.3, δ133.0, δ129.1, δ125.8, δ121.5, δ102.3, δ83.1, δ80.7 and δ0.1. ATR-FTIR data (cm^{-1})**:** 3276 (ν:≡C-H), 1624 (ν:C=O *keto-enol* form, with intermolecular H bonds), 1524 (ν_{ar}:C-C, skeleton vibrations), 1393 (ν:B-O), 824 (ν_{ar}:C-H ρ-disubstituted and δ_{oop}: CH), 652 (δ:≡C-H). MS MALDI-TOF (m/z): calc. for $C_{23}H_{15}BF_2O_2$[M]: 372.11; found $[M-1]^-$: 371.87. Elemental analysis calculated for **3**·DCM ($C_{24}H_{15}BF_2O_2Cl_2$): C, 64.01; H, 3.65. Found; C, 64.59; H, 3.82.

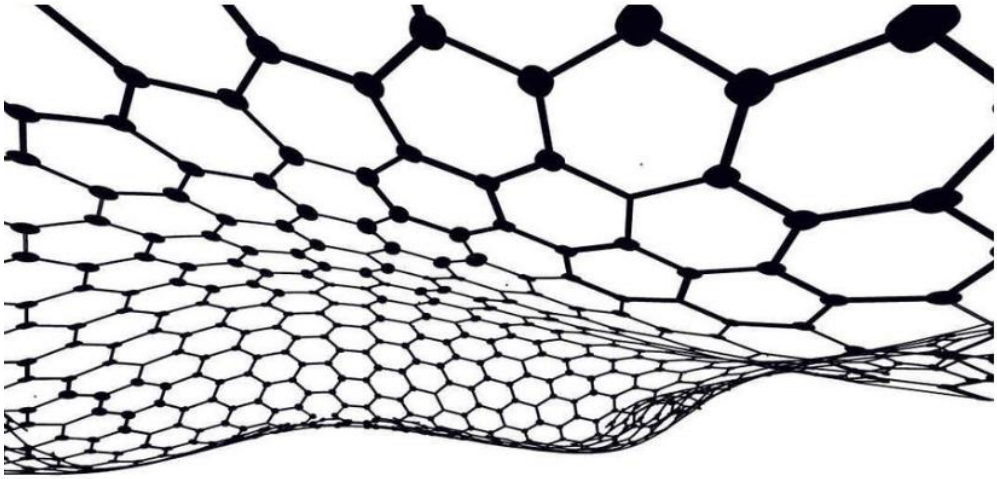

APPENDIX I

APPENDIX I. SUPPLEMENTARY FIGURES

^{1}H NMR spectra

^{1}H NMR (360 MHz, $CDCl_3$) δ=15.81 (s, 1H), δ=7.64 (d, $^3J_{HH}$ = 15.8 Hz, 2H), δ=7.51 (s, 8H), δ=6.63 (d, $^3J_{HH}$ = 15.8 Hz, 2H), δ=5.85 (s, 1H), δ=3.20 (s, 2H).

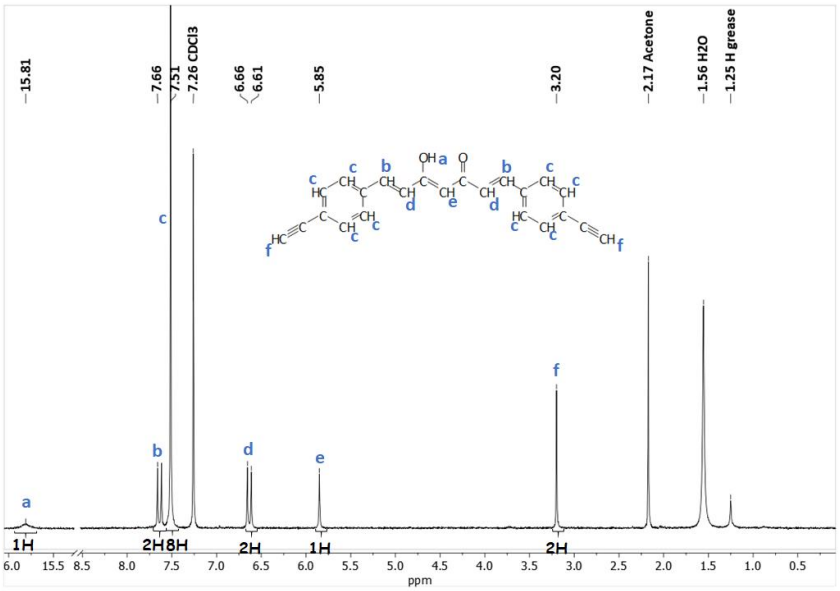

*Figure A 1.1: ^{1}H RMN spectrum of AlkCCMoid **1**.*

^{1}H NMR (360 MHz, $CDCl_3$) δ=15.82 (s, 1H), δ=7.63 (d, $^3J_{HH}$ = 15.7 Hz, 2H), 7.47 (s, 8H), 6.62 (d, $^3J_{HH}$ = 15.8 Hz, 2H), 5.83 (s, 1H), 0.26 (s, 18H).

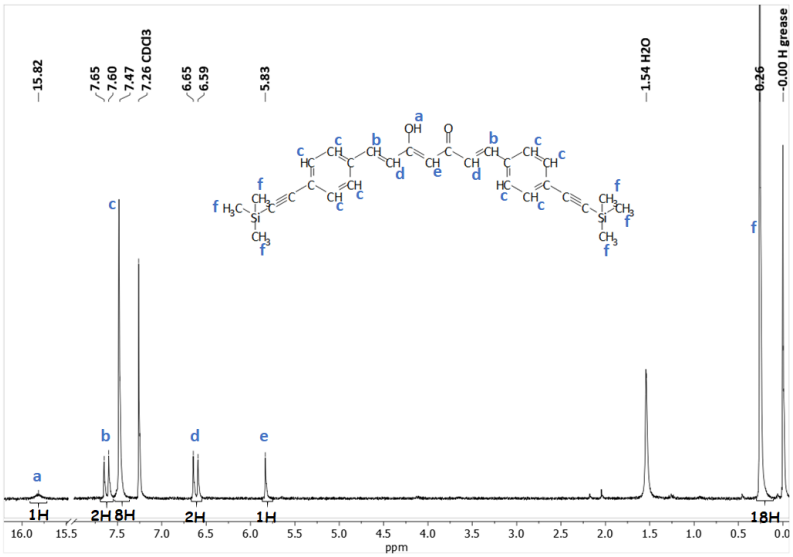

*Figure A 1.2: ^{1}H RMN spectrum of AlkTMSCCMoid **2**.*

^{1}H NMR (360 MHz, $CDCl_3$) δ=8.04 (d, $^{3}J_{HH}$ = 15.6 Hz, 2H), 7.56 (q, $^{3}J_{HH}$ = 8.43 Hz, 8H), 6.74 (d, $^{3}J_{HH}$ = 15.6 Hz, 2H), 6.12 (s, 1H), 3.27 (s, 2H).

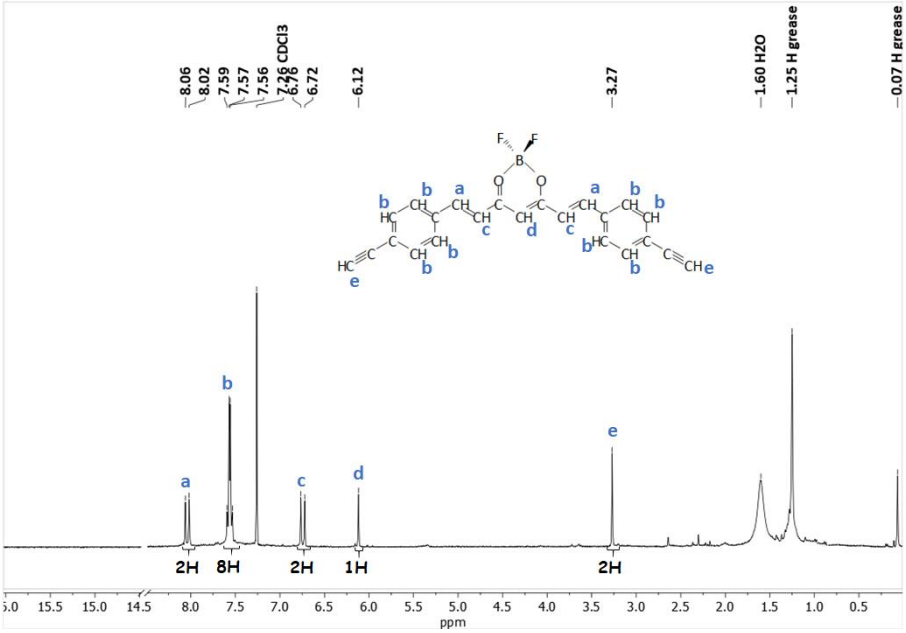

*Figure A 1.3: ^{1}H RMN spectrum of AlkCCMoidBF$_2$ **3**.*

^{13}C{^{1}H}-NMR spectra

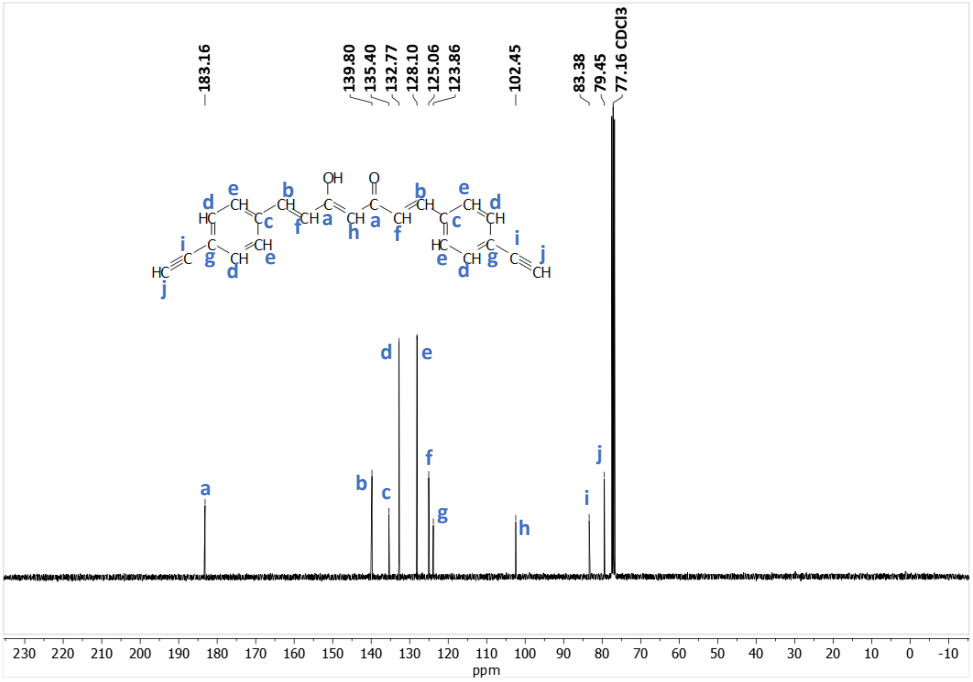

*Figure A 4: ^{13}C RMN spectrum of AlkCCMoid **1**.*

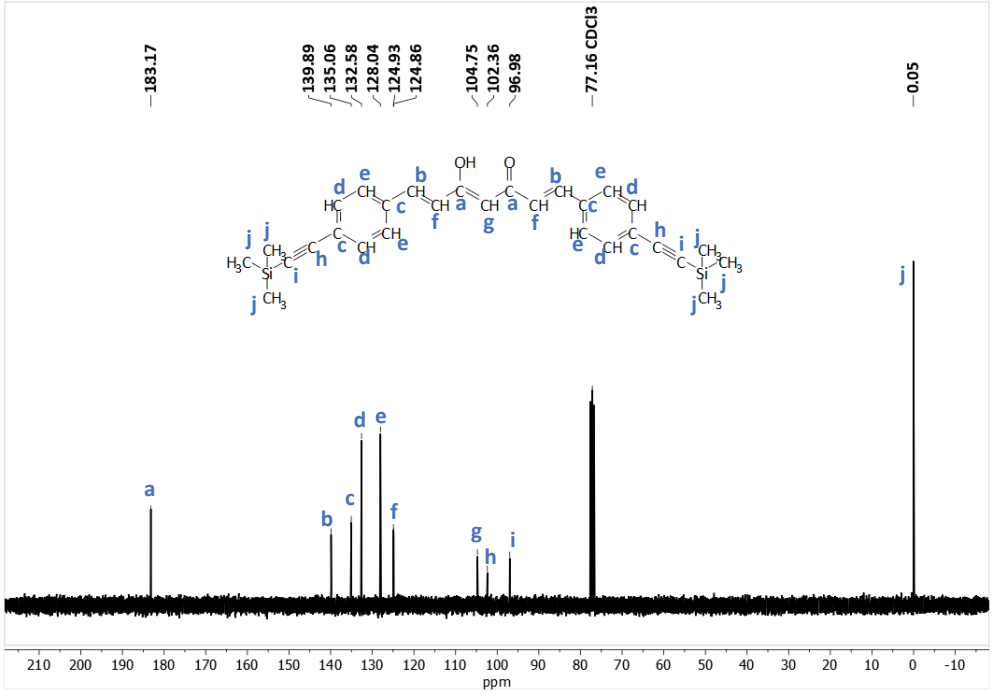

***Figure A 5**: ^{13}C RMN spectrum of AlkTMSCCMoid **2**.*

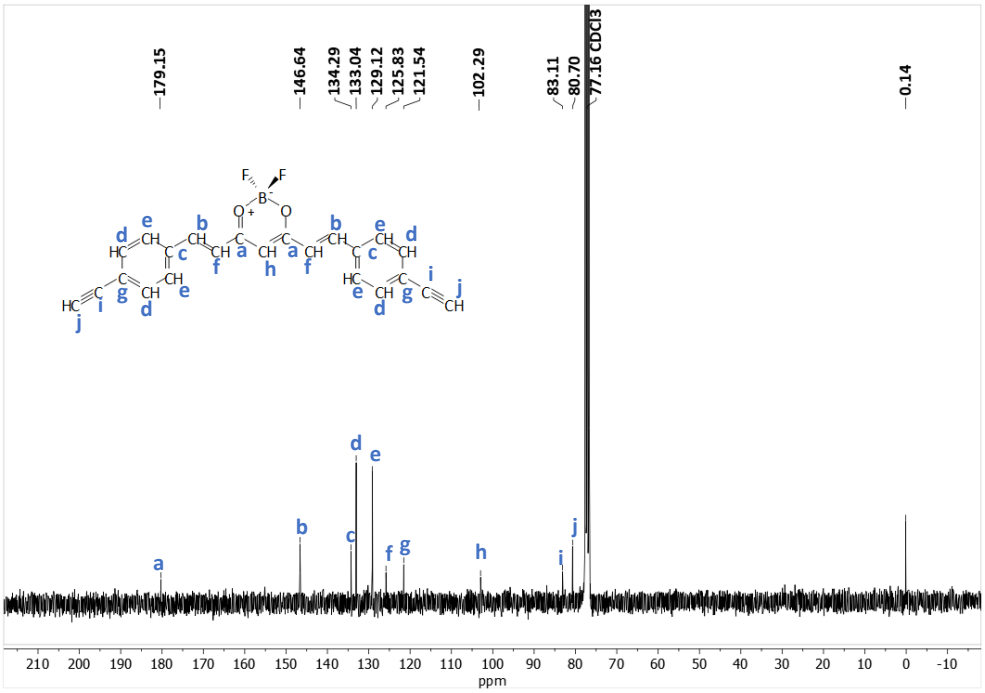

***Figure A 6**: ^{13}C RMN spectrum of AlkCCMoidBF$_2$ **3**.*

ATR-FTIR spectra

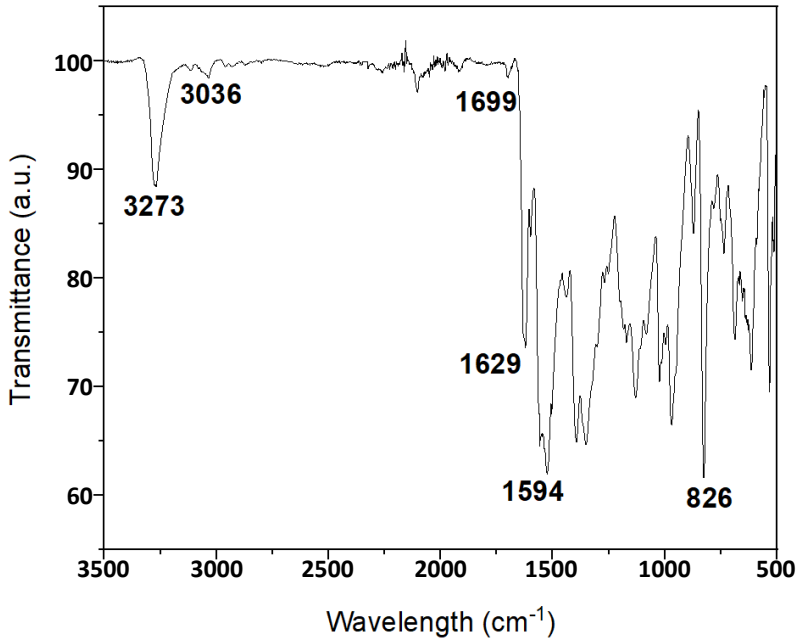

Figure A 7: *ATR-FTIR spectrum of AlkCCMoid **1**.*

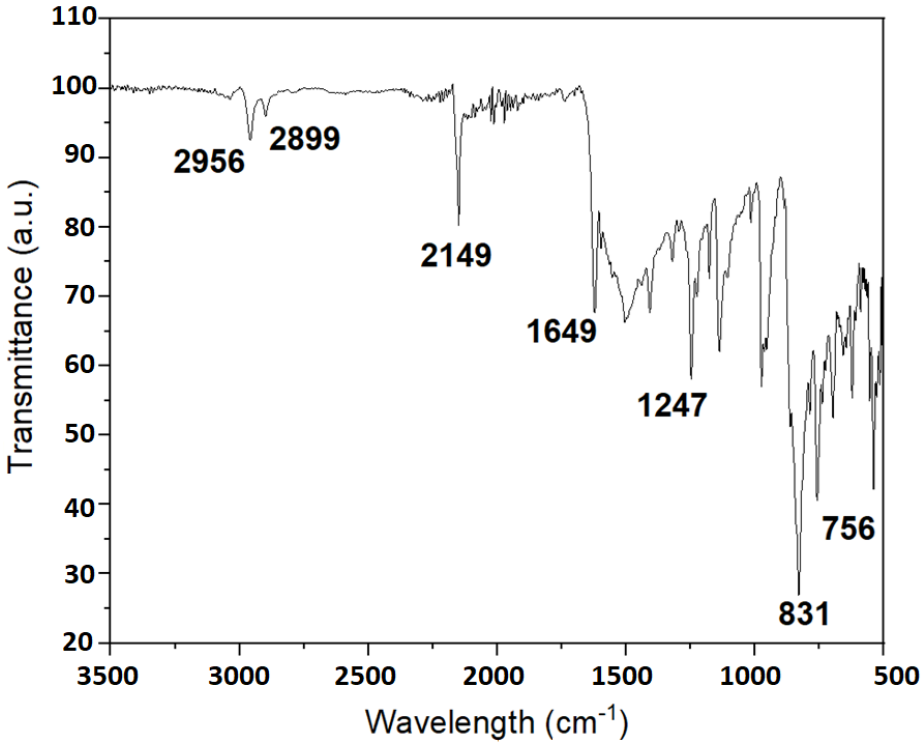

Figure A 1.8*: ATR-FTIR spectrum of AlkTMSCCMoid **2**.*

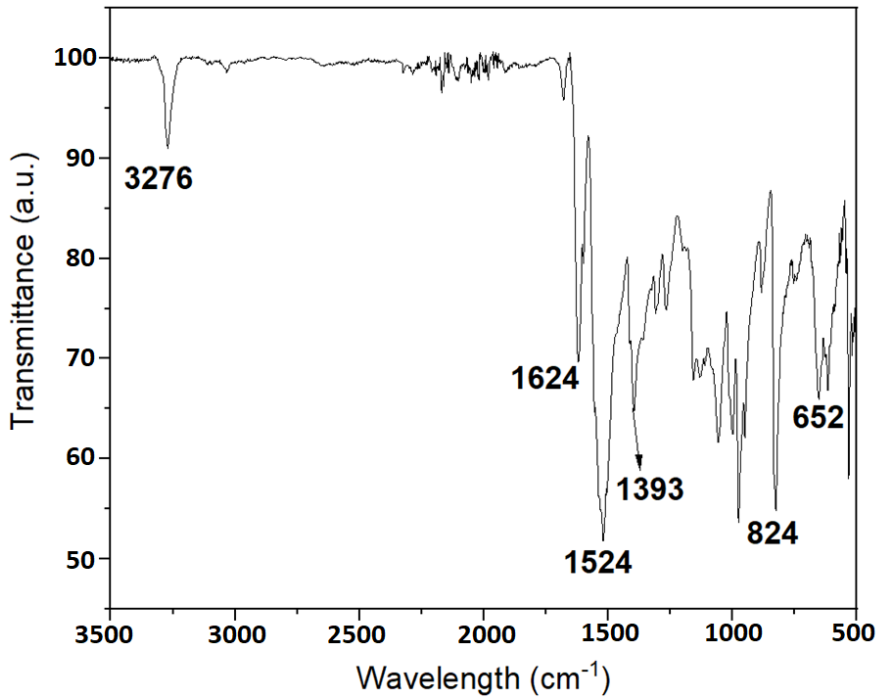

***Figure A 8**: ATR-FTIR spectrum of AlkCCMoidBF$_2$ **3**.*

Raman spectra

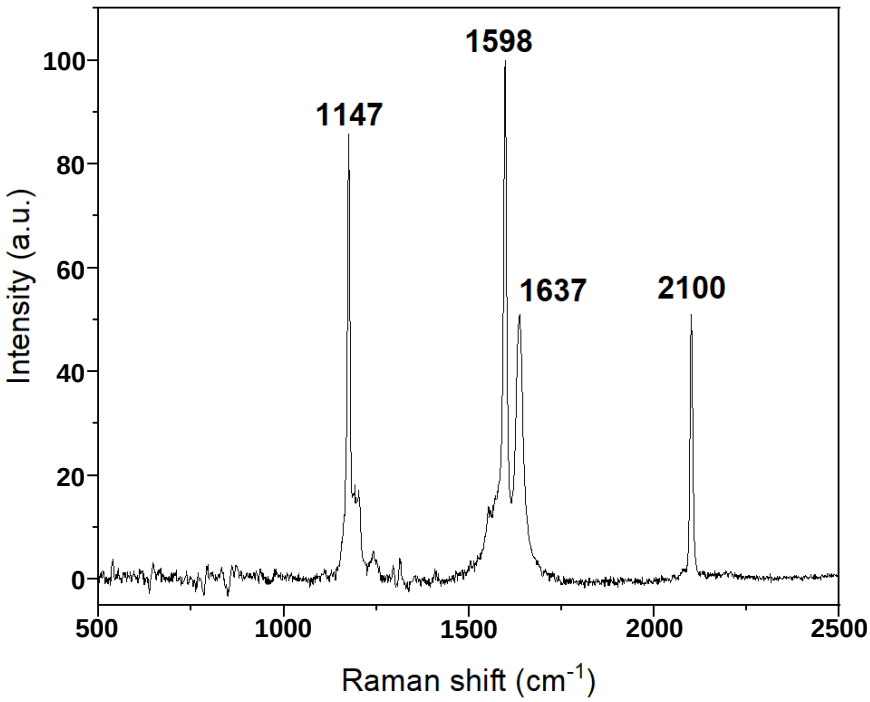

***Figure A 910**: Raman spectrum of AlkCCMoid **1**.*

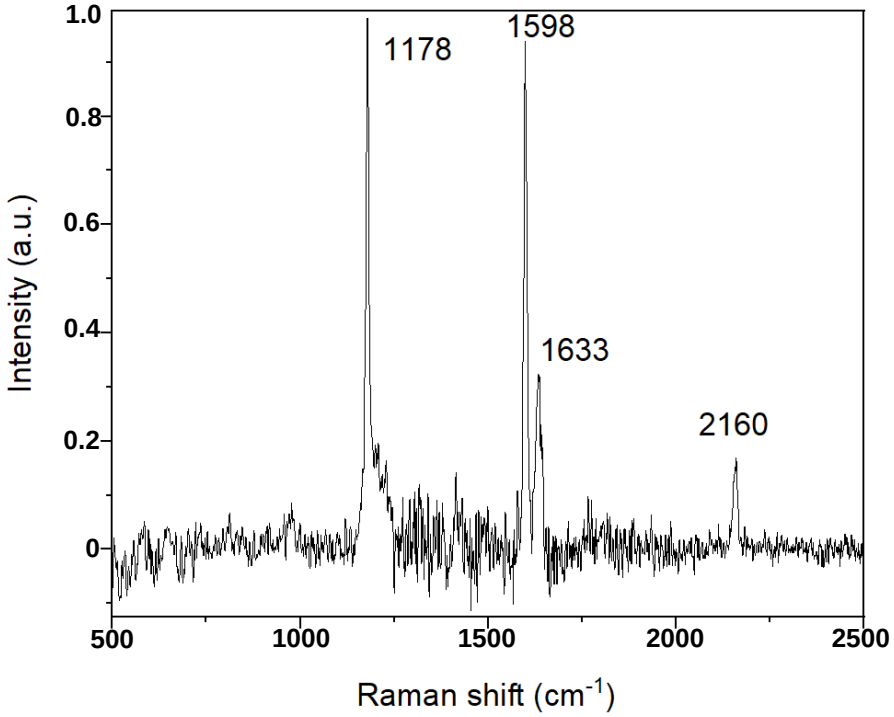

Figure A 1011**: Raman spectrum of AlkTMSCCMoid **2.

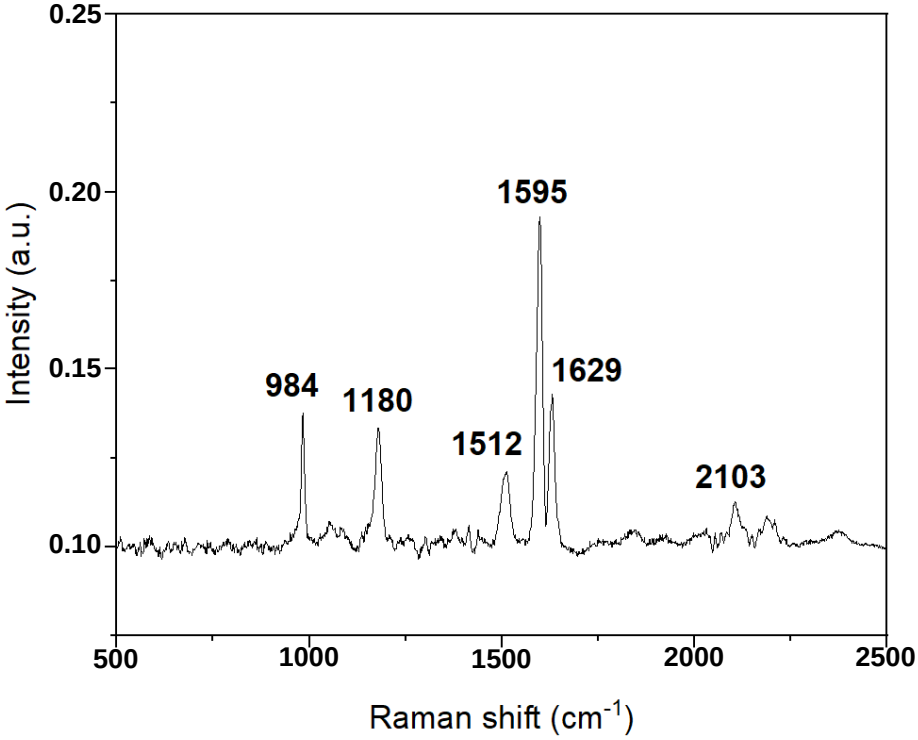

***Figure A 112**: Raman spectrum of AlkCCMoidBF$_2$ **3**.*

UV-VIS spectra in solution (DCM) and in solid state (KBr PELLETS)

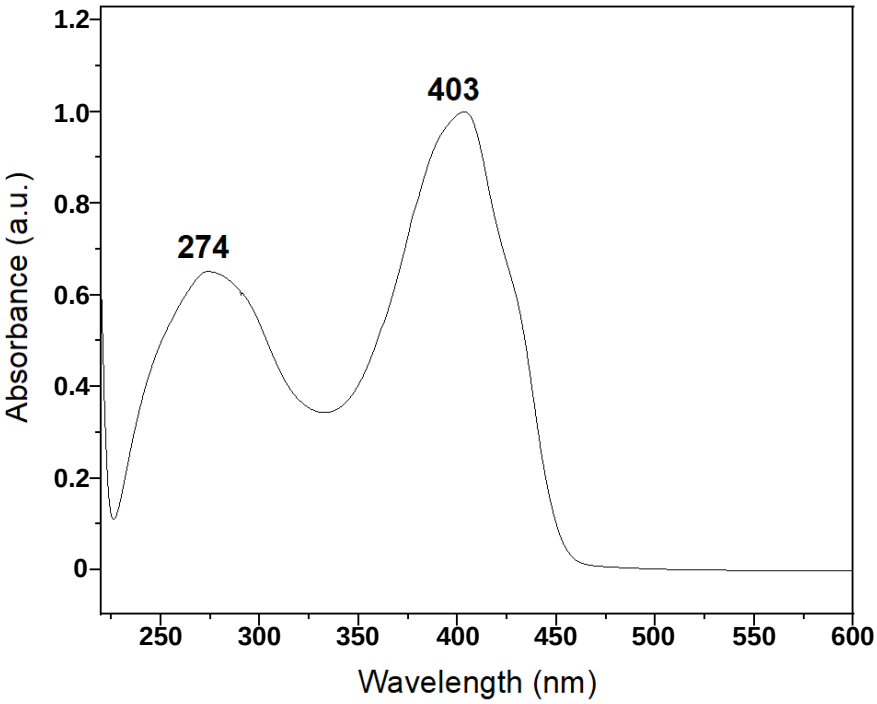

Figure A 12: *UV-Vis solution spectrum of AlkCCMoid **1**.*

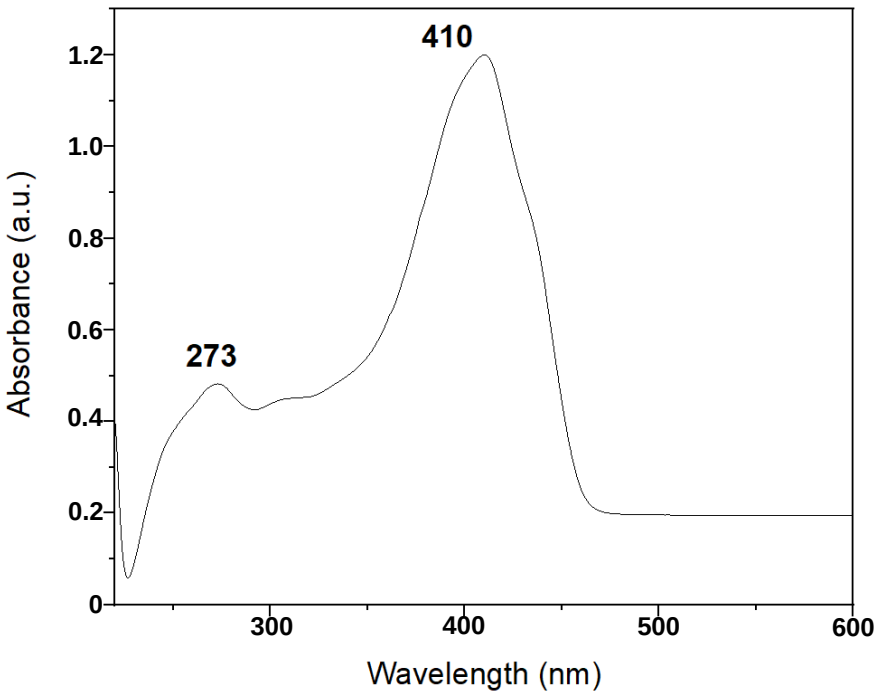

Figure A 13: *UV-Vis solution spectrum of AlkTMSCCMoid **2.***

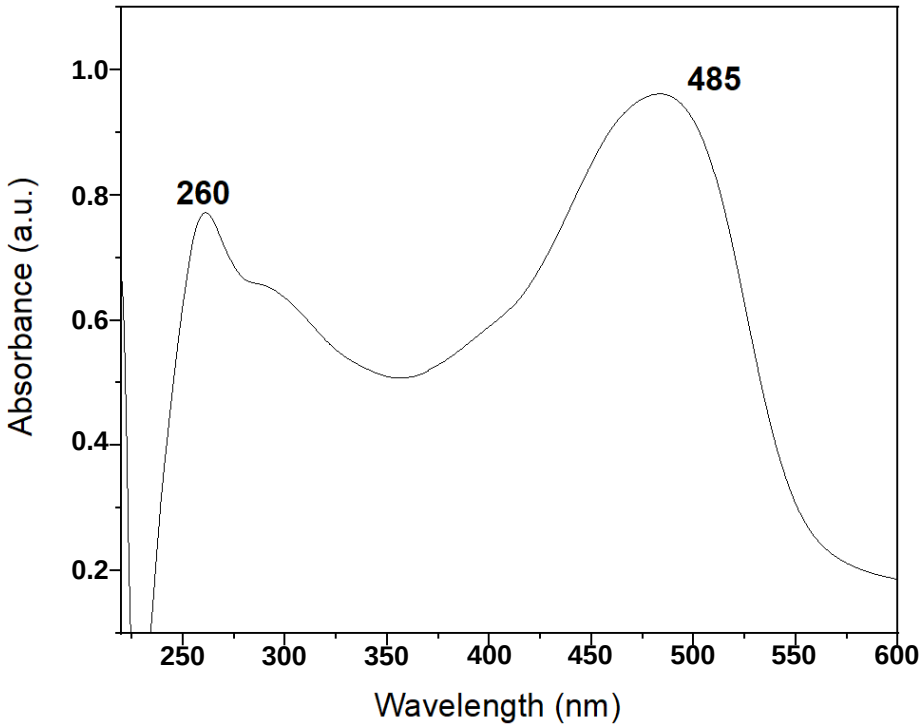

***Figure A 14**: UV-Vis solution spectrum of AlkCCMoidBF$_2$ **3**.*

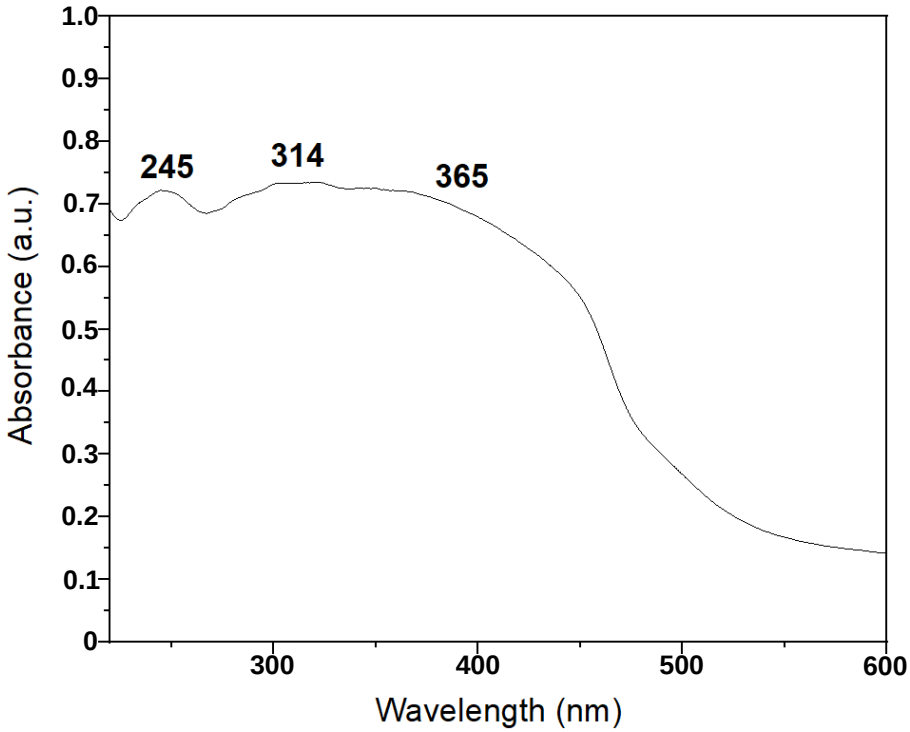

***Figure A 15**: UV-Vis solid spectrum of AlkCCMoid **1**.*

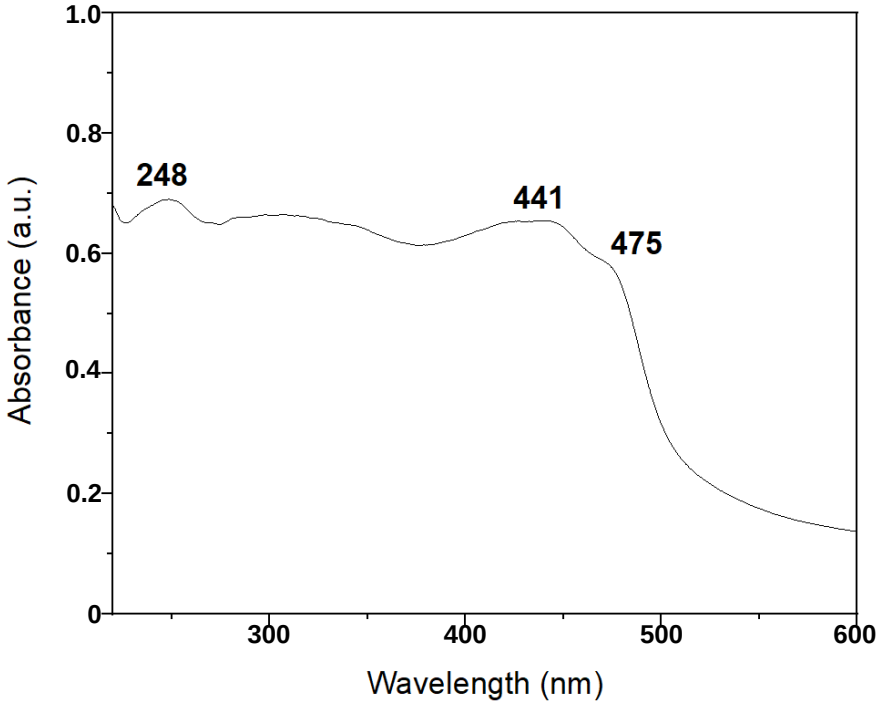

Figure A 16**: UV-Vis solid spectrum of AlkTMSCCMoid **2.

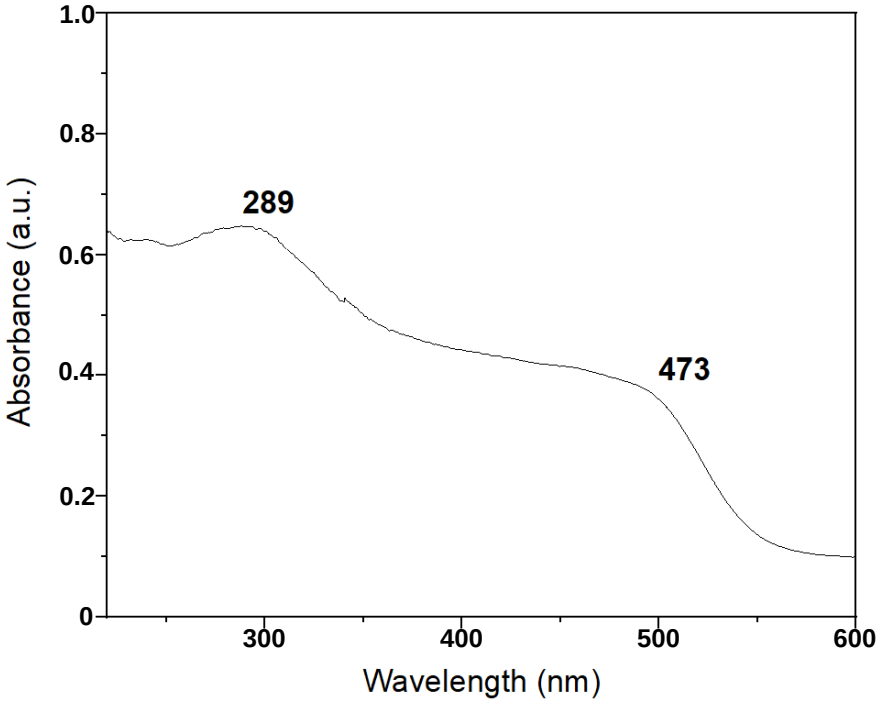

***Figure A 17**: UV-Vis solid spectrum of AlkCCMoidBF$_2$ **3**.*

Electrochemistry spectra

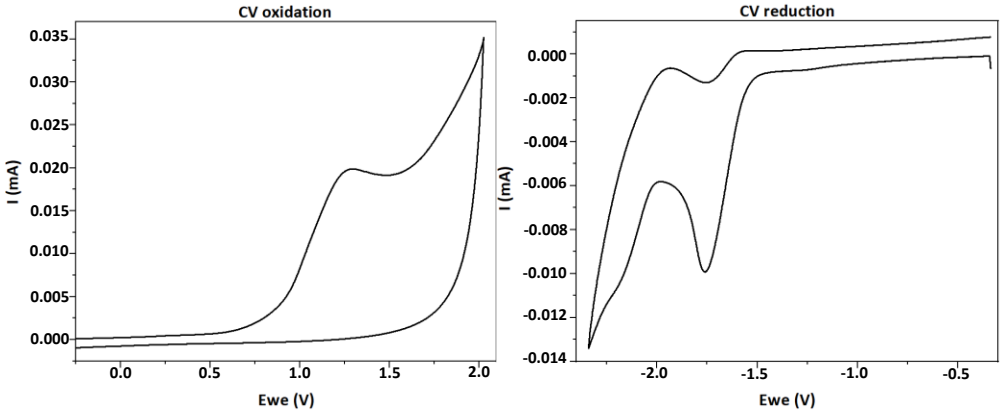

Figure A 18**: Oxidation and reduction cyclic voltammogram spectra of AlkCCMoid **1.

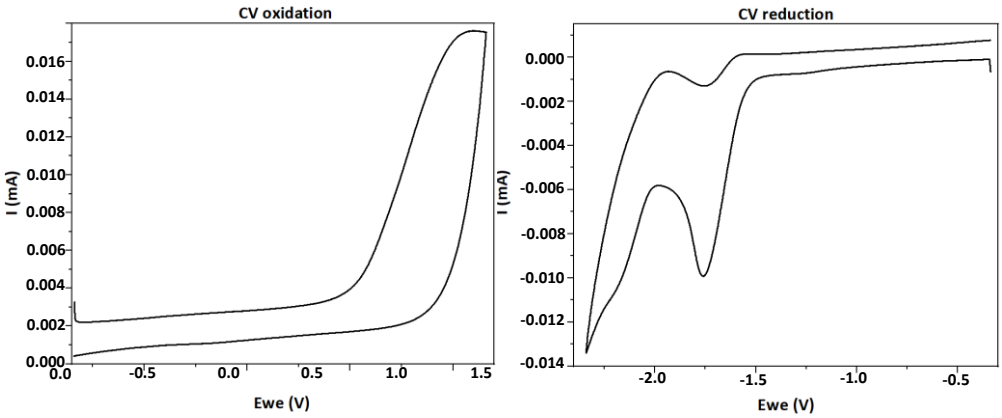

Figure A 19**: Oxidation and reduction cyclic voltammogram spectra of AlkTMSCCMoid **2.

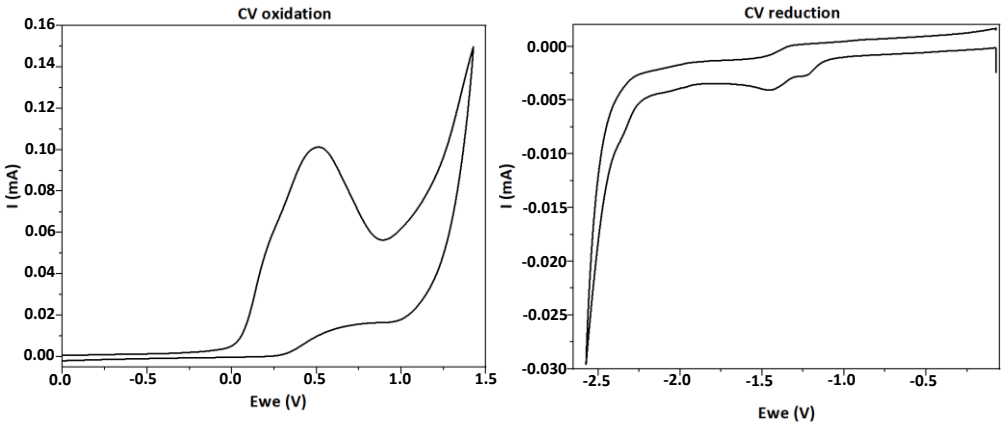

Figure A 20**: Oxidation and reduction cyclic voltammogram spectra of AlkCCMoidBF_2 **3.

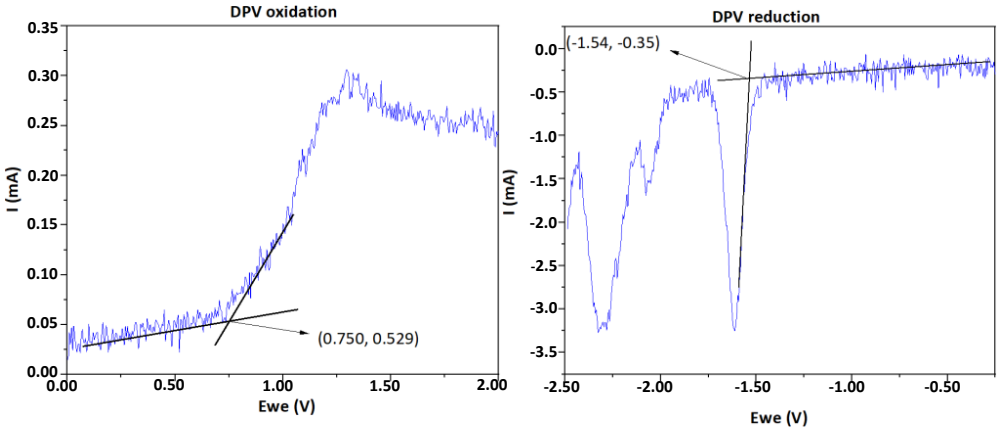

Figure A 21**: Oxidation and reduction differential pulse voltammogram spectra of AlkCCMoid **1.

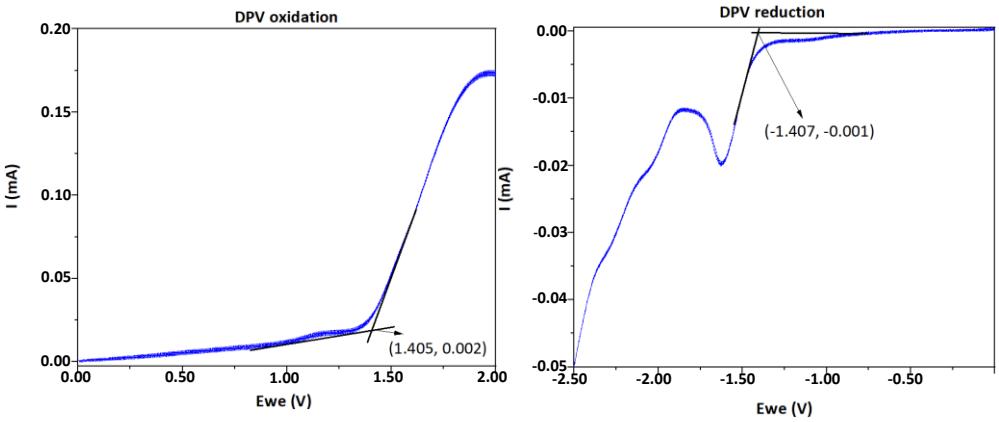

Figure A 22:** Oxidation and reduction differential pulse voltammogram spectra of AlkTMSCCMoid **2.

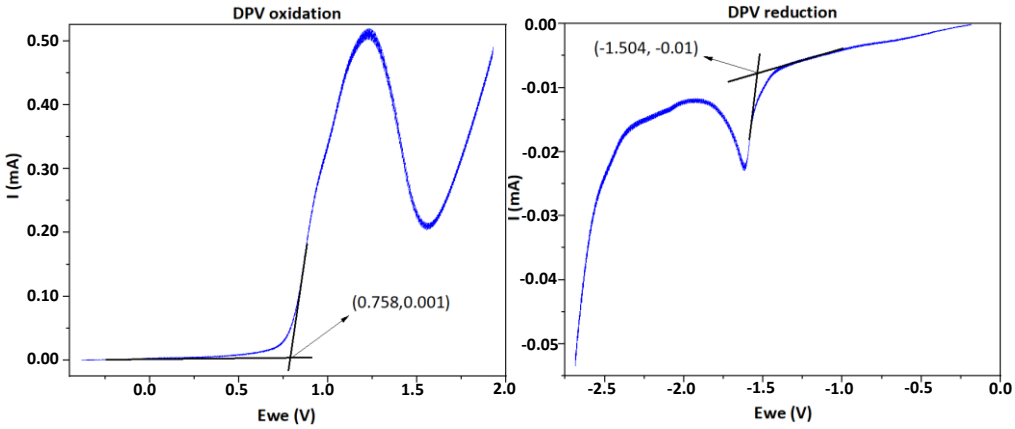

Figure A 23**. Oxidation and reduction differential pulse voltammogram spectra of AlkCCMoidBF_2 **3.

MALDI- MASS spectra

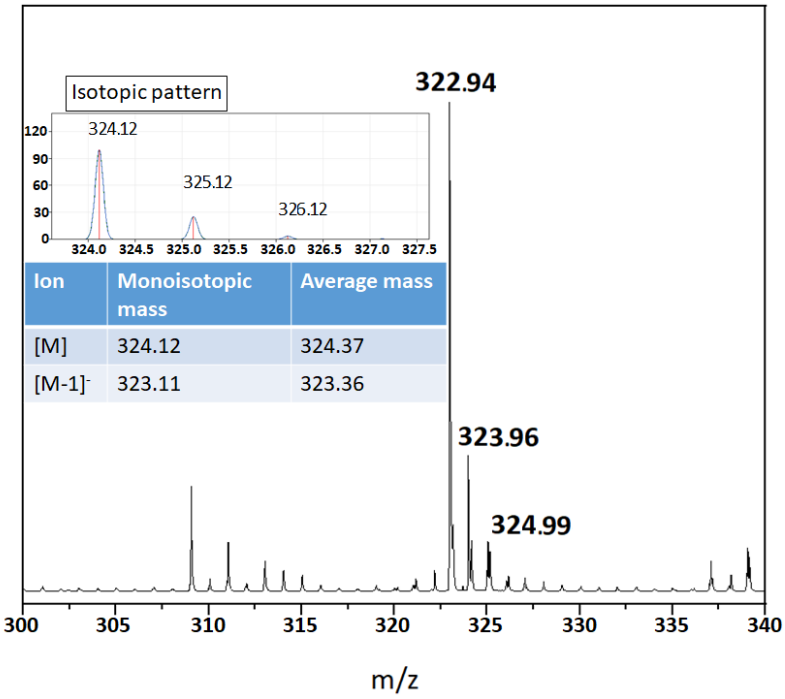

Ion	Monoisotopic mass	Average mass
[M]	324.12	324.37
[M-1]⁻	323.11	323.36

Figure A 24: *Mass spectrum of AlkCCMoid **1** (Negative mode).*

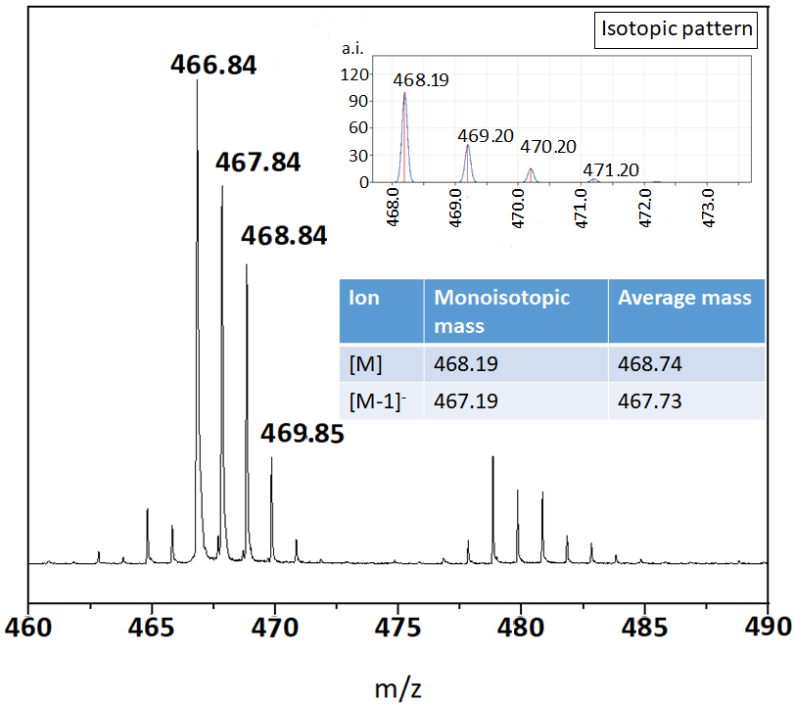

Ion	Monoisotopic mass	Average mass
[M]	468.19	468.74
[M-1]⁻	467.19	467.73

Figure A 25: *Mass spectrum of AlkTMSCCMoid **2** (Negative mode).*

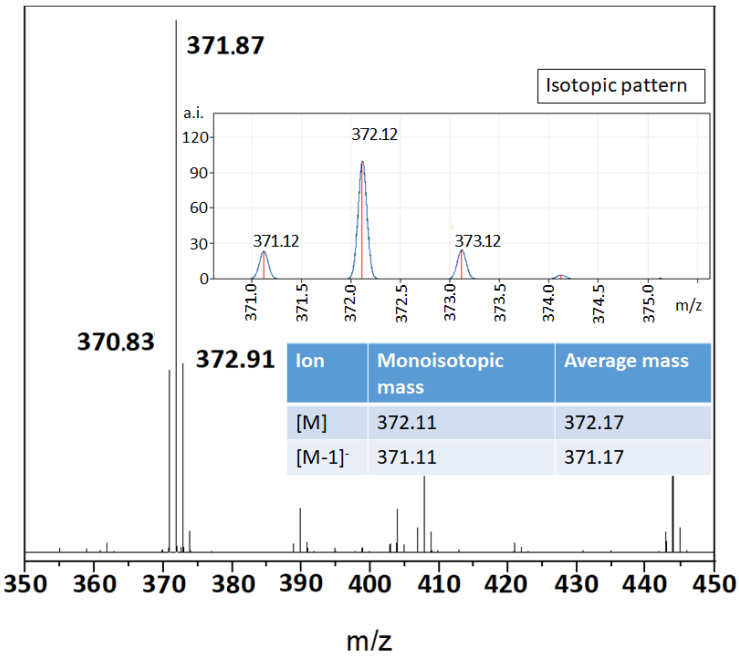

***Figure A 26**: Mass spectrum of AlkCCMoidBF$_2$ **3** (Positive mode).*

Thermogravimetric analysis spectra (TGA)

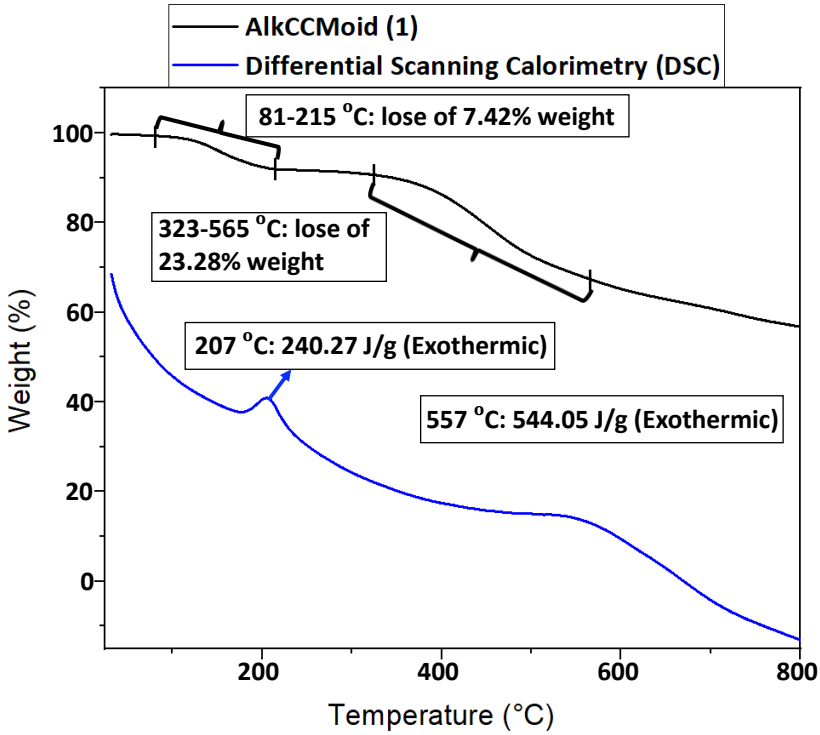

***Figure A 27:** Thermogravimetric spectrum of AlkCCMoid **1** under N$_2$ atmosphere.*

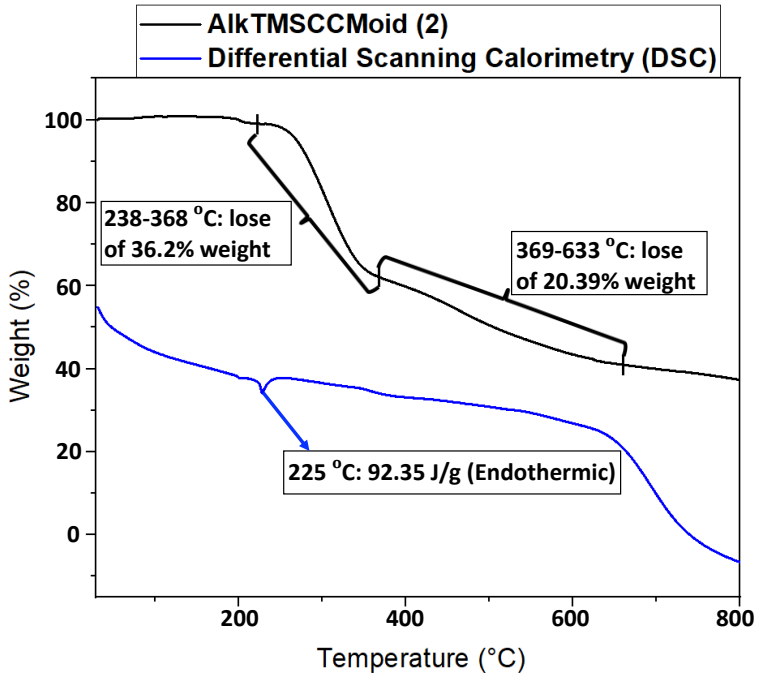

***Figure A 28**: Thermogravimetric spectrum of AlkTMSCCMoid **2** under N_2 atmosphere.*

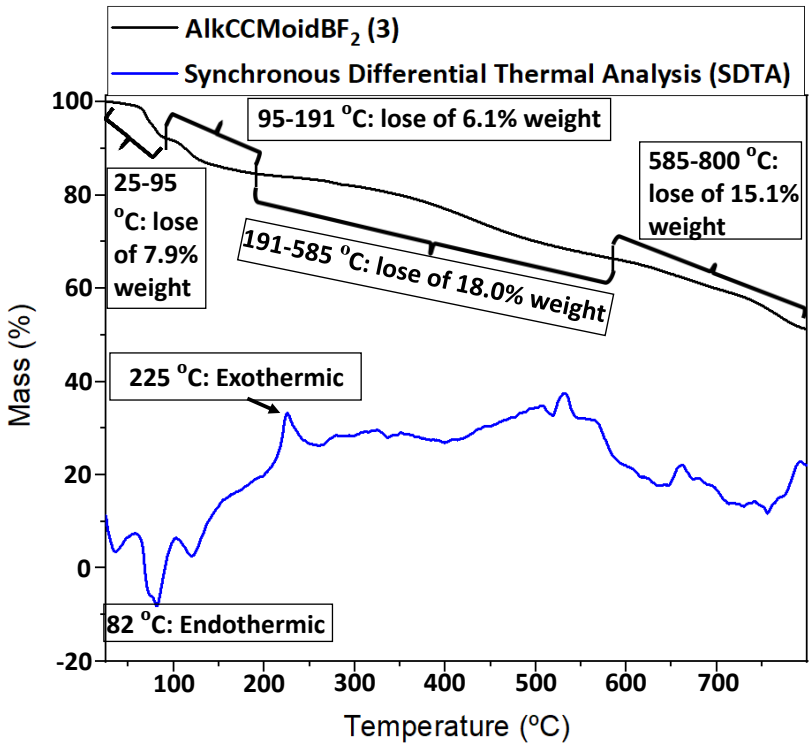

***Figure A 29**: Thermogravimetric spectrum of AlkCCMoidBF$_2$ **3** under N_2 atmosphere.*

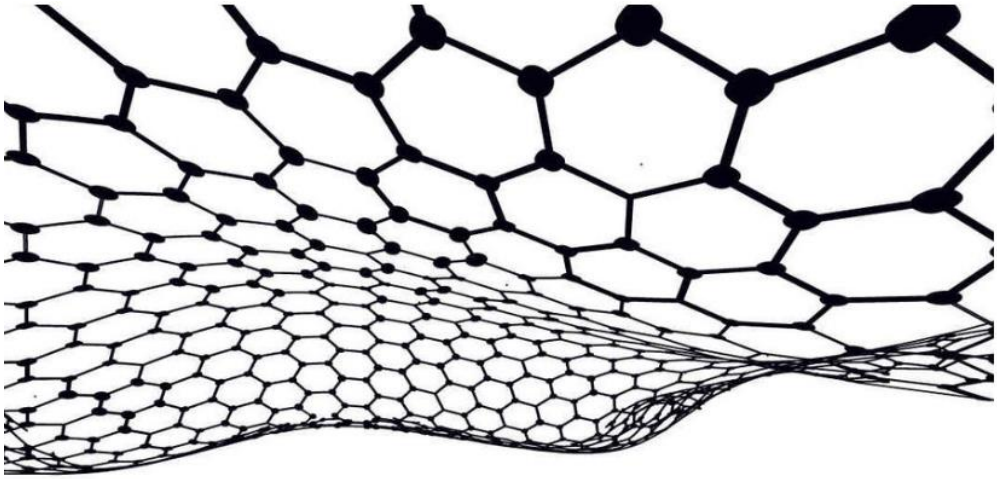

CHAPTER II

2. CHAPTER II: SYNTHESIS AND CHARACTERIZATION OF GRAPHENE-LIKE CCMOIDS

2.1 INTRODUCTION

Chips made from silicon have been, and continue to be, the basis for the rapid development of the technology, although, this industry faces current limitations in the miniaturization process such as the heat generated and the occurrence of quantum effects in the electron behaviour that would make the system unreliable in the creation of repeatable and robust devices at levels of a few nanometers.[59] An alternative to overcome part of these problems is the use of single molecules as active components in the electronic devices to create functional electrical circuits. Regarding this matter, carbon electrode-molecule junctions have been attracted more attention, with graphene being most widely used as the electrode.[60,61,90]

Graphene is a unique carbon material that is known for its charge transfer properties and the freedom in the electronic movement in its structure, thanks to that, it has been used as a platform for sensors, electrodes in field-effect transistors, and as transparent contacts for photovoltaic devices.[140-142] Interestingly, graphene could also be either covalent or noncovalent functionalized, making the first an interference with the extended carbon network and modifying their electronic properties.[143] On the other hand, examples of noncovalent functionalization relate to weak intermolecular forces, such as electrostatics, π-stacking, or hydrogen bonding, that allows to maintain the structural integrity of the nanocarbon network.[144]

Considering the latest, during the last years our group has focused on the contacting molecules to graphene elements meanwhile using π-stacking interactions. For that, in the past, the synthesis of a family of CCMoids containing various aromatic groups (some of them shown in Figure 52) was achieved.

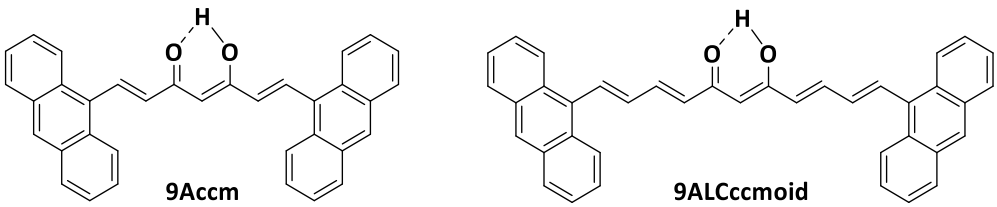

***Figure 52**: Structure of 9Accm and 9ALCccmoid molecules.*

In the past, the two anthracene-modified CCMoids (9Accm[37] and 9ALCccmoid[38]) were used as molecular wires in graphene-based three-terminal devices. They were deposited, in solution and at room temperature, over a nanogap formed between few-layer graphene-based electrodes (Figure 53). It was demonstrated that these CCMoid systems allow the electronic transport between both electrodes, acting as a bridge, thanks to the π-π stacking coupling interaction of the aromatic groups of the CCMoids to the graphene electrodes.

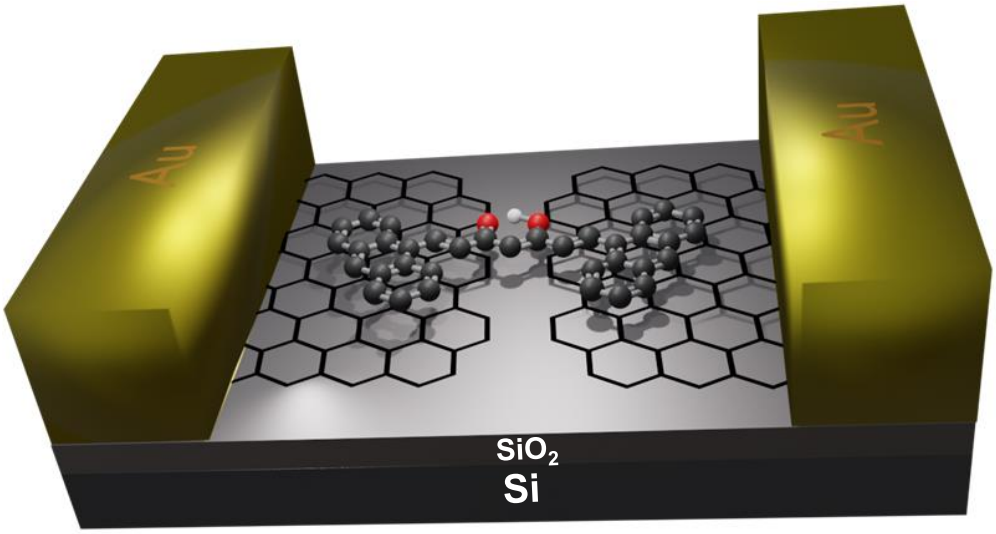

***Figure 53**: Idealized model of the electronic three terminal device used for the deposition of 9Accm and 9ALCCMoid molecules.[37,38] The model only uses one layer of graphene for simplicity.*

The results obtained indicate that both molecules, after being deposited over the device gap, display a similar increase of conductance at low temperatures. Considering that 9ALCCCmoid is larger than 9Accm (approx. 21 Å *vs*. 17 Å) and that the gap between the flakes of graphene is approximately 1-2 nm at the shortest distances, the conductance value for the first was expected to be smaller. However, the results show that the improvement of the π-π interactions between the anthracene groups for the 9ALCCCmoid and the graphene surfaces compensates for the possible limitations that a longer length in the molecule might bring. Once again, it highlights the relevance of the molecule-electrode anchoring in the conductance, supported by theoretical results.[38]

Therefore, the purpose of this new chapter was to explore the preparation of new curcuminoid-based molecules that contained a larger number of aromatic rings on their arms and that, consequently, should provide better

contact sites with the graphene electrodes than the aforementioned molecules. Moreover, the preparation of new curcuminoids with reactive groups on the arms, which allow the enlarge of the arms will be also objective of study. Finally, the new and relatively small PAH-molecules prepared in this chapter will open the possibility to create of graphene nanoribbons with a CCMoid skeleton, Figure 54.

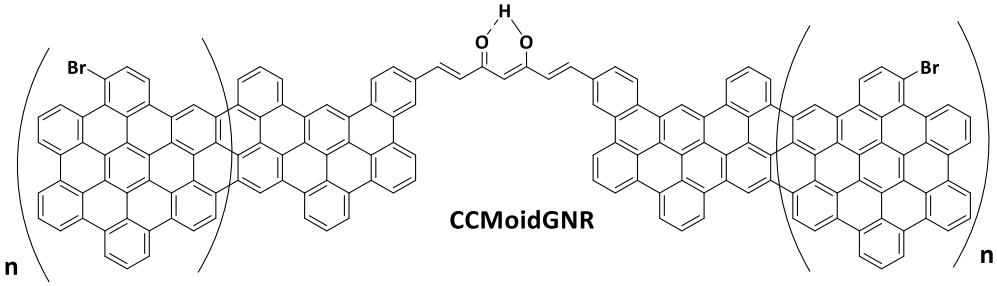

Figure 54*: Chemical structure of the ideal CCMoid graphene nanoribbons (CCMoidGNRs), where n stands for the number of PAH sequences that can be introduced.*

2.2 OBJECTIVES

The main objective of this chapter is the establishment of a reliable bottom-up methodology for the synthesis of a new generation of CCMoids containing PAHs groups in their arms that may include reactive groups, allowing the growth of their arms (Figure 55). This has resulted in two structures containing small nanographene (NGs) units (**5** and **7**).

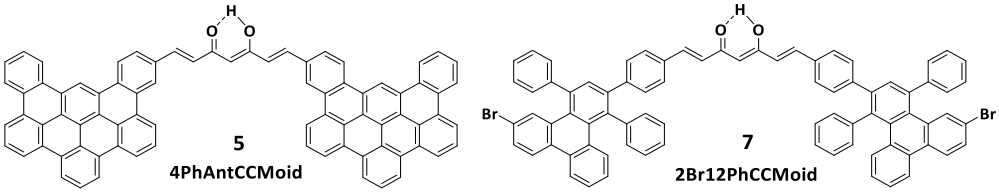

***Figure 55**: Chemical structure of CCMoids **5** and **7**.*

Due to the novelty of such molecular systems and foreseen characteristics coming from the PAH moieties (e.g.: planarity, insolubility), an important aim here was the identification of the most useful techniques that could assist in the characterization of such materials.

For that, to characterize the new CCMoid systems it has been necessary comparative studies with already known PAH molecules using both, solution and solid-state techniques. Furthermore, as done in the third chapter, the optical and electric bandgaps of them and their BF_2 derivatives were studied by UV-Vis spectroscopy and electrochemistry.

2.3 RESULTS AND DISCUSSION

2.3.1. Synthesis of 10PhCCMoid 4 and 4PhAntCCMoid 5

Scheme **2.1**2.1 shows the general path toward the synthesis of CCMoids **4** and **5**, containing three main steps**Error! Reference source not found.**. This synthetic pathway was designed in collaboration with the group of Professor Diego Peña, from CIQUS in the University of Santiago de Compostela (USC). His group has an extended experience in the synthesis of PAHs either on surface and in solution, so they have assisted finding the suitable conditions for the synthesis of molecule **5**. Part of the work was performed during a two-month stay at the installations of Prof. Peña´s group.

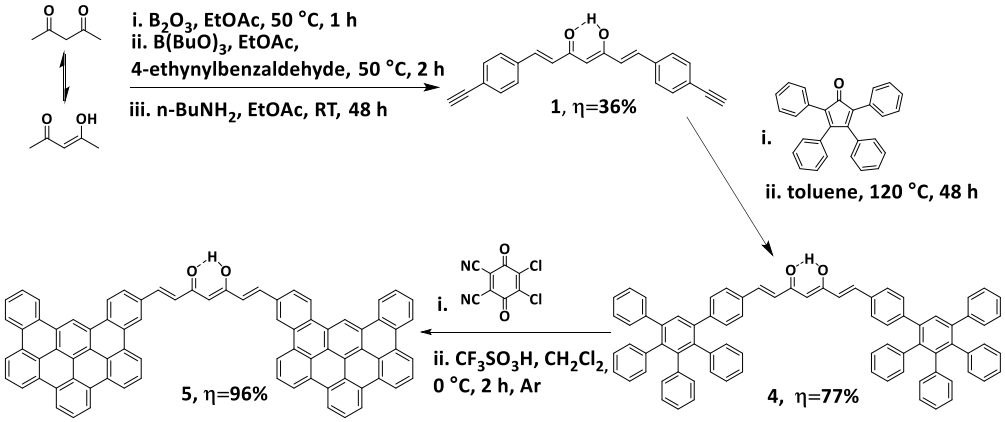

***Scheme 2.1**: General path of the synthesis proposed to obtain CCMoid **5**.*

The proposed synthesis started using the phenylacetylene **1** described in chapter 1. Then, the next step involved the pericyclic Diels-Alder [4+2] cycloaddition reaction between the alkynyl groups of **1,** acting as dienophile, and the diene groups of the commercially available 2,3,4,5-tetraphenylcyclopenta-2,4-dien-1-one, giving rise to the polycyclic CCMoid **4**.[102] For this reaction, several conditions were tested which are summarized in 103,104,145

Table [103,104,145]

Table 2.1: Conditions for the reaction of the formation of CCMoid **4**.. Among all of them, entry 6, which involves the use of toluene as solvent, gave the best yields. Moreover, the use of this solvent allowed an easier purification process by recrystallization with acetonitrile.[103,104,145]

***Table 2.1**: Conditions for the reaction of the formation of CCMoid **4**.*

Entry	Solvent	Equivalents	Colour	Yield (%)
1	Diphenyl ether	2	Dark brown	27
2	Diphenyl ether	3	Dark brown	55
3	Xylene	2	-	-
4	Xylene	3	White	30
5	Toluene	2	Brown	37
6	Toluene	3	Brown	77

Finally, the last step involved the intramolecular cyclodehydrogenation (Scholl reaction)[146-148] of system **4** to produce the planar polycyclic aromatic hydrocarbon **5**. The Scholl reaction consisted of an intramolecular oxidative reaction producing new C-C bonds between two benzenoid rings as shown in Figure 56. This reaction has been widely used in the synthesis of a variety of polyarylbenzenes to produce the corresponding planar PAHs.[149-151]

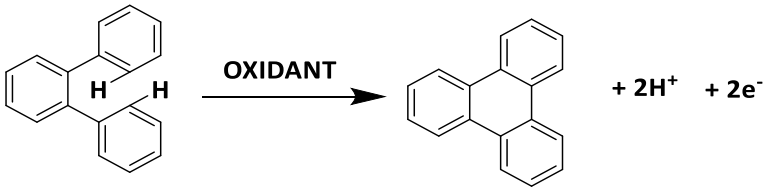

***Figure 56**: Intramolecular oxidative C-C bond formation.*

The mechanism of this reaction displays certain complexity, presenting some debate, taking into account that are two plausible possibilities for this reaction, which share similar characteristics and presented an easy

interchangeability of the reactive intermediates: a cationic-radical pathway and the creation of an arenium-ion system. However, between the two, a large amount of experimental evidence has been accumulated in favour of the first (cation-radical pathway, Figure 57)[152-155] as opposed to the second (arenium-ion, Figure 58).[146,156] The cation-radical involves as a key step the formation of a dicationic intermediate radical arising from the coupling of two benzenoid cation radicals or through a coupling of the cation radical with its neutral counterpart followed by a 1e$^-$ oxidation. All the processes shown in Figure 57 have been demonstrated by spectroscopic methods in the past.[146,154]

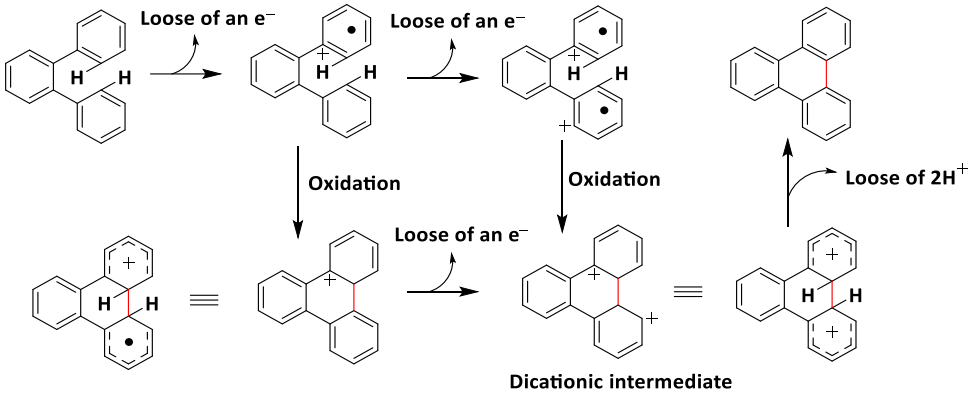

***Figure 57**: Cation radical mechanism for Scholl reaction.*

The second mechanism occurs via arenium ion intermediates due to the presence of acidic media. This mechanism is accelerated as it proceeds due to the formation of 2 equivalent of acid by C-C bond formation. Furthermore, such C-C bond formation is achieved only if protonation occurs at the least preferred site producing a non-aromatic cyclohexadiene derivative.[146] Exposure to strong acids (such as sulphuric or trifluoroacetic acid) generates a paramagnetic cation radical from electron-rich aromatic donors which would promote the start of the process.[153]

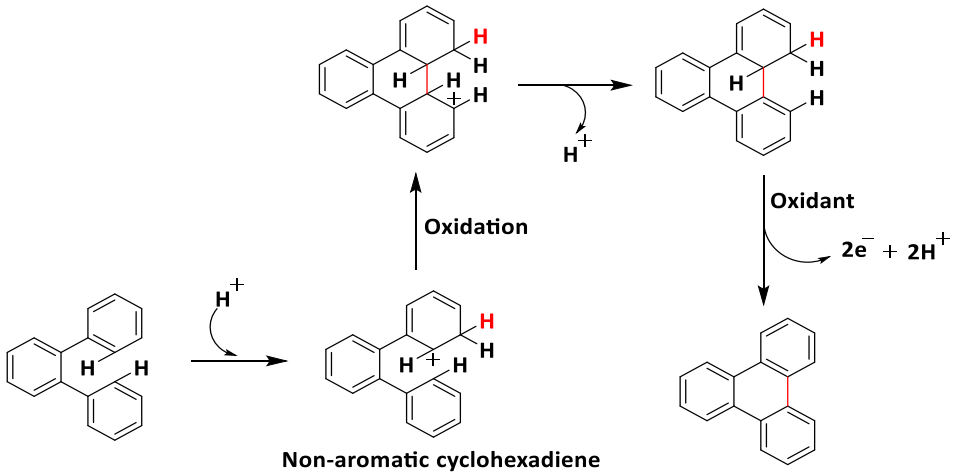

***Figure 58**: Arenium ion radical mechanism for Scholl reaction.*

Beyond the mechanism of the reaction, the reaction of dehydrogenated aryl-aryl bond formation can be carried out in many ways. From treatment with a Lewis acid,[146,157] to the use of a base,[158] or by irradiation in the presence of oxidant,[159] and by heterogeneous catalysis at high temperature.[160-162]

It is known that, quinones molecules (such as tetrachloro-*p*-benzoquinone or 2,3-dichloro-5,6-dicyano-1,4-benzoquinone (DDQ)) in the presence of an strong acid readily oxidize a variety of aromatic electron donors to the corresponding cation radicals and enhance the electron-transfer process.[153,163] Moreover, it is also well-stablished that a number of highly reactive Scholl precursors do not undergo cyclodehydrogenation or produce non-aromatic cyclohexadiene derivatives when exposed only to strong acids or Lewis acids for prolonged periods; to do so, one equivalent of DDQ per C-C bond must be added, being identified as one of the key steps in the reaction.

Therefore, our first attempts toward the creation of the CCMoid-NGs included the reaction of a Lewis acid ($FeCl_3$) mixed with an oxidant such as nitromethane (CH_3NO_2), diluted in DCM. However, this protocol provided ambiguous results without the possibility of identifying system **5**. In part, this method was abandoned due to the possibility of coordination between the Fe(III) species and the *keto-enol* moiety of system **4**. Then, the use of a strong protonic acid such as trifluoromethanesulfonic acid (CF_3SO_3H) was decided together with DDQ, as oxidant agent, getting **5** under mild conditions and in quantitative yields (90-100 %).[150] To achieve the best result for this reaction several conditions, which are shown in

Table 4.2, were modified, such as: the amount of **4** used, the equivalents of DDQ and CF_3SO_3H, the reaction time and the order of addition of the reagents, finding that the best ones are entries 7 and 8. These different trials showed that best results were achieved by increasing the amount of reagents. In addition, with bigger quantities the time of reaction seemed to have no effect and similar results were obtained with reaction times of 2 h and 24 h.

Table 4.2*: List of the different conditions for the formation of CCMoid* ***5****.*

Entry	Reagent order addition	CCMoid 4 (mg)	DDQ (eq)	CF_3SO_3H (eq)	Yield (%)	Colour of the powder	Time of reaction
1	1st acid 2nd DDQ	20	8	8	0	-	24h
2	1st acid 2nd DDQ	20	12	12	43	Red	24h
3	1st DDQ 2nd acid	20	8	8	10	Black	24h
4	1st DDQ 2nd acid	20	8	8	0	-	2h
5	1st DDQ 2nd acid	20	12	12	90	Black	24h
6	1st DDQ 2nd acid	20	12	12	15	Black	2h
7	1st DDQ 2nd acid	50	12	12	96	Black	2h
8	1st DDQ 2nd acid	50	12	12	96	Black	24h

As a result, **5** was obtained as a blackish insoluble powder, features that prevented further characterisation of the system in solution (e.g.: NMR). Great efforts were then devoted towards the characterization of **5** with solid-state techniques, and results were systematically compared with the whole set of CCMoids prepared in the present work, previous chapter, and to similar PAHs described in the literature. The solid-state techniques include mass spectrometry (MALDI-TOF), ATR-FTIR, UV-vis and RAMAN. Among them, solid state-^{13}C NMR was discarded due to the amorphous nature of system **5**, presenting poor resolution of the shifts in initial trials.[40]

2.3.2. Synthesis of 2Br12PhCCMoid 7

This molecule and precursors were designed in collaboration with the group of Professor Diego Peña. As mentioned before, part of the work of this synthesis was performed in a two-month stay at the installations of the group at the University of Santiago. The synthesis of molecule **7** is represented in Scheme 2.2. CCMoid **7** could have three conformational isomers: the two -Br groups looking up (as it is represented in Figure 55), looking down or looking one up and one down, all three are conformational isomers of the same molecule as the arms of the molecule can rotate freely.

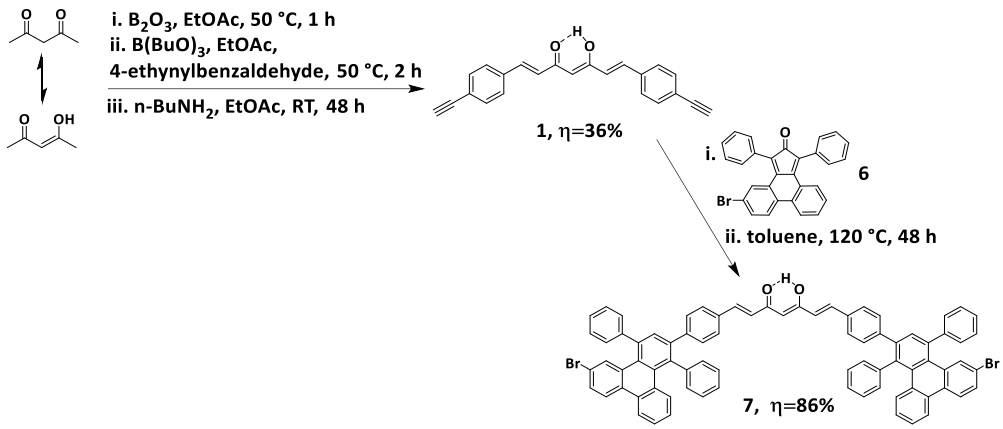

***Scheme 2.2**: Synthetical pathway proposed to obtain molecule **7**.*

To synthesize system **7**, we followed a similar methodology to that reported before. The difference between this procedure and the previous is that the step involving the diels-alder reaction to give **7** use the ketone ligand **6** which was previously synthesized in the laboratory and contains a reactive Br ending group (Scheme 2.3). The conditions used in this diels-alder reaction were the same as the ones used for the synthesis of CCMoid **4**, providing acceptable yields as explained in the experimental section.

System **6** was obtained following the procedure indicated in Scheme 2.3 performing a two-step reaction and following the conditions published in the bibliography.[105,164,165] This procedure consisted in exposing the 9,10-phenanthrenedione to a bromination reaction using 1 equivalent of *n*-bromosuccinimide to obtain de mono-bromated product **8**. Then, in a second reaction the Knoevenagel condensation of **8** using of the 1,3-diphenylpropan-2-one, give ketone-based system **6**.

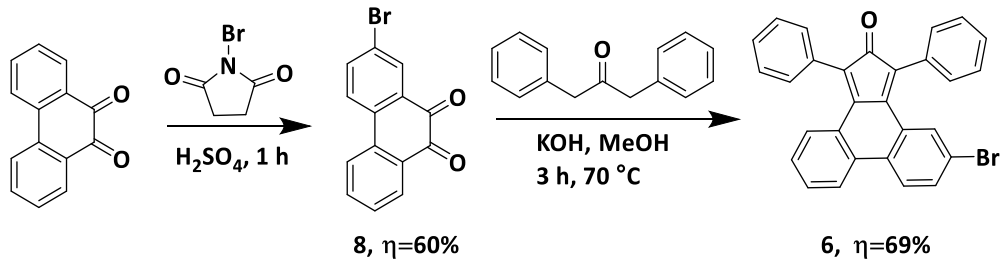

***Scheme 2.3**: Methodology followed for the synthesis of the precursors: CCMoids **6** and **8**.*

2.3.3. Synthesis of 10PhCCMoidBF$_2$ 9, 4PhAntCCMoidBF$_2$ 10 and 2Br12PhCCMoidBF$_2$ 11

As in the previous chapter, the -BF$_2$ derivatives of **4** and **7** (**9** and **11** respectively, Scheme 4) were also prepared to explore the plausible changes in the optical and electrical properties of the coordinated systems in comparison with the free CCMoid molecules. The subsequent -BF$_2$ derivatives were obtained by reaction with BF$_3$·OEt$_2$ under microwave conditions. Nevertheless, due to the low solubility of **10** and to be sure its proper obtention, two synthetic routes in solution and in solid state were tested. The first one (A) is a two-step reaction involving first, the coordination reaction with BF$_3$ of **4**, giving **9** and then performing the ring closing cyclodehydrogenation reaction to form **10**. The second route (B) involves the coordination of -BF$_2$ in solid state[166-168] of **5** giving directly **10**. Both synthetic routes gave similar results that were analysed with the same solid-state techniques used for CCMoid **5**.

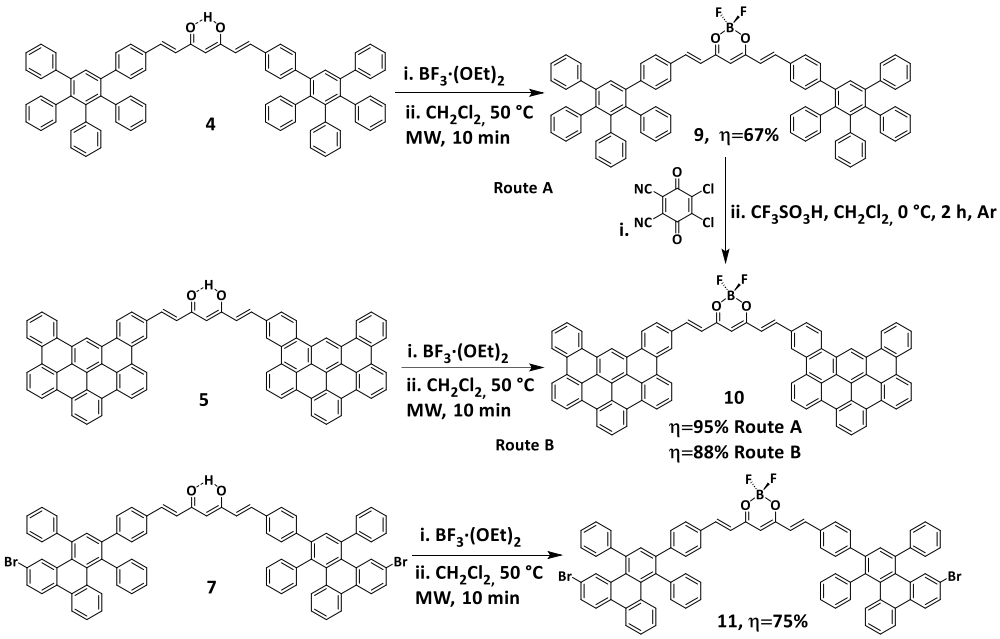

***Scheme 4**: Synthetic strategy for the synthesis of the -BF$_2$ derivatives: CCMoids **9**, **10** and **11**.*

In solution, CCMoids **4**, **7**, **9** and **11** were characterized by NMR, although not all the aromatic signals were straightforward assigned, all the systems display the characteristic features of CCMoid skeletons, which corroborate the creation of the final systems. In addition, other characterization techniques (IR, MALDI, UV-Vis and EA, among others) have been performed to properly

analyse these molecules. In the case of systems **5** and **10**, as explained before, great efforts have been focused on characterization by solid-state techniques such as ATR-FTIR, UV-Vis, RAMAN spectroscopy, X-ray photelectron spectroscopy (XPS), elemental analysis (EA) and mass spectrometry (MALDI-TOF). Additionally, fluorescence spectroscopy has also been used with the purpose of gathering further information.

2.3.4. ^{1}H-NMR and ^{13}C-NMR spectroscopy for CCMoids 4, 7, 9 and 11

The ^{1}H and ^{13}C NMR characterization of most of the CCMoids was performed in deuterated chloroform however, for molecules **7** and **9** the ^{13}C NMR spectra were performed in deuterated DCM due to better solubility. Figure 59 and Figure **60** show the comparison of CCMoids **4**, **7, 9** and **11**.

In the case of ^{1}H NMR (Figure 59), the aromatic region displays abundant and broad signals, as expected, making challenging the assignment and integration of each proton. However, it was possible to identify the typical signals of the central part of each CCMoid and some of the aromatic regions that agree and confirm the proposed structures.

Starting with the assignment, the signals at the lowest fields, H_a and H_f, of molecules **4** and **7**, respectively, correspond to the enol proton of the *keto-enol* group (15.89 and 15.92 ppm) and as expected, this signal is not observed in the BF_2-CCMoids. Next, in molecules **4**, **9** and **11** the signals from the doublets: H_b, H_j and H_p are identified as the alkene protons in *trans* ($^{3}J_{HH}$=15.0-16.0 Hz), the furthest from the *keto-enol* group which, as occurred in the previous chapter, shifted to lower fields. **4**, **7**, **9** and **11** showed the other two *trans* protons H_d, H_h, H_m and H_q, in that order, at higher fields, easily identified because of the coupling signal.[38] Interestingly, in CCMoid **4** the signal H_b appear as the sum of the aforementioned doublet *trans* protons and a singlet attributed to the only aromatic proton that has no other protons in its vicinity. Following the explanation, in CCMoids **4** and **9**, the doublets H_c and H_l, both with similar coupling constants ($^{3}J_{HH}$= 8.02 Hz) were assigned to the first two aromatic protons of the ring closest to the CCMoid core. Then, for all the CCMoids, the signal H_e, H_i, H_n and H_r correspond to the central methine proton of the molecules and finally, in CCMoids **9** and **11** appear the signals H_g and H_o assigned to the protons near the bromo groups.

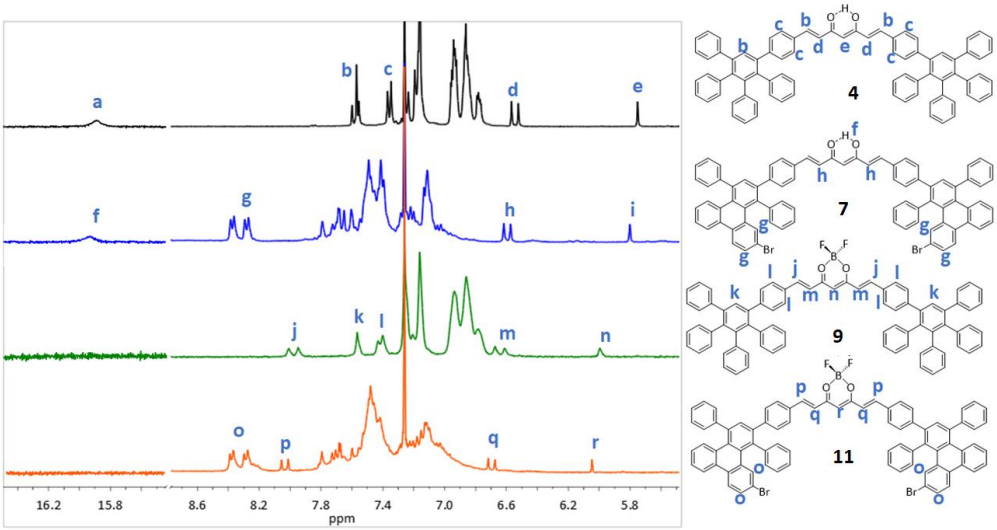

***Figure 59**: ^{1}H NMR spectra comparison between **4** (black), **7** (blue), **9** (green) and **11** (orange) in $CDCl_3$ at 360 MHz.*

Then, for the ^{13}C NMR analysis in solution (Figure 60), as before, all the systems are compared except for **11** because of its poor solubility in deuterated $CDCl_3$ or CD_2Cl_2 (and other deuterated solvents). Although different deuterated solvents were used, all molecules shared very similar shifts. For all of them, the signals that appear at lower fields are related with the *keto-enol* moiety, appearing C_a, C_f and C_k as single signals, which is explained by the easy/fast interconversion between both functional groups. The aromatic units and the conjugated alkene chain are found in the region between 140-120 ppm where the most intense signals correspond to the aromatic carbons and the least intense ones to the quaternary carbons due to the relaxation time of each nucleus.[13] From this region, we were able to assign the signals of the alkene chain where the ones that appear at lower fields: C_b, C_g and C_l are assigned to the *trans* alkene carbons that are the furthest from the *keto-enol* moiety. The other two *trans* alkene carbons: C_d, C_i and C_q are located between 124-120 ppm and finally the central carbon of the alkene chain: C_e, C_j and C_r (for **4**, **7** and **9**, respectively) appeared at the higher fields 103-101 ppm due to the shielding effect of the *keto-enol* group. As it happened in chapter 3, the CCMoids with BF_2 present significant shifting in the carbons near this functional group (C_l, C_k and C_q).

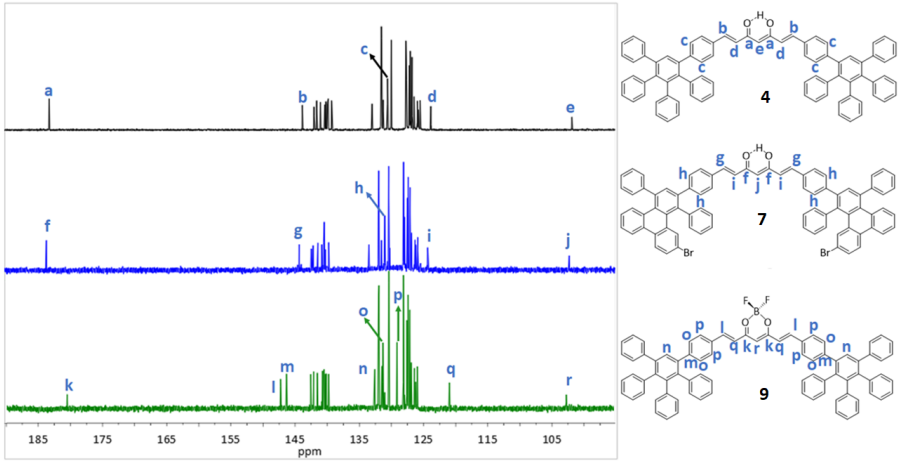

***Figure 60**: Comparison of ^{13}C NMR spectra of **4** (black) and **7** (blue) in $CDCl_3$* at 90 MHz *and **9** (green) in CD_2Cl_2* at 90 MHz,

As mentioned before, for **5**, solid-state ^{13}C NMR analysis was attempted, however, no good results were obtained as the spectra presented broad signals that could not be analysed. Most likely this is due to the poor crystallinity of the system, achieved after a rapid precipitation.

2.3.5. ATR-FTIR spectroscopy for CCMoids 4, 5, 7, 9, 10 and 11

The ATRFTIR spectroscopy technique allowed us to make the comparison between the soluble and insoluble systems, being an efficient technique to confirm the formation of systems **5** and **13**. Figure 61 shows the different spectra obtained for **4**, **5** and **7** and Figure 62 for **9**, **13** and **11**, respectively***Error! Reference source not found.***.

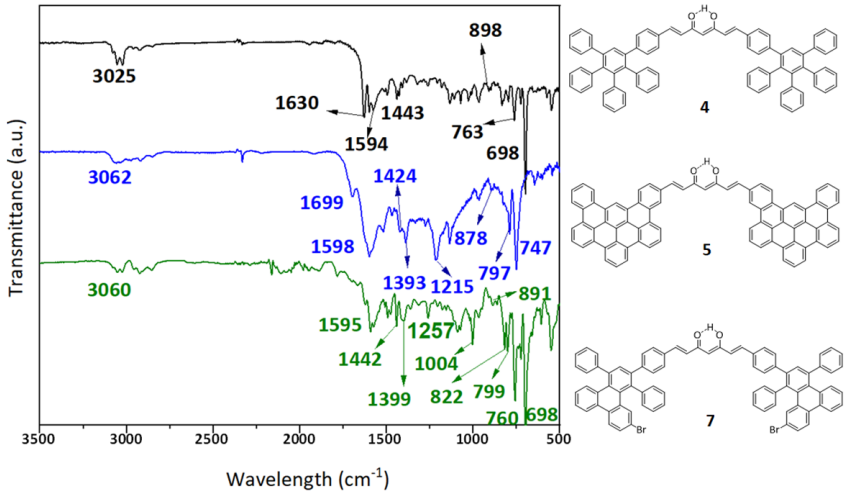

*Figure 61: Comparative ATR-FTIR spectrum between **4** (black), **5** (blue) and **7** (green).*

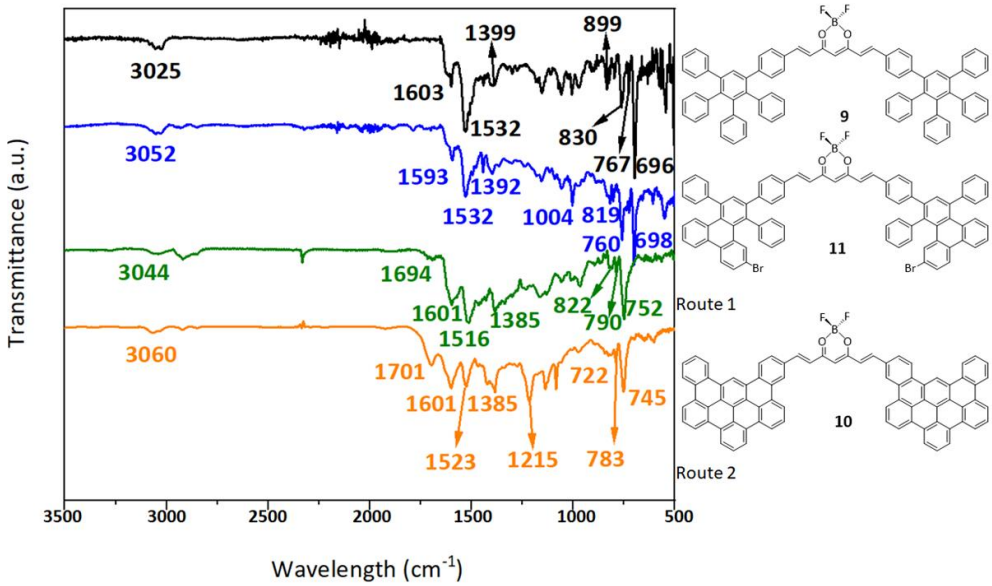

*Figure 62: Comparative ATR-FTIR spectrum between **9** (black), **7** (blue), and **10** (route A, green and route B, orange).*

In all molecules, a stretching broad band is observed between 1603-1593 cm^{-1} that is related to the ν_{ar}(C-C) band. In **4**, this band is overlapped with the stretching C-O bond of the *keto-enol* ν(C-O, around 1630 cm^{-1}).[120] Between 1399-1383 cm^{-1} the bending mode δ(=CH, aromatic and alkenyl chain) appeared, moreover, for molecules with $-BF_2$ moieties; in this region it also appears the stretching ν(B-O) signal. Then, for **7** and **11** the ν(C-Br) vibrational band at 1004 cm^{-1} can be identified.

Finally, CCMoids **4, 7, 9** and **11** shared a very similar shape in the region between 1000-500 cm^{-1}: the *mono*-substituted aromatic ring signals (around 898, 763 and 696 cm^{-1}) the *penta*-substituted and the *para-di*-substituted bands (around 840 cm^{-1}). Nevertheless, in CCMoids **5** and **13**, the shape of this region signals changed, and it can be observed the *neighbouring tri*-substituted (752-745 cm^{-1}), the *o-di*-substituted (797-783 cm^{-1}) and the *1,2,4-tri*-substituted (827-822 cm^{-1}) bands, correspondingly. In addition, it is worth noting the disappearance of the sharp frequency at 696 cm^{-1}, another confirmation that the reaction was complete with no indications of molecule **4**.[120,169]

With the help of a graphical interface Avogadro, it was possible to propose the length of CCMoids **4** (31.19 Å) and **5** (31.02 Å), respectively (Figure A 97 and Figure **A 98**). Also, with the help of a graphical interface running Gaussian calculations (*GaussView*) and the assistance of Prof. Eliseo Ruiz, from the University of Barcelona, it was possible to compare the spectra of these molecules with the simulated ones (Figure 63) confirming the different bands (always with a certain shift from the experimental). Some peaks are not observed in the experimental spectra, such as: the stretching ν(O-H) around 3180 cm^{-1} of the enol group and the ν(C=O) corresponding to the tautomer *keto-enol* group due to the fact that simulations take under consideration both tautomers and the intensity of the bands should not be taken into account.

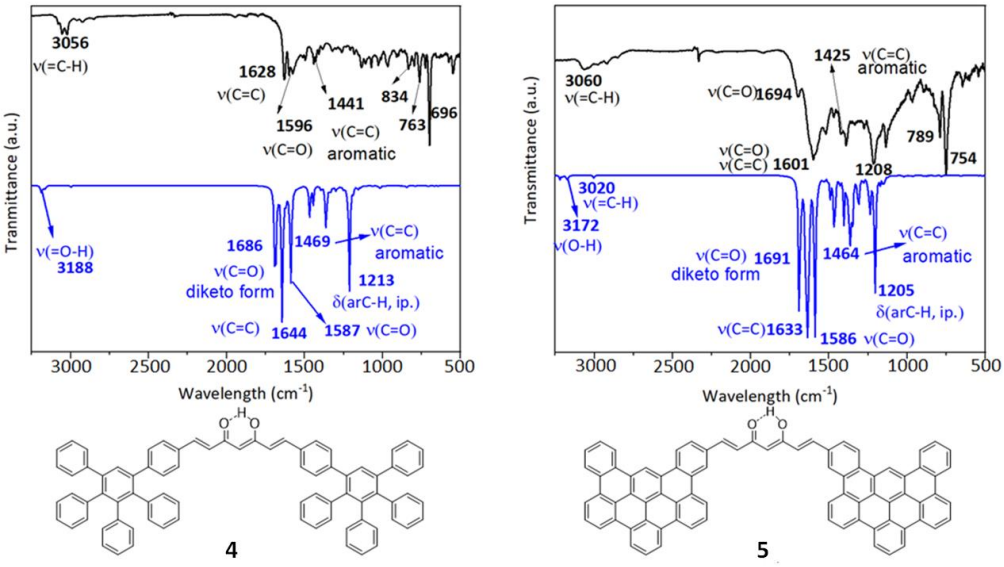

***Figure 63**: Comparative ATR-FTIR spectra of: A) Experimental CCMoid **4** (black) and simulation (blue) and B) experimental CCMoid **5** (black) and simulation (blue).*

2.3.6. Raman spectroscopy for CCMoids 4, 5, 7, 9, 10 and 11

Raman spectroscopy was used for the comparison of the different functional groups of all the molecules too. Interestingly, it could be observed, in Figure 64, that CCMoids **5** and **10** do not share the same shape as the other synthesized molecules, in fact, they present more similarities with some PAH units from reported studies, confirming also their graphene-like structure.[170-172]

Carefully analysing each of them, for CCMoids **4**, **7**, **9** and **11** some shared bands could be observed as at 1150-1190 cm^{-1} corresponding to the stretching and bending ν and δ(C-C-H) vibrations of the alkene chain and the aromatic ring, respectively. Then, at 1360 cm^{-1} appeared the bending δ(C-O-H) of the enol group. Next, at 1590 cm^{-1} the stretching ν_{ar}(C=C) vibration was found and finally at 1630 cm^{-1} was related to the signal of the stretching ν(C=O). Furthermore, the most remarkable difference observed within the -BF_2 units (**9** and **11**) is that the latter contain an additional signal in the 1500 cm^{-1} range consisting with the ν(B-O) vibration, which was not visible in the graphitic-like molecules due to the width of the nearby peaks. All the values agree with those found in reported studies of curcumin.[51,123,127] Interestingly, in the spectra of CCMoids **5** and **10** the signals were broader, and slightly shifted. As already explained and according to some reported publications,

these phenomena could be explained for the graphitic behaviour of the substances.[123,127,173] Furthermore, the same bands that appear in a graphene nanoribbon spectrum are observed: the first-order G band at 1597 cm^{-1} corresponding to ν(C-C) vibration (Ag symmetry: which is the symbol corresponding to the molecular vibration which presents symmetry respect to the centre and the principal axis of symmetry)[174] and the first-order D band at around 1300-1400 cm^{-1}, related to the breathing-like vibrations of the six-carbon-atom rings (representation of this vibration modes in Figure 65).[172] In addition, after suppression of the fluorescence within the experiments, it was possible to observe the second order 2G (only visible in CCMoid **5**), 2D and D+G bands which are located around 3200, 2950 and 2550 cm^{-1}, respectively.[173,175]

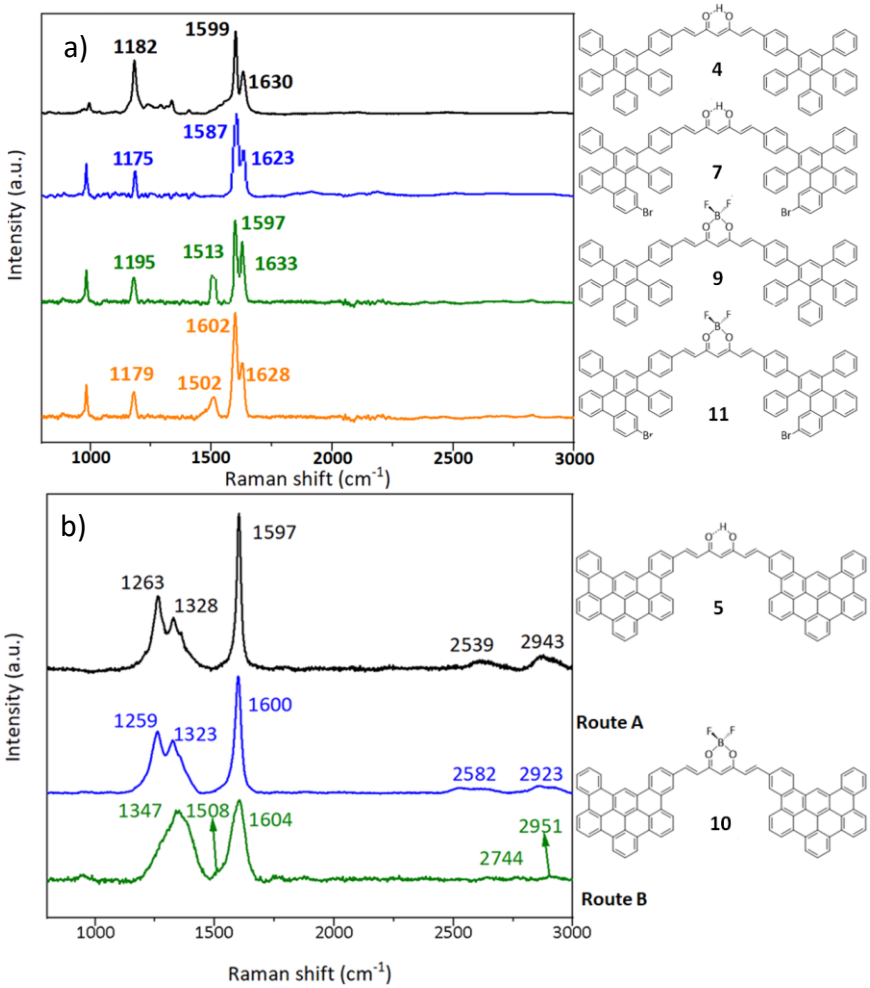

***Figure 64**: Raman spectra comparison of the different CCMoids: a) **4** (black), **7** (blue), **9** (green), and **11** (orange), and b) **5** (black) and **10** (blue route A and green route B).*

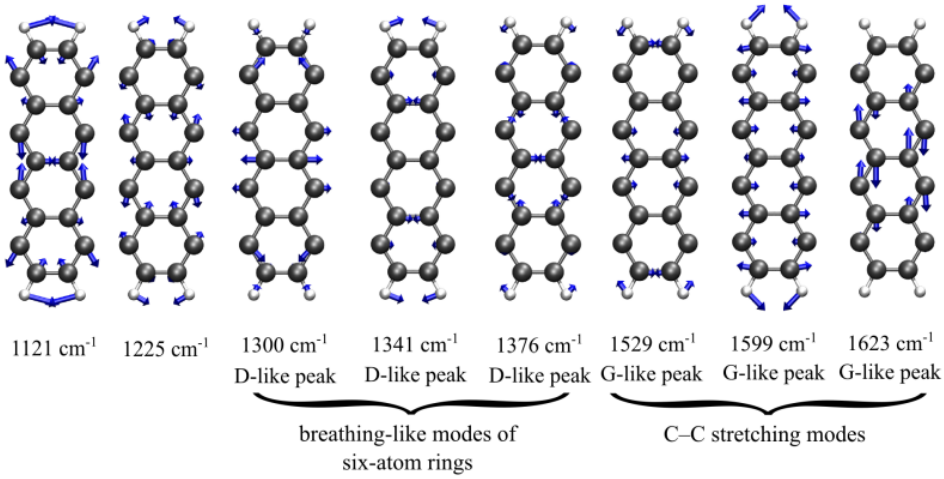

Figure 65: Representation of the Raman-active vibration modes of the 9-AGNR. Blue arrows indicate amplitude and direction of atomic displacements. Reprinted with permission from *ACS Nano*. 2017, 11 (2), 1380–1388.[171] Copyright 2017 American Chemical Society.

As for the ATR-FTIR spectra, simulations were performed to confirm the different functional groups of CCMoids **4** and **5** by comparing them with the experimental ones (Figure 66). For **4**, most of the bands in the simulated spectrum appeared closer than those appearing in the experimental one, only the stretching ν(C=O) band at 1630 cm^{-1} is shifted appearing at 1690 cm^{-1}. Nevertheless, for CCMoid **5** the experimental spectrum is very different compared to the simulated, due to the graphitic behaviour explained above and not reflected in the simulated spectrum. However, the area in the spectrum and overall shape agree with the experimental obtained for **5**.

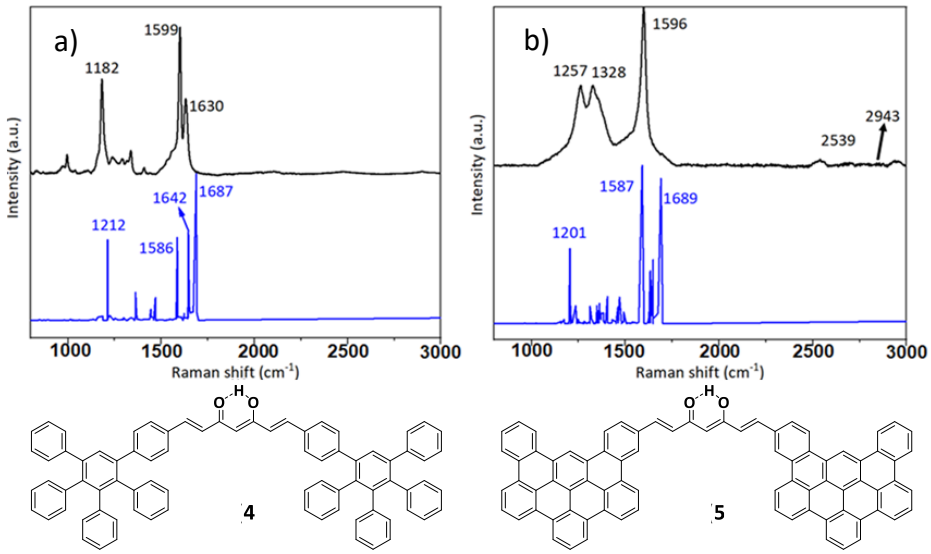

*Figure 66: Raman spectra comparison between a) CCMoid **4** (black) and the simulation (blue), and b) CCMoid **5** (black) and the simulation (blue).*

2.3.7. X-ray photoelectron spectroscopy (XPS) for CCMoid 10

XPS technique was used for the recognition of the -BF_2 functional group. In our case, it was exclusively used in a qualitative way, to recognize the presence of the B and F elements in system **10** deposited over an Au surface, Figure 67 and Figure **68**, respectively.[176-180] This way, it can be seen that in the B region, which the B atoms of the *keto-enol* group, can be integrated into two different bands that are related with the B-F and B-O bonds, respectively. In the F region it could be extracted also as two different bands related to B-F bond and the other as an excess of F^- reagent still remaining in the molecule, even after the cleaning procedure.[181]

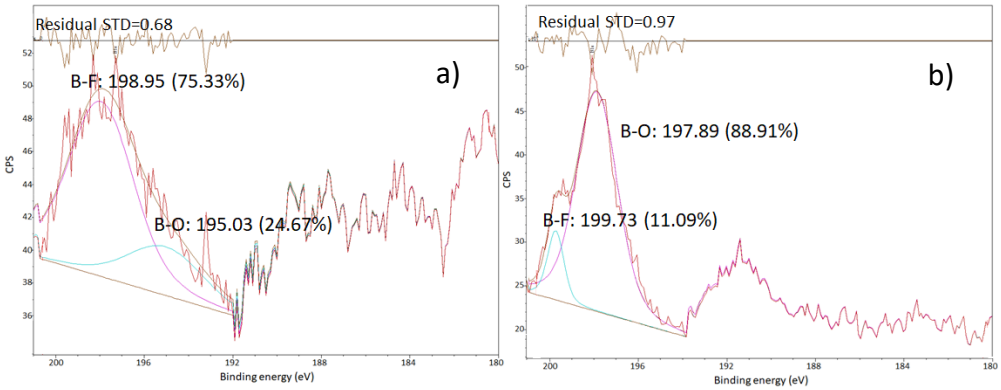

*Figure 67: Boron region of the XPS spectrum for a) **10** route **A** and b) **10** route **B**.*

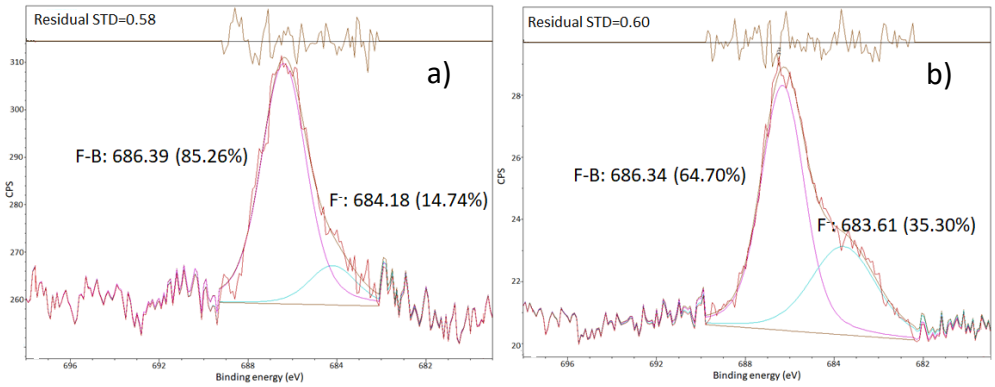

*Figure 68: Fluor region of the XPS spectrum for a) **10** route **A** and b) **10** route **B**.*

2.3.8. UV-Vis absorption studies in solution and in solid state for CCMoids 4, 5, 7, 9, 10 and 11

Once again, UV-Vis absorption studies in solution and in the solid state were performed in an attempt to further characterize, systems **4**, **7**, **9** and **11** while extracting electronic information, including the calculation of the optical band gap (E_g^{op}) in the case of the solid state.

As in previous chapter, the experiments were carried out in DCM with a concentration of 10^{-5} M. Again, for the systems with -BF_2, a shifting towards the near-infrared region (bathochromic shift) was observed due to the presence of the -BF_2 group in the band corresponding to the π-π* transitions of the *keto-enol* moiety situated between 403-484 nm (Figure 69).[50,114,118,119]

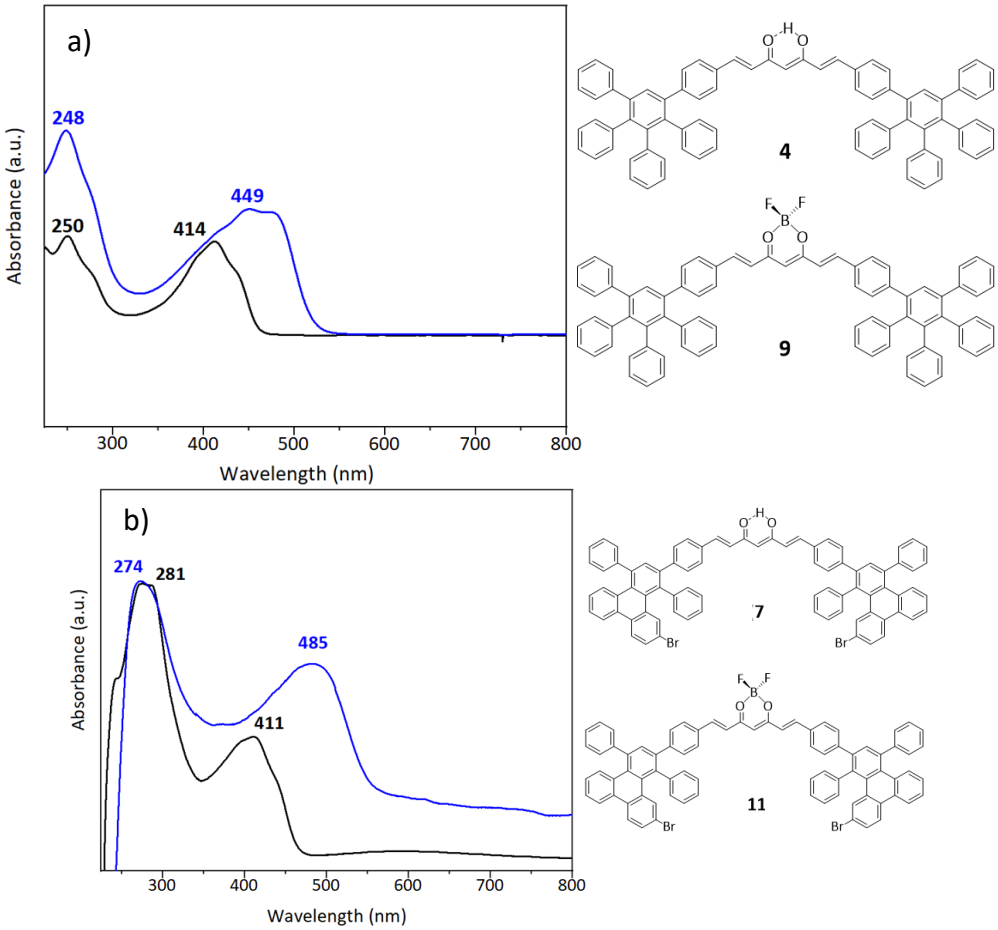

***Figure 69**: Comparative UV-Vis spectra in solution (DCM 10^{-5} M) for: a) **4** (black) and **9** (blue) and b) **7** (black) and **11** (blue).*

Then, moving to the solid-state studies, the same shifting phenomenon towards higher wavelengths for the π-π* transition of the *keto-enol* could be observed for CCMoids **4**, **7**, **9** and **11** in the bands around 390-480 nm (Figure

70). For systems **5** and **10** (Figure 71), however, the observed band between 370-377 nm appear closely as in similar PAH structures in the literature and is assigned to the π-band. Next, the band at 509 nm is also identified in the literature as the α-band.[41,81,112,182,183] Nevertheless, the bathochromic shifting for **10** was not observed. A possible explanation could be that the bands are broader for the presence of a huge number of highly conjugated aromatic rings or the formation of aggregation of various molecules by π-π stacking, which promotes charge delocalization that has great influence in the solid-state UV-Vis technique; also, we cannot discard the idea of having an incomplete reaction and therefore a degree of molecules that could not react with $-BF_2$ units due to the insolubility of the system.[184]

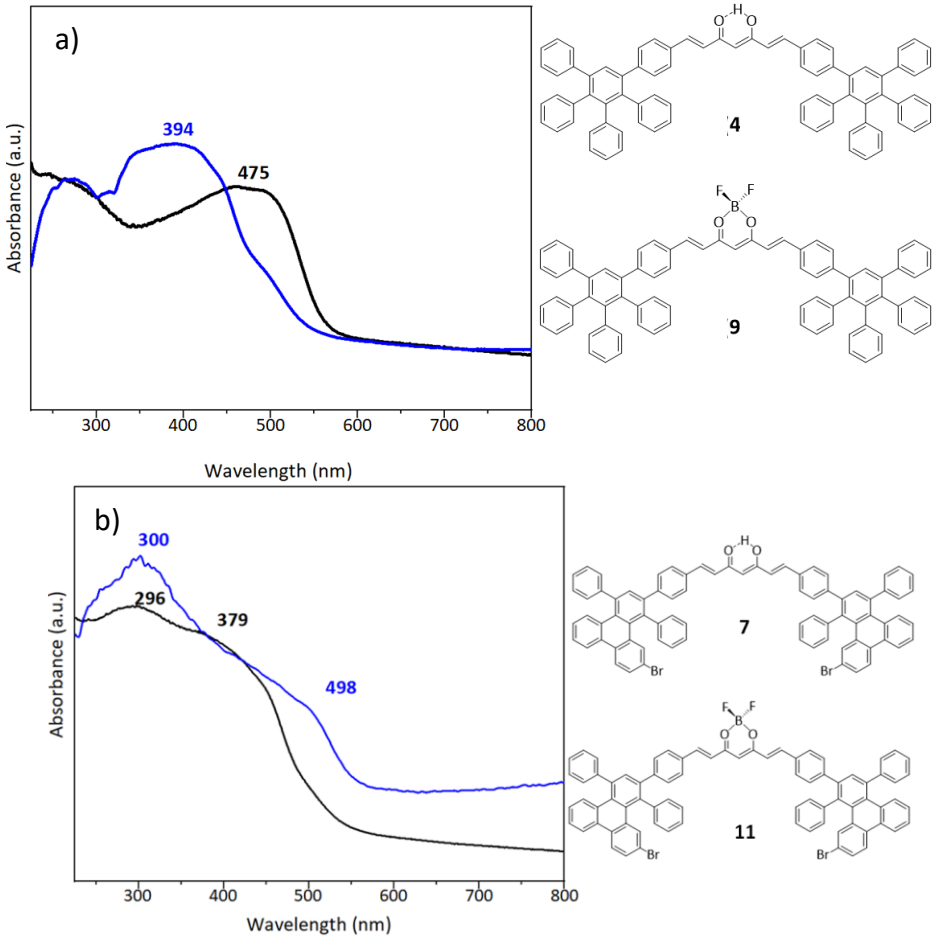

***Figure 70**: Comparative UV-Vis spectrum in solid state with KBr pellets (10^{-6} M) for: a) **4** (black) and **9** (blue) and b) **7** (black) and **11** (blue),*

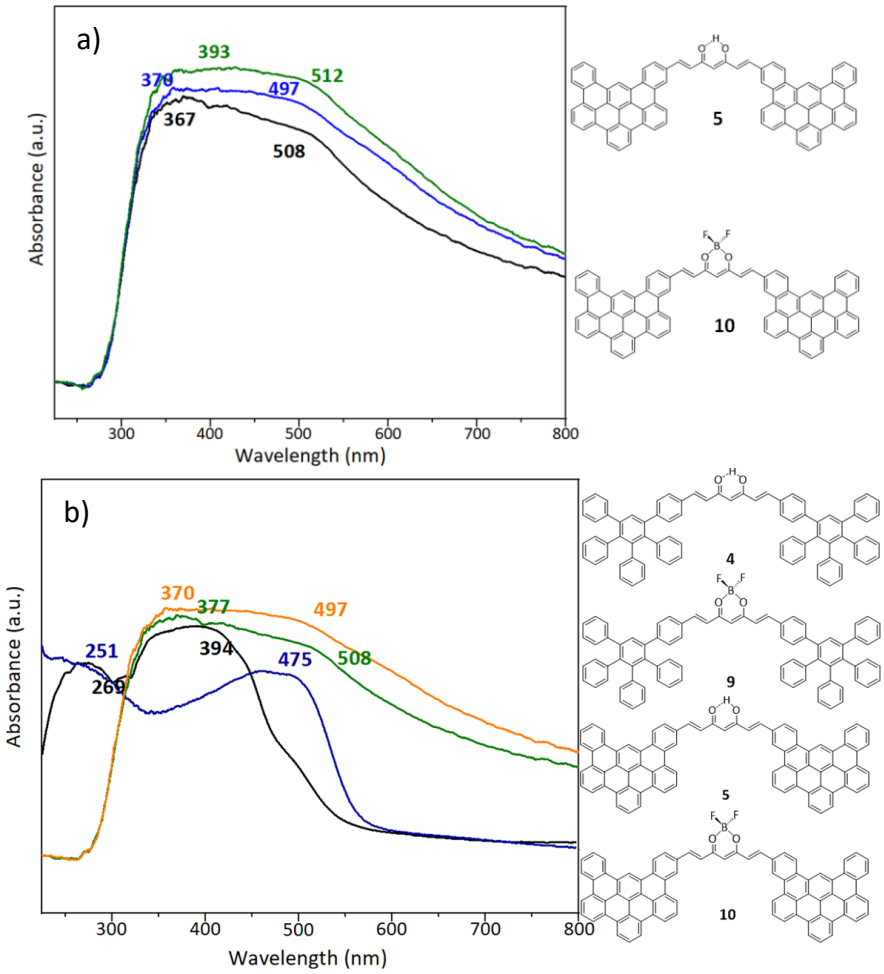

***Figure 71**: Comparative UV-Vis spectrum in solid state with KBr pellets (10^{-6} M) for: a) **5** (black), **10** (route A, blue), **10** (route B, green) and b) **4** (black), **9** (blue), **5** (green) and **10** (route A, orange).*

For the quantitative analysis, the calculation of the optical band gap for each molecule was performed in the solid state. To do that, Tauc's plot was used as explained in previous chapter. The comparison of all the CCMoids is represented in Figure 72.

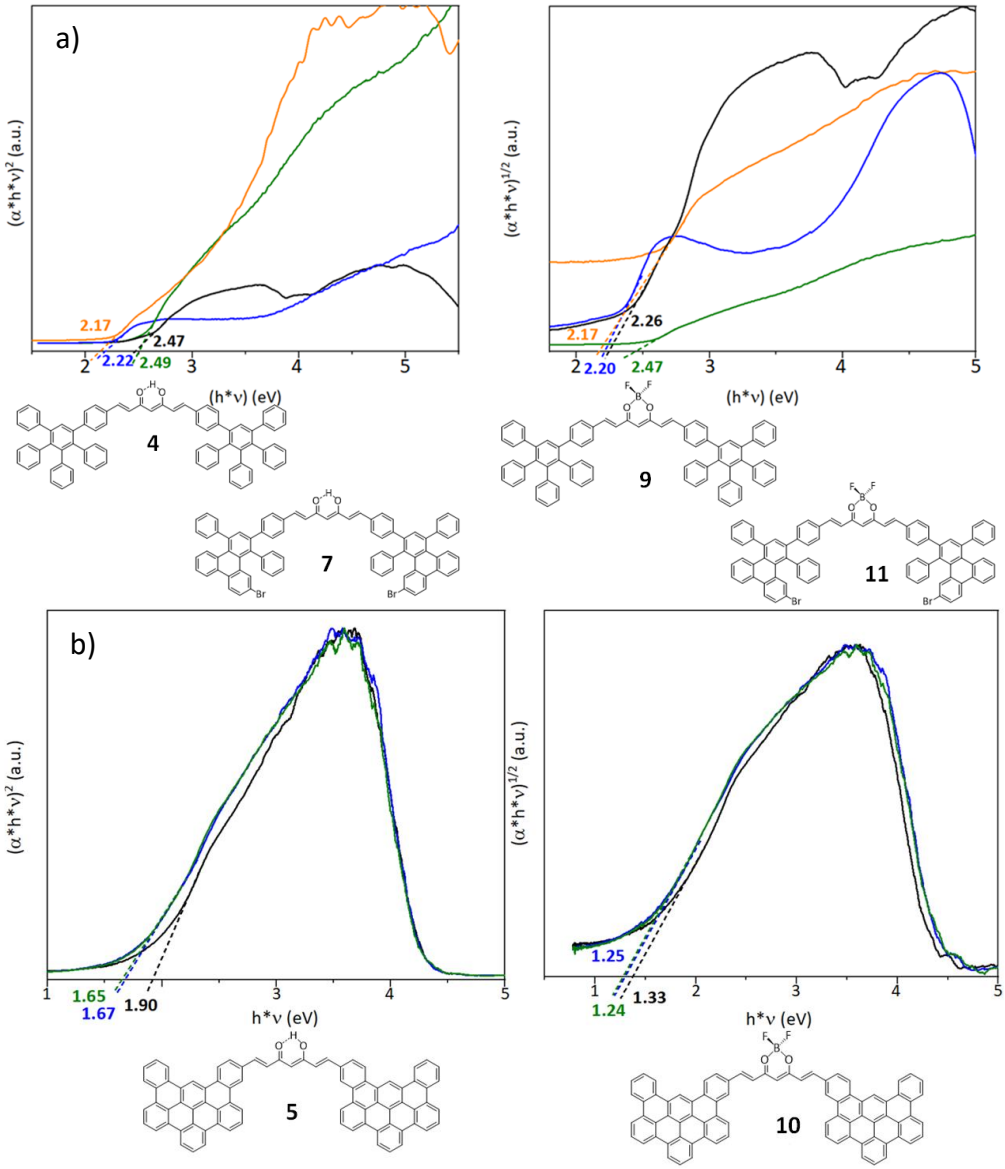

Figure 72: *Comparative UV-Vis spectrum using the Tauc's plot representation for the analysis of the optical band gap of: a)* ***4*** *(black),* ***9*** *(blue),* ***7*** *(green) and* ***14*** *(orange) and b)* ***5*** *(black),* ***10*** *(route A, blue) and* ***10*** *(route B, green).*

For all the systems it appears that those containing a -BF_2 group exhibit the smallest optical gaps in contrast to the free CCMoids, even in the case of the graphitic systems. Interestingly, for CCMoids **5** and **10**, it appears to be a bigger decrease of the energetic bandgap levels, which could mean that the molecule is more prone to behave as a semiconductor (Eg < 3 eV).[185] Such values, are below 2, which are remarkable, taking into account that in chapter 3 the overall electronic characterization of system **1** show a global insulator

behaviour. This way, it could be foreseen that systems **4**, **7**, **9** and **11** may behave in a similar way as **1** (by comparing the E_g values) meanwhile the electronic characteristics of systems **5** and **10** may differ from previous. Table 2.2 displays a summary of the data in solution and in solid state.

***Table 2.2**: Summary of the optical properties of **4, 5, 7, 9, 10** and **11**. Band gap energies are displayed in eV. Egop stand for the optical energy gap.*

CCMoid	E_g^{op} solid state	Colour of the powder
4	2.37	Brown
7	2.48	Yellow
9	2.21	Red
11	2.17	Red
5	1.65	Brown/black
10 (route A)	1.53	Brown/black
10 (route B)	1.46	Brown/black

2.3.9. Electrochemistry (Cyclic Voltammetry and Differential Pulse Voltammetry) for CCMoids 4, 7, 9 and 11

The calculation of the optical band gap was compared with the analysis of the electrical band gap (E_g^{ec}), using cyclic voltammetry and differential pulse voltammetry. This technique was only performed for the soluble molecules **4**, **7**, **9** and **11**, respectively. As in the previous chapter, each measurement was done dissolving the sample with DCM in a concentration of 10^{-3} M and using $TBAPF_6$ as electrolyte in an inert atmosphere of Ar. The spectra were recorded at 100 mV/s. Figure 73 and Figure **74** display the reduction (right) and oxidation (left) pattern of the four systems.

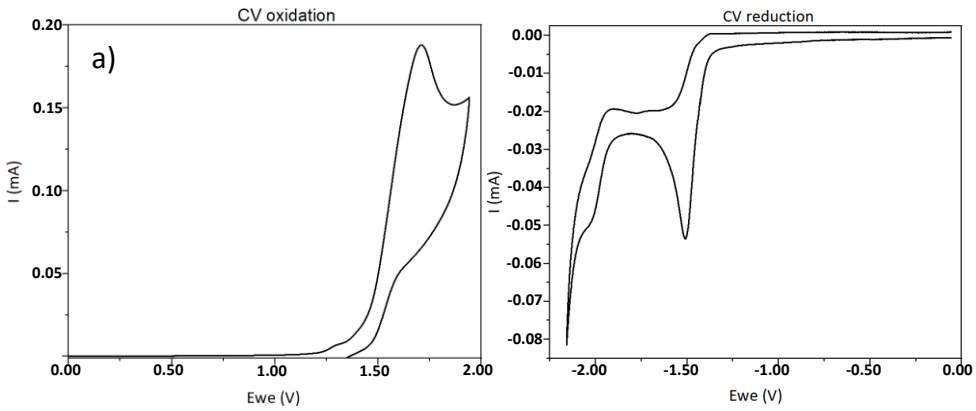

b)

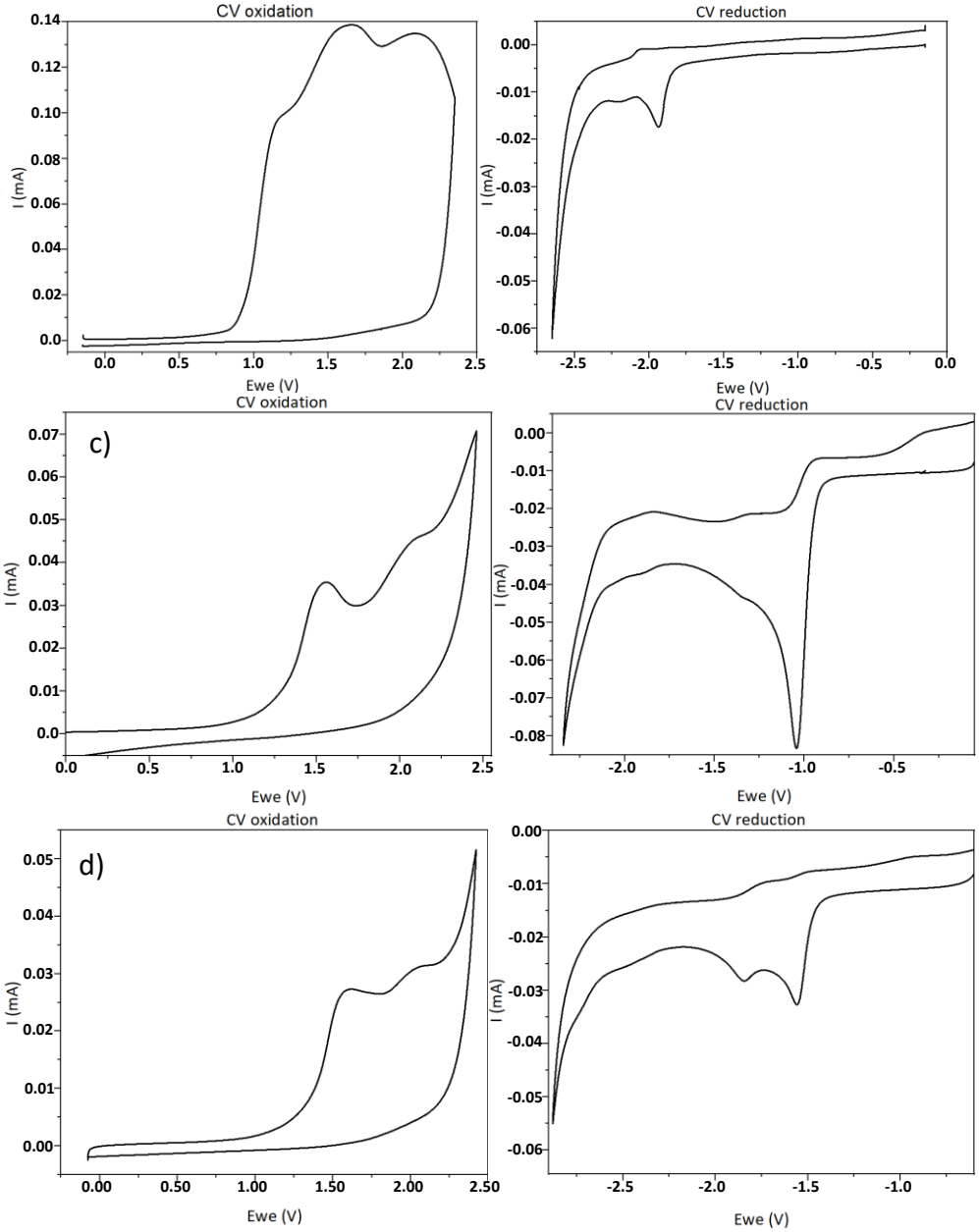

***Figure 73**: Oxidation and reduction cyclic voltammogram spectra of a) **4**, b) **7**, c) **9** and d) **11**.*

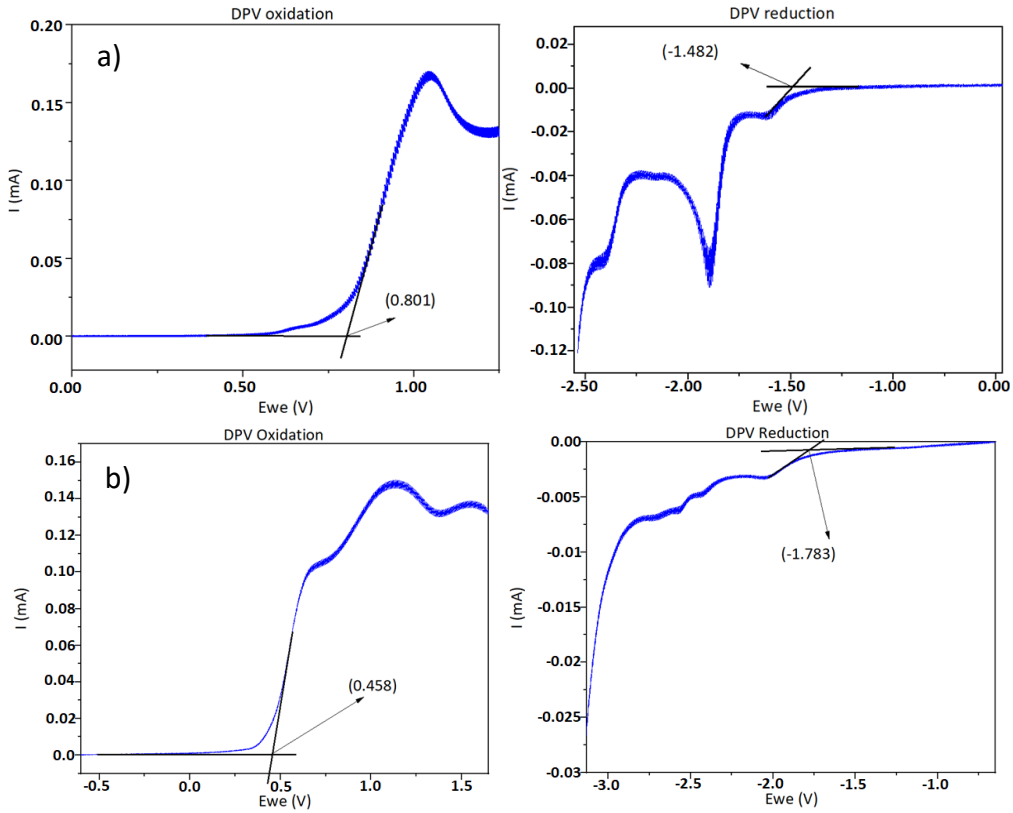
DPV oxidation
a)
I (mA)
Ewe (V)
(0.801)
DPV reduction
(-1.482)
I (mA)
Ewe (V)
DPV Oxidation
b)
I (mA)
Ewe (V)
(0.458)
DPV Reduction
(-1.783)
I (mA)
Ewe (V)

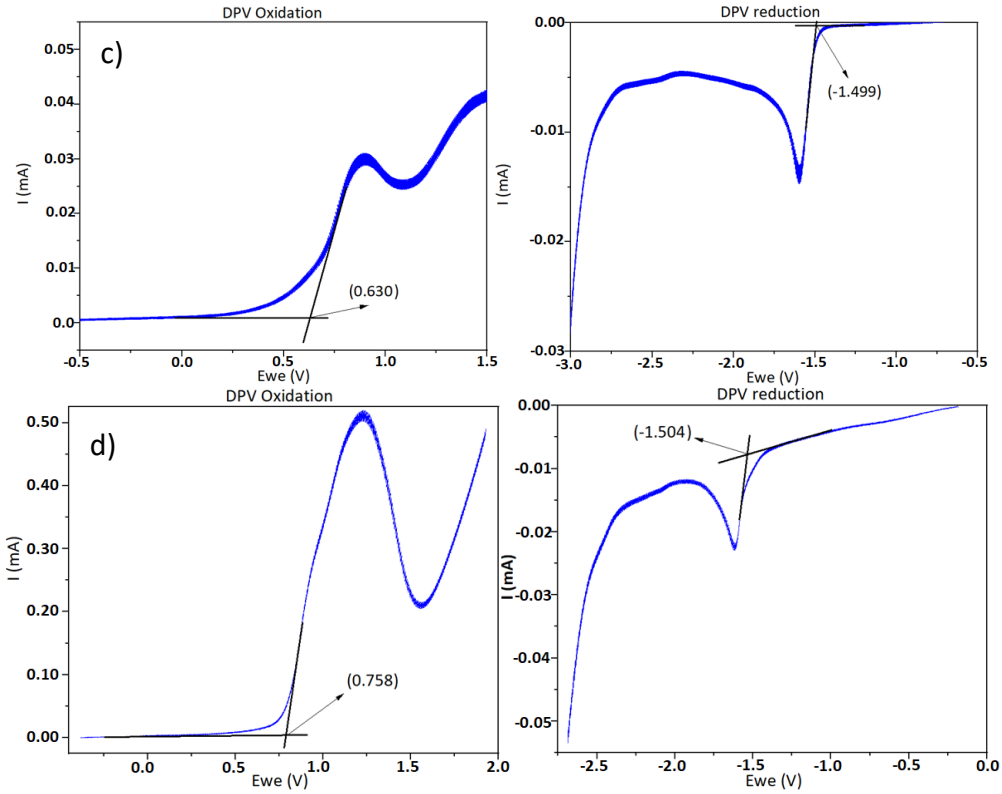

***Figure 74**: Oxidation and reduction differential pulse voltammogram spectra of a) **4**, b) **7**, c) **9** and d) **11**.*

As in the previous chapter, all the systems display irreversible bands for the oxidation and reduction processes, in a window between -2.75 and 2.5 V, correspondingly. In this range, the oxidation section always displays a broad process, and in the reduction process most of them present an intense first band. This pattern is typical for most of CCMoids described in the literature.[58] The electrochemical gaps are provided by the differential between the gap of the HOMO process (first oxidation observed) and the gap of the LUMO process (first reduction process), considering that they rely to the extraction and addition of electrons in the outer molecular orbitals.[45,117,135]

To compare with the values from the UV-Vis absorption studies in solution, the values obtained for the electrochemical band gap energy levels are compared to the optical ones for the four molecules (Table 2.3, Figure 75).

***Table 2.3**: Summary of the physical properties of **4**, **7**, **9** and **11**. Potential values in V, referenced to Fc/Fc$^+$. Band gap energies in eV. Eg^{ec} and Eg^{op} stand for the electrochemical and optical energy gaps, respectively.*

CCMoid	1st Oxid.	1st Red.	E_{HOMO}	E_{LUMO}	E_g^{ec}	E_g^{op}	Colour of the powder
4	0.80	-1.48	-5.60	-3.11	2.28	2.37	Brown
7	0.46	-1.78	-5.26	-3.02	2.24	2.48	Yellow
9	0.63	-1.50	-5.43	-3.30	2.13	2.21	Red
11	0.47	-1.59	-5.27	-3.21	2.06	2.17	Red

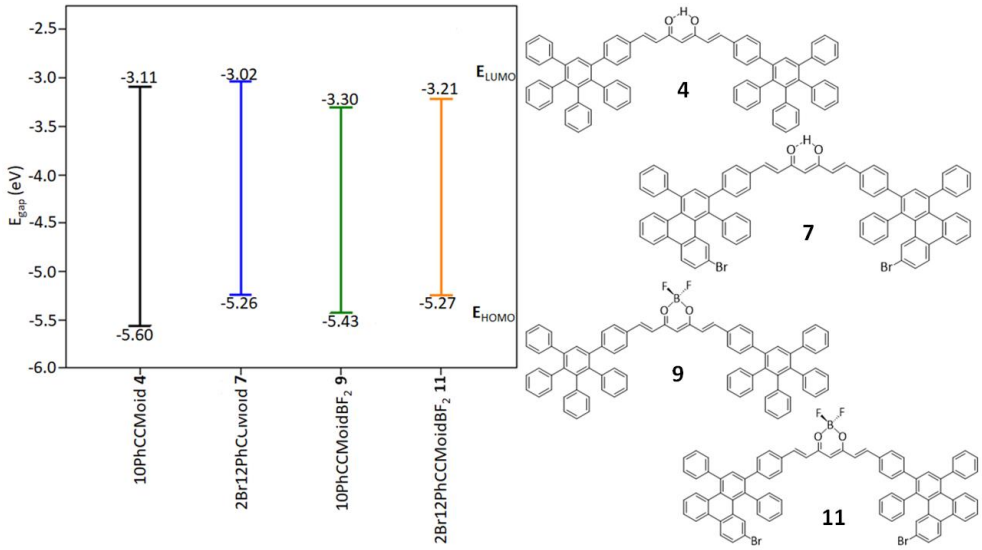

*Figure 75: HOMO and LUMO levels of **4**, **7**, **9** and **11** CCMoids.*

The comparison between the HOMO-LUMO values shows that when the molecules **4** and **7** are coordinated with the BF_2 a change in the E_g^{ec} they present a lowering of the values giving the molecules a more conductive behaviour. Comparing the values obtained with the ones from the previous chapter (Figure 76, Table 2.4) it could be seen that all the molecules of chapter **1** show a higher E_g^{ec}. These values mean that the molecules from this chapter have a stronger semiconductor character compared with previous, which could be explained with the presence of a higher number of aromatic groups that promotes an enhancement of the π-conjugation system.

The energy band gap values assessed from the optical and electrochemical experiments, agreed well, being in both cases similar, and consistent with other CCMoids in the literature, showing a more significant semiconductor character.[60]

*Table 2.4: Summary of the electrical properties of **1, 2, 3, 4, 7, 9** and **11** CCMoids. Potential values in V, referenced to Fc/Fc⁺. Band gap energies in eV. Eg^{ec} and Eg^{op} stand for the electrochemical and optical energy gaps, respectively.*

CCMoid	1st Oxid.	1st Red.	E_{HOMO}	E_{LUMO}	E_g^{ec}	E_g^{op}	Colour of the powder
1	0.86	-1.54	-5.66	-3.26	2.44	2.48	Brown
2	0.41	-1.95	-5.21	-2.85	2.36	2.40	Yellow
3	0.85	-1.47	-5.66	-3.33	2.32	2.20	Red
	1st Oxid.	**1st Red.**	**E_{HOMO}**	**E_{LUMO}**	**E_g^{ec}**	**E_g^{op}**	**Colour of the powder**
4	0.80	-1.48	-5.60	-3.11	2.28	2.37	Brown
7	0.46	-1.78	-5.26	-3.02	2.24	2.48	Yellow
9	0.63	-1.50	-5.43	-3.30	2.13	2.21	Red
11	0.47	-1.59	-5.27	-3.21	2.06	2.17	Red

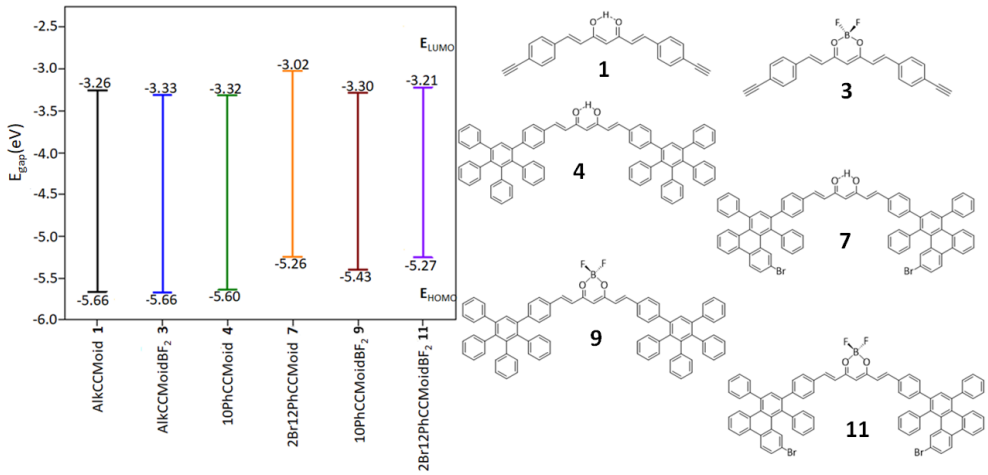

***Figure 76**: HOMO and LUMO levels of **1, 3, 4, 7, 9,** and **11** CCMoids.*

2.3.10. Fluorescence emission studies for CCMoids 4, 5, 9 and 10

Regarding the fluorescence emission studies, it is known that PAHs exhibit fluorescence emission in the range between 400-650 nm when the molecules are dissolved in some common solvents, such as toluene, tetrachloroethane and cyclohexane.[80] Nevertheless, in the solid state, an aggregation process occurs between planar chromophores leading to the formation of π-aggregates/excimers and as a result the fluorescence emission can drop or even cancelled.[186-188]

Considering this information, we performed initial trials to measure the emission fluorescence of the CCMoids obtained before and after the cyclodehydrogenation reaction (**4**, **9**, **5** and **10**, Figure 77). On one hand, it was possible to observe some bands in the range of 500-600nm for **4** and **9**, where **9** presented a shift of the emission band towards the 600 nm due to the same phenomena already explained of the bathochromic shift of the -BF_2 moiety. On the other hand, for CCMoids **5** and **10** it was confirmed the aforementioned aggregation phenomena, which enables us to distinguish the fluorescent emission bands viewed in the previous molecules. In order to overcome this problem for future experiments the arms of molecules **5** and **10** will be modified, adding functional groups that may facilitate the solubility of these molecules and hence overcome the aggregation problems.

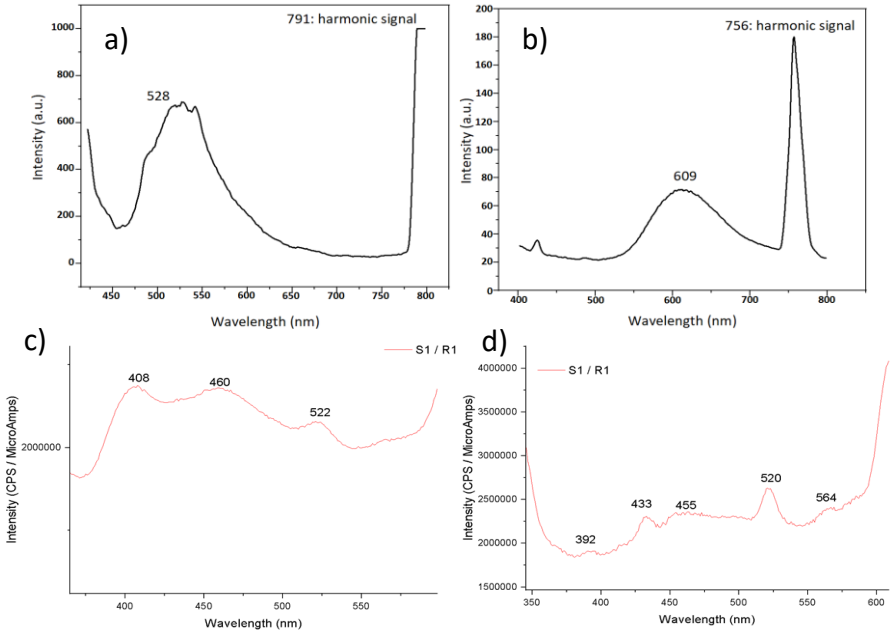

***Figure 77**: a) Emission fluorescence spectra with excitation at 400 nm for **4**, conditions of the measurement: PMT voltage (High), excitation light aperture (10), emission light aperture (5), smoothing (on). b) Emission fluorescence spectra with excitation at 380 nm for **9**, conditions of the measurement: PMT voltage (Medium), excitation light aperture (10), emission light aperture (5), smoothing (on). c) Emission fluorescence spectra with excitation at 320 nm for **5**, conditions of the measurement: PMT voltage (High), excitation light aperture (10), emission light aperture (5), smoothing (on). d) Emission fluorescence spectra with excitation at 320 nm for **10**, route A, conditions of the measurement: PMT voltage (High), excitation light aperture (10), emission light aperture (5), smoothing (on).*

2.3.11. TGA, melting and sublimation point measurements for CCMoids 4, 5, 7, 9 and 11

Despite what happened in chapter 1, no information regarding the thermal stability of the samples was obtained with the melting point measurements, showing in all cases a change of the CCMoids turning them into black with inconclusive analyses. Moreover, something similar happened when the sublimation point was tried to be found obtaining only molecule **4** a sublimation point at 265 °C under a pressure of $1 \cdot 10^{-3}$ bar, once again, in all the other molecules, the solid suffered a change of colour turning them into black with inconclusive analyses.

Subsequently, thermogravimetric analyses were performed to identify the temperature at which the different molecules suffer structural and decomposition changes (Figure A 76 and Figure **A 80**). To do the analysis, the molecules were heated up to 800 °C under N_2 with a mass flow rate of 100 mL/min and a heat ramp of 10 °C/min. For all CCMoids the molecule starts to suffer a first change between 200-250 °C, where the common trend is the loss of solvent molecules as acetonitrile or more abrupt changes as the loss of the *keto-enol* moiety. Then, for CCMoids **4** and **5** at 250 °C it could be seen an exothermic band that for the other CCMoids is present at around 500 °C, which indicates that, the molecule suffered a melting or a sublimation process (see Appendix of this chapter).

2.3.12. Deposition of 5 on surface

We performed some experiments of the deposition of molecule **5** on graphene surfaces to find suitable conditions for the final deposition process over the three-terminal device and how to characterize properly the system (similar to the image shown in Figure 53). These experiments were done by putting a drop of a solution of **5** in DCM or tetrachloroethane (TCE) and letting dry the graphene substrate overnight. The samples were then analysed without further clean-up process. During the process, it was observed by optical microscopy and scanning electron microscopy (SEM) that the surface suffered some mechanical stress due the removal of the droplet during the evaporation process, Figure 78b and c. In addition, it was seen the presence of large clusters of the molecule, due to the aggregation of CCMoids, which could be another drawback because they could cover future devices and block the nano-gap region.

Due to lack of time, no further studies were performed in this direction, and as a future prospect, different procedures to avoid the presence of big clusters can be tried such as: sonication studies of the sample, filtering of the

emulsion and playing with different concentrations. In the case of the delivering of the sample an alternative to the drop casting methodology could be the dip coating methodology, which consisted of depositing the graphene device into a suspension of the molecule and then let it dry by air.

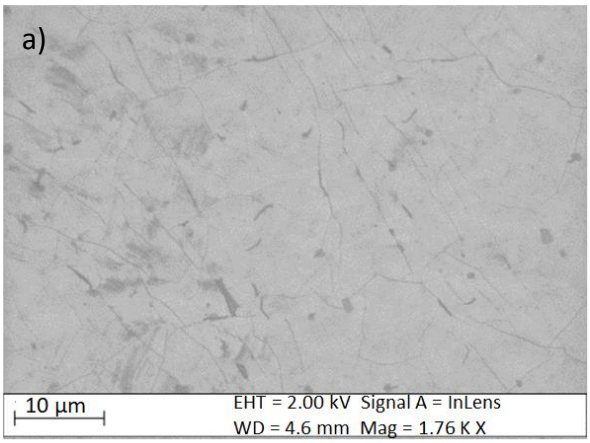

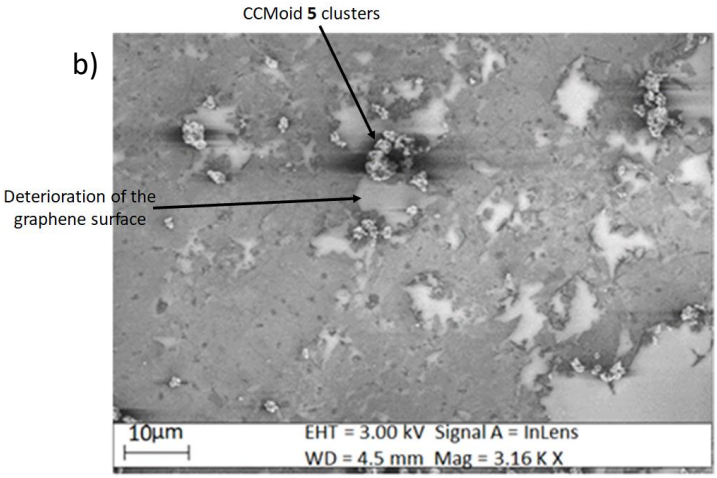

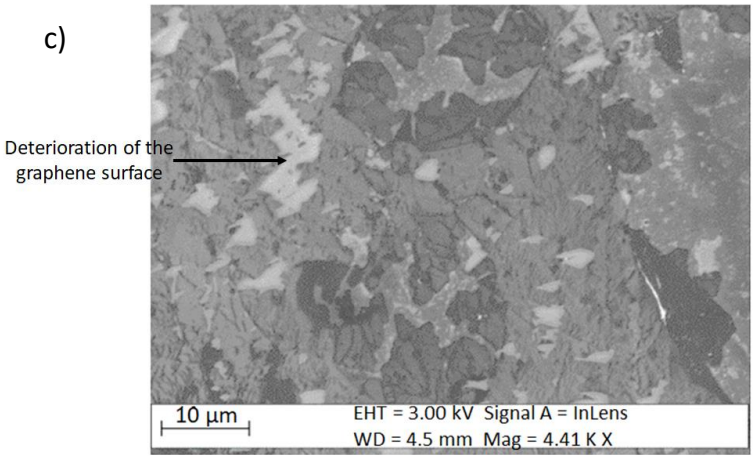

***Figure 78**: SEM images of: a) before the deposition of mixture solution of **5** over a graphene surface and b) after the deposition by drop casting with DCM and c) after the deposition using TCE.*

2.4 CONCLUSIONS

In this chapter, the synthesis of new PAH-CCMoids (**5** and **7**) were successfully achieved using three and two steps methodologies in an overall yield of 27 and 31% yields. Moreover, CCMoid **7** would allow us to obtain another molecule that contains a much larger PAH at the arms position that could resemble a GNR.

Using solid-state techniques, like Raman spectroscopy, MS-MALDI-TOF, ATR-FTIR and XPS, it was possible to characterize and overcome the high insolubility of the final system and its -BF_2 derivatives.

The comparison between the HOMO-LUMO values for molecules **4**, **5** and **7** shows that the -BF_2 group induces a reduction of the energy gap, conferring to the molecules a more semiconductor behaviour, in comparison with what it has been seen in the previous chapter. Moreover, it can be observed that all the molecules in chapter 3 show a more insulating behaviour with higher values of the electrochemical and optical energy gap, which could be explained with the presence of a higher number of aromatic groups could promote a higher freedom of electrons to move towards the π-conjugation system and therefore a higher capacity to conduct electrons. The optical and electrical bandgap of all the molecules before closing the rings presented values between 2-3 eV meaning that they can act as semiconductors, whereas the electrical bandgap calculated for molecules **5** and **10** in the solid state gave values < 2 eV, meaning a higher semiconductor behaviour than the others.

The deposition of molecule **5** on graphene surfaces by drop casting show big aggregations of the CCMoid on the surface, which produced some mechanical stress during the evaporation of the solvent and consequently the deterioration of the surface indicating that another type of deposition procedure has to be developed, among other proposed approaches and modifications in the employed methodology.

2.5 FUTURE WORK

As future work of this project, molecule **7** could be used as a starting point to obtain another molecule possessing a much larger PAH at the arms position as shown in Scheme 5.

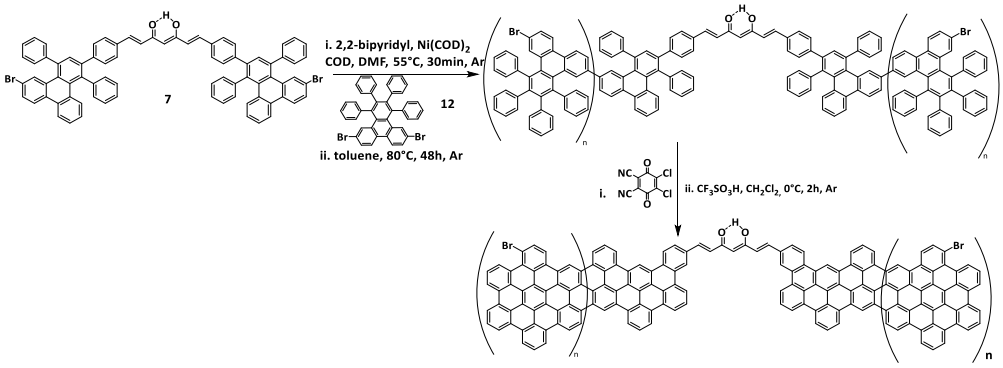

***Scheme 5**: Synthetic pathway of the possible path to obtain the final GNRCCMoid.*

This synthesis consists first of the Yamamoto coupling[188,190] reaction with ligand **12**. The Yamamoto coupling is based on a carbon-carbon bond coupling between two aryl halide groups mediated with a metal catalyst of nickel (0) (bis(cyclooctadiene)nickel ($Ni(cod)_2$)). An advantage that the Yamamoto coupling offers over the other coupling reactions (Suzuki, Sonogashira, Negishi, etc.) is that it requires only a single halogen-functionalized monomer, which speeds up the process. The mechanism of this reaction is illustrated in Figure 79.

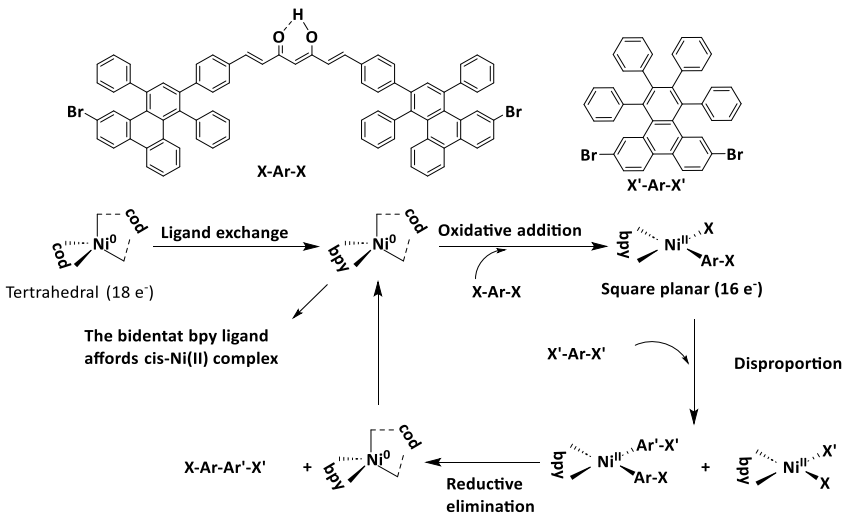

***Figure 79**: Yamamoto's coupling mechanism.*

It is known that first, the $Ni(cod)_2$ metal catalyst undergoes a ligand exchange between one of the cods and a bipyridine ligand which acts as a stabilizer of the transition alkyl- metal bond. Next, one of the diaryl complexes is added to the catalytic cycle through an oxidative addition process that changes the central metal core from Ni(0) to Ni(II) and promotes a square planar complex. Following the mechanism, a disproportion process proceeds where, the other diaryl reagent is introduced and enhances the formation of a complex containing the two aryl molecules arranged in *cis* position. Finally, the last step of the cycle is the reductive elimination process, which gives our desired diaryl complex and reduces the central Ni(II) metal core back to Ni(0) to start again the process. Once this reaction is accomplished, the product undergoes a cyclodehydrogenation reaction, to obtain the final GNRCCMoid.

Moreover, ligand **12** was obtained following the same procedure previously mentioned for ligands **6** and **8** but with slight changes, as explained in published literature (Scheme 6).[105,164,165] This procedure consisted, firstly, in subjecting 9,10-phenanthrenedione to a bromination reaction using *n*-bromosuccinimide, which, by doubling the equivalents of this bromination reagent with respect with those used to obtain molecule **8**, the dibrominated molecule **13** can be obtained. Then, the next reaction consists of the Knoevenagel condensation using the 1,3-diphenylpropan-2-one, giving the ketone **14**. Finally, with molecule **14**, a diels-alder reaction with diphenylacetylene produced the dibromated PAH **12**.

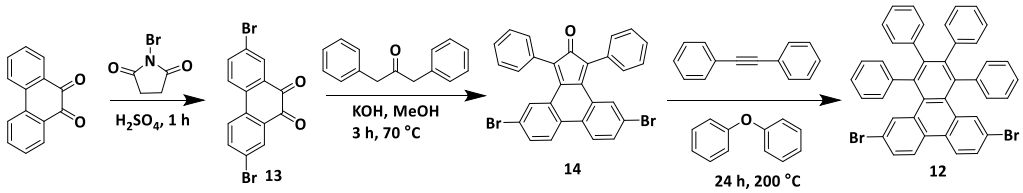

***Scheme 6**: Scheme of the synthetic path to obtain the ligand molecule **12**.*

Nevertheless, once the Yamamoto coupling process was carried out in the laboratory, only few trials were performed due to the lack of quantity of ligands and the time needed to obtain and properly characterize them. In all the cases, the starting reagents were always obtained with a degree of impurities, so it was concluded that the conditions of this reaction should be further optimized as future work. As mentioned before, this is in collaboration with Professor Diego Peña and future work will be carried out in collaboration.

Furthermore, as future work, additional studies should be carried out to improve the deposition of molecule **5** on the three-terminal device. To avoid the presence of big clusters of CCMoids (**5**) initial solutions should be sonicated and filtered prior deposition. In addition, upon delivery of the sample onto the surface, one could attempt to dip the sample into the solution, wash it and gently dry it the next day instead of the drop-casting procedure.

2.6 EXPERIMENTAL SECTION

2.6.1. Measurements

Explained in chapter 3

2.6.2. Materials

2,3,4,5-tetraphenylcyclopenta-2,4-dien-1-one ($C_{29}H_{20}O$), trifluoromethanesulfonic acid (CF_3SO_3H), 2,3-dichloro-5,6-dicyano-1,4-benzoquinone (DDQ), boron trifluoride diethyl etherate ($BF_3{\cdot}OEt_2$), phenanthrene-9,10-dione ($C_{14}H_8O_2$), H_2SO_4 (98%), n-bromosuccinimide (NBS), 1,3-diphenylacetone ($C_{15}H_{14}O$), diphenylacetylene ($C_{14}H_{10}$), potassium hydroxide (KOH) were provided by Sigma Aldrich and Fluorochem. Ethyl Acetate (EtOAc), hexane, toluene, methanol (MeOH), acetonitrile (MeCN), chloroform ($CHCl_3$) and 1,1,2,2-tetrachloroethane ($C_2H_2Cl_4$), diphenyl ether (Ph_2O) are supplied by Carlo Erba. Dicloromethane (DCM) was provided by ChemLab. Deuterium chloroform ($CDCl_3$), deuterium dimethylsulfoxide (DMSO-d^6) and deuterium DCM (CD_2Cl_2) was provided by Eurisotop.

2.6.3. Synthesis of 4. (1E,4Z,6E)-5-hydroxy-1,7-bis(4-{4,5,6-triphenyl-[1,1'-biphenyl]-2-yl}phenyl)hepta-1,4,6-trien-3-one

200 mg (0.6 mmol) of **1** and 690 mg of 2,3,4,5-tetraphenylcyclopenta-2,4-dien-1-one (3 eq, 1.8 mmol) were solubilized in 6 mL of toluene. When the ketone was added, the mixture changed its colour from yellow to violet, then the solution was stirred and heated under reflux at 120 °C for 48 h. TLC was used to monitor the progress of the reaction (hexane/DCM: 95/5, Rf: 0.31). Finally, the reaction was cooled down to RT, then hexane was added to the solution and a brown-yellowish precipitate was obtained. The solid was filtered and washed with hexane. The further purification of the system and recrystallization process were performed with MeOH and MeCN. **4** was obtained as a brown solid in a 77% yield. ^{1}H NMR (δ in ppm, 360 MHz, $CDCl_3$): 15.89 (s, 1H), 7.57 (d+s, $^3J_{HH}$ = 15.66 Hz, 4H), 7.36 (d, $^3J_{HH}$ = 8.02 Hz, 2H), 7.16 (m, 12H), 6.88 (m, 32H), 6.58 (d, $^3J_{HH}$ = 15.66 Hz, 2H), 5.75 (s, 1H). $^{13}C\{^1H\}$ NMR (δ in ppm, 90 MHz, $CDCl_3$): 183.3, 143.9, 142.1, 141.7, 141.1, 140.4, 140.2, 139.9, 139.9, 139.8, 139.3, 133.0, 131.6, δ131.5, 131.3, 130.6, 130.1, 127.8, 127.7, 127.6, 127.2, 127.1, 126.8, 126.5, 125.9, δ125.8, δ125.5, 123.9 and 101.8. ATR-FTIR (cm^{-1}): 3025 (ν:=C-H and ν_{ar}:C-H), 1630 (ν:C=O *keto-enol*, enol

form with intermolecular H-bonds), 1594 (ν_{ar}:C-C, skeleton vibrations), 835 (ν_{ar}:C-H ρ-disubstituted and ν_{ar}:C-H pentasubstituted), 763 (ν_{ar}:C-H monosubstituted) and 696 (ν_{ar}:C-H monosubstituted). Raman (cm^{-1}): 1629 (ν:C=O), 1600 (ν:C=C, aromatic ring), 1336 (δ: C-O-H, enol group and δ: C-C-H, aromatic ring), 1180 (δ: C-O-C, *keto-enol* group and ν and δ: C-C-H, aromatic ring). MS MALDI-TOF (m/z): calc. for $C_{79}H_{56}O_2$[M]: 1036.32; found $[M]^-$: 1036.08. Elemental analysis calculated for **4**·2MeCN ($C_{83}H_{72}N_2O_2$): 89.06 C, 5.58 H. Found: 89.30 C, 5.20 H.

2.6.4. Synthesis of 5. (1E,4Z,6E)-7-{decacyclo[22.10.2.02,15.03, 8.04,33.09,14.017,35.018,23.028,36.029,34]hexatriaconta-1(35),2(15),3(8),4,6,9(14),10,12,16,18, 20,22, 24,26, 28 (36),29(34),30,32-octadecaen-11-yl}-5-hydroxy-1-{undecacyclo[24.12.0.02,15.03,8.04,37.09,14.013,18.016,25.017,22.027,32.033,38]octatriaconta-1(26),2(15),3(8),4,6,9(14),10,12,16(25),17(22),18,20,23,27(32),28,30,33(38),34,36-nonadecaen-30-yl} hepta-1,4,6-trien-3-one

50 mg (0.05 mmol) of **4** was mixed with 130 mg of DDQ (12 eq, 0.58 mmol) under Ar and both reagents were solubilized in 4 mL of dry DCM. Then, the mixture was brought to 0 °C with an ice bath and 50 μL of CF_3SO_3H (12 eq, 0.58 mmol) was added to the solution. After that, the mix was brought to RT and let it stir for 2 h. TLC was used to control the disappearance of the starting material **4** (hexane/DCM: 95/5, Rf: 0.31). After this time, 2 x 5 mL of $NaHCO_{3(aq)}$ was added to the mixture and the solid obtained was centrifuged for 5 min in 6000 rpm obtaining a black solid and a yellow solution. Then, the same procedure of washing and centrifugation was done with distilled H_2O, cold MeOH, cold $CHCl_3$ and 1,1,2,2-tetrachloroethane until the centrifuge solution has no colour. Finally, the resulting black solid **5** was let it dry in the vacuum obtaining a 96% yield. ATR-FTIR (cm^{-1})**:** 3062 (ν:-C-H), 1699 (ν:C=O diketo form), 1598 (ν_{ar}**:**C-C, skeleton vibrations), 878 (ν_{ar}:C-H pentasubstituted), 747 (ν_{ar}: C-H o-disubstituted), 877 and 797 (ν_{ar}:C-H 1,2,4-trisubstituted), 797 (ν_{ar}: C-H vec-trisubstituted). Raman (cm^{-1}): 3197 (second order G band), 2943 (second order G+D band), 2539 (second order D band), 1597 (first order G band, ν:C-C) 1328 (first order D band, breathing-like vibrations of six carbon atom ring) and 1263 (first order D band, breathing-like vibrations of six carbon atom ring). MS MALDI-TOF (m/z): m/z calc. for $C_{79}H_{40}O_2$[M]: 1020.42; found $[M-3]^-$: 1017.34. Elemental analysis calculated for **5** ($C_{79}H_{40}O_2$): 93.08 C, 3.86 H. Found; 75.44 C, 2.59 H.

2.6.5. Synthesis of 9. 2,2-difluoro-4,6-bis((E)-2-(3',4',5'-triphenyl-[1,1':2',1''-terphenyl]-4-yl)vinyl)-2H-1λ^3,3,2λ^4-dioxaborinine

50 mg (0.05 mmol) of **4** and 10 μL of $BF_3{\cdot}OEt_2$ (1.4 eq, 0.07 mmol) were solubilized in 1.5 mL of DCM. The mixture was heated with the microwave in a dynamic program of 50 °C for 10 min at 6000 rpm. TLC was used to monitor the progress of the reaction (hexane/EtOAc: 8/2, Rf: 0.28). Finally, the reaction was cooled down to RT, the solid obtained was filtered, washed with Et_2O and MeOH and recrystallized with MeOH. **9** was obtained as a red powder in a 67% yield. ^{1}H NMR (δ in ppm, 360 MHz, $CDCl_3$): 7.98 (d, $^3J_{HH}$ = 15.46 Hz, 2H), 7.57 (s, 2H), 7.42 (d, $^3J_{HH}$ = 8.13 Hz, 4H), 7.22 (d, $^3J_{HH}$ = 8.13, 4H), 7.16 (s, 8H), 6.89 (m, 32H), 6.65 (d, $^3J_{HH}$ = 15.46 Hz, 2H), 5.75 (s, 1H). $^{13}C\{^1H\}$ NMR (δ in ppm, 90 MHz, $CDCl_3$): 179.6, 141.2, 140.8, 139.7 139.5, 139.3, 139.2, 138.9, 131.2, 131.1, 129.7, 128.4, 127.4, 126.9, 126.8, 126.5, 126.2, 125.7, 125.3, 101.9. ATR-FTIR (cm^{-1})**:** 3025 (ν:=C-H and ν_{ar}:C-H), 1603 (ν:C=O *keto-enol* form with intermolecular H-bonds), 1532 (ν_{ar}:C-C, skeleton vibrations), 1399 (ν:B-O), 899 (ν_{ar}:C-H monosubstituted), 830 (ν_{ar}:C-H ρ-disubstituted and ν_{ar}:C-H pentasubstituted), 767 (ν_{ar}:C-H monosubstituted), 696 (ν_{ar}:C-H monosubstituted). Raman (cm^{-1}): 1634 (ν:C=O), 1607 (ν: C=C, aromatic ring), 1512 (ν: B-O, δ:O-H enol group and δ: C-C-H, aromatic ring), 1186 (δ: C-O-C, *keto-enol* group and ν and δ: C-C-H, aromatic ring). MS MALDI-TOF (m/z): calc. for $C_{79}H_{55}BF_2O_2$ [M]: 1084.43; found $[M-1]^-$: 1083.99. Elemental analysis calculated for **9** ($C_{79}H_{55}BF_2O_2$): 87.45 C, 5.11 H. Found; 87.30 C, 4.94 H.

2.6.6. Synthesis of 10. 4-[(1E)-2-{decacyclo[22.10.2.02,15.03,8.04,33.09,14.017,35.018,23.028,36.029,34]hexatriaconta-1(35),2(15),3(8),4,6,9(14),10,12,16,18,20,22,24,26,28(36),29(34),30,32-octadecaen-11-yl}ethenyl]-2,2-difluoro-6-[(1E)-2-{undecacyclo[24.12.0.02,15.03,8.04,37.09,14.013,18.016,25.017,22.027,32.033,38]octatriaconta-1(26),2(15),3(8),4,6,9(14),10,12,16(25),17(22),18,20,23,27(32),28,30,33(38),34,36-nonadecaen-30-yl}ethenyl]-2H-1λ^3,3,2λ^4-dioxaborinin-1-ylium-2-uide

Two synthetic routes (A and B) were used to obtain **10**.

A) 50 mg (0.05 mmol) of **9** was mixed with 130 mg of DDQ (12 eq, 0.58 mmol) under Ar and were solubilized in 4 mL of dry DCM. Then, the mixture was brought to 0 °C with an ice bath, afterwards 50 μL of CF_3SO_3H (12 eq, 0.58 mmol) was added to the solution and the mix was brought to room

temperature and let it stir for 2 h. TLC was used to control the disappearance of the starting material **9** (Hexane/EtOAc: 8/2, Rf: 0.28). After this time, 2 x 5 mL of $NaHCO_{3\ (aq)}$ was added to the mixture and the solid obtained was centrifuged for 5 min using 6000 rpm/min, obtaining a black solid and a yellow solution. Then, the same procedure of washing and centrifuge was done with distilled H_2O, cold MeOH and $CHCl_3$ and 1,1,2,2-tetrachloroethane until the centrifuge solution had no colour. Finally, the resulting black solid **10** was dry at vacuum obtaining a 95% yield. ATR-FTIR (cm^{-1})**:** 3068 (ν:-C-H), 1686 (ν:C=O diketo form), 1594 (ν_{ar}:C-C, skeleton vibrations), 1385 (ν:B-O), 842 (ν_{ar}:C-H pentasubstituted), 753 (ν_{ar}:C-H o-disubstituted), 796 and 700 (ν_{ar}:C-H 1,2,4-trisubstituted) and ν_{ar}:C-H vec-trisubstituted). Raman (cm^{-1}): 2923 (second order G+D band), 2582 (second order D band), 1600 (first order G band, ν:C-C), 1323 (first order D band, breathing-like vibrations of six carbon atom ring) and 1259 (first order D band, breathing-like vibrations of six carbon atom ring). MS MALDI-TOF (m/z): m/z calc. for $C_{79}H_{39}O_2BF_2$ [M]: 1070.30; found $[M+3]^+$: 1073.72. Elemental analysis calculated for **10** ($C_{79}H_{39}BF_2O_2$): 89.01 C, 3.60 H. Found; 75.44 C, 2.59 H.

B) 11 mg (0.05 mmol) of **5** and 10 μL of $BF_3{\cdot}OEt_2$ (1.4 eq, 0.07 mmol) were solubilized in 400 μL of 1,1,2,2-tetrachloroethane. The mixture was heated 2 h at 60 °C under Ar atmosphere. The reaction was cooled down to RT, the solid obtained was filtered off and washed with Et_2O and dried. **10** was obtained as a black powder in 88% yield. ATR-FTIR (cm^{-1})**:** 3068 (ν:-C-H), 1701 (ν:C=O diketo form), 1601 ν_{ar}:C-C, skeleton vibrations), 1523 (ν_{ar}:C=C), 1385 (ν:B-O and δ:=CH), 1215 (δ_{ar}:C-H) 891 (ν_{ar}:C-H pentasubstituted), 745 (ν_{ar}:C-H o-disubstituted), 867, 811 and 697 (ν_{ar}:C-H 1,2,4-trisubstituted) and 789 and 697(ν_{ar}:C-H vec-trisubstituted). Raman (cm^{-1}): 2951 (second order G+D band), 2744 (second order D band), 1604 (first order G band, ν:C-C), 1508 (ν:B-O, δ:O-H enol group and δ:C-C-H, aromatic ring), 1347 (first order D band, breathing-like vibrations of six carbon atom ring) and 1259 (first order D band, breathing-like vibrations of six carbon atom ring). MS MALDI-TOF (m/z): m/z calc. for $C_{79}H_{39}O_2BF_2$[M]: 1070.30; found $[M-2]^-$: 1068.36.

2.6.7. Synthesis of 8 and 13. Synthesis of 2-bromophenanthrene-9,10-dione and 2,7-dibromophenanthrene-9,10-dione

Following the described methodology,[105,164,165] 2 g of phenanthrene-9,10-dione (9.69mmol) was mixed with 30 mL of concentrated H_2SO_4. Once the acid is added, the solution acquires a black colour and every 15 min small

amounts of n-bromosuccinimide were added until reaching 1.1 equivalents to obtain **8** as the major product and 2.2 equivalents to obtain **13**.

Once finished, the reactions were let stirring for three hours at room temperature. The reaction was monitored by TLC (DCM 100% Rf: 0.48 **8**, Rf: 0.63 **13**) until the signal of the starting material disappeared (Rf: 0.7). Then, the mixture was cooled down to 0 °C with ice, and cold MiliQ-water is added to the solution that immediately changes colour from black to orange. Afterwards, the solution was stirred for 1 h and then extractions with DCM (3x20 mL) were performed. The organic phase was dried with $MgSO_4$ and filtered off with a filtering plate and then, it was concentrated. Finally, the systems were purified with a silica column using DCM 100% as a mobile phase. CCMoids **8** and **13** were obtained as an orange powder in a 60% of the yield, respectively.
8: ^{1}H NMR (δ in ppm, 360 MHz, DMSO-d^6) δ 8.30 (d, $^3J_{HH}$ = 10.0 Hz, 1H), 8.26 (s, 1H), 8.07 – 8.03 (dd, $^3J_{HH}$ = 12.6, $^4J_{HH}$ =1.9 Hz, 1H), 7.98-7.95 (dd, $^3J_{HH}$ = 8.5 Hz, $^4J_{HH}$ = 2.3 Hz, 1H), 7.81-7.77 (t, $^3J_{HH}$ = 7.7 Hz, $^4J_{HH}$ = 2.3, 1H), 7.59 – 7.55 (t, $^3J_{HH}$ = 7.7 Hz, 1H).
13: ^{1}H NMR (δ in ppm, 300 MHz, DMSO-d^6) δ 8.25 (d, $^3J_{HH}$ = 8.6 Hz, 2H), 8.08 (d, $^4J_{HH}$ = 2.3 Hz, 2H), 7.96 (dd, $^3J_{HH}$ = 8.5, $^4J_{HH}$ = 2.3 Hz, 2H).

2.6.8. Synthesis of 6 and 14. Synthesis of 5-bromo-1,3-diphenyl-2H-cyclopenta[l]phenanthren-2-one and 5,10-dibromo-1,3-diphenyl-2H-cyclopenta [l]phenanthren -2-one

Following the described methodology,[105,164,165] 500 mg of **8** (1.74 mmol) or **13** (1.36 mmol) and 1.2 eq. of commercially available 1,3-diphenylacetone was mixed and dissolved in MeOH (0.02 M) giving an orange solution. Then, the mixture was brought to reflux. Once reached the reflux temperature solution of KOH (pellets, 0.3 M) in MeOH was added dropwise to the mixture using an addition funnel with a pressure-equalization arm and the reaction was stirred for 2 h under reflux temperature. When the KOH was added the solution changes from orange to green-black colour for molecule **8** or red-black colour for molecule **13**. The progress of the reaction was monitored by TLC (DCM 100%, Rf: 0.67 for both CCMoids), then once it was finished, it was cooled down to 0 °C with an ice bath, and the solid precipitated was filtered off and washed with cold MeOH. The remain solid was used in the next step without further purification obtaining a black-green powder in a 69% of yield for **6** and a black-violet powder in a 30% yield for **14**.

6: ^{1}H NMR (δ in ppm, 360 MHz, $CDCl_3$) δ 7.77-7.75 (d, $^3J_{HH}$ = 8.2 Hz, 1H), 7.67-7.65 (d+d, $^3J_{HH}$ = 8.0 Hz, 2H), 7.56-7.53 (d, $^3J_{HH}$ = 8.0 Hz, 1H), 7.48-7.37 (m, 11H), 7.30-7.28 (d, $^3J_{HH}$ = 7.8 Hz, 1H), 6.96 (t, $^3J_{HH}$ = 7.7 Hz, 1H).
14: ^{1}H NMR (δ in ppm, 360 MHz, $CDCl_3$) δ 7.66 (s, 2H), 7.61 (d, $^3J_{HH}$ = 8.6 Hz, 2H), 7.49-7.42 (m, 6H), 7.39-7.36 (d, $^3J_{HH}$ = 7.6 Hz, 6H).

2.6.9. Synthesis of 12. Synthesis of 6,11-dibromo-1,2,3,4-tetraphenyltriphenylene 2-bromophenanthrene-9,10-dione

Following the described methodology,[105,164,165] 100 mg **14** was mixed with 1 eq. of diphenylacetylene and dissolved in Ph_2O (0.24 M). The solution went from dark green to pale brown and the reaction was warmed up to reflux and was let it stir during 48 h. The reaction was monitored by TLC (hexane/DCM: 5/5 Rf: 0.23). When it finished, first, it was cooled down to room temperature, concentrated and purified using a silica column and a step gradient of Hexane/DCM (a total of 50 mL from 0 to 70% DCM at 5% increments). The product **12** was obtained with a 49% yield as a white powder.^{1}H NMR (δ in ppm, 360 MHz, $CDCl_3$-d) δ 8.21-2.19 (d, $^3J_{HH}$ = 8.6 Hz, 2H), 7.66 (s, 2H), 7.49-7.47 (d, $^3J_{HH}$ = 9.1 Hz, 2H), 7.19 – 6.98 (m, 10H), 6.91 (d, $^3J_{HH}$ =5.9 Hz, 6H), 6.70 (d, $^3J_{HH}$ = 6.5 Hz, 4H).

2.6.10. Synthesis of 7. (1E,4Z,6E)-1,7-bis(4-(6-bromo-1,4-diphenyltriphenylen-2-yl)phenyl)-5-hydroxyhepta-1,4,6-trien-3-one

50 mg (0.124 mmol) of **1** and 177.8 mg of molecule **11** (2.5 eq, 1.8 mmol) are solubilized in 1.5 mL of toluene. The mixture changed from yellow to dark green colour when the ketone was added, then the mixture was stirred and heated under reflux at 120 °C for 48 h. TLC was used to monitor the progress of the reaction (Hexane/EtOAc: 9/1, Rf: 0.25). Finally, the reaction was cooled down to room temperature, after that hexane was added obtaining a brown-yellowish precipitate. The solid was filtered off and washed with hexane and, finally, it was purified with a silica column and a step gradient of Hexane/EtOAc (a total of 50 mL from 0 to 30% EtOAc at 0.25% increments). **7** was obtained as a yellow solid in an 86% yield. ^{1}H NMR (δ in ppm, 360 MHz, $CDCl_3$) δ=15.92 (s, 1H), 8.32 (dd, $^3J_{HH}$ = 8.4 Hz, $^4J_{HH}$ = 2.1, 4H), 7.86-7.57 (m, 10H), 7.45 (m, 22H), 7.12 (m, 10H), 6.60 (d, $^3J_{HH}$ = 15.8Hz, 2H), 5.81 (s, 1H). $^{13}C\{^1H\}$ NMR (δ in ppm, 90 MHz, CD_2Cl_2) 183.2, 143.8, 141.9, 141.7, 140.9, 140.3, 140.0, 139.9, 139.8, 139.2, 132.9, 131.8, 131.5, 131.0, 130.5, 129.9,

129.6, 129.3, 127.6, 127.4, 126.9, 126.8, 126.6, 126.3, 125.8, 123.8 and 101.7. ATR-FTIR (cm^{-1}): 3060 (ν:=C-H and ν_{ar}:C-H), 1593 (ν:C=O *keto-enol* form with intermolecular H-bonds), 1414 (ν_{ar}:C-C, skeleton vibrations), 1004 (ν:C-Br), 822 (ν_{ar}:C-H ρ-disubstituted and ν_{ar}:C-H pentasubstituted), 799 (ν_{ar}:C-H ρ-disubstituted) 760 (ν_{ar}:C-H o-disubstituted) and 698 (ν_{ar}:C-H monosubstituted). Raman (cm^{-1}): 1623 (ν:C=O), 1597 (ν:C=C, aromatic ring), 1175 (δ: C-O-C, *keto-enol* group and ν and δ: C-C-H, aromatic ring). MS MALDI-TOF (m/z): calc. for $C_{79}H_{50}Br_2O_2$ [M]: 1188.22; found $[M]^{\cdot}$: 1188.80. Elemental analysis calculated for **7**·2MeOH ($C_{81}H_{56}Br_2O_4$): C, 77.51; H, 4.66. Found: C, 77.30; H, 4.28.

2.6.11. Synthesis of 11. 4,6-bis((E)-4-(6-bromo-1,4-diphenyltriphenylen-2-yl)styryl)-2,2-difluoro-2H-1λ³,3,2λ⁴-dioxaborinine

50 mg (0.04 mmol) of **7** and 8 μL of $BF_3{\cdot}OEt_2$ (1.4 eq, 0.06 mmol) were solubilized in 0.5 mL of DCM. The mixture was heated with the microwave in a dynamic program of 50 °C for 10 min at 6000 rpm. TLC was used to monitor the progress of the reaction (hexane/EtOAc: 8/2, Rf: 0.30). Once no starting material was found, the reaction was cooled down to RT, the solid obtained was filtered off, washed with cold Et_2O, cold MeOH and recrystallized with MeOH. CCMoid **11** was obtained as a red powder in 75% yield. ^1H NMR (360 MHz, $CDCl_3$) δ=8.33 (dd, $^3J_{HH}$ = 8.5 Hz, $^4J_{HH}$ = 2.1, 4H), 8.03 (d, $^3J_{HH}$ = 15.5Hz, 2H), 7.86 – 7.58 (m, 8H), 7.56 – 7.36 (m, 22H), 7.12 (s, 10H), 6.70 (d, $^3J_{HH}$ = 15.6 Hz, 2H), 6.05 (s, 1H). ATR-FTIR data (cm^{-1})**:** 3052 (ν:=C-H and ν_{ar}:C-H), 1593 (ν:C=O *keto-enol* form with intermolecular H-bonds), 1540 (ν_{ar}:C-C, skeleton vibrations), 1392 (ν:B-O, δ_{ar}:=CH), 1004 (ν:C-Br), 819 (ν_{ar}:C-H ρ-disubstituted and ν_{ar}:C-H pentasubstituted), 760 (ν_{ar}:C-H monosubstituted), 698 (ν_{ar}:C-H monosubstituted). Raman (cm^{-1}): 1628 (ν:C=O), 1602 (ν:C=C, aromatic ring), 1509 (ν:B-O), enol group and δ: C-C-H, aromatic ring), 1179 (δ: C-O-C, *keto-enol* group and ν and δ: C-C-H, aromatic ring). MS MALDI-TOF (m/z): calc. for $C_{79}H_{50}Br_2BF_2O_2$ [M]: 1236.22; found $[M+1]^+$: 1237.54. Elemental analysis calculated for **11**·1DCM ($C_{80}H_{51}Cl_2Br_2O_2BF_2$): C, 72.78; H, 3.92. Found; C, 72.72; H, 4.57.

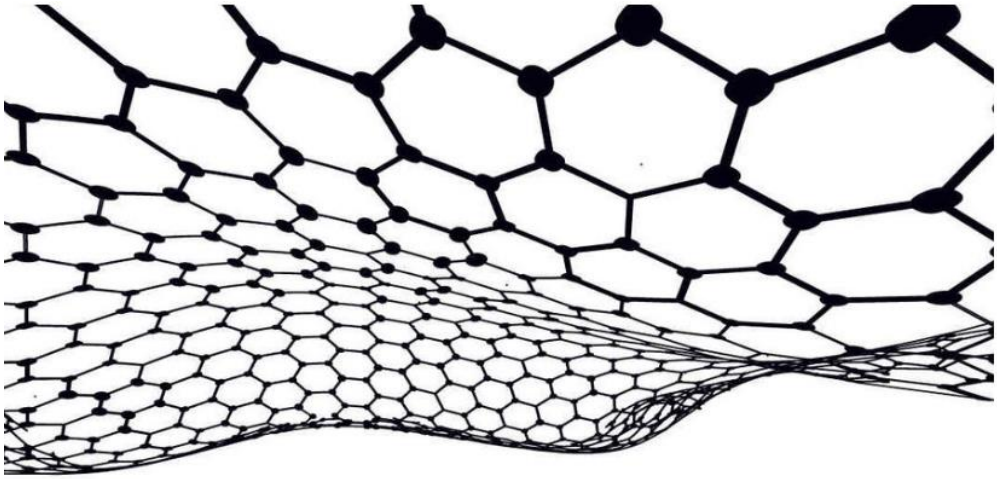

APPENDIX II

APPENDIX II. SUPPLEMENTARY FIGURES

^{1}H NMR spectra

^{1}H NMR (360 MHz, $CDCl_3$) δ=15.89 (s, 1H), 7.57 (d+s, $^3J_{HH}$ = 15.66 Hz, 4H), 7.36 (d, $^3J_{HH}$ = 8.02 Hz, 4H), 7.16 (m, 12H), 6.88 (m, 32H), 6.58 (d, $^3J_{HH}$ = 15.66 Hz, 2H), 5.75 (s, 1H).

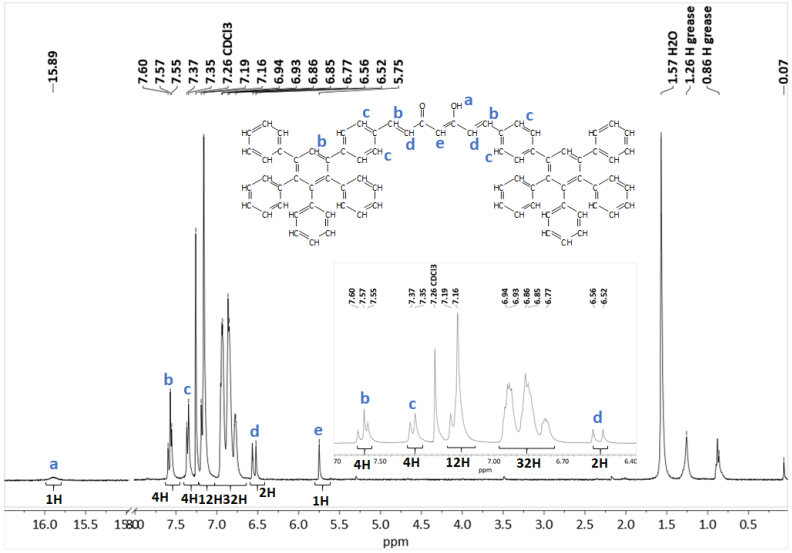

*Figure A 2.1: ^{1}H RMN spectrum of 10PhCCMoid **4**.*

^{1}H NMR (360 MHz, $CDCl_3$-d) δ 7.77-7.75 (d, $^3J_{HH}$ = 8.2 Hz, 1H), 7.67-7.65 (d+d, $^3J_{HH}$ 8.0 Hz, 2H), 7.56-7.53 (d, $^3J_{HH}$ = 8.0 Hz, 1H), 7.48-7.37 (m, 11H), 7.30-7.28 (d, *J* = 7.8 Hz, 1H), 6.96 (t, *J* = 7.7 Hz, 1H).

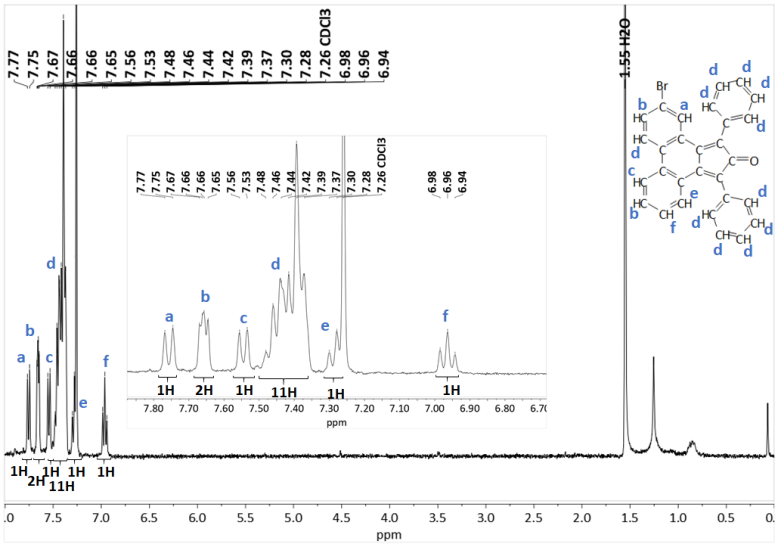

*Figure A 2.2: ^{1}H RMN spectrum of 5-bromo-1,3-diphenyl-2H-cyclopenta[l]phenanthren-2-one **6**.*

^{1}H NMR (360 MHz, $CDCl_3$) δ=15.92 (s, 1H), 8.32 (dd, $^3J_{HH}$ = 8.4 Hz, $^4J_{HH}$ = 2.1 Hz, 4H), 7.86-7.57 (m, 10H), 7.45 (m, 22H), 7.12 (m, 10H), 6.60 (d, $^3J_{HH}$ = 15.8 Hz, 2H), 5.81 (s, 1H).

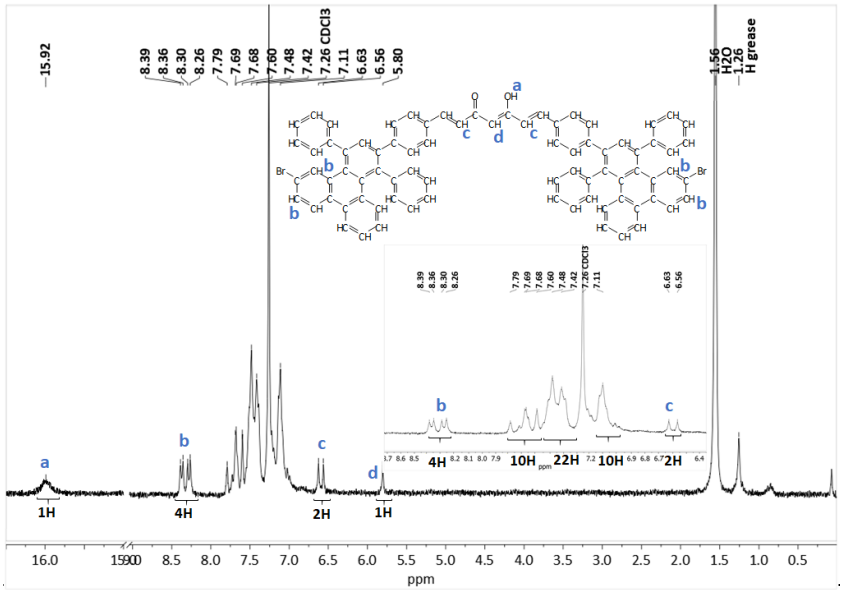

*Figure A 2.3: ^{1}H RMN spectrum of 2Br12PhCCMoid **7**.*

^{1}H NMR (360 MHz, DMSO-d^6) δ 8.30 (d, $^3J_{HH}$ = 10.0 Hz, 1H), 8.26 (s, 1H), 8.07 – 8.03 (dd, $^3J_{HH}$ = 12.6, $^4J_{HH}$ =1.9 Hz, 1H), 7.98-7.95 (dd, $^3J_{HH}$ = 8.5 Hz, $^4J_{HH}$ = 2.3 Hz, 1H), 7.81-7.77 (t, $^3J_{HH}$ = 7.7 Hz, $^4J_{HH}$ = 2.3 1H), 7.59 – 7.55 (t, $^3J_{HH}$ = 7.7 Hz, 1H).

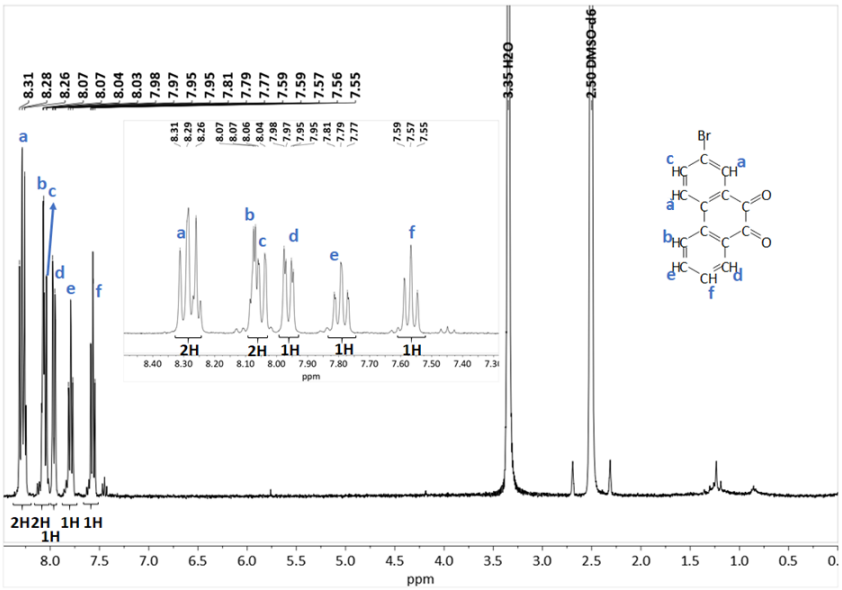

*Figure A 2.4: ^{1}H RMN spectrum of 2-bromophenanthrene-9,10-dione **8**.*

^{1}H NMR (360 MHz, $CDCl_3$) δ=7.98 (d, $^3J_{HH}$ = 15.46 Hz, 2H), 7.57 (s, 2H), 7.42 (d, $^3J_{HH}$ = 8.13 Hz, 4H), 7.22 (d, $^3J_{HH}$ = 8.13 Hz, 4H), 7.16 (s, 8H), 6.89 (m, 32H), 6.65 (d, *J* = 15.46 Hz, 2H), 6.00 (s, 1H).

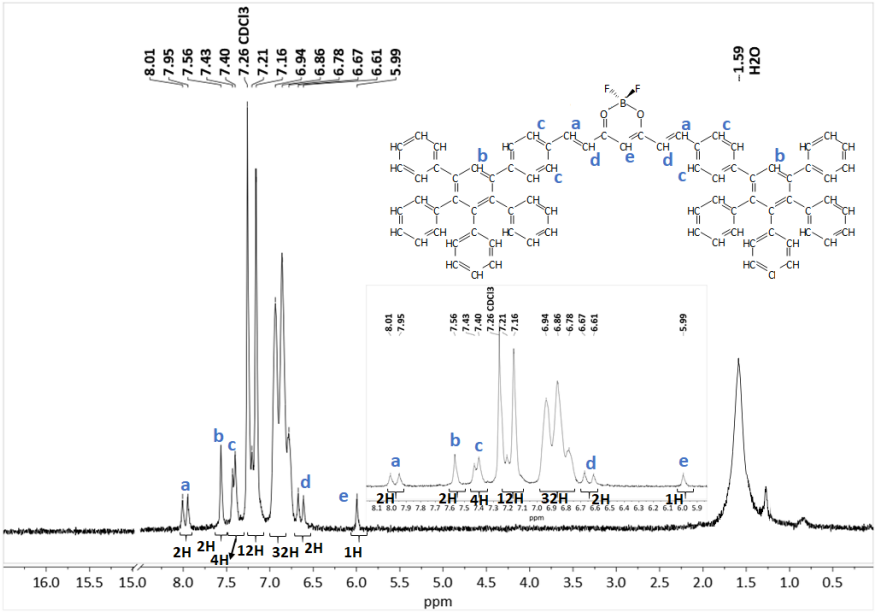

*Figure A 2.5: ^{1}H RMN spectrum of 10PhCCMoidBF$_2$ **9**.*

^{1}H NMR (360 MHz, $CDCl_3$) δ=8.33 (dd, $^3J_{HH}$ = 8.5 Hz, $^4J_{HH}$ = 2.1 Hz, 4H), 8.03 (d, $^3J_{HH}$ = 15.5 Hz, 2H), 7.86 – 7.58 (m, 8H), 7.56 – 7.36 (m, 22H), 7.12 (s, 10H), 6.70 (d, *J* = 15.6 Hz, 2H), 6.05 (s, 1H).

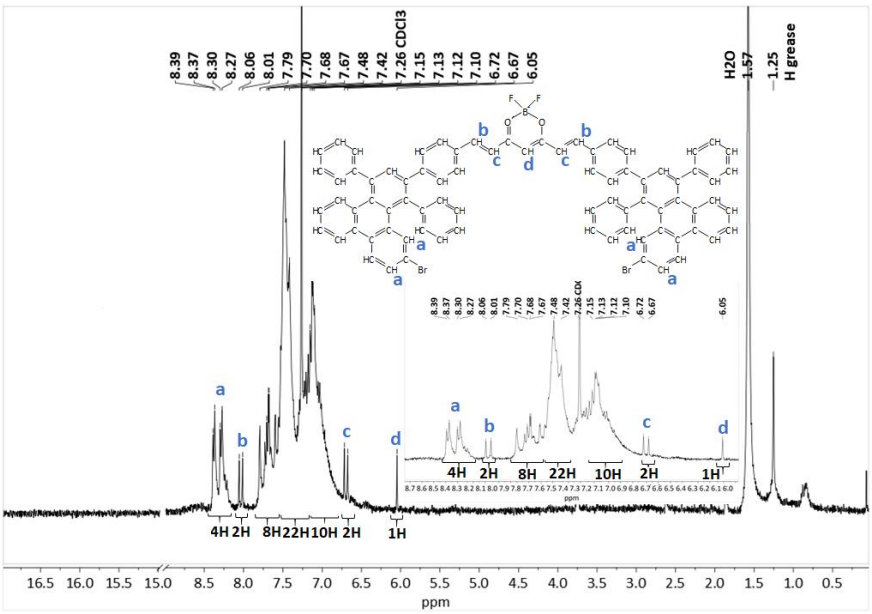

*Figure A 2.6: ^{1}H RMN spectrum of 2Br12PhCCMoidBF$_2$ **11**.*

^{1}H NMR (360 MHz, $CDCl_3$) δ 8.21-2.19 (d, $^{3}J_{HH}$ = 8.6 Hz, 2H), 7.66 (s, 2H), 7.49-7.47 (d, $^{3}J_{HH}$ = 9.1 Hz, 2H), 7.19 – 6.98 (m, 10H), 6.91 (d, $^{3}J_{HH}$ = 5.9 Hz, 6H), 6.70 (d, $^{3}J_{HH}$ = 6.5 Hz, 4H).

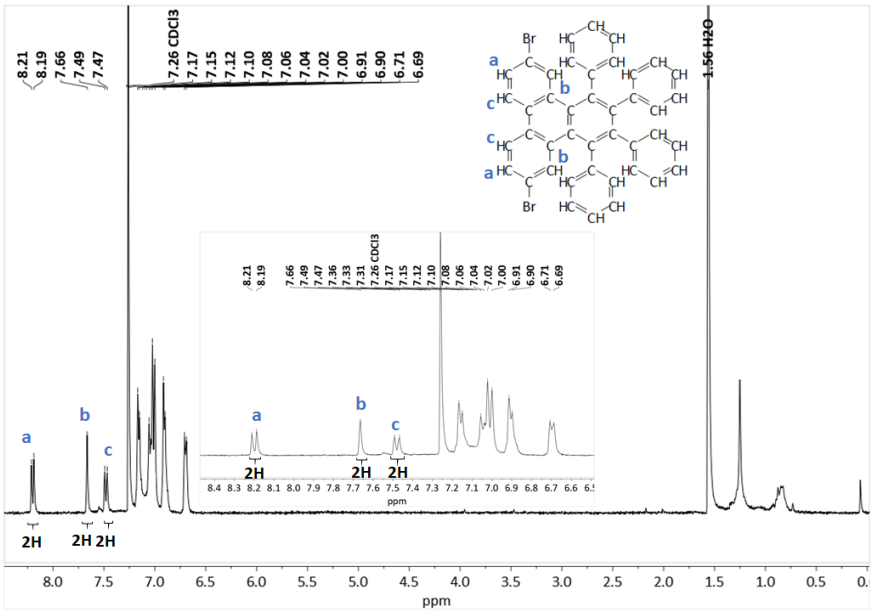

*Figure A 30: 6,11-dibromo-1,2,3,4-tetraphenyltriphenylene **12**.*

^{1}H NMR (300 MHz, DMSO-d^{6}) δ 8.25 (d, $^{3}J_{HH}$ = 8.6 Hz, 2H), 8.08 (d, $^{3}J_{HH}$ = 8.5 Hz, 2H), 7.96 (dd, $^{3}J_{HH}$ = 8.5, 2.3 Hz, 2H).

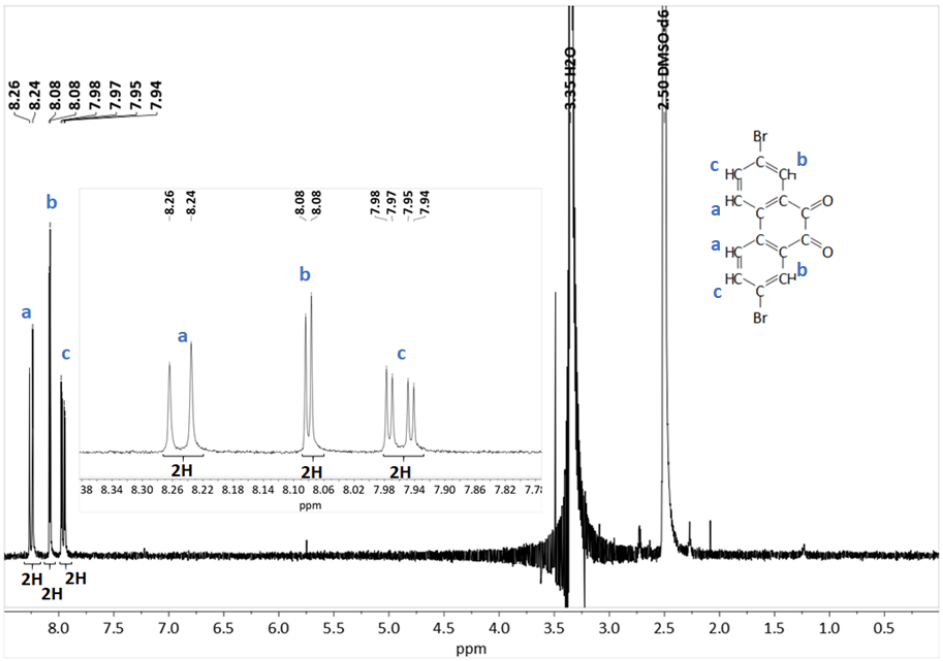

*Figure A 31: ^{1}H RMN spectrum of 2,7-dibromophenanthrene-9,10-dione **13**.*

^{1}H NMR (360 MHz, $CDCl_3$-d) δ 7.66 (s, 2H), 7.61 (d, $^{3}J_{HH}$ = 8.6 Hz, 2H), 7.49-7.42 (m, 6H), 7.39-7.36 (d, $^{3}J_{HH}$ = 7.6 Hz, 6H).

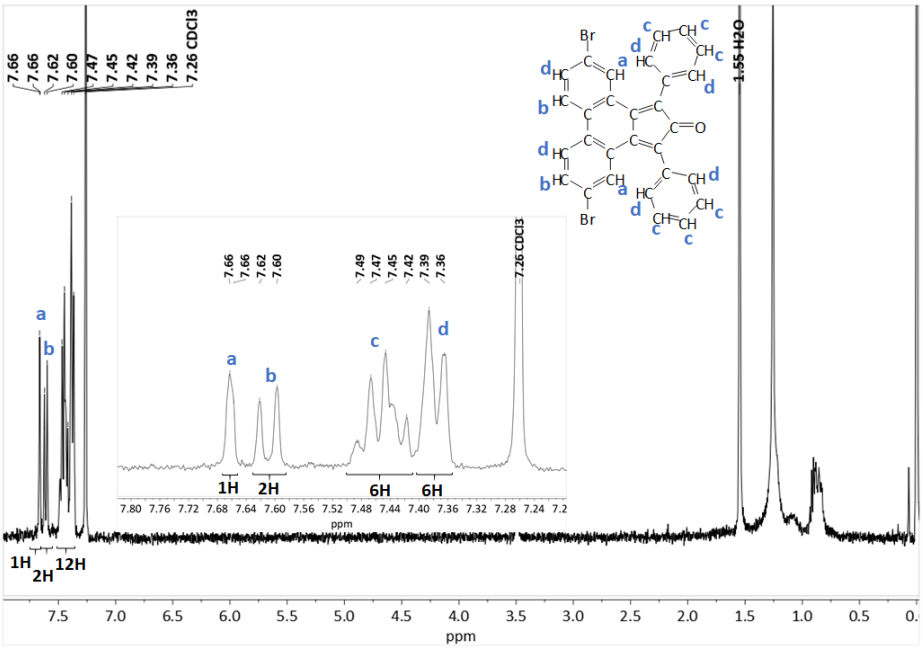

*Figure A 32: ^{1}H RMN spectrum of 5,10-dibromo-1,3-diphenyl-2H-cyclopenta[l]phenanthren-2-one **14**.*

^{13}C{^{1}H}-NMR spectra

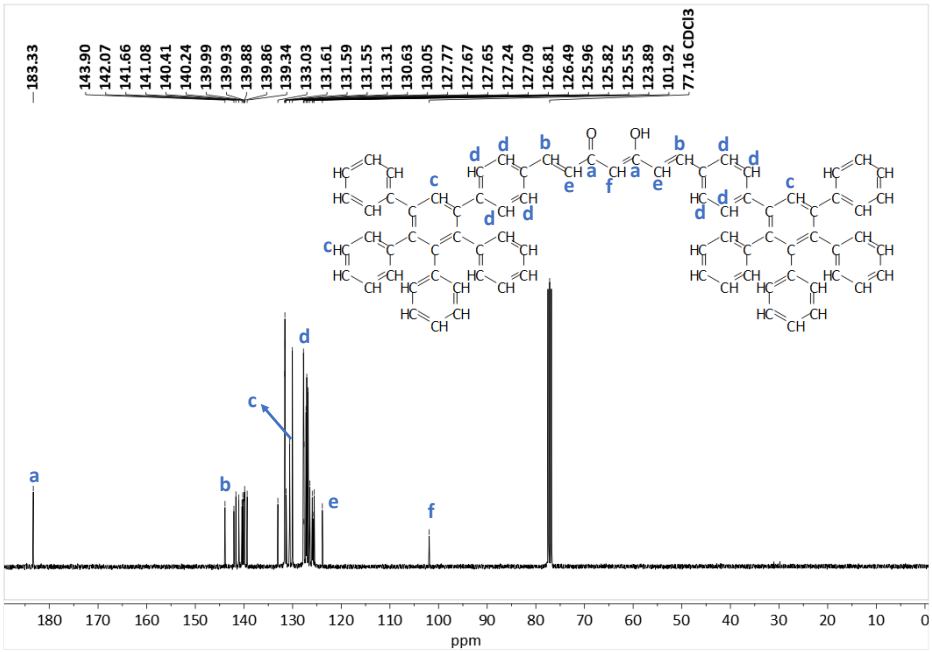

*Figure A 33: ^{13}C RMN spectrum of 10PhCCMoid **4**.*

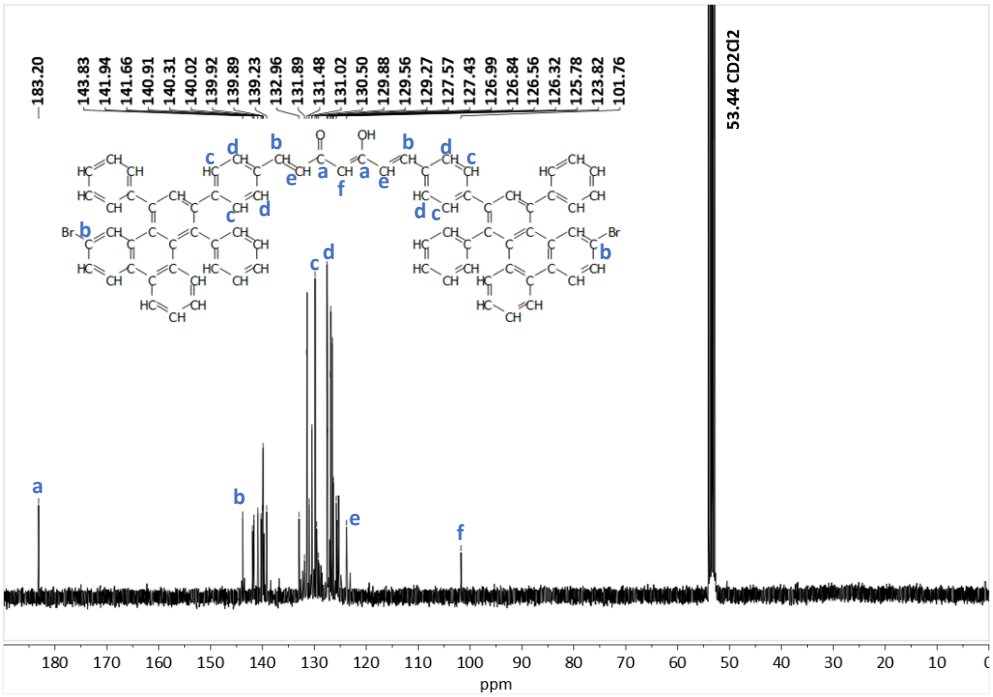

*Figure A 34: ^{13}C RMN spectrum of 2Br12PhCCMoid **7**.*

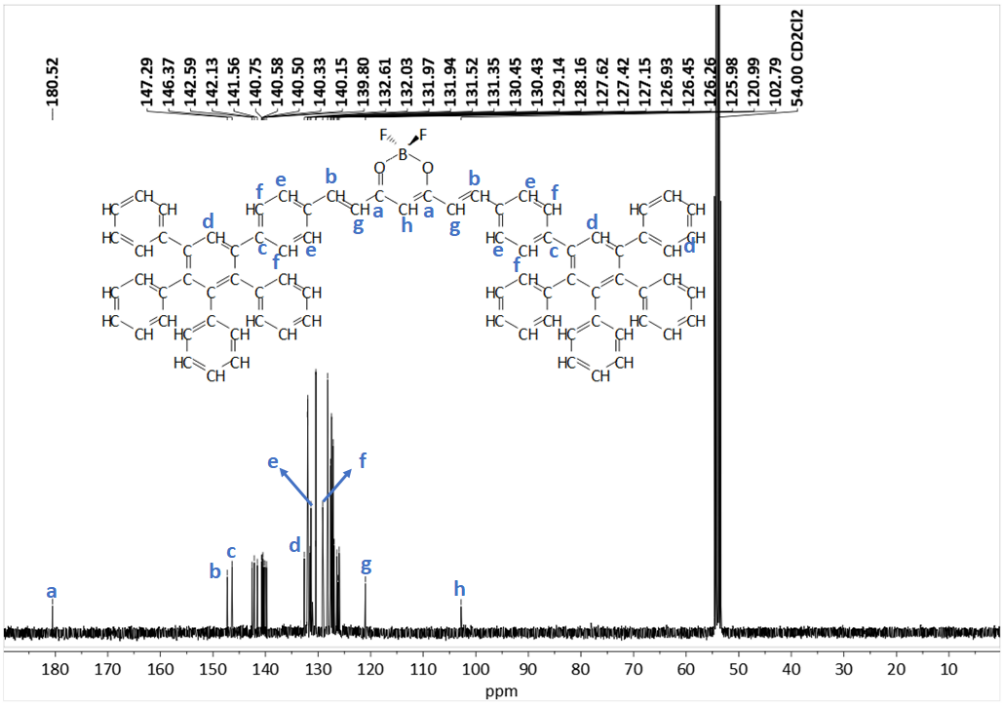

*Figure A 35: ^{13}C RMN spectrum of 10PhCCMoidBF$_2$ **9**.*

ATR-FTIR spectra

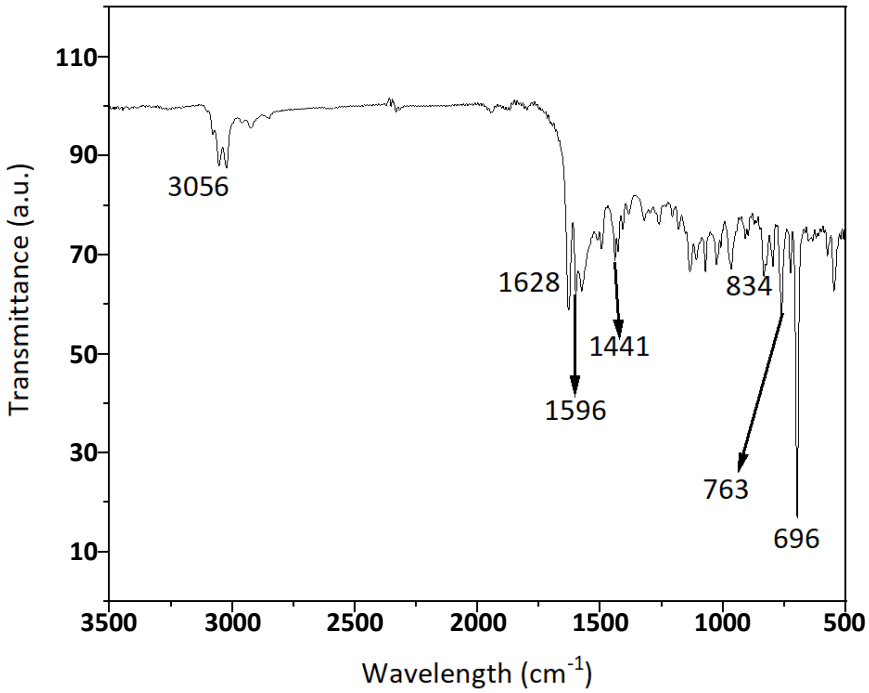

Figure A 36: *ATR-FTIR spectrum of 10PhCCMoid* ***4****.*

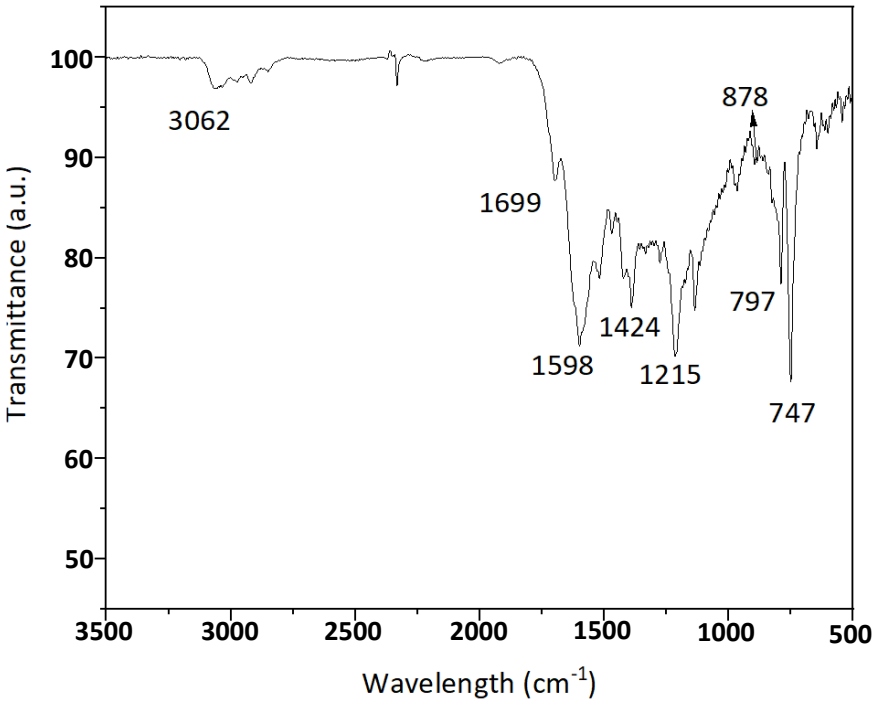

Figure A 37*: ATR-FTIR spectrum of 4PhAntCCMoid* ***5****.*

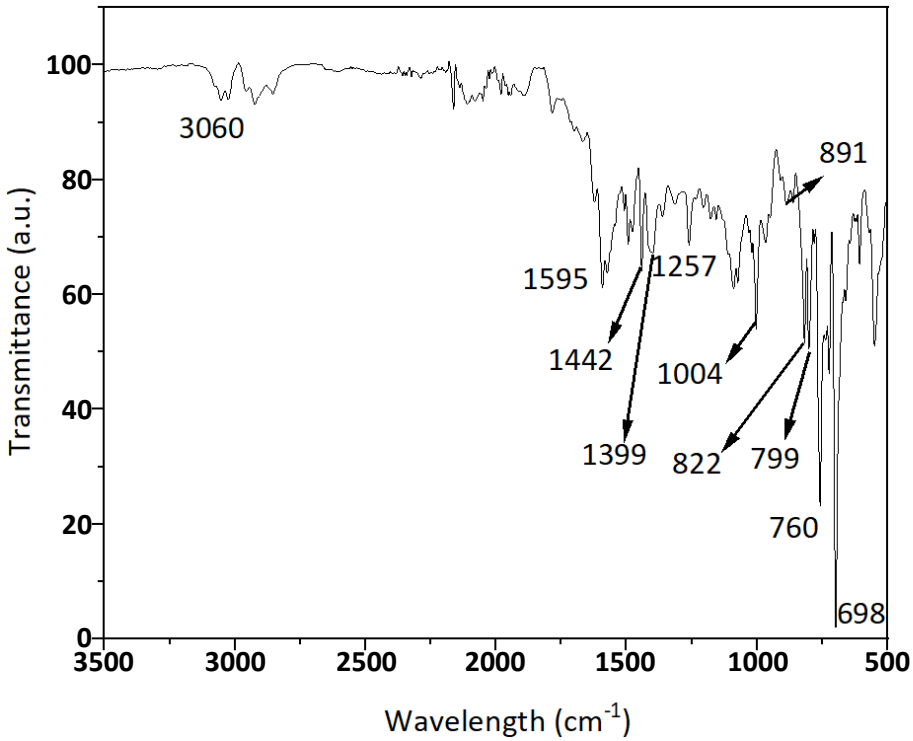

***Figure A 38**: ATR-FTIR spectrum of 2Br12PhCCMoid **7**.*

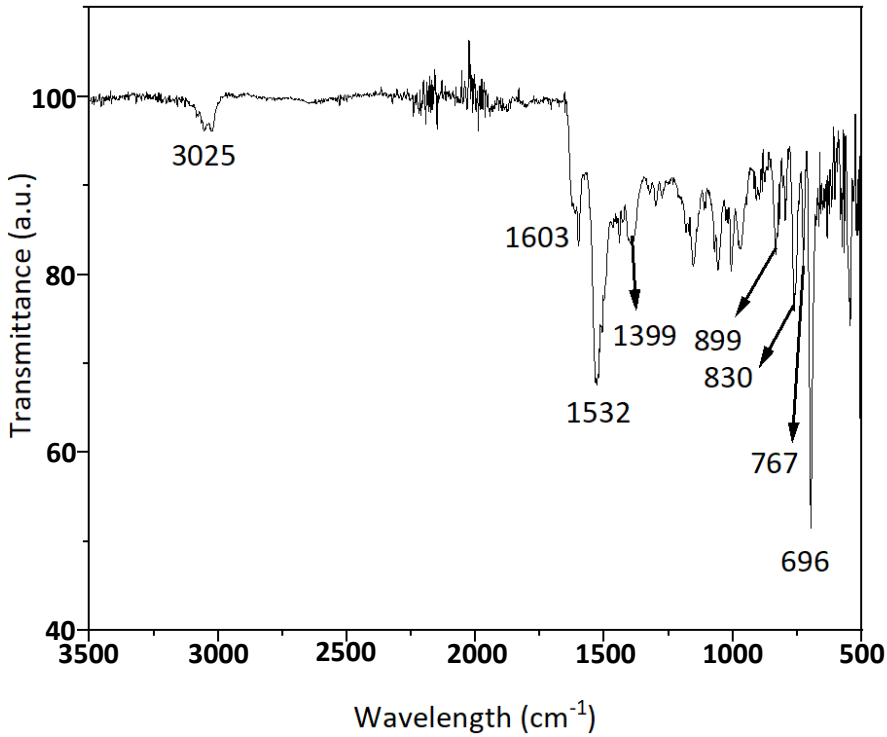

***Figure A 39**: ATR-FTIR spectrum of 10PhCCMoidBF$_2$ **9**.*

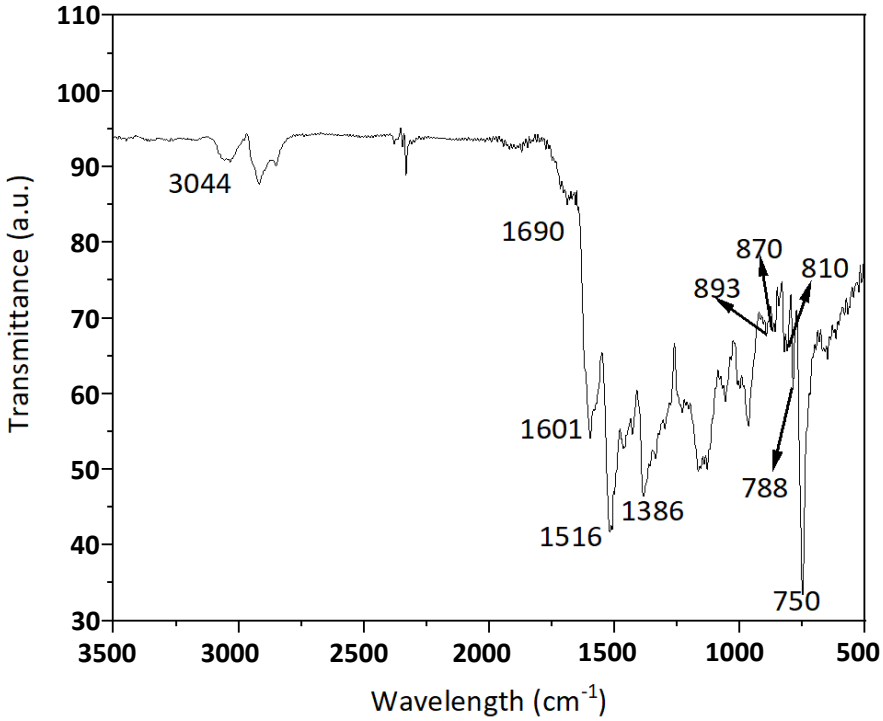

***Figure A 40**: ATR- FTIR spectrum of 4PhAntCCMoidBF$_2$ **10** (Route A).*

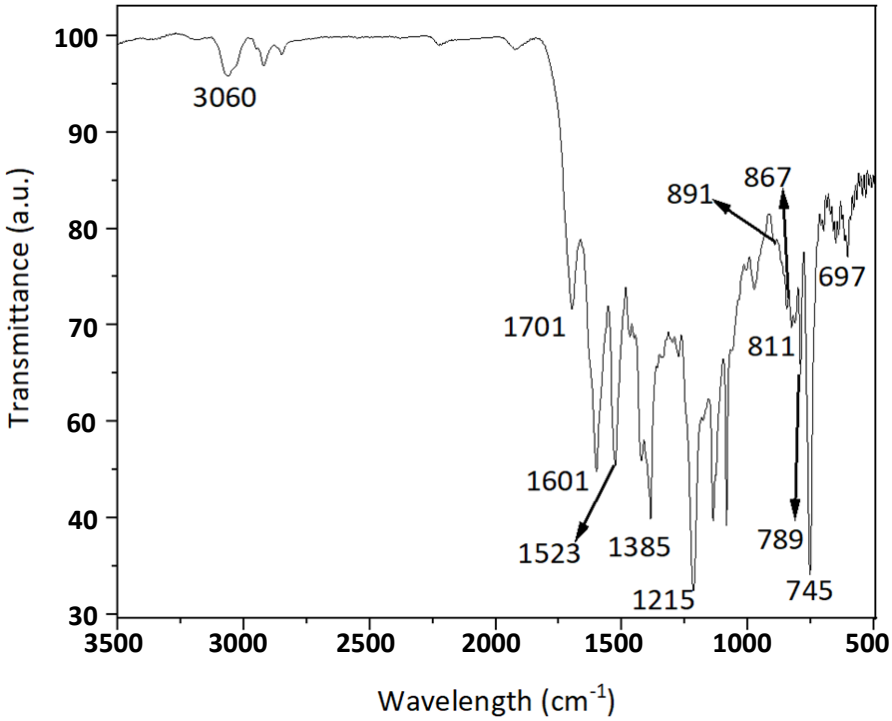

***Figure A 41**: ATR-FTIR spectrum of 4PhAntCCMoidBF$_2$ **10** (Route B).*

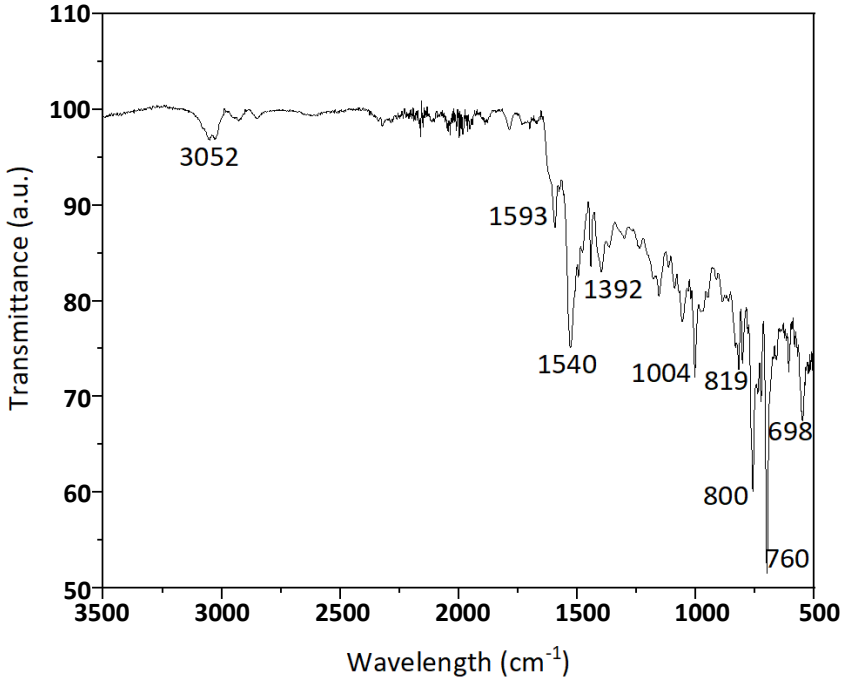

***Figure A 42**: ATR-FTIR spectrum of 2Br12PhCCMoidBF$_2$ **11**.*

Raman spectra

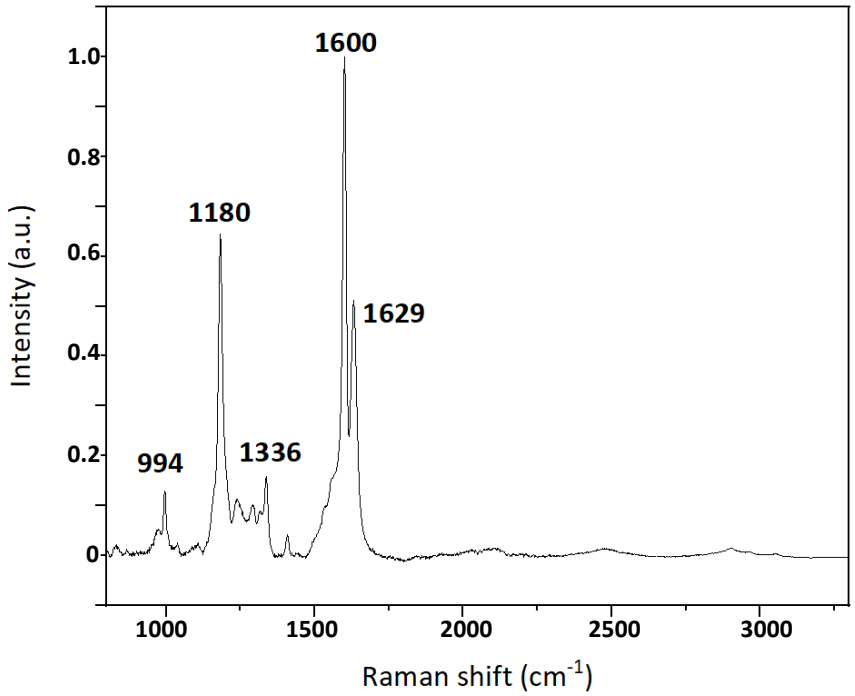

***Figure A 43**: Raman spectrum of 10PhCCMoid **4**.*

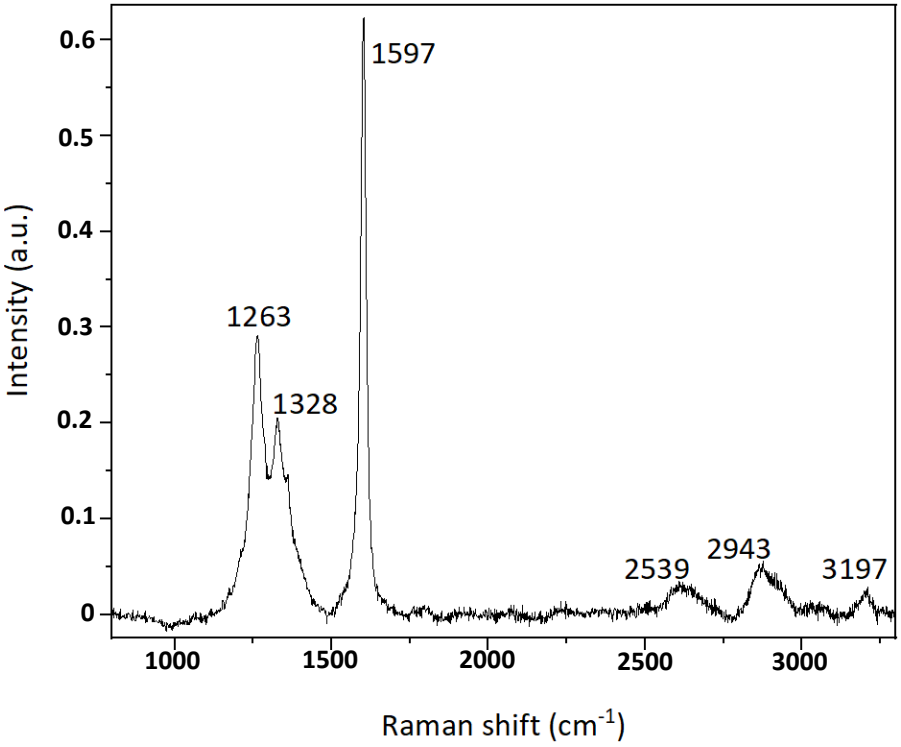

***Figure A 44**: Raman spectrum of 4PhAntCCMoid **5**.*

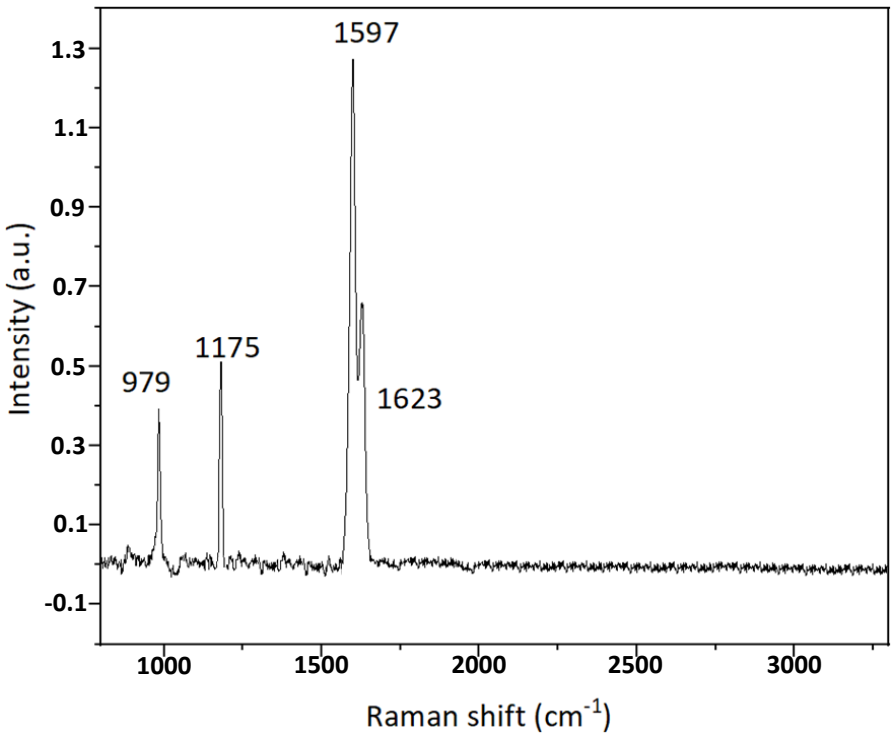

Figure A 45**: Raman spectrum of 2Br12PhCCMoid **7.

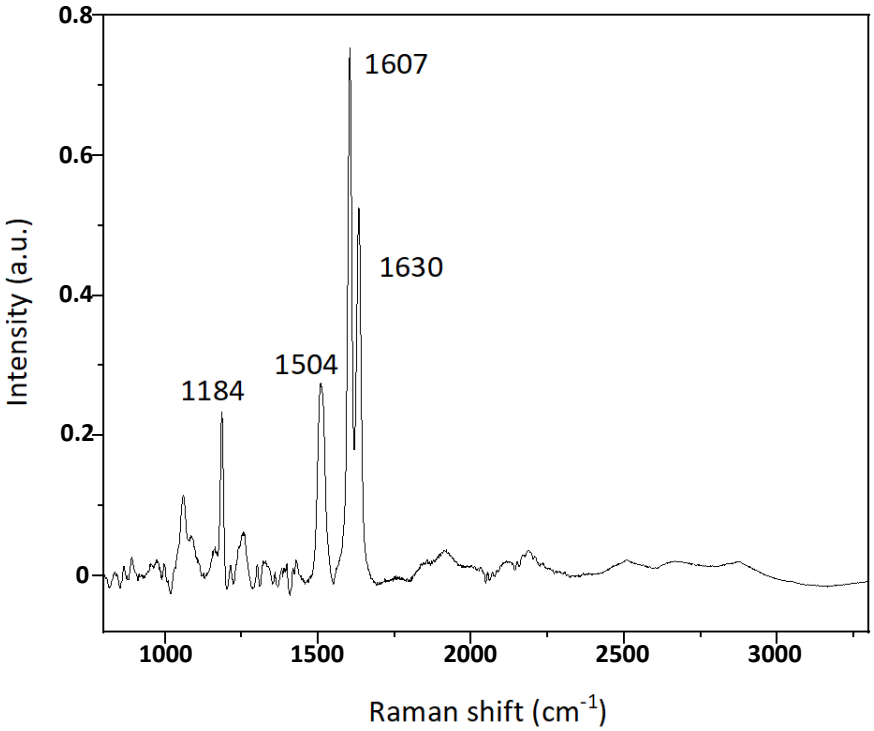

***Figure A 46**: Raman spectrum of 10PhCCMoidBF$_2$ **9**.*

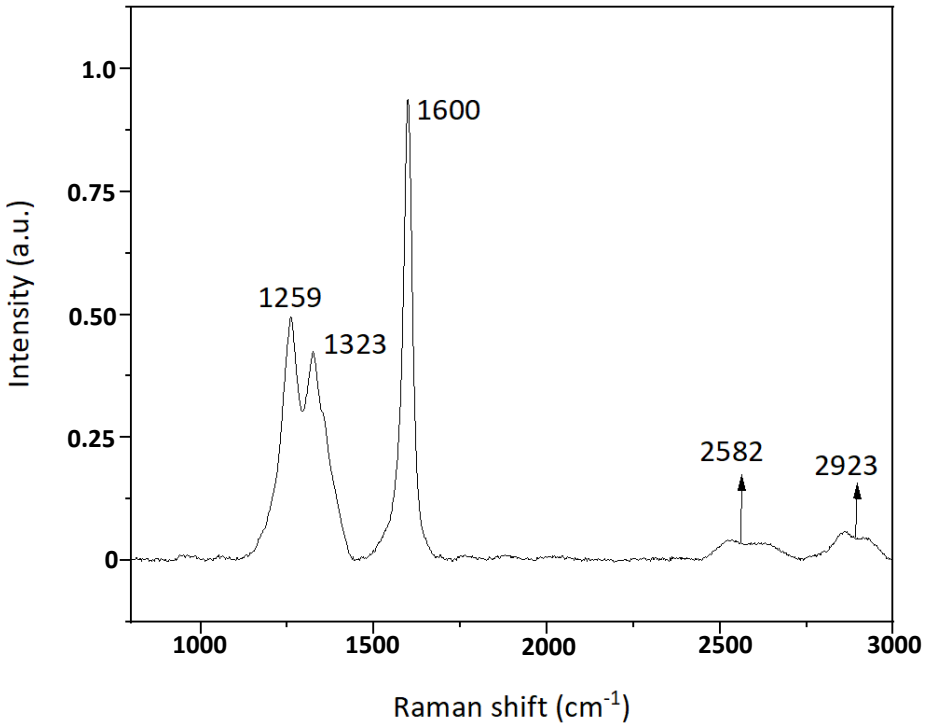

***Figure A 47**: Raman spectrum of 4PhAntCCMoidBF$_2$ **10** (route, A).*

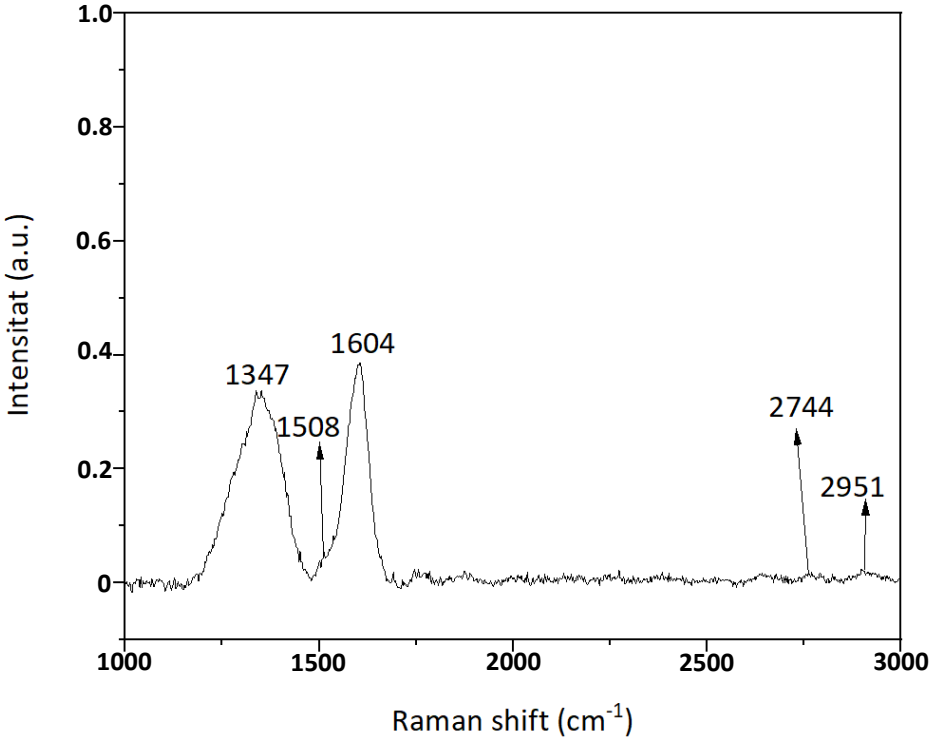

***Figure A 48**: Raman spectrum of 4PhAntCCMoidBF$_2$ **10** (route, B).*

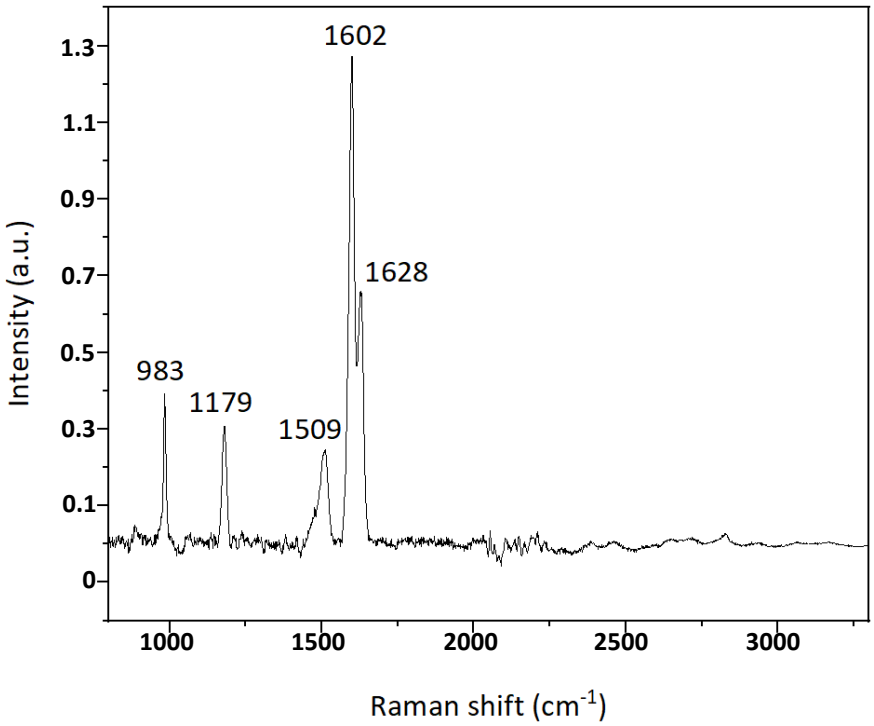

***Figure A 49**: Raman spectrum of 2Br12PhCCMoidBF$_2$ **11**.*

UV-VIS spectra in solution (DCM) and in solid state (KBr PELLETS)

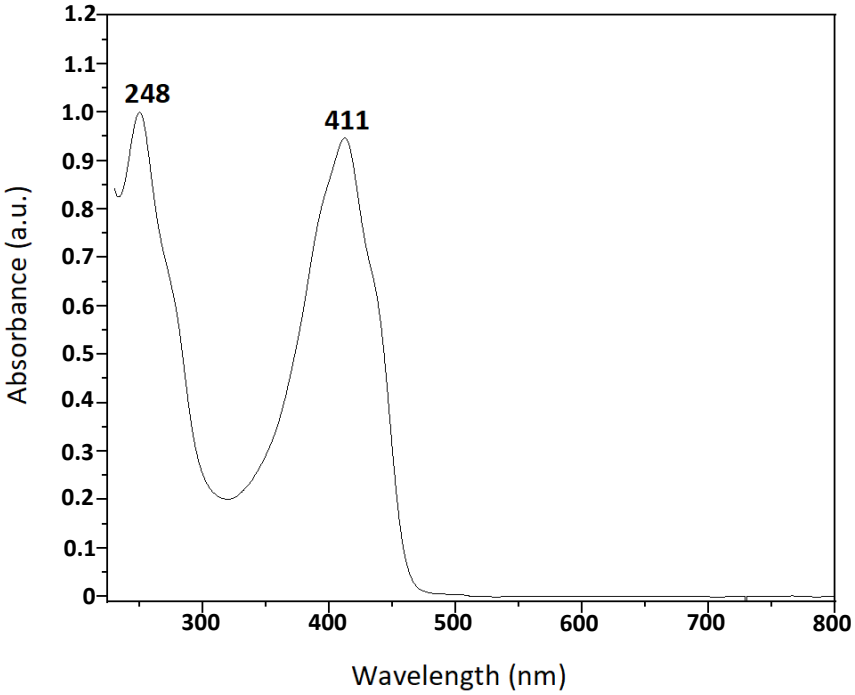

***Figure A 50**: UV-Vis solution spectrum of 10PhCCMoid **4**.*

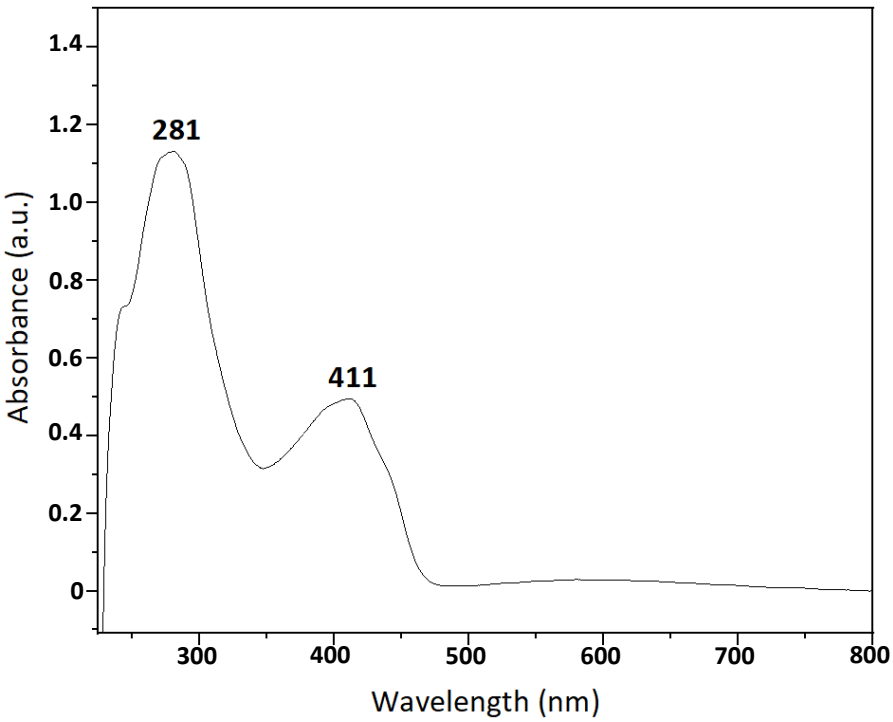

***Figure A 51**: UV-Vis solution spectrum of 2Br12PhCCMoid **7**.*

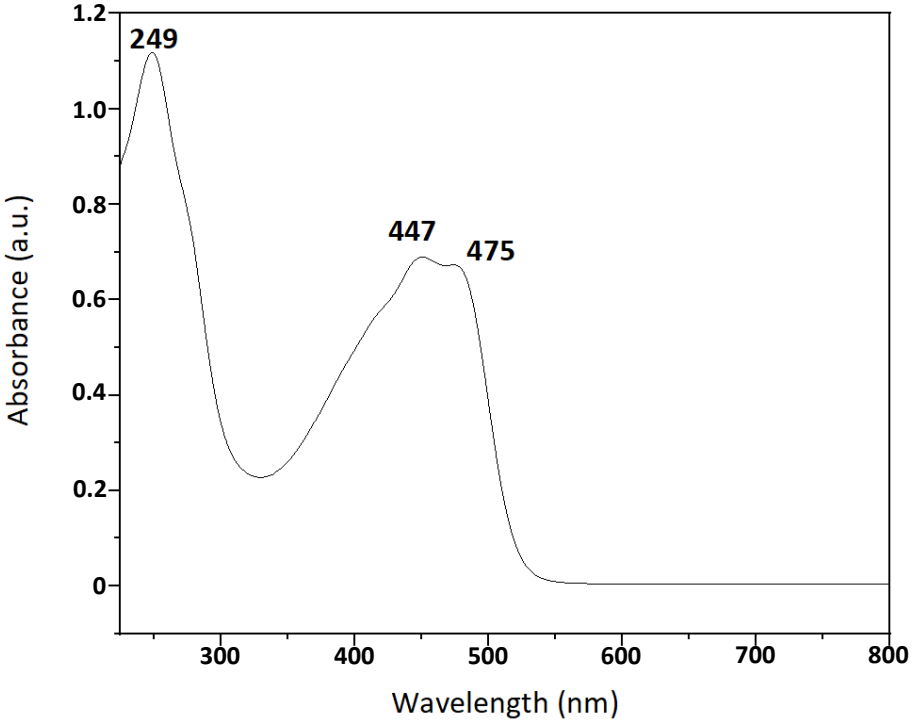

***Figure A 52**: UV-Vis solution spectrum of 10PhCCMoidBF$_2$ **9**.*

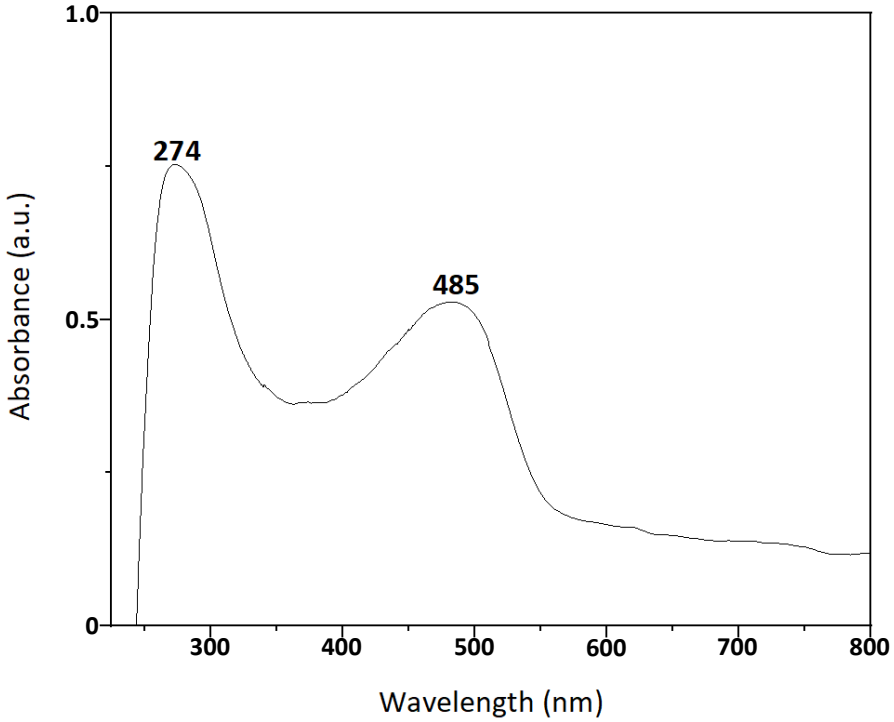

***Figure A 53**: UV-Vis solution spectrum of 2Br12PhCCMoidBF$_2$ **11**.*

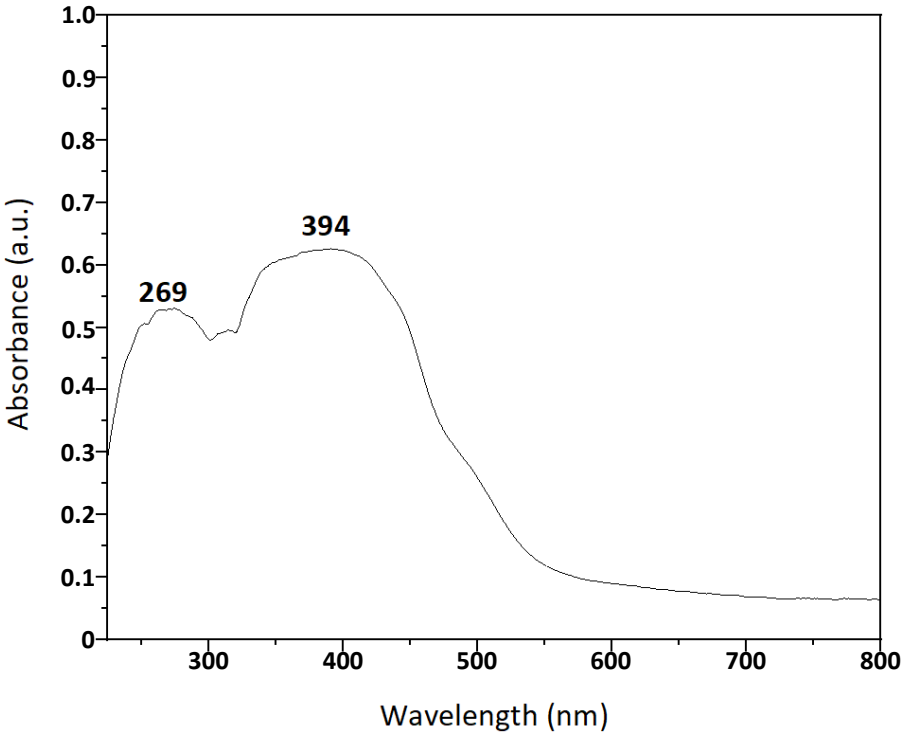

***Figure A 54**: UV-Vis solid spectrum of 10PhCCMoid **4**.*

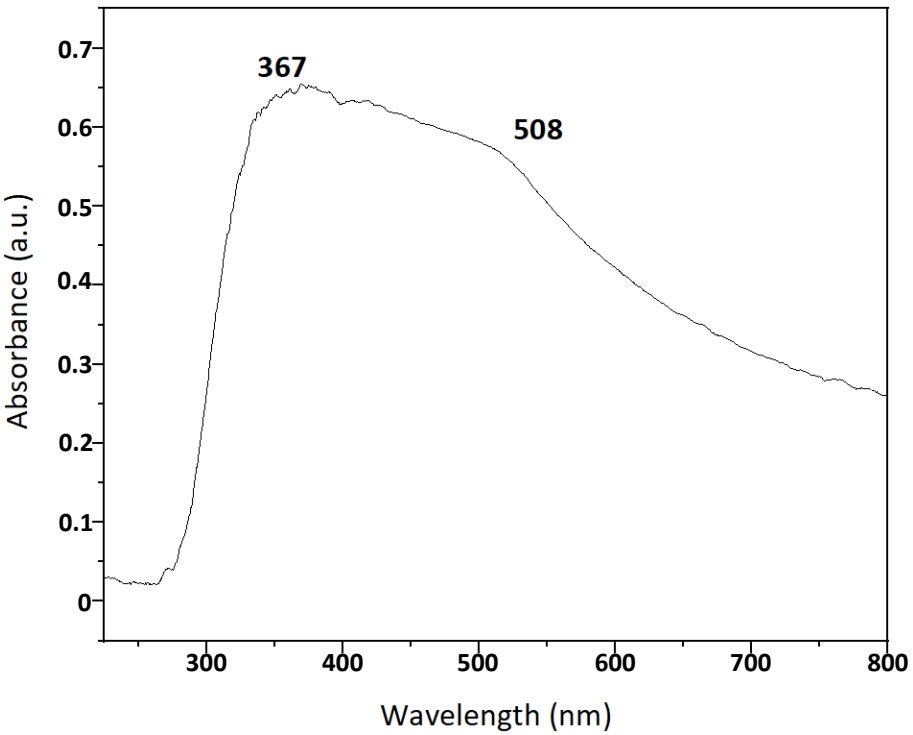

***Figure A 55**: UV-Vis solid spectrum of 4PhAntCCMoid **5**.*

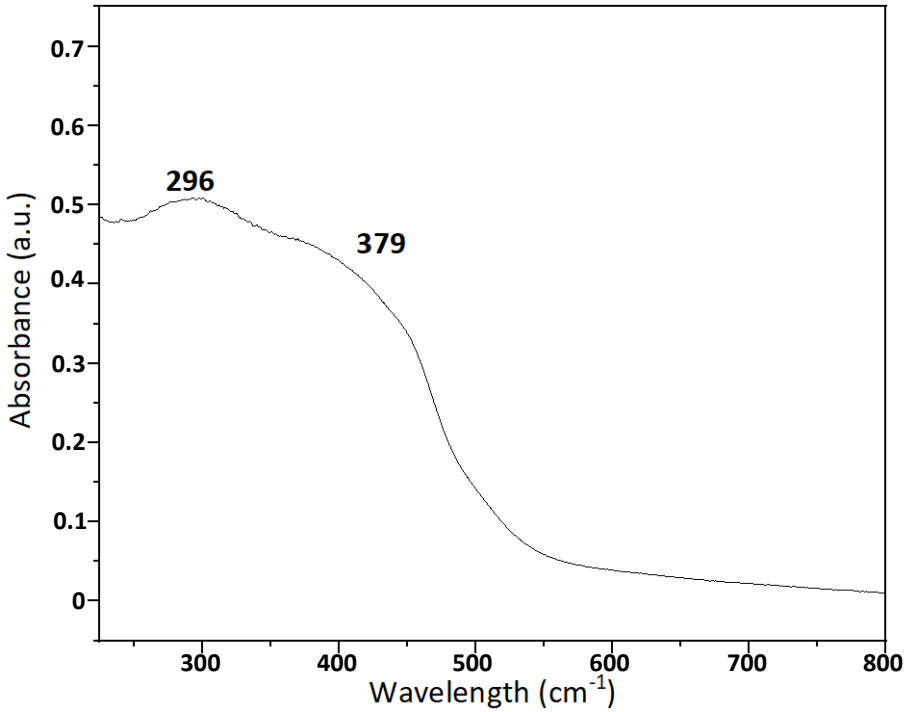

***Figure A 56**: UV-Vis solid spectrum of 2Br12PhCCMoid **7**.*

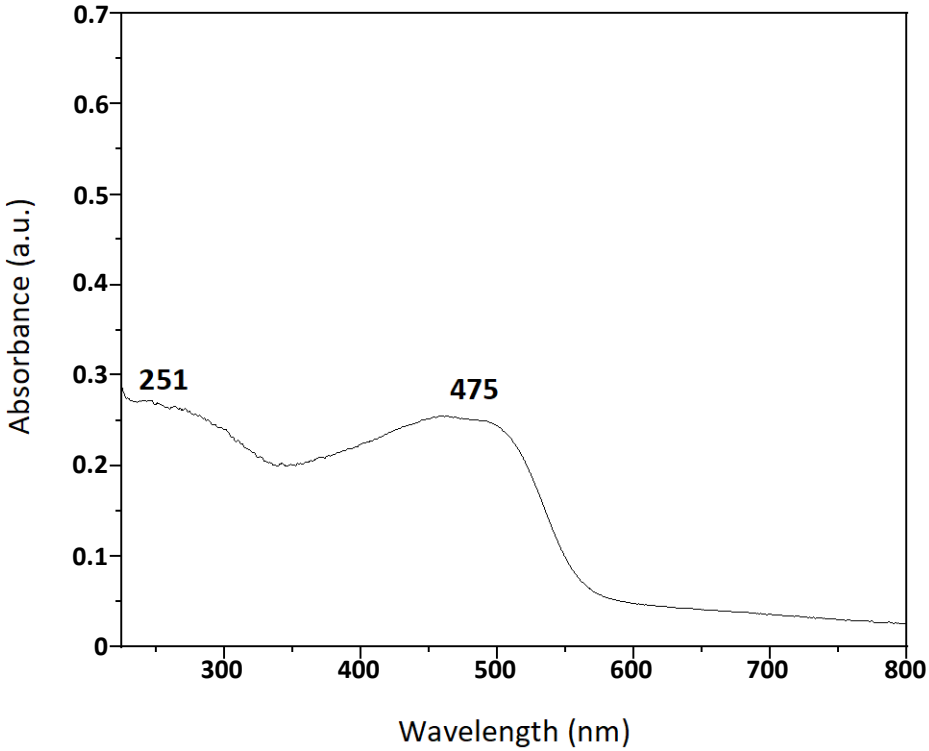

***Figure A 57**: UV-Vis solid spectrum of 10PhCCMoidBF$_2$ **9**.*

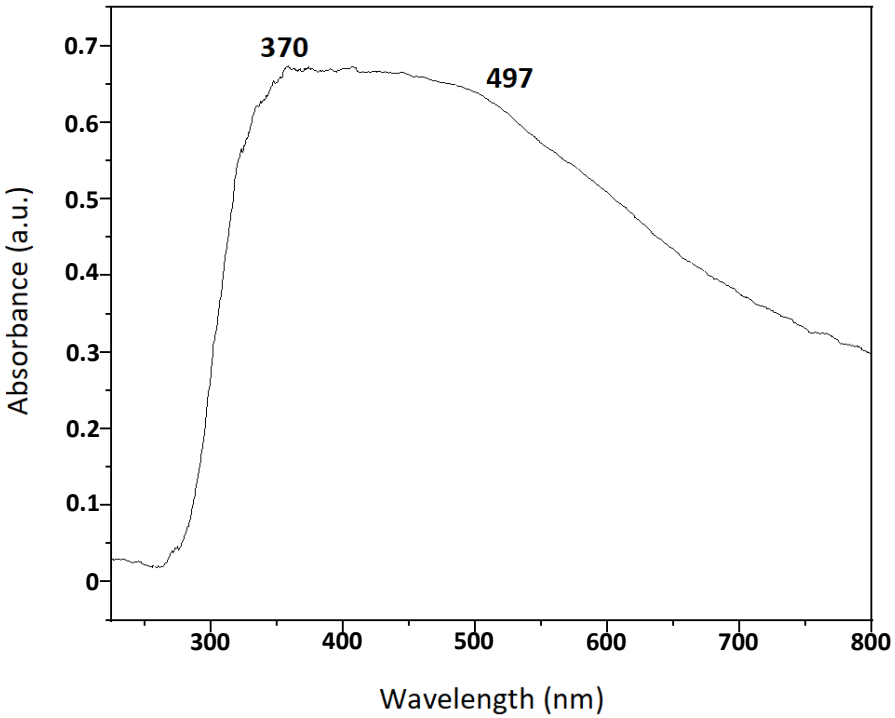

***Figure A 58**: UV-Vis solid spectrum of 4PhAntCCMoidBF$_2$ **10** (route A).*

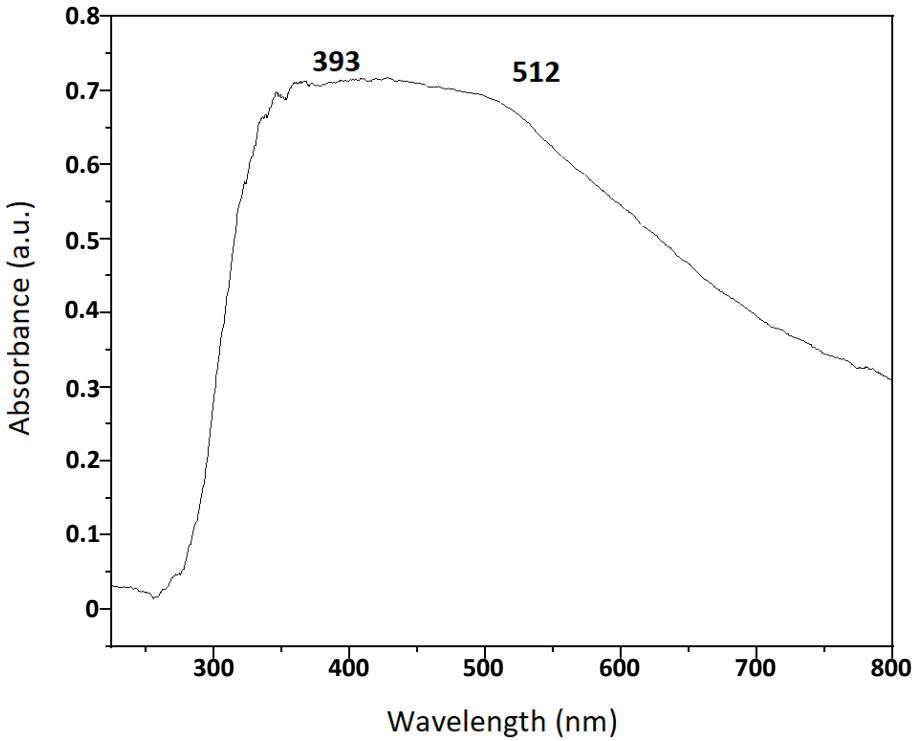

***Figure A 59**: UV-Vis solid spectrum of 4PhAntCCMoidBF$_2$ **10** (route B).*

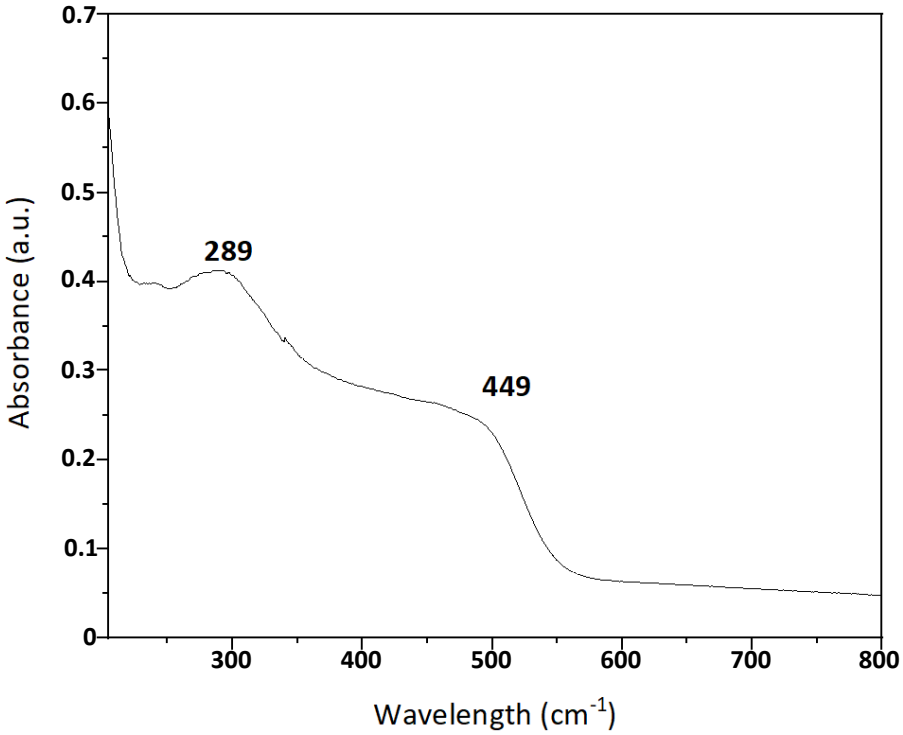

***Figure A 60**: UV-Vis solid spectrum of 2Br12PhCCMoid **11**.*

Electrochemistry spectra

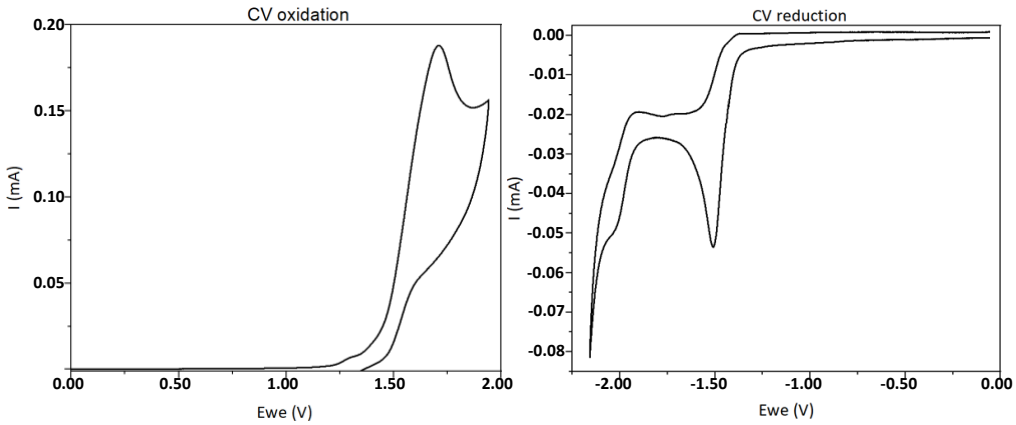

Figure A 61**: Oxidation and reduction cyclic voltammogram spectra of 10PhCCMoid **4.

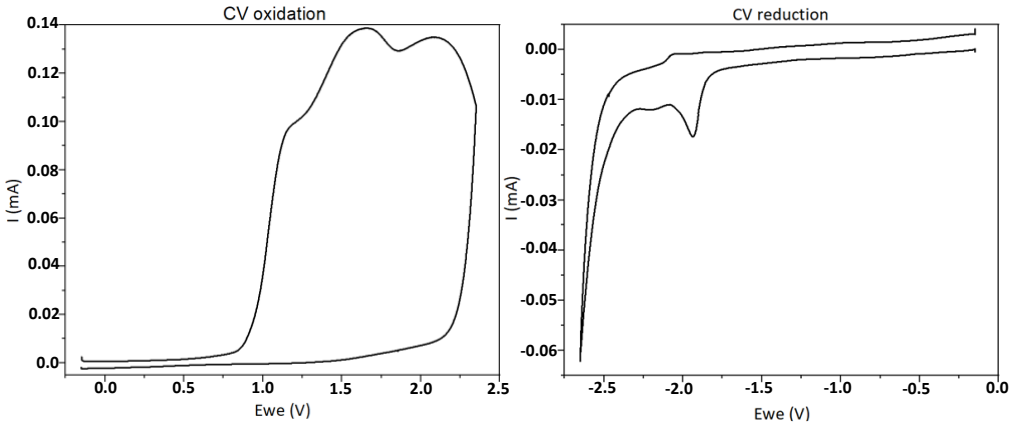

Figure A 62**: Oxidation and reduction cyclic voltammogram spectra of 2Br12PhCCMoid **7.

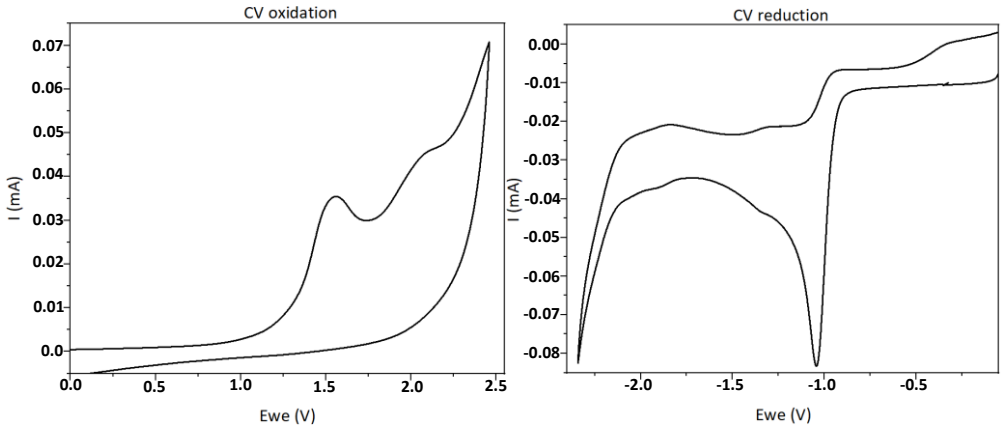

Figure A 63**: Oxidation and reduction cyclic voltammogram spectra of 10PhCCMoidBF$_2$ **9.

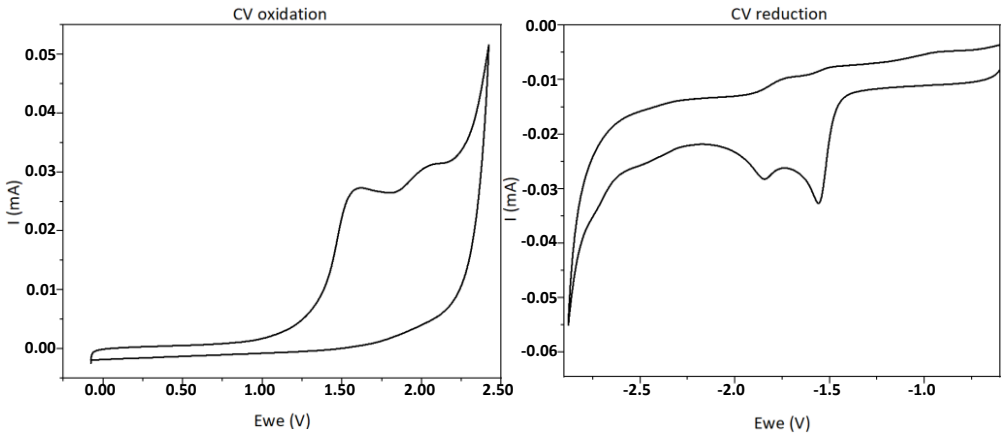

Figure A 64**: Oxidation and reduction cyclic voltammogram spectra of 2Br12CCMoidBF$_2$ **11.

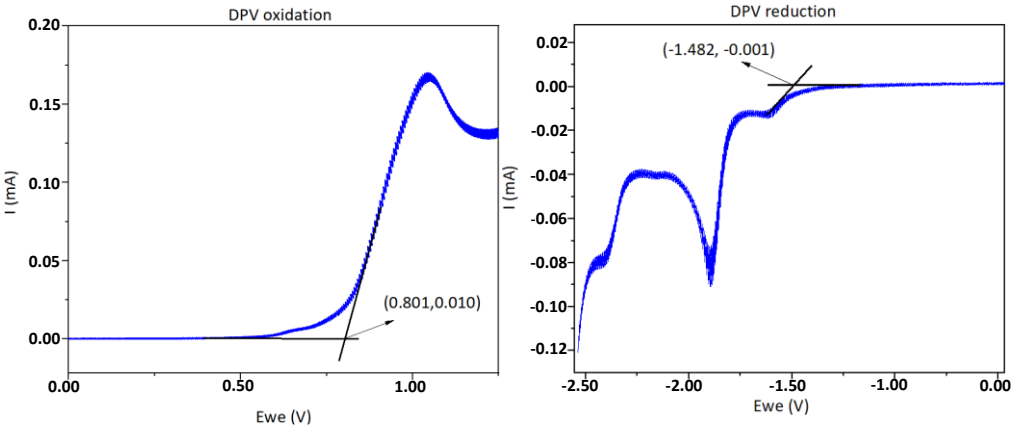

Figure A 65**: Oxidation and reduction voltammogram spectra of 10PhCCMoid **4.

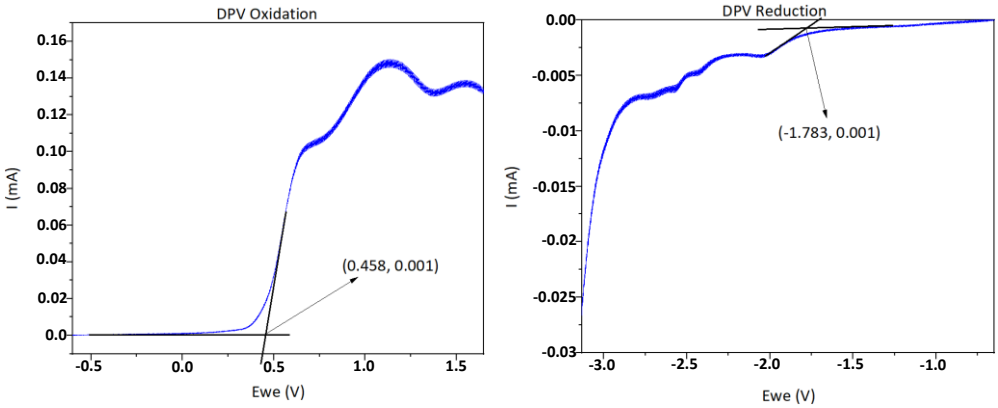

Figure A 66**: Oxidation and reduction voltammogram spectra of 2Br12PhCCMoid **7.

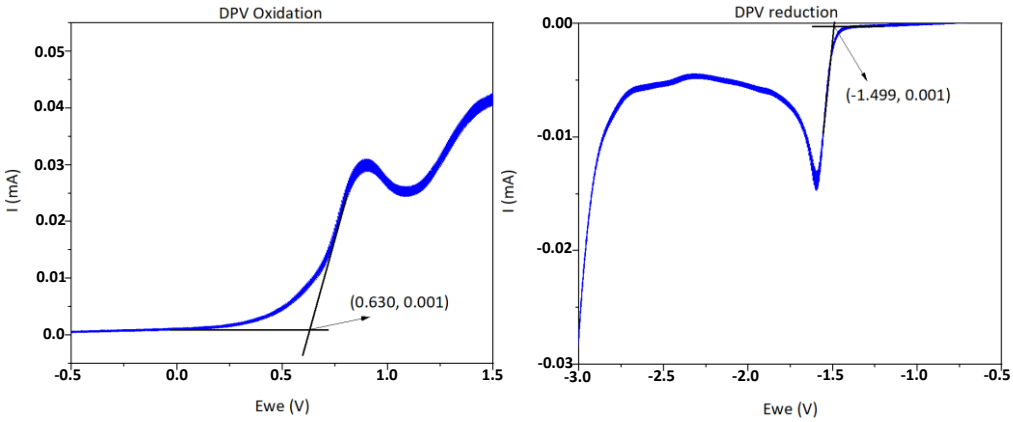

Figure A 67**: Oxidation and reduction voltammogram spectra of 10PhCCMoidBF_2 **9.

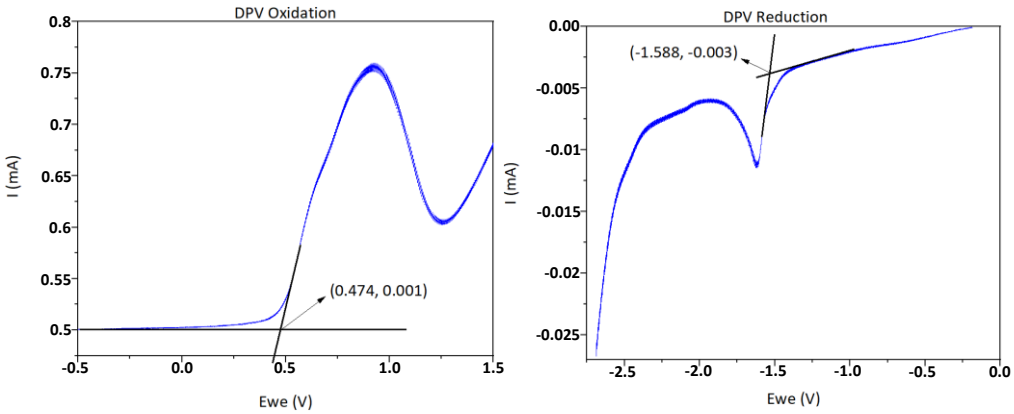

Figure A 68**: Oxidation and reduction voltammogram spectra of 2Br12PhCCMoidBF$_2$ **11.

MALDI- MASS spectra

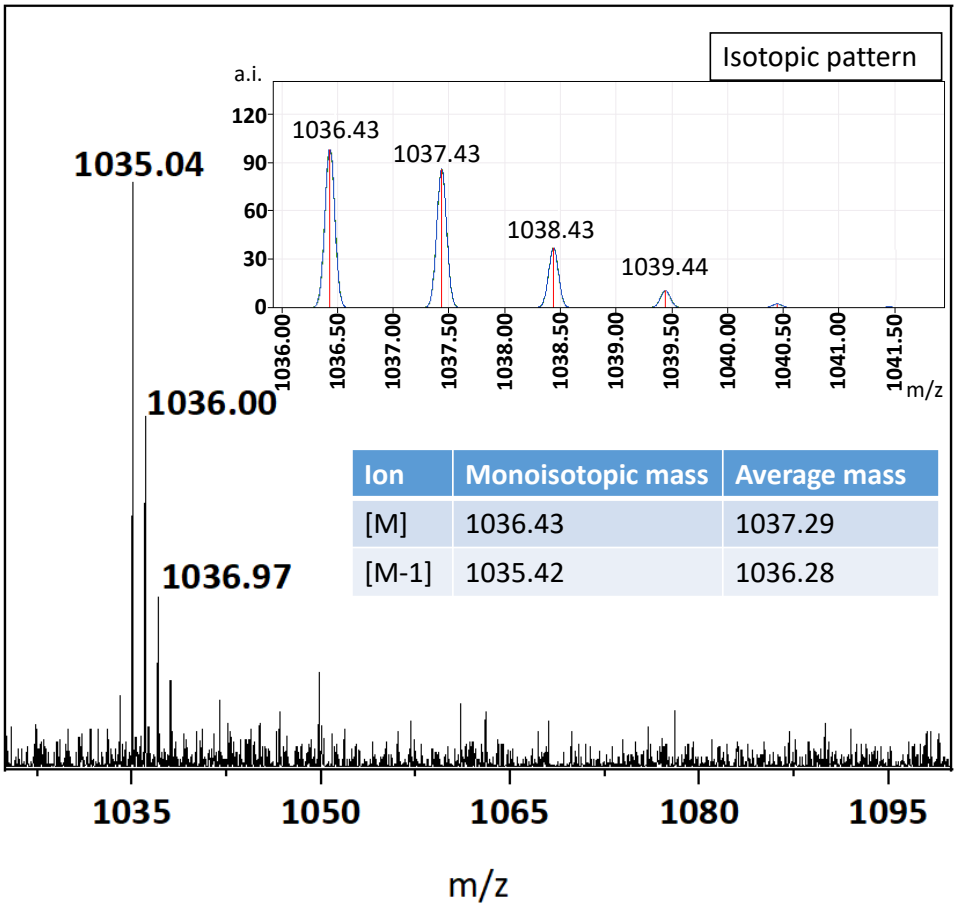

Ion	Monoisotopic mass	Average mass
[M]	1036.43	1037.29
[M-1]	1035.42	1036.28

***Figure A 69:** Mass spectrum of 10PhCCMoid **4** (Negative mode).*

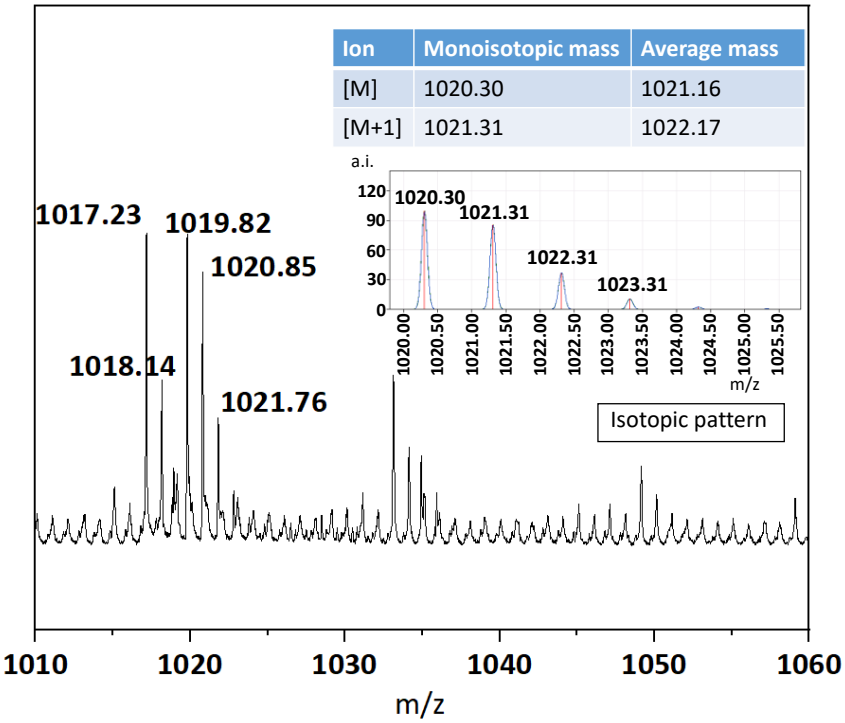

***Figure A 70**: Mass spectrum of 4PhAntCCMoid **5** (Negative mode).*

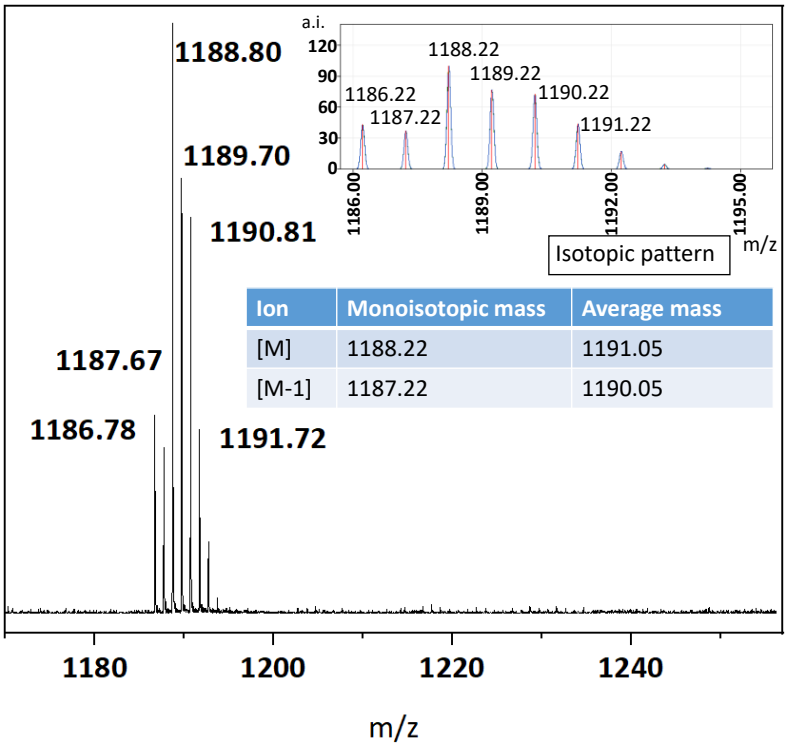

***Figure A 71**: Mass spectrum of 2Br12PhCCMoid **7** (Positive mode).*

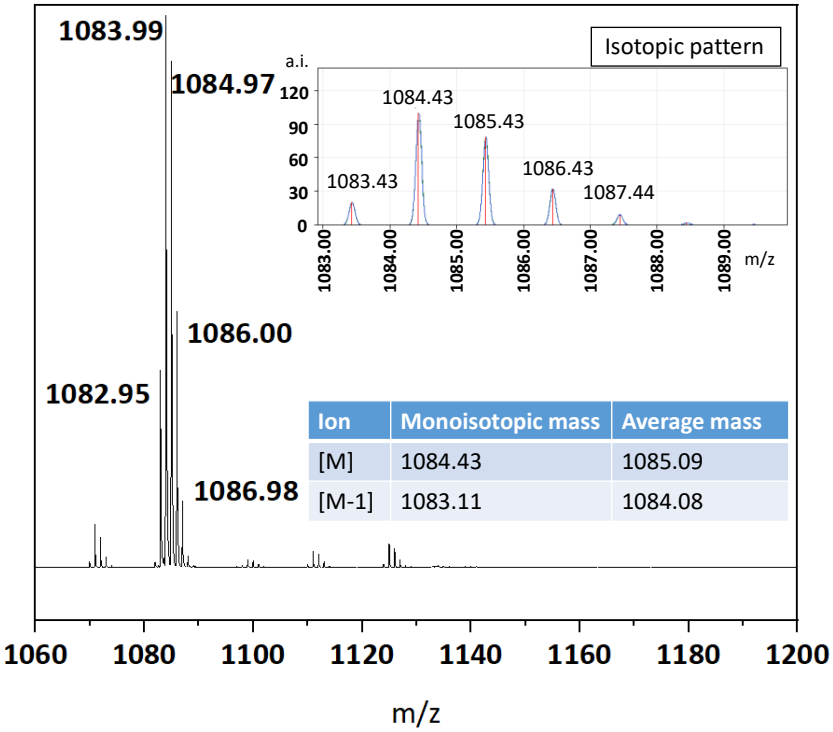

Ion	Monoisotopic mass	Average mass
[M]	1084.43	1085.09
[M-1]	1083.11	1084.08

***Figure A 72**: Mass spectrum of 10PhCCMoidBF$_2$ **9** (Negative mode).*

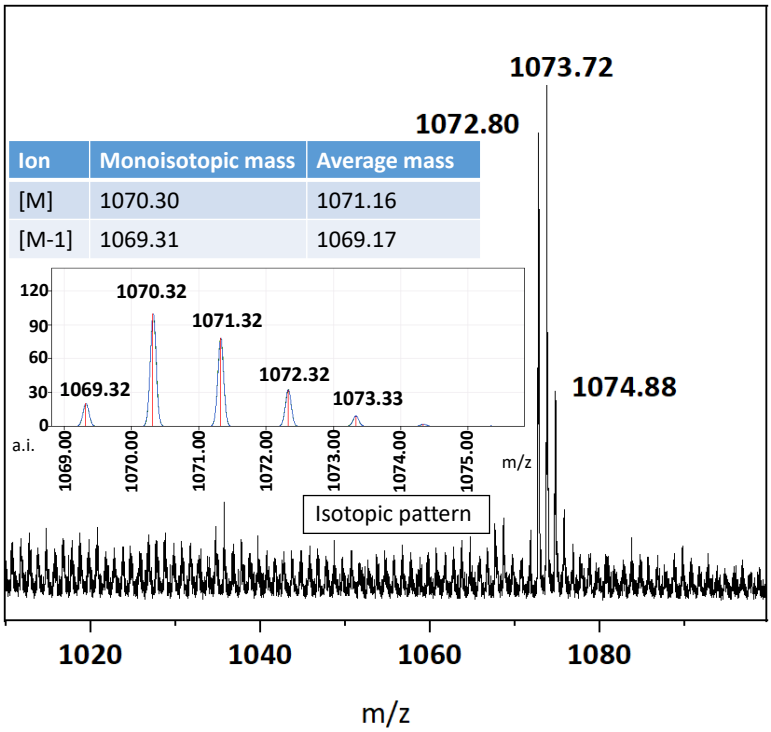

Ion	Monoisotopic mass	Average mass
[M]	1070.30	1071.16
[M-1]	1069.31	1069.17

***Figure A 73**: Mass spectrum of 4PhAntCCMoidBF$_2$ **10** (route **A,** positive mode).*

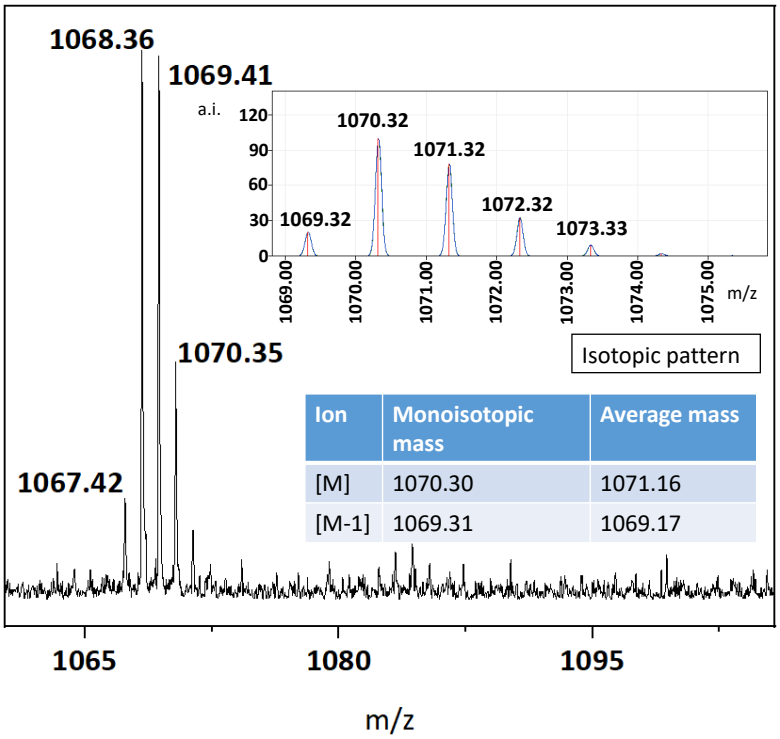

Ion	Monoisotopic mass	Average mass
[M]	1070.30	1071.16
[M-1]	1069.31	1069.17

***Figure A 74**: Mass spectrum of 4PhAntCCMoidBF$_2$ **10** (route **B**, negative mode).*

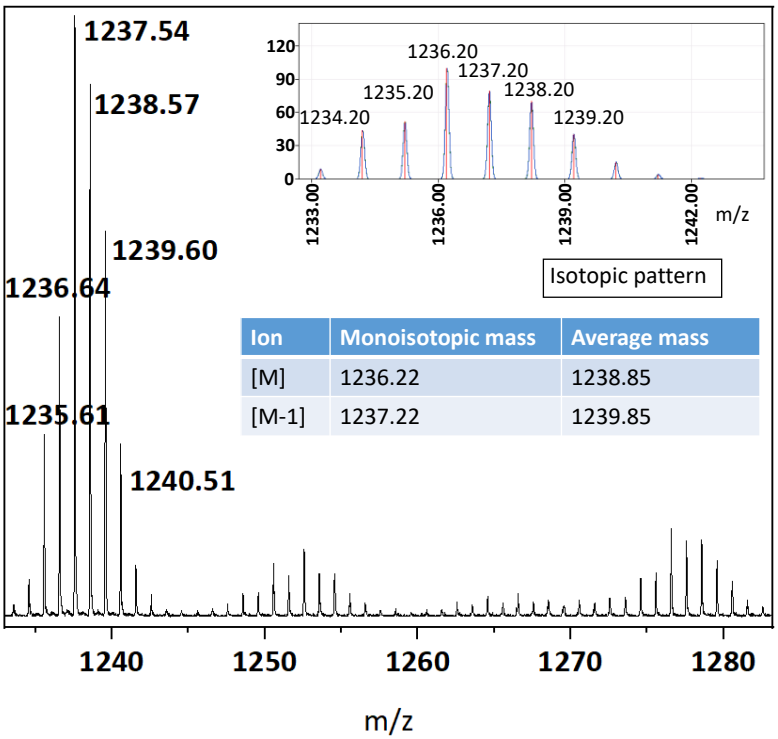

Ion	Monoisotopic mass	Average mass
[M]	1236.22	1238.85
[M-1]	1237.22	1239.85

***Figure A 75**: Mass spectrum of 2Br12PhCCMoidBF$_2$ **11** (Positive mode).*

Thermogravimetric analysis spectra (TGA)

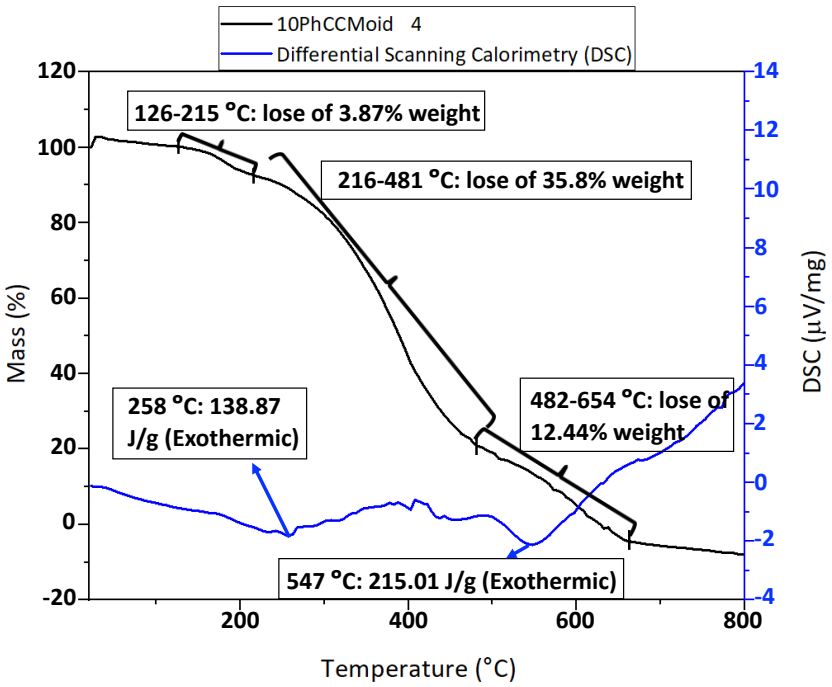

Figure A 76: *Thermogravimetric spectra of 10PhCCMoid **4** under N_2 atmosphere.*

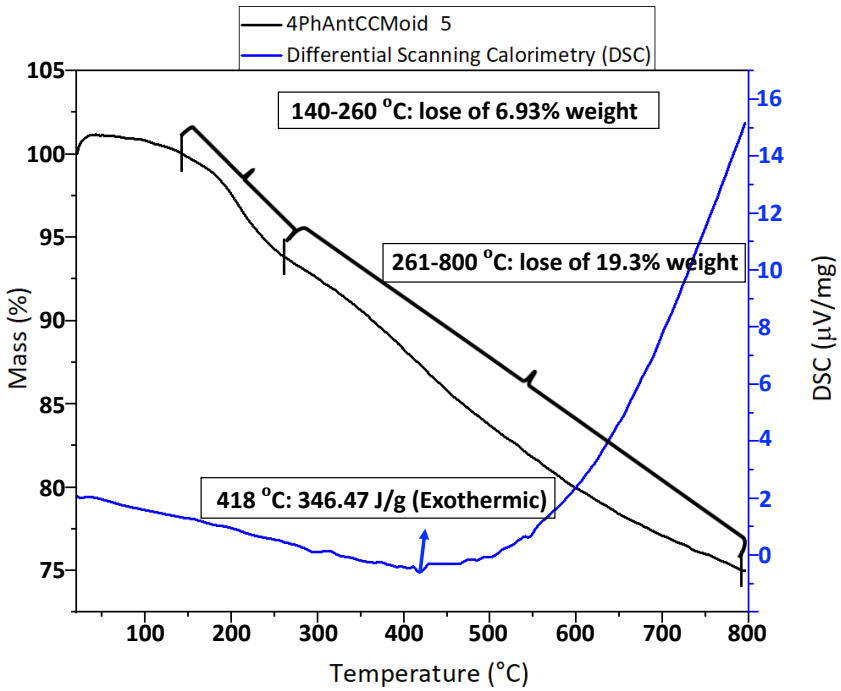

Figure A 77*: Thermogravimetric spectra of 4PhAntCCMoid **5** under N_2 atmosphere.*

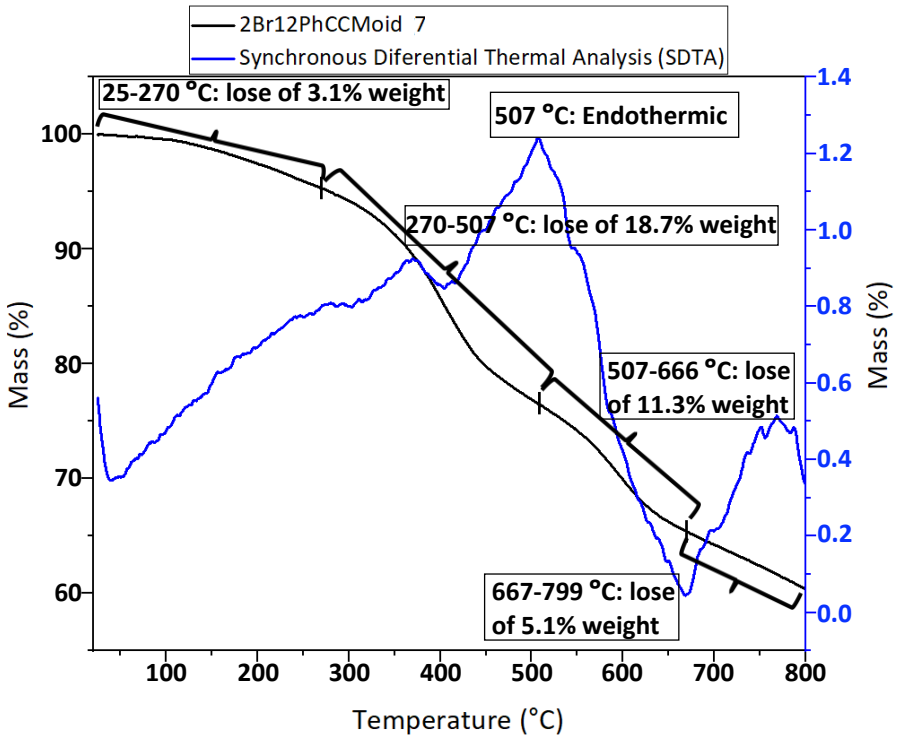

***Figure A 78**: Thermogravimetric spectra of 2Br12PhCCMoid **7** under N_2 atmosphere.*

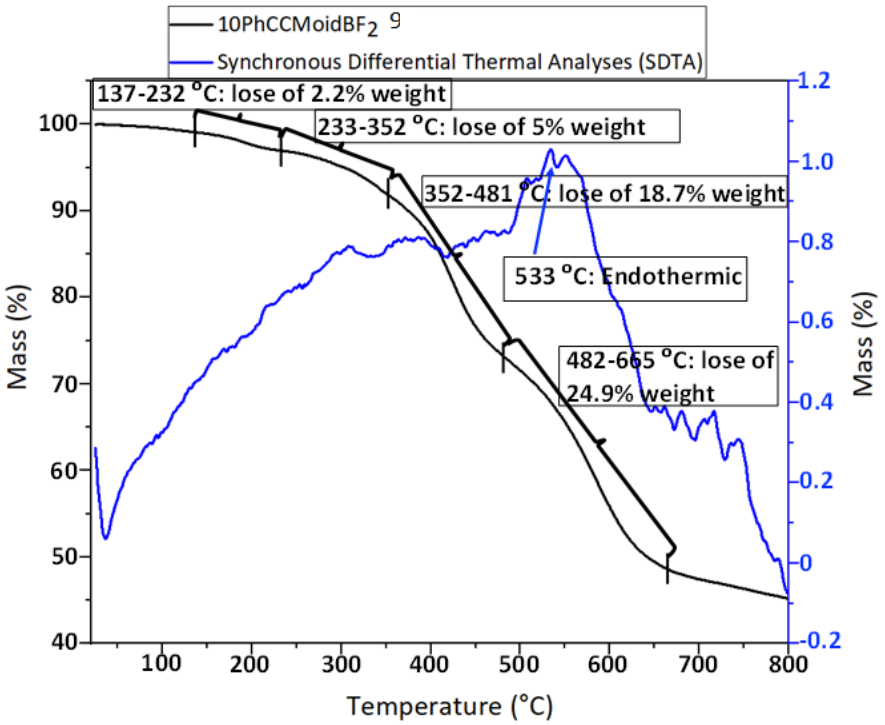

***Figure A 79**: Thermogravimetric spectra of 10PhCCMoidBF$_2$ **9** under N_2 atmosphere.*

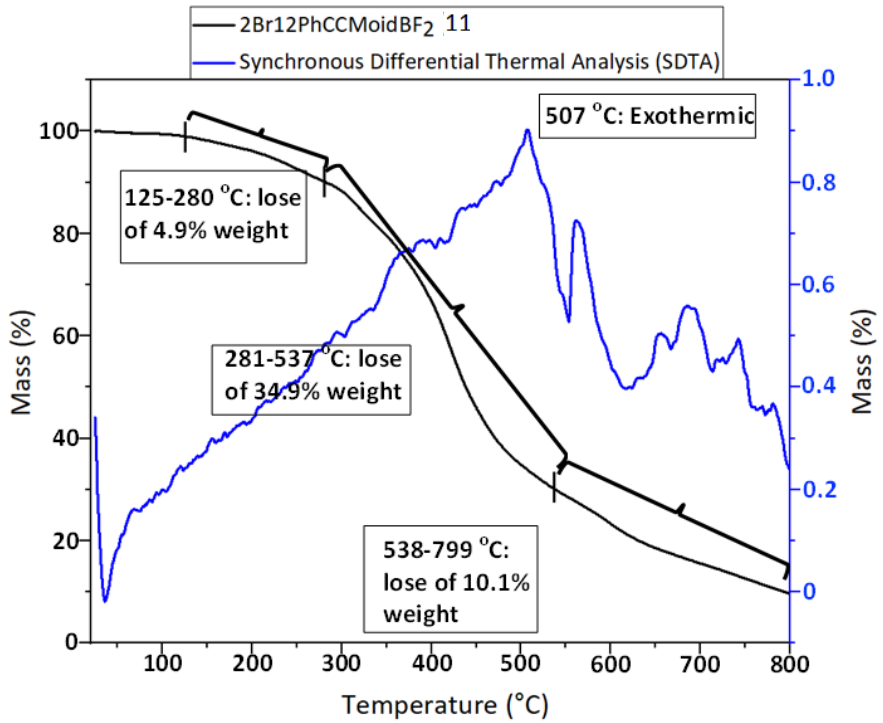

***Figure A 80**: Thermogravimetric spectra of 2Br12PhCCMoidBF$_2$ **11** under N$_2$ atmosphere.*

X-ray Photoelectron Spectra

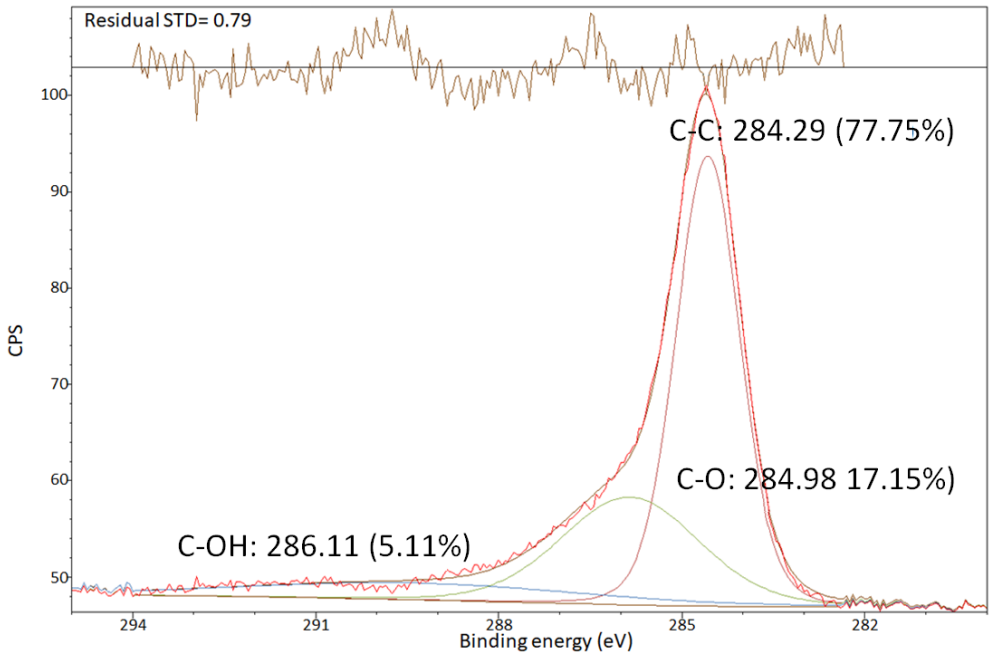

***Figure A 81**: C region XPS spectrum for 10PhCCMoid **4**.*

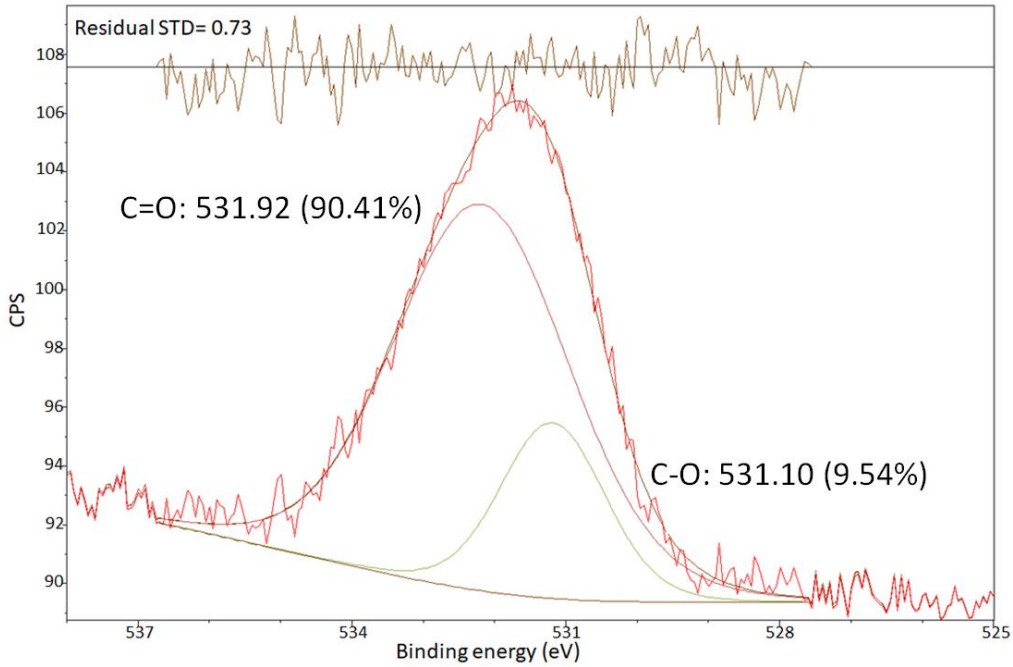

***Figure A 82**: O region XPS spectrum for 10PhCCMoid **4**.*

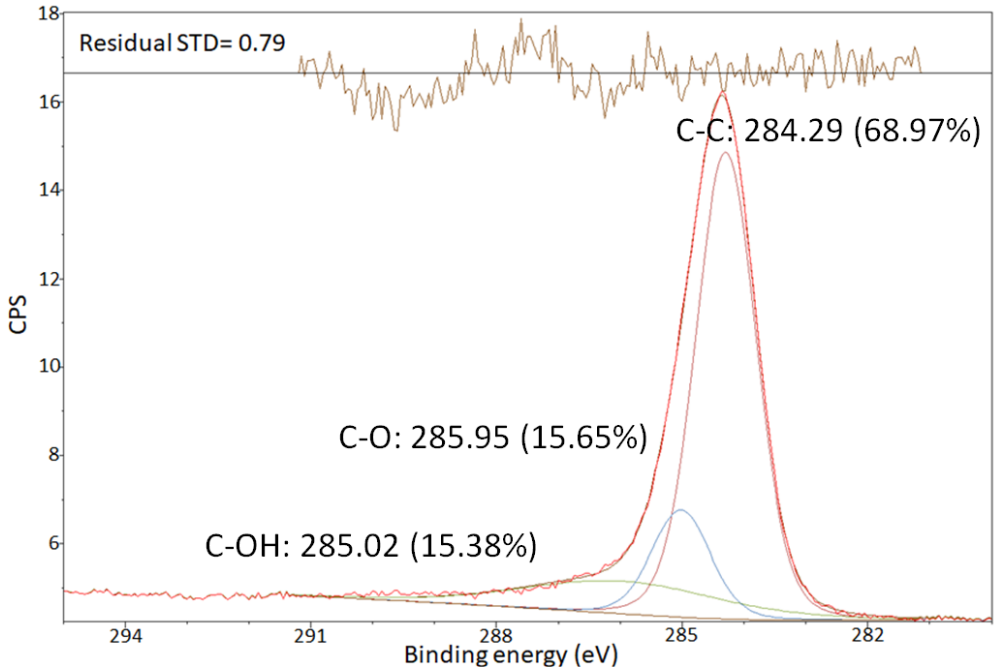

***Figure A 83**: C region XPS spectrum for 4PhAntCCMoid **5**.*

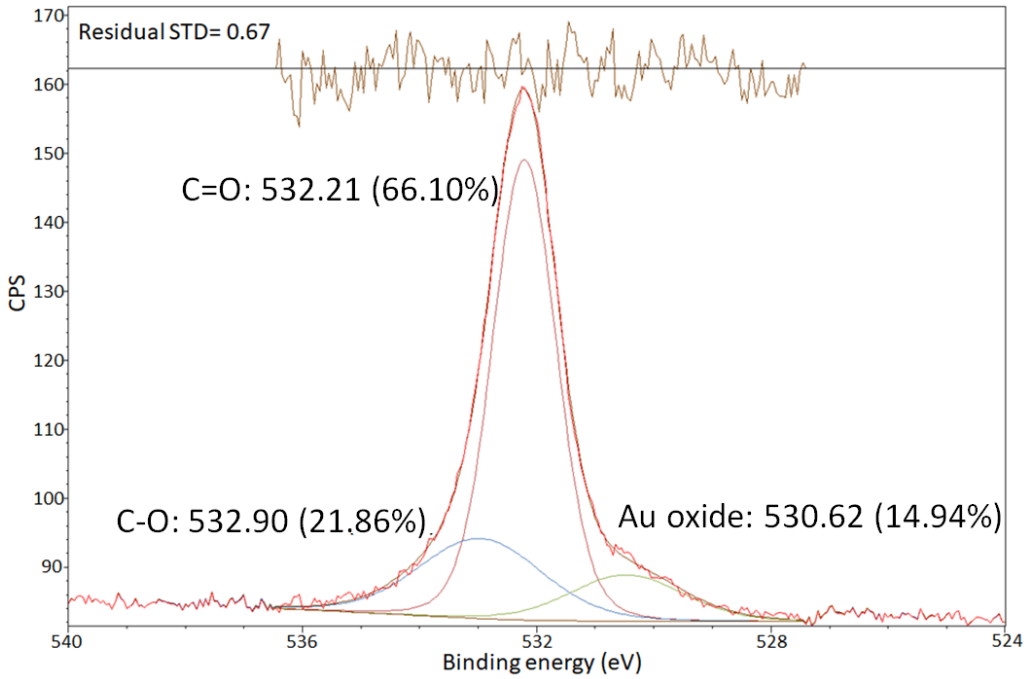

***Figure A 84**: O region XPS spectrum for 4PhAntCCMoid **5**.*

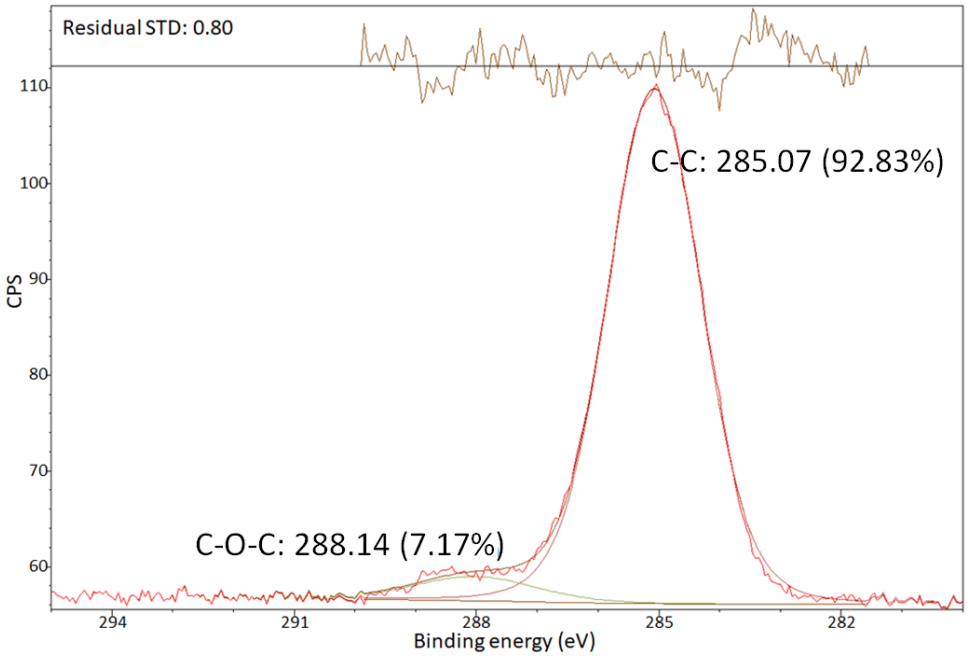

***Figure A 85**: C region XPS spectrum for 4PhAntCCMoidBF$_2$ **10**, route A.*

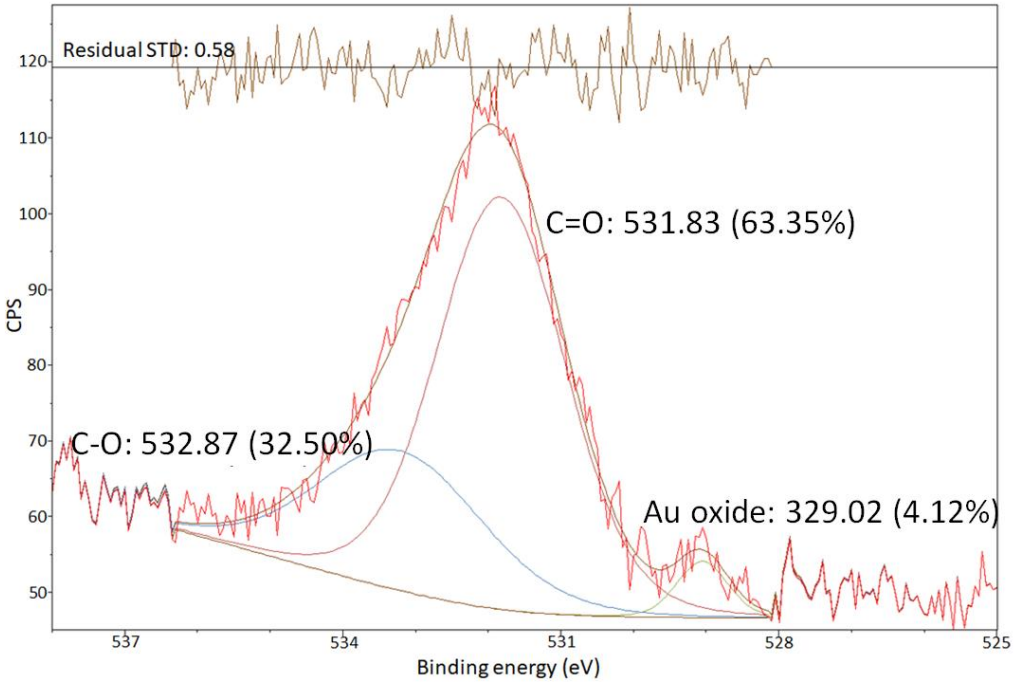

***Figure A 86**: O region XPS spectrum for 4PhAntCCMoidBF$_2$ **10**, route A.*

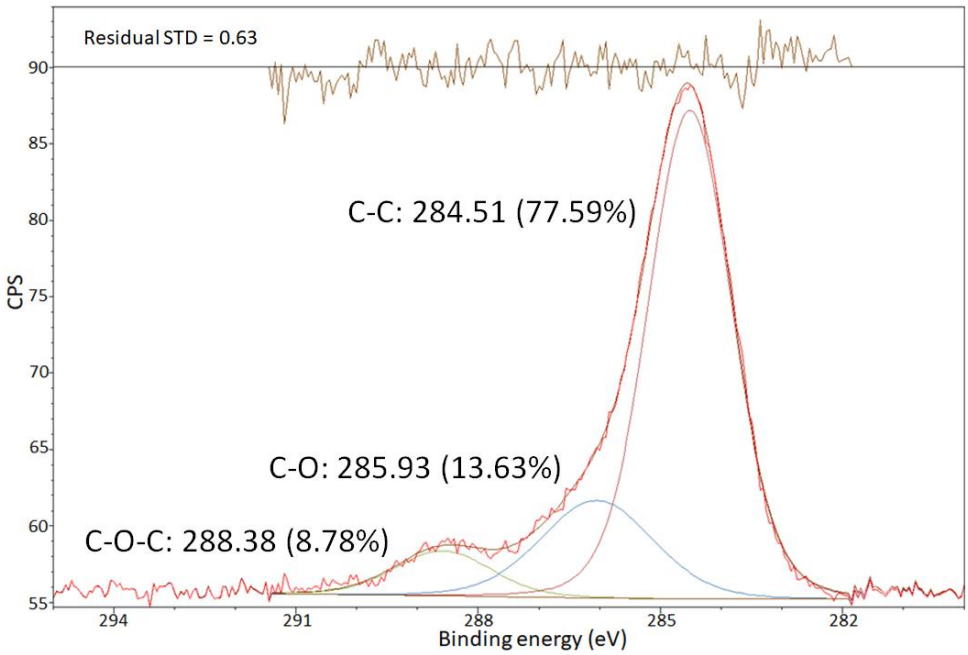

***Figure A 87**: C region XPS spectrum for 4PhAntCCMoidBF$_2$ **10**, route B.*

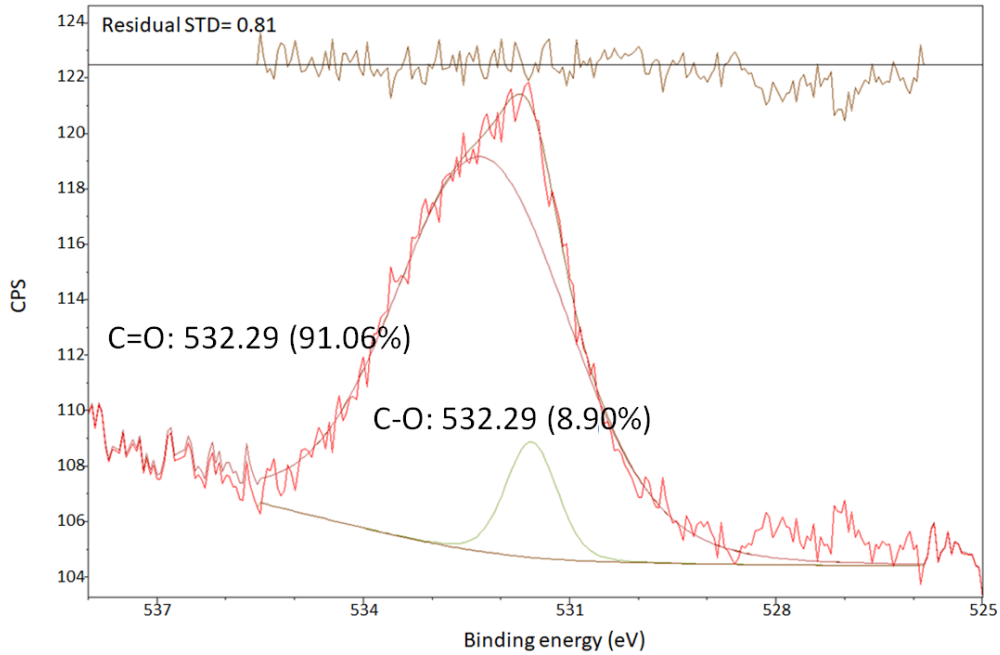

Figure A 88: *O region XPS spectrum for 4PhAntCCMoidBF$_2$* ***10****, route B.*

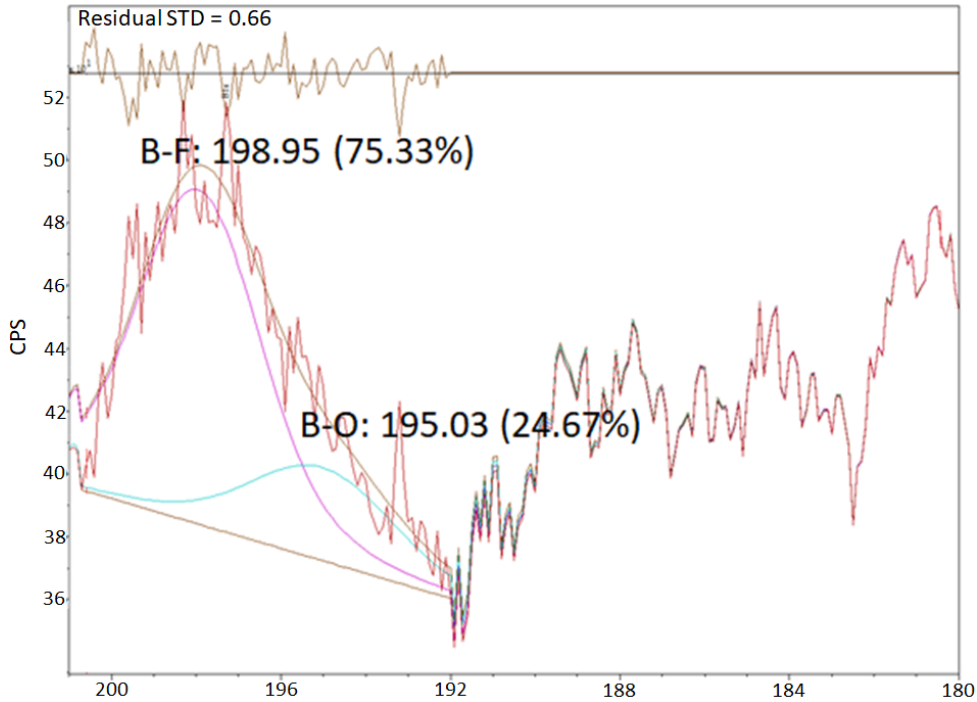

Figure A 89*: B region XPS spectrum for 4PhAntCCMoidBF$_2$* ***10****, route A.*

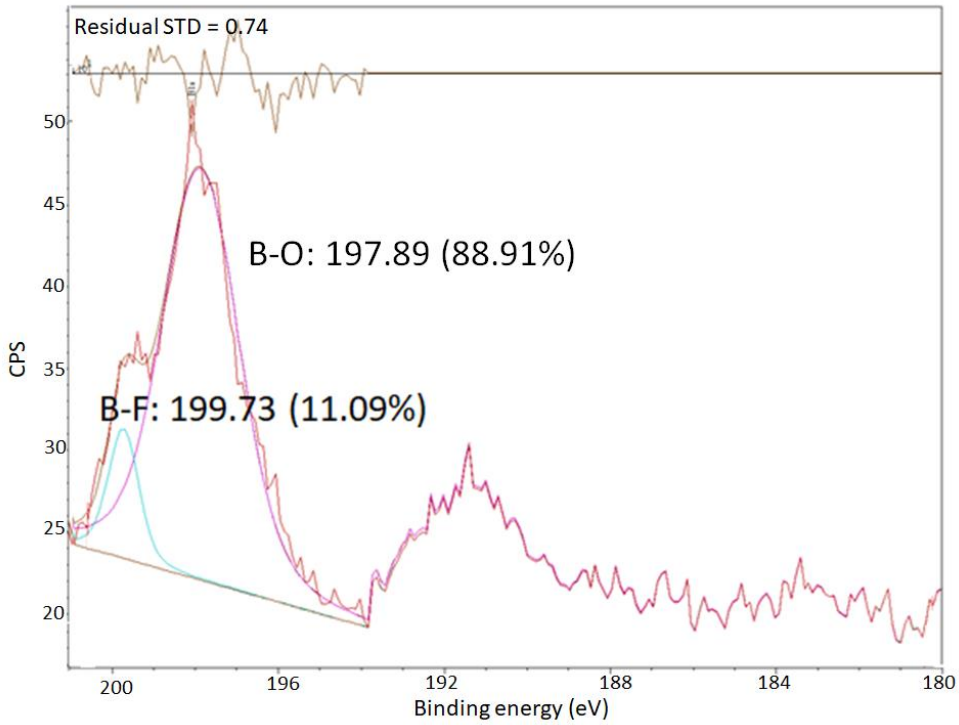

***Figure A 90**: B region XPS spectrum for 4PhAntCCMoidBF$_2$ **10**, route B.*

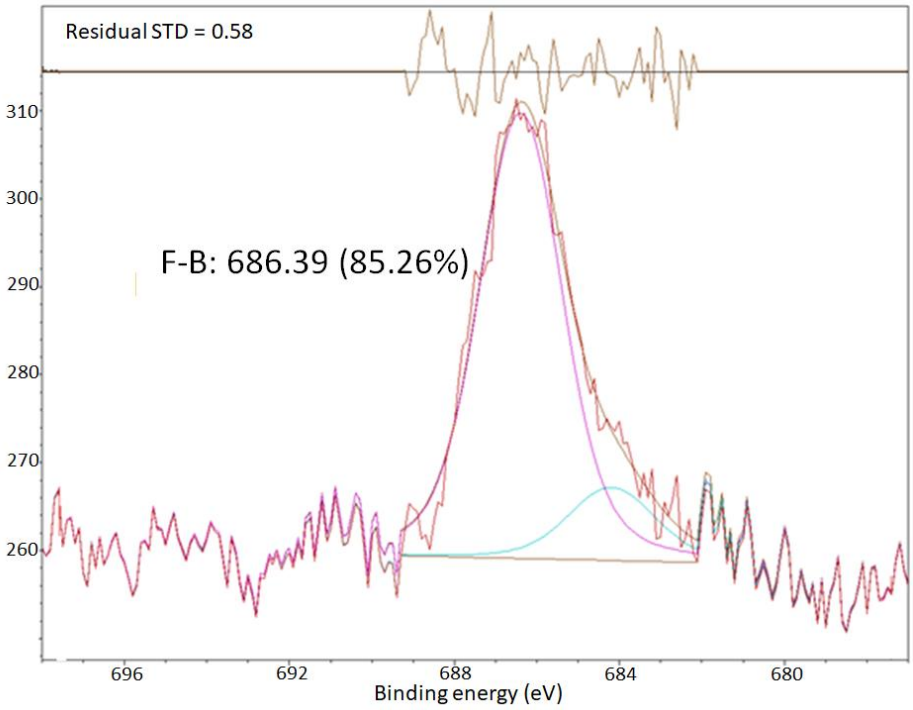

***Figure A 91**: F region XPS spectrum for 4PhAntCCMoidBF$_2$ **10**, route A.*

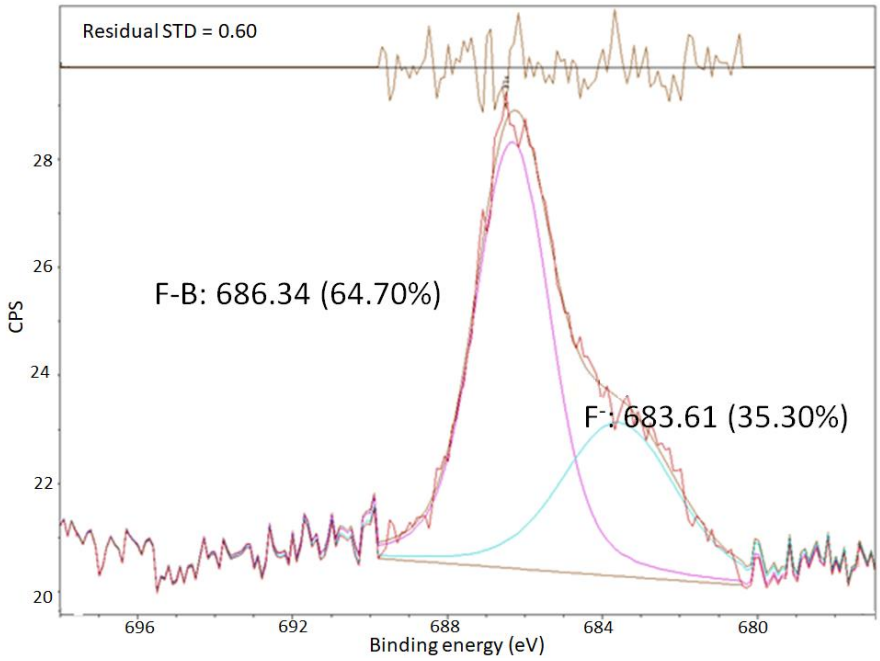

***Figure A 92**: F region XPS spectrum for 4PhAntCCMoidBF$_2$ **10**, route B.*

Fluorescence Spectra

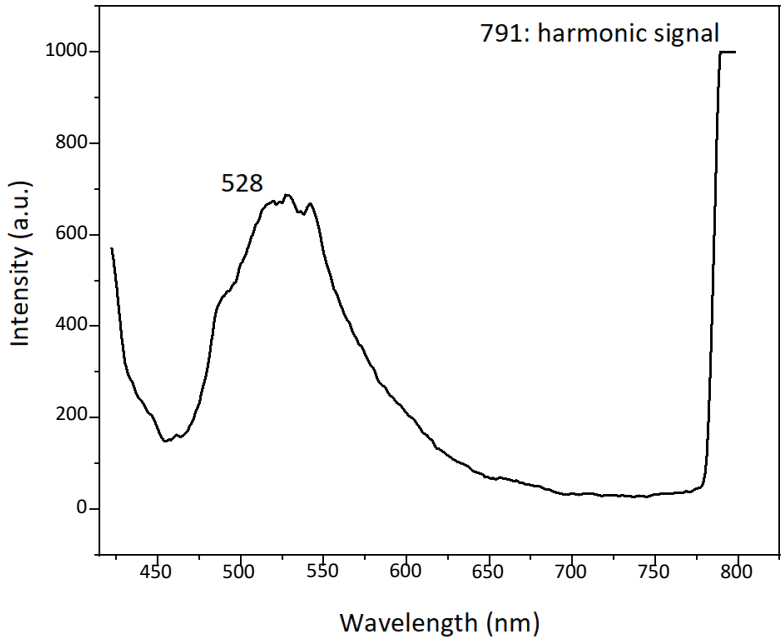

***Figure A 93**: Emission fluorescence spectra with excitation at 400 nm for 10PhCCMoid **4**, conditions of the measurement: PMT voltage (High), excitation light aperture (10), emission light aperture (5), smoothing (on).*

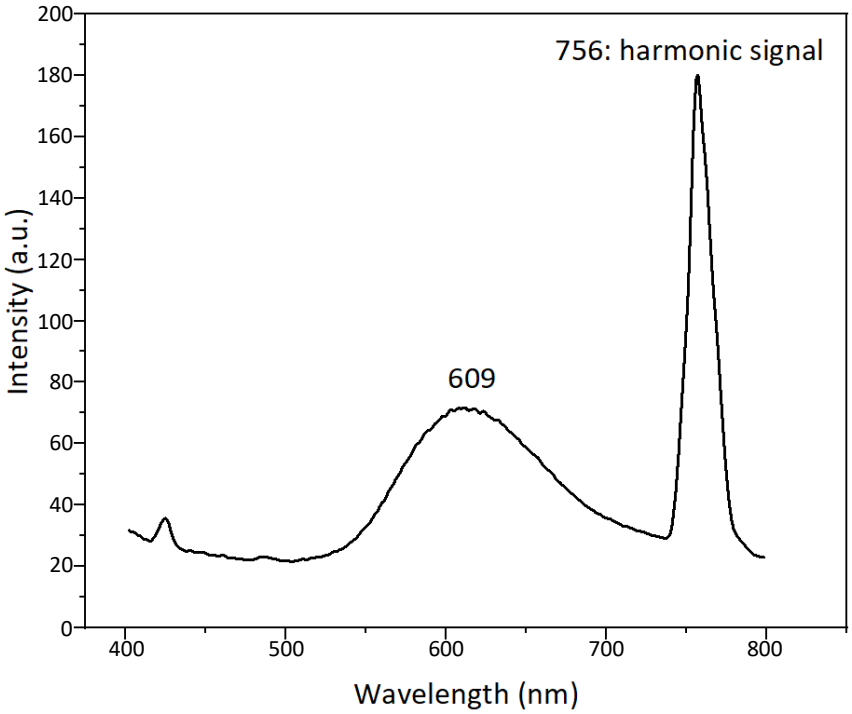

***Figure A 94**: Emission fluorescence spectra with excitation at 380 nm for 10PhCCMoidBF$_2$ **9**, conditions of the measurement: PMT voltage (Medium), excitation light aperture (10), emission light aperture (5), smoothing (on).*

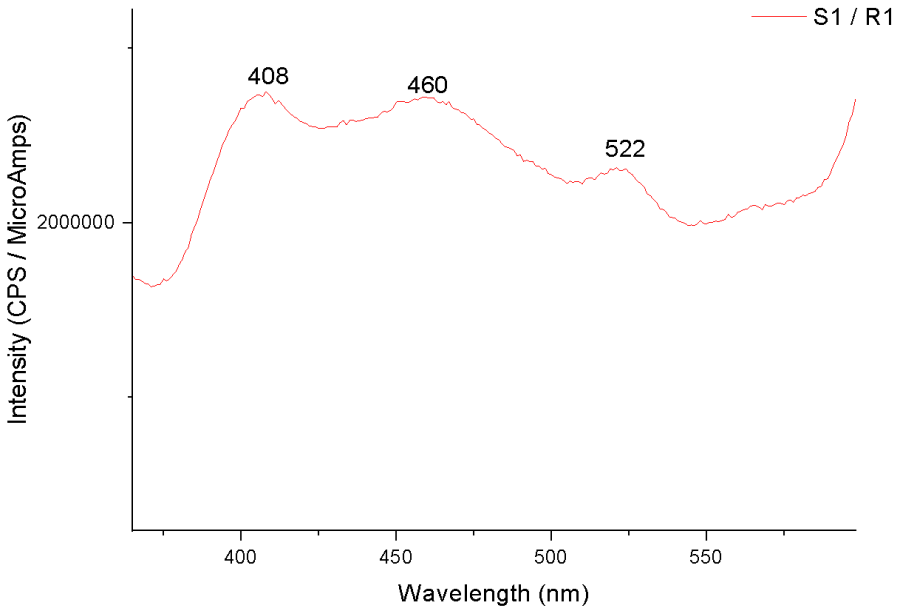

***Figure A 95:** Emission fluorescence spectra with excitation at 320 nm for 4PhAntCCMoid **5**, conditions of the measurement: PMT voltage (High), excitation light aperture (10), emission light aperture (5), smoothing (on).*

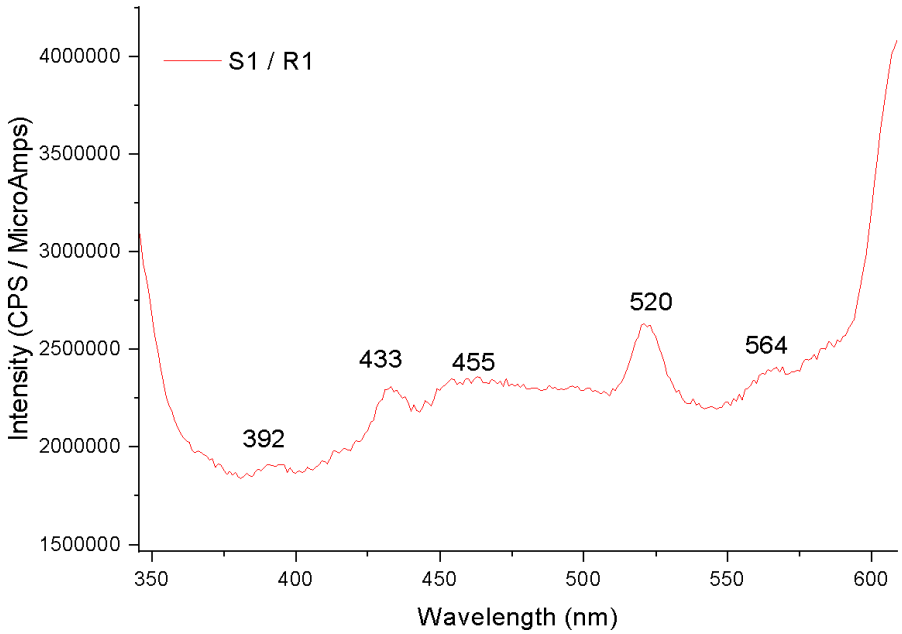

***Figure A 96**: Emission fluorescence spectra with excitation at 320 nm for 4PhAntCCMoidBF$_2$ **10**, route A, conditions of the measurement: PMT voltage (High), excitation light aperture (10), emission light aperture (5), smoothing (on).*

Schematic representation of CCMoids structure

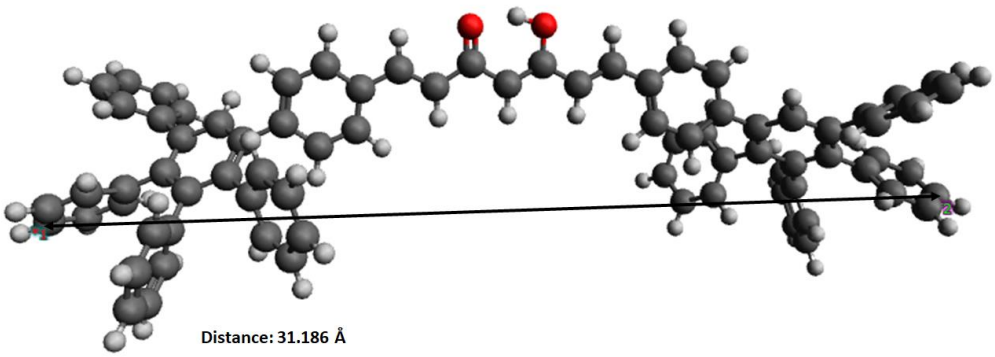

***Figure A 97**: Representation of CCMoid **4** using Avogadro program.*

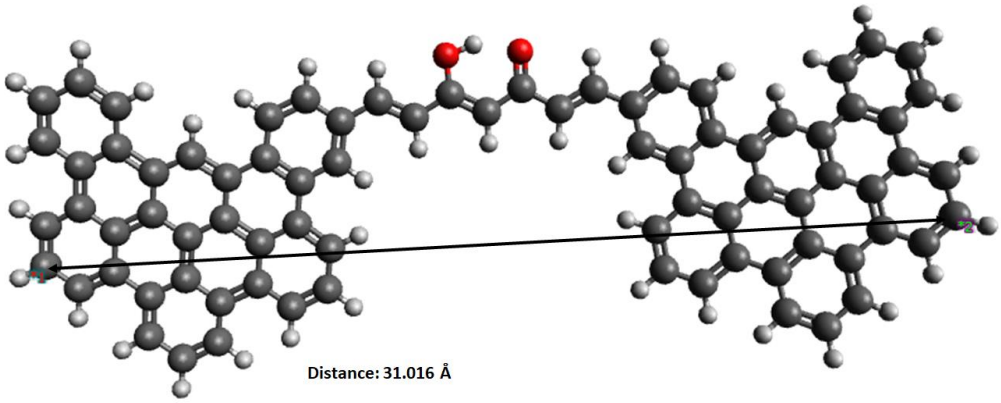

***Figure A 98**: Representation of CCMoid **5** using Avogadro program.*

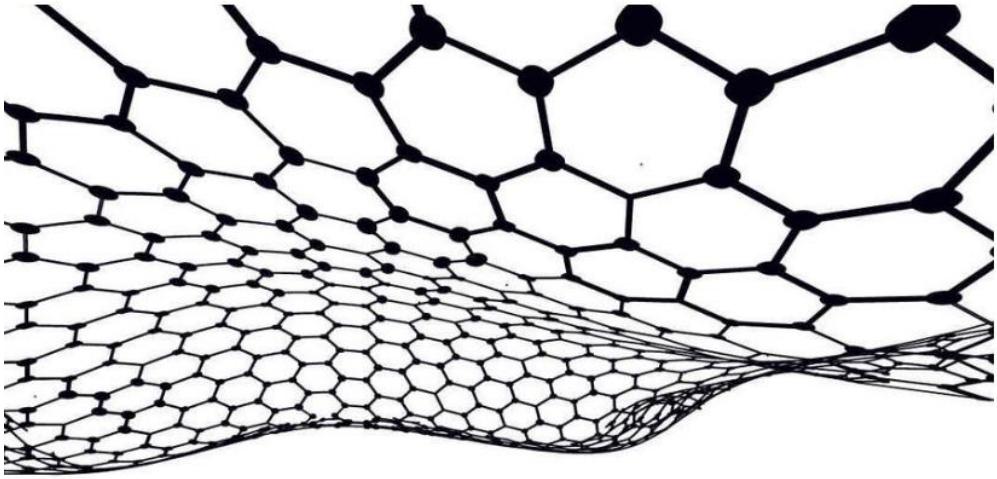

CHAPTER III

3. CHAPTER III: SYNTHESIS OF T-SHAPED CCMOIDS

3.1 INTRODUCTION

As mentioned throughout this thesis, graphene could undergo noncovalent interactions by intermolecular forces (π-π stacking) with other molecular systems.[37,38,57] This matter was examined in chapter 4 as the main key for the design of new CCMoid molecules containing PAH groups at the arms, capable of stablishing in the future strong interactions with the graphene electrodes in hybrid devices (Figure 55, chapter 2). In addition to this issue, there are other outstanding concerns related to the control in single molecules along with the stability, performance and reproducibility of graphene hybrid devices once the molecules are deposited. [37,38,57] All of these are crucial issues in the development of the topic of single molecule electronics and its evolution. The first one, links with the difficulty of positioning single molecules in strategic locations, considering that known methods like the anchoring through a covalent bond or the deposition of a suspension of molecules to the system among others, are not sensitive enough to work at that scale.

There is not a simple approach toward such limitation, and the general procedure is based on the use of dissolution methodologies and mild conditions, which limits the possibility of selectively operating on the device and aggravates the risk of its degradation.[37,38,57] Here again, the idea of reinforcing the molecule-electrode interface, improving the quality of the junction, is basic. This part, as mentioned above, has been discussed in the previous chapter 2. In addition, it should be mentioned that the effect of temperature on the device will favour the vibration of the molecules, hindering intermolecular bonds with graphene and causing sliding movements that would deteriorate the bonding and performance of the devices in the short and medium term. Therefore, the additional challenge lies in fixing the molecule so as to minimize such effects while improving electrode contact along with reproducibility and performance of the final devices. Guo *et al*.[61] have accomplished something similar in nanographs of 8-12 nm, where with the assistance of chemical reactions they have accomplished the coordination of molecules to the sides of functionalized graphene electrodes, proving that their devices provide good yields and are stable and function after more than one year. This supports the concept that

improvements will come from actively working at the interface between electrodes and molecules from a chemical point of view.

On the other hand, the field of surface science and, precisely, that including the reactivity and chemical functionalization of substrates has been extensively studied.[61,90,91,108,191-193] In solution, a multitude of routes describing the coordination between the outermost atoms on the surface of inorganic materials with organic molecules of all kinds have been described and effectively developed.[194] In particular, and given its relevance in technological applications, there are a large number of pathways describing the reactivity of SiO_2 substrates in the creation of SAMs (self-assembled monolayers).[109,110] Some of these studies[195] describe the relevance of the 3d orbitals of silicon material, which play an important role in enhancing the stability of the possible systems (molecule+substrate) that could be formed. Comparing the Si-O bond with the closest system, which is the C-O bond, the d-orbitals of silicon are available to be occupied with the electron density donated by the 2*p* orbitals of oxygen that formed a kind of π-bonding between d_π- and p_π-orbitals.[196,197] This donation strengthens the Si-O bond promoting a lower basicity of this bond. This makes the Si-O bond very reactive towards the formation of a O-Si-O polymerisation system.[198-200]

In this matter, our group has extensive experience in the deposition and reactivity of polysilicon substrates,[53,54,201-203] in particular, in the functionalization of CCMoids molecules for binding to previously functionalized surfaces, and the creation of molecular patterns on substrates by soft micro-contact printing (μ-CP) technique[53,54,201,203] for the study of new CCMoids acting as sensors.[51,204,205]

A new methodology in the construction of graphene devices, which has not yet been explored in the literature, is the one based on the symbiosis of the ideas described above, taking into account that the gate of the desired devices is usually of Si covered by SiO_2, as insulator. In this way, the molecular deposition could be performed in solution and with soft methods. The attachment of the molecules to the gate would provide the ability to fix the molecules to the third electrode, while getting rid of the excess of extra molecules, by cleaning the final device with organic solvents, without damaging the device. The attachment of the molecule will minimize the sliding of the system which, at the same time, will contain arms that will

enhance the π-π stacking with the graphene electrodes (source and drain). Figure 80 shows a general picture of what the final systems could look like.

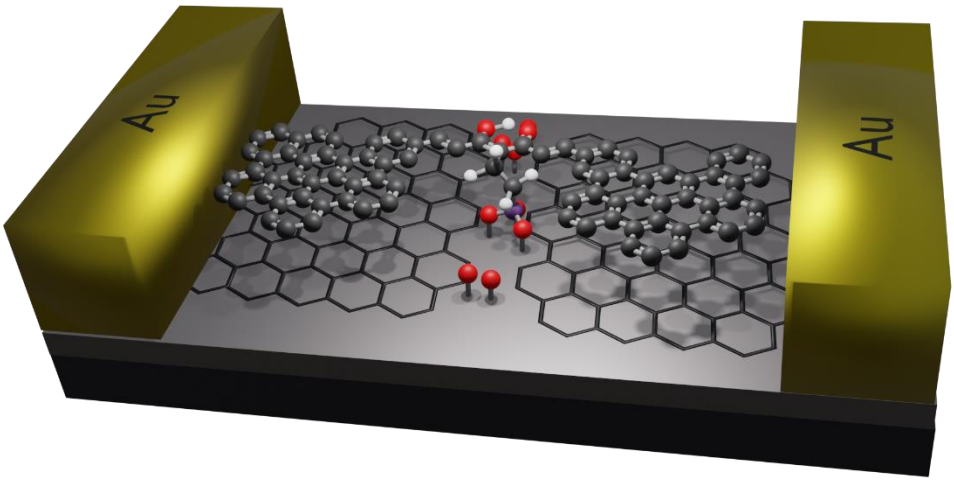

Figure 80*: Representation of the three-terminal device with the desired T-shaped CCMoid, where carbon atoms are in grey, hydrogens in white and silicon in purple.*

3.2 OBJECTIVES

In order to proceed to a better molecule+electrode hybridization and to perform it under mild conditions, in solution, the molecular design must be suitable and fine-tuned to the dimensions and nature of the electrodes. Chapter 4 shows the bottom-up methodology stablished for the synthesis of CCMoids containing PAHs groups. Now, the main objective of chapter 5, which is the synthesis of T-shaped CCMoids with PAHs in their arms involve:

Searching for a synthetic procedure to achieve PAH-based CCMoids containing, in addition, short and reactive functional group in the central part of the CCMoid skeleton (leg position), allowing this type of approach the synthesis of functional T-shaped CCMoids.

For this purpose, the application of the techniques described in the previous chapters, including the calculation of the optical and electrical band gaps of the different T-shaped CCMoid systems, has been of great help. Moreover, the comparison between molecules with and without legs (chapters 4 and 5) has also been planned to determine the effect of the leg on the electronic nature of the final molecules.

3.3 RESULTS AND DISCUSSION

3.3.1. Synthesis of 4PhAntpropCCMoid 19 and 4PhAntallylCCMoid 24

Here, a new synthetic approach was proposed, using the knowledge gathered in previous chapters and targeting the creation of T-shaped CCMoids. The synthetic pathway includes therefore both ideas, the inclusion into the CCMoid skeleton of PAH arms, to strength the π-π interactions with graphene, and a functionalized leg prone to react with SiO_2 layer through the Si-OH formed once the layer is activated.

Scheme 7 and Scheme **8** display the routes that were followed toward the attainment of such goal. Both diagrams share a similar strategy, starting both with the addition of the leg, and differing in their ending groups: a terminal propargyl group in the case of Scheme 7 and a terminal allyl group in Scheme 8. As a result, the synthetic path displays symmetric CCMoids **15**-**24** as intermediate and final systems and obtaining overall yields for CCMoids **19** and **24** of 2.2 and 1.2%, respectively. Furthermore, all these molecules include the 7-carbon conjugated chain with a central *keto-enol* functional group, containing bulky aromatic-based rings, as it happens in chapter 2.

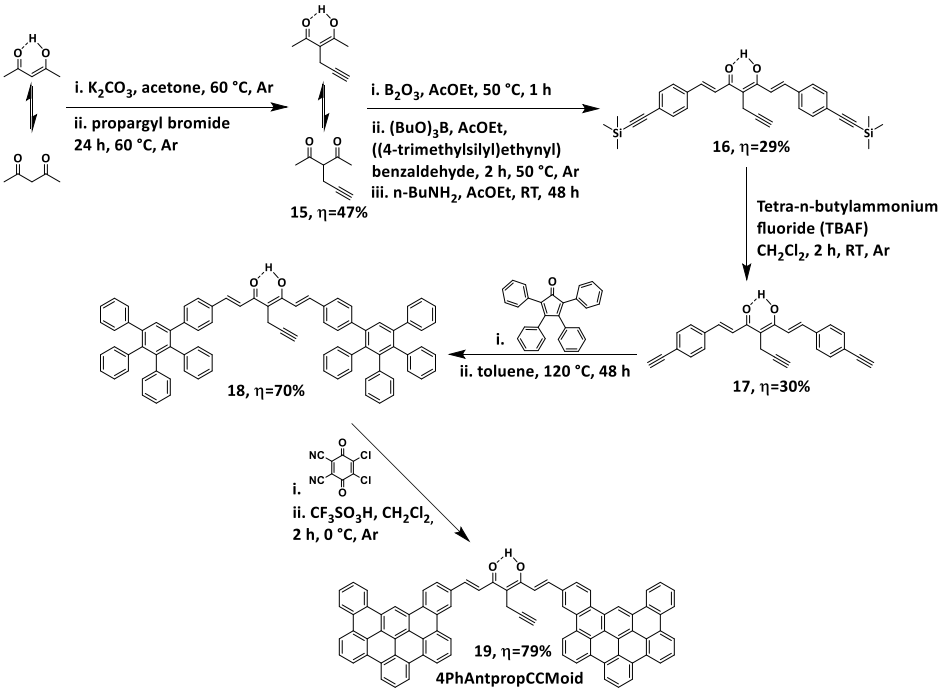

***Scheme 7**: Scheme of the synthesis proposed for the attainment of CCMoid **19**.*

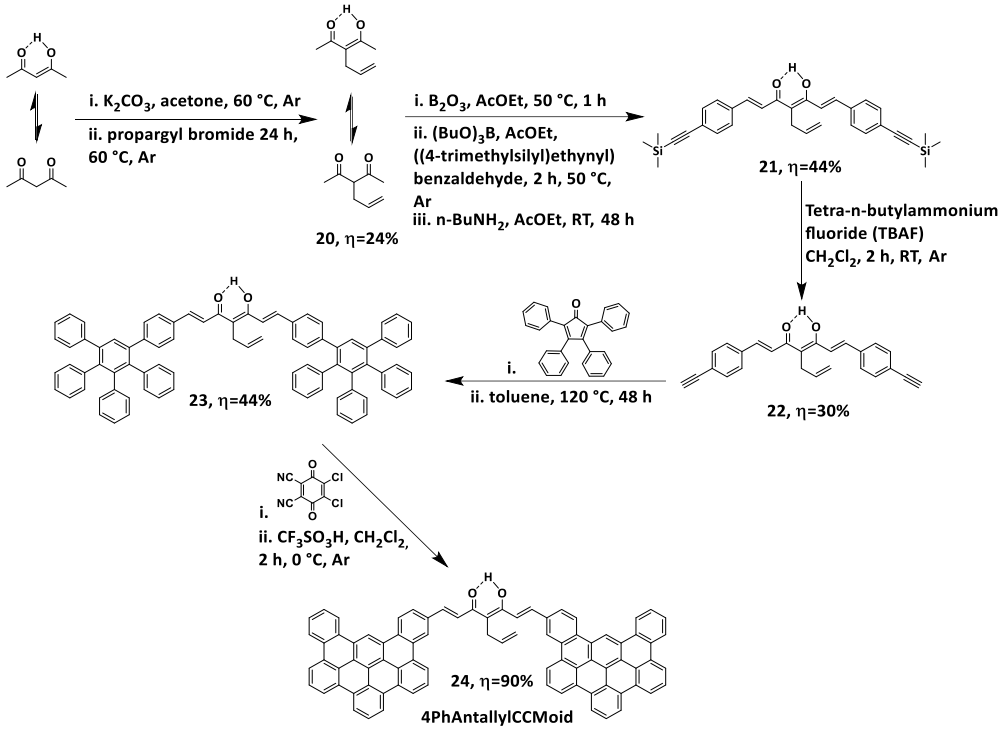

***Scheme 8**: Scheme of the synthesis proposed for the achievement of CCMoid **24**.*

This way, the two proposed syntheses started with the introduction of the propargyl bromide or allyl bromide groups in the acetylacetonate structure (**15** and **20**).[2,3,206,207] Next, the application of Pabon's methodology[5] gave CCMoids **16** and **21**, using in both cases 4-(trimethylsilyl)benzaldehyde, as the aldehyde selected for this reaction. The two reactions gave satisfactory yields and straightforward purifications (shown in the experimental section).

A challenging step here was the achievement of systems **17** and **22**, which involves the removal of the trimethylsilyl protecting groups. The methodology of applying potassium carbonate and methanol, used in previous chapter 3, promoted ambiguous results indicating the removal of the leg from the CCMoids, together with the appearance of unwanted byproducts, not possible to separate by column chromatography or recrystallization techniques. Instead, the use of the quaternary ammonium salt tetrabutylammonium fluoride gave the desired molecules in a straightforward way and good yields.

Continuing with the schemes, both show Diels-Alder [4+2] cycloaddition reactions using 2,3,4,5-tetraphenylcyclopenta-2,4-dien-1-one, providing the

polycyclic CCMoids **18** and **23**, respectively.[102] At this stage, the two systems display always small traces of impurities (see characterization section) that were not possible to separate; however, their origin was not CCMoid and therefore the compounds were used in the following reactions.

Finally, the last steps in both schemes were those already explained in previous chapter, involving intramolecular cyclodehydrogenations (Scholl reaction)[146-148] to produce the planar polycyclic aromatic hydrocarbons **19** and **24**. As in chapter 2, the final products were insoluble dark brown solids, that were characterized with solid-state techniques discussed previously.

3.3.2. ^{1}H-NMR and ^{13}C-NMR spectroscopy for CCMoids 16, 16, 18, 21, 22 and 23

Figure 81-Figure **84** show the ^{1}H and ^{13}C NMR spectra comparing CCMoids **16**, **17** and **18** and CCMoids **21**, **22** and **23**, respectively. Regarding the overall appearance of the ^{1}H and ^{13}C chemical shifts, a similar trend is observed in the case of the backbone of all CCMoids, having in common comparable signals for the linear alkene chain and the aromatic groups except for CCMoids **18** and **23**.

In the ^{1}H NMR spectra (Figure 81 and Figure **82**), the assignment and integration of the signals for CCMoids **16**, **17**, **21** and **22** were clearly made, as they have a similar shape as CCMoids **1** and **2** of chapter 3. Nevertheless, as occurred in CCMoid **4**, the analysis of the spectra of CCMoids **18** and **23** (Figure 81 and Figure **82**) were tougher due to the presence of broad signals in the aromatic regions. However, here it was easier to compare the T-shaped CCMoids with those shown before, without legs, presenting all compounds a similar appearance. In addition, the presence of the leg signals (region between 3.5-2 ppm, for propargyl system and, 6-3 ppm for the allyl systems) and the absence of signals from the triple and double bonds present in CCMoids **17** and **22** (Figure 81 and Figure **82**), encouraged us to keep going with the following reactions proposed in the synthetic routes. As mentioned before, the presence of some impurities were always observed, but clearly differentiated from the final systems.

In the signal assignment process at the lowest fields always appeared the enol proton of the *keto-enol* group H_a, H_h and H_o for CCMoids **16**, **17**, **18** (Figure 81), H_a, H_i and H_q for CCMoids **21**, **22** and **23** (Figure 81) (17.45-17.20 ppm). Then, the signal from the doublets H_b and H_i, for molecules **16** and **17**, and H_b,

H_j and H_r for molecules **21**, **22** and **23** respectively, were identified as the alkene protons in *trans* ($^3J_{HH}$ =16.0-15.0 Hz) because they are the closest to the *keto-enol* group and suffer the most the deshielding effect from it. The other two protons H_d, H_k for CCMoids **16** and **17** and H_d, H_l, for systems **21** and **22**, in that order, were observed at higher fields (≈7 ppm); interestingly, this last signal could not be identified for CCMoids **18** and **23** due to the presence of the broad aromatic bands in the 7-6.75 ppm region of the NMR spectra. Next, the signals H_c, H_j, for CCMoids **16** and **17**, and H_c, H_k for **21** and **22**, correspondingly, are related to the aromatic protons closer to the *keto-enol* moiety that in the cases of systems **16** and **17** integrates as a doublet of doublets and possess a coupling constant $^3J_{HH}$ = 8.4 Hz.

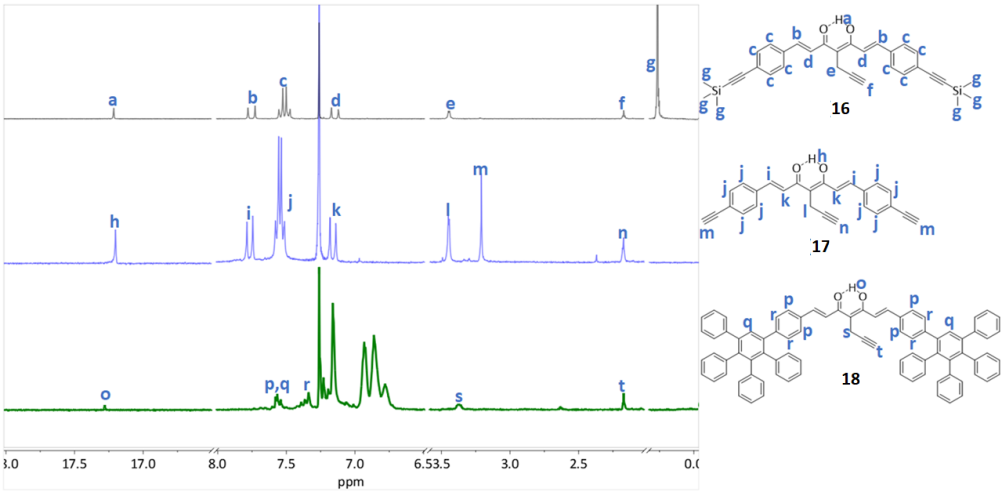

***Figure 81**: ^{1}H NMR spectra comparison between **16** (black), **17** (blue) and **18** (green).*

Finally, the remaining part of the spectra to comment is that related to the leg fragments. In the cases of CCMoids with triple bond legs (**16**, **17** and **18**, Figure 81) it was always found a doublet around 3.44-3.37 ppm (H_e, H_l and H_s), with a coupling constant $^4J_{HH}$ = 2.7 Hz which correspond to the methylene group. Moreover, it was always observed a singlet around 2.0 ppm (H_f, H_n and H_t) which agrees well with the expected shift for acetylene protons. In this region, for CCMoid **17** a singlet around 2.17 ppm was seen as well, assigned to the H_m proton of the acetylene group in the arms.

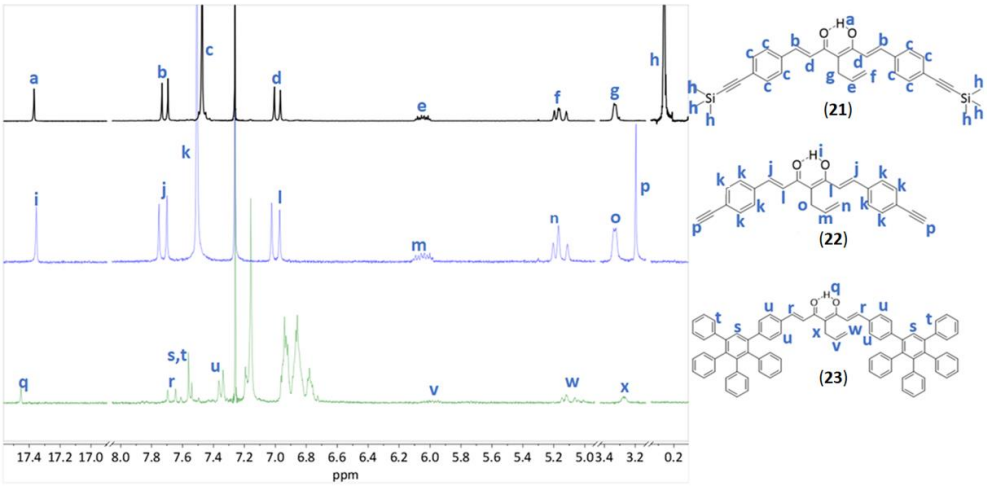

***Figure 82**: ^{1}H NMR spectra comparison between **21** (black), **22** (blue) and **23** (green).*

For the T-shaped CCMoids **21**, **22** and **23** (Figure 82), that present an ending double bond in their legs, respectively, a similar shape in the aromatic region, as the previous CCMoids, was observed which promoted a similar identification of the signals. Particularly, comparing systems **23** and **18** (Figure 81), the signals of CCMoid **23** appeared sharper and therefore easier to analyse than for CCMoid **18**. Regarding the leg unit, it was seen a broad signal around 6.10-5.95 ppm which is assigned to the protons H_e, H_m and H_v (Figure 82). This signal is seeing at the same time the terminal vinylic protons (H_f, H_n and H_w) and the methylene ones (H_g, H_o and H_x) nevertheless their multiplicity is difficult to distinguish, to do that a stronger magnetic field will be needed giving theoretically a doublet of doublets of triplets. A possible explanation of this existing multiplicity is that the two vinylic protons (H_f, H_n and H_w) could possess different coupling constants in addition to that expected for the two methylene protons (H_g, H_o and H_x).

The signals H_f, H_n and H_w (Figure 82), related to the terminal vinylic protons appear as a doublet of doublets between 5.27-4.97 ppm and finally the signals of the methylenic protons: H_g, H_o and H_x appear in all cases as a doublet around 3.33-3.28 ppm. Moreover, as before in the case of compound **17** (H_m, Figure 81), CCMoid **23** also contain a singlet that appears at 3.21 ppm assigned to the H_p proton of the acetylene group in the arms.

The comparision of the ^{13}C NMR spectra between CCMoids **16**, **17**, **21** and **22**, respectively, and between **18** and **23**, in that order, presents many similarities with few particular carbon shifts. This way, for **16**, **17** and **18** (Figure 83), the *keto-enol* carbons (C_a, C_o and C_β, 182.7, 182.6 and 183.9 ppm) appear as a

unique signal as well as for **21**, **22** and **23** (Figure 84) (C_a, C_o and C_β, 183.6, 183.2 and 183.4). The region comprising 145-120 ppm contains the aromatic and conjugated alkene chain signals. In this region, the most intense are those related to the aromatic carbons C_d, C_e, C_r, C_s for CCMoids **16** and **17** and C_e, C_f, C_s, C_t for CCMoids **21** and **22**, respectively. Here, the less intense ones correspond to the quaternary one carbons C_c, C_f, C_q, C_t for CCMoids **16** and **17** and C_c, C_g, C_q, C_u for CCMoids **21** and **22**. The remaining shifts in this region come from the body alkene chain: C_b, C_g, C_p, C_u, C_γ, C_δ for CCMoids **16**, **17** and **18** and C_b, C_h, C_p, C_v, C_δ, C_ε for CCMoids **21**, **22** and **23**. The carbon atoms of the triple bonds in the arms: C_i, C_j, for CCMoid **16** and C_k, C_l, for CCMoid **21**, appear between 83-79 ppm, in agreement with similar units described in the literature.[120] Here, the same signals for **17** (C_w, C_y) and **22** (C_y, C_z) are shifted to lower fields compared to the others because of the steric interactions caused by the presence of trimethylsilyl groups, which influences the nucleus of the alkynyl group promoting a deshielding effect as happened in chapter 3.

Finally, the region that involves the shifts of the leg segment showed that for CCMoids **16**, **17** and **18** the acetylene signals appear between 73-65 ppm (C_k, C_l, C_x, C_z, C_ζ and C_η) and the methylene C_m, C_α and C_θ at 17-16 ppm. For CCMoids **21**, **22** and **23** the signals of the double bond leg appear in the same region as the alkene chain at around 133-116 ppm C_d, C_i, C_r, C_w, C_γ and C_ζ and again the methylene C_m, C_α and C_θ at 30-29 ppm, that appear at lower fields than the methylene groups of CCMoids **16**, **17** and **18** due to the shielding effect of the acetylene moiety.

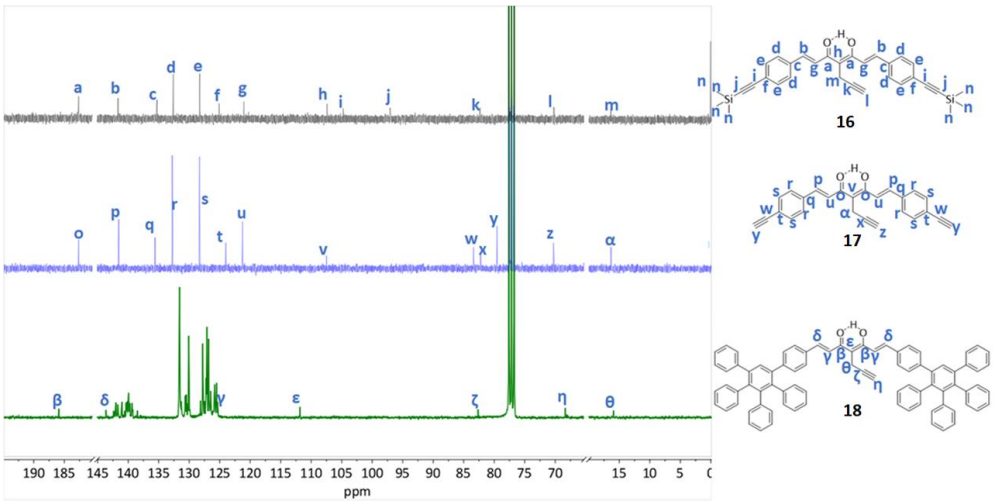

***Figure 83**: ^{13}C NMR spectra comparison between **16** (black), **17** (blue) and **18** (green).*

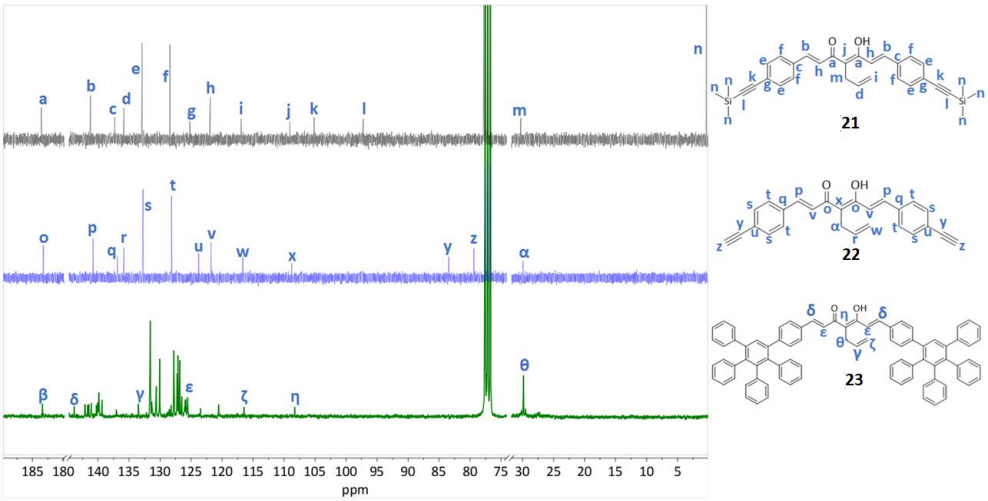

*Figure 84: ^{13}C NMR spectra comparison between **21** (black), **22** (blue) and **23** (green).*

3.3.3. ATR-FTIR spectroscopy for CCMoids 16, 17, 18, 19,21, 22, 23 and 24

ATR-FTIR was also performed to compare the different functional groups possessed of each CCMoid in both synthetic routes and to characterize the insoluble final systems (**19** and **24**) present in this chapter. **Figure 85**: Comparative ATR-FTIR spectra of CCMoids **16**, (black), **17** (blue), **18** (green) and **19** (orange).Figure 85 and Figure **86** showed the spectra for **16**, **17**, **18**, **19** and **21**, **22**, **23**, **24**, respectively***Error! Reference source not found.***.

For molecules **17**, **18** and **19** (Figure 85) characteristic sharp bands corresponding to the ν(≡C-H) appears around 3296-3247 cm^{-1} in the three cases, for CCMoid **16**, however, this band is not present but it can be seen the band at 2087 cm^{-1} which corresponds to the ν(C≡C) as in CCMoid **2** of the chapter 3 (Figure 29). Also, in all of the systems, a broad band is observed between 1619-1596 cm^{-1} that is related to the ν_{ar}(C-C) band. This band overlaps with a small band related to the *keto-enol* form ν(C-O, around 1633 cm^{-1}).[148] The bands appearing at 1445-1403 cm^{-1} and 1262-1208 cm^{-1} are related to the δ(=CH, aromatic and alkenyl chain). Moreover, for CCMoids **16**, **17**, **21** and **22** (Figure 85 and Figure **86**) a sharp band can be observed around 830-817 cm^{-1} corresponding to the *para-di*-substituted aromatic ring. CCMoids **18**, and **23** (Figure 85 and Figure **86**) share a very similar shape in the bands between 900-500 cm^{-1} presenting the *mono*-substituted aromatic ring (around 910, 763-756 and 698 cm^{-1}). Finally, in the graphitic-based CCMoids, systems **19** and **24** (Figure 85 and Figure **86**), the bands of the neighbouring

tri-substituted (755-750 cm^{-1}) and the *o-di*-substituted (806-787 cm^{-1}) could be distinguished; this, together with the disappearance of the sharp signal at 696 cm^{-1} (*mono*-substituted) is noteworthy and a confirmation that the system is pure (with no traces of CCMoids **18** and **23**).[120,169]

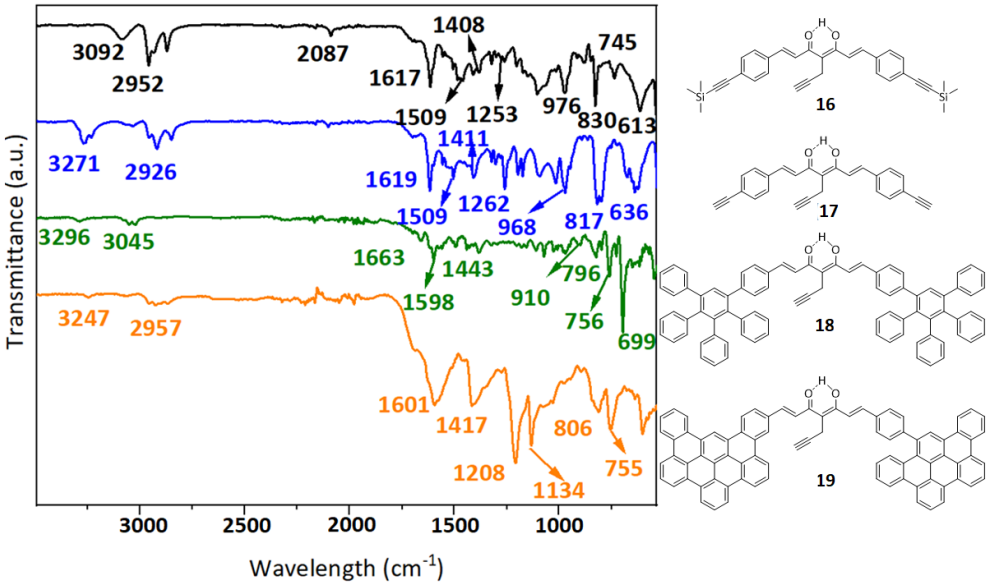

***Figure 85**: Comparative ATR-FTIR spectra of CCMoids **16**, (black), **17** (blue), **18** (green) and **19** (orange).*

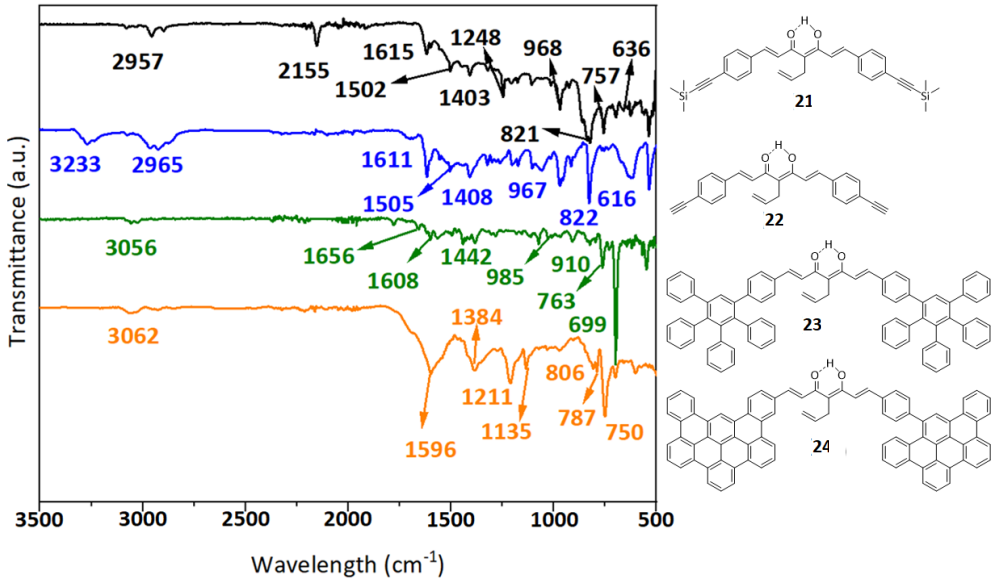

***Figure 86**: Comparative ATR-FTIR spectra of CCMoids **21** (black), **22** (blue), **23** (green) and **24** (orange).*

3.3.4. Raman spectroscopy for CCMoids 16, 17, 18, 19, 21, 22, 23 and 24

As for ATR-FTIR, Raman experiments allow confirming the different functional groups for each CCMoid. In addition, it could be observed (Figure 87 and Figure **88**) that molecules **19** and **24** present broad bands as occurred in the previous chapter for systems **5** and **10**, giving a Raman spectrum similar to the pristine graphene and to the isolated units that form the arms of these molecules.[170-172]

It can also be observed that all CCMoids containing an alkynyl group presented a shared peak around 2100-2200 cm^{-1} assigned to the ν(C≡C), except for molecule **20** (Figure 87) that presented a large amount of fluorescence in this region of the spectrum overlapping the alkynyl signal. In addition, in the case molecules **16** and **21**, this band is slightly shifted due to the presence of trimethylsilyl groups. By carefully analysing each of them, it was possible to observe at 1174-1185 cm^{-1} the ν and δ(C-C-H) vibrations of the alkene chain and aromatic ring. In addition, at 1313-1340 cm^{-1} the δ(C-O-H) of the enol group can be seen, and around 1600 cm^{-1} the ν_{ar}(C=C) appears. All these values agree with those found in the reported studies of curcumin.[51,123,127]

Interestingly, as it happened in the spectra of CCMoids **5** and **10** (chapter 2, Figure 64) in the cases of systems **20** and **24** the signals were broader, and slightly shifted. As already explained, these phenomena could be explained for the graphitic behaviour of the substances[124,128,173] and the signals are assigned to the first-order G band at 1598 cm^{-1} corresponding to ν(C-C) motion (Ag symmetry: which is the symbol corresponding to the molecular vibration which presents symmetry respect to the centre and the principal axis of symmetry)[172] and the first-order D band at 1330 cm^{-1} related to the breathing-like vibrations of six-carbon-atom ring.[173] In addition, after fluorescence suppression, it was possible to observe with some difficulty the second order, 2D and D+G bands that are located around 2928 and 2660 cm^{-1}, respectively.[171,173]

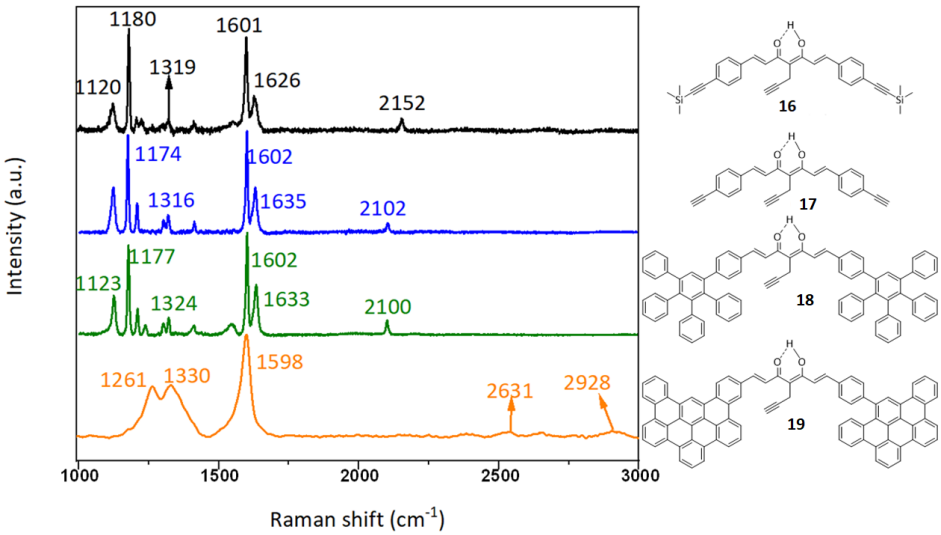

*Figure 87: Comparative Raman spectrum between CCMoids **16** (black), **17** (blue), **18** (green) and **19** (orange), respectively.*

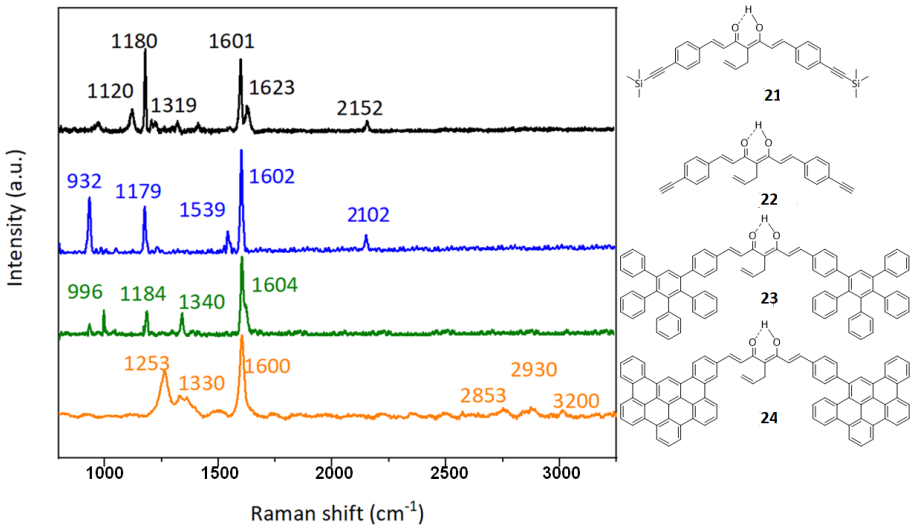

*Figure 88: Comparative Raman spectra of CCMoids **21** (black), **22** (blue), **23** (green) and **24** (orange), respectively.*

3.3.5. MALDI-TOF spectroscopy for CCMoids 19 and 24

To support the obtention of our CCMoids, MALDI-TOF spectra were recorded giving in all the cases the expected molecular mass, using either the positive or the negative mode, all the spectra can be seen in the appendix section (Figure A 155-Figure **A 162**). As the presence of the leg section in CCMoids **20** and **24** was not possible to be confirmed by Raman, MALDI-TOF technique

was a useful tool to analyse further our data, showing the proper molecular peak of both systems, containing legs (Figure 89).

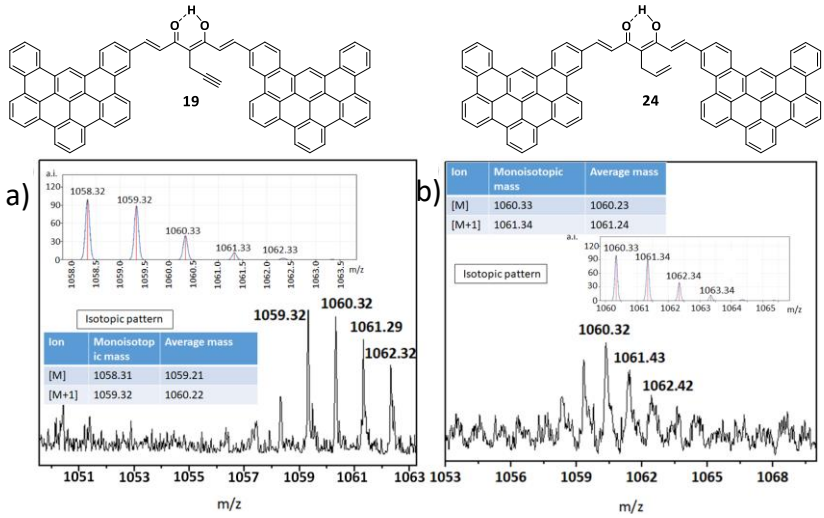

***Figure 89**: MALDI-TOF spectra in positive mode for CCMoids **19** and **24**.*

3.3.6. Thermogravimetric analyses (TGA), melting and sublimation point measurements for CCMoids 16, 17, 18, 21, 22 and 23

Regarding the information about thermal stability of the CCMoids, melting points measurements were performed showing only for CCMoids **17** and **21** a melting point of 223 and 205 °C, respectively. For the remaining CCMoids no further information could be obtained because the systems did not show melting points at the detection limits of the equipment (300 °C). Similarly, no sublimation character was observed for any of the systems, using a standard sublimation system at 1 mbar of pressure.

Then, thermogravimetric analyses were performed to identify the temperature at which the different molecules suffer structural and decomposition changes (Figure A 163-Figure **A 168**). To do the analysis, the molecules were heated up to 800 °C under N_2 atmosphere with a mass flow rate of 100 mL/min and a heat ramp of 10 °C/min. For all CCMoids the molecule starts to suffer a first small change before 200-250 °C, where the common trend shows us the loss of solvent molecules as acetonitrile or the *keto-enol* moiety. In general, the system displayed the bigger loss around 20% of the weight, which could be related with the loss of one arm or the aromatic rings of the arms in the case of molecules **18** and **23**. Moreover, all CCMoids present endothermic bands around 500°C, which indicates that the molecule suffered a fusion or a sublimation process, however, for molecules **19** and **23**

it could be seen a sharp exothermic band around 170-200 °C indicating that the samples are going through a melting or sublimation point.

3.3.7. UV-Vis absorption studies in solution and in solid state for CCMoids 16, 17, 18, 19, 21, 22, 23 and 24

UV-Vis absorption studies in solution and in the solid state were performed to further characterize systems **16-24**, while extracting electronic information, as the optical band gap (E_g^{op}) in the case of the solid state.

In solution, all CCMoids except **19** and **24** were measured (Figure 90). As in previous chapters, the experiments were carried out in DCM with a concentration of 10^{-5} M. Furthermore, all systems were also measured in the solid state to, once again, analyse the optical bandgap. The solid-state experiments were performed using KBr pellets until concentrations close to $1 \cdot 10^{-6}$ mmol of molecule/mg of KBr.

Similar as in chapter 2, for CCMoids **16**-**23,** the π-π* band of the *keto-enol* moieties were observed between 414-466 nm (Figure 91). For **19** and **24**, the bands at 403 and 362 nm appear closely as in similar PAH structures in the literature as the π-band. Next, the band at 515-517 nm could be identified also from the literature as the α but it also could be assigned as a π- band as happened in molecules synthesized in our group.[41,84,112,182,183]

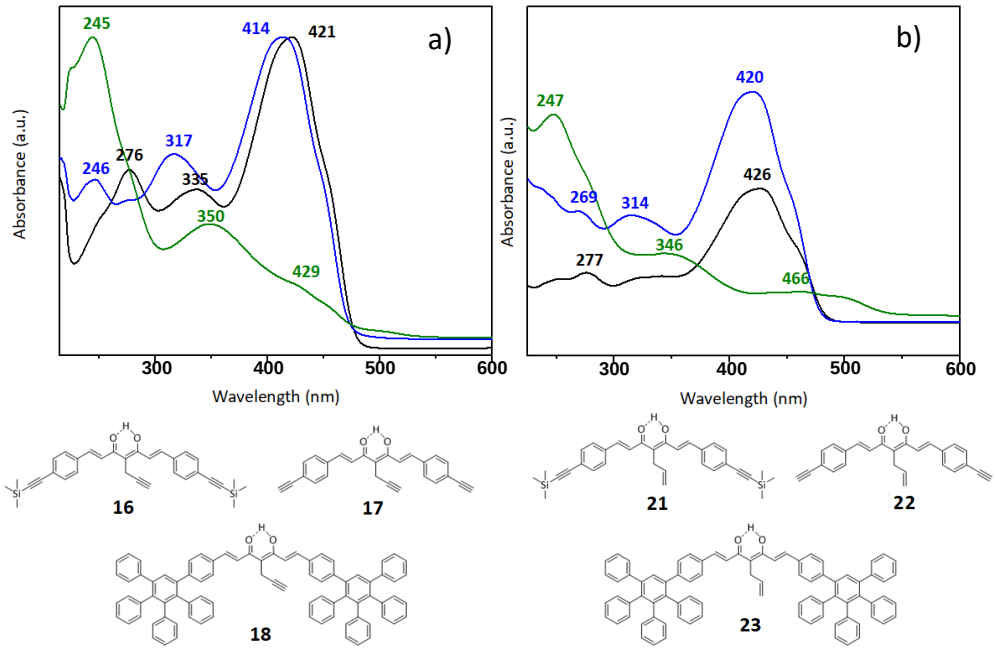

***Figure 90**: Comparative UV-Vis spectra in solution (DCM 10^{-5}M) among: a) **16** (black), **17** (blue) and **18** (green) and b) **21** (black), **22** (green) and **23** (blue), respectively.*

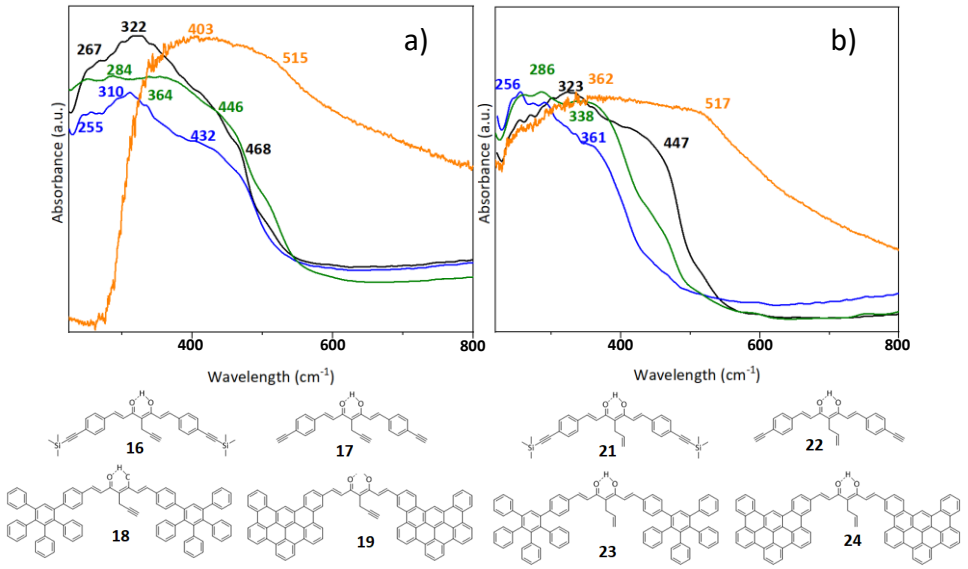

***Figure 91**: Comparative UV-Vis spectra in solid state among: a) **16** (black), **17** (blue), **18** (green) and **19** (orange); b) **21** (black), **22** (green), **23** (blue) and **24** (orange).*

The calculation of the optical band gap for each molecule was performed in solid state. To do that, Tauc's plot was used as explained in previous

chapters.[132-134] The comparison of all the CCMoids is represented in Figure 92 and Figure **93**.

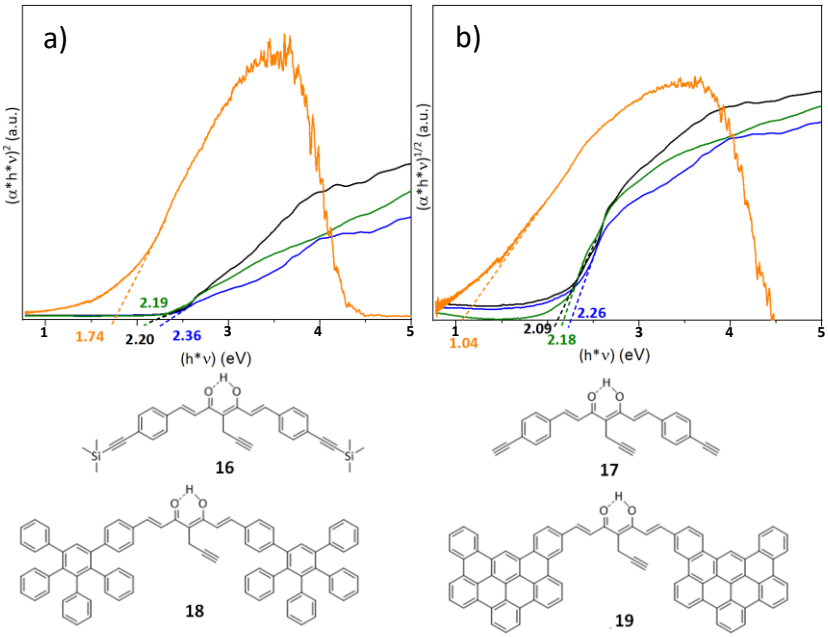

***Figure 92**: Comparative UV-Vis spectra using the Tauc's plot representation for the analysis of the optical band gap of **16** (black), **17** (blue), **18** (green) and **19** (orange), respectively, in solid state.*

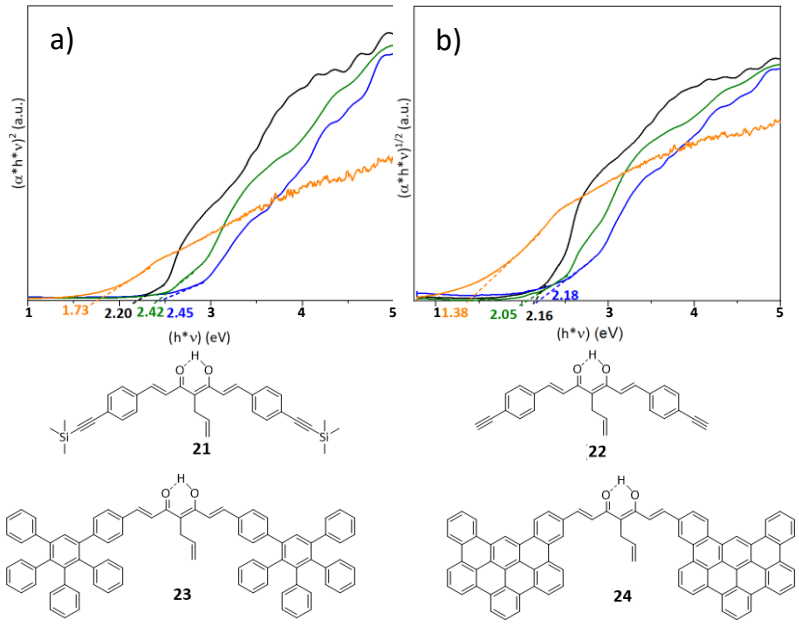

***Figure 93**: Comparative UV-Vis spectra using the Tauc's plot representation for the analysis of the optical band gaps of **21** (black), **22** (blue), **23** (green) and **24** (orange), respectively, in solid state.*

Considering all the systems, CCMoids **19** and **24**, display both a decrease in the values of their energetic bandgap levels, which could mean that the molecules improve their semiconductor behavior with respect to the rest and it could be observed the dramatic change promoted by the planarization of the arms of the molecules, respectively.[184] Following the results, the remaining systems (**16-18** and **21-23**) behave in a similar way as previous CCMoids from chapters 1 and 2, except for CCMoids **5** and **10** (chapter 2) that are closer to the values of CCMoids **19** and **24**. Table 3.1**Table 2.2** displays a summary of the data in solution and in solid state.

Table 3.1: *Summary of the optical properties of **16, 17, 18, 19, 21, 22, 23** and **24**. Band gap energies are displayed in eV. E_g^{op} stand for the optical energy gap.*

CCMoids	E_g^{op} solid state	Colour of the powder
16	2.15	Yellow
17	2.27	Brown
18	2.19	Yellow
19	1.39	Brown/black
21	2.18	Yellow
22	2.31	Brown
23	2.24	Yellow
24	1.56	Brown/black

Comparation between CCMoids with and without leg (T-shaped vs. chapter 2 systems)

Gathering all the information, it was possible to compare the differences in the UV-Vis absorption spectra of the molecules with and without legs (Figure 94). This way, it could be observed that the shape of the spectra of the molecules with allyl or propargyl legs (double and triple bond, respectively) are very similar in solution and in the solid state but differ with the CCMoids without leg (chapter 2). However, when the arms of the molecules are planar (systems **5**, **19** and **24**) the shape of each spectrum becomes almost identical abd their broad bands (as explained in chapter 2) could be explained due to the presence of a huge number of highly conjugated aromatic rings or the formation of aggregation of various molecules by π-π stacking, which promotes charge delocalization that has great influence in the solid-state UV-Vis technique.

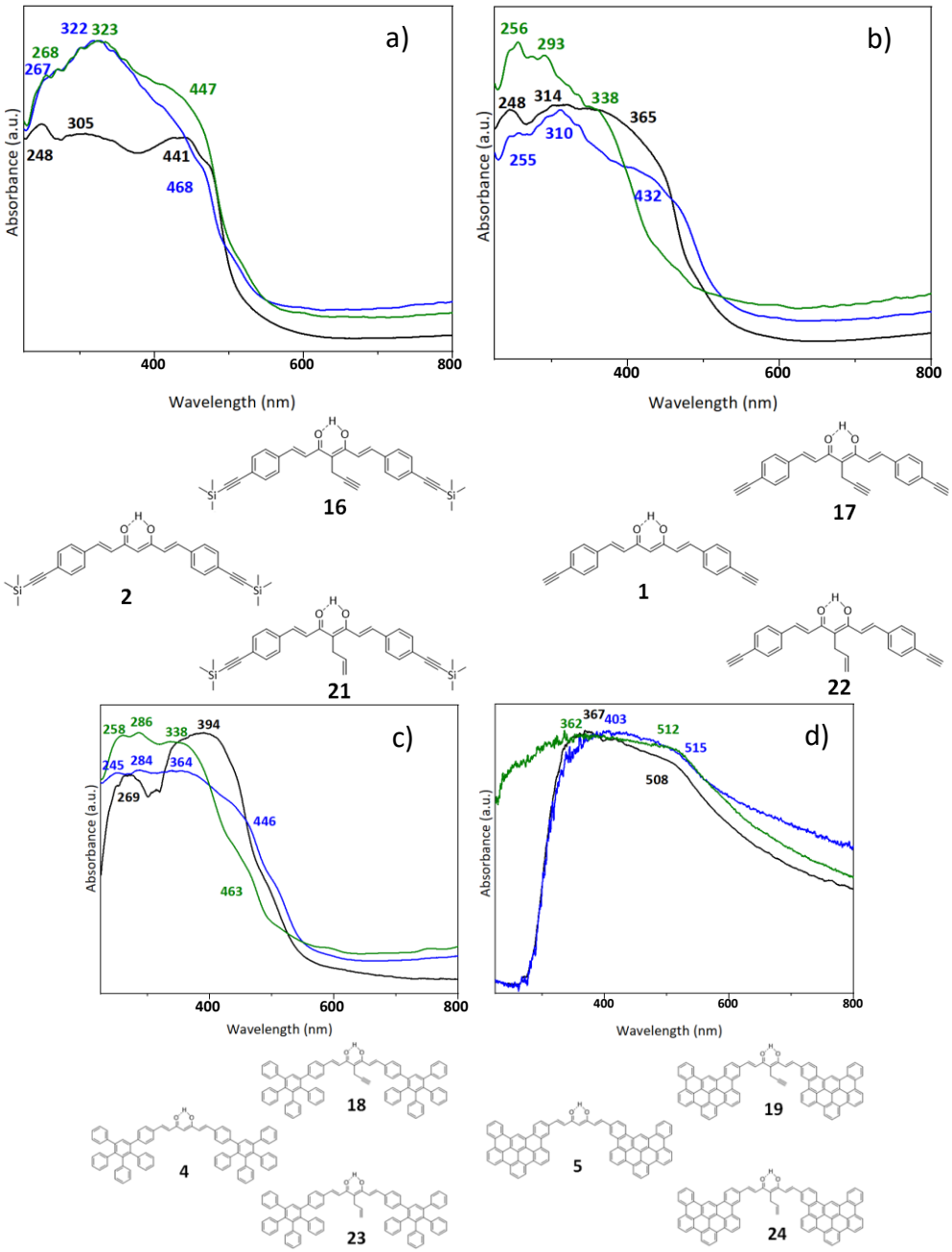

Figure 94: *Comparison of normalized UV-Vis absorption spectra, in the solid state, of CCMoids: a)* ***2*** *(black),* ***16*** *(blue) and* ***21*** *(green); b)* ***1****, (black),* ***17*** *(blue) and* ***22*** *(green); c)* ***4*** *(black),* ***18*** *(blue) and* ***23*** *(green); d)* ***5*** *(black),* ***29*** *(blue) and* ***24*** *(green).*

Next, looking for the effect that the leg could produce to the optical bandgap of the molecules the Tauc's plot gave us the values, which are represented in

Table 4. The values show that there is a general trend where the T-shaped CCMoids have a lower optical bandgap than CCMoids without the leg unit, conferring the first with a more semiconductive behavior.

***Table 4**: Comparison between all the CCMoids with and without the leg functionality. Band gap energies are displayed in eV. E_g^{op} stand for the optical energy gap.*

CCMoids	E_g^{op} solid state	Colour
AlkTMSCCMoid (2)	2.40	Yellow
AlkTMSpropCCMoid (16)	2.15	Yellow
AlkTMSallylCCMoid (21)	2.18	Yellow
AlkCCMoid (1)	2.48	Brown
AlkpropCCMoid (17)	2.27	Brown
AlkallylCCMoid (22)	2.31	Brown
10PhCCMoid (4)	2.37	Brown
10PhpropCCMoid (18)	2.19	Yellow
10PhallylCCMoid (23)	2.24	Yellow
4PhAntCCMoid (5)	1.65	Black/brown
4PhAntpropCCMoid (19)	1.39	Black/brown
4PhAntallylCCMoid (24)	1.56	Black/brown

3.3.8. Electrochemistry (Cyclic Voltammetry, CV and Differential Pulse Voltammetry, DPV)

Using cyclic voltammetry and differential pulse voltammetry (CV and DPV, respectively) for the soluble CCMoids **18**, **19**, **20**, **23**, **24** and **25**, the calculation of their optical band gaps was compared with the analyses of their corresponding electrochemical band gaps (E_g^{ec}). These studies were carried out dissolving the samples in DCM, in concentration of 10^{-3} M, using $TBAPF_6$ as electrolyte under an inert atmosphere of Ar. The spectra were recorded at 100 mV/s. Figure 95 and Figure **96** displays the reduction (right) and oxidation (left) processes of the six systems, for the CV and DPV studies, respectively.

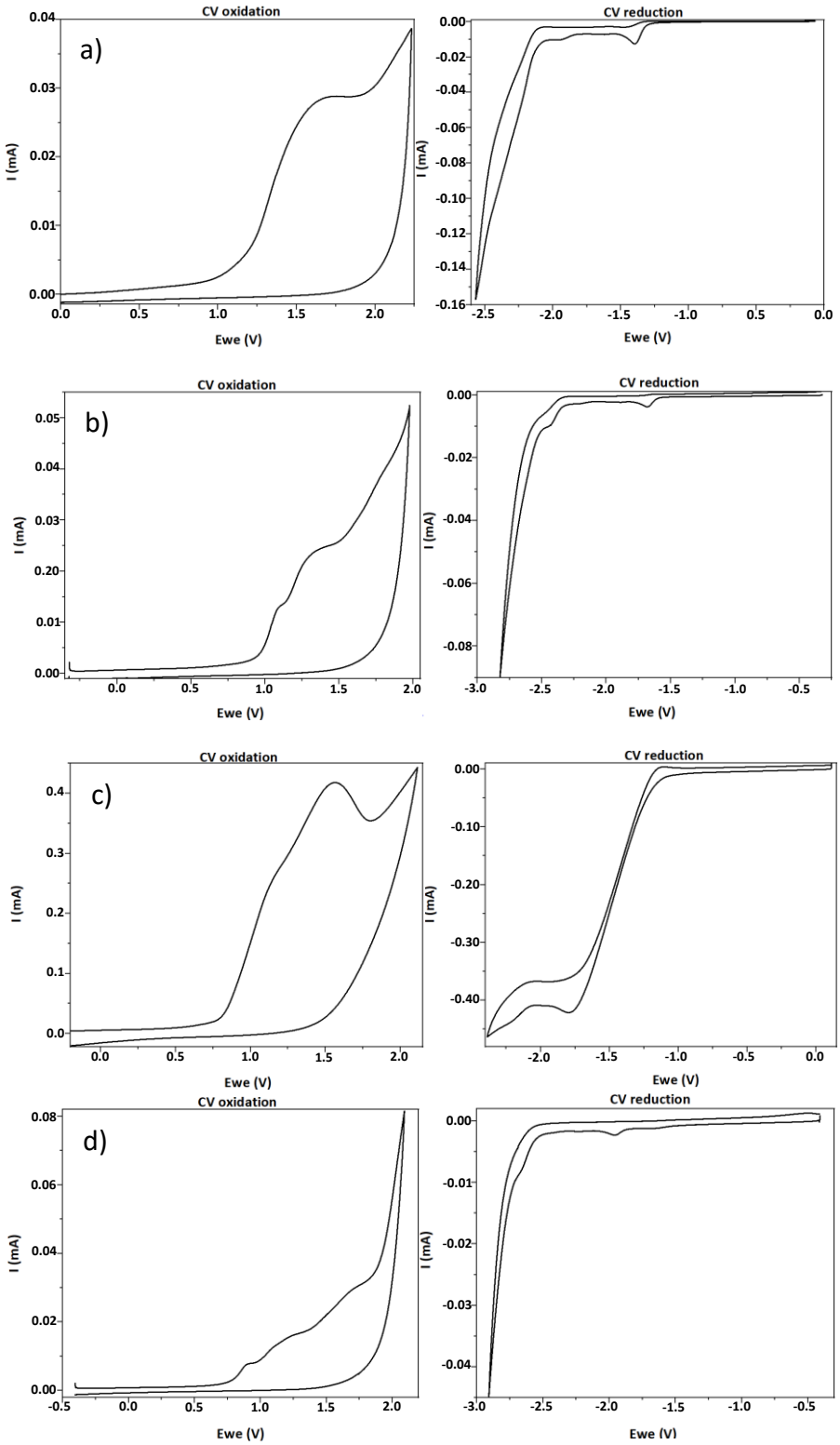
a)
CV oxidation
I (mA)
Ewe (V)
CV reduction
I (mA)
Ewe (V)
b)
CV oxidation
I (mA)
Ewe (V)
CV reduction
I (mA)
Ewe (V)
c)
CV oxidation
I (mA)
Ewe (V)
CV reduction
I (mA)
Ewe (V)
d)
CV oxidation
I (mA)
Ewe (V)
CV reduction
I (mA)
Ewe (V)

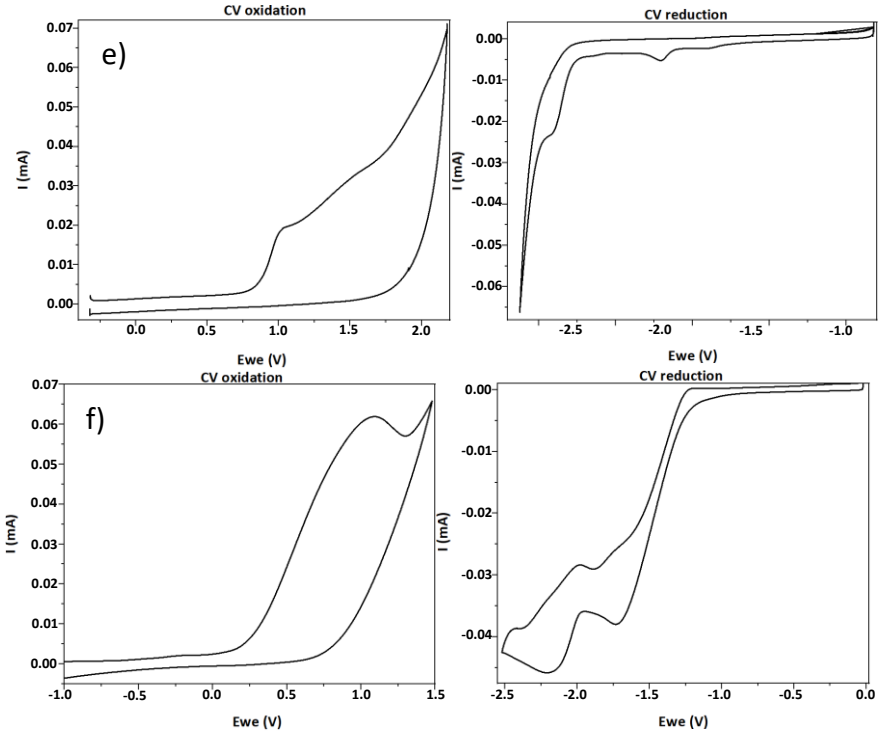

***Figure 95**: Oxidation and reduction cyclic voltammogram of CCMoids: a) **16**, b) **17**, c) **18**, d) **21**, e) **22** and f) **23**.*

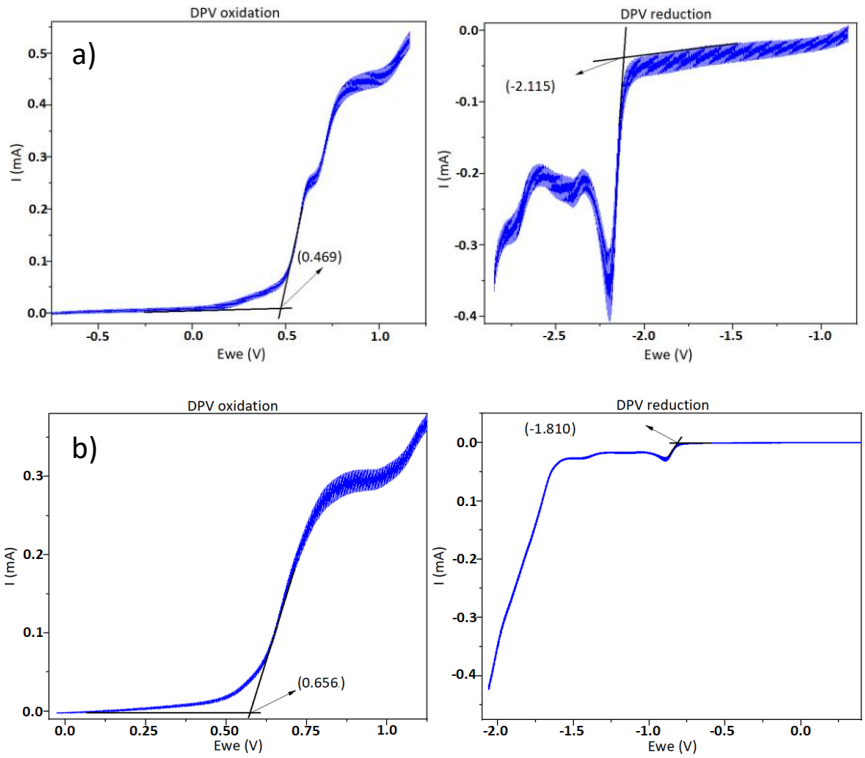

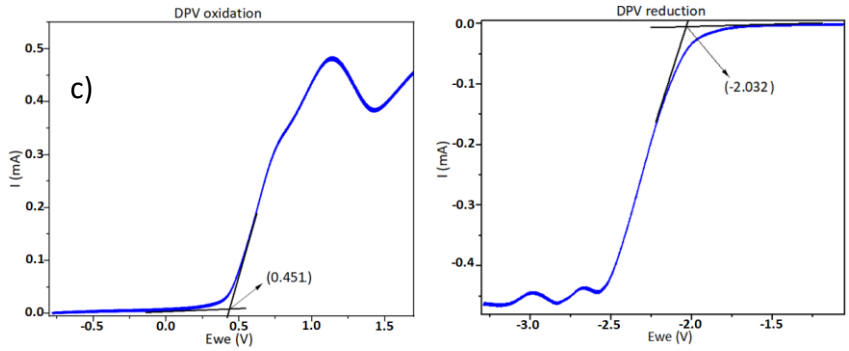
c)
DPV oxidation
I (mA)
Ewe (V)
(0.451)
DPV reduction
I (mA)
Ewe (V)
(-2.032)

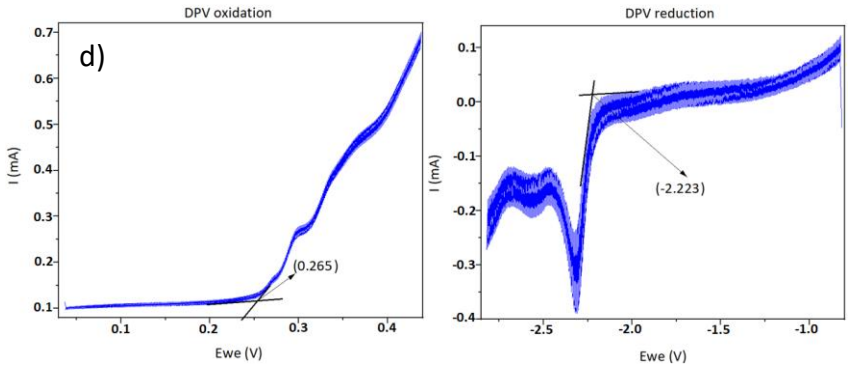
d)
DPV oxidation
I (mA)
Ewe (V)
(0.265)
DPV reduction
I (mA)
Ewe (V)
(-2.223)

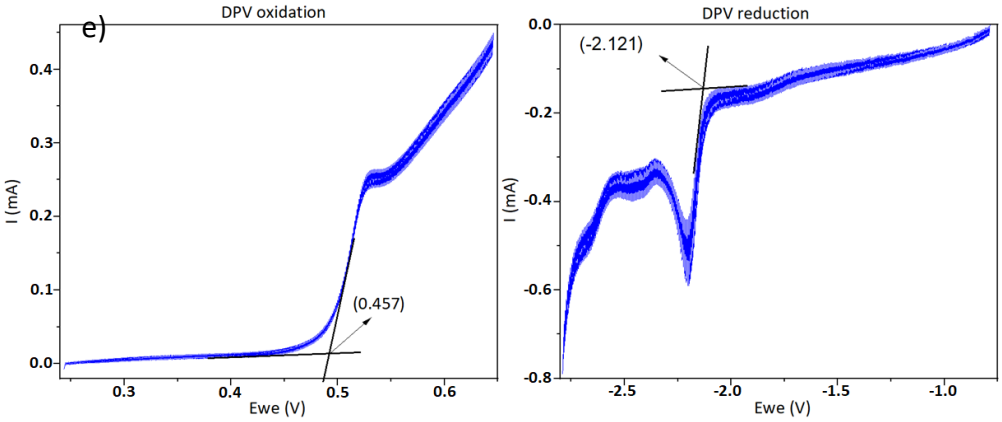
e)
DPV oxidation
I (mA)
Ewe (V)
(0.457)
DPV reduction
I (mA)
Ewe (V)
(-2.121)

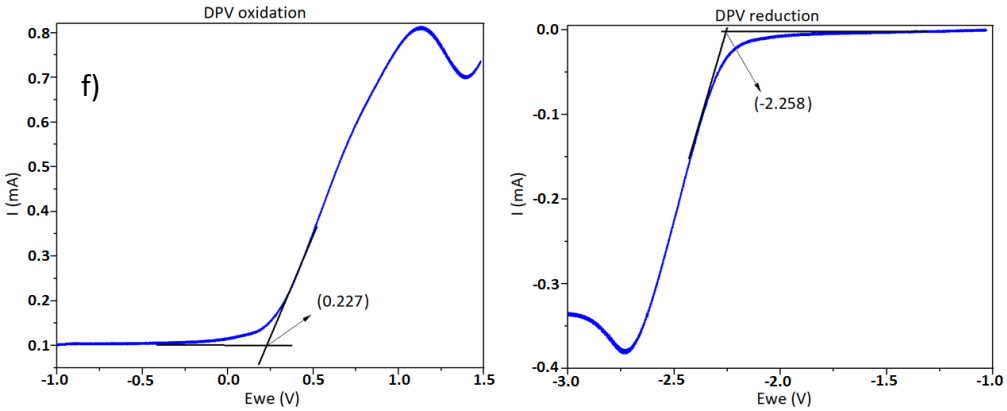

***Figure 96**: Oxidation and reduction differential pulse voltammogram of CCMoids: a) **16**, b) **17**, c) **18**, d) **21**, e) **22** and f) **23**.*

As in the other chapters, all the systems display several irreversible bands, oxidation and reduction processes, in a window between -3.0 and 2.0 V. The electrochemical band gap is obtained from the differential between the gap of the HOMO process (first oxidation band) and the LUMO process (first reduction process) considering that they rely to the extraction and addition of electrons in the outer molecular orbitals.[51,117,138]

Table 5 and Figure 97 displays the values from the UV-Vis absorption studies in solution obtained for the electrochemical band gap energy levels and the optical ones.

***Table 5**: Summary of the electrochemical properties of **16**, **17**, **18**, **21**, **22** and **23**. Potential values in V, referenced to Fc/Fc^+. Band gap energies in eV. Eg^{ec} and Eg^{op} stand for the electrochemical and optical energy gaps, respectively.*

CCMoid	1st Oxid.	1st Red.	E_{HOMO}	E_{LUMO}	E_g^{ec}	E_g^{op}	colour
16	0.47	-2.11	-5.27	-2.69	2.58	2.15	Yellow
17	0.66	-1.81	-5.46	-2.99	2.47	2.27	Brown
18	0.45	-2.03	-5.25	-2.77	2.48	2.19	Yellow
21	0.26	-2.23	-5.06	-2.57	2.49	2.18	Yellow
22	0.46	-2.12	-5.26	-2.68	2.58	2.31	Brown
23	0.23	-2.26	-5.03	-2.54	2.48	2.24	Yellow

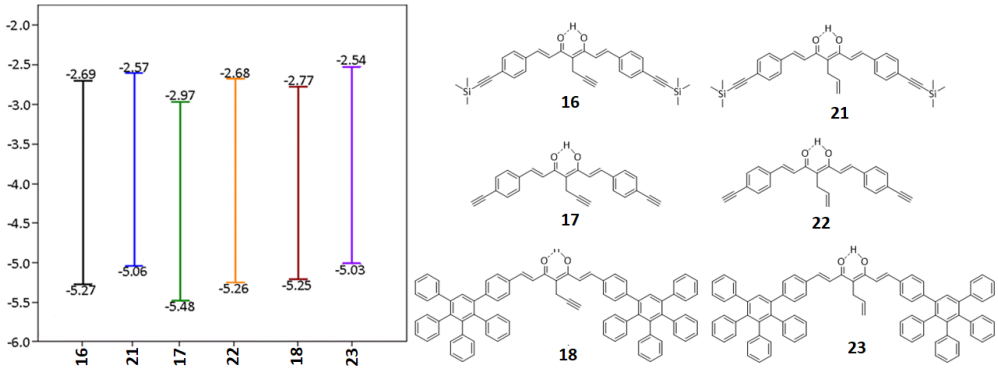

***Figure 97**: HOMO and LUMO levels of **16**, **17**, **18**, **21**, **22** and **23** CCMoids.*

The comparison of the estimated HOMO-LUMO values from the electrochemical experiments shows that all CCMoids presented very similar band gaps and energy displacements, always higher than those from the optical energy gaps. Moreover, it can be highlighted that the propargylic leg CCMoids (propargyl ones) have E_{HOMO} and E_{LUMO} values higher than allylic leg CCMoids (allyl ones).

Comparison between CCMoids with and without leg (T-shaped CCMoids vs. CCMoids from chapter 2)

Comparing here the estimated energy gap values of T-shaped molecules, with those without the leg unit (Table 6 and Figure 98), it can be seen that the first contain larger energy gaps (electrochemical and optical) than those without the leg moiety. This phenomena could be explained because of the presence of an alkyl chain in the middle of the molecule could reduce the capacity to conduct the electrons as confirmed in the literature, where molecules that contain aromatic groups functionalized with electro-donor groups display a similar behaviour.[208,209] Furthermore, the representation of the E_{HOMO} and E_{LUMO} levels of each CCMoid showed that molecules whose arms contain a trimethylsilyl protecting group present lower E_{HOMO} and E_{LUMO} energy levels than those without this group.

***Table 6**: Summary of the electrical properties of **1**, **2**, **4**, **16**, **17**, **18**, **21**, **22** and **23**. Potential values in V, referenced to Fc/Fc⁺. Band gap energies in eV. Eg^{ec} stands for the electrochemical and optical energy gaps, respectively.*

CCMoid	1st Oxid.	1st Red.	E_{HOMO}	E_{LUMO}	E_g^{ec}	E_g^{op}	Colour of the powder
2	0.41	-1.95	-5.21	-2.85	2.36	2.40	Yellow
16	0.47	-2.11	-5.27	-2.69	2.58	2.15	Yellow
21	0.26	-2.23	-5.06	-2.57	2.49	2.18	Yellow
1	0.86	-1.54	-5.66	-3.26	2.44	2.48	Brown
17	0.68	-1.83	-5.48	-2.97	2.51	2.27	Brown
22	0.46	-2.12	-5.26	-2.68	2.58	2.31	Brown
4	0.80	-1.48	-5.60	-3.11	2.28	2.37	Brown
18	0.45	-2.03	-5.25	-2.77	2.48	2.19	Yellow
23	0.23	-2.26	-5.03	-2.54	2.48	2.24	Yellow

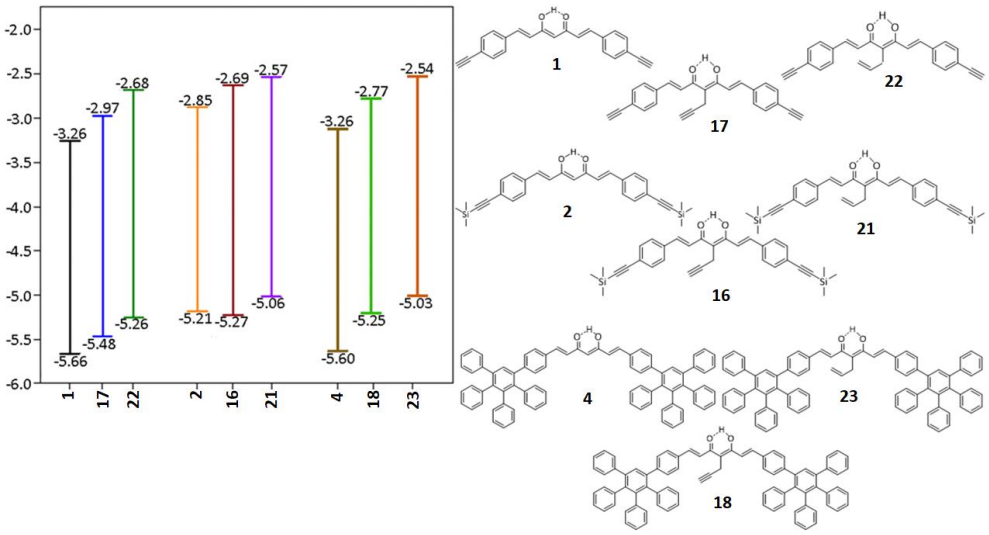

***Figure 98**: HOMO and LUMO levels of **1**, **2**, **4**, **16**, **17**, **18**, **21**, **22** and **23** CCMoids, correspondingly.*

3.4 CONCLUSIONS

In this chapter the synthesis of T-shaped PAH-based CCMoids **19** and **24** were successfully achieved using a five-step methodology with overall yields of 2 and 1%, respectively. Once again, the use of solid-state techniques, for the characterization of the CCMoids, allowed us to confirm the presence of the desired CCMoids.

UV-Vis spectroscopy in solution and in solid-state and electrochemistry were used to calculate the bandgap of all molecules showing similar behaviour with the previous CCMoids shown in the previous chapters. Before the planarization reaction in the arms of the CCMoids, the bandgap values are between 2-3 eV which means that they present insulator-semiconductors behaviour, whereas the values obtained for CCMoids **19** and **24** were < 2 eV, as it happened for CCMoids **5** and **10** in chapter 2, show higher semiconductor behaviour than the rest of CCMoids.

Furthermore, comparing the band gap values obtained for T-shaped molecules and without the leg units it was observed that T-shaped molecules contain a bigger energy gap than those without the leg. This difference could be explained with the presence of the alkyl chain in the leg position that interferes in the capacity of the CCMoid skeleton to conduct the electrons. Further theoretical studies will assist the corroboration of the data.

3.5 FUTURE WORK

The introduction of this chapter mentions our objective of fixing CCMoid systems on surfaces through additional points than those coming from the π-π stacking of the arms, using for this purpose the leg position. Hence, molecules **19** and **24** could be further modified to contain silane groups at the end of the leg units with the aim of performing a covalent bond with the hydroxyl groups of the SiO_2 layer of the device as showed in Figure 99.

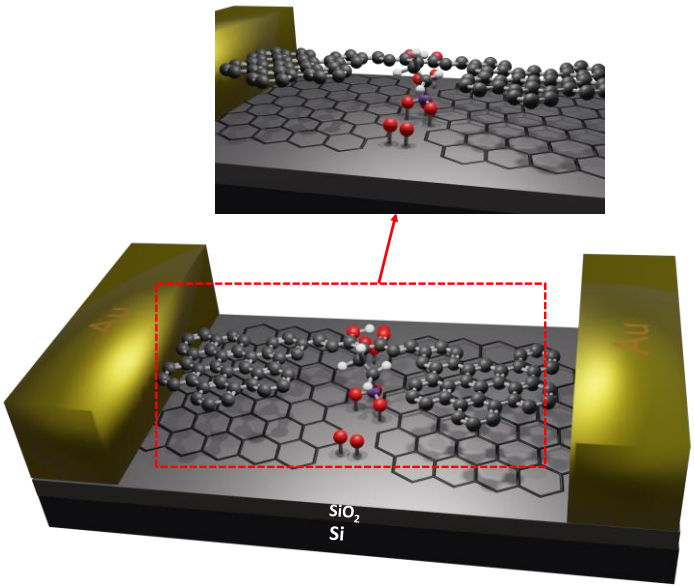

***Figure 99**: Schematic representation of the CCMoids interaction with the SiO_2 layer of the device, where the grey balls are carbons, the white balls are hydrogens, the red ones are oxygen and the purple is silicon.*

So, as future work, molecules **19** and **24** could be used as starting materials to obtain PAH-based CCMoids with silyl groups in the leg positions through hydrosylilation reactions[210,211] as shown in Scheme 9.

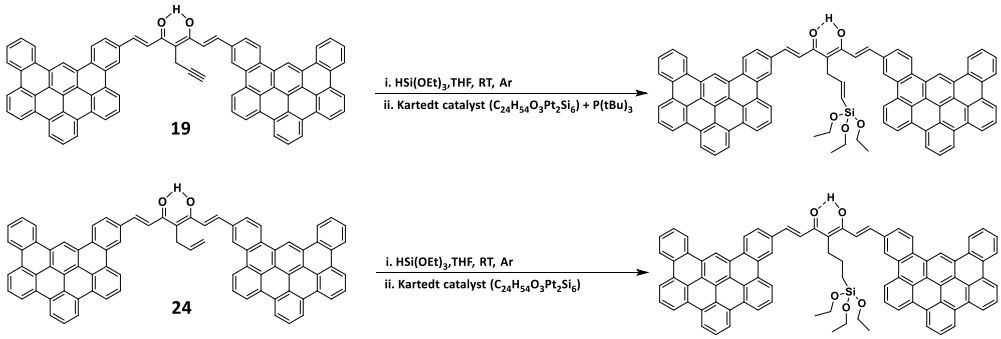

***Scheme 9**: Synthetic pathway to obtain the final GNRCCMoidlegs.*

In this hydrosilylation reaction a Pt^0-based catalyst is necessary that in our case would be the Karstedt's catalyst (KC). KC is a bulky stereoselective catalyst, it allows the hidrosilation insertion towards the less hindered position of an insaturated bond. Moreover, if the catalyst is coordinated with another bulky ligand like the phosphines, it enhances even more the stereoselectivity of the reaction. The mechanism of this reaction undergoes a catalytic cycle represented in Figure 100.[212,213]

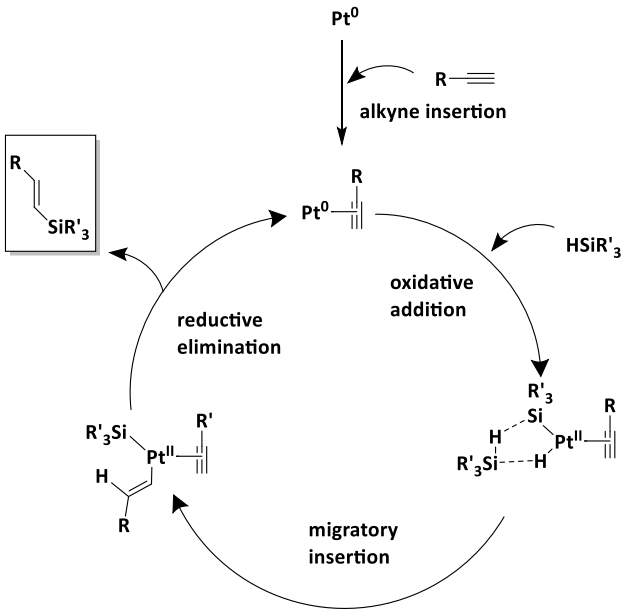

***Figure 100**: Mechanism for the hydrosilylation reaction.*

This type of reaction should be carried out under argon atmosphere, to avoid polymerization of the silanes and decrease in the efficiency of the catalyst used. First, in the case of the propargyl CCMoid, the platinum catalyst should be mixed with a phosphine ligand, which produce the hydrosilylation addition

on the β-position of the propargylic group and in *trans* position as a major product and for the allyl one, the phosphine ligand would not be necessary.[210,211,214-216] Next, the CCMoid will be mixed with triethoxysilane $HSi(OEt)_3$ in another flask and, afterwards, the catalyst mixture should be added over the flask containing our CCMoid. The reaction can be monitored with TLC and ^{1}H NMR and, once finished, the work-up procedure must be performed also under inert conditions avoiding the moisture.

A first trial of this reaction with molecules **18** and **23** was performed (figures 3.22 and 3.23), to evaluate the suitable conditions to obtain CCMoids **19** and **24**. For the allyl leg CCMoid, the catalyst was not mixed with a phosphine giving rise to a saturated chain. Unfortunately, these first attempts provided in all cases mixture of byproducts (by ^{1}H NMR), without being able to distinguish them over the desired products and making the purification techniques very difficult and more challenging with the high sensitivity of the final product toward the presence of moisture.

Therefore, as future work, further studies should be carried out such as: study of optimization of the reaction times, modification of the solvent/s, working harder towards the purification of CCMoids **18** and **23**, among others.

Once the desired silyl molecules will be achieved, the deposition of the systems on the three-terminal device could be performed using mild conditions as described in previous chapters.

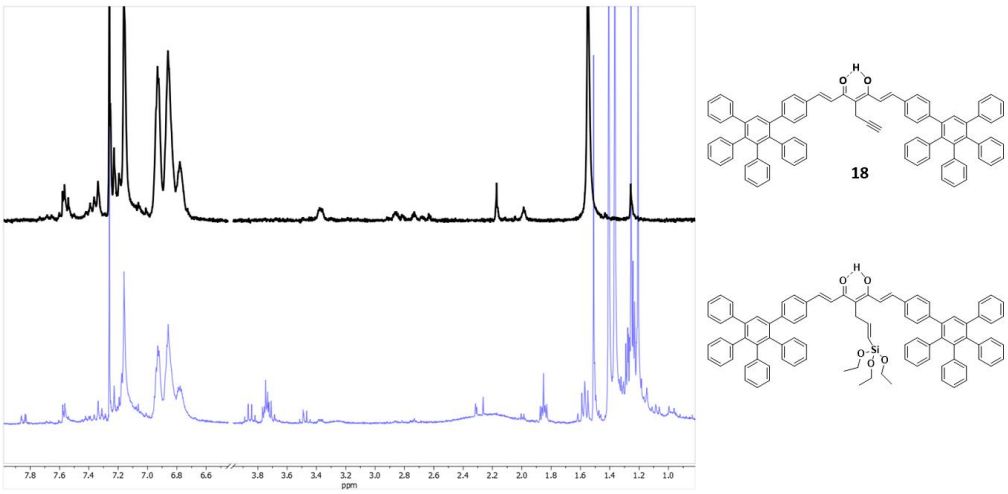

***Figure 3.22**: ^{1}H NMR spectra comparison between **19** (black) and GNRCCMoidleg (blue).*

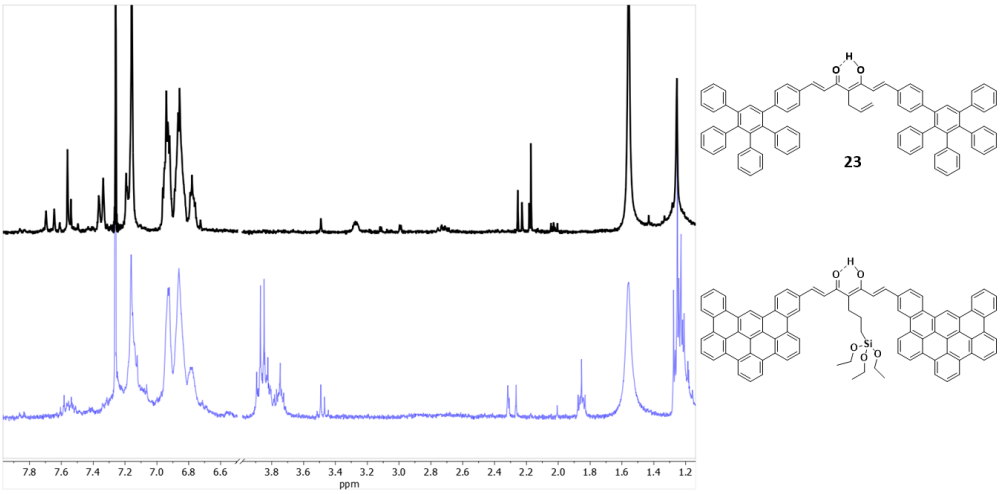

***Figure 3.23**: ^{1}H NMR spectra comparison between **23** (black) and GNRCCMoidleg (blue).*

3.6 EXPERIMENTAL SECTION

3.6.1. Measurements.

Explained in chapter 3

3.6.2. Materials.

Potassium carbonate (K_2CO_3), acetylacetonate (acac, $C_5H_8O_2$), propargyl bromide (C_3H_3Br), allyl bromide (C_3H_5Br), boron trioxide (B_2O_3), tributyl borate ($(BuO)_3B$), 4-[(trimethylsilyl)ethynyl] benzaldehyde ($C_{12}H_{14}OSi$), n-butylamine (n-$BuNH_2$, $C_4H_{11}N$), tetrabutylammonium fluoride monohydrated (TBAF, $C_{16}H_{38}FNO$), 2,3,4,5-tetraphenylcyclopenta-2,4-dien-1-one ($C_{29}H_{20}O$), trifluoromethane-sulfonic acid (CF_3SO_3H), 2,3-dichloro-5,6-dicyano-1,4-benzoquinone ($C_6O_2Cl_2N_2$, DDQ), chlorohydric acid (HCl, 37%), sodium chloride (NaCl) and sodium hydroxide carbonate ($NaHCO_3$) were provided by Sigma Aldrich and Fluorochem. Acetone (C_3H_6O), ethyl acetate ($C_4H_8O_2$, EtOAc), toluene (C_7H_8), methanol (CH_3OH, MeOH), acetonitrile (CH_3CN, MeCN), chloroform ($CHCl_3$) and 1,1,2,2-tetrachloroethane ($C_2H_2Cl_4$) were supplied by Carlo Erba. Dicloromethane (CH_2Cl_2, DCM) was provided by ChemLab.

536.3. Synthesis of 15. 3-(prop-2-yn-1-yl)pentane-2,4-dione

Following the described methodology,[2,206] 5 g of acac (49.94 mmol) and 8.3 g of K_2CO_3 (59.93 mmol) were solubilized with 100 mL of dry acetone (0.08 M) giving a white solution. Then, 890 μL of propargyl bromide (9.90 mmol) was added and the mixture was brought to reflux under inert atmosphere and let it stir for 24 h. The reaction was controlled by TLC (hexane/EtOAc: 2/1, Rf: 0.1), then once it was finished, the reaction was cooled down to room temperature and filtered off. The solution was concentrated in the rotatory evaporator and purified with a silica column and a step gradient of hexane/EtOAc (a total of 400 mL from 0 to 20 % EtOAc at 5 % increments). Molecule **15** was obtained as a yellow oil in a 47 % yield. ^{1}H NMR (δ in ppm, 300 MHz, $CDCl_3$) δ=16.54 (s, 1H), 3.85 (t, $^3J_{HH}$ = 7.6 Hz, 1H), 3.11 (d, $^4J_{HH}$ = 2.7 Hz, 2H), 2.70 (dd, $^3J_{HH}$ = 7.5, $^4J_{HH}$ = 2.7 Hz, 2H), 2.25 (s, 6H), 2.22 (s, 6H), 2.03 (t, $^4J_{HH}$ = 2.7 Hz, 2H).

3.6.4. Synthesis of 16. (1E,4Z,6E)-5-hydroxy-4-(prop-2-yn-1-yl)-1,7-bis(4-((trimethylsilyl)ethynyl)phenyl)hepta-1,4,6-trien-3-one

200 mg (1.43 mmol) of **15** and 70 mg of B_2O_3 (0.70 eq, 1.00 mmol) were solubilized in 1.2 mL of EtOAc. The mixture was stirred and heated at 50 °C for 1 hour. Then 800 μL (2.97 mmol) of $(BuO)_3B$ was added, followed by the addition of a solution of 595 mg of 4-[(trimethylsilyl)ethynyl] benzaldehyde (2.94 mmol) in 1 mL of EtOAc. The reaction was stirred at 50 °C for two hours and then cooled to room temperature. Next, a solution of n-$BuNH_2$ (110 μL, 1.11 mmol) in EtOAc (0.8 mL) was added dropwise and the reaction was left stirred at room temperature for two days. TLC was used to monitor the progress of the reaction (hexane/DCM: 7/3, Rf: 0.25). Finally, an aqueous HCl solution (0.1 M) was added to the solution and the mixture was stirred at 40 °C for 1 h. The resulting precipitate was filtered off and washed with cold MeOH. Recrystallisation was achieved by dissolving the solid in MeCN and leaving the solution in the refrigerator at 0 °C. **16** was obtained as a yellow powder in 29% yield. ^{1}H NMR (300 MHz, $CDCl_3$) δ=17.21 (s, 1H), 7.75 (d, $^3J_{HH}$ = 15.5 Hz, 2H), 7.51 (q, $^3J_{HH}$ = 8.3 Hz, 8H), 7.12 (d, $^3J_{HH}$ = 15.5 Hz, 2H), 3.44 (d, $^4J_{HH}$ = 2.6 Hz, 2H), 2.17 (s, 1H).^{13}C{^{1}H} NMR (δ in ppm, 75 MHz, $CDCl_3$) 182.7, 141.7, 135.3, 132.6, 128.3, 125.1, 121.0, 107.4, 104.8, 97.1, 82.3, 70.2, 16.4 and 0.1. ATR-FTIR data (cm^{-1})**:** 3092 (ν:=C-H and ν_{ar}:C-H), 2952 (ν:-C-H), 2087 (ν:-C≡C-), 1617 (ν:C=O *keto-enol* form, with intermolecular H bonds), 1509 (ν_{ar}:C-C, skeleton vibrations), 1408 (δ_{ar}:=CH), 1253 (δ_{sim}: Si-CH_3) 976 (δ_{oop}:CH) 830 (ν_{ar}:C-H ρ-disubstituted and δ_{oop}:CH) 745 (γ:Si-CH_3). Raman (cm^{-1}): 2152 cm^{-1} (ν:-C≡C-), 1626 cm^{-1} (ν:C=O), 1601 cm^{-1} (ν:C=C, aromatic ring), 1319 cm^{-1} (δ:C-O-H, enol group and δ:C-C-H, aromatic ring), 1180 cm^{-1} (δ:C-O-C, *keto-enol* group and ν and δ:C-C-H, aromatic ring). MS MALDI-TOF (m/z): calc. for $C_{32}H_{35}O_2Si_2$[M]: 506.22; found[M+1]$^+$: 507.21. Elemental analysis calculated for **16**·MeCN ($C_{34}H_{37}N_1O_2Si_2$): C, 74.54; H, 6.81. Found; C, 74.92; H, 6.53.

3.6.5. Synthesis of 17. (1E,4Z,6E)-1,7-bis(4-ethynylphenyl)-5-hydroxy-4-(prop-2-yn-1-yl)hepta-1,4,6-trien-3-one

100 mg (0.19 mmol) of **16** was diluted in dry DCM (17 mL, 0.01M) under Ar atmosphere. Then 2.2 eq of TBAF (117 mg, 0.45 mmol) was added to the solution and the reaction was let stirred for 2 h at room temperature. TLC was used to monitor the progress of the reaction (hexane/EtOAc: 9/1, Rf: 0.30). Once the reaction was finished, the solution was concentrated in the rotatory evaporator and extractions with EtOAc/brine (3x20 mL) were performed. **17**

was obtained as a pale brown solid in a 30% yield. ^{1}H NMR (δ in ppm, 360 MHz, $CDCl_3$) δ=17.20 (s, 1H), 7.77 (d, $^{3}J_{HH}$ = 15.5 Hz, 2H), 7.65 – 7.47 (q, $^{3}J_{HH}$ = 8.4 Hz, 8H), 7.16 (d, $^{3}J_{HH}$ = 15.5 Hz, 2H), 3.45 (d, $^{4}J_{HH}$ = 2.7 Hz, 1H), 3.21 (s, 2H), 2.17 (s, 1H). ^{13}C NMR (δ in ppm, 90 MHz, $CDCl_3$) 182.6, 141.6, 135.6, 132.8, 132.8, 128.3, 123.9, 121.2, 107.5, 83.4, 82.2, 79.5, 70.3, 16.4. ATR-FTIR data (cm^{-1}): 3271 (ν:≡C-H), 3040 (ν:=C-H and ν_{ar}:C-H), 2926 (ν:-C-H), 1619 (ν:C=O *keto-enol* form with intermolecular H-bonds), 1509 (ν_{ar}:C-C, skeleton vibrations), 1404 (δ_{ar}:=CH), 1136 ($\delta_{ip\ ar}$:C-H), 968 (δ_{oop}:CH), 817 (ν_{ar}:C-H ρ-disubstituted and δ_{oop}:CH) and 636 (δ:≡C-H). Raman (cm^{-1}): 2102 (ν:-C≡C-), 1635 (ν:C=O), 1602 (ν:C=C, aromatic ring), 1316 (δ:C-O-H, enol group and δ:C-C-H, aromatic ring), 1174 (δ:C-O-C, *keto-enol* group and ν: and δ:C-C-H, aromatic ring). MS MALDI-TOF (m/z): calc. for $C_{26}H_{17}O_2$[M]: 361.12; found [M]$^{-}$: 360.97. Elemental analysis calculated for **17·2**MeCN ($C_{30}H_{24}N_2O_2$): C, 86.16; H, 5.01. Found; C, 82.97; H, 4.82.

3.6.6. Synthesis of 18. (1E,4Z,6E)-5-hydroxy-4-(prop-2-yn-1-yl)-1,7-bis(3',4',5'-triphenyl-[1,1':2',1''-terphenyl]-4-yl)hepta-1,4,6-trien-3-one

100 mg (0.28 mmol) of **17** and 210 mg of 2,3,4,5-tetraphenylcyclopenta-2,4-dien-1-one (2 eq, 0.28 mmol) were solubilized in 3 mL of toluene (0.1 M). When the ketone was added, the mixture changed its colour from brown to black, and then the reaction was stirred and heated under reflux at 120 °C for 48 h. TLC was used to monitor the progress the reaction (hexane/EtOAc: 7/3, Rf: 0.55). Finally, the reaction was cooled down to room temperature, then hexane was added to the solution and a dark brown precipitate was obtained. The solid was filtered and washed with hexane. For the further purification of the CCMoid, recrystallization was performed with MeCN and MeOH. **18** was obtained as a brown solid in a 70% yield. ^{1}H NMR (400 MHz, $CDCl_3$) δ=17.28 (s, 1H), 7.56 (s+d, $^{3}J_{HH}$ = 7.5 Hz, 6H), 7.36 (d, $^{3}J_{HH}$ = 7.6 Hz, 4H), 7.20 – 7.16 (m, 10H), 6.93 – 6.78 (m, 30H), 3.37 (d, $^{4}J_{HH}$ = 2.9 Hz, 2H), and 1.99 (s, 1H). ^{13}C{^{1}H} NMR (δ in ppm, 100 MHz, $CDCl_3$): 183.9, 142.4, 142.0, 141.7, 141.0, 140.6, 140.3, 140.2, 140.1, 140.0, 139.9, 139.7, 139.4, 139.3, 138.5, 131.6, 131.3, 130.6, 130.5, 130.0, 130.1, 128.1, 127.8, 127.4, 127.2, 127.1, 126.81, 126.47, 125.9, 125.5, 125.3, 111.9, 82.6, 68.3 and 16.8. ATR-FTIR (cm^{-1}): 3296 (ν:≡C-H), 3045 (ν:=C-H and ν_{ar}:C-H), 2190 (ν:-C≡C-), 1663 (ν:C=O *keto-enol* form with intermolecular H-bonds), 1598 (ν_{ar}:C-C, skeleton vibrations), 1443 (ν_{ar}:C-C, skeleton vibrations), 910 (ν_{ar}:C-H monosubstituted), 796 (ν_{ar}:C-H ρ-disubstituted) 756 (ν_{ar}:C-H o-disubstituted) and 699 (ν_{ar}:C-H monosubstituted). Raman (cm^{-1}): 2100 (ν:-C≡C-), 1633 cm^{-1} (ν:C=O), 1602 cm^{-}

[1] (ν:C=C, aromatic ring), 1324 cm^{-1} (δ:C-O-H, enol group and δ:C-C-H, aromatic ring), 1177 cm^{-1} (δ:C-O-C, *keto-enol* group and ν: and δ:C-C-H, aromatic ring). MS MALDI-TOF (m/z): calc. for $C_{82}H_{57}O_2$[M]: 1074.44; found[M-1]$^-$: 1073.00. Elemental analysis calculated for **18·2**MeCN ($C_{90}H_{64}N_2O_2$): 89.67 C, 5.35 H; found: 88.95 C, 5.10 H.

3.6.7. Synthesis of 19. (1E,4Z,6E)-1,7-bis(dibenzo[fg,ij]phenanthrol[9, 10,1,2,3-pqrst]pentaphen-3-yl)-5-hydroxy-4-(prop-2-yn-1-yl)hepta-1,4, 6 -trien-3-one

25 mg (0.02 mmol) of **18** was mixed with 63 mg of DDQ (12 eq, 0.28 mmol) under argon atmosphere and 2 mL of dry DCM. Then, the mixture was cooled down to 0°C with an ice bath and 24 μL of CF_3SO_3H (12 eq, 0.28 mmol) was added to the solution. After that, the mixture was brought to room temperature and stirred for 2 h. TLC was used to control the disappearance of the starting material **19** (hexane/EtOAc: 8/2, Rf: 0.1). After this time, 2 x 5 mL of $NaHCO_{3\ (aq)}$ was added to the mixture and the solid obtained was centrifuged for 5 min in 6000 rpm obtaining a black solid and a yellow solution. Then, the same procedure of washing and centrifuge was done with distilled H_2O, cold MeOH, cold $CHCl_3$ and $C_2H_2Cl_4$ until the solution has no colour. Finally, the resulting black solid was dried under vacuum obtaining a 79% yield. ATR-FTIR data (cm^{-1})**:** 3247 (ν:≡C-H), 2957 (ν:-C-H), 1601 (ν_{ar}:C-C, skeleton vibrations), 1417 (ν_{ar}:C-C), 1208 (δ_{ar}:C-H), 1134 (δ:C-O-C, *keto-enol* group and ν: and δ: C-C-H, aromatic ring), 806 (ν_{ar}:C-H 1,2,4-trisubstituted and vec-trisubstituted) and 755 (ν_{ar}:C-H o-disubstituted). Raman (cm^{-1}): 2901 cm^{-1} (second order G+D band), 2653 cm^{-1} (second order D band), 2527 cm^{-1} (second order D band), 1598 cm^{-1} (first order G band, ν C-C) 1330 (first order D band, breathing-like vibrations of six carbon atom ring) and 1261 (first order D band, breathing-like vibrations of six carbon atom ring). MALDI-TOF (m/z): calc. for $C_{82}H_{43}O_2$[M]: 1058.42; found[M+1]$^+$: 1059.32.

3.6.8. Synthesis of 20. 3-allylpentane-2,4-dione

Following the described methodology,[3,207] 5 g of acac (13.40 mmol) and 6.50 g of K_2CO_3 (46.96 mmol, 3.5 eq) were solubilized with 40 mL of dry acetone (0.33 M) giving a white solution. Then, 5.3 mL of allyl bromide (61.33 mmol) was added and the mixture was refluxed under inert atmosphere and stirred for 24 h. The progression of the reaction was monitored by TLC (hexane/EtOAc: 7/2, Rf: 0.6), then cooled down to room temperature and

filtered off. The solution was concentrated in the rotatory evaporator and destilled under reduced pressure (≈3 mbar, 55 °C). **22** was obtained as a yellow oil in a 24 % yield. ^{1}H NMR (360 MHz, $CDCl_3$) δ 16.73 (s, 1H), 5.95 – 5.79 (m, 0.2H), 5.77 – 5.63 (m, 1H), 5.15 – 4.93 (m, 6H), 3.73 (t, $^3J_{HH}$ = 7.4 Hz, 0.2H), 2.99 (d, $^3J_{HH}$ = 5.3 Hz, 2H), 2.63 – 2.56 (m, 0.3H), 2.18 (s, 6H), 2.10 (s, 1H).

3.6.9. Synthesis of 21. (1E,4Z,6E)-4-allyl-5-hydroxy-1,7-bis(4-((trimethylsilyl)ethynyl) phenyl) hepta-1,4,6-trien-3-one

324 mg (2.31 mmol) of CCMoid **20** and 112 mg of B_2O_3 (0.7 eq, 1.00 mmol) were solubilized in 2.40 mL of EtOAc (1 M). The mixture was stirred and heated at 50 °C for 1 h. Then 1.250 mL (4.64 mmol) of $(BuO)_3B$ was added, followed by the addition of a solution of 935 mg of 4-[(trimethylsilyl)ethynyl] benzaldehyde (4.63 mmol) in 2.50 mL of EtOAc. The reaction was stirred at 50 °C for two hours and then cooled down to room temperature. Next, a solution of n-$BuNH_2$ (175 µL, 1.73 mmol) in EtOAc (1 mL) was added dropwise and the reaction was stirred at room temperature for two days. TLC was used to monitor the progress of the reaction (hexane/DCM: 8/2, Rf: 0.1). Finally, an aqueous HCl solution (0.1 M) was added to the solution and the mixture was left stirring at 40 °C for 1 h. The resulting precipitate was filtered and washed with cold MeOH. Recrystallisation was achieved by dissolving the solid in MeOH and MeCN leaving the solution in the refrigerator at 0 °C. **21** was obtained as a yellow powder in 44% yield. ^{1}H NMR (400 MHz, $CDCl_3$) δ 17.51 – 17.29 (m, 1H), 7.71 (d, ^{3}JHH = 15.6 Hz, 2H), 7.47 (s, 8H), 6.99 (d, $^3J_{HH}$ = 15.5, 2H), 6.05 (ddt, $^3J_{HH}$ = 16.8, 10.0, 4.9 Hz, 1H), 5.27 – 5.05 (dd, $^3J_{HH}$ = 10.9 and $^2J_{HH}$ = 16.8 2H), 3.33 (d, $^3J_{HH}$ = 5.3 Hz, 2H), 0.27 (s, 18H). ^{13}C NMR (δ in ppm, 100 MHz, $CDCl_3$) 185.6, 141.2, 137.3, 135.8, 132.9, 128.4, 125.2, 121.9, 116.9, 109.1, 105.1, 97.2, 30.3, 0.4. ATR-FTIR data (cm^{-1})**:** 3088 (ν:=C-H and ν_{ar}:C-H), 2957 (ν:-C-H), 2155 (ν:-C≡C-), 1615 (ν:C=O *keto-enol*, with intermolecular H-bonds), 1503 (ν_{ar}:C-C, skeleton vibrations), 1403 (δ_{ar}:=CH), 1248 (δ_{sim}:Si-CH_3), 968 (δ_{oop}:CH), 821 (ν_{ar}: C-H ρ-disubstituted and δ_{oop}:CH), 751 (γ: Si-CH_3) and 636 (δ:≡C-H). Raman (cm^{-1}): 2151 cm^{-1} (ν:-C≡C-), 1627 cm^{-1} (ν:C=O), 1596 cm^{-1} (ν:C=C, aromatic ring), 1176 cm^{-1} (δ:C-O-C, *keto-enol* group and ν: and δ:C-C-H, aromatic ring). MS MALDI-TOF (m/z): calc. for $C_{32}H_{34}O_2Si_2$[M]: 508.22; found[M]$^{\cdot}$: 508.19. Elemental analysis calculated for **21**·**1**MeCN ($C_{32}H_{36}N_1O_2Si_2$): C, 75.35; H, 6.85. Found; C, 75.15; H, 6.36.

3.6.10. Synthesis of 22. (1E,4Z,6E)-1,7-bis(4-ethynylphenyl)-5-hydroxy-4-(prop-2-yn-1-yl) hepta-1,4,6-trien-3-one

150 mg (0.19 mmol) of CCMoid **23** was diluted in dry DCM (30 mL, 0.01 M) under Ar atmosphere. Then, TBAF (170 mg, 2.20 eq) was added to the solution and the reaction was let it stirring for 2 h stirring at room temperature. TLC was used to monitor the progress the reaction (Hexane/EtOAc: 5/1, Rf: 0.70). Once the reaction was finished, the solution was concentrated in the rotatory evaporator and extractions with EtOAc/brine (3x20 mL) were performed. **22** was obtained as a pale brown solid in a 30% yield. ^{1}H NMR (300 MHz, $CDCl_3$) δ 17.35 (s, 1H), 7.73 (d, $^{3}J_{HH}$ = 15.5 Hz, 2H), 7.51 (s, 8H), 7.00 (d, $^{3}J_{HH}$ = 15.5 Hz, 2H), 6.09 – 6.00 (m, 1H), 5.20 – 5.11 (dd, $^{3}J_{HH}$ = 10.9 and $^{2}J_{HH}$ = 16.8 2H), 3.33 (d, $^{3}J_{HH}$ = 4.8 Hz, 2H), 3.20 (s 2H). ^{13}C NMR (δ in ppm, 75 MHz, $CDCl_3$) 183.2, 140.8, 136.9, 135.8, 132.7, 128.1, 123.8, 121.8, δ 116.66, 108.8, 83.4, 79.4, 29.9. ATR-FTIR data (cm^{-1}): 3233 (ν:≡C-H), 3075 (ν:=C-H and ν_{ar}:C-H), 2965 (ν:-C-H), 1695 (ν:C=O *keto-enol*), 1611 (ν:C=O *keto-enol*, with intermolecular H-bonds), 1505 (ν_{ar}:C-C, skeleton vibrations), 1408 (δ_{ar}:=CH ar), 967 (δ_{oop}:CH), 822 (ν_{ar}:C-H ρ-disubstituted and δ $_{oop}$:CH) and 619 (δ:≡C-H). Raman (cm^{-1}): 1602 (ν:C=C, aromatic ring), 1539 cm^{-1} (δ:O-H enol group and δ:C-C-H, aromatic ring), 1316 (δ:C-O-H, enol group and δ:C-C-H, aromatic ring), 1179 (δ:C-O-C, *keto-enol* group and ν: and δ:C-C-H, aromatic ring). MS MALDI-TOF (m/z): calc. for $C_{26}H_{18}O_2$ [M]: 364.23; found [M-2]$^{-}$: 362.14. Elemental analysis calculated for **22**·**1**MeCN ($C_{34}H_{26}N_2O_2$): C, 82.57; H, 5.30. Found; C, 81.97; H, 5.21.

3.6.11. Synthesis of 23. (1E,4Z,6E)-5-hydroxy-4-(prop-2-yn-1-yl)-1,7-bis(3',4',5'-triphenyl-[1,1':2',1''-terphenyl]-4-yl)hepta-1,4,6-trien-3-one

130 mg (0.35 mmol) of **22** and 335 mg of 2,3,4,5-tetraphenylcyclopenta-2,4-dien-1-one (2.5 eq, 0.88 mmol) were solubilized in 3.5 mL of toluene (0.1 M). When the ketone was added, the mixture changed its colour from brown to violet, and then the reaction was stirred and heated under reflux at 120 °C for 48 h. TLC was used to monitor the progress the reaction (Hexane/EtOAc: 9/1, Rf: 0.2). Finally, the reaction was cooled down to room temperature, then hexane was added to the solution and a dark brown precipitate was obtained. The solid was filtered and washed with hexane. To the further purification of the molecule, recrystallization was performed with MeCN and Et_2O. **25** was obtained as a yellow solid in a 44% yield. ^{1}H NMR (400 MHz, $CDCl_3$) δ 17.48 (s, 1H), δ 7.85 (d, $^{3}J_{HH}$ = 7.5 Hz, 4H), 7.58 – 7.54 (m, 8H), 7.42 (d, $^{3}J_{HH}$ = 6.6 Hz,

2H), 7.16 – 7.07 (m, 8H), 6.97 – 6.76 (m, 26H), 6.70 (d, $^3J_{HH}$ = 7.5 Hz, 4H), 6.54 (d, $^3J_{HH}$ = 8.2 Hz, 2H), 5.88-5.80 (m, 1H), 5.05 – 4.99 (m, 2H), 3.28 (d, $^3J_{HH}$ = 5.1 Hz 2H). $^{13}C\{^1H\}$ NMR (δ in ppm, 100 MHz, $CDCl_3$): 183.4, 143.8, 142.1, 141.7, 141.5, 141.1, 140.3, 140.2, 140.0, 139.9, 139.9, 139.4, 137.0, 133.5, 131.6, 131.6, 131.3, 130.6, 130.06, 128.5, 128.2, 127.8, 127.3, 127.1, 126.8, 126.5, 125.9, 125.8, 125.5, 123.5,120.5, 116.4, 108.3 and 29.8. ATR-FTIR (cm^{-1}): 3056 (ν:=C-H and ν_{ar}:C-H), 1656 (ν:C=O *keto-enol*), 1602 (ν_{ar}:C-C, skeleton vibrations), 1442 (ν_{ar}:C-C, skeleton vibrations), 985 (ν:-CH vinyl wags), 910 (ν_{ar}:C-H monosubstituted), 801 (ν_{ar}:C-H ρ-disubstituted) 761 (ν_{ar}:C-H o-disubstituted) and 698 (ν_{ar}:C-H monosubstituted). Raman (cm^{-1}): 1604 cm^{-1} (ν:C=C, aromatic ring), 1340 cm^{-1} (δ:C-O-H, enol group and δ:C-C-H, aromatic ring), 1184 cm^{-1} (δ:C-O-C, *keto-enol* group and ν and δ:C-C-H, aromatic ring). MS MALDI-TOF (m/z): calc. for $C_{82}H_{59}O_2$ [M]: 1076.45; found $[M-1]^-$: 1075.61. Elemental analysis calculated for **23·2**MeCN ($C_{90}H_{66}N_2O_2$): 89.52 C, 5.51 H. Found: 89.15 C, 5.28 H.

3.6.12. Synthesis of 24. (1E,4Z,6E)-1,7-bis(dibenzo[fg,ij]phenanthrol[9, 10,1,2,3-pqrst]pentaphen-3-yl)-5-hydroxy-4-(prop-2-yn-1-yl)hepta-1,4, 6-trien-3-one

20 mg (0.02 mmol) of **23** was mixed with 51 mg of DDQ (12 eq, 0.28 mmol) under argon atmosphere and 2 mL of dry DCM (0.01M). Then, the mixture was cooled down to 0°C with an ice bath and 24 μL of CF_3SO_3H (12 eq, 0.28 mmol) was added to the solution. After that, the mix was brought to room temperature and let it stir for 2 h. TLC was used to monitor the progress of the reaction (Hexane/EtOAc: 9/1, Rf: 0.2). After this time, 2 x 5 mL of $NaHCO_{3\,(aq)}$ was added to the mixture and the solid obtained was centrifuged for 5 min in 6000 rpm obtaining a black solid and a yellow solution. Then, the same procedure of washing and centrifuge was done with distilled H_2O, cold MeOH, cold $CHCl_3$ and $C_2H_2Cl_4$ until the solution has no colour. Finally, the resulting black solid was dried under vacuum obtaining a 90% yield. ATR-FTIR data (cm^{-1})**:** 3065 (ν:=C-H and ν_{ar}:C-H), 1605 (ν_{ar}:C-C, skeleton vibrations), 1386 (δ:=CH), 1215 (δ_{ar}:C-H), 988 and 910 (C-H, vinyl wags), 789 (ν_{ar}:C-H 1,2,4-trisubstituted and vec-trisubstituted) and 754 (ν_{ar}:C-H o-disubstituted). Raman (cm^{-1}): 3200 cm^{-1} (second order G band), 2930 cm^{-1} (second order G+D band), 2853 cm^{-1} (second order G+D band), 1600 cm^{-1} (first order G band, ν C-C) 1330 (first order D band, breathing-like vibrations of six carbon atom ring) and 1253 (first order D band, breathing-like vibrations of six carbon atom ring). MS MALDI-TOF (m/z): m/z calc. for $C_{82}H_{44}O_2$[M]: 1060.33; found$[M]^{\cdot}$: 1060.69.

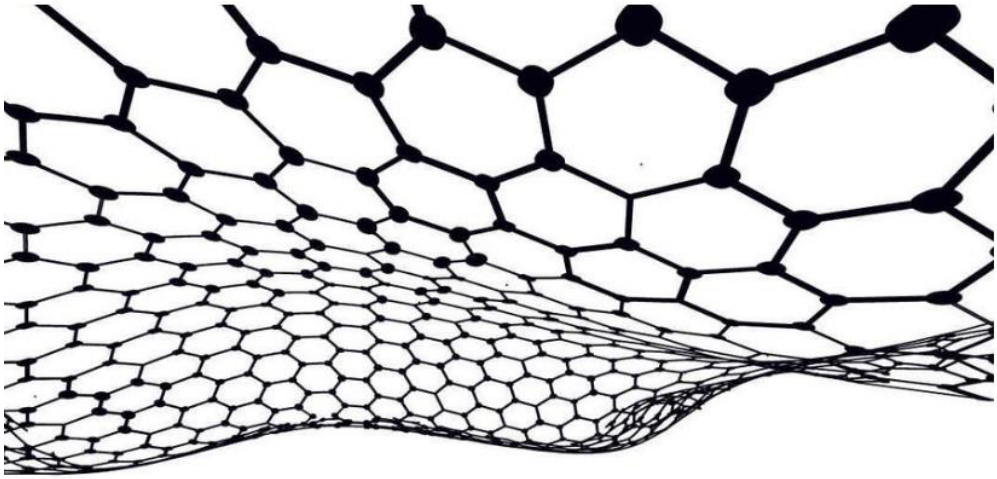

APPENDIX III

APPENDIX III. SUPPLEMENTARY FIGURES

^{1}H NMR spectra

^{1}H NMR (300 MHz, $CDCl_3$) δ=16.54 (s, 1H), 3.85 (t, $^3J_{HH}$ = 7.6 Hz, 1H), 3.11 (d, $^4J_{HH}$ = 2.7 Hz, 2H), 2.70 (dd, $^3J_{HH}$ = 7.5, $^4J_{HH}$ = 2.7 Hz, 2H), 2.25 (s, 6H), 2.22 (s, 6H), 2.03 (t, $^4J_{HH}$ = 2.7 Hz, 2H).

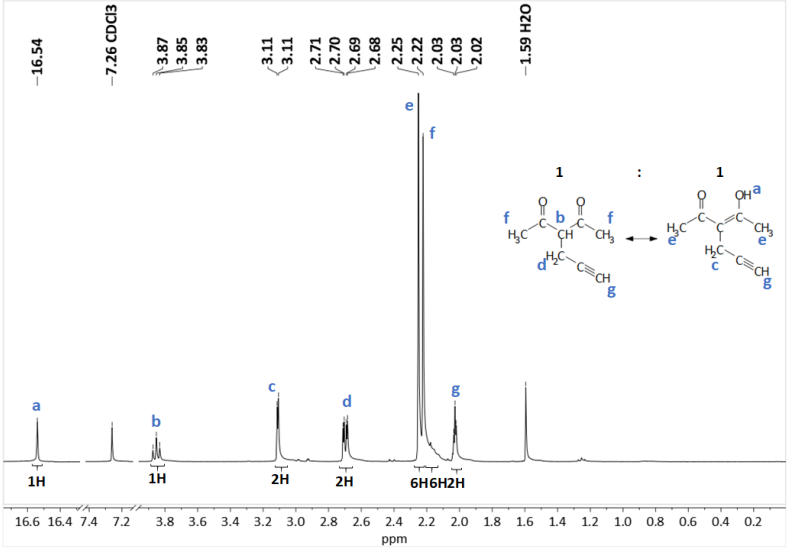

*Figure A 99: ^{1}H RMN spectrum of propACAC **15**.*

^{1}H NMR (300 MHz, $CDCl_3$) δ=17.21 (s, 1H), 7.75 (d, $^3J_{HH}$ = 15.5 Hz, 2H), 7.51 (q, $^3J_{HH}$ = 8.3 Hz, 8H), 7.12 (d, $^3J_{HH}$ = 15.5 Hz, 2H), 3.44 (d, $^4J_{HH}$ = 2.6 Hz, 2H), 2.17 (s, 1H).

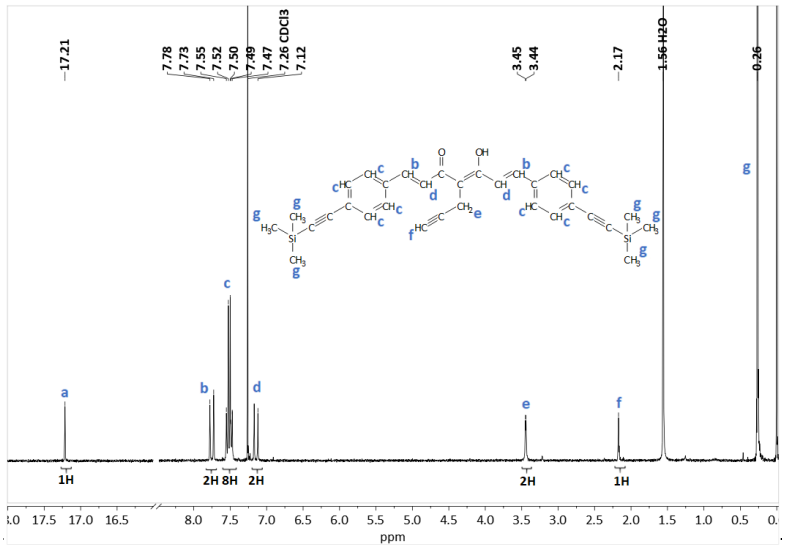

*Figure A 100: ^{1}H RMN spectrum of AlkTMSpropCCMoid **16**.*

^{1}H NMR (360 MHz, $CDCl_3$) δ=17.20 (s, 1H), 7.77 (d, $^{3}J_{HH}$ = 15.5 Hz, 2H), 7.65 – 7.47 (q, $^{3}J_{HH}$ = 8.4 Hz, 8H), 7.16 (d, $^{3}J_{HH}$ = 15.5 Hz, 2H), 3.45 (d, $^{4}J_{HH}$ = 2.7 Hz, 1H), 3.21 (s, 2H), 2.17 (s, 1H).

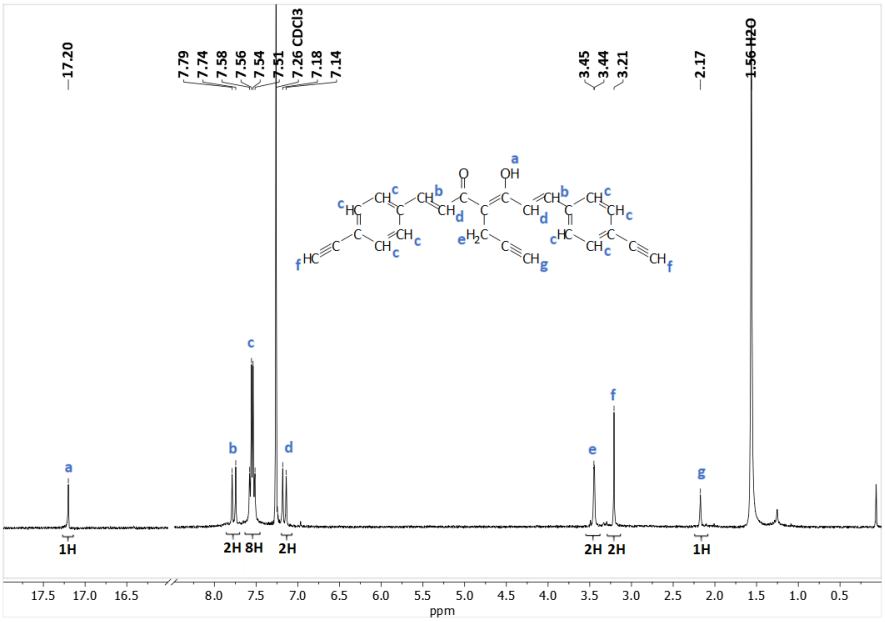

***Figure A 101**: ^{1}H RMN spectrum of AlkpropCCMoid **17**.*

^{1}H NMR (400 MHz, $CDCl_3$) δ=17.28 (s, 1H), 7.56 (s+d, $^{3}J_{HH}$ = 7.5 Hz, 6H), 7.36 (d, $^{3}J_{HH}$ = 7.6 Hz, 4H), 7.20 – 7.16 (m, 10H), 6.93 – 6.78 (m, 30H), 3.37 (d, $^{4}J_{HH}$ = 2.9 Hz, 2H), and 1.99 (s, 1H).

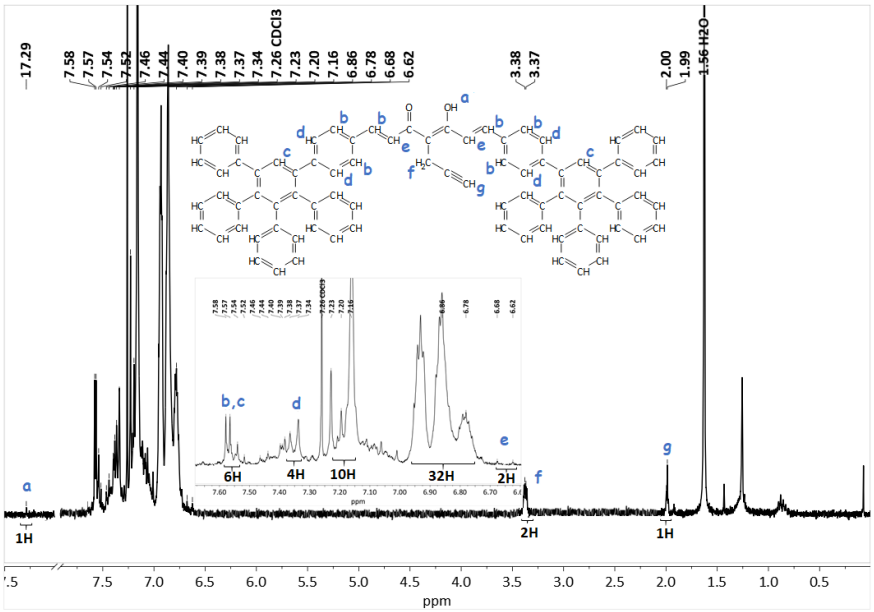

***Figure A 102**: ^{1}H RMN spectrum of 10PhpropCCMoid **18**.*

^{1}H NMR (360 MHz, $CDCl_3$) δ 16.73 (s, 1H), 5.95 – 5.79 (m, 0.2H), 5.77 – 5.63 (m, 1H), 5.15 – 4.93 (m, 6H), 3.73 (t, $^3J_{HH}$ = 7.4 Hz, 0.2H), 2.99 (d, $^3J_{HH}$ = 5.3 Hz, 2H), 2.63 – 2.56 (m, 0.3H), 2.18 (s, 6H), 2.10 (s, 1H).

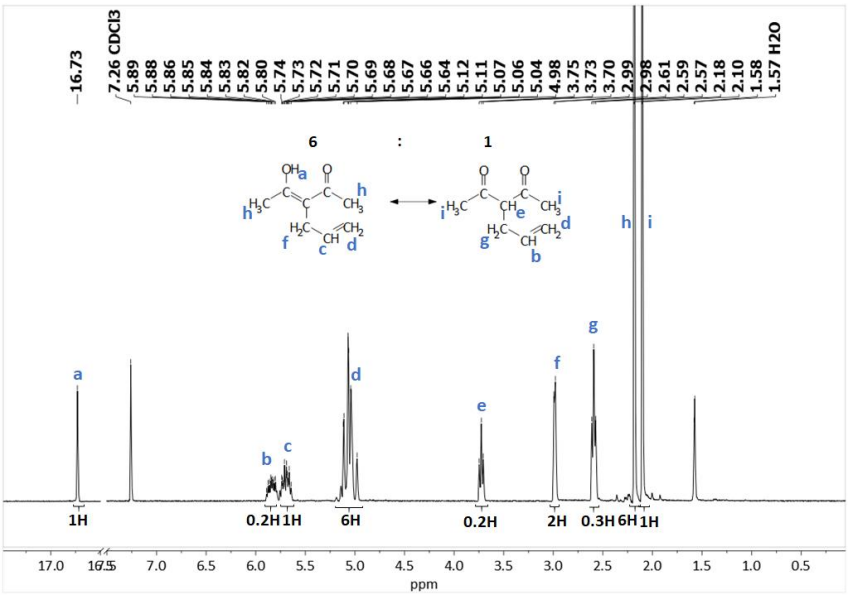

***Figure A 103**: ^{1}H RMN spectrum of allylACAC **20**.*

^{1}H NMR (400 MHz, $CDCl_3$) δ 17.51 – 17.29 (m, 1H), 7.71 (d, $^3J_{HH}$ = 15.6 Hz, 2H), 7.47 (s, 8H), 6.99 (d, $^3J_{HH}$ = 15.5, 2H), 6.05 (ddt, $^3J_{HH}$ = 16.8, 10.0, 4.9 Hz, 1H), 5.27 – 5.05 (dd, $^3J_{HH}$ = 10.9 and $^2J_{HH}$ = 16.8 2H), 3.33 (d, $^3J_{HH}$ = 5.3 Hz, 2H), 0.27 (s, 18H).

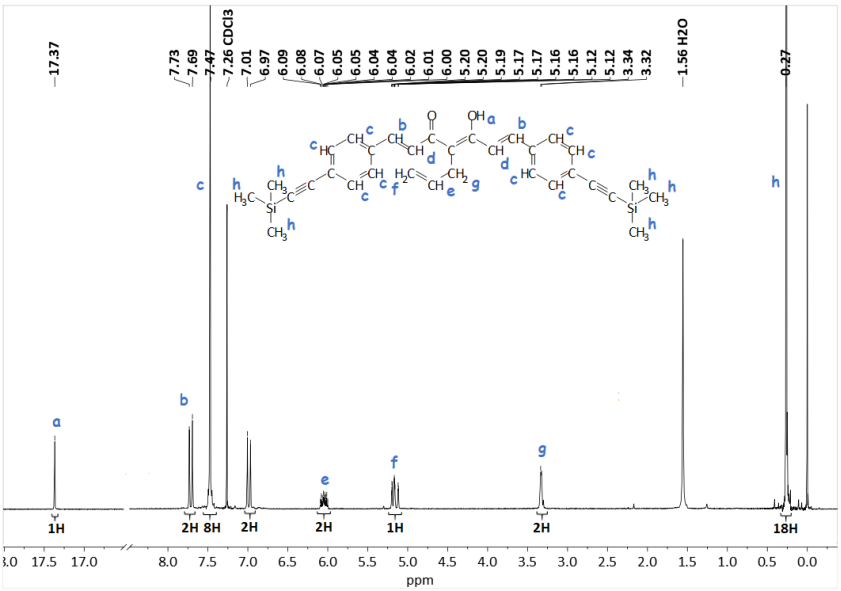

***Figure A 104**: ^{1}H RMN spectrum of AlkTMSallylCCMoid **21**.*

^{1}H NMR (300 MHz, $CDCl_3$) δ 17.35 (s, 1H), 7.73 (d, $^{3}J_{HH}$ = 15.5 Hz, 2H), 7.51 (s, 8H), 7.00 (d, $^{3}J_{HH}$ = 15.5 Hz, 2H), 6.09 – 6.00 (m, 1H), 5.20 – 5.11 (dd, $^{3}J_{HH}$ = 10.9 and $^{2}J_{HH}$ = 16.8 2H), 3.33 (d, $^{3}J_{HH}$ = 4.8 Hz, 2H), 3.20 (s 2H).

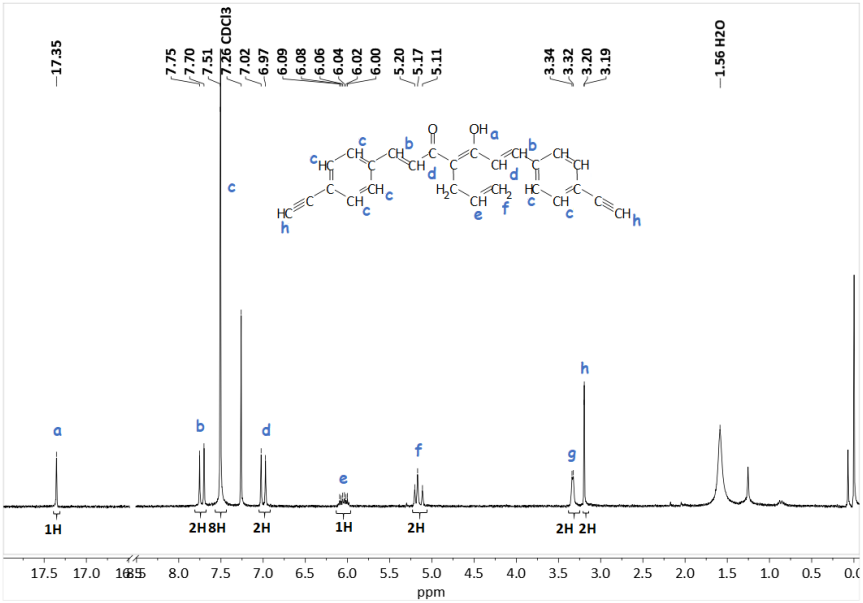

*Figure A 105: ^{1}H RMN spectrum of AlkallylCCMoid **22**.*

^{1}H NMR (400 MHz, $CDCl_3$) δ 17.48 (s, 1H), δ 7.85 (d, $^{3}J_{HH}$ = 7.5 Hz, 4H), 7.58 – 7.54 (m, 8H), 7.42 (d, $^{3}J_{HH}$ = 6.6 Hz, 2H), 7.16 – 7.07 (m, 8H), 6.97 – 6.76 (m, 26H), 6.70 (d, $^{3}J_{HH}$ = 7.5 Hz, 4H), 6.54 (d, $^{3}J_{HH}$ = 8.2 Hz, 2H), 5.88-5.80 (m, 1H), 5.05 – 4.99 (m, 2H), 3.28 (d, *J* = 5.1 Hz 2H).

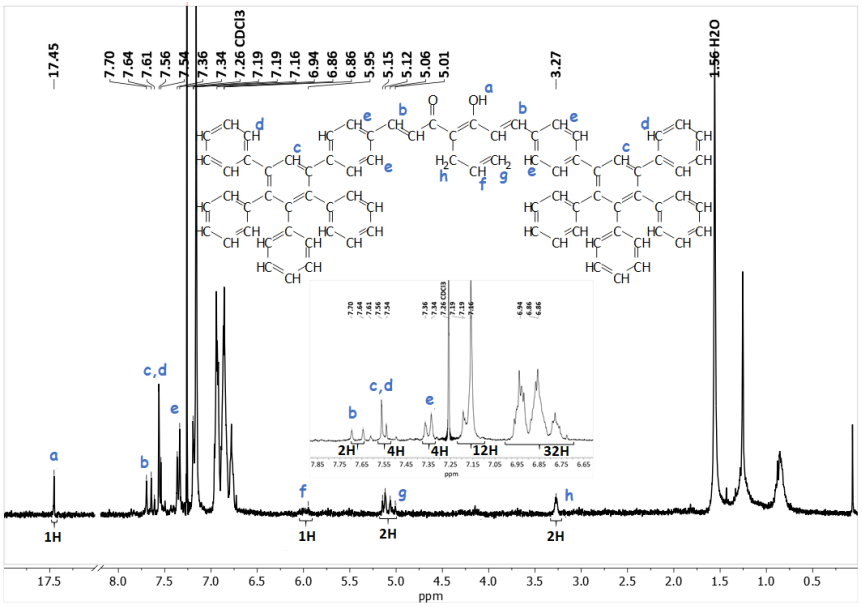

*Figure A 106: ^{1}H RMN spectrum of 10PhallylCCMoid **23**.*

^{13}C NMR spectra

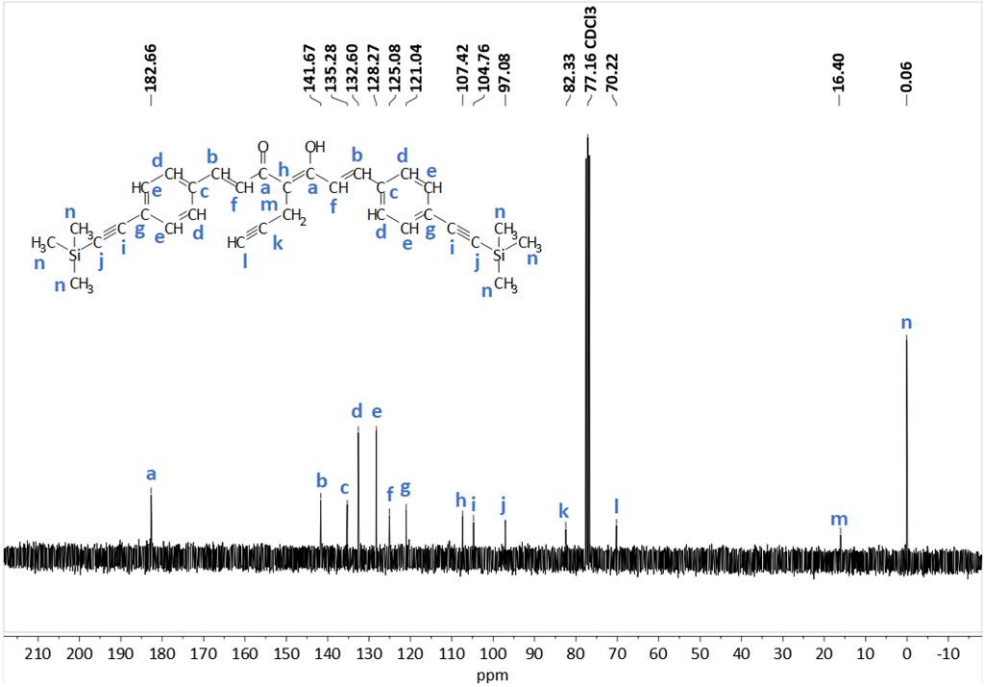

***Figure A 107**: ^{13}C RMN spectrum of AlkTMSpropCCMoid **16**.*

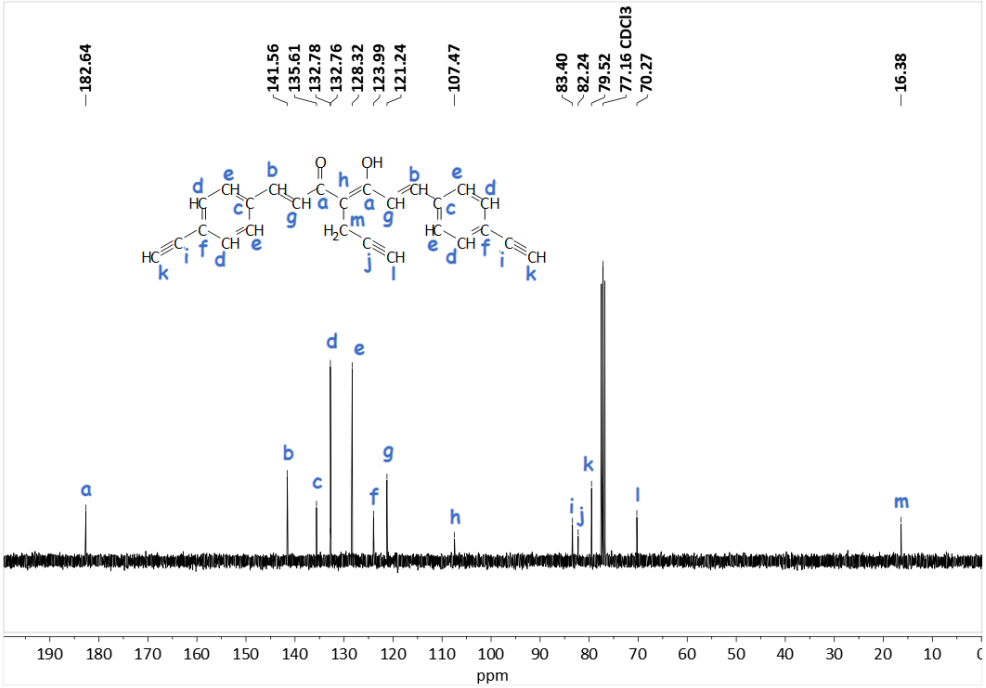

***Figure A 108**: ^{13}C RMN spectrum of AlkpropCCMoid **17**.*

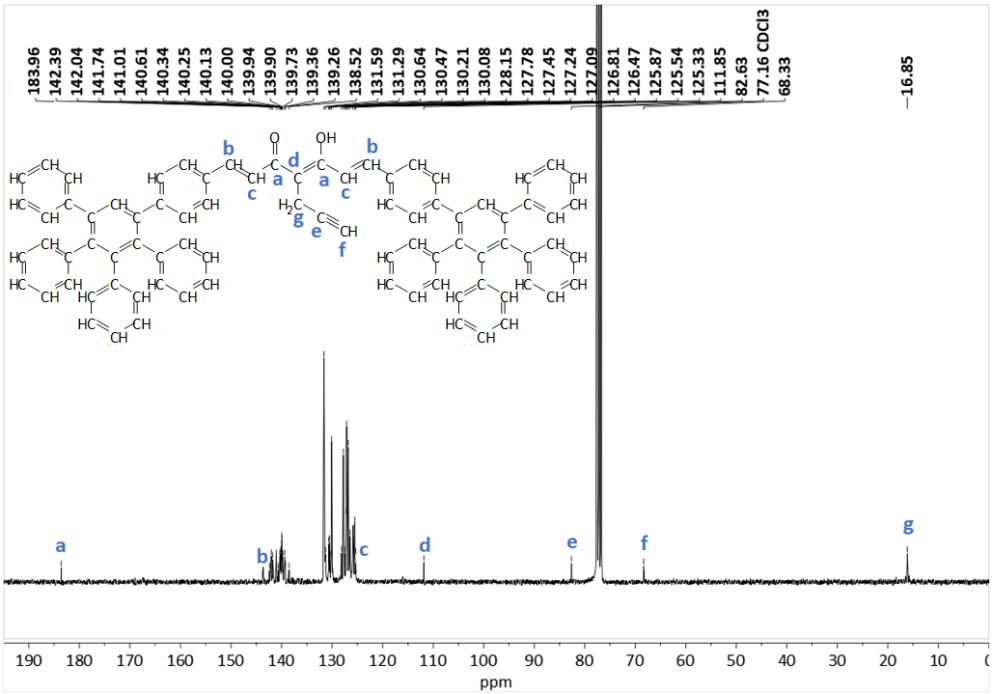

***Figure A 109**: ^{13}C RMN spectrum of 10PhpropCCMoid **18**.*

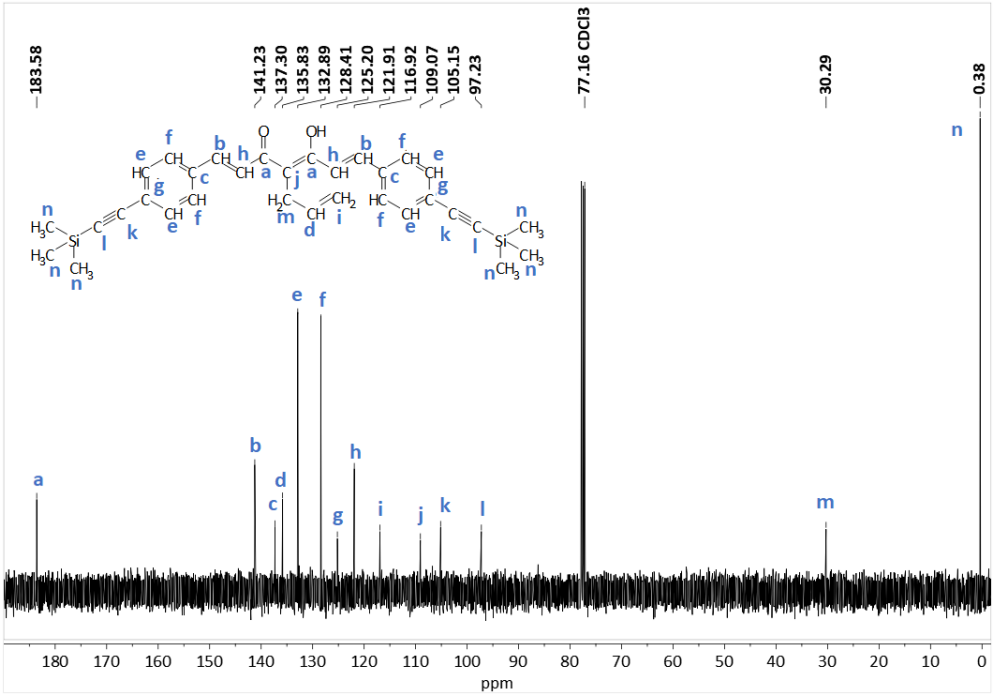

***Figure A 110**: ^{13}C RMN spectrum of AlkTMSallylCCMoid **21**.*

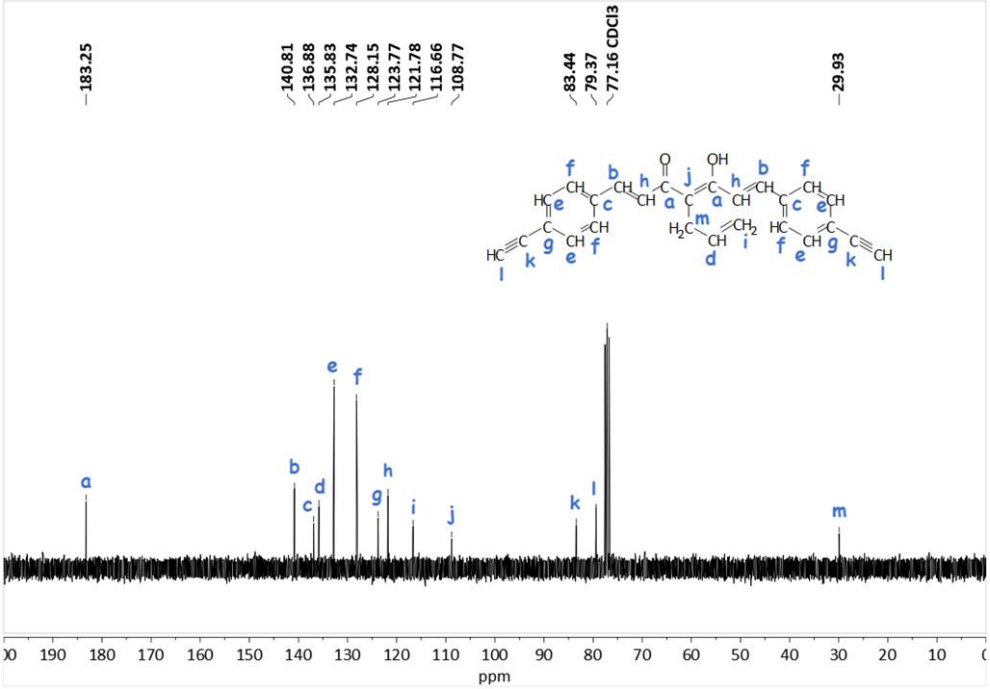

***Figure A 1113**: ^{13}C RMN spectrum of AlkallylCCMoid **22**.*

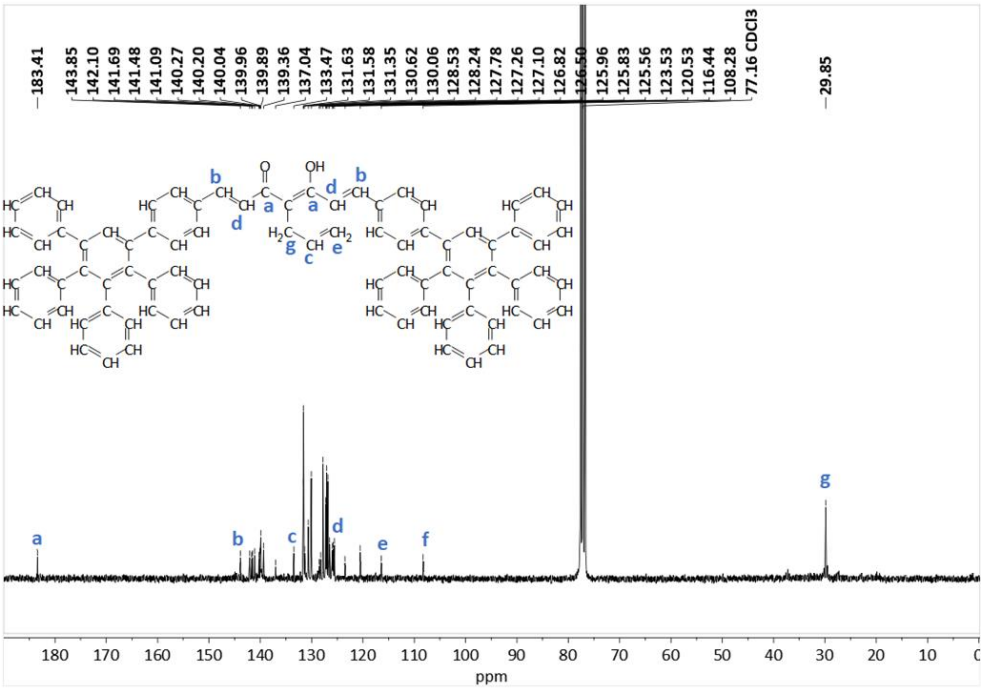

***Figure A 112**: ^{13}C RMN spectrum of 10PhallylCCMoid **23**.*

ATR-FTIR spectra

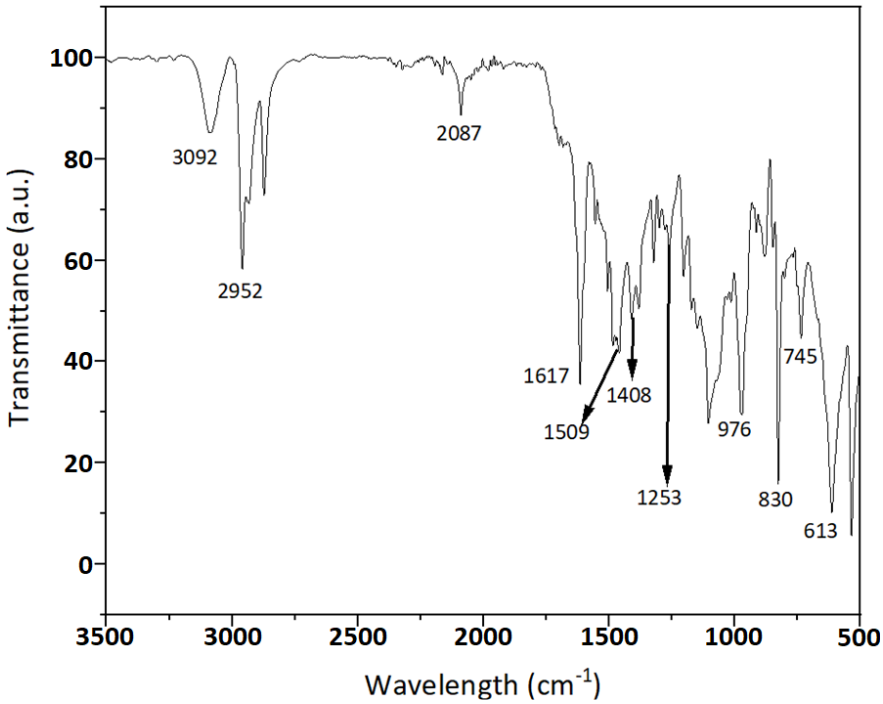

***Figure A 113**: ATR-FTIR spectrum of AlkTMSpropCCMoid **16**.*

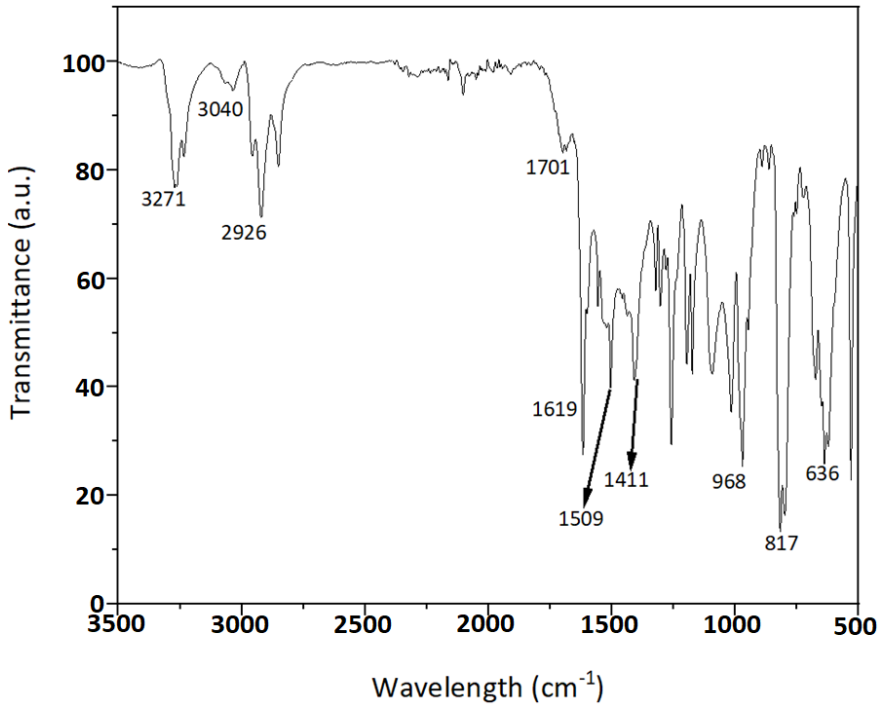

***Figure A 114**: ATR-FTIR spectrum of AlkpropCCMoid **17**.*

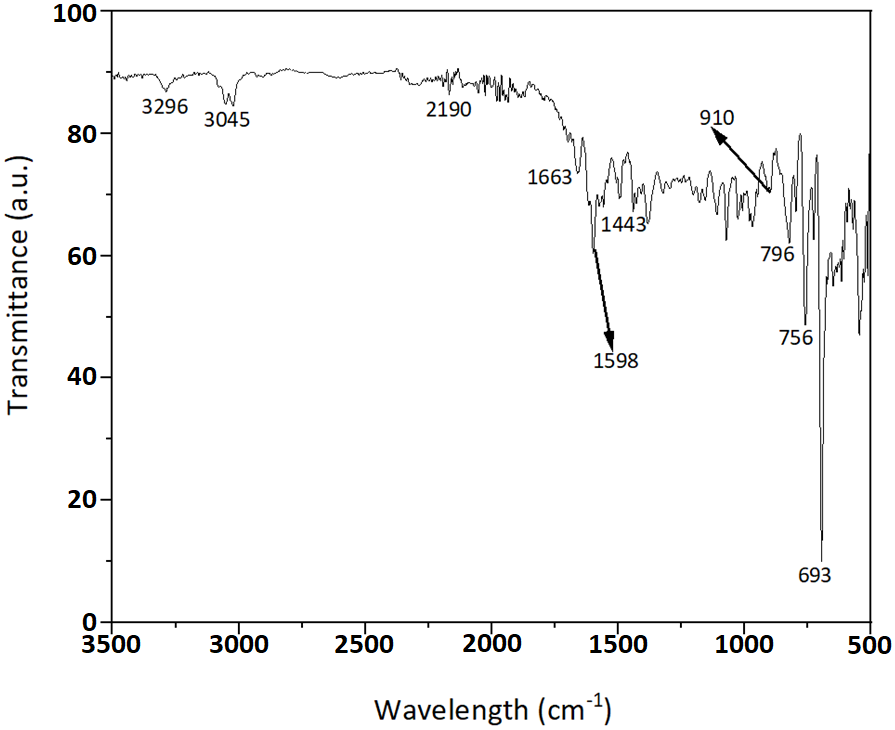

***Figure A 115**: ATR-FTIR spectrum of 10PhpropCCMoid **18**.*

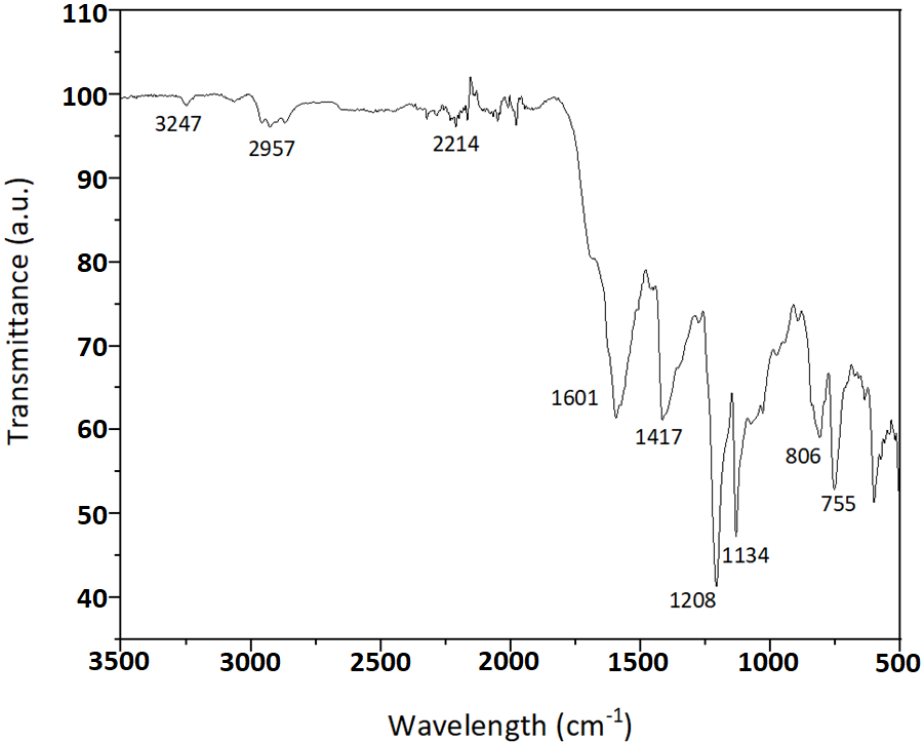

***Figure A 116**: ATR-FTIR spectrum of 4PhAntpropCCMoid **19**.*

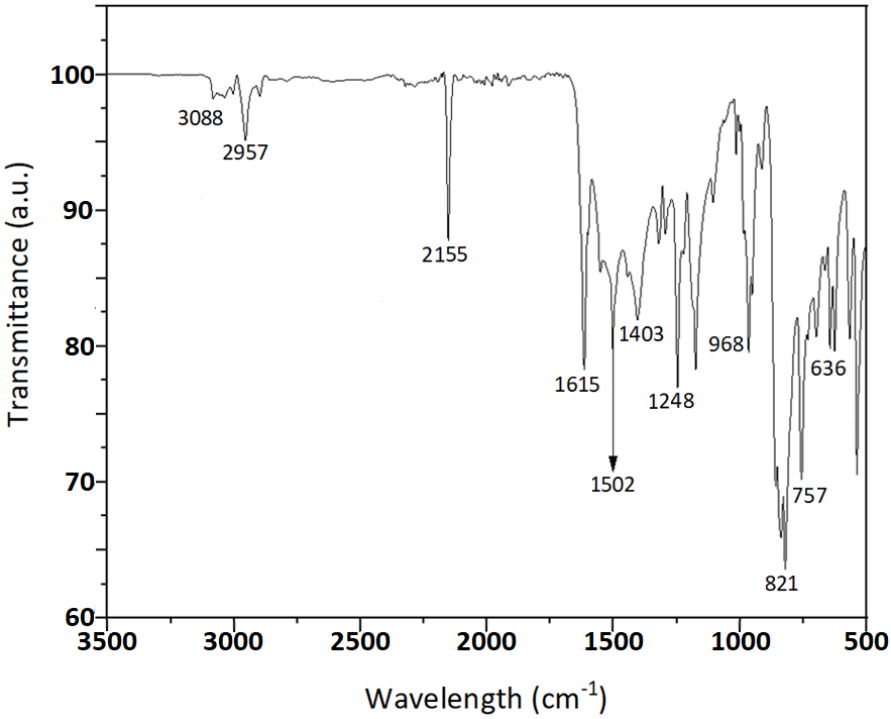

***Figure A 117**: ATR-FTIR spectrum of AlkTMSallylCCMoid **21**.*

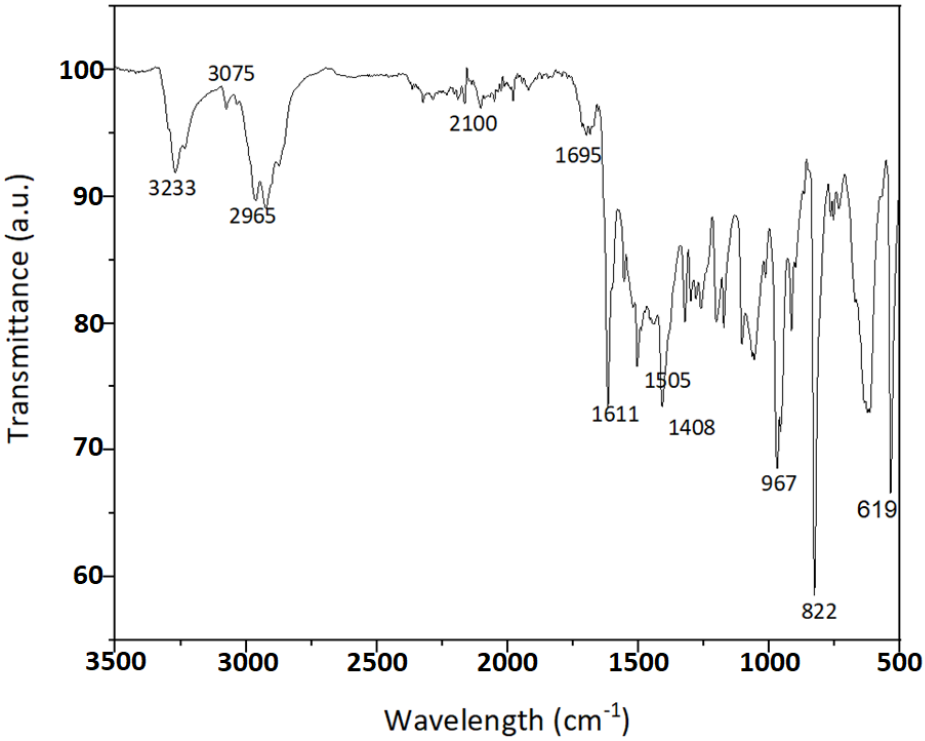

***Figure A 118**: ATR-FTIR spectrum of AlkallylCCMoid **22**.*

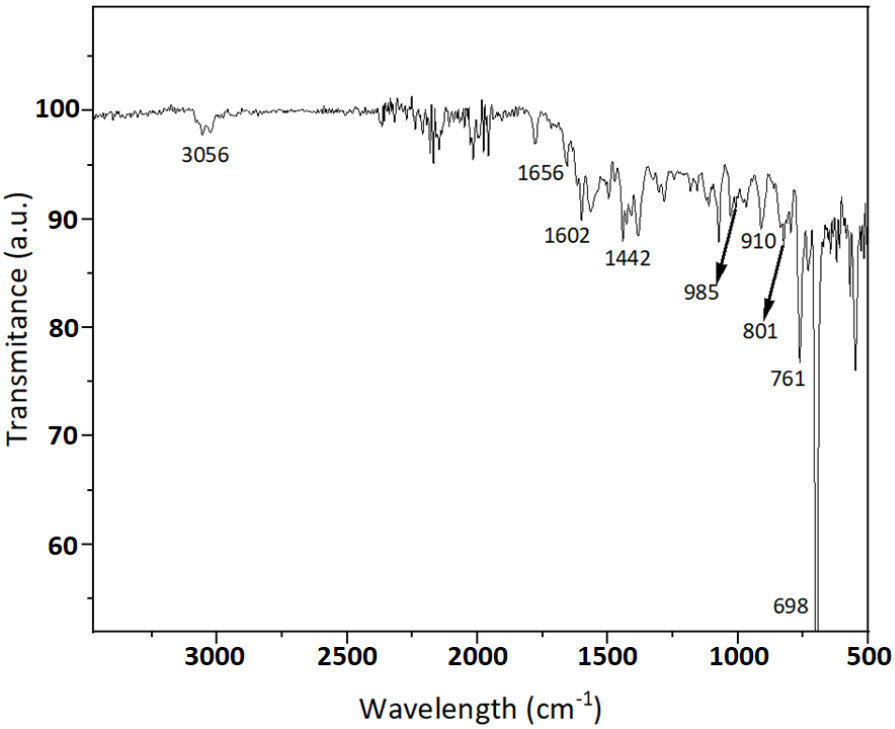

***Figure A 119**: ATR-FTIR spectrum of 10PhallylCCMoid **23**.*

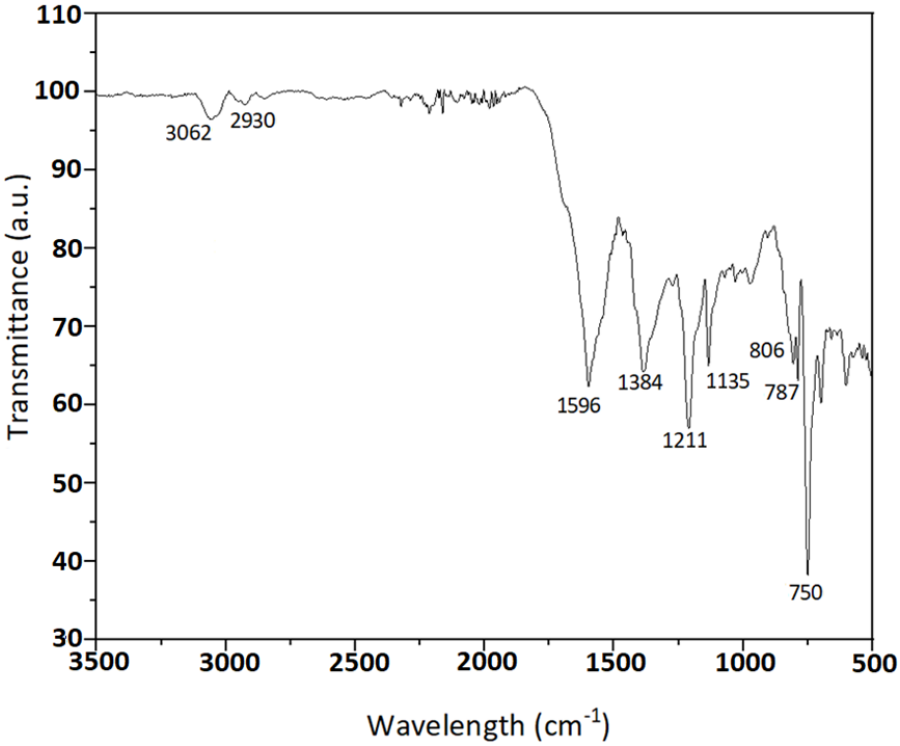

***Figure A 120**: ATR-FTIR spectrum of 4PhAntallylCCMoid **24**.*

Raman spectra

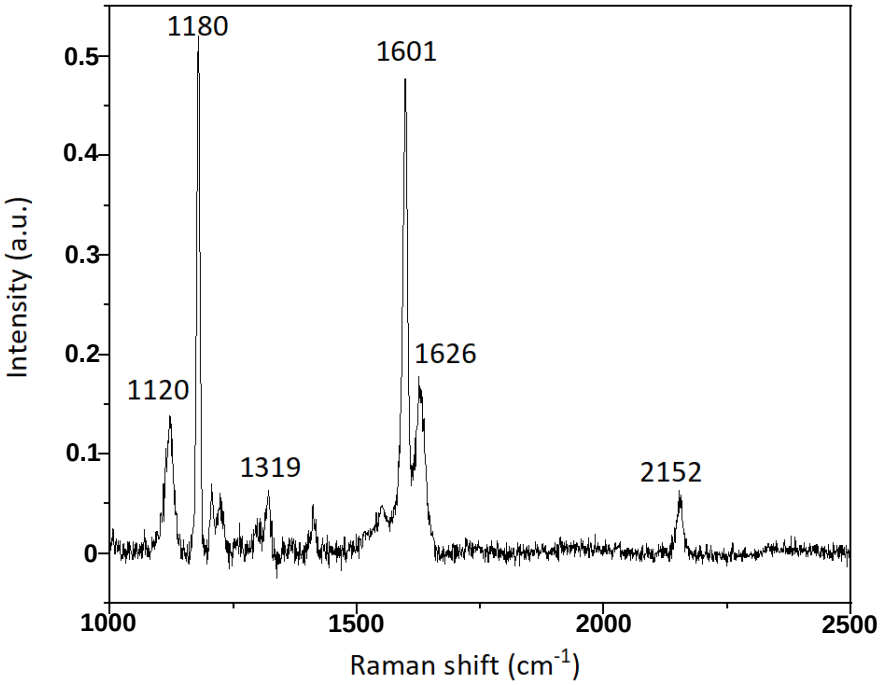

***Figure A 121**: Raman spectrum of AlkTMSpropCCMoid **16**.*

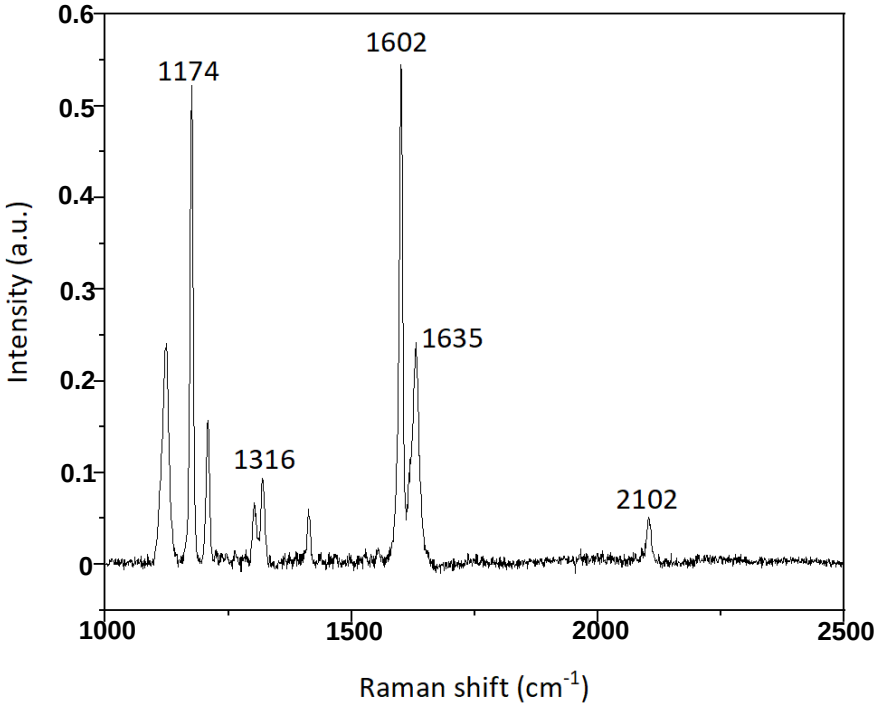

***Figure A 122:** Raman spectrum of AlkpropCCMoid **17**.*

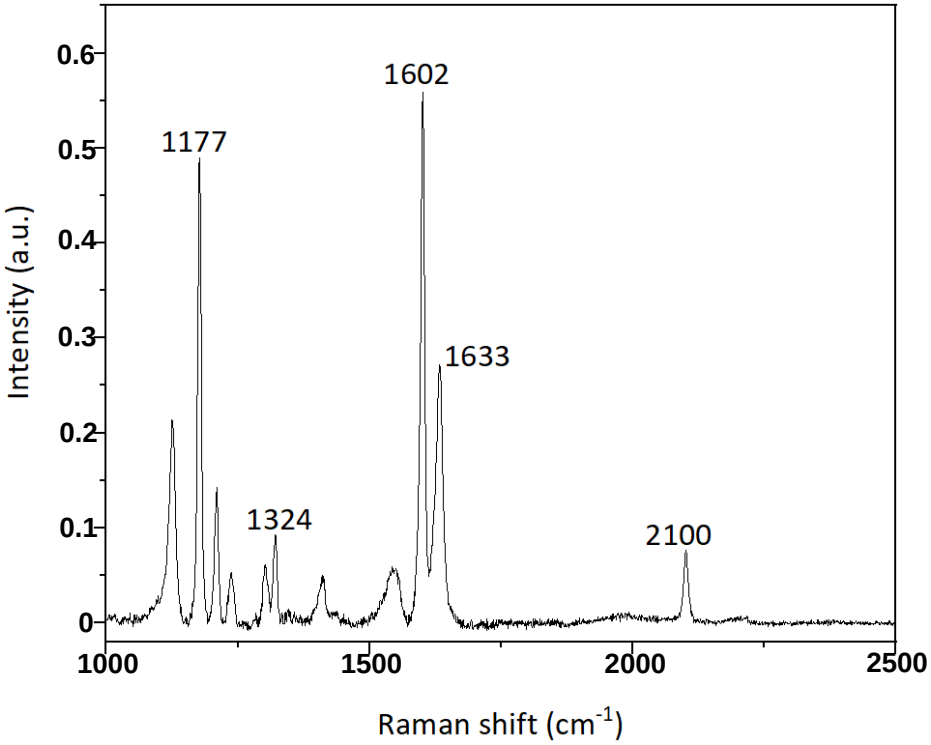

Figure A 123: *Raman spectrum of 10PhpropCCMoid* ***18****.*

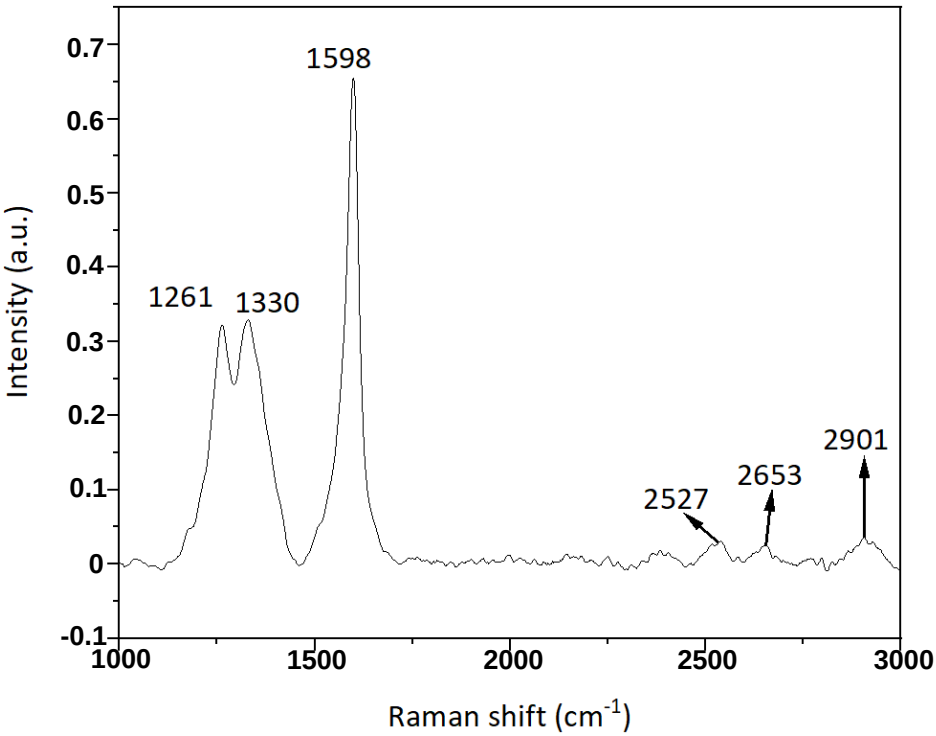

Figure A 124*: Raman spectrum of 4AntpropCCMoid* ***19****.*

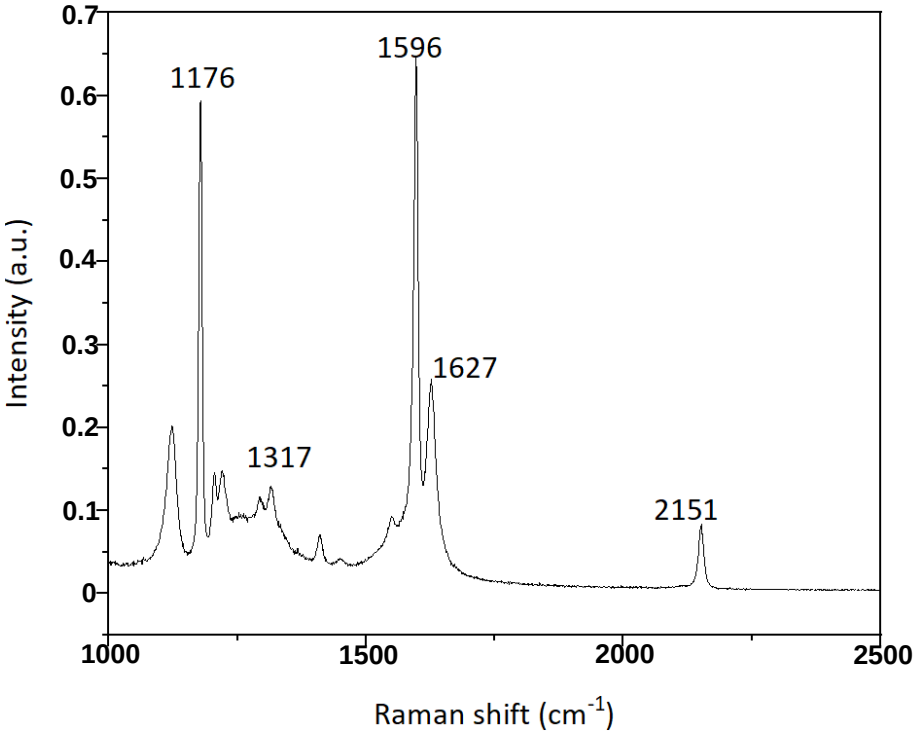

Figure A 125: *Raman spectrum of AlkTMSallylCCMoid* ***21****.*

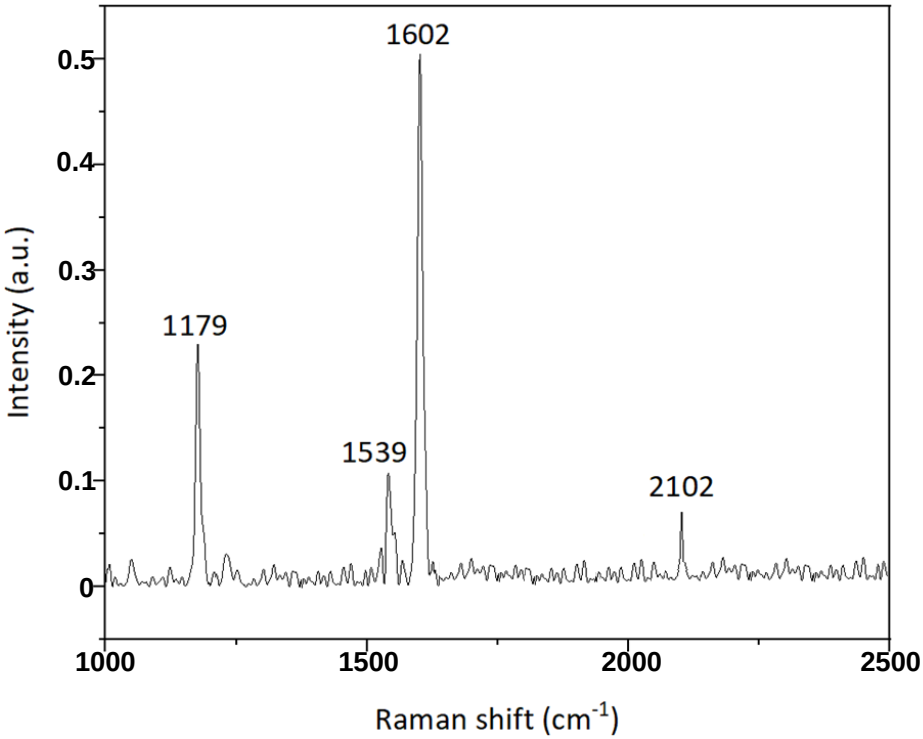

Figure A 126*: Raman spectrum of AlkallylCCMoid* ***22****.*

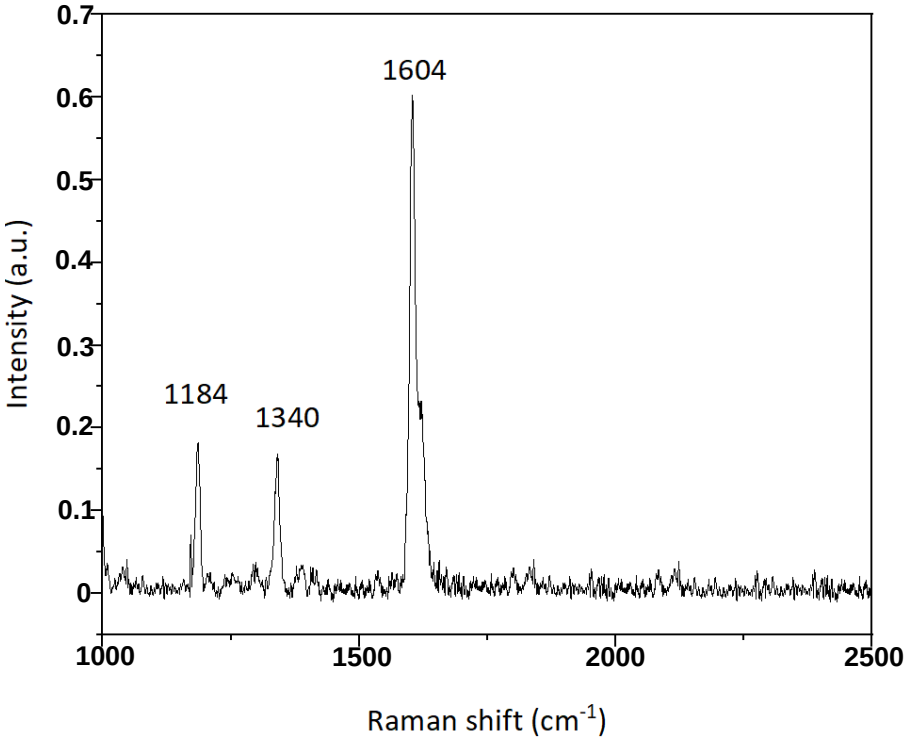

***Figure A 127**: Raman spectrum of 10PhallylCCMoid **23**.*

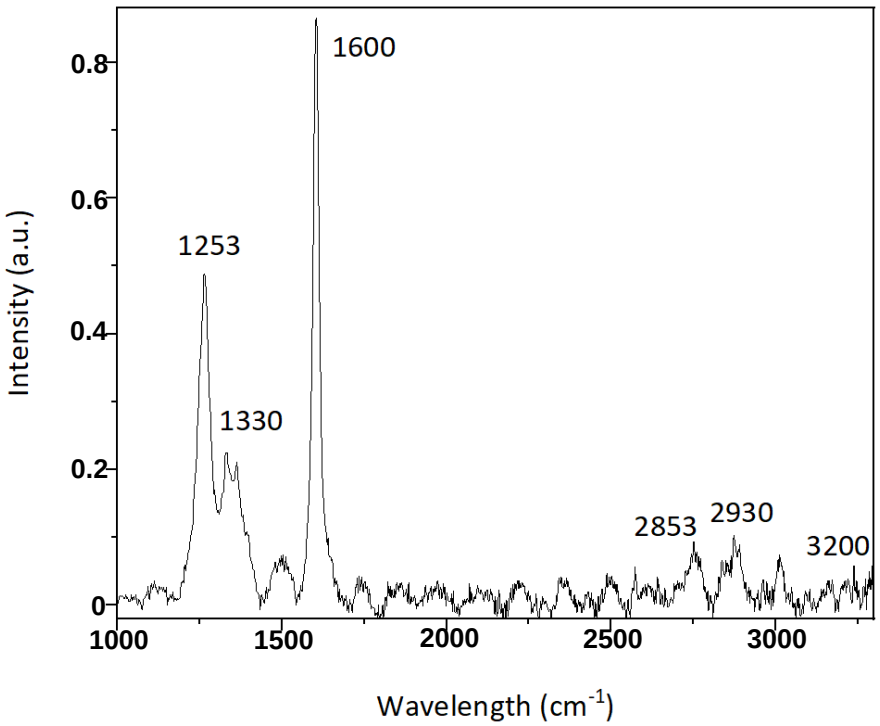

***Figure A 128**: Raman spectrum of 4PhAntallylCCMoid **24**.*

UV-VIS spectra in solution (DCM) and in solid state (KBr PELLETS)

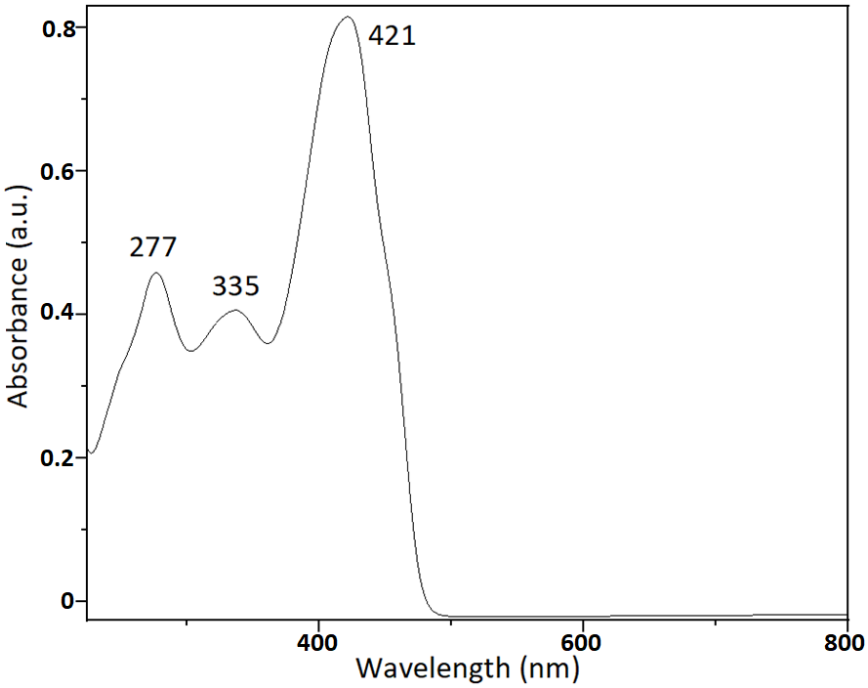

Figure A 129**: UV-Vis solution spectrum of AlkTMSPropCCMoid **16.

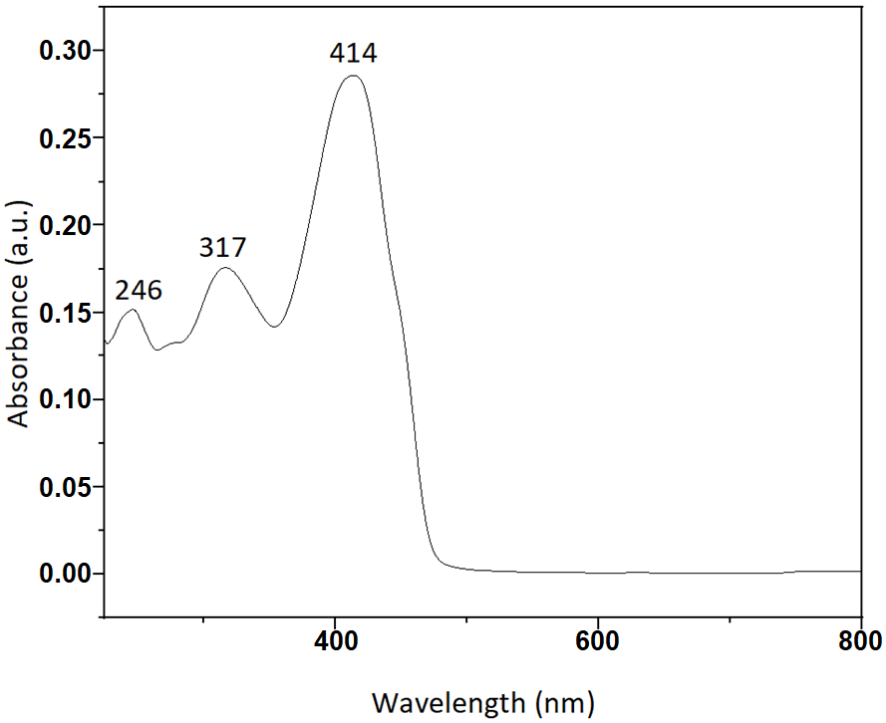

***Figure A 130**: UV-Vis solution spectrum of AlkPropCCMoid **17**.*

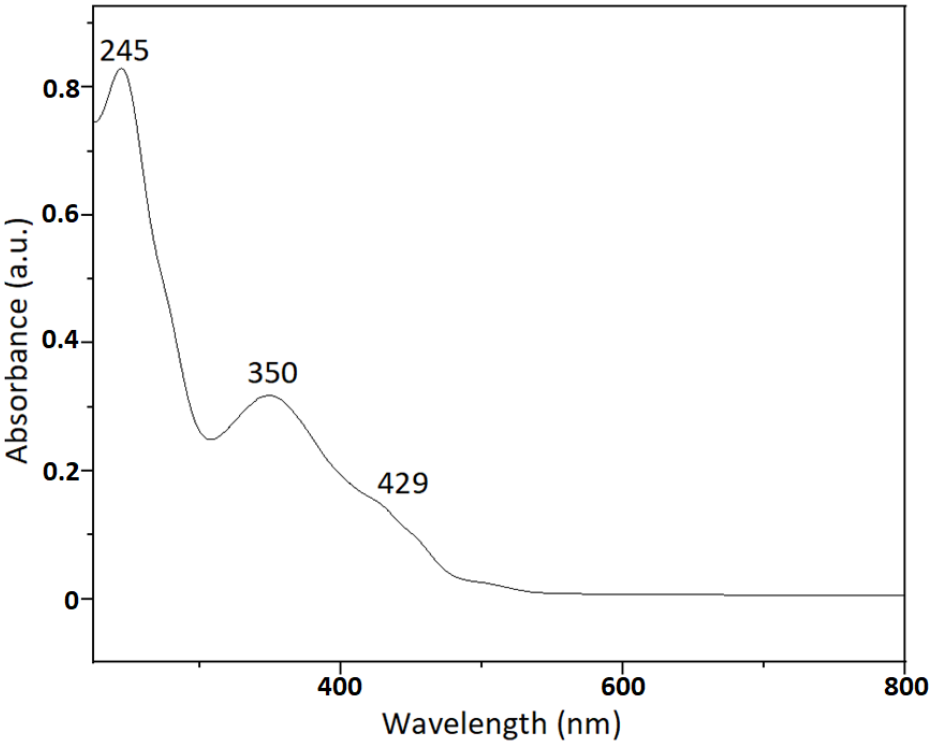

***Figure A 131**: UV-Vis solution spectrum of 10PhpropCCMoid **18**.*

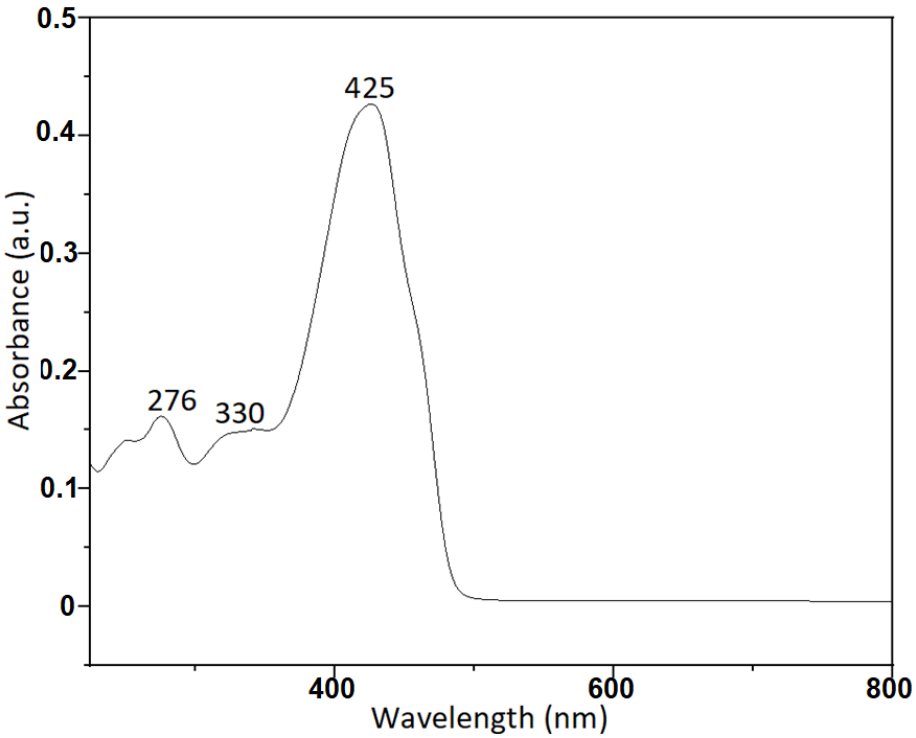

***Figure A 132**: UV-Vis solution spectrum of AlkTMSallylCCMoid **21**.*

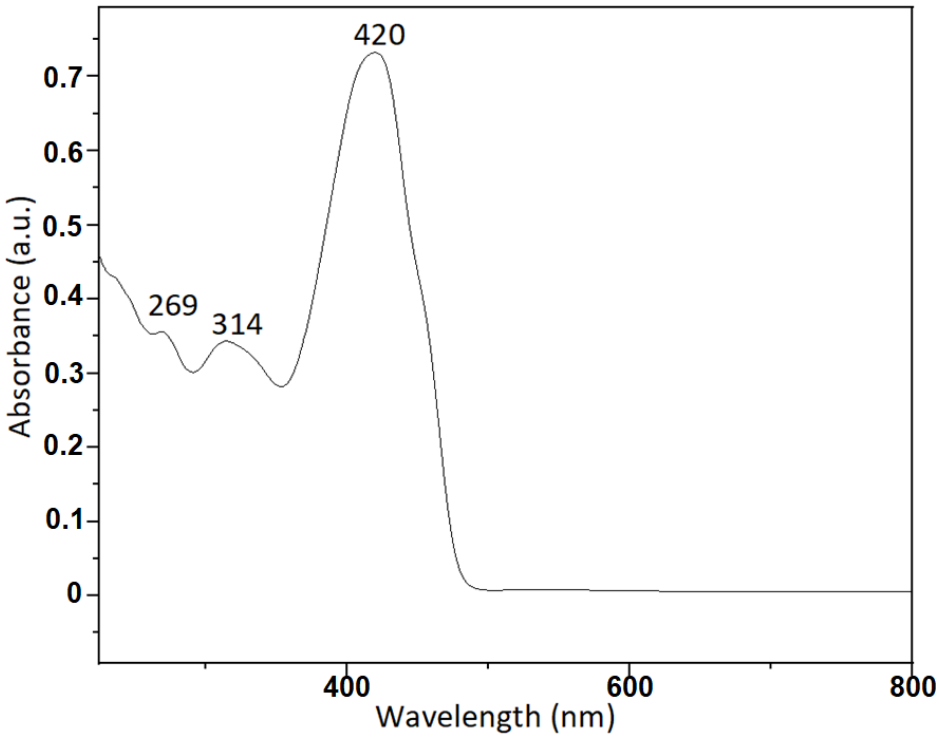

***Figure A 133**: UV-Vis solution spectrum of AlkallylCCMoid **22**.*

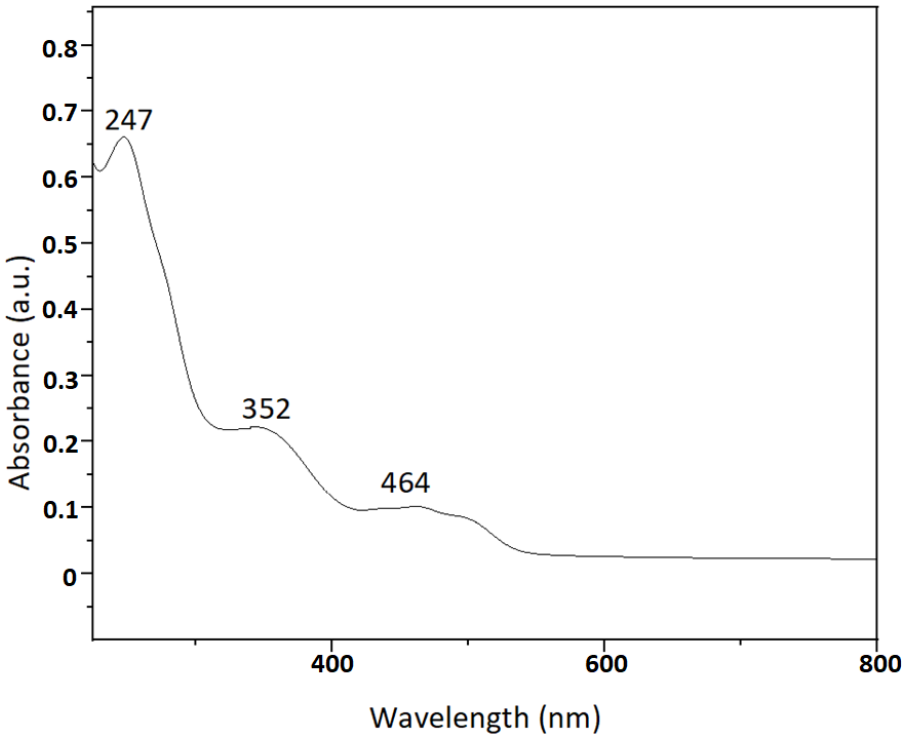

***Figure A 134**: UV-Vis solution spectrum of 10PhallylCCMoid **23**.*

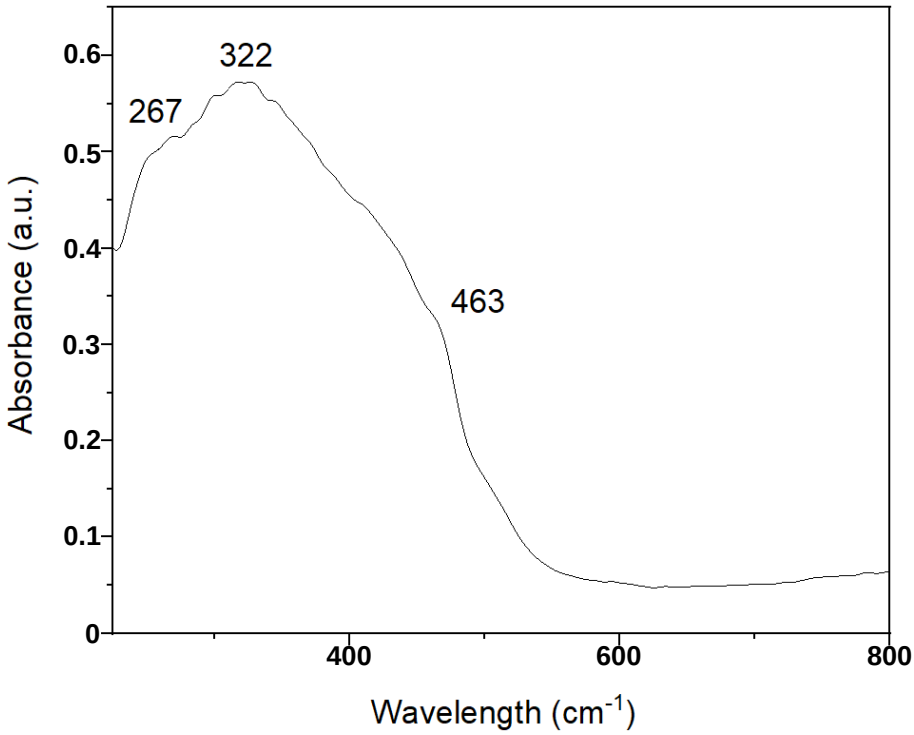

Figure A 135: *UV-Vis solid spectrum of AlkTMSpropCCMoid* ***16****.*

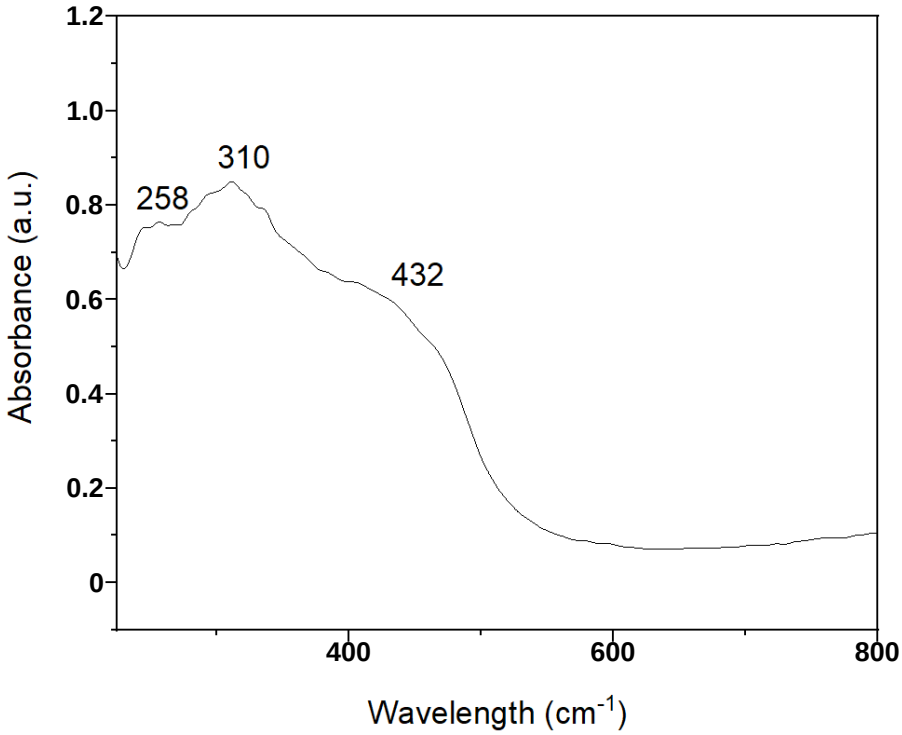

Figure A 136*: UV-Vis solid spectrum of AlkpropCCMoid* ***17****.*

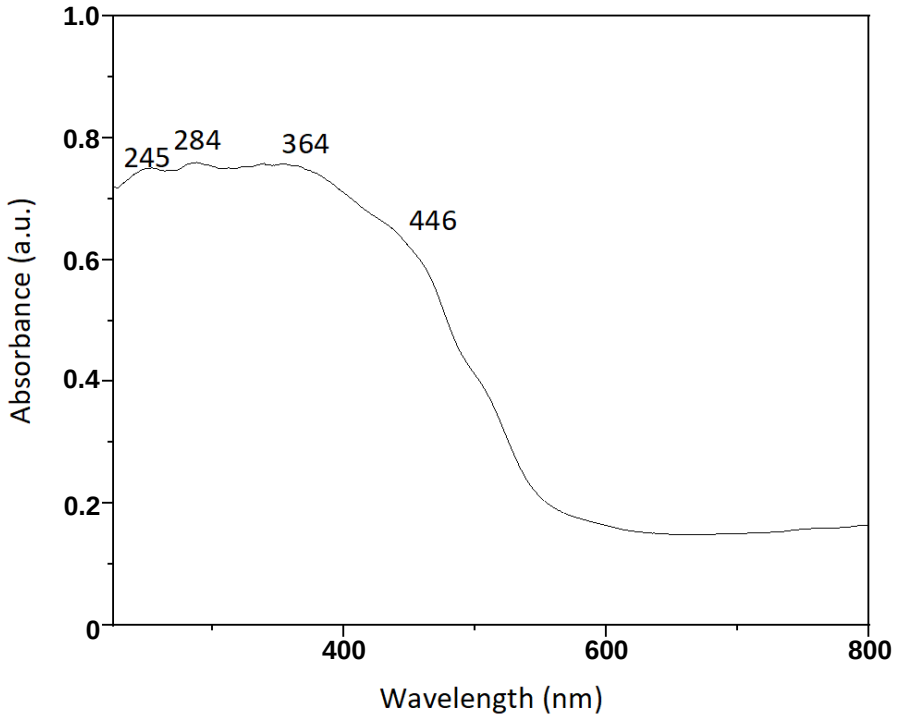

***Figure A 137**: UV-Vis solid spectrum of 10PhpropCCMoid **18**.*

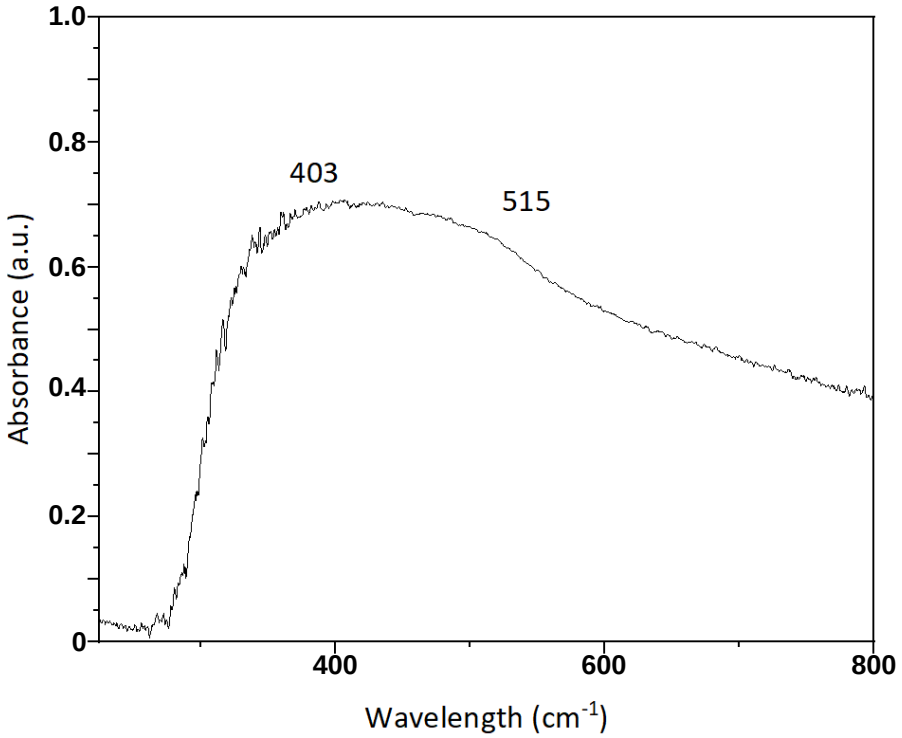

***Figure A 138**: UV-Vis solid spectrum of 4PhAntpropCCMoid **19**.*

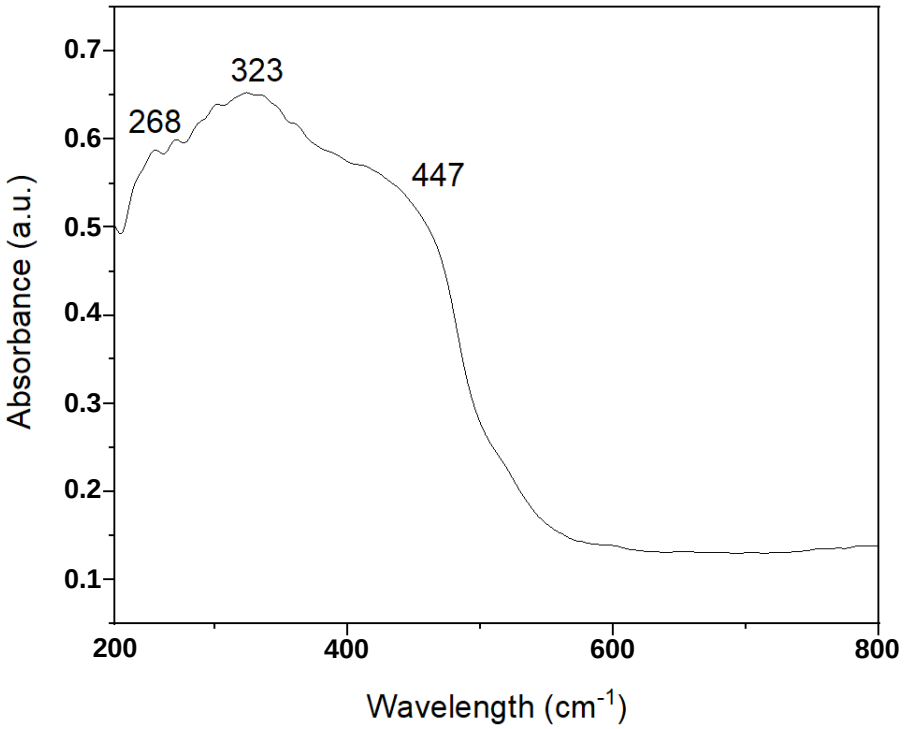

***Figure A 139**: UV-Vis solid spectrum of AlkTMSallylCCMoid **21**.*

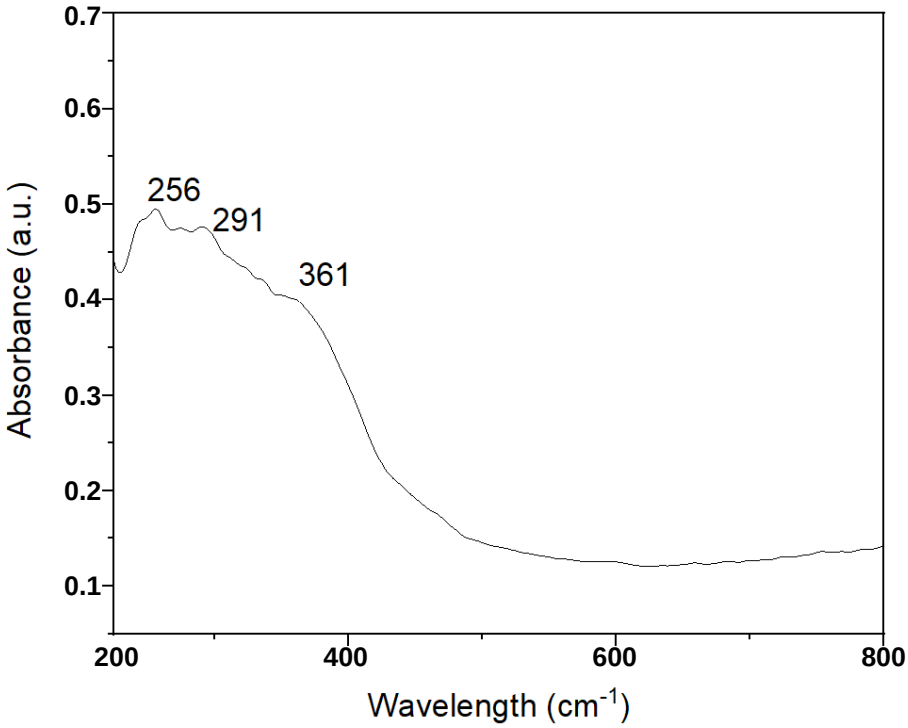

***Figure A 140**: UV-Vis solid spectrum of AlkallylCCMoid **22**.*

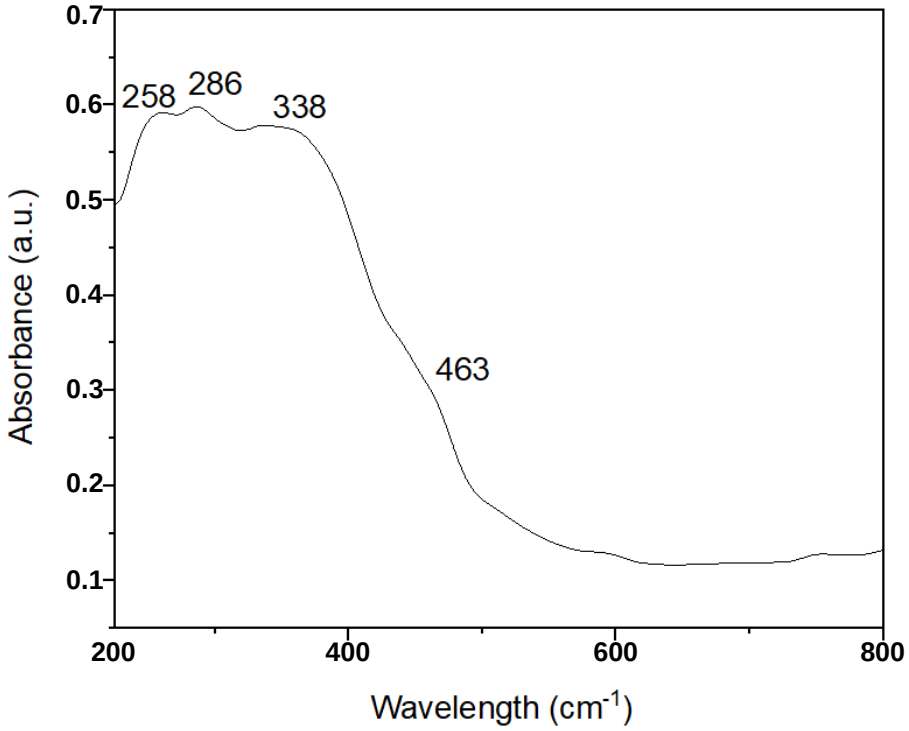

***Figure A 141**: UV-Vis solid spectrum of 10PhallylCCMoid **23**.*

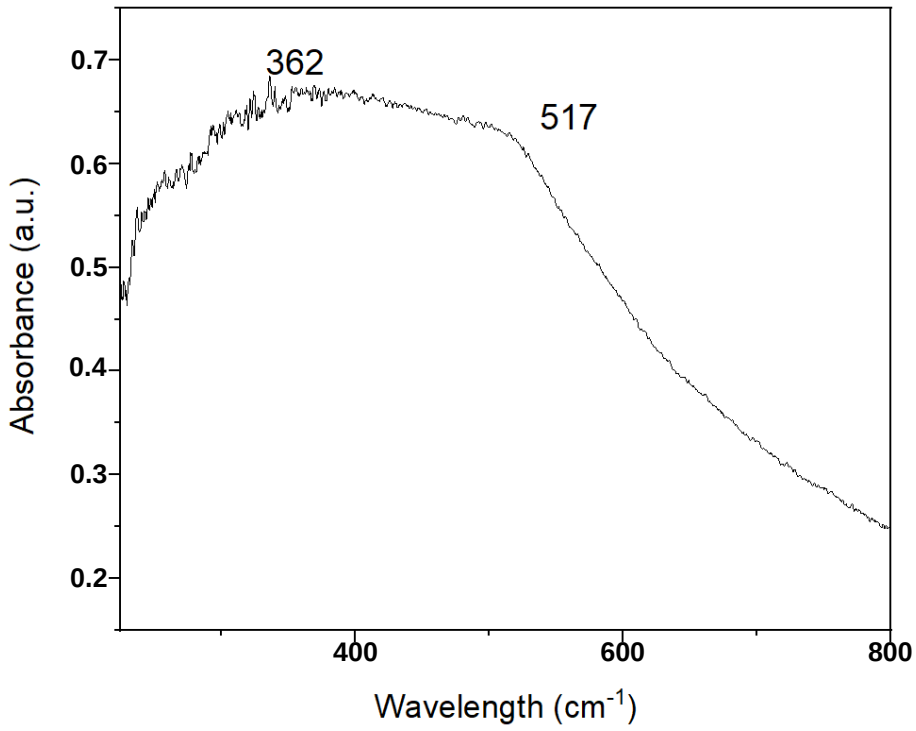

***Figure A 142**: UV-Vis solid spectrum of 4PhAntallylCCMoid **24**.*

Electrochemistry spectra

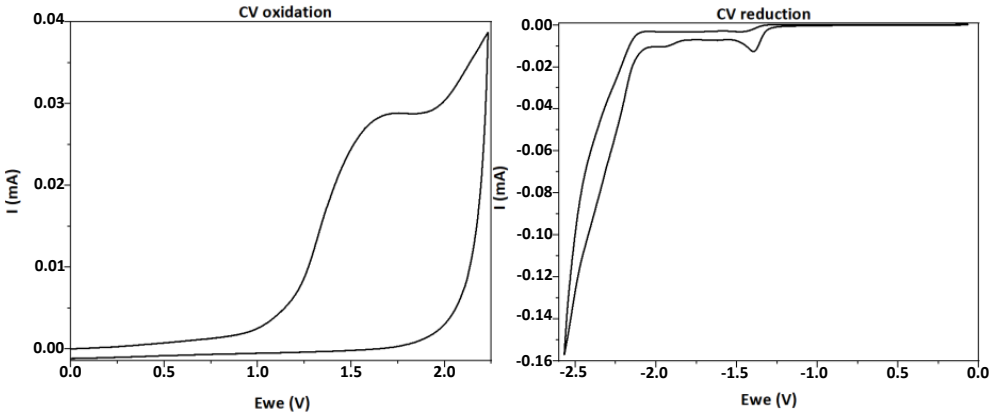

Figure A 143: *Oxidation and reduction cyclic voltammogram spectrum of AlkTMSpropCCMoid* ***16****.*

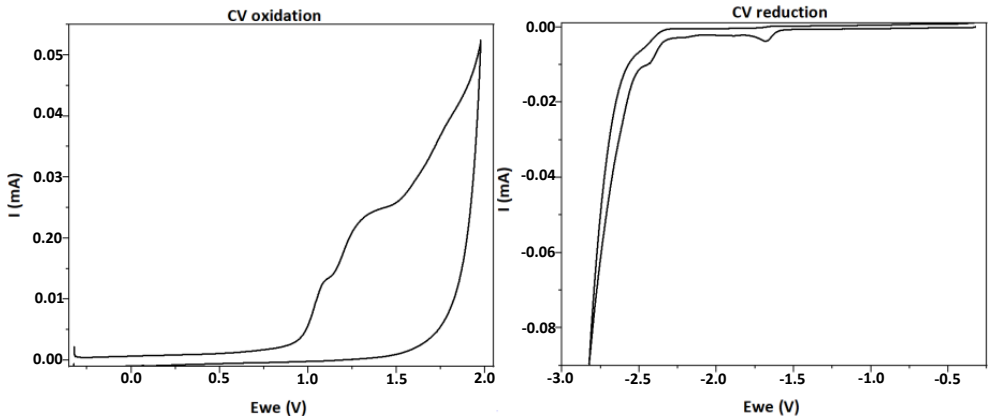

Figure A 144*: Oxidation and reduction cyclic voltammogram spectrum of AlkpropCCMoid* ***17****.*

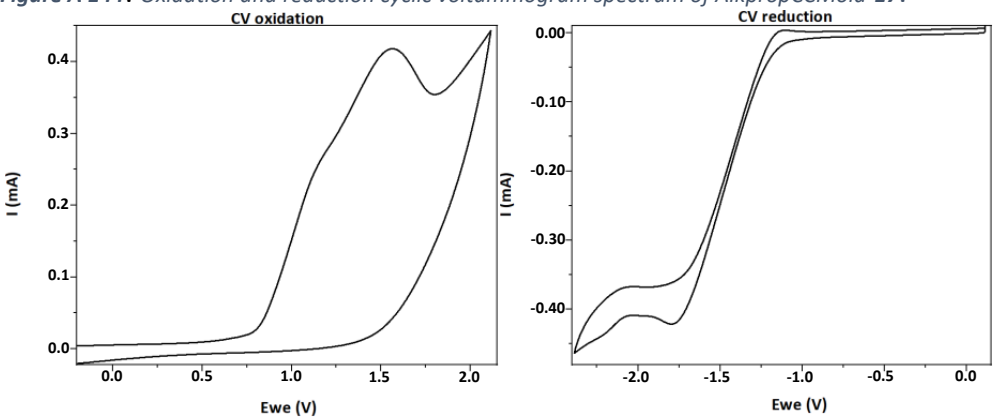

Figure A 145*: Oxidation and reduction cyclic voltammogram spectrum of 10PhpropCCMoid* ***18.***

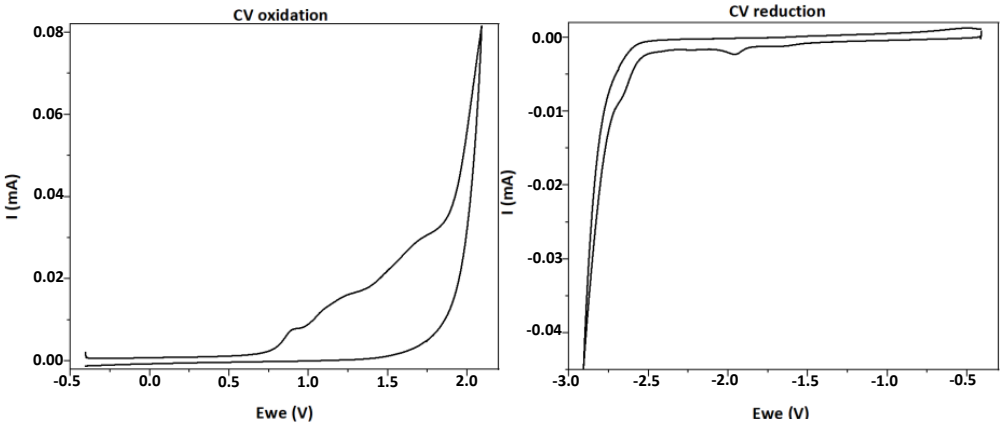

Figure A 146**: Oxidation and reduction cyclic voltammogram spectrum of AlkTMSallylCCMoid **21.

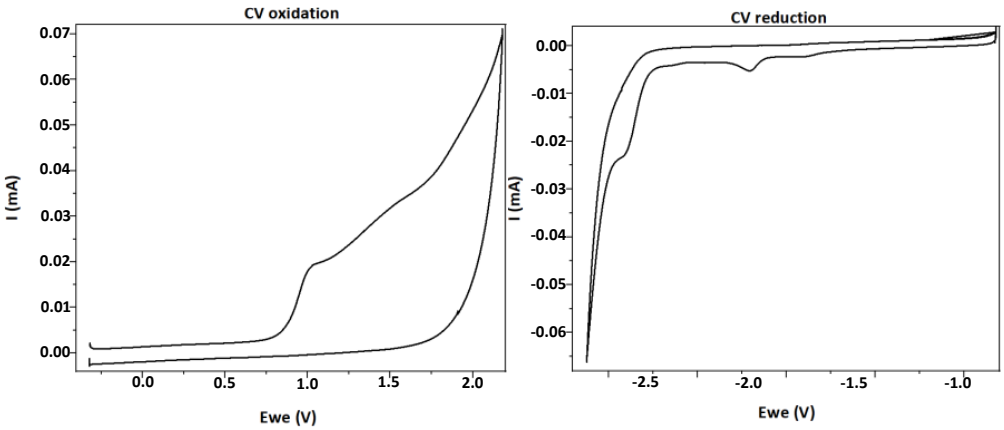

Figure A 147**: Oxidation and reduction cyclic voltammogram spectrum of AlkallylCCMoid **22.

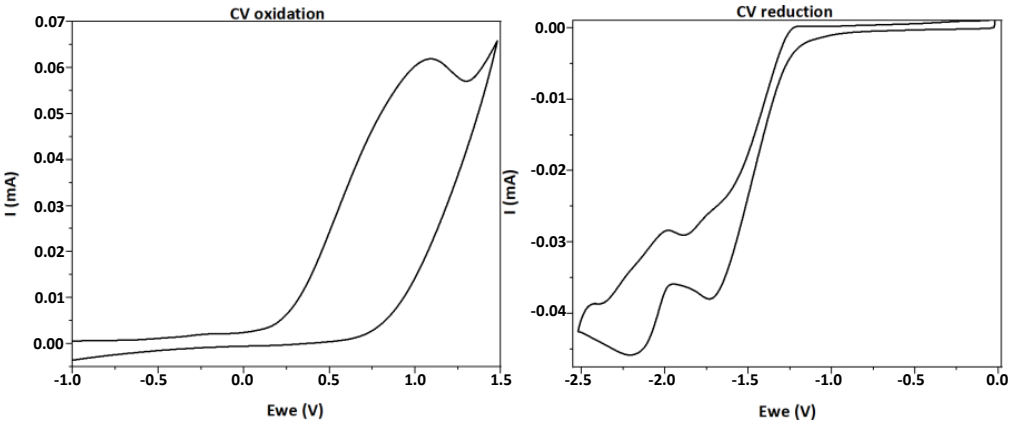

Figure A 148**: Oxidation and reduction cyclic voltammogram spectrum of 10PhallylCCMoid **23.

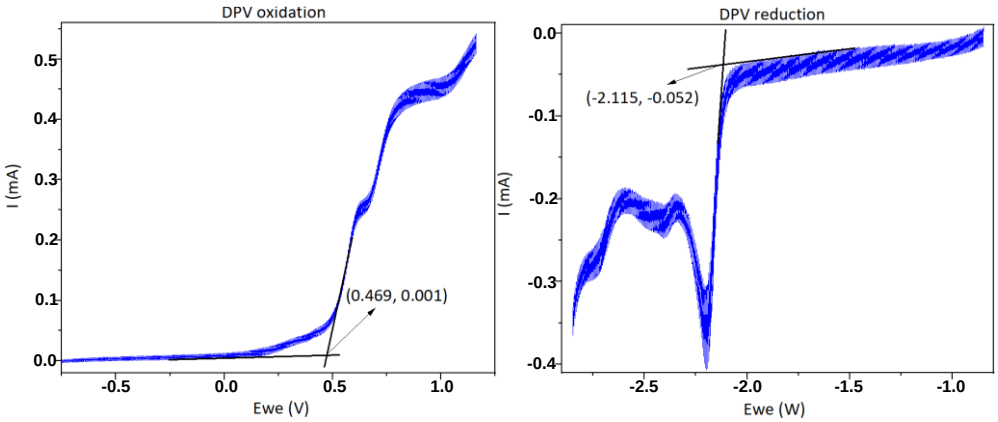

Figure A 149**: Oxidation and reduction differential pulse voltammogram spectrum of AlkTMSpropCCMoid **16.

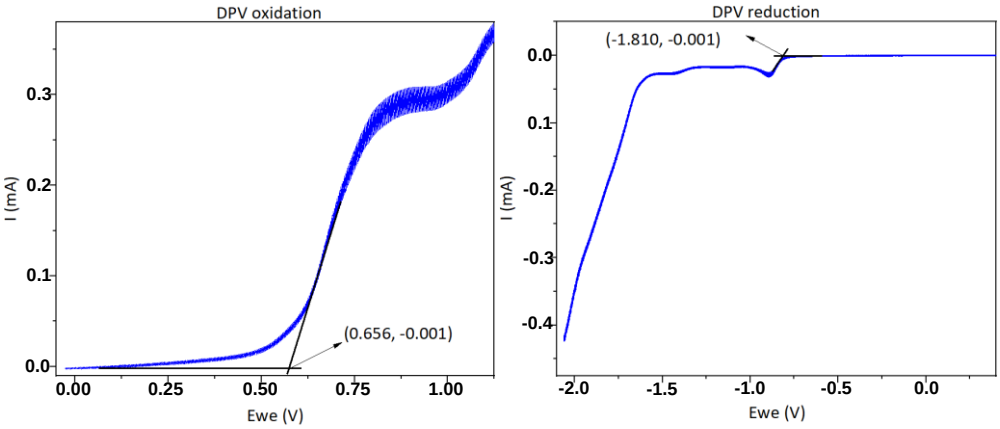

Figure A 150:** Oxidation and reduction differential pulse voltammogram spectrum of AlkpropCCMoid **17.

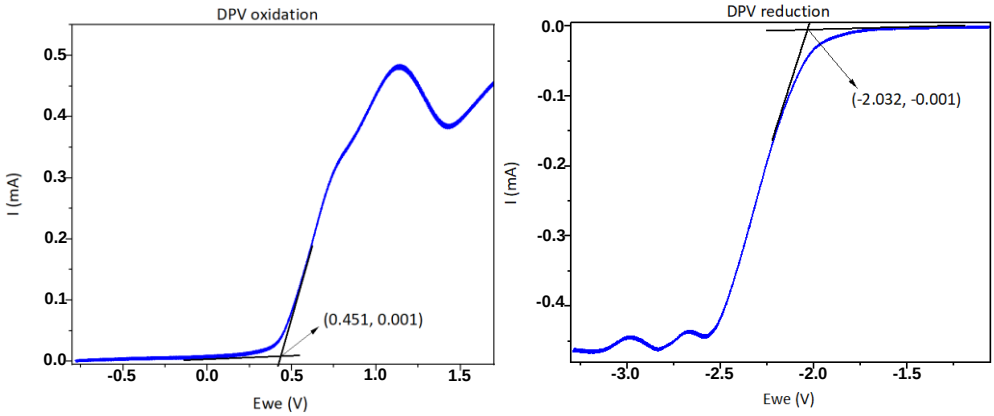

Figure A 151**: Oxidation and reduction differential pulse voltammogram spectrum of 10PhpropCCMoid **18.

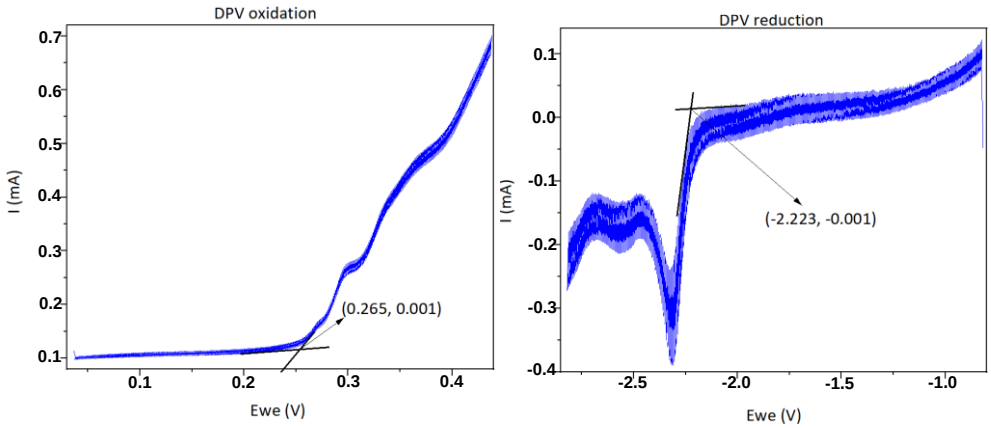

Figure A 152**: Oxidation and reduction differential pulse voltammogram spectrum of AlkTMSallylCCMoid **21.

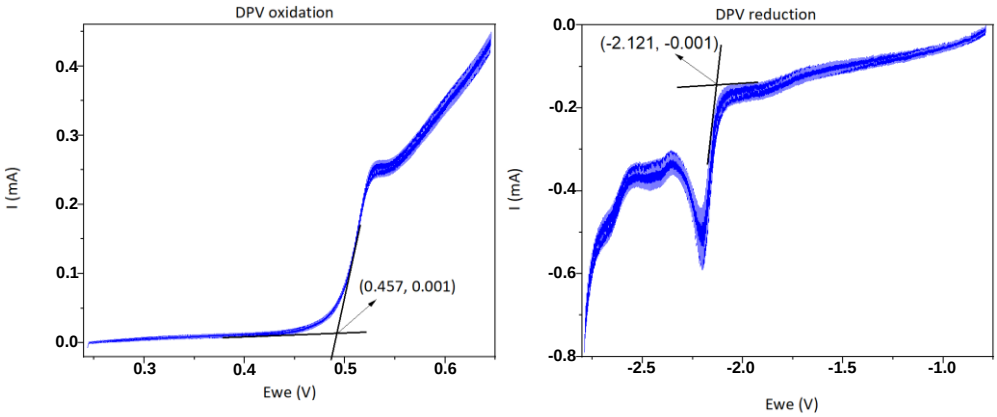

Figure A 153**: Oxidation and reduction differential pulse voltammogram spectrum of AlkallylCCMoid **22.

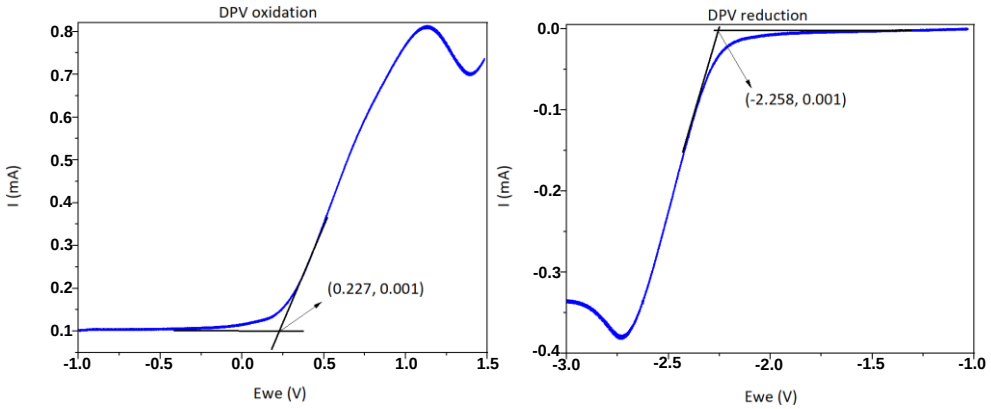

***Figure A 154**: Oxidation and reduction differential pulse voltammogram spectrum of 10PhallylCCMoid **23**.*

MALDI- MASS spectra

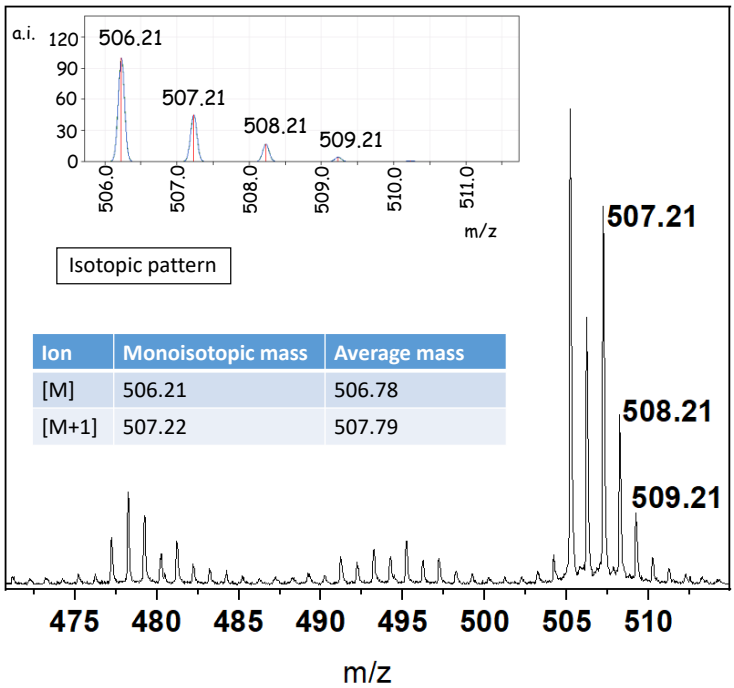

Ion	Monoisotopic mass	Average mass
[M]	506.21	506.78
[M+1]	507.22	507.79

Figure A 155: *Mass spectrum of AlkTMSpropCCMoid* ***16*** *(Positive mode).*

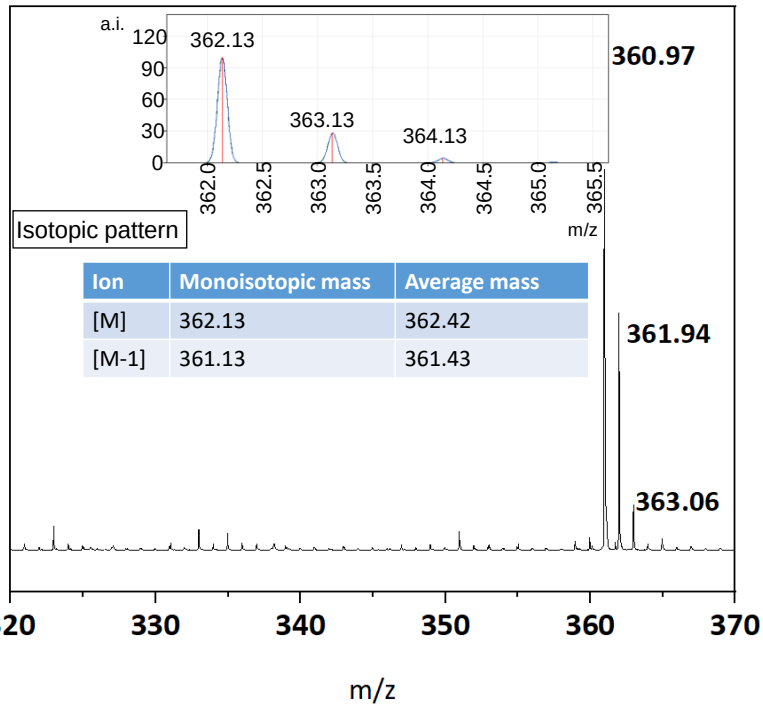

Ion	Monoisotopic mass	Average mass
[M]	362.13	362.42
[M-1]	361.13	361.43

Figure A 156*: Mass spectrum of AlkpropCCMoid* ***17*** *(Negative mode).*

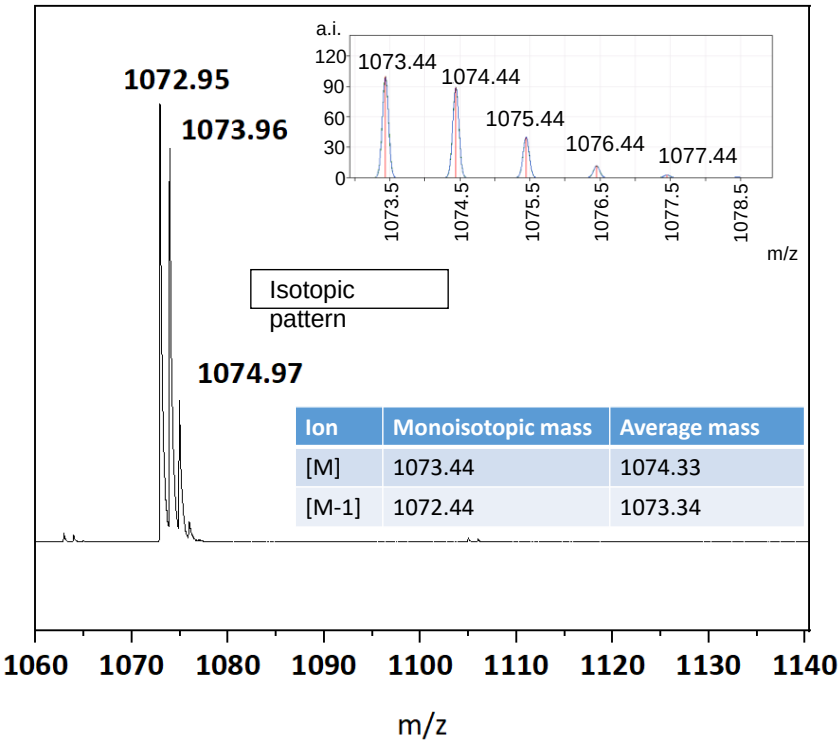

Ion	Monoisotopic mass	Average mass
[M]	1073.44	1074.33
[M-1]	1072.44	1073.34

Figure A 157: *Mass spectrum of 10PhpropCCMoid **18** (Negative mode).*

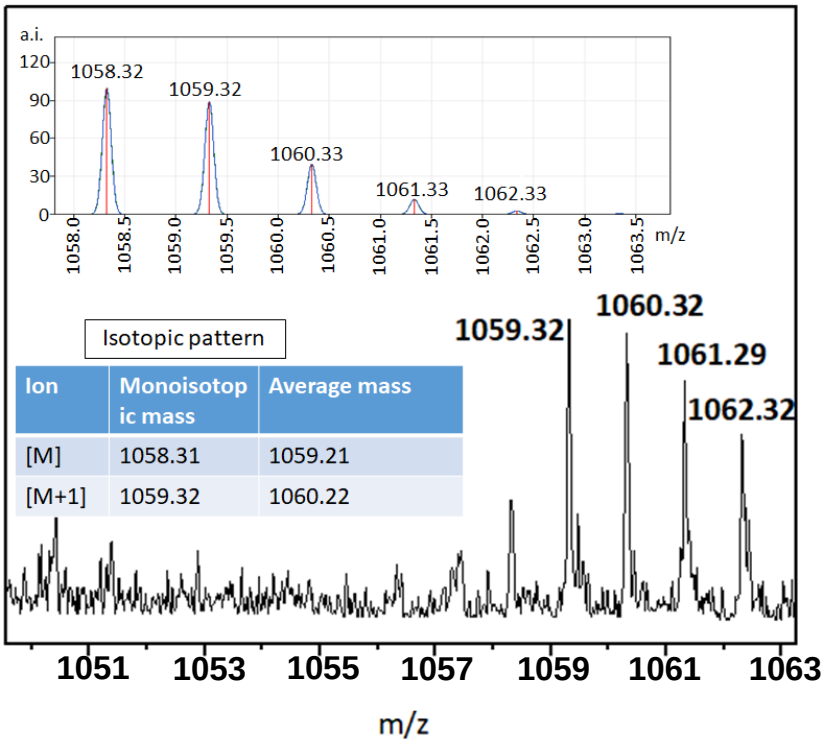

Ion	Monoisotopic mass	Average mass
[M]	1058.31	1059.21
[M+1]	1059.32	1060.22

Figure A 158*: Mass spectrum of 4PhAntpropCCMoid **19** (Positive mode).*

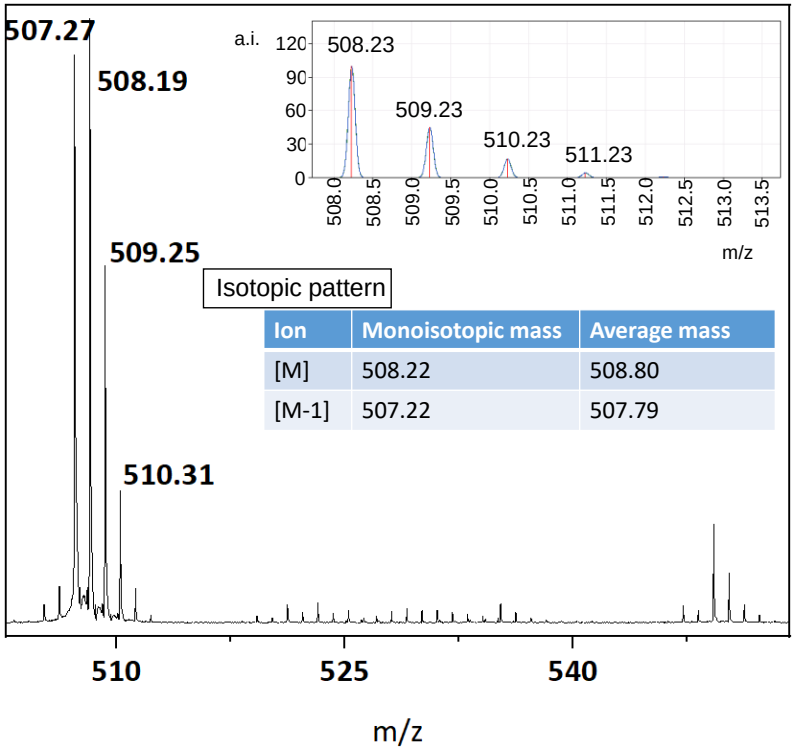

Ion	Monoisotopic mass	Average mass
[M]	508.22	508.80
[M-1]	507.22	507.79

Figure A 159: *Mass spectrum of AlkTMSallylCCMoid* ***21*** *(Negative mode).*

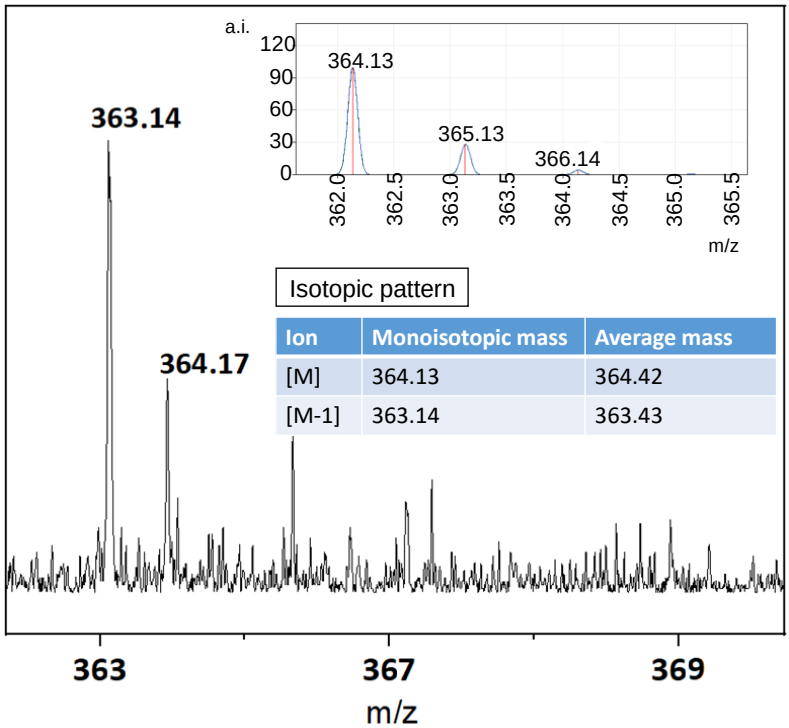

Ion	Monoisotopic mass	Average mass
[M]	364.13	364.42
[M-1]	363.14	363.43

Figure A 160*: Mass spectrum of AlkallylCCMoid* ***22*** *(Negative mode).*

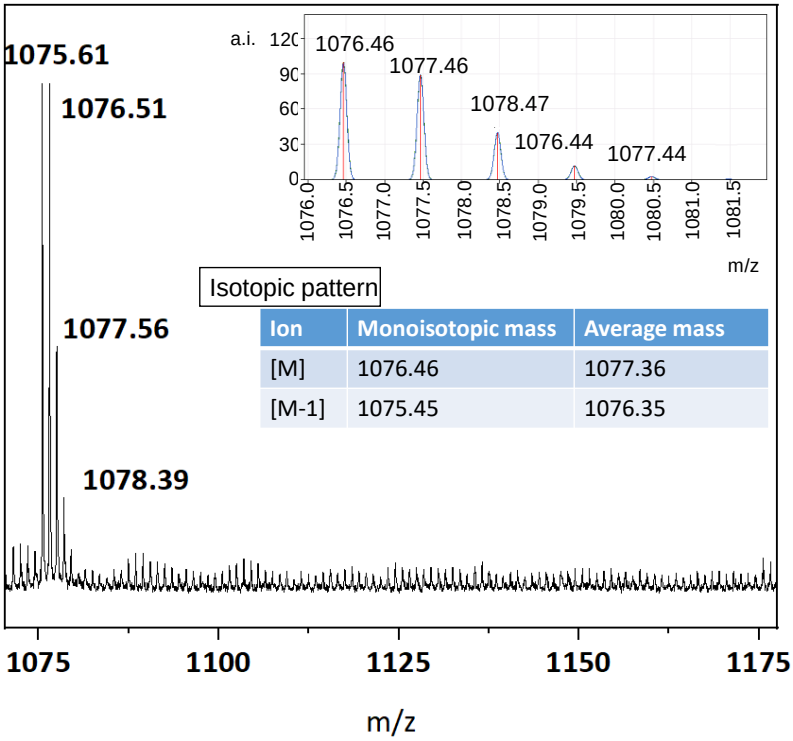

Ion	Monoisotopic mass	Average mass
[M]	1076.46	1077.36
[M-1]	1075.45	1076.35

***Figure A 161**: Mass spectrum of 10PhallylCCMoid **23** (Negative mode).*

Ion	Monoisotopic mass	Average mass
[M]	1060.33	1060.23
[M+1]	1061.34	1061.24

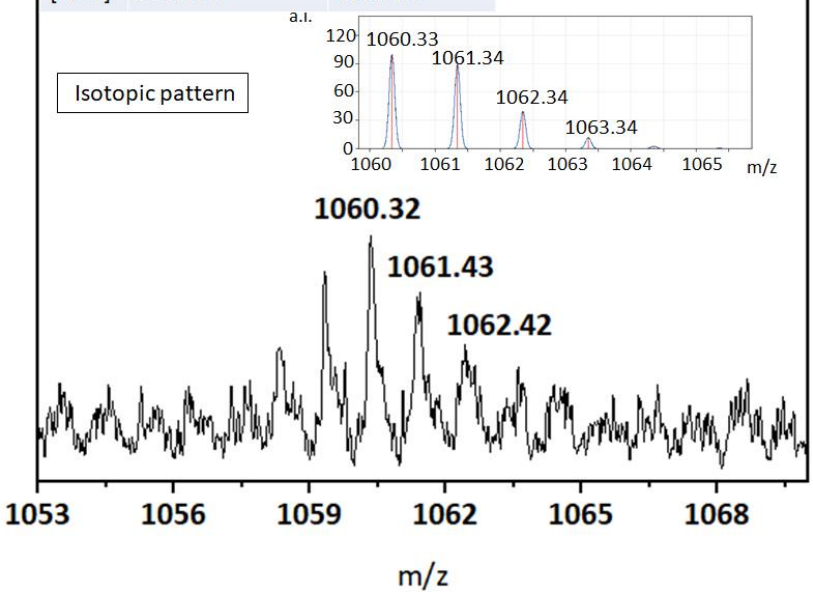

***Figure A 162:** Mass spectrum of 4PhAntallylCCMoid **24** (Positive mode).*

Thermogravimetric analysis spectra (TGA)

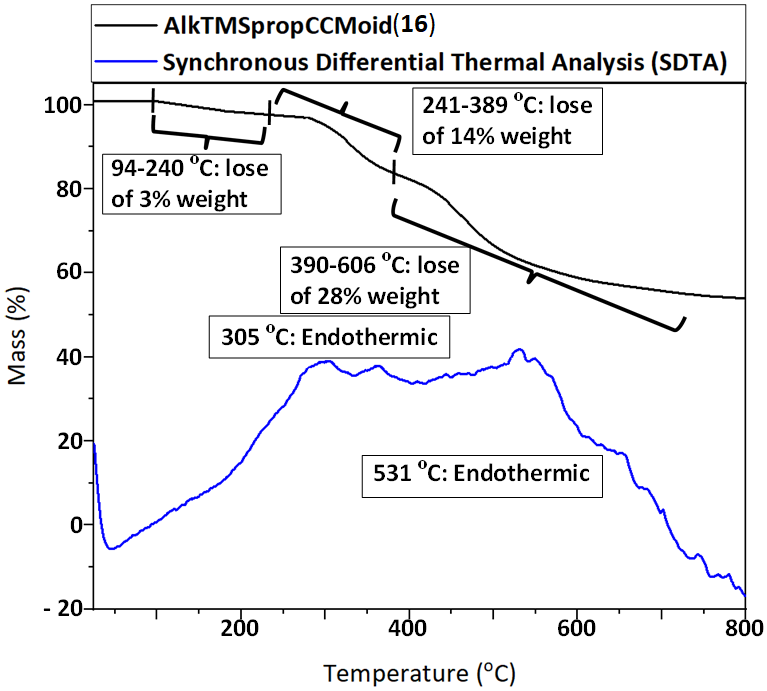

***Figure A 163**: TGA spectrum of AlkTMSpropCCMoid **16**.*

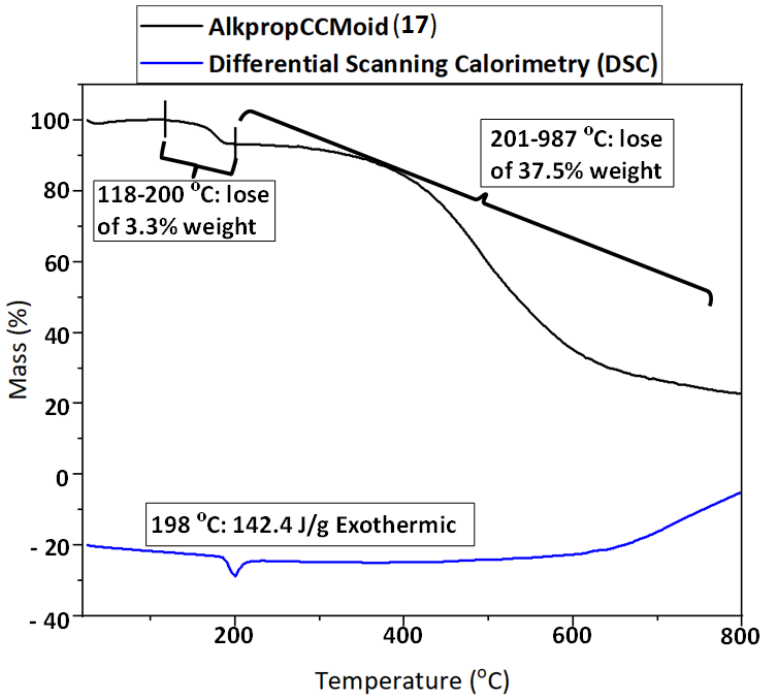

***Figure A 164**: TGA spectrum of AlkpropCCMoid **17**.*

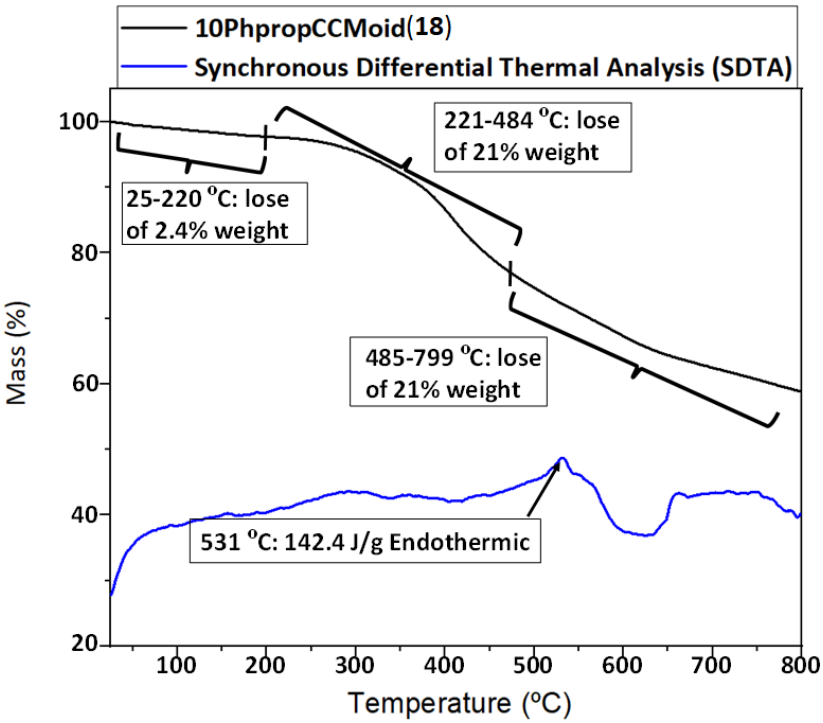

***Figure A 165**: TGA spectrum of 10PhpropCCMoid **18**.*

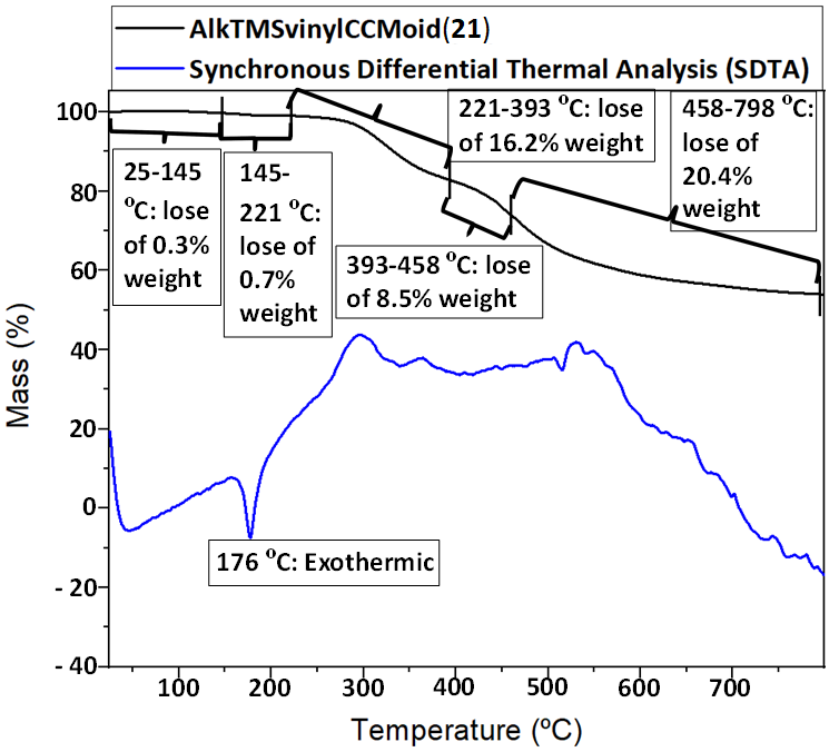

***Figure A 166**: TGA spectrum of AlkTMSallylCCMoid **21**.*

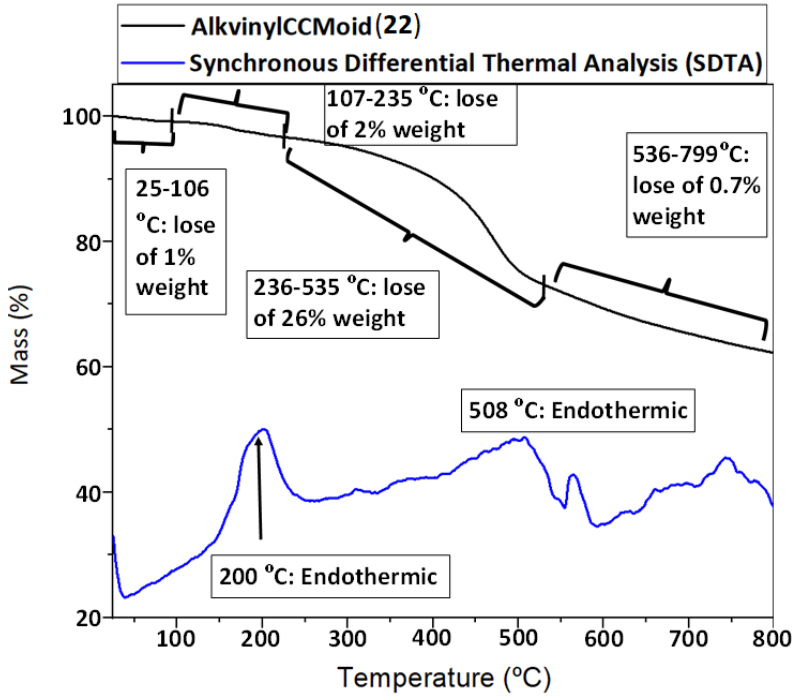

***Figure A 167**: TGA spectrum of AlkallylCCMoid **22**.*

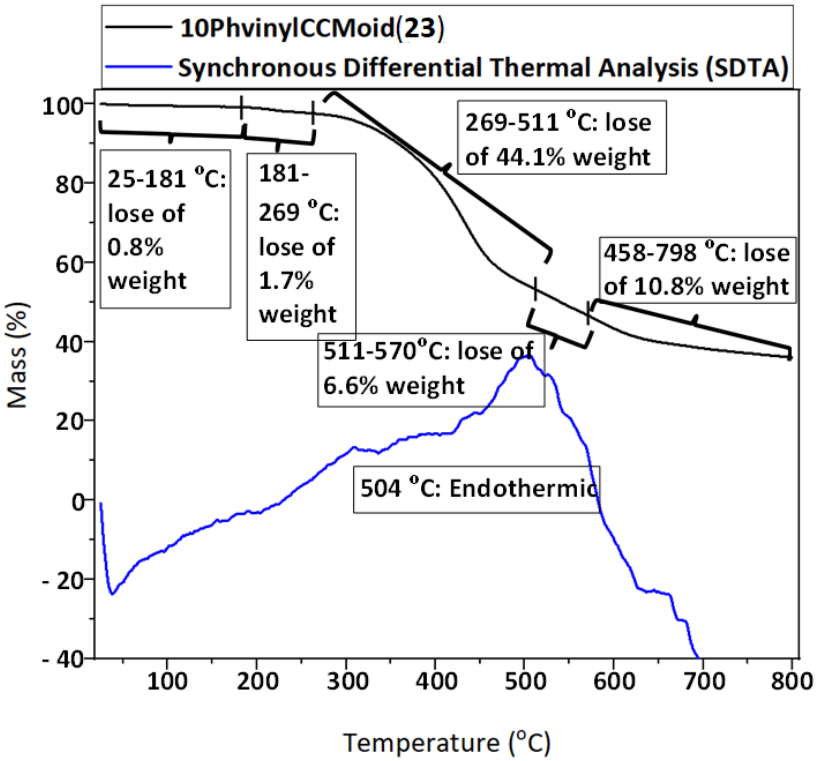

***Figure A 168**: TGA spectrum of 10PhallylCCMoid **23**.*

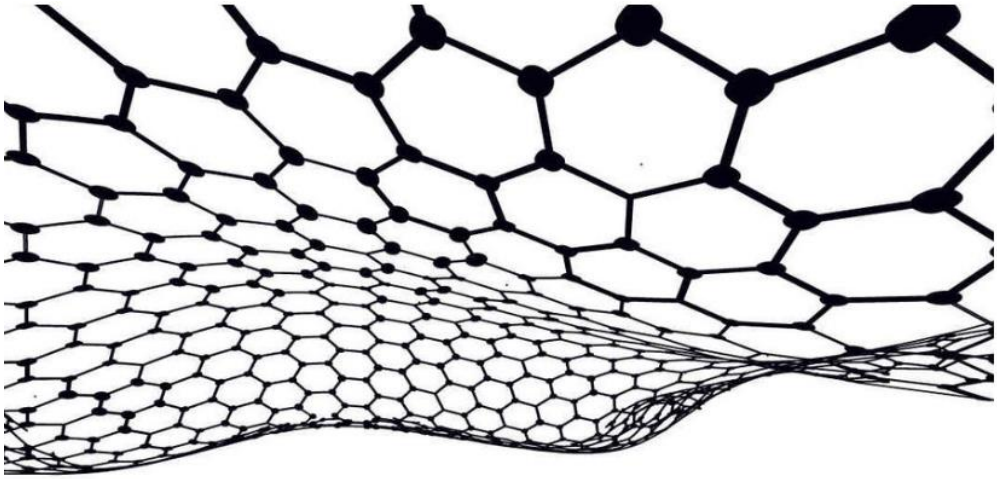

GENERAL

CONCLUSIONS

GENERAL CONCLUSIONS

Here, the general conclusions drawn from the studies elaborated in this thesis are summarized:

- The synthetic protocols proposed in the various chapters of this thesis have resulted in successful CCMoids of different nature, from the simplest, and small but highly reactive, to the most complicated, the T-shaped ones, all of them with reasonable yields. This way, for CCMoid **1**, its straightforward reaction presented a yield of 36% and the additional two-step reaction provided an overall yield of 32%. For the PAH-CCMoids (**5** and **7**), the three- and two-steps synthetic paths proposed provided overall yields of 27 and 31% yields, respectively. Finally, the most challenging T-shaped PAH-based CCMoids (**19** and **24**) the proposed five-step methodology gave total yields of 2% and 1%, respectively. Although at first sight, and in some cases, the final yields are low, it should be noted that the structural complexity/functionality/number of reaction steps ratio is optimal compared to other types of similar molecular systems (e.g. other CCMoids systems, porphyrins).

- Raman spectroscopy, UV-Vis, MS-MALDI-TOF, FTIR and XPS are the most powerful solid-state techniques for understanding the final systems, both their structure and properties. Considering the high insolubility of the final CCMoids **5**, **10**, **19** and **24**, respectively.

- The electrochemical and optical data in correlation with the structure of each CCMoid allowed the estimation of values for the energy bandgaps of all the CCMoids which are represented in **Figure 101**, the comparison of such values provided relevant information related to the electronic nature of the molecules and how it is affected by differences in the arms or the leg functionalization. For small CCMoids and those with non-planar and bulky aromatic systems (CCMoids **1**, **2**, **3**, **4**, **7**, **9**, **11**, **16**, **17**, **18**, **21**, **22** and **23**), the estimated HOMO-LUMO energy values are in the boundaries found for insulators-semiconductors molecular-based systems. However, the values obtained for the CCMoids with nanographene-like arms, **5**, **10**, **19** and **24**, respectively, are always < 2 eV, showing a more semiconducting behaviour. In addition, the coordination of the CCMoids with $-BF_2$

units through their keto-enol moieties (CCMoids **3**, **9**, **10** and **11**) promotes a reduction of the energy gap as well, conferring to the molecules a more semiconducting behaviour, which was also corroborated with previous reported works with such coordinating moiety. Finally, the comparison between the T-shaped CCMoids and those without the leg unit, showed that the first ones contain a larger energy bandgap than those without the leg. This difference could be explained as an interference of the leg with the CCMoid skeleton. Further theoretical studies will assist the corroboration of the data

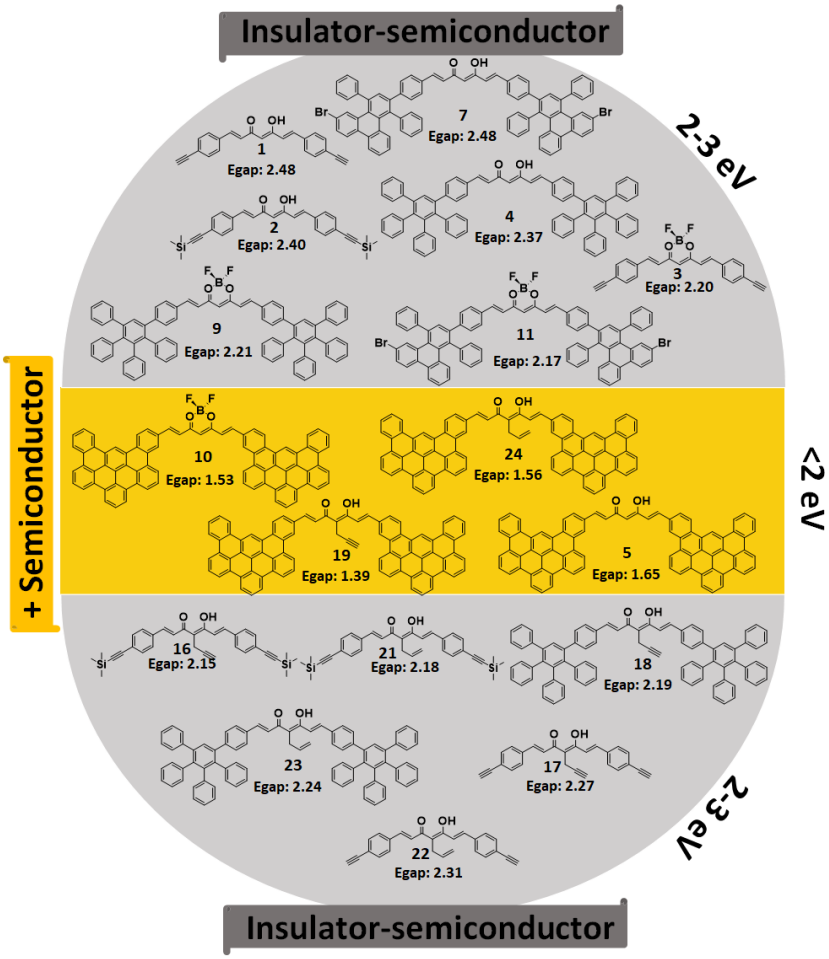

***Figure 101**: Schematic representation of the bandgap of the CCMoids in this thesis.*

- As an additional remark in this thesis, CCMoid **1** which could be sublimated, was deposited this way on Au (111) and Si/SiO_2 substrates obtaining thin and stable aggregates in short periods of time (<60

minutes). The deposition process was also investigated directly on a three-terminal hybrid device, by the use of a home-made sublimation device, and as a result, straightforward electrical measurements at ambient and also at vacuum conditions (<10^{-5} mbar) corroborated that: (i) the material showed an insulating behaviour, which similar values of conductivity and resistivity of the sublimated and single-crystal molecules. (ii) Due to its insulating behaviour, dielectric measurements manifested that no significant variations in conductivity were observed at either low or high frequencies. (iii) No temperature dependence of the conductivity was obtained after experiments heating from 15 ˚C to 55 ˚C, presenting only small and reversible variations. (iv) However, the irreversible increase in permittivity observed in the bulk of the sample was related to a structural change in the supramolecular morphology of **1**, supported by XRD analysis and DFT theoretical calculations. The above results and sublimation method used, to deposite directly our molecules on different substrates/devices have provide a straightforward and clair analysis on the electronic properties of **1**,.

- In addition, initial deposition on graphene surfaces of CCMoid **5** by drop-casting have been also performed showing the formation of big aggregates of this CCMoid on the surface, which resulted in some mechanical stress during evaporation of the solvent and consequently the deterioration of the substrate. The results indicated that further understanding on the deposition method and factors that may affect the substrate should be studied before moving to graphene-based three-terminal device.

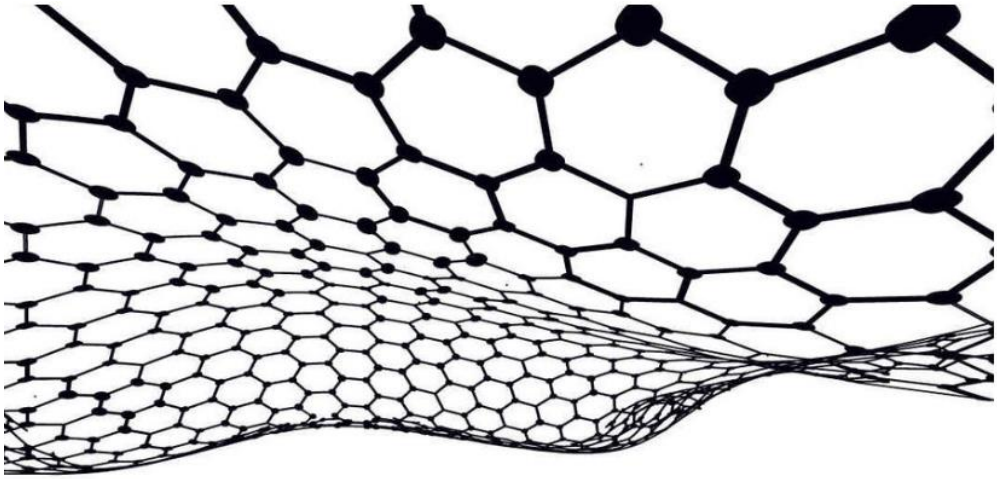

REFERENCES

REFERENCES

1. Y. Cao, R.X. Xu and Z. Liu. A high-throughput quantification method of curcuminoids and curcumin metabolites in human plasma via high-performance liquid chromatography/tandem mass spectrometry. *J.Chromatogr. B*. **2014**, 949-950, 70-78.
2. J.A. Lenhart, X. Ling, R. Gandhi, T.L. Guo, P.M. Gerk, D.H. Brunzell and S. Zhang. "Clicked" bivalent ligands containing curcumin and cholesterol as multifunctional Aβ oligomerization inhibitors: Design, synthesis, and biological characterization. *J. Med. Chem.* **2010**, 53 (16), 6198–6209.
3. D. Kalaitzakis, J.D. Rozzell, I. Smonou and S. Kambourakis. Synthesis of valuable chiral intermediates by isolated ketoreductases: Application in the synthesis of α-alkyl-β-hydroxy ketones and 1,3-diols. *Adv. Synth. Catal.* **2006**, 348 (14), 1958–1969.
4. Y. Manolova, V. Deneva, L. Antonov, E. Drakalska, D. Momekova and N. Lambov. The effect of the water on the curcumin tautomerism: A quantitative approach. *Spectrochim. Acta A Mol. Biomol. Spectrosc.* **2014**, 132, 815–820.
5. H. J. J. Pabon. A synthesis of curcumin and related compounds. *Rec. Trav. Chim. Pays Bas*. **1964**, 83 (4), 379–386.
6. U. Pedersen, P. B. Rasmussen, and S. O. Luwesson. Synthesis of Naturally Occurring Curcuminoids and Related Compounds. *Liebigs Ann. Chem*. **1985**, 1557-1569.
7. K.I. Priyadarsini. The chemistry of curcumin: From extraction to therapeutic agent. *Molecules*. MDPI AG, **2014**, 20091–20112.
8. H. Gopinath and K. Karthikeyan. Turmeric: A condiment, cosmetic and cure. *Indian J. Dermatol. Venereol. Leprol*. Wolters Kluwer Medknow Publications, **2018**, 16–21.
9. D. Bandyopadhyay. Farmer to pharmacist: curcumin as an anti-invasive and antimetastatic agent for the treatment of cancer. *Front. Chem.* **2014**, 2.
10. M. Vogel. On curcumine. *Lond. Edinb. Dublin philos. mag. j. sci*. **1842**, 21 (137), 233–234.
11. J. Miłobędzka, St. V. Kostanecki and V. Lampe. Zur Kenntnis des Curcumins. *Ber. Dtsch. Chem. Ges.* **1910**, 43 (2), 2163–2170.

12. V. Lampe and J. Milobedzka. Studien über Curcumin. *Ber. Dtsch. Chem. Ges.* **1913**, 46 (2), 2235–2240.
13. H. Steinberg and D.L. Hunter. Preparation and Rate of Hydrolysis of Boric Acid Esters. *Ind. Eng. Chem.* **1957**, 49 (2), 174–181.
14. P. J. Roughley and D. A. Whiting. Experiments in the Biosynthesis of Curcumin. *J. Chem. Soc.*, *Perkin Trans.* 1. **1973**, 2379.
15. H. W. D. Matthes, B. Luu and G. Ourisson. Cytotoxic Components of Zingiber Zerumbet, Curcuma Zedoarza and C. Domestica. *Phytochemistry*. **1980**, 19 (12), 2643-2650.
16. A. Mukhopadhyay, N. Basu, N. Ghatak and P.K. Gujral. Anti-inflammatory and irritant activities of curcumin analogues in rats. *Agents Actions*. **1982**, 12 (4), 508-515.
17. W. Wichitnithad, U. Nimmannit, S Wacharasindhu and P. Rojsitthisak. Synthesis, Characterization and Biological Evaluation of Succinate Prodrugs of Curcuminoids for Colon Cancer Treatment. *Molecules*. **2011**, 16, 1888-1900.
18. P. Cornago, P. Cabildo, D. Sanz, R.M. Claramunt, M. C. Torralba, M.R. Torres and J. Elguero. Structures of Hemi-Curcuminoids in the Solid State and in Solution. *Eur. J. Org. Chem*. **2013**, 27, 6043-6054.
19. P. Cornago, R.M. Claramunt, L. Bouissane, I. Alkorta and J. Elguero. A study of the tautomerism of b-dicarbonyl compounds with special emphasis on curcuminoids. *Tetrahedron*. **2008**, 64, 8089–8094.
20. E. Kim, A. Felouat, E. Zaborova, J.C. Ribierre, J.W. Wu, S. Senatore, C. Matthews, P.F. Lenne, C. Baffert, A. Karapetyan, M. Giorgi, D. Jacquemin, M. Ponce-Vargas, B. Le Guennic, F. Fages and A. D'Áleo. Borondifluoride complexes of hemicurcuminoids as bio-inspired push-pull dyes for bioimaging. *Org Biomol. Chem.* **2016**, 14 (4),1311-24.
21. M.A. Khan, R. El-Khatib, K.D. Rainsford and M.W. Whitehouse. Synthesis and anti-inflammatory properties of some aromatic and heterocyclic aromatic curcuminoids. *Bioorg. Chem.* **2012**, 40 (1), 30–38.
22. S.S. Ghosh, T.W.B. Gehr and S. Ghosh. Curcumin and chronic kidney disease (CKD): Major mode of action through stimulating endogenous intestinal alkaline phosphatase. *Molecules* **2014**, 19 (12), 20139–20156.
23. R.A. Sharma, A.J. Gescher and W.P. Steward. Curcumin: The story so far. *Eur. J. Cancer* **2005**, 41 (13), 1955–1968.

24. P. Anand, A.B. Kunnumakkara, R.A. Newman and B.B. Aggarwal. Bioavailability of curcumin: Problems and promises. *Molecular Pharmaceutics*. November 2007, pp 807–818.
25. D.K. Agrawal and P.K. Mishra. Curcumin and its analogues: Potential anticancer agents. *Med. Res. Rev.* **2010**, 30 (5), 818–860.
26. W. Wichitnithad, U. Nimmannit, P.S. Callery and P. Rojsitthisak. Effects of different carboxylic ester spacers on chemical stability, release characteristics, and anticancer activity of mono-PEGylated curcumin conjugates. *J. Pharm. Sci.* **2011**, 100 (12), 5206–5218.
27. Y. Ilieva, K. Kaloyanov, D. Yosifov, B. Robev, I. Zhelezova, M. Genova, A. Mihova, G. Balatzenko, M. M. Zaharieva, M. R. Berger, S. M. Konstantinov. Antineoplastic potential of curcumin (cooperative study in Bulgaria and Germany). *Phytochem. Rev.* **2014**, 13 (2), 459–469.
28. A. Pal, B. Sung, B.A.B. Prasad, P.T. Schubert, Jr, S. Prasad, B.B. Aggarwal and W.G. Bornmann. Curcumin glucuronides: Assessing the proliferative activity against human cell lines. *Bioorg. Med. Chem.* **2014**, 22 (1), 435–439.
29. B.B. Aggarwal, L. Deb and S. Prasad. molecules Curcumin Differs from Tetrahydrocurcumin for Molecular Targets, Signaling Pathways and Cellular Responses. *Molecules* **2015**, 20, 185–205.
30. A.B. Hegge, T.T. Nielsen, K.L. Larsen, E. Bruzell and H.H. Tønnesen. Impact of curcumin supersaturation in antibacterial photodynamic therapy-effect of cyclodextrin type and amount: Studies on curcumin and curcuminoides XLV. *J. Pharm. Sci.* **2012**, 101 (4), 1524–1537.
31. A.B. Hegge, E. Bruzell, S. Kristensen and H.H. Tønnesen. Photoinactivation of Staphylococcus epidermidis biofilms and suspensions by the hydrophobic photosensitizer curcumin - Effect of selected nanocarrier: Studies on curcumin and curcuminoides XLVII. *Eur. J. Pharm. Sci.* **2012**, 47 (1), 65–74.
32. F. Dai, W.-F. Chen, B. Zhou, L. Yang and Z.-L. Liu. Antioxidative effects of curcumin and its analogues against the free-radical-induced peroxidation of linoleic acid in micelles. *Phytother. Res.* **2009**, 23 (9), 1220–1228.
33. R. Ciochina, C. Savella, B. Cote, D. Chang and D. Rao. Synthesis and characterization of new curcumin derivatives as potential chemotherapeutic and antioxidant agents. *Drug. Dev. Res.* **2014**, 75 (2), 88–96.

34. M. Y. Khorasani, H. Langari, S. B. T. Sany, M. Rezayi and A. Sahebkar. The role of curcumin and its derivatives in sensory applications. Mat. Sci. Eng. C 2019, 103, 109792, 1-25.
35. K. Ponnuvel, K. Santhiya and V. Padmini. Curcumin based chemosensor for selective detection of fluoride and cyanide anions in aqueous media. Photochem. Photobiol. Sci. 2016,15, 1536.
36. E. Castro, M.R. Cerón, A.H. Garcia, Q. Kim, A. Etcheverry-Berrios, M.J. Morel, R. Díaz-Torres, W. Qian, Z. Martínez, L. Mendes, F. Perez, C.A. Santoyo, R. Gimeno-Muñoz, R. Esper, D.A. Gutierrez, A. Varela-Ramirez, R.J. Aguilera, M. Llano, M. Soler, N. Aliaga-Alcalde and L. Echegoyen. A new family of fullerene derivatives: Fullerene-curcumin conjugates for biological and photovoltaic applications. RSC Adv. 2018, 8 (73), 41692–41698.
37. F. Prins, A. Barreiro, J.W. Ruitenberg, J.S. Seldenthius, N. Aliaga-Alcalde, L.M.K. Vandersypen and H.S.J. van der Zant. Room-temperature gating of molecular junctions using few-layer graphene nanogap electrodes. Nano. Lett. 2011, 11 (11), 4607–4611.
38. E. Burzurí, J.O. Island, R. Díaz-Torres, A. Fursina, A. González-Campo, O. Roubeau, S.J. Teat, N. Aliaga-Alcalde, E. Ruiz and H.S.J. van der Zant. Sequential electron transport and vibrational excitations in an organic molecule coupled to few-layer graphene electrodes. ACS Nano. 2016, 10 (2), 2521–2527.
39. D. Riba-López, R. Zaffino, D. Herrera, R. Matheu, F. Silvestri, J.F. da Silva, E.C. Sañudo, M. Mas-Torrent, E. Barrena, R. Pfattner, E. Ruiz, A. González-Campo and N. Aliaga-Alcalde. Dielectric behaviour of curcuminoid polymorphs on different substrates by direct soft vacuum deposition. iScience 2022, 105686, 1-29.
40. L. Rodríguez-Cid, E.C. Sañudo, A.M. López-Periago, A. González-Campo, N. Aliaga-Alcalde and M.C. Domingo. Novel Zn(II) Coordination Polymers Based on the Natural Molecule Bisdemethoxycurcumin. Cryst. Growth Des. 2020, 20 (10), 6555–6564.
41. R. Díaz-Torres, M. Menelaou, A. González-Campo, S.J. Teat, E.C. Sañudo, M. S. Jaumá and N. Aliaga-Alcalde. Comparative magnetic studies in the solid state and solution of two isostructural 1D coordination polymers containing CoII/NiII-curcuminoid moieties. *Magnetochemistry* **2016**, 2 (3), 29.

42. N. Aliaga-Alcalde and L. Rodríguez. Solvatochromic studies of a novel Cd 2+-anthracene-based curcuminoid and related complexes. *Inor. Chim. Acta* **2012**, 380 (1), 187–193.
43. N. Aliaga-Alcalde, L. Rodríguez, M. Ferbinteanu, P. Höfer and T. Weyhermüller. Crystal structure, fluorescence, and nanostructuration studies of the first Zn II anthracene-based curcuminoid. *Inorg. Chem.* **2012**, 51 (2), 864–873.
44. M. Menelaou, F. Ouharrou, L. Rodríguez, O. Roubeau, S.J. Teat and N. Aliaga-Alcalde. DyIII- and YbIII-curcuminoid compounds: Original fluorescent single-ion magnet and magnetic near-IR luminescent species. *Chem. Eur. J.* **2012**, 18 (37), 11545–11549.
45. R. Díaz-Torres, M. Menelaou, O. Roubeau, A. Sorrenti, G. Brandariz-de-Pedro, E.C. Sañudo, S.J. Teat, J. Fraxedas, E. Ruiz and N. Aliaga-Alcalde. Multiscale study of mononuclear CoII SMMs based on curcuminoid ligands. *Chem. Sci.* **2016**, 7 (4), 2793–2803.
46. B.A. da Silva, P. Pitasse-Santos, V. Sueth-Santiago, A.R.M. Monteiro, R.K.F. Marra, G.P. Guedes, R.R. Ribeiro, M.E.F. de Lima, D. Decoté-Ricardo and A.P. Neves. Effects of Cu(II) and Zn(II) coordination on the trypanocidal activities of curcuminoid-based ligands. *Inorganica Chim. Acta* **2020**, 501, 119237.
47. A. Felouat, A. D'Aléo and F. Fages. Synthesis and photophysical properties of difluoroboron complexes of curcuminoid derivatives bearing different terminal aromatic units and a meso-aryl ring. *J. Org. Chem.* **2013**, 78 (9), 4446–4455.
48. N. Aliaga-Alcalde, P. Marqués-Gallego, M. Kraaijkamp, C. Herranz-Lancho, H. den Dulk, H. Görner, O. Roubeau, S.J. Teat, T. Weyhermüller and J. Reedijk. Copper curcuminoids containing anthracene groups: Fluorescent molecules with cytotoxic activity. *Inorg. Chem.* **2010**, 49 (20), 9655–9663.
49. I. Berlanga, Á. Etcheverry-Berríos, A. Mella, D. Jullian, A. Gómez, A. Victoria, N. Aliaga-Alcalde, V. Fuenzalida, M. Flores and M. Soler. Formation of self-assembled monolayer of curcuminoid molecules on gold surfaces. *Appl. Surf. Sci.* **2017**, 392, 834–840.
50. I.J. Olavarría-Contreras, A. Etcheverry-Berríos, W. Qian, C. Gutiérrez-Cerón, A. Campos-Oleguín, E.C. Sañudo, D. Dulić, E. Ruiz, N. Aliaga-Alcalde, M. Soler and H.S.J. van der Zant. Electric-field induced bistability in single-molecule conductance measurements for boron coordinated curcuminoid compounds. *Chem. Sci.* **2018**, 9 (34), 6988–6996.

51. R. Díaz-Torres. Doctoral thesis: Synthesis, characterization and deposition on surfaces of curcuminoids-based systems, University of Barcelona, **2018**.
52. D. Dulić, A. Rates, E. Castro, J. Labra-Muñoz, D. Aravena, A. Etcheverry-Berrios, D. Riba-López, E. Ruiz, N. Aliaga-Alcalde, M. Soler, L. Echegoyen and H.S.J. van der Zant. Single-Molecule Transport of Fullerene-Based Curcuminoids. *J. Phys. Chem. C* **2020**, 124 (4), 2698–2704.
53. A. González-Campo, M. Brasch, D.A. Uhlenheuer, A. Gómez-Casado, L. Yang, L. Brunsveld, J. Huskens and P. Jonkheijm. Supramolecularly oriented immobilitzation of proteins using Cucurbit[8]uril. *Langmuir.* **2012**, 28, 16364−16371.
54. Y. Gil, R. Gimeno-Muñoz, R. C. de Santana, N. Aliaga-Alcalde, P. Fuentealba, D. Aravena, A. González-Campo and E. Spodine. Luminiscence of macrocyclic mononuclear Dy^{III} complexes and their immobilitzation on functionalized silicon-based surfaces. *I*norg. Chem. **2022**, 61, 41, 16347–16355.
55. L. Rodríguez-Cid, W. Qian, J. Iribarra-Araya, A. Etcheverry-Berrios, E. Martínez-Olmos, D. Choquesillo-Lazarte, E.C. Sañudo, O.Roubeau, A.M. López-Periago, A. González-Campo, J.G. Planas, M. Soler, C. Domingo and N. Aliaga-Alcaled. Broadening the scope of high structural dimensionality nanomaterials using pyridine-based curcuminoids. *Dalton Trans.* **2021**, 50 (20), 7056–7064.
56. W. Qian. Doctoral thesis: Preparation and processing of molecular materials with optoelectronic properties, Institut de Ciència de Materials de Barcelona (ICMAB), Barcelona, **2018**.
57. J.O. Island, A. Holovchenko, M. Koole, P.F.A. Alkemade, M. Menelaou, N. Aliaga-Alcalde, E. Burzurí and H.S.J. van der Zant. Fabrication of hybrid molecular devices using multi-layer graphene break junctions. *J. Phys.: Condens. Matter.* **2014**, 26, 474205, 1-5.
58. A. Etcheverry-Berríos, I. Olavarría, M.L. Perrin, R. Díaz-Torres, D. Jullian, I. Ponce, J.H. Zagal, J. Pavez, S.O. Vásquez, H.S.J. van der Zant, D. Dulić, N. Aliaga-Alcalde and M. Soler. Multiscale Approach to the Study of the Electronic Properties of Two Thiophene Curcuminoid Molecules. *Chem. Eur. J.* **2016**, 22 (36), 12808–12818.
59. M.M. Waldrop. The chips are down for Moore's law. *Nature* **2016**, 530 (7589), 144–147.
60. J.R. Heath and M.A. Ratner. Molecular electronics. *Phys. Today* **2003**, 56 (5), 43–49.

61. D. Xiang, X. Wang, C. Jia, T. Lee and X. Guo. Molecular-Scale Electronics: From Concept to Function. *Chem. Rev*. American Chemical Society. **2016**, 4318–4440.
62. M. Ratner. A brief history of molecular electronics. *Nat. Nanotechnol* **2013**, 8 (6), 378–381.
63. J. M. Tour, W. A. Reinerth, L. Jones, T. P. Burgin, C. W. Zhou, C. J. Muller, M. R. Deshpande and M. A. Reed. Recent Advances in Molecular Scale Electronics. *Ann. N. Y. Acad. Sci.* **1998**, 852, 197−204.
64. J. R. Heath. Analytical Chemistry in Molecular Electronics. *Annu. Rev. Mater. Res*. **2009**, 39, 1−23.
65. C. R. Kagan and M. A. Ratner. Molecular Transport Junctions: An Introduction. *MRS Bull*. **2004**, 29, 376−384.
66. M. Tsutsui and M. Taniguchi. Single Molecule Electronics and Devices. *Sensors*. **2012**, 12 (6),7259-98.
67. N. Portolés-Gil, A. Lanza, N. Aliaga-Alcalde, J.A. Ayllón, M. Gemmi, E. Mugnaioli, A. M. López-Periago and C. Domingo. Crystalline Curcumin bioMOF Obtained by Precipitation in Supercritical CO2 and Structural Determination by Electron Diffraction Tomography. *ACS Sustain. Chem. Eng*. **2018**, 6 (9), 12309–12319.
68. H. Su, F. Sun, J. Jia, H. He, A. Wang and G. Zhu. A highly porous medical metal–organic framework constructed from bioactive curcumin. *Chem. Comm.* **2015**, 51 (26), 5774–5777.
69. D. Xiang, H. Jeong, T. Lee and D. Mayer. Mechanically controllable break junctions for molecular electronics. *Adv. Mater*. **2013**, 25 (35), 4845–4867.
70. B. Xu, J. Hamill and K. Wang. Characterizing molecular junctions through the mechanically controlled break-junction approach. *Reports in Electrochemistry.* **2014**, 4, 1-11.
71. K. Moth-Poulsen and T. Bjørnholm. Molecular electronics with single molecules in solid-state devices. *Nat. Nanotechnol.* **2009**, 4, 551–6
72. J.A. Mol, C.S. Lau, W.J.M. Lewis, H. Sadeghi, C. Roche, A. Cnossen, J.H. Warner, C.J. Lambert, H.L. Anderson and G.A.D. Briggs. Graphene-porphyrin single-molecule transistors. *Nanoscale* **2015**, 7 (31), 13181–13185.
73. P. Puczkarski, P. Gehring, C.S. Lau, J. Liu, A. Ardavan, J.H. Warner, G.A.D. Briggs and J.A. Mol. Three-terminal graphene single-

electron transistor fabricated using feedback-controlled electroburning. *Appl Phys Lett* **2015**, 107 (13).
74. E. Burzurí, F. Prins and H.S.J. van der Zant. Characterization of Nanometer-Spaced Few-Layer Graphene Electrodes. *Graphene* **2012**, 01 (02), 26–29.
75. P.T. Mathew and F. Fang. Advances in Molecular Electronics: A Brief Review. *Engineering* **2018**, 4 (6), 760–771.
76. J. Liu, Z. Yin, X. Cao, F. Zhao, A. Lin, L. Xie, Q. Fan, F. Boey, H. Zhang and W. Huang. Bulk heterojunction polymer memory devices with reduced graphene oxide as electrodes. *ACS Nano.* **2010**, 4 (7), 3987–3992.
77. C.A. Di, D. Wei, G. Yu, Y. Liu, Y. Guo and D. Zhu. Patterned graphene as source/drain electrodes for bottom-contact organic field-effect transistors. *Adv. Mater.* **2008**, 20 (17), 3289–3293.
78. X. Wang, L. Zhi and K. Müllen. Transparent, conductive graphene electrodes for dye-sensitized solar cells. *Nano. Lett.* **2008**, 8 (1), 323–327.
79. V. Berry. Impermeability of graphene and its applications. *Carbon*, **2013**, 62, 1-10.
80. R. Rieger and K. Müllen. Forever young: Polycyclic aromatic hydrocarbons as model cases for structural and optical studies. *J. Phys. Org. Chem.* **2010**, 23 (4), 315–325.
81. A. Luch. Carcinogenic Effects Polycyclic Aromatic Hydrocarbons; London, Imperial College Press; **2005**.
82. J. Wu, W. Pisula and K. Müllen. Graphenes as potential material for electronics. *Chem. Rev.* **2007**, 107 (3), 718–747.
83. X. Feng, V. Marcon, W. Pisula, M.R. Hansen, J. Kirkpatrick, F. Grozema, D. Andrienko, K. Kremer, K. Müllen. Towards high charge-carrier mobilities by rational design of the shape and periphery of discotics. *Nat. Mater.* **2009**, 8 (5), 421–426.
84. M.G. Schwab, A. Narita, Y. Hernandez, et al. Structurally defined graphene nanoribbons with high lateral extension. *J. Am. Chem. Soc.* **2012**, 134 (44), 18169–18172.
85. B. Limburg, J.O. Thomas, G. Halloway, H. Sadeghi, S. Sangtarash, I.C.Y. Hou, J. Cremers, A. Narita, K. Müllen, C.J. Lambert, G.A.D. Briggs, J.A. Mol and H.L. Anderson. Anchoring groups for graphene-porphyrin single-molecule transistors. *Adv. Funct. Mater*. **2018**, 1803629, 1-11.
86. Y. Li, X. Tu, H. Wang, S. Sanvito and S. Hou. First-principles investigation on the electronic efficiency and binding energy of the

contacts formed by graphene and poly-aromatic hydrocarbon anchoring groups. *J. Chem. Phys.* **2015**, 142 (16) 1-7.

87. H.S.J. van der Zant, Y.V Kervennic, M. Poot, K. O'Neill, Z. de Groot, J.M. Thijssen, H.B. Heersche, N. Stuhr-Hansen, T. Bjørnholm, D. Vanmaekelbergh, C.A. van Walree and L.W. Jenneskens. Molecular three-terminal devices: fabrication and measurements. *Faraday Discuss.* **2006**, 131, 347-356.
88. S. Caneva, P. Gehring, V.M. García-Suárez, A. García-Fuente, D. Stefani, I.J. Olavarría-Contreras, J. Ferrer, C. Dekker and H.S.J. van der Zant. Mechanically controlled quantum interference in graphene break-junctions. *Nat. Nanotech*. **2018**, 13, 1126–1131.
89. J. O. Thomas, B. Limburg, J.K. Sowa, K. Willick, J. Baugh, G.A.D. Briggs, E.M. Gauger, H.L. Anderson and J.A. Mol. Understanding resonant charge transport through weakly coupled single-molecule junctions. *Nat. Commun.* **2019**, 10, 1-9.
90. Y. Cao, S. Duong, S. Liu, L. He, L. Gan, X. Yu, M.L. Steigerwald, X. Wu, Z. Liu and X. Guo. Building high-throughput molecular junctions using indented graphene point contacts. *Angew. Chem. Int. Ed. Engl.* **2012**, 51 (49), 12228-12232.
91. C. Yang, A. Qin, B. Z. Tang and X. Guo. Fabrication and functions of graphene-molecule-graphene single-molecule junctions. *J. Chem. Phys*. **2020**, 152, 120902.
92. M. El Abbassi, S. Sangtarash, X. Liu, M. L. Perrin, O. Braun, C. Lambert, H. S. J. van der Zant, S. Yitzchaik, S. Decurtins, S.-X. Liu, H. Sadeghi and M. Calame. Robust graphene-based molecular devices. *Nat. Nanotech.* **2019**, 14, 957-961.
93. M.E. Abbassi, M.L. Perrin, G.B. Barin, S. Sangtarash, J. Overbeck, O. Braun, C.J. Lambert, Q. Sun, T. Prechtl, A. Narita, K. Müllen, P. Ruffieux, H. Sadeghi, R. Fasel, and M. Calame. Controlled Quantum-Dot Formation in AtomicallyEngineered Graphene Nanoribbons Field-Effect Transistors. *ACS Nano.* **2020**, 14, 5, 5754–5762.
94. O. Braun, J. Overbeck, M.E. Abbassi, S. Käser, R. Furrer, A. Olziersky, A. Flasby, G.B. Barin, Q. Sun, R. Darawish, K. Müllen, P. Ruffieux, R. Fasel, Shorubalko. M.L. Perrin and M. Calame. Optimized graphene electrodes for contacting graphene nanoribbons. *Carbon*. **2021**, 184, 331-339.

95. D. Aswal, S. Lenfant, D. Guerin, J. Yakhmi, and D. Vuillaume. Self-assembled monolayers on silicon for molecular electronics. *Anal. Chem. Acta*. **2006**, 568, 84–108.
96. S. A. DiBenedetto, A. Facchetti, M. A. Ratner and T. J. Marks, Molecular self-assembled monolayers and multilayers for organic and unconventional inorganic thin-film transistor applications. *Adv. Mater.* **2009**, 21 (14), 1407–1433.
97. A. V. Krasnoslobodtsev and S. N. Smirnov. Efect of water on silanization of silica by trimethoxysilanes. *Langmuir*. **2002**, 18 (8), 3181–3184.
98. D. Carrascal, V.M. García-Suáreza and J. Ferrer. Impact of edge shape on the functionalities of graphene-based single-molecule electronics devices. *Phys. Rev. B Condens. Matter. Mater Phys* **2012**, 85 (19).
99. L.M. Deck, L.A. Hunsaker, T.A.V. Jagt, L.J. Whalen, R.E. Royer and D.L.V. Jagt. Activation of anti-oxidant Nrf2 signaling by enone analogues of curcumin. *Eur. J. Med. Chem.* **2018**, 143, 854–865.
100. E. Ferrari, M. Asti, R. Benassi, F. Pignedoli and M. Saladini. Metal binding ability of curcumin derivatives: A theoretical vs. experimental approach. Dalton Trans. 2013, 42 (15), 5304–5313.
101. C.H. Görbitz and A. Mostad. Structural Studies of Curcuminoids. VII. Crystal and Molecular Structure of 1,7-diphenyl-4-propenyl-1,6-heptadiene-3,5-dione. Acta Chem. Scand. 1993, 47, 509–513.
102. P.Y. Bruice. Organic chemistry; Pearson Education, 2016.
103. S. Kawai, T. Yamaguchi, T. Kato, S. Hatano and J. Abe. Entropy-controlled thermal back-reaction of photochromic [2.2]paracyclophane-bridged imidazole dimer. Dyes Pigm. 2012, 92 (2), 872–876
104. T. Weil, U.M. Wiesler, A. Herrmann, R. Bauer, J. Hofkens, F.C. De Schryver and K. Müllen. Polyphenylene dendrimers with different fluorescent chromophores asymmetrically distributed at the periphery. *J. Am. Chem. Soc.* **2001**, 123 (33), 8101–8108.
105. T.H. Vo, M. Shekhirev, D.A. Kunkel, M.D. Morton, E. Berglund, L. Kong, P.M. Wilson, P.A. Dowben, A. Enders and A. Sinitskii. Large-scale solution synthesis of narrow graphene nanoribbons. *Nat Commun* **2014**, 5, 1–8
106. F. Albrecht, D. Rey, S. Fatayer, F. Schulz, D. Pérez, D. Peña and L. Gross. Intramolecular Coupling of Terminal Alkynes by Atom Manipulation. *Angew. Chem., Int. Ed. Engl.* **2020**, 59 (51), 22989–22993.

107. S. Ciampi, M. James, N. Darwish, E. Luais, B. Guan, J.B. Harper, and J.J. Gooding. Oxidative acetylenic coupling reactions as a surface chemistry tool. *Phys. Chem. Chem. Phys.* **2011**, 13 (34), 15624–15632.
108. H.Y. Gao, H. Wagner, D. Zhong, J.H. Franke, A. Studer and H. Fuchs. Glaser coupling at metal surfaces. *Angew. Chem., Int. Ed. Engl.* **2013**, 52 (14), 4024–4028.
109. D. Brunel, V. Jangid, E.S. Adaime, D. Duché, A.K. Bharwal, M. Abel, M. Koudia, T. Buffeteau, C. Lebouin and J.J. Simon. Click chemistry: An efficient tool to control the functionalization of metallic surfaces with alkyl chains possessing two reactive end groups. *Appl. Surf. Sci.* **2021**, 566, 150731.
110. T. Lummerstorfer and H. Hoffmann. Click Chemistry on Surfaces: 1,3-Dipolar Cycloaddition Reactions of Azide-Terminated Monolayers on Silica. *J. Phys. Chem. B* **2004**, 108 (13), 3963–3966.
111. J.F. Da Silva. University of Southampton. Master thesis: The Synthesis and Characterisation of Curcumin Derivatives for use in Single Molecule, Molecular Junctions, **2017**.
112. M. Menelaou, T. Weyhermüller, M. Soler and N. Aliaga-Alcalde. Novel paramagnetic-luminescent building blocks containing manganese(II) and anthracene-based curcuminoids. *Polyhedron* **2013**, 52, 398–405.
113. V.A. Reutov, E. v Gukhman and E.E. Kafitulova. Boron difluoride >-diketonates: III. 1 boron difluoride 3-organylpenta-2,4-dionates. *Russ. J. Gen. Chem.* **2003**, 73 (9), 1525–1528.
114. K. Kamada, T. Namikawa, S. Senatore, C. Matthews, P.F. Lenne, O. Maury, C. Andraud, M. Ponce-Vargas, B. Le Guennic, D. Jacquemin, P. Agbo, D.D. An, S.S. Gauny, X. Liu, R.J. Abergel, F. Fages and A. D'Áleo. Boron difluoride curcuminoid fluorophores with enhanced two-photon excited fluorescence emission and versatile living-cell imaging properties. *Chem. Eur. J.* **2016**, 22 (15), 5219-5232.
115. M. Rivoal, E. Zaborova, G. Canard, A. d'Áleo and F. Fages. Synthesis, electrochemical and photophysical studies of the borondifluoride complex of a meta-linked biscurcuminoid. *New J. Chem* **2016**, 40, 1297.
116. Á. Etcheverry Berríos. Universidad de Chile. Doctoral thesis: Diseño y síntesis de sistemas curcuminoides para aplicaciones en electrónica molecular, **2018**.
117. L. Rodríguez-Cid. Universitat Autònoma de Barcelona, ICMAB. Doctoral thesis: Synthesis and characterization of curcuminoids and their derived polymeric systems, **2021**.

118. H. Weiss, J. Reichel, H. Görls, K.R.A. Schneider, M. Micheel, M. Pröhl, M. Gottschaldt, B. Dietzek and W. Weigand. Curcuminoid–BF_2 complexes: Synthesis, fluorescence and optimization of BF_2 group cleavage. *Beilstein J. Org. Chem.* **2017**, 13, 2264–2272.
119. S. Bellinger, M. Hatamimoslehabadi, S. Bag, F. Mithila, J. La, M. Frenette, S. Laoui, D.J. Szalda, C. Yelleswarapu and J. Rochford. Photophysical and photoacoustic properties of quadrupolar borondifluoride curcuminoid dyes. *Chem. Eur. J.* **2018**, 24 (4), 906–917.
120. E. Pretsch, P. Bühlmann and M. Badertscher. Structure determination of organic compounds: Tables of spectral data; Springer Berlin Heidelberg, **2009.**
121. R.P. Sperline, W.B. Beaulieu and D.M. Roundhill. ^{1}H and ^{31}P nuclear magnetic resonance spectroscopy of substituted phosphinito and phosphite complexes of platinum (II). Analysis of the ^{31}P spectrum of an AA'BB'-AA'BB'X spin system showing second-order effects in coupling with ^{195}Pt. *Bull. Am. Phys. Soc* **1977**, 17 (7), 2032–2035.
122. B. Wrackmeyer and K. Horchler. Nmr parameters of alkynes; Pergamon Press plc. **1990**; Vol. 22.
123. L. Miloudi, F. Bonnier, D. Bertrand, H.J. Bryne, X. Perse, I. Chourpa and E. Munnier. Quantitative analysis of curcumin-loaded alginate nanocarriers in hydrogels using Raman and attenuated total reflection infrared spectroscopy. *Anal. Bioanal. Chem.* **2017**, 409 (19), 4593–4605.
124. T.M. Kolev, E.A. Velcheva, B.A. Stamboliyska and M. Spiteller. DFT and experimental studies of the structure and vibrational spectra of curcumin. *Int. J. Quantum Chem.* **2005**, 102 (6), 1069–1079.
125. B. Pan, J. Xiao, J. Li, P. Liu, C. Wang and G. Yang. Materials: Carbyne with finite length: The one-dimensional sp carbon. *Sci. Adv.* **2015**, 1 (9), 1-10.
126. Y. Chen, J.Q. Ren, X.G. Zhang, D.Y. Wu, A.G. Shen and J.M. Hu. Alkyne-modulated surface-enhanced raman scattering-palette for optical interference-free and multiplex cellular imaging. *Anal. Chem.* **2016**, 88 (12), 6115–6119.
127. H. Singh, Q. Shu, G. King, Z. Liang, Z. Wang, W. Cao, M. Huttula and T. Fabritius. Structure and viscosity of $CaO–Al_2O_3–B_2O_3–BaO$ slags with varying mass ratio of BaO to CaO. *J. Am. Ceram. Soc.* **2021**, 104 (9), 4505–4517.
128. A.K. Yadav and P. Singh. A Review of Structure of Oxide Glasses by Raman Spectroscopy. *RSC Adv.* **2015**, 5 (83), 67583-67609.

129. K. Nakamoto. Infrared and Raman Spectra of Inorganic and Coordination Compounds, 6th ed.; Wiley, Ed.; **2009.**
130. A.M. Abu-Dief, R. Díaz-Torres, E.C. Sañudo, L.H. Abdel-Rahman and N. Aliaga-Alcalde. Novel sandwich triple-decker dinuclear NdIII-(bis-N,N'-p- bromo-salicylideneamine-1,2-diaminobenzene) complex. *Polyhedron* **2013**, 64, 203–208.
131. L. Nardo, A. Andreoni, M. Masson, T. Haukvik and H.H. Tønnesen. Studies on curcumin and curcuminoids. XXXIX. Photophysical properties of bisdemethoxycurcumin. *J. Fluoresc.* **2011**, 21 (2), 627–635.
132. B.D. Viezbicke, S. Patel, B.E. Davis and D.P. Birnie. Evaluation of the Tauc method for optical absorption edge determination: ZnO thin films as a model system. *Phys. Status Solidi (B): Basic Res.* **2015**, 252 (8), 1700–1710.
133. J. Tauc. Optical Properties and Electronic Structure of Amorphous. *Mat. Res. Bull.* **1967**, 3, 37–46.
134. P. Makuła, M. Pacia and W. Macyk. How to correctly determine the band gap energy of modified semiconductor photocatalysts based on UV-Vis spectra. *J. Phys. Chem. Lett.* **2018**, 9 (23), 6814–6817.
135. A. Shafiee and M. Yahaya. Determination of HOMO and LUMO of [6,6]-Phenyl C61-butyric acid 3-ethylthiophene ester and poly (3-octyl-thiophene-2, 5-diyl) through voltametry characterization. *Sains Malays.* **2011**, 40 (2), 173–176.
136. Patent application filed out (22/02/2022), application number: P202230143 (Ref. Number: ES1641.1728). Title: Device for vacuum sublimation. Owner entity: Consejo Superior de Investigaciones Científicas (CSIC). https://www.csic.es/sites/www.csic.es/files/leaflet-af-012-2022-03-30.pdf / https://industry.icmab.es/ images/vacuum-sublimation-v.pdf.
137. Unit Manufacturing Processes Issues and Opportunities in Research; National Research Council, Washington, D.C., **1995.**
138. A.A. Dakhel, K.E. Jasim, S. Cassidy and F.Z. Henari. Extraction and dielectric properties of curcuminoid films grown on Si substrate for high-k dielectric applications. *Mater. Sci. Eng. B Solid State Mater. Adv. Technol.* **2013**, 178 (16), 1062–1067.
139. M.P. Hughes, K.D. Rosenthal, N.A. Ran, M. Seifrid, G.C. Bazan and T.Q. Nguyen. Determining the dielectric constants of organic photovoltaic materials using impedance spectroscopy. *Adv. Funct. Mater.* **2018**, 28 (32), 1801542.

140. D.W. Chang, H.J. Choi, A. Filer and J.B. Baek. Graphene in photovoltaic applications: Organic photovoltaic cells (OPVs) and dye-sensitized solar cells (DSSCs). *J. Mater. Chem. A* **2014**, 2 (31), 12136–12149.
141. N.F. Atta, A. Galal and E.H. El-Ads. Graphene — A Platform for Sensor and Biosensor Applications. *Biosensors - Micro and Nanoscale Applications*; InTechOpen, **2015.**
142. F. Chen, Q. Qing, J. Xia and N. Tao. Graphene field-effect transistors: Electrochemical gating, interfacial capacitance, and biosensing applications. *Chem. Asian J.* **2010**, 5 (10), 2144–2153.
143. D. Dasler, R.A. Schäfer, M.B. Minameyer, J.F. Hitzenberger, F. Hauke, T. Drewello and A. Hirsch. Direct covalent coupling of porphyrins to graphene. *J. Am. Chem. Soc.* **2017**, 139 (34), 11760–11765.
144. M. Garrido, M.K. Volland, P.W. Münich, L. Rodríguez-Pérez, J. Calbo, E. Ortí, M.A. Herranz, N. Martín and D.M. Guldi. Mono- and tripodal porphyrins: Investigation on the influence of the number of pyrene anchors in carbon nanotube and graphene hybrids. *J. Am. Chem. Soc.* **2020**, 142 (4), 1895–1903.
145. Z. Wang, Ž. Tomović, M. Kastler, R. Pretsch, F. Negri, V. Enkelmann and K. Müllen. Graphitic molecules with partial “Zig/Zag” periphery. *J. Am. Chem. Soc.* **2004**, 126 (25), 7794–7795.
146. P. Rempala, J. Kroulik and B.T. King. Investigation of the mechanism of the intramolecular Scholl reaction of contiguous phenylbenzenes. *J. Org. Chem.* **2006**, 71 (14), 5067–5081.
147. Y. Honjo, Y. Shibata, E. Kudo, T. Namba, K. Masutomi and K. Tanaka. Room temperature decarboxylative and oxidative [2+2+2] annulation of benzoic acids with alkynes catalyzed by an electron-deficient rhodium(III) complex. *Chem. Eur. J.* **2018**, 24 (2), 317–321.
148. A. Pradhan. Doctoral thesis: Distorted arenes by Scholl cyclizations, towards twisted carbon nanoribbons. Université Sciences et Technologies - Bordeaux I, **2013**.
149. A.J. Berresheim, M. Müller and K. Müllen. Polyphenylene nanostructures. *Chem. Rev.* **1999**, 99 (7), 1747–1785.
150. L. Zhai, R. Shukla, S.H. Wadumethrige and R. Rathore. Probing the arenium-ion (ProtonTransfer) versus the cation-radical (Electron Transfer) mechanism of scholl reaction using DDQ as oxidant. *J. Org. Chem.* **2010**, 75 (14), 4748–4760.
151. M.D. Watson, A. Fechtenkötter and K. Müllen. Big is beautiful - “Aromaticity” revisited from the viewpoint of macromolecular and supramolecular benzene chemistry. *Chem.l Rev.* **2001**, 101 (5),1267–1300.

152. R. Rathore and J.K. Kochi. Acid catalysis vs. electron-transfer catalysis via organic cations or cation-radicals as the reactive intermediate. Are these distinctive mechanisms? *Acta Chem. Scand.* **1998**, 52, 114–130.
153. R. Rathore and J.K. Kochi. Radical-cation catalysis in the synthesis of diphenylmethanes via the dealkylative coupling of benzylic ethers. *J. Org. Chem.* **1995**, 60 (23), 7479-7490.
154. O. Hammerich and V.D. Parker. Kinetics and mechanisms of reactions of organic cation radicals in solution. *Adv. Phys. Org. Chem.* **1984**, 20, 55–189.
155. S.H. Wadumethrige and R. Rathore. A facile synthesis of elusive alkoxy-substituted hexa-peri- hexabenzocoronene. *Org. Lett.* **2008**, 10 (22), 5139–5142.
156. B.T. King, J. Kroulík, C.R. Robertson, P. Rampala, C.L. Hilton, J.D. Korinek and L.M. Gortari. Controlling the Scholl reaction. *J. Org. Chem.* **2007**, 72 (7), 2279–2288.
157. R. Scholl and J. Mansfeld. Meso-benzdianthron (helianthron), meso-naphthodianthron, und ein neuer weg zum flavanthren. *Ber. Dtsch. Chem. Ges.* **1910**, 43 (2), 1734–1746.
158. W. Bradley and F.K. Sutcliffe. 225. The occurrence of direct hydroxylation and self-condensation in the action of potassium hydroxide on three isomeric benzo-derivatives of mesobenzanthrone. *J. Chem. Soc.* **1952**, 0, 1247-1251.
159. F.B. Mallory, C.S. Wood, J.T. Gordon, L.C. Lindquist and M.L. Savitz. Photochemistry of stilbenes. I. *J. Am. Chem. Soc.* **1962**, 84 (22), 4361–4362.
160. D.A. Scola. Dehydrocyclization of Aromatics: A convenient synthesis of triphenylene. *J. Chem. Eng. Data* **1964**, 9 (3), 405–405.
161. P.G. Copeland, R.E. Dean and D. McNeil. 339. The cyclodehydrogenation of o-terphenyl and 1,2′-biphenylyl-3,4-dihydronaphthalene. *J. Chem. Soc.* **1960**, 0 (0), 1687–1689.
162. C. Hansch and C. Geiger. Notes - A new synthesis for triphenylene. *J. Org. Chem.* **1958**, 23 (3), 477–478.
163. R. Rathore, S. v Lindeman and J.K. Kochi. Charge-transfer probes for molecular recognition via steric hindrance in donor-acceptor pairs. *J. Am. Chem. Soc.* **1997**, 119 (40), 9393-9404.
164. M. Saleh, M. Baumgarten, A. Mavrinskiy, T. Schäfer and K. Müllen. Triphenylene-based polymers for blue polymerie light emitting diodes. *Macromolecules* **2010**, 43 (1), 137–143.
165. B. Alameddine, R.S. Anju, F. Al-Sagheer and T.A. Jenny. Tribenzopentaphene derivatives with lateral aromatic groups: the

effect of the nature and position of substituents on emission properties. *New J. Chem.* **2016**, 40 (12), 10363–10370.
166. Y. Manabe, K. Wada, Y. Baba, T. Yoneda, T. Ogoshi and Y. Inokuma. Supramolecular Conformational Control of Aliphatic Oligoketones by Rotaxane Formation. *Org. Lett.* **2020**, 22 (8), 3224–3228.
167. M. Holler, T. Stoerkler, A. Louis, F. Fischer and J.F. Nierengarten. Mechanochemical solvent-free conditions for the synthesis of pillar[5]arene-containing [2]rotaxanes. *Eur. J. Org. Chem.* **2019**, 2019 (21), 3401–3405.
168. V.I. Spitsyn. Interaction of boron trifluoride with primary butylamine. *Zh. Neorg. Khim.* **1975**, 20 (1), 54–56.
169. W. Hendel, Z.H. Khan and W. Schmidt. Hexa-peri-benzocoronene, a candidate for the origin of the diffuse interstellar visible absorption bands? *Tetrahedron* **1986**, 42 (4), 1127–1134.
170. A.C. Ferrari and D.M. Basko. Raman spectroscopy as a versatile tool for studying the properties of graphene. *Nat. Nanotechnol.* **2013**, 8 (4), 235–246.
171. L. Escobar-Alarcón, M.E. Espinosa-Pesqueira, D.A. Solis-Casados, J. Gonzalo, J. Solis, M. Martínez-Orts and E. Haro-Poniatowski. Two-dimensional carbon nanostructures obtained by laser ablation in liquid: effect of an ultrasonic field. *Appl. Phys. A Mater. Sci. Process* **2018**, 124 (2), 1–7.
172. C. Sánchez-Sánchez, T. Dienel, A. Nicolaï, N. Kharche, L. Liang, C. Daniels, V. Meunier, J. Liu, X. Feng, K. Müllen, J.R. Sánchez-Valencia, O. Gröning, P. Ruffieux and R. Fasel. On-surface synthesis and characterization of acene-based nanoribbons incorporating four-membered rings. *Chem. Eur. J.* **2019**, 25 (52), 12074-12082.
173. L. Talirz, H. Söde, T. Dumslaff, S. Wang, J.R. Sánchez-Valencia, J. Liu, P. Shinde, C.A. Pignedoli, L. Liang, V. Munier, N.C. Plumb, M. Shi, X. Feng, A. Narita, K. Müllen, R. Fasel and P. Ruffieux. On-surface synthesis and characterization of 9-atom wide armchair graphene nanoribbons. *ACS Nano.* **2017**, 11 (2), 1380–1388.
174. D. Tuschel. Practical group theory and raman spectroscopy, Part I: normal vibrational modes; Spectroscopy Solutions for Materials Analysis, **2014.**
175. A.C. Ferrari and J. Robertson. Interpretation of raman spectra of disordered and amorphous carbon. *Phys. Rev. B* **2000**, 61 (20), 14095–14107.
176. R. Liu, H. Liu, Y. Li, Y. Yi, X. Shang, S. Zhang, X. Yu, S. Zhang, H. Cao and G. Zhang. Nitrogen-doped graphdiyne as a metal-free catalyst for high-

performance oxygen reduction reactions. *Nanoscale* **2014**, 6 (19), 11336–11343.
177. R. Blume, D. Rosenthal, J.P. Tessonnier, H. Li, A. Knop-Gericke and R. Schögl. Characterizing graphitic carbon with x-ray photoelectron spectroscopy: a step-by-step approach. *Chem. Cat. Chem.* **2015**, 7 (18), 2871–2881.
178. J.H. Cavka, S. Jakobsen, U. Olsbye, N. Guillou, C. Lamberti, S. Bordiga and K.P. Lillerud. A new zirconium inorganic building brick forming metal organic frameworks with exceptional stability. *J. Am. Chem. Soc.* **2008**, 130 (42), 13850–13851.
179. W.M.E.M.M. Daniyal, Y.W. Fen, J. Abdullah, H.S. Hashim, N.M. Fauzi, N. Chanlek and M.A. Mahdi. X-ray photoelectron study on gold/nanocrystalline cellulose-graphene oxide thin film as surface plasmon resonance active layer for metal ion detection. *Thin Solid Films* **2020**, 713, 138340.
180. J.F. Moulder, W.F. Stickle, P.E.' Sobol, K.D. Bomben and J. Chastain. Handbook of x-ray photoelectron spectroscopy a reference book of standard spectra for identification and interpretation of XPS data; Chastain, J., Ed.; **1993.**
181. G. Beamson and D. Briggs. High resolution XPS of organic polymers: the scienta ESCA300 database; Wiley J., & sons, Eds.; **1992.**
182. Y. Li and Z. Wang. Bis-N-annulated quaterrylene: An approach to processable graphene. *Org Lett* **2009**, 11 (6), 1385–1387.
183. E. Clair, C.T. Ironside and M. Zander. The electronic interaction between benzenoid rings in condensed aromatic hydrocarbons. 1:12-2.3-4.5-6:7-8:9-10:11-Hexabenzocoronene, 1:2-3:4-5:6-10:11-Tetrabenzoanthanthrene, and 4:5-6:7-11:12-13:14-Tetrabenzoperopyrene. *J. Chem. Soc.* **1958**, 142 (0), 142–147.
184. L. Giribabu, K. Sudhakar, G. Sabapathi and R.K. Kanaparthi. Intramolecular photoinduced reactions in corrole-pyrene and corrole-fluorene dyad systems. *J. Photochem. Photobiol A Chem.* **2014**, 284, 18–26.
185. C. Kittel. Introduction to Solid State Physics, 6th ed.; **1985**; Vol. 8.
186. Y. Liu, Y. Lv, X. Zhang, S. Chen, J.W.Y. Lam, P. Lu, R.T.K. Kwok, H.S. Kwok, X. Tao and B.Z. Tang. From a fluorescent chromophore in solution to an efficient emitter in the solid state. *Chem. Asian J.* **2012**, 7 (10), 2424–2428.
187. A. Goel, V. Kumar, S. Chaurasia, M. Rawat, R. Prasad and R.S. Anand. Synthesis, electrochemical and optical properties of stable yellow fluorescent fluoranthenes. *J. Org. Chem.* **2010**, 75 (11), 3656–3662.

188. Z.Y. Xia, J.H. Su, H.H. Fan, K.W. Cheah, H. Tian and C.H. Chen. Multifunctional diarylamine-substituted benzo[k]fluoranthene derivatives as green electroluminescent emitters and nonlinear optical materials. *J. Phys. Chem. C* **2010**, 114 (26), 11602–11606.
189. T. Yamamoto, A. Morita, Y. Miyazaki, T. Maruyama, H. Wakayama, Z. Zhen-Hua, Y. Nakamura, T. Kanbara, S. Sasaki and K. Kubota. Preparation of π-conjugated poly(thiophene-2,5-diyl), poly(p-phenylene), and related polymers using zerovalent nickel complexes. Linear structure and properties of the π-conjugated polymers. *Macromolecules* **1992**, 25 (4), 1214–1223.
190. T. H. Vo, M. Shekhirev, A. Lipatov, R. A. Korlacki and A. Sinitskii. Bulk properties of solution-synthesized chevron-like graphene nanoribbons. *Faraday Discuss* **2014**, 173, 105–113.
191. Y. Cao, S. Dong, S. Liu, Z. Liu and X. Guo. Toward functional molecular devices based on graphene-molecule junctions. *Angew. Chem. Int. Ed.* **2013**, 52, 3906–3910.
192. S. Zint, D. Ebeling, T. Schlöder, S. Ahles, D. Mollenhauer, H.A. Wegner and A. Schirmeisen. Imaging successive intermediate states of the on-surface Ullmann reaction on Cu(111): role of metal coordination. *ACS Nano*. **2017**, 11, 4183−4190.
193. H.Y. Gao, P.A. Held, M. Knor, C. Mück-Lichtenfeld, J. Neugebauer, A. Sruder and H.Fuchs. Decarboxylative polymerization of 2,6-naphtalenedicarboxylic acid at surfaces. *J. Am. Chem. Soc.* **2014**, 136, 9658−9663.
194. S. H. Mir, L. A. Nagahara, T. Thundat, P. Mokarian-Tabari, H. Furukawa and A. Khosla. Review—organic-inorganic hybrid functional materials: An integrated platform for applied technologies *J. Electrochem. Soc*. **2018**, 165 (8) B3137-B3156.
195. F. Dankert and C. von Hänisch. Siloxane Coordination Revisited: Si−O Bond Character, Reactivity and Magnificent Molecular Shapes. *Eur. J. Inorg. Chem*. **2021**, 29, 2907–2927.
196. F.G.A. Stone and D. Seyferth. The chemistry of silicon involving probable use of d-type orbitals; Pergamon Press Ltd, **1955**; Vol. I.
197. D.P. Craig, A. Maccoll, R.S. Nyholm, L.E. Orgel and L.E. Sutton. Chemical bonds involving d-orbitals. Part I. *J. Chem. Soc.,* **1954**, 0, 332-353.
198. R. West, L.S. Wilson and D.L. Powell. Basicity of siloxanes, alkoxysilanes and ethers toward hydrogen bonding. *J. Organomet. Chem*. **1979**, 178, 5-9.

199. W.A. Zisman. Surface chemistry of plastics reinforced by strong fibers. *Ind. Eng. Chem. Prod. Res. Dev*. **1969**, 8, 2, 98–111.
200. J. Sagiv. Organized monolayers by absorption. 1. Formation and structure of oleophobic mixed monolayers on solid surfaces. *J. Am. Chem. Soc.* **1980**, 102, 1, 92–98.
201. S. Giraldo, M.E. Alea-Reyes, D. Limón, A. González, M. Duch, J.A. Plaza, D. Ramos-López, J. de Lapuente, A. González-Campo and Ll. Pérez-García.π-donor/π-acceptor interactions for the encapsulation of neurotransmitters on functionalized polysilicon-based microparticles. *Pharmaceutics*. **2020**, 12, 724, 1-19.
202. L. Ye, A. González-campo, T. Kudernac, R. Nuñez, M.P. de Jong, W.G. van der Wiel and J. Huskens. Monolayer contact doping from a silicon oxide source substrate. *Langmuir*. **2017**, 33(15), 3635-3638.
203. A. González-Campo, S.H. Hsu, L. Puig, J. Huskens, D.N. Reinhoudt and A.H. Velders. Orthogonal covalent and noncovalent functionalization of cyclodextrin-alkyne patterned surfaces. *J. Am. Chem. Soc.* **2010**, 132, 11434–11436.
204. S. Giraldo. University Autonomous of Barcelona. Master thesis: Synthesis and characterization of new curcuminoid ligands for their immobilization on surfaces. **2014.**
205. R. Gimeno-Muñoz. University Autonomous of Barcelona. Doctoral thesis in progress.
206. C. Shih, Q. Shi and H.K. Wang. Compounds with (1e, 6e)-1,7-bis-(3,4-dimethoxyphenyl)-4,4-disstituted-hepa-1,6-diene-3,5-dione structural scaffold, their biological activity, and uses thereof. WO/2013/192091, **2013.**
207. Y.G. Borisova, G.Z. Raskildina and S.S. Zlotskii. Gem-dichlorocyclopropanes containing acetylacetone fragment in the side chain. *Russ. J. Gen. Chem*. **2016**, 2126–2128.
208. Z. Ali, S. Abdalla, E.A. Hassan, Y. Umar and M.M. Al-Mogren. Theoretical study of electronic and optical properties of functionalized Indigo and Alizarin as potential organic semi-conductors for solar cells applications. *Mat. Tod. Comm.* **2022**, 32, 104048.
209. M.B.A. Siddique, R. Hussain, S.A. Siddique, M.Y. Mehboob, Z. Irshad, J. Iqbal and M. Adnan. Designing triphenylamine-configured donor materials with promising photovoltaic properties for highly efficient organic solar cells. *Chem. Sel.* **2020**, 5 (25), 7358–7369.
210. L. N. Lewis, K. G. Sy, G. L. Bryant, Jr., and P. E. Donahue. Platinum-catalyzed hydrosilylation of alkynes. *Organometallics*, **1991**, 10 (10), 3750-3759.

211. A. Ferrer-Ugalde, A. González-Campo, C. Viñas, J. Rodríguez-Romero, R. Santillan, N.Farfan, R. Sillanpää, A. Sousa-Pedrares, R. Núñez and F. Teixidor. Fluorescence of new o-carborane compounds with different fluorophores: can it be tuned?. *Chem. Eur. J.* **2014**, 20, 9940 – 9951.
212. L.N. Lewis. On the mechanism of metal colloid catalyzed hydrosilylation: proposed explanations for electronic effects and oxygen cocatalysis; **1990**; Vol. 112.
213. M. Planellas, W. Guo, F. Alonso, M. Yus, A. Shafir, R. Pleixats and T. Parella. Hydrosilylation of internal alkynes catalyzed by tris-imidazolium salt-stabilized palladium nanoparticles. *Adv. Synth. Catal*. **2014**, 356 (1), 179–188.
214. D.-W. Chung and T.G. Kim. Solvent effect on the hydrosilylation reactions for the synthesis of polydimethylsiloxane grafted with polyoxyethylene catalyzed by speier's catalyst; **2007**; Vol. 13.
215. W. Wu, X.Y. Zhang, S.X. Kang and Y.M. Gao. Tri(t-butyl)phosphine-assisted selective hydrosilylation of terminal alkynes. *Chin. Chem. Lett.* **2010**, 21 (3), 312–316.
216. A. Franczyk, K. Stefanowska, M. Dutkiewicz, D. Frąckowiak and B. Marciniec. A highly selective synthesis of new alkenylsilsesquioxanes by hydrosilylation of alkynes. *Dalton Trans.* **2017**, 46 (1), 158–164.

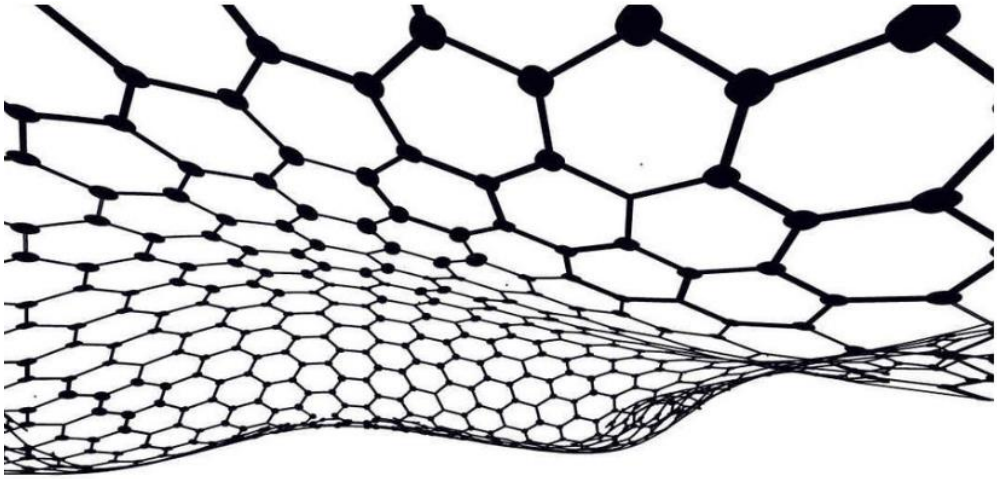

APPENDIX IV

iScience

CellPress
OPEN ACCESS

Article

Dielectric behavior of curcuminoid polymorphs on different substrates by direct soft vacuum deposition

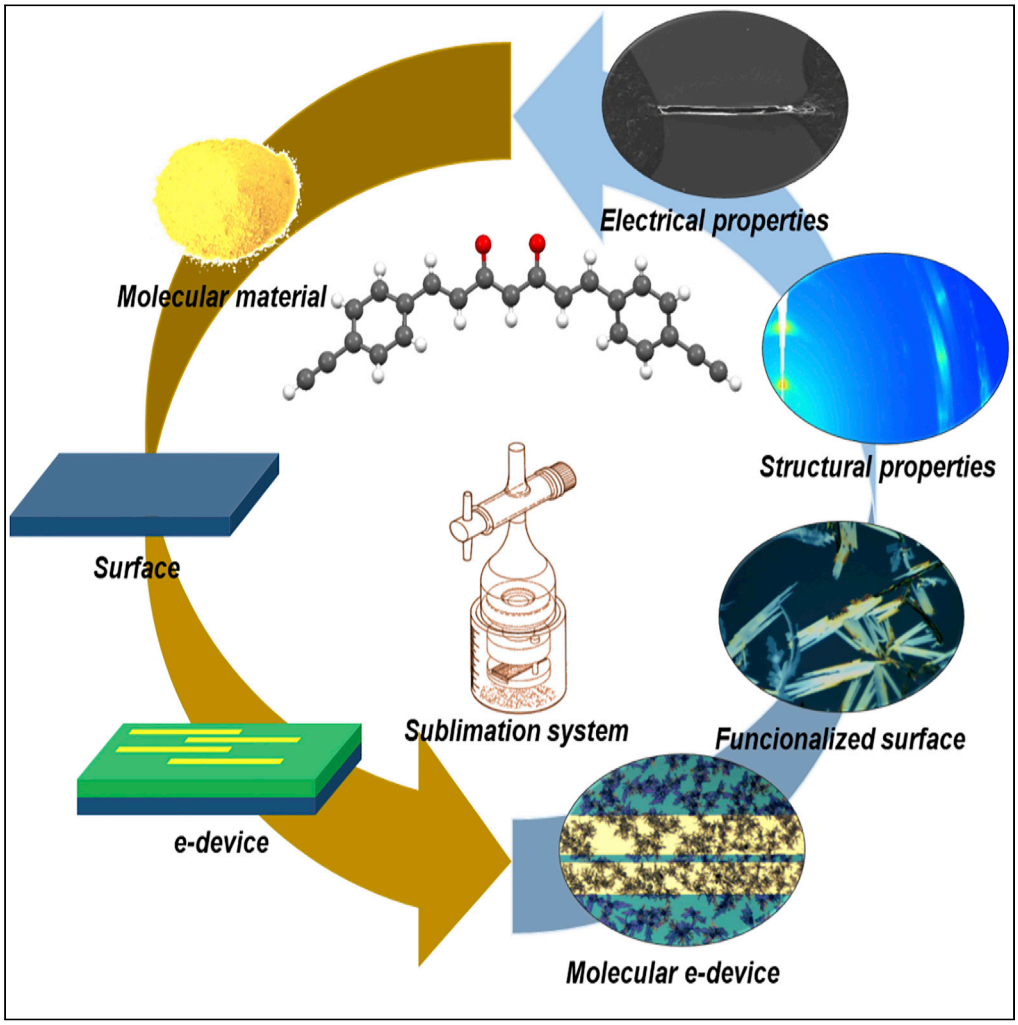

Daniel Riba-López, Rossella Zaffino, Daniel Herrera, ..., Eliseo Ruiz, Arántzazu González-Campo, Núria Aliaga-Alcalde

rpfattner@icmab.es (R.P.)
agonzalez@icmab.es (A.G.-C.)
nuria.aliaga@icrea.cat (N.A.-A.)

Highlights

A new curcuminoid with triple bonds ending groups shows dielectric behavior

Direct sublimation of the curcuminoid on substrates is achieved under mild conditions

Structural-electronic correlation on surfaces is a strong analytical tool

Permittivity is greatly affected by polymorphism

Riba-López et al., iScience *25*, 105686
December 22, 2022
https://doi.org/10.1016/j.isci.2022.105686

iScience

CellPress
OPEN ACCESS

Article

Dielectric behavior of curcuminoid polymorphs on different substrates by direct soft vacuum deposition

Daniel Riba-López,[1,7] Rossella Zaffino,[1,7] Daniel Herrera,[1] Roc Matheu,[2,3] Francesco Silvestri,[1] Jesse Ferreira da Silva,[1,4] Eva Carolina Sañudo,[3,5] Marta Mas-Torrent,[1] Esther Barrena,[1] Raphael Pfattner,[1,*] Eliseo Ruiz,[2,3] Arántzazu González-Campo,[1,*] and Núria Aliaga-Alcalde[1,6,8,*]

SUMMARY

Our work examines the structural-electronic correlation of a new curcuminoid, AlkCCMoid, as a dielectric material on different substrates. For this purpose, we show a homemade sublimation method that allows the direct deposition of molecules on any type of matrix. The electronic properties of AlkCCMoid have been evaluated by measurements on single crystals, microcrystalline powder, and sublimated samples, respectively. GIWAXS studies on surfaces and XRD studies on powder have revealed the existence of polymorphs and the effect that substrates have on curcuminoid organization. We describe the dielectric nature of our system and identify how different polymorphs can affect electronic parameters such as permittivity, all corroborated by DFT calculations.

INTRODUCTION

The practical use of molecules as active components in electronic devices depends on the intrinsic electronic properties of the molecular system under study and their assembly in the solid state. For realistic applications, the substrate on which the molecules are deposited plays an important role as it influences molecular growth and ordering. As a result, new polymorphic forms can develop, which are often not observed in bulk single-crystals.[1–4] To ensure robust and efficient molecular elements, regardless of their electronic behavior, it is necessary to understand the impact that the assembly and substrate have on the parameters governing their final electronic properties.[5–7] This is in line with the study of new materials, analyzing in detail their structure-properties correlation, and the use of simple methods for their manipulation, with the aim of identifying and redesigning low-cost, environmentally friendly and high-performance molecular systems at the nano- and micro-scale.[8]

Curcuminoids (CCMoids) are a family of molecules extensively studied in the field of biomedicine, the best known of which is curcumin.[9] A large number of such systems and simple methodologies for their synthesis are now available,[10,11] together with reports on their physicochemical properties.[12–17] The versatility in their design is remarkable, functioning as molecular platforms, where variations in the different parts (central skeleton, diketone moiety, and aromatic groups, Figure 1A top) give rise to new structural compositions, with modified biological, optical and electronic behavior.[18] These diarylheptanoid systems are dyes, readily coordinate with transition metals and metalloids,[19,20] and often exhibit solvatochromic properties.[21] This has led to an expansion of the use of CCMoids in other areas of nanoscience and nanotechnology, attracting attention as key components in coordination polymers (CPs),[22] MOFs[17,23] and photovoltaic cells,[24,25] among others. In relation to the field of molecular electronics, CCMoids have been studied mainly in solution, showing band gap values of the order of 2-3 eV,[13,26] tuned through the coordination of the β-diketone group and the nature of the aromatic sides. As far as electronic devices are concerned, there are only a few examples reported with curcumin and coordinated systems, listed as appealing for ecofriendly applications in the framework beyond-CMOS devices,[27] although it is important to note that there has been increasing interest in boron difluoride CCMoids due to their potential optoelectronic applications.[28–30] Taking into account CCMoids structural diversity, their projection in molecular-based electronics is promising, but still limited,[27–36] with an increasing need to gather information and improve designs. Beyond their use as an active layer in electronic devices, wide band gap materials can be of interest as a dielectric in capacitors and transistors combined with different electronic elements.[37] In

[1]Institut de Ciència de Materials de Barcelona (ICMAB-CSIC) Campus Universitari, 08193 Bellaterra, Spain

[2]Institut de Recerca de Química Teòrica i Computacional, Universitat de Barcelona, Diagonal 645, 08028 Barcelona Spain

[3]Departament de Química Inorgànica i Orgànica, Universitat de Barcelona, C/Martí i Franqués 1-11, 08028 Barcelona, Spain

[4]University of Southampton, Chemistry, Highfield, Southampton, UK

[5]Institut de Nanociència i Nanotecnologia. Universitat de Barcelona, Av. Diagonal 645, 08028 Barcelona, Spain

[6]ICREA (Institució Catalana de Recerca i Estudis Avançats) Passeig Lluïs Companys 23, 08010 Barcelona, Spain

[7]These authors contributed equally

[8]Lead contact

*Correspondence: rpfattner@icmab.es (R.P.), agonzalez@icmab.es (A.G.-C.), nuria.aliaga@icrea.cat (N.A.-A.)

https://doi.org/10.1016/j.isci.2022.105686

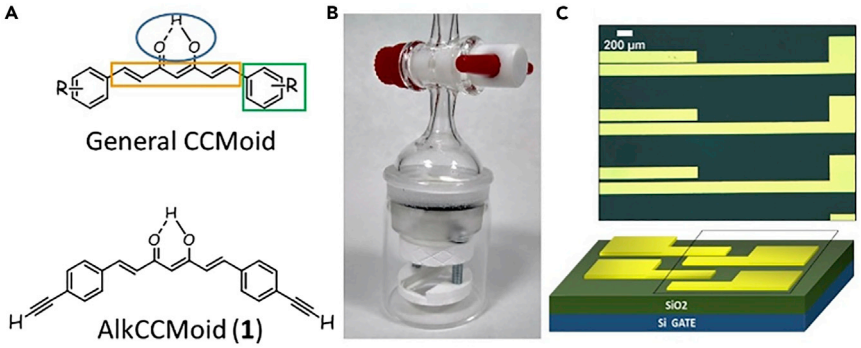

Figure 1. Illustration of molecules, sublimation system, and FET device

(A) Top. ChemDraw scheme of a general symmetric CCMoid (highlighting the β-diketone group, CCMoid skeleton, and aromatic groups in blue, orange, and green, respectively). Bottom. ChemDraw scheme of AlkCCMoid (1).

(B) Picture of the custom-designed sublimation system used in this work.

(C) Pictures of three-terminal devices on Si/SiO_2 substrate containing source and drain electrodes made of Au.

this regard, stable films of organic molecules with insulating properties, which can be easily deposited on a substrate by sublimation, could provide an environmentally sustainable alternative to standard oxides and insulators used in the manufacture of metal-insulator-semiconductor (MIS) and metal-oxide-semiconductor (MOS) devices. Some of us have performed single-molecule electronic transport studies using CCMoids as nanowires, by electrical controlled break junction (BJ) and mechanically controlled break junction (MCBJ) techniques, with conductance values on the order of other small, conjugated molecules; some CCMoids have been studied at room temperature in hybrid graphene devices and in other cases the critical factors for them to show electric-field induced bistability have been identified.[31–35]

Here we show a new synthetic CCMoid, the AlkCCMoid (1, Figure 1A bottom), highlighting its electrochemical and crystalline properties, focusing on its deposition studies. To avoid solvent interference, we exploited its ability to sublimate crystallizing on different surfaces and identify the conditions under which the system polymerizes. For that, we developed a homemade setup (patent pending, Figure 1B) which presents the advantage of carrying the sublimation directly on surfaces, under mild conditions (STAR Methods). The electrical performance of 1 was examined using microcrystalline powder (1-MP), single crystals (1-SC) and, sublimated material (1-SUB) on three-terminal devices containing Si/SiO_2/Au electrodes (Figure 1C) and related substrates (Au and Si/SiO_2). The analyses of the different crystalline phases were performed using powder XRD (X-ray Diffraction) and GIWAXS (Grazing Incidence Wide Angle X-ray Scattering) techniques. Focusing on the Si/SiO_2 substrates, we compared the diffraction patterns of 1 and evaluated supramolecular changes caused by temperature and sublimation, with the help of DFT calculations, identifying variations in the permittivity of the microcrystalline powder.

RESULTS AND DISCUSSION

AlkCCMoid (1) was synthesized, as a microcrystalline powder (1-MP), following a modification of the Pabonś method[10] according to the procedure shown in Scheme in STAR Methods, using MeCN as precipitating solvent. The experimental section is reported in detail in the SI. 1-MP was analyzed in solution by $^{1}H/^{13}C$ NMR (Figures S1 and S2) and additional techniques (UV-Vis absorption, IR, MALDI, and EA, Figures S5, S6, and S8), showing the expected CCMoid features. The optical band gap of 1-MP was assessed by solid UV-Vis absorption spectroscopy (KBr pellets, Figures S10 and S11, due to the already known solvatochromic behavior of CCMoids)[36,38–41] and the electrochemical energy gap, using CV (cyclic voltammetry, Figure S12).[42] Both measurements display an approximated value of 2.4 eV, corresponding to a behavior close to the boundary of a semiconductor/insulator material.[43] Table S1 shows a summary of the data.

Single crystals of AlkCCMoid (1-SC) were obtained by slow diffusion by dissolving 1-MP in an EtOAc/Hexanes mixture and used to determine the structure by single crystal X-ray diffraction.[15,19,36] 1-SC crystallizes in the monoclinic space group *Cc*. Figure 2A shows its structure and packing characteristics with the most significant crystallographic parameters listed in Table S2. Within the molecule, the C=O/C-OH

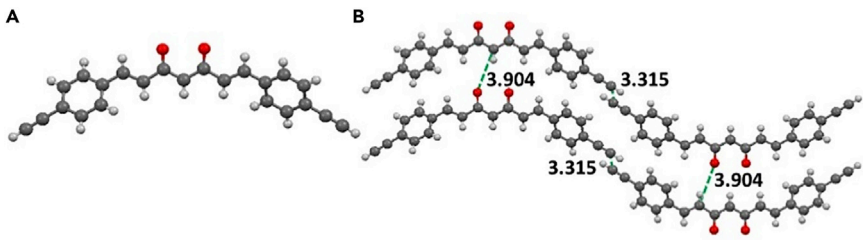

Figure 2. Molecular unit and packing motifs of AlkCCMoid (1)
(A) Molecular structure of 1-SC and (B) supramolecular packing. C atoms are in dark grey, O in red, and H in light gray, respectively. Depicted distances are in Angstrom (Å).

distances of the diketone moiety appear averaged (1.294 Å) and alternating C-C and C=C distances in the linear skeleton between 1.345 and 1.464 Å. As expected, the terminal alkyne groups exhibit the shortest distances, with C≡C lengths of 1.200 Å. The entire molecule presents a smooth sinusoidal shape due to the twisting of the aromatic rings and triple bonds from the plane of the backbone of the molecule, displaying a total length of 20.74 Å (H···H). The supramolecular arrangement shows the combination of two networks of molecular units in opposite directions (Figure 2B), with intermolecular interactions between the units in the same direction through O atoms from the β-diketone moiety of one molecule and the methine group (H-C) of the neighbor further ahead, with distances of 3.904 Å and angles close to 155°, and additional interactions arising through the triple bonds between molecules in opposite directions (C-C distances of 3.315 Å, Figure 2) creating 2D supramolecular networks.

In addition, 1-MP sublimates at 160 °C and 1 mbar of pressure, agreeing well with the thermogravimetric analysis (TGA) and differential scanning calorimetry (DSC, Figure S15). Taking this into account, we directly deposited our CCMoid onto Au(111) and Si/SiO_2 surfaces (1-SUB) using our specially designed sublimation system (Figure 1B and STAR Methods). Briefly, the solid is added to the bottom of a ground glass vessel, which is coupled to a stopcock adapter connected to a vacuum pump. Inside, a cylinder acting as a frame supports the surface to be studied, orienting it toward the solid. We carried out our experiments by fixing the distance between the solid and substrate, as well as the temperature, at 160 °C, while studying the effect of time (1, 2, 6, and 24 h) on the deposition process by Raman spectroscopy and Scanning Electron Microscopy (SEM). For long periods (>6 h), the evolution of the sublimation process collapses due to side reactions of the bulk solid at the bottom of the sublimation system. This is accompanied by a color change of the solid at the bottom, from yellow to brown, most likely due to the presence of polymeric species of CCMoid units bound through ethylene bonds, which gives rise to amorphous and insoluble materials.[44–46] However, our Raman studies indicated non-destructive deposition of the sublimated molecules on both types of substrates (Figures S17 and S18). For this purpose, control experiments were performed by depositing 1-MP by drop casting on the two surfaces. All samples showed the distinct C≡C-H vibrational band at 2100 cm^{-1}, plus additional ones at 1640 and 1600 cm^{-1} corresponding to the C=C and C=O vibrations, respectively, of the CCMoid skeleton.[47,48]

The morphology of 1-SUB on Au(111) and Si/SiO_2 was analyzed by SEM On the Au substrate, aggregates of different shapes (Figure S19) and sizes are formed (some of them with a lateral dimension greater than 30 μm). In contrast to the irregular assembly obtained on Au, the deposition on Si/SiO_2 leads to the formation of regular and elongated microstructures (Figure 3), with some of them exceeding 100 μm in length.

Topographical data acquired by atomic force microscopy (AFM) provided an amplified view confirming the formation of microcrystals with a wide variation in heights exposing flat surfaces (Figures S20-22), concluding that the CCMoid molecules tend to show better organization on Si/SiO_2 than on Au, displaying facetted microcrystals.

As mentioned earlier, molecular packing, crystal structure, and the interplay between molecular structure and substrate surfaces have an important impact on the electrical properties of materials.[49–52] To gain insight into the correlation between the AlkCCMoid structure with its electrical properties we used 1-SC, 1-MP, and 1-SUB (onto Si/SiO_2 surfaces) to perform XRD, GIWAXS, and electrical measurements.

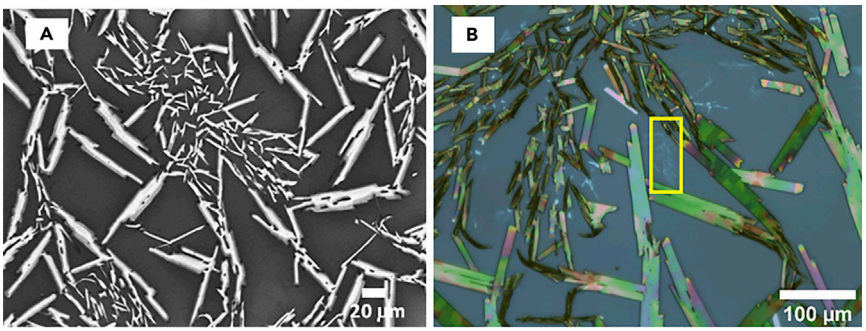

Figure 3. Microscopy information at the micro- and macroscale

(A) SEM and (B) optical microscope images of 1-sub sublimated over Si/SiO_2. Yellow inset shows fuzzy branched sheet-like structures, as a first stage toward the creation of microcrystals.

In this regard, Figure 4A compares specular XRD (theta-2theta) obtained for 1-MP (black) and 1-SUB (red) with the calculated from 1-SC (blue). The pattern belonging to 1-SC displays the diffracted intensity from the family of {200} crystalline planes and the (200) peak corresponds to 19.65 Å in the real space (at 2theta ≈ 4.5°, the momentum transfer equals to q = 0.3198 $Å^{-1}$). In the comparison of the three systems, important differences are found for 1-SUB, for which two phases were clearly visible (Figure 4A, red), with peak positions shifted to lower angles with respect to the XRD reflections of the single crystals (1-SC, blue), indicating the existence of two polymorphs. These two are observed in the case of 1-MP (Figure 4A, black), with one of them appearing as a small shoulder (*), again differing from the single-crystal pattern.

1-SUB on Si/SiO_2 was characterized also by GIWAXS to determine the orientation of the crystallites on the sample (Figure 4B). The observation of the Bragg peak (and higher diffraction order peaks) along the specular direction reveals a defined preferential orientation of the microcrystals that agrees with the flat facets observed in the morphology (Figure 3). On Au (111) a similar structure is observed but with a larger angular distribution of crystallite orientations, i.e. more orientation disorder (Figure S22).

In addition, we performed an XRD analysis of the XRD data collected for 1-MP. Based on observed reflections and systematic absences, we finally indexed the powder pattern to the *C2/m* space group and extracted the unit-cell parameters through Pawley refinements of the PXRD pattern of the sample (see Table S4 and Figure S31).

In parallel, to test the electrical properties of this CCMoid, high-quality 1-SC were selected with an optical microscope and transferred electrostatically to a Si/SiO_2 substrate (Figure 5A inset), using graphite paste

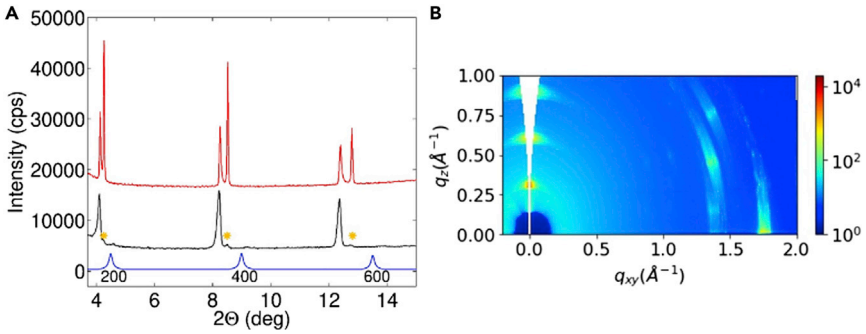

Figure 4. Collection of diffraction images

(A) Specular XRD measurements (th-2th) showing the comparison of the structure in 1-SC (blue), 1-MP (black), and 1-SUB (red) deposited on Si/SiO_2.

(B) 2D GIWAXS measured on the sample obtained by sublimation on Si/SiO_2 (1-SUB).

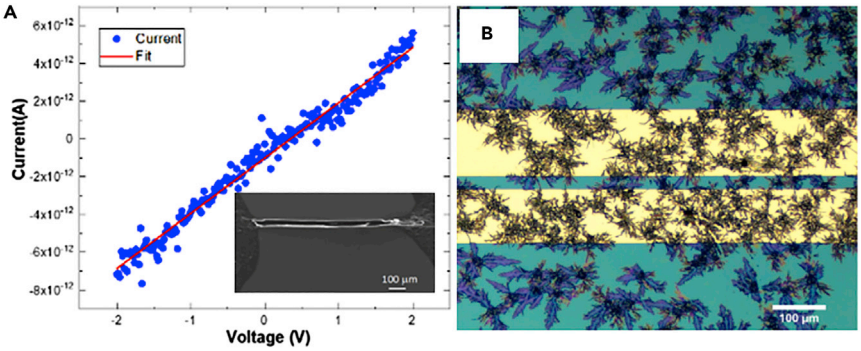

Figure 5. DC electrical measurements and device pictures

(A) Current-Voltage characteristics of a 1-SC electrically connected with graphite electrodes. Inset shows an SEM image of the single crystal.

(B) Electrodes connected by molecular ensembles sublimated on pre-patterned substrates.

to electrically connect both ends of the needle-shaped crystals. From the measured current-voltage characteristics done under vacuum, a conductivity value of about $(8.50 \pm 0.03)\times10^{-10}$S/cm was derived. The application of a gate voltage of $V_G = \pm 40$V did not significantly alter the sample conductivity (Figure S23), indicating that single crystals were insulating in nature (Figure 5).[53] Similar conductivity values, measured in air and vacuum, were also obtained for 1-SUB samples (Figures 5B and S23), which are in good agreement with the DC conductivity values already reported for CCMoid films.[54]

To further characterize the dielectric properties of the AlkCCMoid broadband dielectric spectroscopy measurements were carried out using 1-MP and the setup described in STAR Methods and in SI (Figure S25). Briefly, a 1-MP pellet was loaded into a capacitor cell and measured as prepared and after storage, under ambient conditions, sandwiched between two aluminum contacts, for about one week. Our results indicate that while the electrical ac-conductivity displays only negligible changes, the extracted relative permittivity, shows a clear decrease at low frequencies. Changes in this region can be attributed to variations of the relative humidity. At high frequency ($f > 100$ kHz), the relative permittivity exhibited stable values (3.7 ± 0.1) when comparing samples measured as prepared and after 7 days of storage in air, respectively. Thus, the 1-MP is highly stable under ambient conditions, exhibiting permittivity values in good agreement with those found in the literature for small, conjugated molecules.[55]

However, this was not the case in the measurements of the electrical properties of the 1-MP pellet after soft annealing at temperatures ranging from $15°C < T < 55°C$ (SI). Figures S26–S30 and S6A show the evolution of impedance, phase, conductivity, and permittivity following heating and cooling, and Table S3 summarizes the trends for the parameters extracted from the measurements. We could notice that all values show small and reversible changes with temperature, except in the case of permittivity, for which a consistent and irreversible increase was observed, as shown in Figure 6A. This led us to hypothesize that the variation of the latter could be due to a thermally induced structural change in the morphology of 1-MP, based on the facts that conductance and capacitance are inversely proportional to sample thickness (i.e., pellet thickness), and the sample exhibited only modest and reversible variations in the case of the conductance.

To test our theory, we started by measuring the specular X-ray diffraction of the pristine microcrystalline powder and compared it with the same sample, after mild annealing, recovered from the capacitance measurement cell. Figure 6B displays the corresponding diffraction patterns from the sample before (black) and after annealing (red), where the diffractogram of the single-crystal, 1-SC, is given for comparative reasons (blue). The comparison clearly shows that, in general, the annealed 1-MP sample follows the same pattern, but also exhibits additional structural features of the single crystal, 1-SC. Hence, our findings reinforced the idea of structural changes affecting the permittivity parameter leading to theoretical calculations to provide further information.

DFT calculations were performed to calculate the permittivity values of 1-SC and that from the main polymorph found in 1-MP The calculations were performed with the all-electron FHI-aims computer code (*tight*

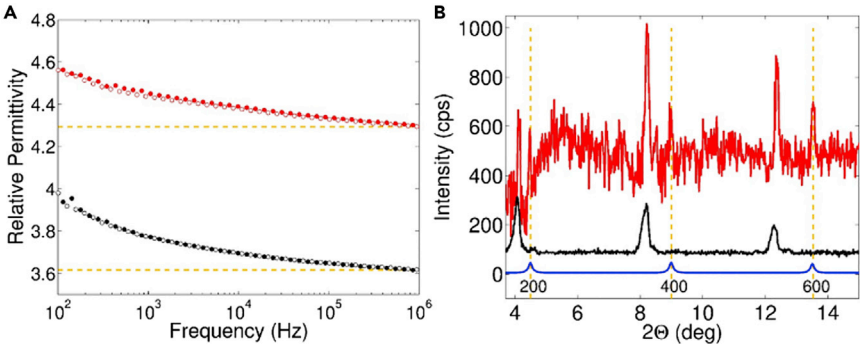

Figure 6. Dielectric and structural properties of AlkCCMoid (1)

(A) Relative permittivity of 1-MP, before (black) and after annealing (red), both measured at room temperature. Open and closed symbols correspond to forward and reverse frequency sweeps, respectively.

(B) Specular X-ray diffraction pattern of 1-MP before (black) and after annealing (red) compared to 1-SC (blue).

option for basis set and 24/12 k-points for small *Cc* and large *C2/m* unit cells, respectively).[56] The unit cell optimizations and dielectric properties, using Density Functional Perturbation Theory (DFPT),[57] were carried out using the PBE exchange-correlation functional,[58] including many-body dispersion contributions[59] (CIF files of the optimized structures, Data S1). The AlkCCMoid structure (1-SC_{theor}) was optimized using 1-SC data with and without symmetry constrain, as a starting point to maintain the same unit cell symmetry (Tables S2 and S5), showing an excellent agreement with the experimental data. The calculated dielectric constant (relative permittivity, see Table S6) for both optimized structures (with and without constrains) was the same, 3.85. This value is slightly different from the experimental value observed for 1-MP after annealing (~4.29 at high frequency, Figure 6A, red) because the precision limit of the DFPT approach is only implemented with the LDA (local density approximation) and GGA (generalized gradient approximation) functionals. Taking into account that the experimental XRD analysis after annealing of 1-MP indicated the existence of the two polymorphs (1-MP/1-SC, Figure 6B, red), the optimized structure for the main polymorph found in the 1-MP sample was initially set by fixing the unit-cell parameters based on the XRD analysis (Table S4). However, the subsequent full optimization, 1-MP_{theor}, gave the same structure, 1-MP, because the calculated gradient was below the convergence tolerances. The comparison between 1-MP_{theor} and 1-SC shows a considerable increase in volume for the former (around 21%, Table S4), being less stable by 8.3 kcal/mol per molecule. Therefore, the calculated dielectric constant for this system, 2.92, was consistent with the lower value found in the experimental data (~3.62 at high frequency, Figure 6A, black). In addition, the bandgaps calculated at PBE level of the 1-MP_{theor} compared to that of the 1-SC_{theor} were very similar, around 2 eV, being the latter only 0.1 eV larger than the former (Figure S33). This result corroborates our hypothesis that changes in permittivity values are due to structural variations, since bandgap and dielectric constant are usually inversely proportional.[60]

Summarizing, we have presented a comprehensive study of the structural and electrical properties of a new CCMoid, the AlkCCMoid (1). To this end, we have characterized our solid-state system in detail, emphasizing single and powder XRD data (1-SC and 1-MP, respectively), together with XRD data from the sublimation of AlkCCMoid directly onto different substrates (1-SUB), which includes FETs, by using a homemade sublimation system.

The electrical properties extracted from 1-SC and 1-SUB (using a FET device architecture) agree with and confirm the dielectric nature of the system. Detailed electrical characterization using 1-MP pellets provided obvious differences in permittivity before and after mild temperature and pressure conditions were applied to the sample. Subsequent structural analysis by powder XRD allowed us to observe a partial transition of the polymorphic 1-MP system to a mixture of polymorphs, 1-MP/1-SC. DFT calculations have corroborated the hypothesis relating the permittivity changes to those involving the existence of different polymorphs. Our findings are applicable to other molecules and provide the necessary tools to deposit and study molecules directly on surfaces as well as to understand new molecular-based systems, where polymorphism and electronics go along together.

Limitations of the study

Our future work may include similar studies, using a range of temperatures and including fluorescence experiments. Our sublimation methodology cannot yet provide precise control of the amount of material deposited, as do UHV-STM and related techniques, however, it can be tuned by controlling sublimation time, temperature, and pressure, and the basic three-terminal devices can be fabricated *in situ*, allowing pre-testing of the electronic properties of the molecules.

STAR★METHODS

Detailed methods are provided in the online version of this paper and include the following:

- KEY RESOURCES TABLE
- RESOURCE AVAILABILITY
  - Lead contact
  - Material availability
  - Data and code availability
- METHOD DETAILS
  - Synthetic methodology
  - Molecular characterization
  - Devices fabrication
  - GIWAXS experiments
  - Theoretical details
  - Additional instruments for characterization
- ADDITIONAL RESOURCES
  - Sublimation system

SUPPLEMENTAL INFORMATION

Supplemental information can be found online at https://doi.org/10.1016/j.isci.2022.105686.

ACKNOWLEDGMENTS

This work has received funding from the European Research Council (ERC) under the European Union's Horizon 2020 R&D program (ERC-724981). This work was also supported by the projects PID2019-108794GB-I00, GENESIS PID2019-111682RB-I00, PID2019-110907GB-I00, and PID2021-122464NB-I00 funded by MCIN/AEI/10.13039/501100011033 from the Ministerio de Ciencia e Innovación. E.C.S. acknowledges the financial support from the Spanish Government, (Grant PGC2018-098630-B-I00). R.P. acknowledges support from the Ramón y Cajal Fellowship (Ref. RyC2019-028474-I). J.dS. thanks to the MChem program of the University of Southampton. E.R. thanks Generalitat de Catalunya by a ICREA Academia award, Spanish Ministry Science for a Maria de Maeztu excellence grant (MDM-2017-0767), and computer resources, technical expertise and assistance provided by the Barcelona Supercomputing Center. R.M. thanks "la Caixa" Foundation (ID 100010434) for a Junior Leader fellowship (LCF/BQ/PI22/11910024). The crystal structures were collected at beamline XALOC at ALBA Synchrotron (Exp. 2017042211). The CSIC authors acknowledge the financial support from the Spanish Ministry Science, through the "Severo Ochoa" Programme for Centres of Excellence (FUNFUTURE,2020-2023). GIWAXS experiments were performed at the beam line BL11 – NCD-SWEET at ALBA Synchrotron with the collaboration of ALBA staff ; we also thank the support from Alba Cazorla.

AUTHORS CONTRIBUTIONS

D.R.L., D.H., and J.dS. investigation, data collection, and data analysis-molecular synthesis and characterization; R.Z. conceptualization, investigation, data collection, and data analysis-Raman spectroscopy, electrical, optical, and SEM characterization; E. B. and F.S. data collection and analysis- GIWAXS; E.B., R.M., E.C.S. data analysis-crystallography, and XRD Patterns; R.P. and M.M. data collection and data analysis-dielectric measurements; E.R. investigation, data collection, and data analysis-theoretical study; R.P., A.G.C., and N.A.A. conceptualization, investigation, data analysis, validation, supervision; A.G.C. and N.A.A. project administration and funding acquisition. All authors contributed to the writing and editing of the article.

DECLARATION OF INTERESTS

Regarding the sublimation system, a patent application has been filed (22/02/2022), with application number: P202230143 (Ref. Number: ES1641.1728). D.H., A.G.C., and N.A.A. are listed as co-inventors of the patents. The rest of the authors declare no competing interests.

Received: October 9, 2022
Revised: November 11, 2022
Accepted: November 28, 2022
Published: December 22, 2022

REFERENCES

1. Sheats, J.R. (2004). Manufacturing and commercialization issues in organic electronics. J. Mater. Res. *19*, 1974–1989. https://doi.org/10.1557/JMR.2004.0275.

2. Fleet, L.R., Stott, J., Villis, B., Din, S., Serri, M., Aeppli, G., Heutz, S., and Nathan, A. (2017). Self-assembled molecular nanowires for high performance organic transistors. ACS Appl. Mater. Interfaces *9*, 20686–20695. https://doi.org/10.1021/acsami.7b01449.

3. Tang, F., Wu, Z., Yang, C., Osenberg, M., Hilger, A., Dong, K., Markötter, H., Manke, I., Sun, F., Chen, L., and Cui, G. (2021). Synchroton X-ray tomography for rechargeable battery research: fundamentals, setups and applications. Small Methods *5*, 2100557. https://doi.org/10.1002/smtd.202100557.

4. Jones, A.O.F., Chattopadhyay, B., Geerts, Y.H., and Resel, R. (2016). Substate-Induced and thin-film phases: polymorphism of organic materials on surfaces. Adv. Funct. Mater. *26*, 2233–2255. https://doi.org/10.1002/adfm.201503169.

5. Reed, G., Littleton, M., Doran, H., Keay, K., Hughes, G.M., and Patrick, D.L. (2020). Bottom-up growth of shape-engineered molecular single crystals. Cryst. Growth Des. *20*, 5043–5047. https://doi.org/10.1021/acs.cgd.0c00194.

6. Taheri, H.E., Ocheje, M.U., St Onge, P.B.J., Rondeau-Gagné, S., and Mirhassani, M. (2021). Computational design of an integrated CMOS readout circuit for sensing with organic field-effect transistors. Front. Electron. *2*, 725008. https://doi.org/10.3389/felec.2021.725008.

7. Liu, R., Wang, Z.L., Fukuda, K., and Someya, T. (2022). Flexible self-charging power sources. Nat. Rev. Mater. *7*, 870–886. https://doi.org/10.1038/s41578-022-00441-0.

8. Qiu, X., and Chiechi, R.C. (2022). Printable logic circuits comprising self-assembled protein complexes. Nat. Commun. *13*, 2312. https://doi.org/10.1038/s41467-022-30038-8.

9. Lampe, V. (1918). Syntheses von curcumin. Ber. Dtsch. Chem. Ges. *51*, 1347–1355. https://doi.org/10.1002/cber.19180510223.

10. Pabon, H.J.J. (1964). A synthesis of curcumin and related compounds. Recl. Trav. Chim. Pays. Bas. *83*, 379–386. https://doi.org/10.1002/recl.19640830407.

11. Pedersen, U., Rasmussen, P.B., and Lawesson, S.O. (1985). Synthesis of naturally occurring curcuminoids and related compounds. Liebigs Ann. Chem. *1985*, 1557–1569. https://doi.org/10.1002/jlac.198519850805.

12. Zhang, Y., Tu, L., Lu, L., Li, Y., Song, L., Qi, Q., Song, H., Li, Z., and Huang, W. (2020). Screening and application of boron difluoride complexes of curcumin as colorimetric and radiometric fluorescent probes for bisulfite. Anal. Methods *12*, 1514–1521. https://doi.org/10.1039/D0AY00173B.

13. Gál, E., and Nagy, L.C. (2021). Photophysical properties and electronic structure of symmetrical curcumin analogues and their BF2 complexes including a phenothiazine substituted derivative. Symmetry *13*, 2299. https://doi.org/10.3390/sym13122299.

14. Cornago, P., Cabildo, P., Sanz, D., Claramunt, R.M., Torralba, M.C., Torres, M.R., and Elguero, J. (2013). Structures of hemicurcuminoids in the solid state and in solution. Eur. J. Org. Chem. *2013*, 6043–6054. https://doi.org/10.1002/ejoc.201300488.

15. Abu-Dief, A.M., Díaz-Torres, R., Sañudo, E.C., Abdel-Rahman, L.H., and Aliaga-Alcalde, N. (2013). Novel sandwich triple-decker dinuclear Nd^{III}-(bis-N, N′-p-bromo-salicylidiene-1, 2-diaminobenzene) complex. Polyhedron *64*, 203–208. https://doi.org/10.1016/j.poly.2013.04.010.

16. Díaz-Torres, R., Menelaou, M., Roubeau, O., Sorrenti, A., Brandariz-De-Pedro, G., Sañudo, E.C., Teat, S.J., Fraxedas, J., Ruiz, E., and Aliaga-Alcalde, N. (2016). Multiscale study of mononuclear Co^{II} SMMs based on curcuminoid ligands. Chem. Sci. *7*, 2793–2803. https://doi.org/10.1039/C5SC03298A.

17. Rodríguez-Cid, L., Qian, W., Iribarra-Araya, J., Etcheverry-Berríos, Á., Martínez-Olmos, E., Choquesillo-Lazarte, D., Sañudo, E.C., Roubeau, O., López-Periago, A.M., González-Campo, A., et al. (2021). Broadening the scope of high dimensionality nanomaterials using pyridine-based curcuminoids. Dalton Trans. *50*, 7056–7064. https://doi.org/10.1039/d1dt00708d.

18. Olavarría-Contreras, I.J., Etcheverry-Berríos, A., Qian, W., Gutiérrez-Cerón, C., Campos-Olguín, A., Sañudo, E.C., Dulić, D., Ruiz, E., Aliaga-Alcalde, N., Soler, M., and van der Zant, H.S.J. (2018). Electric-field induced bistability in single-molecule conductance measurements for boron coordinated curcuminoids compounds. Chem. Sci. *9*, 6988–6996. https://doi.org/10.1039/c8sc02337a.

19. Aliaga-Alcalde, N., Marqués-Gallego, P., Kraaijkamp, M., Herranz-Lancho, C., den Dulk, H., Görner, H., Roubeau, O., Teat, S.J., Weyhermüller, T., and Reedijk, J. (2010). Copper curcuminoids containing anthracene groups: fluorescent molecules with cytotoxicity activity. Inorg. Chem. *49*, 9655–9663. https://doi.org/10.1021/ic101331c.

20. Menelaou, M., Ouharrou, F., Rodríguez, L., Roubeau, O., Teat, S.J., and Aliaga-Alcalde, N. (2012). Dy^{III} and Yb^{III}-Curcuminoid compounds: original fluorescent single-ion magnet and magnetic near-IR luminescent species. Chemistry *18*, 11545–11549. https://doi.org/10.1002/chem.201200955.

21. Aliaga-Alcalde, N., and Rodríguez, L. (2012). Solvatochromic studies of a novel Cd^{2+}-anthracene-based curcuminoid and related complexes. Inorg. Chim. Acta. *380*, 187–193. https://doi.org/10.1016/j.ica.2011.08.052.

22. Rodríguez-Cid, L., Sañudo, E.C., López-Periago, A.M., González-Campo, A., Aliaga-Alcalde, N., and Domingo, C. (2020). Novel Zn(II) coordination polymers based on the natural molecule bisdemethoxycurcumin. Cryst. Growth Des. *20*, 6555–6564. https://doi.org/10.1021/acs.cgd.0c00742.

23. Su, H., Sun, F., Jia, J., He, H., Wang, A., and Zhu, G. (2015). A highly porous medical metal-organic framework constructed from bioactive curcumin. Chem. Commun. *51*, 5774–5777. https://doi.org/10.1039/C4CC10159F.

24. Archet, F., Yao, D., Chambon, S., Abbas, M., D'Aléo, A., Canard, G., Ponce-Vargas, M., Zaborova, E., Le Guennic, B., Wantz, G., and Fages, F. (2017). Synthesis of bioinspired curcuminoid small molecules for solution-processed organic solar cells with high open-circuit voltage. ACS Energy Lett. *2*, 1303–1307. https://doi.org/10.1021/acsenergylett.7b00157.

25. Castro, E., Cerón, M.R., Garcia, A.H., Kim, Q., Etcheverry-Berríos, A., Morel, M., Díaz-Torres, R., Qian, W., Martinez, Z., Mendez, L., et al. (2018). A new family of fullerene derivatives: fullerene-curcumin conjugates for biological and photovoltaic applications. RSC Adv. *8*, 41692–41698. https://doi.org/10.1039/C8RA08334G.

26. Etcheverry-Berríos, A., Olavarría, I., Perrin, M.L., Díaz-Torres, R., Jullian, D., Ponce, I., Zagal, J.H., Pavez, J., Vásquez, S.O., Van der Zant, H.S.J., et al. (2016). Multiscale approach to the study of the electronic properties of two thiophene curcuminoid molecules. Chemistry *22*, 12808–12818. https://doi.org/10.1002/chem.201601187.

27. Portolés-Gil, N., Lanza, A., Aliaga-Alcalde, N., Ayllón, J.A., Gemmi, M., Mugnaioli, E., López-Periago, A.M., and Domingo, C. (2018). Crystalline curcumin bioMOF obtained by precipitation in supercritical CO2 and structural determination by electron diffraction tomography. ACS Sustain. Chem. Eng. *6*, 12309–12319. https://doi.org/10.1021/acssuschemeng.8b02738.

28. Choi, K.R., Kim, D.H., Lee, Y.U., Placide, V., Huynh, S., Yao, D., Canard, G., Zaborova, E., Mathevet, F., Mager, L., et al. (2021). Effect of the electron donating group on the excited-state electronic nature and epsilon-near-zero properties of curcuminoid-borondifluoride dyes. RSC Adv. *11*, 38247–38257. https://doi.org/10.1039/d1ra08025c.

29. Kim, D.H., D'Aléo, A., Chen, X.K., Sandanayaka, A.D.S., Yao, D., Zhao, L., Komino, T., Zaborova, E., Canard, G., Tsuchiya, Y., et al. (2018). High-efficiency electroluminescence and amplified spontaneous emission from a thermally activated delayed fluorescent near-infrared emitter. Nat. Photonics *12*, 98–104. https://doi.org/10.1038/s41566-017-0087-y.

30. D'Aléo, A., Sazzad, M.H., Kim, D.H., Choi, E.Y., Wu, J.W., Canard, G., Fages, F., Ribierre, J.-C., and Adachi, C. (2017). Boron difluoride hemicurcuminoid as an efficient far red to near-infrared emitter: toward OLEDs and laser dyes. Chem. Commun. *53*, 7003–7006. https://doi.org/10.1039/c7cc01786c.

31. Prins, F., Barreiro, A., Ruitenberg, J.W., Seldenthuis, J.S., Aliaga-Alcalde, N., Vandersypen, L.M.K., and Van der Zant, H.S.J. (2011). Room-temperature gating of molecular junctions using few-layer graphene nanogap electodes. Nano Lett. *11*, 4607–4611. https://doi.org/10.1021/nl202065x.

32. Burzurí, E., Island, J.O., Díaz-Torres, R., Fursina, A., González-Campo, A., Roubeau, O., Teat, S.J., Aliaga-Alcalde, N., Ruiz, E., and Van der Zant, H.S.J. (2016). Sequential electron transport and vibrational excitations in an organic molecule coupled to few-layer graphene electrodes. ACS Nano *10*, 2521–2527. https://doi.org/10.1021/acsnano.5b07382.

33. Island, J.O., Holovchenko, A., Koole, M., Alkemade, P.F.A., Menelaou, M., Aliaga-Alcalde, N., Burzurí, E., and Van der Zant, H.S.J. (2014). Fabrication of hybrid molecular devices using multi-layer graphene break junctions. J. Phys. Condens. Matter *26*, 474205. https://doi.org/10.1088/0953-8984/26/47/474205.

34. Xiang, D., Jeong, H., Lee, T., and Mayer, D. (2013). Mechanically controllable break junctions for molecular electronics. Adv. Mater. *25*, 4845–4867. https://doi.org/10.1002/adma.201301589.

35. Perrin, M.L., Burzurí, E., and Van der Zant, H.S.J. (2015). Single-molecule transistors. Chem. Soc. Rev. *44*, 902–919. https://doi.org/10.1039/c4cs00231h.

36. Díaz-Torres, R., Menelaou, M., González-Campo, A., Teat, S., Sañudo, E., Soler, M., and Aliaga-Alcalde, N. (2016). Comparative magnetic studies in the solid state and solution of two isostructural 1D coordination polymers containing CoII/NiII-curcuminoid moieties. Magnetochemistry *2*, 29. https://doi.org/10.3390/magnetochemistry2030029.

37. Lorenz, M., Ramachandra Rao, M.S., Venkatesan, T., Fortunato, E., Barquinha, P., Branquinho, R., Salgueiro, D., Martins, R., Carlos, E., Liu, A., et al. (2016). The 2016 oxide electronic materials and oxide interfaces roadmap. J. Phys. D Appl. Phys. *49*, 433001. https://doi.org/10.1088/0022-3727/49/43/433001.

38. Menelaou, M., Weyhermüller, T., Soler, M., and Aliaga-Alcalde, N. (2013). Novel paramagnetic-luminiscent building blocks containing manganese (II) and anthracene-based curcuminoids. Polyhedron *52*, 398–405. https://doi.org/10.1016/j.poly.2012.08.061.

39. Rieger, R., and Müllen, K. (2010). Forever young: polycyclic aromatic hydrocarbons as model cases for structural and optical studies. J. Phys. Org. Chem. *23*, 315–325. https://doi.org/10.1002/poc.1644.

40. Tauc, J. (1968). Optical properties and electronic structure of amorphous Ge and Si. Mater. Res. Bull. *3*, 37–46. https://doi.org/10.1016/0025-5408(68)90023-8.

41. Viezbicke, B.D., Patel, S., Davis, B.E., and Birnie, D.P. (2015). Evaluation of Tauc method for optical absorption edge determination: ZnO thin films as a model system. Phys. Status Solidi B *252*, 1700–1710. https://doi.org/10.1002/pssb.201552007.

42. Makuła, P., Pacia, M., and Macyk, W. (2018). How to correctly determine the band gap energy of modified semiconductor photocatalyst based on UV-Vis spectra. J. Phys. Chem. Lett. *9*, 6814–6817. https://doi.org/10.1021/acs.jpclett.8b02892.

43. Michaelson, H.B. (1977). The work function of the elements and its periodicity. J. Appl. Phys. *48*, 4729–4733. https://doi.org/10.1063/1.323539.

44. Albrecht, F., Rey, D., Fatayer, S., Schulz, F., Pérez, D., Peña, D., and Gross, L. (2020). Intramolecular coupling of terminal alkynes by atom manipulation. Angew. Chem., Int. Ed. Engl. *59*, 22989–22993. https://doi.org/10.1002/anie.202009200.

45. Gao, H.Y., Wagner, H., Zhong, D., Franke, J.H., Studer, A., and Fuchs, H. (2013). Glaser coupling at metal surfaces. Angew. Chem., Int. Ed. Engl. *52*, 4024–4028. https://doi.org/10.1002/anie.201208597.

46. Ciampi, S., James, M., Darwish, N., Luais, E., Guan, B., Harper, J.B., and Gooding, J.J. (2011). Oxidative acetylenic coupling reactions as a surface chemistry tool. Phys. Chem. Chem. Phys. *13*, 15624–15632. https://doi.org/10.1039/C1CP21450K.

47. Miloudi, L., Bonnier, F., Bertrand, D., Byrne, H.J., Perse, X., Chourpa, I., and Munnier, E. (2017). Quantitative analysis of curcumin-loaded alginate nanocarriers in hydrogels using Raman and attenuated total reflection infrared spectroscopy. Anal. Bioanal. Chem. *409*, 4593–4605. https://doi.org/10.1007/s00216-017-0402-y.

48. Kolev, T.M., Velcheva, E.A., Stamboliyska, B.A., and Spiteller, M. (2005). DFT and experimental studies of the structure and vibrational spectra of curcumin. Int. J. Quant. Chem. *102*, 1069–1079. https://doi.org/10.1002/qua.20469.

49. Peng, B., Wu, R., and Li, H. (2021). Crystallization from a Droplet: single-crystalline arrays and heterojunctions for organic electronics. Acc. Chem. Res. *54*, 4498–4507. https://doi.org/10.1021/acs.accounts.1c00537.

50. Ryu, H.S., Kim, M.J., Lee, Y.W., Lee, S.H., Shin, T.J., Cho, J.H., and Woo, H.Y. (2019). Synthesis, molecular packing, and electrical properties of new regioisomeric n-type semiconducting molecules with modification of alkyl substituents position. ACS Appl. Mater. Interfaces *11*, 47170–47181. https://doi.org/10.1021/acsami.9b17664.

51. Kiriy, N., Kiriy, A., Bocharova, V., Stamm, M., Richter, S., Plötner, M., Fischer, W.J., Krebs, F.C., Senkovska, I., and Adler, H.J. (2004). Conformation, molecular packing, and field effect mobility of regioregular b, b'-dihexylsexithiophene. Chem. Mater. *16*, 4757–4764. https://doi.org/10.1021/cm049686a.

52. Mas-Torrent, M., and Rovira, C. (2011). Role of molecular order and solid-state structure in organic field-effect transistors. Chem. Rev. *111*, 4833–4856. https://doi.org/10.1021/cr100142w.

53. Sun, L., Park, S.S., Sheberla, D., and Dincă, M. (2016). Measuring and reporting electrical conductivity in metal-organic frameworks: Cd2(TTFTB) as a case study. J. Am. Chem. Soc. *138*, 14772–14782. https://doi.org/10.1021/jacs6b09345.

54. Dakhel, A.A., Jasim, K.E., Cassidy, S., and Henari, F.Z. (2013). Extraction and dielectric properties of curcuminoid films grown on Si substrate for high-k dielectric applications. Mater. Sci. Eng., B *178*, 1062–1067. https://doi.org/10.1016/j.mseb.2013.06.003.

55. Hughes, M.P., Rosenthal, K.D., Ran, N.A., Seifrid, M., Bazan, G.C., and Nguyen, T. (2018). Determining the dielectric constants of organic photovoltaic materials using impedance spectroscopy. Adv. Funct. Mater. *28*, 1801542. https://doi.org/10.1002/adfm.201801542.

56. Blum, V., Gehrke, R., Hanke, F., Havu, P., Havu, V., Ren, X., Reuter, K., and Scheffler, M. (2009). Ab initio molecular simulations with numeric atom-centered orbitals. Comput.

Phys. Commun. *180*, 2175–2196. https://doi.org/10.1016/j.cpc.2009.06.022.

57. Shang, H., Raimbault, N., Rinke, P., Scheffler, M., Rossi, M., and Carbogno, C. (2018). All-electron, real-space perturbation theory for homogeneous electric, and application within DFT. New J. Phys. *20*, 073040. https://doi.org/10.1088/1367-2630/aace6d.

58. Perdew, J.P., Burke, K., and Ernzerhof, M. (1996). Generalized gradient approximation made simple. Phys. Rev. Lett. *77*, 3865–3868. https://doi.org/10.1103/PhysRevLett.77.3865.

59. Tkatchenko, A., DiStasio, R.A., Car, R., and Scheffler, M. (2012). Accurate and efficient method for many-body Van der Waals interactions. Phys. Rev. Lett. *108*, 236402. https://doi.org/10.1103/PhysRevLett.108.236402.

60. Choudhary, K., Garrity, K.F., Sharma, V., Biacchi, A.J., Hight Walker, A.R., and Tavazza, F. (2020). High-throughput density functional perturbation theory and machine learning predictions of infrared, piezoelectric, and dielectric responses. NPJ Comput. Mater. *6*, 64. https://doi.org/10.1038/s41524-020-0337-2.

CellPress
OPEN ACCESS

STAR★METHODS

KEY RESOURCES TABLE

REAGENT or RESOURCE	SOURCE	IDENTIFIER
Chemicals		
Acetylacetone	Merck	P7754; CAS: 123-54-6
Boron trioxide	Merck	56,750; CAS: 1303-86-2
Tributyl borate	Merck	90,795; CAS: 688-74-4
N-butyl amine	Fischer Scientific, S.L.	10030462; CAS: 109-72-8
Ethynyl benzaldehyde	Fluorochem	MFCD05664348; CAS: 63697-96-1
4-[(Trimethylsilyl)ethynyl] benzaldehyde	Merck	523380; CAS: 77123-57-0
Potassium bromide	Merck	209619; CAS: 7758-02-3
Hydroclorhidric acid 37%	Carlo Erba	403871; CAS: 7647-01-0
Ethyl acetate	Carlo Erba	528299; CAS: 141-78-6
Methanol	Carlo Erba	528101; CAS: 67-56-1
Acetonitrile	Carlo Erba	P0060228; CAS: 75-05-8
Chloroform D 99.80%D	Eurisotop	D007HAG; CAS: 865-49-6
MilliQ water	Merck	purified with Milli-Q®EQ-700
Acetone	Chem-lab	CAS: 67-64-1
Isopropanol	Chem-lab	CAS: 67-63-0
Deposited data		
CIF file of system **1**	The Cambridge Crystallographic Data Centre	CCDC2206711
CIF file of system **2**	The Cambridge Crystallographic Data Centre	CCDC2206712
Software and algorithms		
OriginPro v.2018	http://originlab.com	
Mercury	http://ccdc.cam.ac.uk	
MNova v.2014	http://mestrelab.com	
MMass	http://mmass.org	
Python	https://www.python.org/	

RESOURCE AVAILABILITY

Lead contact

Further information and requests for resources and CCMoid molecules should be directed to and will be fulfilled by the lead contact, Núria Aliaga-Alcalde (nuria.aliaga@icrea.cat).

Material availability

Materials are available upon request.

Data and code availability

- CCDC 2206711 (**1**) and 2206712 (**2**), contain the supplementary crystallographic data. These data can be obtained free of charge by The Cambridge Crystallographic Data Centre.
- The rest of the data reported in this article are available within the paper and the supplemental information files.
- There is no code associated with this work.

METHOD DETAILS

Synthetic methodology

AlkCCMoid (**1**) and AlkTMSCCMoid, (**2**), were synthesized following a modification of the Pabonś method[10] according to the procedure shown in below scheme.

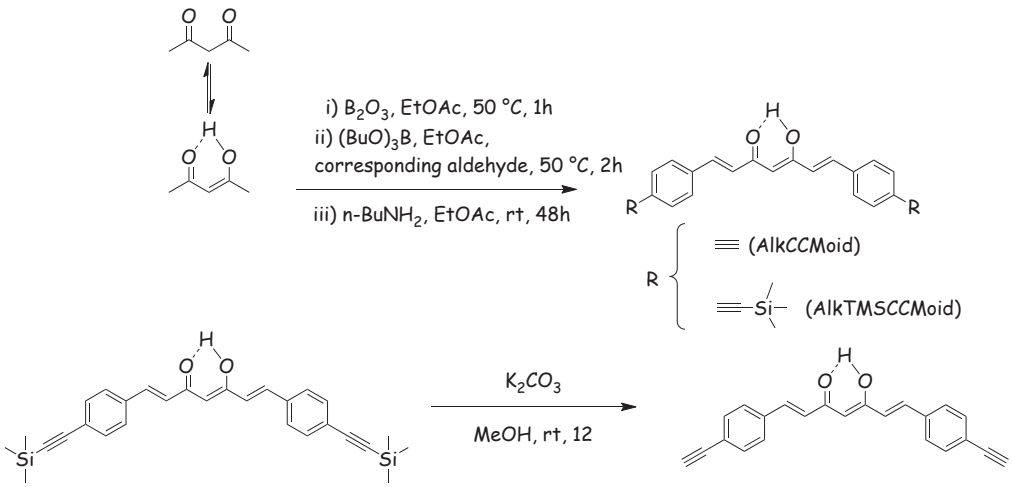

Synthetic paths in the achievement of 1 and 2

Synthesis of AlkCCMoid (**1**). Two synthetic routes (A and B) were used to obtain this molecule.

(A) 200 mg (2 mmol) of acac and 100 mg of B_2O_3 (0.7 eq, 1.4 mmol) were solubilized in 2 mL of EtOAc. The mixture was stirred and heated at 50 ºC for 1 h. Then 1.1 mL (4 mmol) of $(BuO)_3B$ was added, followed by the addition of a solution of 809 mg of 1-ethylbenzaldehyde (4 mmol) in 2 mL of EtOAc. The reaction was stirred at 50 ºC for 2 h and then cooled to room temperature. Next, a solution of *n*-$BuNH_2$ (100 μL, 1 mmol) in EtOAc (1.3 mL) was added dropwise and the reaction was stirred at room temperature for two days. Finally, an aqueous HCl solution (0.1 M) was added to the solution and the mixture was left stirring at 40 ºC for 1 h. The resulting precipitate was filtered off and washed with cold MeOH. Recrystallization was achieved by dissolving the solid in MeCN and leaving the solution in the refrigerator at 0 ºC. AlkCCMoid was obtained as a brown powder in 36% yield. ^{1}H NMR (δ in ppm, 360 MHz, $CDCl_3$): 15.83 (s, 1H), 7.64 (d, *J* = 15.8 Hz, 2H), 7.51 (s, 8H), 6.63 (d, *J* = 15.8 Hz, 2H), 5.85 (s, 1H), 3.20 (s, 2H). $^{13}C\{^1H\}$ NMR (δ in ppm, 90 MHz, $CDCl_3$): 183.2, 139.8, 135.4, 132.8 128.1, 125.1, 123.9, 102.4, 83.4, 79.4. ATR-FTIR (cm^{-1}): 3273 ($\nu_{\equiv C\text{-}H}$), 3033 ($\nu_{=C\text{-}H}$ and $\nu_{arC\text{-}H}$), 2958-2929 ($\nu_{\text{-}C\text{-}H}$), 2162 ($\nu_{\text{-}C\equiv C\text{-}}$), 1698 ($\nu_{C=O}$ β-diketone), 1629 (C=O β-diketone, with intermolecular H-bonds), 1495 ($\nu_{arC\text{-}C}$, skeleton vibrations), 1136 ($\delta_{ip\ ar\ C\text{-}H}$) 974 (δ CH) 822 ($\nu_{arC\text{-}H}$ ρ-disubstituted and $\delta_{oop\ CH}$), 623 ($\delta_{\equiv C\text{-}H}$). MS MALDI-TOF (m/z): calc. for $C_{23}H_{16}O_2$[M-1]: 323.1; found: 322.9. Elemental analysis calculated for AlkCCMoid·2MeCN ($C_{27}H_{22}N_2O_2$): C, 79.78; H, 5.46. Found: C, 79.35; H, 5.08.

(B) The second synthetic route is based on the preparation of the TMS-protected analog CCMoid (AlkTMSCCMoid, **2**) followed by the deprotection in basic media. Full details on the characterization of AlkTMSCCMoid (and AlkCCMoid) are provided in Figures S1–S17 and Tables S1 and S2. Therefore, 200 mg of **2** (2 mmol) and 590 mg of K_2CO_3 (20 mmol) were solubilized in 45 mL of MeOH and the mixture was stirred at room temperature overnight. Then, an aqueous HCl solution (0.1 M) was added, and the resulting solution was concentrated at the rotary evaporator. The final system was extracted with DCM and washed three times with 10 mL brine. AlkCCMoid was obtained without further purification as a brown powder in 70% yield.

Molecular characterization

Tauc's plot of UV-VIS

In solid state, using Tauc's mathematical extrapolation[40,41] estimated band gap values were obtained for AlkCCMoid (**1**) and AlkTMSCCMoid (**2**), respectively. In both cases, these values were obtained by averaging the results of the direct and indirect allowed transitions.

$$(\alpha * h * \nu)^{\frac{1}{n}} = B * (h * \nu - E_g) \quad \text{(Equation 1)}$$

Where:

- α = 2.303·Abs/l (absorption coefficient)
- l = sample thickness
- n = ½ for direct allowed transitions and 2 for indirect allowed transitions

(Figure S11)

Electrochemistry[42]

Using the differential pulse voltammetry (DPV), we calculated the E_g^{ec}.

We used Equations 2 and 3 to calculate the energy of the HOMO and LUMO vs. the ferrocene molecule under vacuum conditions:

$$E_{HOMO} = -\left((E_{onset})^{(oxid)}\right) + 4.8\ eV \quad \text{(Equation 2)}$$

$$E_{LUMO} = -\left((E_{onset})^{(red)}\right) + 4.8\ eV \quad \text{(Equation 3)}$$

The value of 4.8 eV corresponds to the potential of the Fc/Fc^+ couple at the vacuum level. Finally, the energy gap is calculated by:

$$E_g^{ec} = (E_{LUMO}) - (E_{HOMO})\ eV \quad \text{(Equation 4)}$$

(Figures S12 and S13 and Table S1).

Devices fabrication

FETs

Three-terminal devices were fabricated on silicon substrates coated with 300 nm of thermal oxide. A layer of the positive Microposit® resist S1813 by Shipley® was spin coated at 4000 rpm to achieve a final thickness of 1.4 μm and dried during 1 min on a hot plate at 95°C. Then, it was exposed under a 385 nm semiconductor light source using the micro-writer ML3 by Durham Magneto Optics Ltd working at an intensity of 150 mJ/cm^2. Resist development was carried out by dipping the sample in the Microposit® MF 319 developer solution during 40 sec stopped in milliQ water for 30 s and finally dried under a N_2 flow. Thereafter an adhesion layer of Cr with a thickness of 5 nm was evaporated in the evaporation system Auto 360 from Boc Edwards followed by 50 nm of Au. The resulting Au pattern was then revealed through lift-off by immersing the samples in an acetone bath during few minutes followed by rinsing with acetone and isopropanol and dried under a N_2 flow.

The DC electrical characterization of three-terminal devices with sublimated molecules was carried out in a Probe Station by Lakeshore at ambient condition and under vacuum by using two system measurement units (SMU) 2450 from Keithley and a home-made python routine. Resistance measurements were done recording 2 probes current-voltage characteristics applying back and forward voltage sweeps in the range between ±1V. The electrical characterization of the FET was performed under vacuum and applying gate-source voltage V_{GS} between ±40V to the bottom Si acting as a gate electrode. AC electrical characterization was carried out by employing a Novocontrol alpha-A Impedance Analyzer. Temperature sweeps were carried out employing a *Peltier* element which was connected to a PID temperature controller for temperature stabilization.

Sublimated CCMoid-FET setup

The resistivity of the molecular assembly embedded between interdigitated electrodes was obtained from standard 2 probes current-voltage measurements that were operated in air and under vacuum using a

Probe Station from Lakeshore (Figure S23). Under both environmental conditions I(V) data were rather scattered, however for some of the curves (I_g1 and I_g7) it was possible to fit the data to a linear relationship with strong correlation values ($r > 0.85$). We used the values of the resistance obtained by the linear fit to the measured I(V) to evaluate the resistivity according to the Equation 5

$$\rho = \frac{RA}{l} \quad \text{(Equation 5)}$$

Where A is the area (A = W*d, W channel width and d sample thickness, respectively) while l is the channel length of the area between the electrodes covered by the molecules. From this, we obtain for ρ(g1) a value of $6.5 \times 10^4\ \Omega\cdot m$ and $3.7 \times 10^5\ \Omega\cdot m$ for ρ(g7).

Sample preparation for microcrystalline powder (1-MP) measurements

1-MP was ground very fine by employing mortar and pestle under ambient conditions (RH = 45 ± 5%, T = 25 ± 5°C). The powder was loaded into a homemade capacitor cell consisting of Aluminum (~ 35 μm) bottom and top contacts mounted on polycarbonate sheets with about 100 μm thickness (setup, including dimensions in Figure S25). Electrical connections were arranged on opposite sides of the capacitor to avoid high frequency coupling. After loading the cell, it was sandwiched between two rubber pieces and a hydrostatic pressure of about 175 ± 20 kPa was applied. Electrical characterization was carried out by employing a Novocontrol alpha-A Impedance Analyzer. Temperature sweeps were controlled employing a Peltier element which was connected to a PID temperature controller for temperature stabilization. Cell calibration was done by employing a polyimide sheet, *vide infra*.

Calibration of the measurement cell

The measurement cell was calibrated employing a sheet of polyimide with a thickness of d = 125 ± 5 μm, sandwiched between the aluminum contacts. Table S3 and figure S27 show electrical parameters extracted for the broadband dielectric spectroscopy *i.e.* |Impedance|, Phase, Capacitance and Conductivity. Figure S28 shows the calculated relative permittivity of polyimide. The high relative permittivity value at low frequency can be attributed to moisture, since the measurement was done under ambient conditions. At high frequency the relative permittivity converges to a value of: $\varepsilon_r = 3.6 \pm 0.1$, which is in good agreement with literature.

GIWAXS experiments

GIWAXS experiments were performed at the BL11 - NCD-SWEET beamline of the Synchrotron ALBA (Bellaterra, Spain). The energy of the synchrotron X-ray radiation was 14.4 keV. The images (diffraction patterns) were collected with an Rayonix LX255HS area detector. Ten images were collected (exposure time of 0.2 s) and summed up to improve signal-to-noise ratio. The substrates were measured at different incident angles (from 0.09° up to 0.15°), where the data in the Figure 4A corresponds to an incident angle of 0.09° (below the critical angle of the substrate). The data are converted to reciprocal space maps with the out-of-plane (qz) and in-plane (qr) components of the scattering vector corresponding to the directions perpendicular and parallel to the surface, respectively.

Theoretical details

The theoretical permittivity values of **1-SC** and the main polymorph found in **1-MP** were calculated. The DFT calculations were carried out with the all-electron FHI-aims computer code (*tight* option for basis set and 24/12 k-points for small *Cc* and large *C2/m* unit cells, respectively).[56] The unit cell optimizations and dielectric properties, using Density Functional Perturbation Theory (DFPT),[57] were performed using the PBE exchange-correlation functional,[58] including many-body dispersion contributions[59] (Figure S33 and Tables S5and S6).

Additional instruments for characterization

Single crystal X-ray diffraction data for AlkCCMoid (**1**) and AlkTMSCCMoid (**2**) were collected at the XALOC beamline 13 of Alba-CELLS Synchrotron (Spain). Data for **1** using a Bruker D8 Venture diffractometer at 293 K (λ = 0.72932 Å).

The simulated powder patterns were calculated from the single crystal crystallographic data using Mercury 3.7 software. Peak indexing and space-group determination based on X-ray diffraction patterns were performed using the DICVOL5 algorism in Material Studio 8.0 and checked with GSAS-II software. Pawley refinements were performed using GSAS-II software.

Fourier transform infrared (FTIR) spectra were obtained using an FT-IR JASCO 4700LE using the ATR (attenuated total reflectance) accessory in the range between 500 and 4000 cm^{-1}, 2 mg of the powdered samples were deposited covering the crystal of the ATR accessory and pressed with the pressure tip.

Elemental analyses were carried out using a PerkinElmer 2400 series II analyzer.

^{1}H-NMR and ^{13}C-NMR spectra were obtained on a Bruker Advanced at 360 MHz and 298 K.

Thermogravimetric analysis was performed under a N_2 atmosphere from room temperature to 1000 °C at a heating rate of 10 °C min^{-1}, using a simultaneous thermogravimetric analysis (TG)-differential scanning calorimetry/differential thermal analysis (heat flow DSC /DTA) system NETZSCH-STA 449 F1 Jupiter.

MALDI-TOF mass spectra were recorded with an ULTRAFLEXTREME mass spectrometer (Bruker) at Servei de Proteòmica i Biologia Estructural (SePBioEs) from UAB.

UV/Vis absorption spectra of liquid samples were obtained with a Varian Cary 780 spectrometer by using quartz cells with operating range of 200–600 nm, mainly in reflectance or transmittance mode. For solid samples the Diffuse Reflectance Sphere DRA-2500 accessory of a Varian Cary 780 UV/Vis/NIR spectrophotometer was used with operating range of 200–700 nm, mainly in reflectance or transmittance mode.

Raman scattering spectra were measured on a XploraTM Plus system from Horiba Scientific model with a solid-state laser, emitting at 785 nm wavelength. The laser power at the sample was about 10% of 5 mW.

SEM images of molecules sublimated on different surfaces were obtained with a Zeiss Auriga 40 Field Emission microscope at an acceleration voltage of 2kV and a working distance below 4 mm without metallization of the samples.

ADDITIONAL RESOURCES

Sublimation system

Regardless of the method, optimization of practical procedures is crucial to facilitate the screening of the electronic properties of molecules in order to provide faster feedback for redesigning more efficient molecular-based devices. Here, we propose an alternative option in the molecular deposition stage, in which the sublimated material is deposited directly onto the desired substrate or device operating under the conditions that conventional sublimation systems do, using a homemade setup capable of operating in low-medium vacuum conditions. Our design allows for direct use in standard laboratories, with the advantage of one-step deposition of the sublimated material on a variety of surfaces/substrates and pre-formed devices. In addition, the use of common glassware components, together with plastic support parts, make the entire system affordable for conventional characterizations and easily repairable, replaceable, or modifiable.

The solid is added to the bottom of a ground glass vessel, which is coupled to a stopcock adapter connected to a vacuum pump. Inside, a cylinder acting as a frame supports the surface to be studied, orienting it towards the solid.

Patent application filed out (22/02/2022), application number: P202230143 (Ref. Number: ES1641.1728).

Title: Device for vacuum sublimation.

Owner entity: Consejo Superior de Investigaciones Científicas (CSIC).

Readers are welcomed to check the different advertises that CSIC and ICMAB-CSIC have created regarding the capabilities/uses/novelty of this sublimation system.

https://industry.icmab.es/images/vacuum-sublimation-v.pdf